

AD-A065 173

CALSPAN ADVANCED TECHNOLOGY CENTER BUFFALO NY  
STUDIES OF THE EFFECTS OF TRANSITIONAL AND TURBULENT BOUNDARY L--ETC(U)  
DEC 78 M S HOLDEN

F/G 20/4

F44620-76-C-0037

UNCLASSIFIED

CALSPAN-AB-5834-A-2

AFOSR-TR-79-0125

NL

1 OF 4  
ADA  
065173



APOSR-TR- 79-0125

Arvin



AD A0 65173

LEVEL II

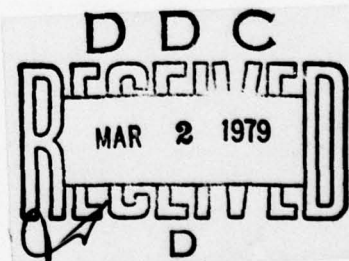
# CALSPAN ADVANCED TECHNOLOGY CENTER



**technical report**

DDC FILE COPY

Approved for public release;  
distribution unlimited.



A DIVISION OF CALSPAN CORPORATION  
AN ARVIN COMPANY P.O. BOX 400 BUFFALO, NEW YORK 14225

79 02 28 150



12

**AD A065173**

DDC FILE COPY

**Calspan Report No. AB-5834-A-2**

**Prepared for:**

Contract No. F44620-76-C-0037

## FINAL SCIENTIFIC REPORT

1 October 1975 - 30 November 1977

ACCESSING for	
DATE	White Section <input checked="" type="checkbox"/> Buff Section <input type="checkbox"/> <input type="checkbox"/>
AUTHORIZED AUTHORIZED	
AUTHORIZED/AVAILABILITY CODES AUTH. CODE/SPECIAL	
A	

REC'D  
MAR 2 1979  
RECEIVED

**AIR FORCE OFFICE OF SCIENTIFIC RESEARCH (AFSC)  
NOTICE OF TRANSMITTAL TO DDC**

This technical report has been reviewed and is approved for public release IAW AFR 190-12 (7b). Distribution is unlimited.

**A. D. BLOSE**

**Technical Information Officer**

79 02 28 150

UNCLASSIFIED

(14) CALSPAN-AB-5834-A-2

SECURITY CLASSIFICATION OF THIS PAGE (When Data Entered)

REPORT DOCUMENTATION PAGE		READ INSTRUCTIONS BEFORE COMPLETING FORM
1. REPORT NUMBER (1) AFOSR/TR. 79-0125	2. GOVT ACCESSION NO.	3. RECIPIENT'S CATALOG NUMBER
4. TITLE (and Subtitle) (2) STUDIES OF THE EFFECTS OF TRANSITIONAL AND TURBULENT BOUNDARY LAYERS ON THE AERODYNAMIC PERFORMANCE OF HYPERSONIC RE-ENTRY VEHICLES IN HIGH REYNOLDS NUMBER FLOWS.	5. TYPE OF REPORT & PERIOD COVERED (1) Final rept. 1 Oct 75 - 30 Nov 77	
6. AUTHOR (10) Michael S. Holden	7. PERFORMING ORG. REPORT NUMBER AB-5834-A-2	
8. CONTRACT OR GRANT NUMBER(s)	(15) F44620-76-C-0037	
9. PERFORMING ORGANIZATION NAME AND ADDRESS Calspan Corporation, Advanced Technology Center Post Office Box 400 Buffalo, New York 14225	10. PROGRAM ELEMENT, PROJECT, TASK AREA & WORK UNIT NUMBERS (16) 2307A1 (17) 61102F	
11. CONTROLLING OFFICE NAME AND ADDRESS Air Force Office of Scientific Research/NA Bolling Air Force Base Washington, D.C. 20332	12. REPORT DATE (11) December 1978	
13. MONITORING AGENCY NAME & ADDRESS (if different from Controlling Office)	13. NUMBER OF PAGES 259 (12) 326 p	
14. MONITORING AGENCY NAME & ADDRESS (if different from Controlling Office)	15. SECURITY CLASS. (if this report) Unclassified	
16. DISTRIBUTION STATEMENT (of this Report)  Approved for public release; distribution unlimited.		
17. DISTRIBUTION STATEMENT (of the abstract entered in Block 20, if different from Report)		
18. SUPPLEMENTARY NOTES		
19. KEY WORDS (Continue on reverse side if necessary and identify by block number) Transition on slender cones Hypersonic flow, separated flow Aerodynamic stability-slender cones Unsteady flow, pressure, heat Transition on blunt bodies transfer, force & moment Nose shaping & aerodynamic stability Particle/shock wave interaction Transition & roughness heating Particle augmented heating		
20. ABSTRACT (Continue on reverse side if necessary and identify by block number) This report describes a series of studies to investigate the underlying aero-thermodynamic phenomena which influence the accuracy and survivability of Ballistic Reentry Vehicles. The influence of transition on the aero- dynamic characteristics of slender RV's is discussed first. Here the pri- mary interest was in determining the influence of the angle of attack and bluntness ratio on the shape of the transition front and the properties of these regions. It was found that a transition occurred first on the leeside over		



of slender cones ( $0 < r_n/R_b < 0.1$ ); while for blunt cones ( $0.1 < r_n/R_b < 0.2$ ), transition was observed first on the windward ray. As the transition moved onto a sharp conical RV, the effects were initially destabilizing; however, a stabilizing effect was observed for the blunt vehicle. The wind-fixed effects observed were small and involved incremental movements of the center of pressure on the cone of the order of ( $\Delta x_{CP}/L = 1\%$ ). A detailed study was made of the influence of asymmetric nose bluntness on the pressure and heat transfer distribution over the cone frustum, and the contribution of the cone frustum to the forces and moments experienced by the total configuration. Particular emphasis was placed on determining the destabilizing effect of the NRV and RTE nose shapes recovered from flight tests. It was found that nose shaping can significantly change the pressure distribution over the conical frustum relative to a spherically-capped configuration; this effect must be accounted for if accurate predictions of cone stability at low altitude are required. Detailed heat transfer and pressure measurements were made on a model of the NRV nose shape for test conditions that duplicated those encountered during reentry. These measurements indicated that regions of flow separation and shock wave boundary-layer interaction were induced over this configuration and produced heating rates in the re-attachment regions on the ablated conical frustum of up to three times those recorded at the stagnation point on the spherical nose tip. We observed significant Reynolds number effects on the distribution of heat transfer and pressure, as well as the structure of the flow field over the NRV nose tip. The contributions of transition, entropy layer and roughness to the heating rates experienced by a number of biconic configurations was the subject of a detailed experimental study. Here we found that calculations based on the Powars roughness heating correlations significantly overpredicted the heating rates to the rough configurations.

In the remaining investigation, we studied the generation of disturbances in the stagnation region of the flow as multiple particles, which were projected upstream from the surface of a blunt body, interacted with the bow shock. This work was directed toward gaining a knowledge of the magnitude and mechanism of heating enhancement. These studies, which were conducted at Mach 6 and 13 on rough and smooth models, demonstrated that there was little heating enhancement as the particle (between 100 and 800  $\mu\text{m}$ .) transversed the shock layer; however, heating levels between 3 and 10 times the stagnation point value can be generated as the particles penetrate the bow shock. Four distinctly different flow regimes were found to exist for different penetration distances and particle trajectories. Of these, the most dramatic is one where a flow instability similar to that encountered over the highly indented nose shapes was observed. The key features of the single particle shock-bow shock interaction phenomena and the gross heating enhancement showed that they are insensitive to the shoulder geometry of the blunt nose tips studied. The principal mode of oscillation observed for multiple particle interactions was associated with pulsation of particle shocks rather than the bow shock, as was the case for a single particle; and the time-averaged heating rates for multiple particle interactions were also found to be considerably larger than those of single particles. The geometric features of the interactions observed in this study were very similar to the ballistic range observations of water droplets. Measurements with rough-walled models under fully turbulent boundary layer conditions indicated that the mechanism of particle-induced heating augmentation or the magnitude of the augmentation factor was not significantly modified by the conditions of the boundary layer or the surface.

## PREFACE

The work described in this final report was performed by Calspan Corporation, Advanced Technology Center (formerly Cornell Aeronautical Laboratory, Inc.), Buffalo, New York, with the support of the U.S. Air Force under the Air Force Office of Scientific Research, Bolling Air Force Base, Washington, D.C. 20332, Contract No. F44620-76-C-0037. The contract monitors for this program, conducted during the period October 1975 to January 1978, were Mr. Milton Rogers and Dr. James Wilson.

The author would like to acknowledge the helpful discussions on this work which he has had with Dr. James Wilson of AFOSR, Captains Hopkins, Taylor and Jones of SAMSO, Mr. Portenier, Mr. Nowlan, Mr. Crowell and Drs. Taylor and Widhopf of the Aerospace Corporation.



## ABSTRACT

In this report, we discuss the results from our current studies to investigate the underlying aero-thermodynamic phenomena which influence the accuracy and survivability of Ballistic Reentry Vehicles. We first discuss our observations on the influence of transition on the aerodynamic characteristics of slender RV's. Our primary interest was in determining the influence of the angle of attack and bluntness ratio on the shape of the transition front and the properties of these regions. We found that a transition occurred first on the leeside of slender cones ( $0 < r_n/R_b < 0.1$ ); while for blunt cones ( $0.1 < r_n/R_b < 0.2$ ), a transition was observed first on the windward ray. As the transition moved onto a sharp conical RV, the effects were initially destabilizing; however, a stabilizing effect was observed for the blunt vehicle. The wind-fixed effects observed were small and involved incremental movements of the center of pressure on the cone of the order of ( $\Delta X_{CP}/L=1\%$ ). A detailed study was made of the influence of asymmetric nose bluntness on the pressure and heat transfer distribution over the cone frustum, and the contribution of the cone frustum to the forces and moments experienced by the total configuration. Particular emphasis was placed on determining the destabilizing effect of the NRV and RTE nose shapes recovered from flight tests. It was found that nose shaping can significantly change the pressure distribution over the conical frustum relative to a spherically-capped configuration; this effect must be accounted for if accurate predictions of cone stability at low altitude are required.

Detailed heat transfer and pressure measurements were made on a model of the NRV nose shape for test conditions that duplicated those encountered during reentry. These measurements indicated that regions of flow separation and shock wave boundary-layer interaction were induced over this configuration and produced heating rates in the reattachment regions on the ablated conical frustum of up to three times those recorded at the stagnation point on the spherical nose tip. We observed significant Reynolds

number effects on the distribution of heat transfer and pressure, as well as the structure of the flow field over the NRV nose tip. The contributions of transition, entropy layer and roughness to the heating rates experienced by a biconic configuration was the subject of a detailed experimental study. Here we found that calculations based on the Powars roughness heating formulae significantly overpredicted the heating rates to the rough configurations.

In the second part of this investigation, we studied, in detail, the generation of disturbances in the stagnation region of the flow as multiple particles, which were projected upstream from the surface of a blunt body, interacted with the bow shock. Here we were primarily interested in gaining a knowledge of the magnitude and mechanism of heating enhancement. These studies which were conducted at Mach 6 and 13, on rough and smooth models, demonstrated that there was little heating enhancement as the particle (between 100 and 800  $\mu\text{m}$ ), transversed the shock layer; however, heating levels between 3 and 10 times the stagnation point value can be generated as the particles penetrate the bow shock. Four distinctly different flow regimes were found to exist for different penetration distances and particle trajectories. Of these, the most dramatic is one where a flow instability similar to that encountered over the highly indented nose shapes was observed.

The salient feature of the single particle shock-bow shock interaction phenomena and the gross heating enhancement showed that they are not sensitive to the shoulder geometry of the blunt nose tips studied here. The aerodynamics of multiple particle interactions were found to be significantly different from those of single particles. The time-averaged heating rates for multiple particle interactions were also found to be considerably larger than those of single particles. The principal mode of oscillation observed for multiple particle interactions was associated with pulsation of particle shocks rather than the bow shock, as was the case for a single particle. The geometric features of the interactions observed in this study were very similar to the ballistic range observations of water droplets. Measurements with rough-walled models under fully turbulent boundary layer conditions indicated that the mechanism of particle-induced heating augmentation or the magnitude of the augmentation factor was not significantly modified by the conditions of the boundary layer or the surface.



## TABLE OF CONTENTS

<u>Section</u>		<u>Page</u>
1	INTRODUCTION. . . . .	1-1
2	STUDIES OF "WIND-FIXED" BOUNDARY LAYER TRANSITION AND ITS INFLUENCE ON SLENDER CONE STABILITY . . . . .	2-1
	2.1 INTRODUCTION . . . . .	2-1
	2.2 EXPERIMENTAL PROGRAMS. . . . .	2-2
	2.2.1 Objectives. . . . .	2-2
	2.2.2 Models and Instrumentation. . . . .	2-2
	2.3 OBSERVATION ON THE MECHANISMS OF BOUNDARY LAYER TRANSITION . . . . .	2-6
	2.4 FACTORS INFLUENCING THE TRANSITION REYNOLDS NUMBER .	2-12
	2.5 INFLUENCE OF ANGLE OF ATTACK AND BLUNTNESS ON TRANSITION PATTERN . . . . .	2-21
	2.6 EFFECTS OF TRANSITION ON AERODYNAMIC STABILITY . . .	2-35
3	STUDIES OF THE AERODYNAMIC EFFECTS RESULTING FROM THE NOSE-TIP SHAPING OF SLENDER BLUNTED VEHICLES AT LOW ALTITUDES . . . . .	3-1
	3.1 INTRODUCTION . . . . .	3-1
	3.2 MODELS AND INSTRUMENTATION . . . . .	3-1
	3.3 RESULTS AND DISCUSSION . . . . .	3-4
	3.3.1 Nose Tip Studies. . . . .	3-4
	3.3.2 Measurements with the Nose Tip-Frustum Combinations. . . . .	3-15
4	STUDIES OF BOUNDARY LAYER TRANSITION, ENTROPY SWALLOWING AND SURFACE ROUGHNESS ON ABLATED NOSE SHAPES .	4-1
	4.1 INTRODUCTION . . . . .	4-1
	4.2 EXPERIMENTAL MODELS AND INSTRUMENTATION. . . . .	4-2
	4.3 RESULTS AND DISCUSSION . . . . .	4-8
5	STUDIES OF THE FLOW AND DISTRIBUTION OF HEAT TRANSFER OVER THE NRV NOSE TIP . . . . .	5-1
	5.1 INTRODUCTION . . . . .	5-1
	5.2 EXPERIMENTAL PROGRAM . . . . .	5-3

## TABLE OF CONTENTS (Cont.)

<u>Section</u>	<u>Page</u>
5.3 RESULTS AND DISCUSSION . . . . .	5-3
5.4 CONCLUSIONS. . . . .	5-27
6 MULTIPLE PARTICLE INDUCED CONVECTIVE HEATING AUGMENTATION TO BLUNT NOSE TIPS . . . . .	6-1
6.1 INTRODUCTION . . . . .	6-1
6.2 EXPERIMENTAL PROGRAM . . . . .	6-15
6.2.1 Program Objectives. . . . .	6-15
6.2.2 Model and Instrumentation . . . . .	6-16
6.3 RESULTS AND DISCUSSION . . . . .	6-18
6.3.1 Test Conditions . . . . .	6-18
6.3.2 Studies of Single Particle-Bow Shock Interaction . . . . .	6-21
6.3.3 Multiple Particle Interactions. . . . .	6-25
6.3.4 Dust Particle - Shock Layer Interaction for Rough Wall Conditions . . . . .	6-28
6.4 CONCLUSIONS. . . . .	6-33
7 CONCLUSIONS . . . . .	7-1
8 REFERENCES. . . . .	8-1
 <u>Appendix</u>	
A EXPERIMENTAL FACILITIES AND MEASUREMENT TECHNIQUES. . . .	A-1



# LIST OF ILLUSTRATIONS

Figure		Page
1-1	NRV, RTE, Blunt and Asymmetric Blunt Force Models . . . .	1-3
2-1	Conical Cone Model with Interchangeable Nose Tips . . . .	2-3
2-2	Drawing of 6° Cone Force, Heat Transfer and Pressure Model Showing Gage Locations. . . . .	2-5
2-3	Measurements on 6° Cone Model for Sharp Nose Configuration - $M_\infty = 13.0$ , $Re/FT = 4.8 \times 10^6$ , $\alpha = 0^\circ-7'$ .	2-40
2-4	Measurements on 6° Cone Model for Sharp Nose Configuration - $M_\infty = 13.0$ , $Re/FT = 4.7 \times 10^6$ , $\alpha = 0^\circ-7'$ .	2-41
2-5	Measurement on 6° Cone Model for 6% Spherical Nose - $M_\infty = 13.0$ , $Re/FT = 4.58 \times 10^6$ , $\alpha = 0^\circ-7'$ . . . . .	2-42
2-6	Measurement on 6° Cone Model for 6% Spherical Nose - $M_\infty = 13.0$ , $Re/FT = 5.0 \times 10^6$ , $\alpha = 3^\circ 3'$ . . . . .	2-43
2-7	Measurements on 6° Cone Model for Sharp Nose Configuration - $M_\infty = 13.3$ , $Re/FT = 3.1 \times 10^6$ , $\alpha = 0^\circ$ . .	2-44
2-8	Measurements on 6° Cone Model for Sharp Nose Configuration - $M_\infty = 13.4$ , $Re/FT = 3 \times 10^6$ , $\alpha = 0^\circ 57'$ . .	2-45
2-9	Measurements on 6° Cone Model for Sharp Nose Configuration - $M_\infty = 12.7$ , $Re/FT = 3 \times 10^6$ , $\alpha = 0^\circ-2'$ . .	2-46
2-10	Measurements on 6° Cone Model for Sharp Nose Configuration - $M_\infty = 12.4$ , $Re/FT = 1.8 \times 10^6$ , $\alpha = 0^\circ 1'$ . .	2-47
2-11	Measurement on 6° Cone Model for 6% Spherical Nose - $M_\infty = 12.5$ , $Re/FT = 2.3 \times 10^6$ , $\alpha = 2^\circ 59'$ . . . . .	2-48
2-12	Measurement on 6° Cone Model for 6% Spherical Nose - $M_\infty = 13.0$ , $Re/FT = 4.9 \times 10^6$ , $\alpha = 2^\circ 3'$ . . . . .	2-49
2-13	Measurement on 6° Cone Model for 6% Spherical Nose - $M_\infty = 12.4$ , $Re/FT = 1.7 \times 10^6$ , $\alpha = 3^\circ$ . . . . .	2-50
2-14	Measurement on 6° Cone Model for 6% Spherical Nose - Configuration - $M_\infty = 13.0$ , $Re/FT = 4.8 \times 10^6$ , $\alpha = 0^\circ 59'$ . . . . .	2-51
2-15	Measurement on 6° Cone Model for NRV Nose Configuration - $M_\infty = 11.4$ , $Re/FT = 1.1 \times 10^7$ , $\alpha = 0^\circ-2'$ . . . . .	2-52
2-16	Measurement on 6° Cone Model for NRV Nose Configuration - $M_\infty = 11.3$ , $Re/FT = 1.0 \times 10^7$ , $\alpha = 2^\circ 57'$ . . . . .	2-53
2-17	Measurement on 6° Cone Model for RTE Nose Configuration - $M_\infty = 11.4$ , $Re/FT = 1.1 \times 10^7$ , $\alpha = 2^\circ 57'$ . . . . .	2-54

# LIST OF ILLUSTRATIONS (Cont.)

Figure		Page
2-18	Measurement on 6° Cone Model for RTE Nose Configuration - $M_\infty = 11.4$ , $Re/FT = 1.1 \times 10^7$ , $\alpha = 1^\circ$ . . . . .	2-55
2-19	Measurement on 6° Cone Model for NRV Nose Configuration - $M_\infty = 11.3$ , $Re/FT = 1.0 \times 10^7$ , $\alpha = 1^\circ$ . . . . .	2-56
2-20	Measurement of 6° Cone Model for NRV Nose Configuration - $M_\infty = 11.0$ , $Re/FT = 4.2 \times 10^6$ , $\alpha = 2^\circ 58'$ . . . . .	2-57
2-21	Measurement on 6° Cone Model for RTE Nose Configuration - $M_\infty = 11.3$ , $Re/FT = 1.1 \times 10^7$ , $\alpha = 0^\circ 2'$ . . . . .	2-58
2-22	Measurements on 6° Cone Model for 21% Spherical Nose Configuration - $M_\infty = 11.4$ , $Re/FT = 1.0 \times 10^7$ , $\alpha = 2^\circ 56'$ . . . . .	2-59
2-23	Measurements on 6° Cone Model for 6%, 0° Blunt Nose Configuration - $M_\infty = 11.3$ , $Re/FT = 1.1 \times 10^7$ , $\alpha = 0^\circ$ . . . . .	2-60
2-24	Measurements on 6° Cone Model for 6%, 45° Blunt Nose Configuration - $M_\infty = 11.4$ , $Re/FT = 1 \times 10^7$ , $\alpha = 0^\circ 5'$ . . . . .	2-61
2-25	Measurements on 6° Cone Model for 6%, 0° Blunt Nose Configuration - $M_\infty = 11.3$ , $Re/FT = 1.0 \times 10^7$ , $\alpha = 0^\circ 5'$ . . . . .	2-62
2-26	Measurements on 6° Cone Model for 21% Spherical Nose Configuration - $M_\infty = 11.4$ , $Re/FT = 1.0 \times 10^7$ , $\alpha = 2^\circ 5'$ . . . . .	2-63
2-27	Measurements on 6° Cone Model for 6%, 0° Blunt Nose Configuration - $M_\infty = 10.9$ , $Re/FT = 2.4 \times 10^6$ , $\alpha = 0^\circ 3'$ . . . . .	2-64
2-28	Measurements on 6° Cone Model for 21% Spherical Nose Configuration - $M_\infty = 11.0$ , $Re/FT = 4.0 \times 10^6$ , $\alpha = 3^\circ 3'$ . . . . .	2-65
2-29	Measurements on 6° Cone Model for 21% Spherical Nose Configuration - $M_\infty = 11.0$ , $Re/FT = 3.8 \times 10^6$ , $\alpha = 2^\circ 3'$ . . . . .	2-66
2-30	Measurements on 6° Cone Model for 6%, 45° Blunt Nose Configuration - $M_\infty = 10.9$ , $Re/FT = 2.5 \times 10^6$ , $\alpha = 3^\circ 3'$ . . . . .	2-67
2-31	Measurements on 6° Cone Model for 6%, 45° Blunt Nose Configuration - $M_\infty = 10.9$ , $Re/FT = 2.6 \times 10^6$ , $\alpha = 0^\circ 3'$ . . . . .	2-68
2-32	Measurements on 6° Cone Model for 6%, 0° Blunt Nose Configuration - $M_\infty = 10.9$ , $Re/FT = 2.6 \times 10^6$ , $\alpha = 0^\circ 3'$ . . . . .	2-69
2-33	Measurements on 6° Cone Model for 6%, 0° Blunt Nose Configuration - $M_\infty = 10.9$ , $Re/FT = 2.6 \times 10^6$ , $\alpha = 1^\circ 2'$ . . . . .	2-70
2-34	Measurements on 6° Cone Model for 6%, 45° Blunt Nose Configuration - $M_\infty = 10.9$ , $Re/FT = 2.6 \times 10^6$ , $\alpha = 1^\circ 2'$ . . . . .	2-71
2-35	Measurements on 6° Cone Model for 6%, 45° Blunt Nose Configuration - $M_\infty = 10.9$ , $Re/FT = 2.5 \times 10^6$ , $\alpha = 1^\circ 2'$ . . . . .	2-72

# LIST OF ILLUSTRATIONS (Cont.)

Figure		Page
2-36	Measurements on 6° Cone Model for 6%, 0° Blunt Nose Configuration - $M_\infty = 10.9$ , $Re/FT = 2.5 \times 10^6$ , $\alpha = 2^\circ 59'$ .	2-73
2-37	Measurements on 6° Cone Model for 6%, 45° Blunt Nose Configuration - $M_\infty = 10.9$ , $Re/FT = 2.6 \times 10^6$ , $\alpha = 2^\circ 59'$ .	2-74
2-38	Measurements on 6° Cone Model for 21%, 0° Blunt Nose Configuration - $M_\infty = 11.3$ , $Re/FT = 1 \times 10^7$ , $\alpha = 0^\circ$ . . . .	2-75
2-39	Measurements on 6° Cone Model for 21%, 45° Blunt Nose Configuration - $M_\infty = 11.3$ , $Re/FT = 1.0 \times 10^7$ , $\alpha = 0^\circ$ . . .	2-76
2-40	Measurements on 6° Cone Model for 21%, 45° Blunt Nose Configuration - $M_\infty = 11.0$ , $Re/FT = 4.0 \times 10^6$ , $\alpha = 1^\circ$ . . .	2-77
2-41	Measurements on 6° Cone Model for 21%, 0° Blunt Nose Configuration - $M_\infty = 11.0$ , $Re/FT = 3.9 \times 10^6$ , $\alpha = 1^\circ$ . . .	2-78
2-42	Measurements on 6° Cone Model for 21%, 0° Blunt Nose Configuration - $M_\infty = 11.0$ , $Re/FT = 3.8 \times 10^6$ , $\alpha = 3^\circ$ . . .	2-79
2-43	Measurements on 6° Cone Model for 21%, 45° Blunt Nose Configuration - $M_\infty = 11.0$ , $Re/FT = 3.8 \times 10^6$ , $\alpha = 3^\circ$ . . .	2-80
2-44	Measurements on 6° Cone Model for Sharp Nose Configuration - $M_\infty = 13.2$ , $Re/FT = 3.0 \times 10^6$ , $\alpha = 3^\circ$ . . .	2-81
2-45	Measurements on 6° Cone Model for Sharp Nose Configuration - $M_\infty = 12.9$ , $Re/FT = 1.1 \times 10^6$ , $\alpha = 3^\circ$ . . .	2-82
2-46	Measurements on 6° Cone Model for Sharp Nose Configuration - $M_\infty = 13.2$ , $Re/FT = 2.9 \times 10^6$ , $\alpha = 2^\circ 2'$ . . .	2-83
2-47	Measurements on 6° Cone Model for Sharp Nose Configuration - $M_\infty = 12.8$ , $Re/FT = 1.2 \times 10^6$ , $\alpha = 2^\circ 2'$ . . .	2-84
2-48	Measurements on 6° Cone Model for Sharp Nose Configuration - $M_\infty = 12.9$ , $Re/FT = 1.9 \times 10^6$ , $\alpha = 2^\circ 2'$ . . .	2-85
2-49	Measurement on 6° Cone Model for 6% Spherical Nose Configuration - $M_\infty = 11.3$ , $Re/FT = 1.1 \times 10^7$ , $\alpha = 0^\circ$ . . .	2-86
2-50	Measurements on 6° Cone Model for 6% Elliptical Nose Configuration - $M_\infty = 11.3$ , $Re/FT = 9.8 \times 10^6$ , $\alpha = 0^\circ 2'$ . . .	2-87
2-51	Measurements on 6° Cone Model for 6% Spherical Nose Configuration - $M_\infty = 11.3$ , $Re/FT = 9.7 \times 10^6$ , $\alpha = 3^\circ 5'$ . . .	2-88
2-52	Measurements on 6° Cone Model for 6% Spherical Nose Configuration - $M_\infty = 11.5$ , $Re/FT = 1.0 \times 10^7$ , $\alpha = 1^\circ 1'$ . . .	2-89
2-53	Measurements on 6° Cone Model for 6% Spherical Nose Configuration - $M_\infty = 11.0$ , $Re/FT = 3.2 \times 10^6$ , $\alpha = 1^\circ 1'$ . . .	2-90



# LIST OF ILLUSTRATIONS (Cont.)

Figure		Page
2-54	Measurements on 6° Cone Model for 6% Elliptical Nose Configuration - $M_\infty = 11.4$ , $Re/FT = 1.0 \times 10^7$ , $\alpha = 1^\circ 1'$ . .	2-91
2-55	Measurements on 6° Cone Model for 6% Spherical Nose Configuration - $M_\infty = 11.3$ , $Re/FT = 1.1 \times 10^7$ , $\alpha = 0^\circ 30'$ . .	2-92
2-56	Measurements on 6° Cone Model for 6% Elliptical Nose Configuration - $M_\infty = 11.3$ , $Re/FT = 1.0 \times 10^7$ , $\alpha = 3^\circ$ . . .	2-93
2-57	Measurements on 6° Cone Model for 6% Elliptical Nose Configuration - $M_\infty = 10.9$ , $Re/FT = 2.4 \times 10^6$ , $\alpha = 3^\circ$ . . .	2-94
2-58	Transition Boundaries on 6° Cone Model for Sharp Nose Configuration - $M_\infty = 13.0$ , $Re/FT = 4.8 \times 10^6$ , $\alpha = 0^\circ - 7'$ . .	2-95
2-59	Transition Boundaries on 6° Cone Model for Sharp Nose Configuration - $M_\infty = 13.0$ , $Re/FT = 4.7 \times 10^6$ , $\alpha = 0^\circ - 7'$ . .	2-95
2-60	Transition Boundaries on 6° Cone Model for Sharp Nose Configuration - $M_\infty = 13.3$ , $Re/FT = 3.1 \times 10^6$ , $\alpha = 0^\circ$ . . .	2-96
2-61	Transition Boundaries on 6° Cone Model for Sharp Nose Configuration - $M_\infty = 13.4$ , $Re/FT = 3.0 \times 10^6$ , $\alpha = 0^\circ 57'$ . .	2-96
2-62	Transition Boundaries on 6° Cone Model for Sharp Nose Configuration - $M_\infty = 12.7$ , $Re/FT = 3 \times 10^6$ , $\alpha = 0^\circ - 2'$ . .	2-97
2-63	Transition Boundaries on 6° Cone Model for Sharp Nose Configuration - $M_\infty = 13.2$ , $Re/FT = 3.0 \times 10^6$ , $\alpha = 3^\circ$ . . .	2-97
2-64	Transition Boundaries on 6° Cone Model for Sharp Nose Configuration - $M_\infty = 13.2$ , $Re/FT = 2.9 \times 10^6$ , $\alpha = 2^\circ 2'$ . .	2-98
2-65	Transition Boundaries on 6° Cone Model for 6% Spherical Nose Configuration - $M_\infty = 13.9$ , $Re/FT = 5.0 \times 10^6$ , $\alpha = 3^\circ 3'$ . . . . .	2-98
2-66	Transition Boundaries on 6° Cone Model for 6% Spherical Nose Configuration - $M_\infty = 11.3$ , $Re/FT = 9.7 \times 10^6$ , $\alpha = 3^\circ 5'$ . . . . .	2-99
2-67	Transition Boundaries on 6° Cone Model for 6% Spherical Nose Configuration - $M_\infty = 11.5$ , $Re/FT = 1.0 \times 10^7$ , $\alpha = 1^\circ 1'$ . . . . .	2-99
2-68	Transition Boundaries on 6° Cone Model for 21% Spherical Nose Configuration - $M_\infty = 11.4$ , $Re/FT = 1.0 \times 10^7$ , $\alpha = 2^\circ 56'$ . . . . .	2-100
2-69	Transition Boundaries on 6° Cone Model for 6% Elliptical Nose Configuration - $M_\infty = 11.4$ , $Re/FT = 1.0 \times 10^7$ , $\alpha = 1^\circ 1'$ . . . . .	2-101



# LIST OF ILLUSTRATIONS (Cont.)

<u>Figure</u>		<u>Page</u>
2-70	Transition Boundaries on 6° Cone Model for 6% Elliptical Nose Configuration - $M_\infty = 11.3$ , $Re/FT = 1.0 \times 10^7$ , $\alpha = 3^\circ$ . . . . .	2-101
2-71	Transition Boundaries on 6° Cone Model for 6%, 45° Blunt Nose Configuration - $M_\infty = 11.4$ , $Re/FT = 1.0 \times 10^7$ , $\alpha = 0^\circ 5'$ . . . . .	2-102
2-72	Transition Boundaries on 6° Cone Model for 6%, 0° Blunt Nose Configuration - $M_\infty = 11.3$ , $Re/FT = 1.0 \times 10^7$ , $\alpha = 0^\circ 5'$ . . . . .	2-102
2-73	Schlieren Photograph Showing the Development of Transition of a Conical Boundary Layer in Hypersonic Flow . . . . .	2-7
2-74	Formation of "Wave-Like" Instabilities at the Edge of the Boundary Layer Preceding the Gross Instabilities. . .	2-8
2-75	Schlieren Photograph Showing Regular Bursting Which Precedes the Nonlinear Breakdown into Turbulence . . . .	2-9
2-76	Studies of Boundary Layer Transition on a Sharp 6° Semi-Angle Cone, Conducted on Calspan's 96" Shock Tunnel. . . . .	2-13
2-77	Correlation of Transition Showing the Effects of Tunnel Size . . . . .	2-11
2-78	Correlation of the Flat Plate Transition Data in Terms of the Parameters Suggested by Pate and Schueler. . . . .	2-14
2-79	Correlation of Transition Measurements in the Calspan Shock Tunnels with Ballistic and Downrange Measurements. . . . .	2-15
2-80	Transition Reynolds Number Vs Unit Reynolds Number; Present Data Vs Krogmann and Stetson. . . . .	2-17
2-81	Transition Reynolds Number Vs Wall-to-Adiabatic Wall Temperature Ratio; Present Data Vs Potter and Sheetz. . . . .	2-18
2-82	Transition Reynolds Number Vs Unit Reynolds Number; Present Data Vs Potter and Sheetz . . . . .	2-19
2-83	Transition Reynolds Number Vs Wall-to-Adiabatic Wall Temperature Ratio; Present Data Vs Stetson and Krogmann. . . . .	2-20

# LIST OF ILLUSTRATIONS (Cont.)

<u>Figure</u>		<u>Page</u>
2-84	Correlation of the Eddy Reynolds Number with Transition Measurements on the Flat Plates . . . . .	2-22
2-85	Turbulent Boundary Layer Displacement and Momentum Thickness from Shock Tunnel Nozzle Data . . . . .	2-23
2-86	Variation of Transition Location Non-Dimensionalized by Entropy Swallowing Distance for Blunted Cones at $\alpha = 0^\circ$ as Determined by Stetson and Rushton. . . . .	2-25
2-87	Finson's Correlation of Stetson and Rushton's Transition Measurements in Terms of Reynolds Number Based on Local Momentum Thickness at Transition . . . . .	2-26
2-88	The Distribution of Heat Transfer Through a Transition Region of a $6^\circ$ Cone in Hypersonic Flow. . . . .	2-27
2-89	Variation of Nondimensional Transition Front Location on Sharp Cones with Angle of Attack. . . . .	2-29
2-90	Comparison Between Range, Shock Tunnel and Ludwig Tube Measurements of Transition Front Location Variation with Angle of Attack for Sharp Slender Cones. . . . .	2-30
2-91a	Transition Zone Asymmetry; Comparison with Other Data, $.15 < (\alpha / \theta_c) < .25$ . . . . .	2-31
2-91b	Transition Zone Asymmetry; Comparisons with Other Data, $.35 \leq (\alpha / \theta_c) \leq .50$ . . . . .	2-32
2-92	Variation of Transition Front Location on Slightly Blunted Cones with Angle of Attack. . . . .	2-33
2-93	Variation of Nondimensional Transition Front Location on Blunt Cones with Angle of Attack . . . . .	2-34
2-94	Correlation of Transition Front Locations on Sharp and Blunt Slender Cones at Angle of Attack. . . . .	2-36
2-95	Variation of the Maximum Transition Induced Increment in Pitching Moment (About the Base) with Bluntness Ratio for a $6^\circ$ Cone . . . . .	2-38
3-1	NRV (Right) and RTE Force, Epoxy Replica and Nose Tip Models (Top to Bottom). . . . .	3-2
3-2	NRV RTE Blunt and Asymmetric Blunt Force Models . . . . .	3-3
3-3	NRV Force Model Installed in the 96" Shock Tunnel . . . . .	3-5

# LIST OF ILLUSTRATIONS (Cont.)

<u>Figure</u>		<u>Page</u>
3-4	6" Conical Force Model with NRV and Asymmetric Nose Tips . . . . .	3-6
3-5	Photographs of Some of the Nose Tips which will be Used with the 6° Cone Model. . . . .	3-7
3-6a	Model Designs for 2 Times Full Scale Force Models . . . .	3-8
3-6b	Accelerometer Balance for NRV & RTE Force Models. . . . .	3-9
3-7	Schlieren Photographs of the Flow Over the NRV Nose Tip (Model Rotated Between Runs). . . . .	3-12
3-8	Flow Over the NTE Nose Tip. . . . .	3-13
3-9	Schlieren Photographs of the Flow Over the Blunt and 45° Blunt Models at Mach 8.6. . . . .	3-14
3-10	Comparison Between Measured Pressure Distribution and Theory for Spherically Capped 6° Cone at 0° Incidence . .	3-15
3-11	Comparison Between Measured Pressure Distribution and Theory for Spherically Capped 6° Cone at 3° Incidence . .	3-19
3-12	Correlation of Heat Transfer Measurements on Slender Cones at Angle of Attack. . . . .	3-20
3-13	Comparison Between Measured Pressure Distribution on a 6° Cone Capped with the NRV and a Spherical Nose Cap at 3° of Model Incidence. . . . .	3-21
3-14	Comparison Between Frustum Pressure Measurement on a 6° Cone Capped with Spherical and NRV Nose Tips . . . . .	3-22
3-15	Variation of the Frustum Force Coefficient with Angle of Attack for 21° Blunt 6° Cones Equipped with the Nose Tips Denoted on the Caption. . . . .	3-23
3-16	Variation of the Center of Pressure Position with Angle of Attack for the Nose Tip - Frustum Combination Denoted in the Caption. . . . .	3-24
3-17	Variation of the Total Normal Force Coefficient with Angle of Attack for 21° Blunt 6° Cones Equipped with Nose Tips Denoted in the Caption. . . . .	3-27
3-18	Variation of the Frustum Center of Pressure Position with Angle of Attack for the Nose Tip - Frustum Combinations Denoted in the Caption. . . . .	3-28



# LIST OF ILLUSTRATIONS (Cont.)

<u>Figure</u>		<u>Page</u>
4-1	Blunt Bi-Conic Configuration Mounted in Calspan 96" Shock Tunnel. . . . .	4-3
4-2	Nose Tip Configurations . . . . .	4-4
4-3	Thin Film Gage to Establish the Surface Heating Rate to a Rough Surface . . . . .	4-5
4-4	Schematic-Arrangement of Apparatus for Calibration of Radiative Absorption Characteristics of Thin-Film, Heat-Transfer Gages. . . . .	4-6
4-5	Schematic-Circuit for Calibration of Radiant Heat Transfer Characteristics of Thin Film Gages . . . . .	4-7
4-6	A Schlieren Photograph Typical of Those Obtained Over the Biconic Configurations ( $M = 11$ ) . . . . .	4-25
4-7	Comparison Between the Shock Shape Determined by the Godunov Code and the Experimental Measurements. . . . .	4-26
4-8	Heat Transfer Measurements on the Sharp Bi-Conic Configuration . . . . .	4-27
4-9	Heat Transfer Measurements on the Medium Bi-Conic Configuration . . . . .	4-31
4-10	Heat Transfer Measurements on the Blunt-Bi-Conic Configuration . . . . .	4-34
4-11	Comparison Between Powars Correlation and Recent Measurements by Holden and Brandon & Masek. . . . .	4-38
4-12	Comparison Between Grabor and White Correlation of the PANT Data and the Recent Calspan Measurements of Roughness Heating on Bi-Conic and MRV Configurations. . . . .	4-39
5-1	NRV Heat Transfer & Pressure, Force, Epoxy Replica and Nose Tip Models (Clockwise from Top Left) . . . . .	5-2
5-2	Drawing of NRV Pressure and Heat Transfer Model Showing Location of Instrumentation . . . . .	5-4
5-3a	Installation of NRV Heat Transfer and Pressure Model in 96" Shock Tunnel . . . . .	5-5
5-3b	View of NRV Heat Transfer and Pressure Model Showing Gage Locations. . . . .	5-6
5-4	Schlieren Photograph of the Flow Over the NRV Heat Transfer and Pressure Model ( $M = 11.3$ $Re/FT = 10 \times 10^6$ ) . . . . .	5-13



# LIST OF ILLUSTRATIONS (Cont.)

<u>Figure</u>		<u>Page</u>
5-5a	Heat Transfer Distribution Over the NRV Configuration - M = 11, Re/FT = $10 \times 10^6$ , $\alpha = 0^\circ$ . . . . .	5-15
5-5b	Pressure Distribution Over the NRV Configuration - M = 11, Re/FT = $10 \times 10^6$ , $\alpha = 0^\circ$ . . . . .	5-16
5-6a	Heat Transfer Distribution Over the NRV Configuration - M = 11, Re/FT = $10 \times 10^6$ , $\alpha = 1^\circ$ . . . . .	5-17
5-6b	Pressure Distribution Over the NRV Configuration - M = 11, Re/FT = $10 \times 10^6$ , $\alpha = 1^\circ$ . . . . .	5-18
5-7a	Heat Transfer Distribution Over the NRV Configuration - M = 11, Re/FT = $10 \times 10^6$ , $\alpha = 2^\circ$ . . . . .	5-19
5-7b	Pressure Distribution Over the NRV Configuration - M = 11, Re/FT = $10 \times 10^6$ , $\alpha = 2^\circ$ . . . . .	5-20
5-8a	Heat Transfer Distribution Over the NRV Configuration - M = 11, Re/FT = $1 \times 10^6$ , $\alpha = 0^\circ$ . . . . .	5-21
5-8b	Pressure Distribution Over the NRV Configuration - M = 11, Re/FT = $1 \times 10^6$ , $\alpha = 0^\circ$ . . . . .	5-22
5-9a	Heat Transfer Distribution Over the NRV Configuration - M = 11, Re/FT = $4.6 \times 10^6$ , $\alpha = 0^\circ$ . . . . .	5-23
5-9b	Pressure Distribution Over the NRV Configuration - M = 11, Re/FT = $4.6 \times 10^6$ , $\alpha = 0^\circ$ . . . . .	5-24
5-10a	Heat Transfer Distribution Over the NRV Configuration - M = 13, Re/FT = $4.8 \times 10^6$ , $\alpha = 0^\circ$ . . . . .	5-25
5-10b	Pressure Distribution Over the NRV Configuration - M = 13, Re/FT = $4.8 \times 10^6$ , $\alpha = 0^\circ$ . . . . .	5-26
6-1a	Shock-Particle Interaction Over a Blunt Ellipsoid . . . . .	6-2
6-1b	Shock-Particle Interaction Over a Blunted Cone. . . . .	6-3
6-2	Vortex Generation Resulting from Particle Rebound, a Sequence Taken in the Boeing Mach 6 Tunnel. . . . .	6-4
6-3	Heating Augmentation Associated with Particle-Induced Ring Vortex Interaction . . . . .	6-6
6-4	"Stable" Flow Resulting from Small Penetration. . . . .	6-7
6-5	Particle-Induced Large Scale Oscillation (E) (Mach 6.5) . . . . .	6-9
6-6	Particle-Induced Large Scale Oscillation (E) of Flow Field (Mach 13). . . . .	6-11

# LIST OF ILLUSTRATIONS (Cont.)

<u>Figure</u>		<u>Page</u>
6-7	"E" Oscillation on AO Configuration at Zero Angle of Attack . . . . .	6-13
6-8	Heat Transfer Distribution to Mode Face for a Single Particle Launch . . . . .	6-14
6-9	Particle Launch Model Equipped with Three Particle Launchers, 105 Heat Transfer Gages, 27 Pressure Gages and 4 Skin Friction Gages . . . . .	6-17
6-10	Impact Particle Launcher. . . . .	6-19
6-11	Typical Heat Transfer Record from Thin Film Gages . . . .	6-22
6-12	Photographic Sequence from Single Particle Launch . . . .	6-22
6-13	Multiple Particle Interactions Over the Blunt Nose Tip .	6-26
6-14	Heating Rates Resulting from Multiple Particle Interactions. . . . .	6-29
6-15	Dust Interactions in the Shock Layer. . . . .	6-30
6-16	Heat Transfer Augmentation in a Dust Environment. . . . .	6-32
6-17	Sequential Laser Photographs of Debris from Water Drop Impact . . . . .	6-33

# LIST OF TABLES

<u>Table</u>		<u>Page</u>
2-1	6° Cone Force Data. . . . .	2-103
2-2	6° Cone Force Transition Studies. . . . .	2-104
2-3	6° Cone Force Test Conditions . . . . .	2-105
2-4	6° Cone Force Heat Transfer Data. . . . .	2-108
2-5	6° Cone Force Final Pressure Data . . . . .	2-119
2-6	6° Cone Force Data. . . . .	2-121
3-1	6° Cone Force Asymmetric Bluntness Effects. . . . .	3-10
3-2	Nose Tip Force Measurements . . . . .	3-11
3-3	Test Conditions for NRV Nose Tip Force Studies. . . . .	3-16
4-1	Biconic I Heat Transfer and Pressure Test . . . . .	4-11
4-2	Biconic I Heat Transfer Computations. . . . .	4-12
4-3	Biconic II Heat Transfer Computations . . . . .	4-20
5-1	Heat Transfer and Pressure Locations on the NRV Tip . . .	5-7
5-2	Test Conditions for NRV Heat Transfer and Pressure Test .	5-8
5-3	Heat Transfer Computations for NRV. . . . .	5-9
5-4	Pressure Computations for NRV . . . . .	5-12
6-1	Test Conditions for Particle Launch Program . . . . .	6-20



## Section 1

### INTRODUCTION

The development of the technology to design accurate and dependable IRBM's and ICBM's represents a key area in the research and development being pursued by the United States Air Force. In part, this technology depends upon the ability to predict the aero-thermodynamic characteristics of a nose tip and frustum combination under conditions where boundary layer transition develops over the vehicle. As boundary layer transition propagates forward on the surface of slender, high  $\beta$  reentry vehicles flying at small incidence, significant perturbations are observed on the lift and moment coefficients in both windward and yawing planes. These perturbations can cause disturbances in vehicle trajectory which can seriously compromise the accuracy of the system.

Analysis of flight data demonstrates that there are two regimes where boundary layer transition has a marked influence on vehicle stability. The first occurs when transition moves from the base of the cone to the cone frustum. Here, the aerodynamic disturbances are of such a nature that perturbations to the vehicle motion are found to build up and decay smoothly. However, a net lateral velocity is built up as a result of an asymmetry in the coning motion. Analysis of flight data suggests that increasing nose bluntness decreases the perturbations in lateral velocity, and recent studies at Calspan (to be discussed later) have supported this observation. However, highly blunted vehicles appear to suffer more severely from the second destabilizing phenomena, which occurs when transition moves from the conical surface of the vehicle to the formerly spherical nose tip.

This second aero-thermodynamic phenomena, which can cause a degradation in RV accuracy, is believed to occur as a result of "nose shaping". Nose shaping, or the asymmetric ablation of a nose tip, can occur if the transition region spreads over the nose tip forming an asymmetric pattern, either as a result of vehicle incidence, or nonuniformities on the ablation, or roughness characteristics of the nose tip. Recent studies have suggested that the

transitional process is intrinsically three dimensional in character, and the probability of generating a completely symmetric transition on or downstream of the nose is extremely small. In fact, the two nose tips which have been recovered from flight tests, at the instant when transition was spreading over the tip, the NRV and the RTE nose tips shown in Figure 1-1, exhibit marked three dimensional ablation patterns. Studies at Calspan have demonstrated that these nose shapes develop significant side forces at zero incidence, and the rolling moment generated by the tip alone may contribute to a "roll down" which could seriously compromise vehicle accuracy.

While the flight data allows us to determine the magnitude of the accuracy problem with the current vehicles and flight trajectories, the limited numbers and accuracy of the onboard instrumentation does not provide us with sufficient information to define accurately the aero-thermodynamic mechanisms leading to the high and low altitude inaccuracy problems. Clearly, this does not place us in a favorable position to select either the optimum configurations to trace most accurately trajectories currently planned, or introduce new construction materials and fly more aggressive trajectories. Therefore, an important objective of any technology program to upgrade the accuracy of RV's must be to address the complex questions associated with the development of transition over the frustum and nose tip.

An important aspect of the design of RV's is the prediction of their performance in "weather", i.e., through clouds of ice particles or dust. While the erosion of nose tips, resulting from particle impact, represents an important problem area, recently it has been demonstrated that the increase in heating as particles rebound or are ejected into the shock layer can represent a significant fraction of the heating experience in a particle-laden environment. While studies conducted in dust tunnels demonstrated the importance of particle-induced convected heating augmentation, only in the recent studies conducted at Calspan have the basic aerodynamic mechanisms responsible for heating augmentation been identified. In these studies, minute particles were launched from the model surface and the interaction between the particles and the shock layer were studied with the aid of high speed cinematography and high frequency heat transfer

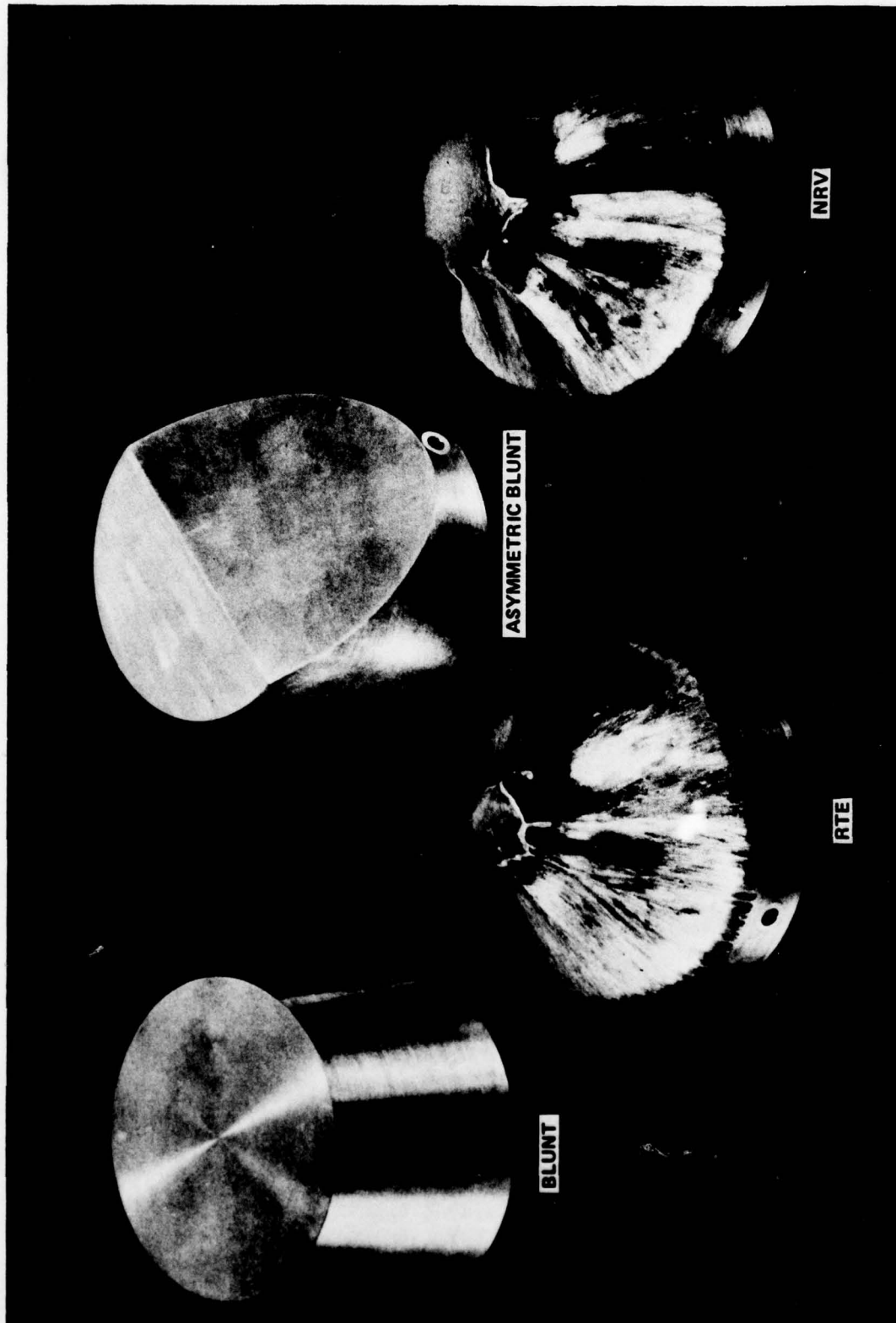


Figure 1-1 NRV, RTE, BLUNT AND ASYMMETRIC BLUNT FORCE MODELS



and pressure gages mounted in the surface of the model. These studies have identified five flow regimes where heating enhancement and the corresponding spatially and temporally resolved measurements of heat transfer and pressure occurs. Two basic flow mechanisms, particle-induced vortices and shear layer reattachment resulting from shock-shock interaction, were shown to be those of greatest importance in heating augmentation. However, further efforts were required to model these flows successfully. Further experimental studies were required to identify the effect of nose tip shape, multiple particle interaction and model roughness on convective heating augmentation.

In this report, we describe the results from our current experimental studies and analysis designed to investigate the underlying aero-thermodynamic disturbances which influence the accuracy and survivability of slender reentry vehicles. In the following section, we review the results from recent theoretical and experimental studies of transitional flows over slender cone frusta and nose tips which are relevant to the RV accuracy problem. Here we will discuss material which illuminates the underlying mechanisms creating the force and moment perturbations leading to variation in trajectory. We then describe an experimental study to examine the effects of nose shaping on the stability of slender RV's. Here six-component force and moment measurements as well as pressure and heat transfer measurements were made on a series of nose tips and nose tip-frusta combinations for models with asymmetric and indented nose shapes. These studies demonstrated that the effect of nose tip shaping was to decrease the stability of blunt RVs and significantly modify the pressure distribution over the conical frusta. In Section 4 we describe studies, performed with idealized ablated nose shapes, to investigate the separate and combined effects of surface roughness and entropy swallowing on the distribution of heat transfer in laminar, transitional and turbulent boundary layer flows over biconic nose shapes. We found that calculations based on Powars roughness heating formulae significantly overpredicted the heating rates to the rough configurations. The detailed heat transfer and pressure measurements made on the NRV nose tip are then described. It was observed that the flow pattern and the large heat transfer rates generated in the reattachment regions on this nose tip were dependent

upon Reynolds number. Finally, the experimental program to examine the particle-induced convective heating augmentation to blunt nose tip is discussed. In these studies, we examined the effects of both single and multiple particle shock-bow shock interactions on the flow structure and the surface heating rates and patterns on a blunt nose tip.

## Section 2

### STUDIES OF "WIND-FIXED" BOUNDARY LAYER TRANSITION AND ITS INFLUENCE ON SLENDER CONE STABILITY

#### 2.1 INTRODUCTION

While hypersonic boundary layer transition has been studied extensively over the past two decades, only recently have strenuous efforts been made to determine the mechanism by which boundary layer transition influences the aerodynamic stability of slender cones. As discussed in the Section 1, flight test data indicate that perturbations occur to the trajectory of slender conical RV's which can be linked directly to destabilizing forces generated during boundary layer transition. At "high" altitude, this can be associated with asymmetric transition on the cone frustum, while at "low" altitude asymmetric nose shaping is believed to be the underlying mechanism. The high altitude phenomena is characterized by perturbations which build up and subside smoothly over several cycles. A net lateral velocity results from nonlinearities in the coning motion of the RV. In contrast, the perturbations observed at low altitudes occur over a period of less than one cycle. Flight data suggests that the magnitude of the net lateral velocity, which results when frustum transition occurs, decreases with nose bluntness ( $r_n/R_b$ ); whereas, the lateral perturbations at low altitude increase with increased bluntness ratio.

Studies of full scale flight transition on slender RVs suggest that both "naturally developed" and tripped transition regions can develop. Surface discontinuities at the nose tip-cone junction and antenna windows have been suggested as potential sources of transition regions which appear "body-fixed" on vehicles which are undergoing changes in angle of attack. Gouges and regions of roughness on the nose tip have also been cited as sources for tripped transition regions. However, most of the flight measurements and those on smooth bodies in ballistic ranges and wind tunnels suggest the onset of transition is relatively well ordered in terms of free stream properties



and the preceeding length of laminar run. Transition onset is also influenced by both angle of attack and nose tip bluntness on smooth non-ablating slender cones. Recently, studies at Calspan have shed further light on this latter problem, and we will discuss some of the results in this section.

## 2.2 EXPERIMENTAL PROGRAM

### 2.2.1 Objectives

The objective of this study was to measure the destabilizing/stabilizing forces associated with the movement of regions of wind-fixed transition onto the frustum of sharp and blunted slender cones and establish how these forces and the characteristics of the transition regions vary with bluntness ratio, angle of attack and free stream conditions. The bluntness ratio ( $0 < r_n/R_B < 0.21$ ) and the nose shape (sharp, spherical, elliptical and flat-ended) of the cone was varied in these studies. The  $6^\circ$ -conical model (shown in Figure 2-1) was chosen so that when tested at Mach numbers between 11 and 13 and Reynolds numbers from  $20 \times 10^6$  to  $5 \times 10^6$  there was a duplication of conditions of Mach number, Reynolds number and wall-to-free stream stagnation temperature ratio with typical conditions for ICBM velocities over  $9^\circ$  cones.

### 2.2.2 Models and Instrumentation

In the study of transition one cannot guarantee the transition region on two models of nominally the same dimensions and tested at nominally the same free stream conditions will be identical in size and properties. Therefore, a key aspect of the current program was the simultaneous measurement of model forces and the pressure and heat transfer on the cone surface. The extremely small changes in normal force ( $\Delta C_N = 0.001$ ) and moments associated with boundary layer transition made highly accurate force measurements essential. The acceleration compensated force balance used on this work, which was capable of making such measurements, was essentially two balances mounted in one model, a six component strain gage balance and a six-component accelerometer

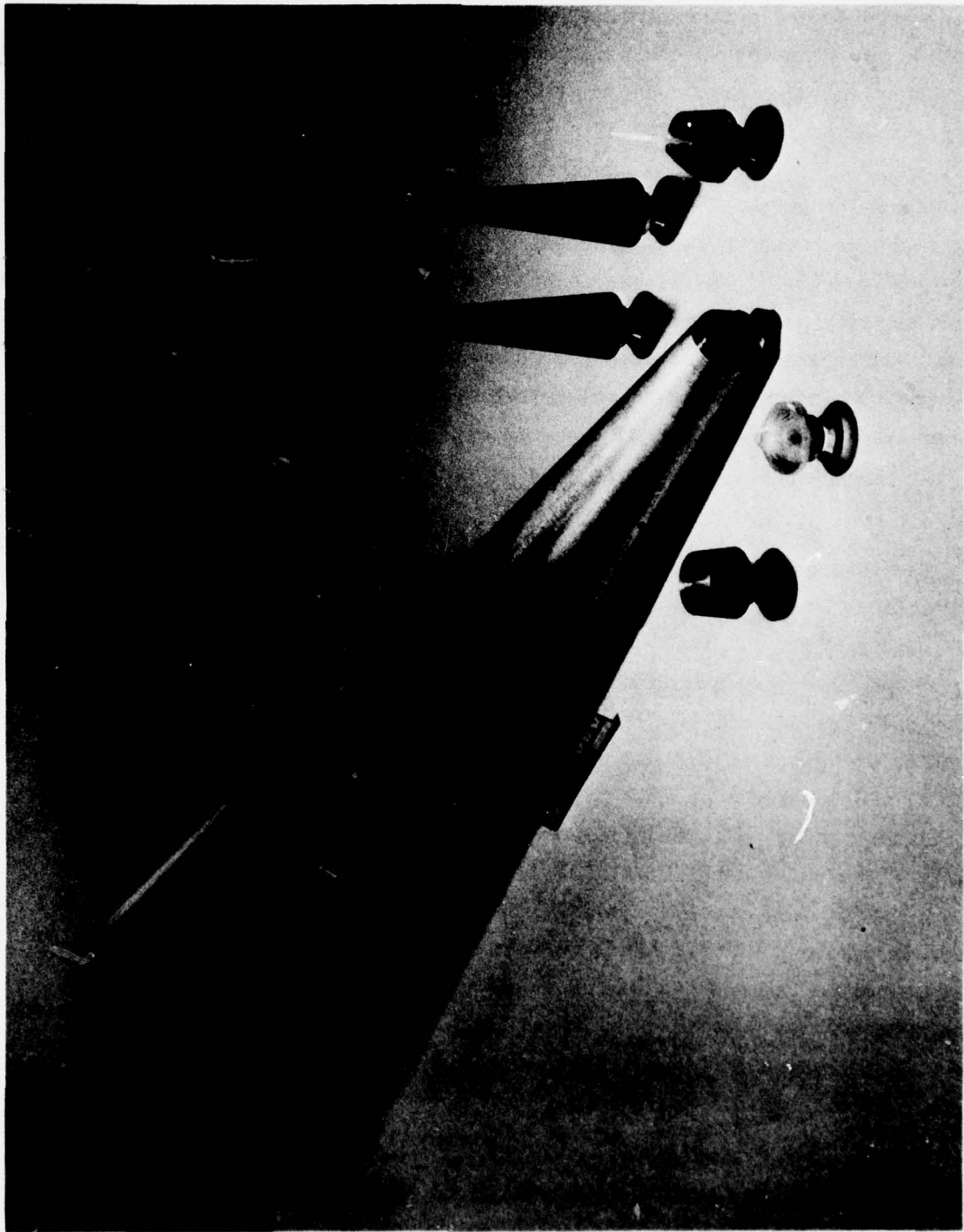


Figure 2-1 CONICAL CONE MODEL WITH INTERCHANGABLE NOSE TIPS

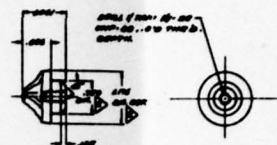
balance. These balances were linked through a small computer so that acceleration loads experienced by the model were completely cancelled. By employing acceleration compensation we could instrument the force model with 48 heat transfer gages and 22 pressure gages without sacrificing accuracy. Details and the instrumentation are given in Appendix A.

A drawing of the 6°-cone model showing the locations of the pressure and heat transfer gages, as well as details of the nose tip configurations, is given in Figure 2-2. The windward and leeside rays of the model contained the major quantity of heat transfer and pressure instrumentation; while, additional heat transfer gages were placed on the 90°, 135°, 270° and 315° rays, to provide information with which to determine the shape of the transition front. The position of these gages are tabulated in Table 2-1. *(Tables 2-1 through 2-6 appear at the end of this section.)*

The studies of transitional flow over sharp and blunted cones at angle of attack, were performed at Mach numbers from 11 to 13 for free stream Reynolds numbers from  $2.5 \times 10^6$  to  $10 \times 10^6$ . A run matrix and detailed listing of the free stream conditions at which these studies were performed is given in Tables 2-2 and 2-3, respectively. Measurements of the detailed distribution of heat transfer and pressure over the conical frustum were obtained at model incidences of 0°, 1° and 3° for sharp, spherical and elliptical nose shapes with bluntness ratios ( $r_n/R_b$ ) of 0, 6 and 18 percent. A listing of the model configurations and the test conditions at which they were run is given in Table 2-2. Tabulations of the heat transfer and pressure measurements obtained in this study are presented in Tables 2-4 and 2-5 and these measurements are plotted in Figures 2-3 through 2-57. Diagrams of the transition boundaries determined from the heat transfer measurements (see Section 2.5) are shown in Figures 2-58 through 2-72. *(Figures 2-3 through 2-72 appear at the end of this section.)*

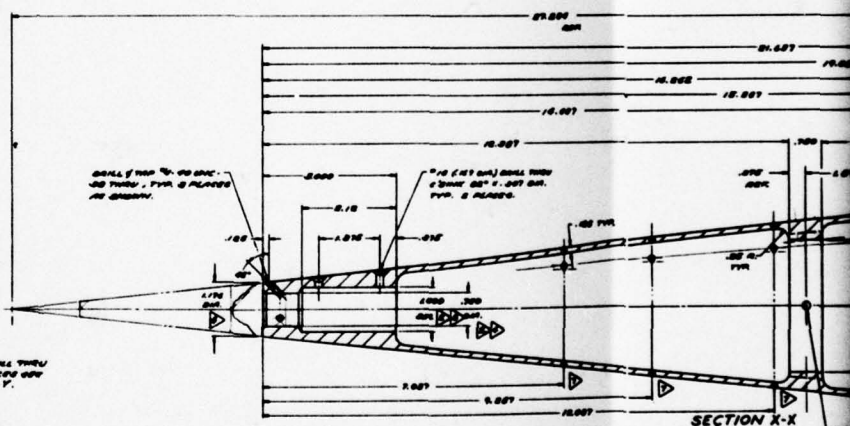
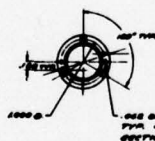
In this investigation, we attempted to examine first, the major mechanisms involved in transition over the conical model; this will be discussed



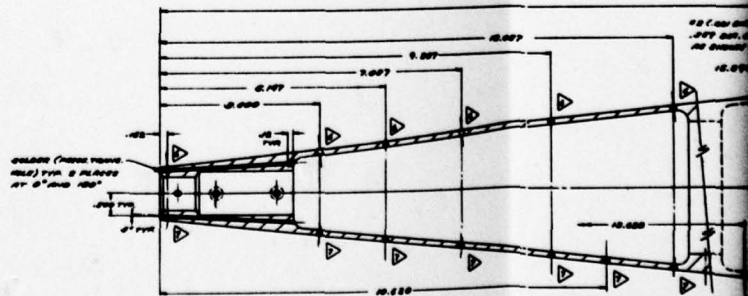


NRV #1  
② ADJUSTED NOISE TH

② **BASE COVER**



**SECTION X-X**

[illegible]

**SECTION Y-Y**

① BODY



in the following section. Then, we compared the measurements of transition Reynolds numbers made in the present with those obtained earlier at Calspan, together with measurements in the ballistic range and from flight. Finally, we present an analysis of the measurements to determine the effect of model incidence and nose tip bluntness ratio on the position of the transition and the shape of the transition front on the cone and the forces and moments which were associated with each transition pattern.

### 2.3 OBSERVATIONS ON THE MECHANISM OF BOUNDARY LAYER TRANSITION

A typical photograph of the development of a transition region over a sharp slender cone at Mach 13 is shown in Figure 2-73. The first evidence of transition is provided by the appearance of a system of regular instabilities in the boundary layer, which subsequently breaks down into a random structure as transition proceeds. We observe transition as a growth of the boundary layer in the Schlieren photographs not only because the momentum thickness increases but also because the optical properties, particularly the position of the maximum density gradient, change. The heat transfer distribution in the transition region exhibits an intermittent character as illustrated in Figure 2-73, which shows records from the gages positioned along the model. The first indication of transition appears as "spikes" in the records as indicated at Station 1 in Figure 2-73. The magnitude and frequency of these "spikes" increase with downstream distance until at the end of the transition process they coalesce to give a larger heating rate with considerably less intermittency. The heat transfer measurements also suggest that secondary vortices are developed as the major disturbances move down the cone. Spatial and temporal correlations of these measurements suggest that close to their point of origin the disturbances are convected downstream at a little under half the free stream velocity, while toward the end of transition this figure has risen to approximately 85% of the free stream velocity. The regular instabilities which precede transition can be seen more easily in Figure 2-74, taken under conditions where we lowered the Reynolds number to delay the start of transition. Close examination reveals that instabilities of this kind always precede transition, and in some cases can be classed as turbulent bursts as illustrated



[illegible]

RUN NO. 3 MODEL INCIDENCE,  $\theta = 0^\circ$   
 $M = 13.0 \text{ Re/FT} = 5 \times 10^6$

**Figure 2-73 SCHLIEREN PHOTOGRAPH SHOWING THE DEVELOPMENT OF TRANSITION OF A CONICAL BOUNDARY LAYER IN HYPERSONIC FLOW**

FORMATION OF "WAVE-LIKE" INSTABILITIES AT THE EDGE OF THE BOUNDARY LAYER  
PRECEDING THE GROSS INSTABILITIES SHOWN IN THE FOLLOWING FIGURE

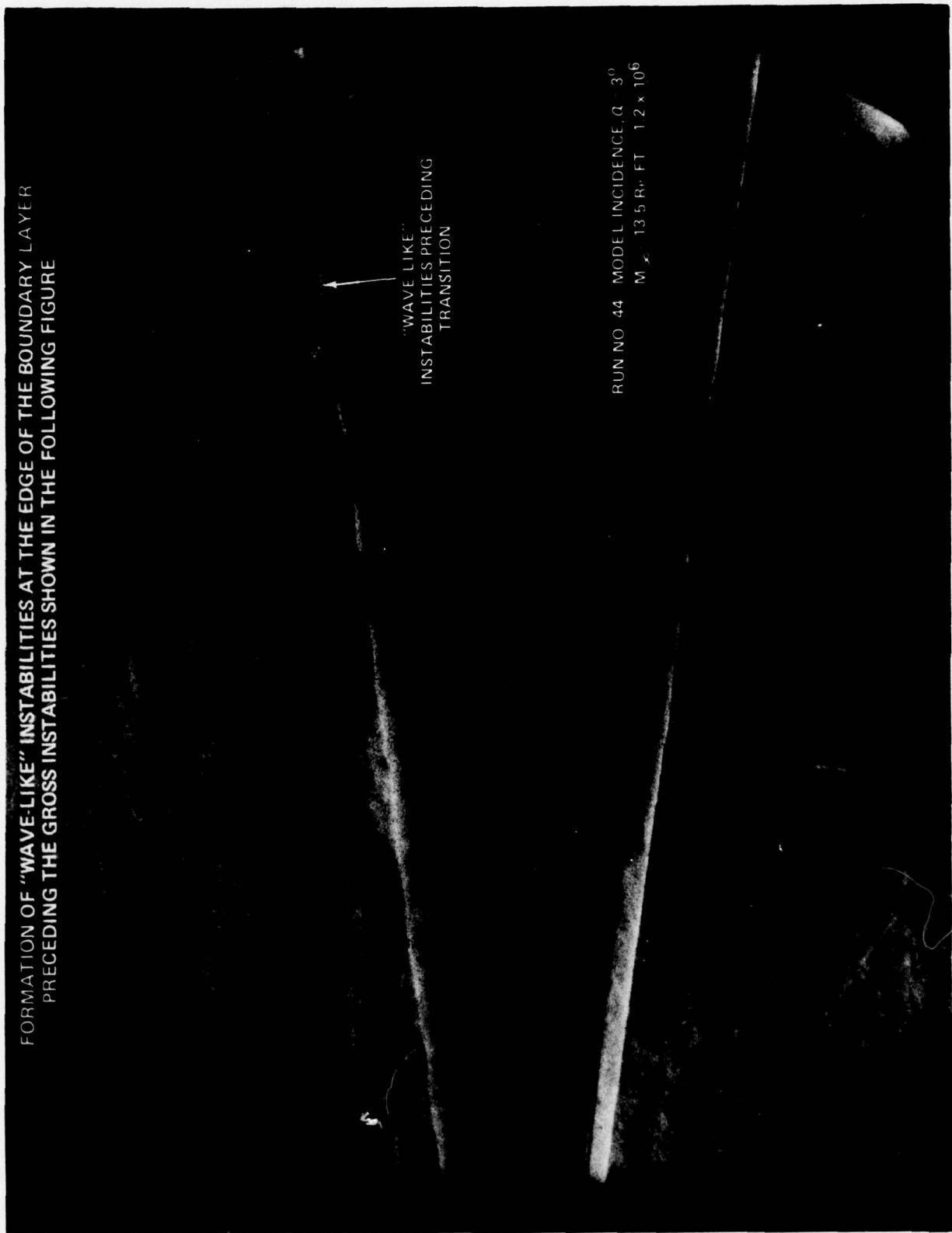


Figure 2-74 FORMATION OF "WAVE-LIKE" INSTABILITIES AT THE EDGE OF THE  
BOUNDARY LAYER PRECEDING THE GROSS INSTABILITIES

in Figure 2-75. Our studies suggest that the instabilities originate at the edge of the boundary layer as demonstrated in Figure 2-76. We believe these disturbances are basically three dimensional in character, possibly a streamwise vortex system, which breaks up into random motion as transition develops.

#### 2.4 FACTORS INFLUENCING THE TRANSITION REYNOLDS NUMBER

Since the early studies of Osborne Reynolds<sup>2</sup>, it has been recognized that the transition of boundary layers or free shear layers from laminar to turbulent flow is influenced by both the local Reynolds number and by the level of internally generated or background disturbance. Thus, experiments to define a specific transition Reynolds number, for given model configuration and free stream conditions, are of little general value unless it can be shown that the instability modes of the boundary layer remain unexcited by disturbances in the free stream or respond to stronger disturbances generated, for example, by surface roughness. While the transition Reynolds number can be influenced by disturbances generated on the model or in the free stream, such disturbances do not appear to influence the basic mechanisms involved in the transition process. However, a high degree of background noise may trigger instability modes which "by-pass" the weaker modes such as the Tollmien-Schlichting<sup>2</sup> instability.

The studies of Pate and Schueler<sup>3</sup>, and the extensive measurements made at NASA Langley<sup>4</sup>, have demonstrated that in conventional supersonic wind tunnels, the Reynolds number at which transition occurs is strongly influenced by the fluctuating pressure level in the free stream. Pate and Schueler further demonstrated that the level of pressure fluctuation could be related to geometric features of the tunnels and the characteristic of the boundary layer on the tunnel walls. A direct result of Pate and Schueler's studies is that a decrease in tunnel size for the same free stream conditions should result in a decrease in the transition Reynolds number. Thus, when we compared our transition measurements obtained in the 96" shock tunnel, equipped with a 24" diameter A nozzle, with those obtained in the same tunnel equipped with the 48" diameter D nozzle, we anticipated a significant difference. However, as



A SCHLIEREN PHOTOGRAPH SHOWING REGULAR BURSTING WHICH PRECEDES  
THE NON-LINEAR BREAKDOWN INTO TURBULENCE.

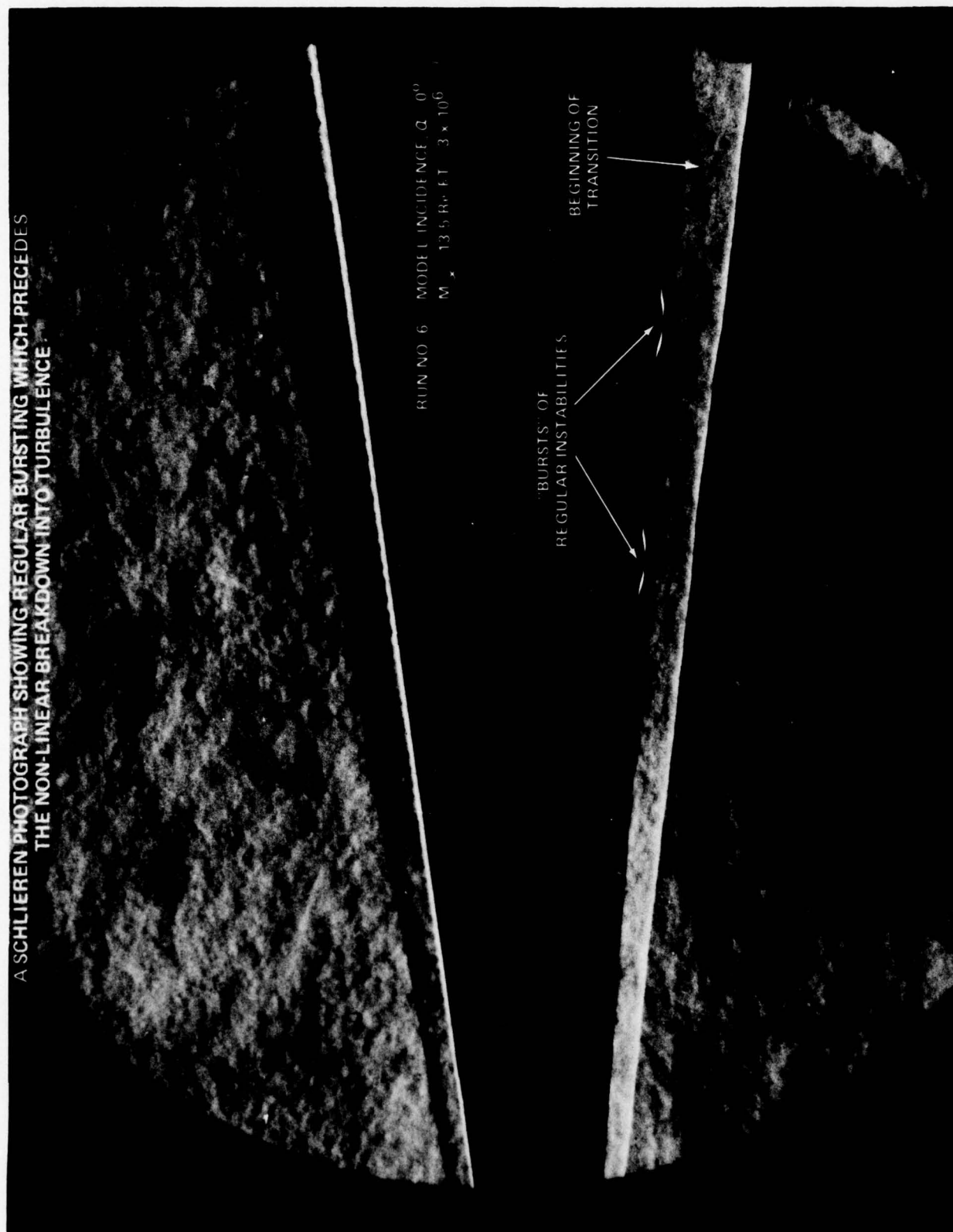
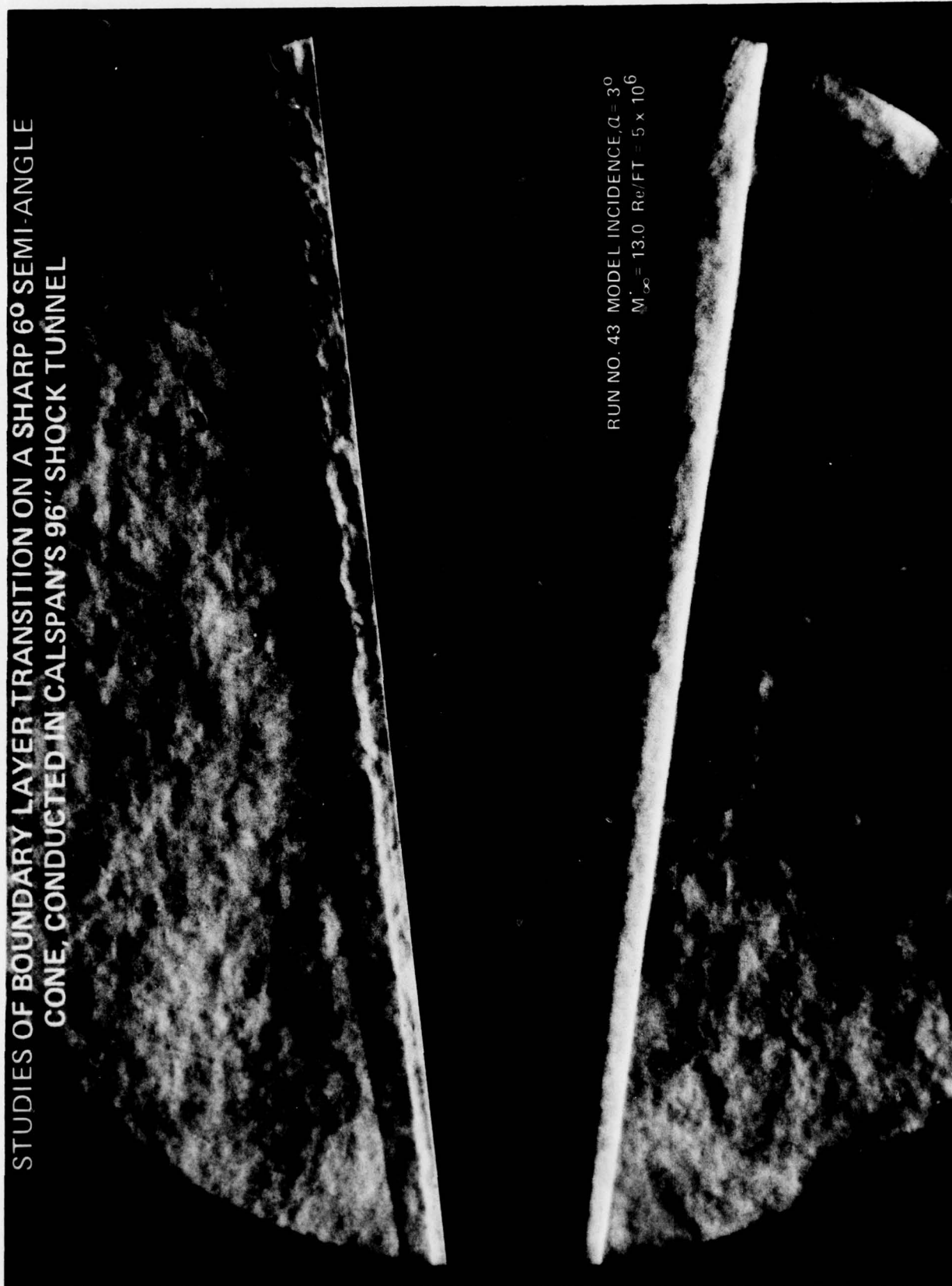


Figure 2-75 SCHLIEREN PHOTOGRAPH SHOWING REGULAR BURSTING WHICH  
PRECEDES THE NONLINEAR BREAKDOWN INTO TURBULENCE

STUDIES OF BOUNDARY LAYER TRANSITION ON A SHARP 6° SEMI-ANGLE  
CONE, CONDUCTED IN CALSPAN'S 96" SHOCK TUNNEL



RUN NO. 43 MODEL INCIDENCE,  $\alpha = 3^\circ$   
 $M_\infty = 13.0$   $Re/FT = 5 \times 10^6$

Figure 2-76 STUDIES OF BOUNDARY LAYER TRANSITION ON A SHARP 6° SEMI-ANGLE CONE, CONDUCTED IN CALSPAN'S 96" SHOCK TUNNEL

demonstrated in Figure 2-77, where we have plotted  $Re_g^{0.2}$  versus the free-stream unit Reynolds number, the Pate and Schueler scaling does not appear to apply, even though a unit Reynolds variation is evident. It should be mentioned that the Calspan studies were conducted at Mach numbers and Reynolds numbers well above those used by Pate and Schueler in their studies. As a result, we believe that in our test environment, the magnitude of the noise radiated from the walls and its intensity on the tunnel axis was significantly less than those found in the experiments analyzed by Pate and Schueler. Transition Reynolds numbers of over  $200 \times 10^6$  are predicted if the Pate and Schueler correlation is extrapolated to the tunnel configurations and free-stream test conditions at which our studies were performed. Clearly, such values are well in excess of physical meaningful quantities. Thus, it was not surprising to find that the measurements made in the Calspan studies fall below the Pate and Schueler correlation as shown in Figure 2-78. These results suggest that in our studies, pressure fluctuations resulting from acoustic radiation from the tunnel walls may not be a dominant disturbance in the free-stream. Thus, the position of transition on the model examined in the present study may be controlled by disturbances more complex than simple acoustic noise. It remains to be determined whether transition can be related to the fluctuating pressure level in the free stream, which, in turn, might be related to fluctuations in the reservoir conditions. However, because of the large expansion ratios in the A and B nozzles, we must look to fluctuations in the enthalpy in the reservoir, as opposed to velocity fluctuations, as a potential source of free stream disturbances.

One of the most successful formats that we have found for comparing and correlating the transition measurements made in the 48" and 96"-shock tunnels at Calspan with measurements from ballistic ranges and flight tests has been in terms of the Reynolds number based on local momentum thickness and the local Mach number  $M_{LOCAL}$ . A correlation of the transition measurements made on sharp cones and flat plates in the present and earlier studies at Calspan, flight measurements reported by TRW, and measurements in the ballistic ranges at AEDC and NSWC are shown in Figure 2-79. We see that there is relatively good agreement between the shock tunnel measurements and those obtained in free flight. A further comparison between our measurements and those made



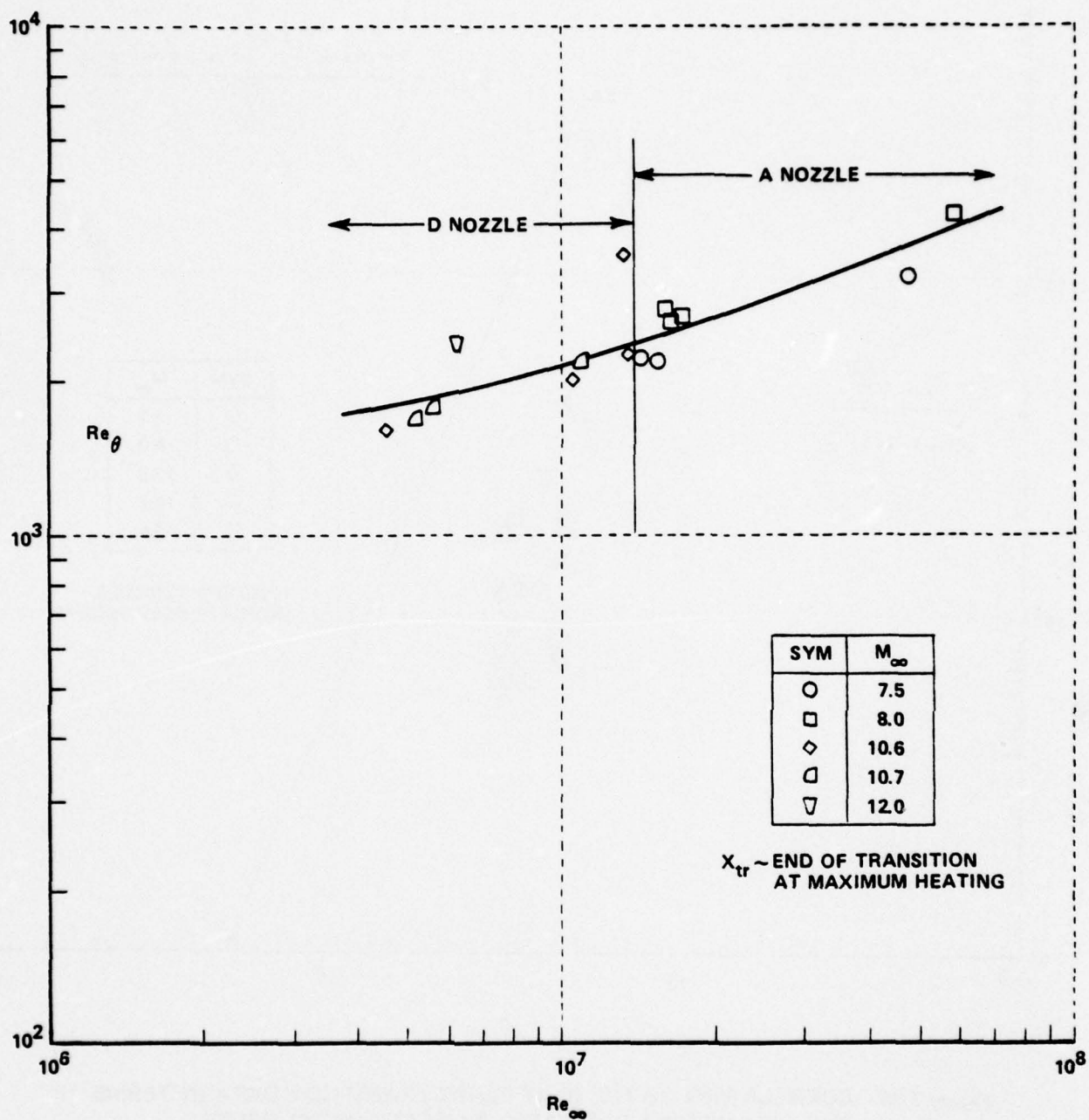


Figure 2-77 CORRELATION OF TRANSITION SHOWING THE EFFECTS OF TUNNEL SIZE

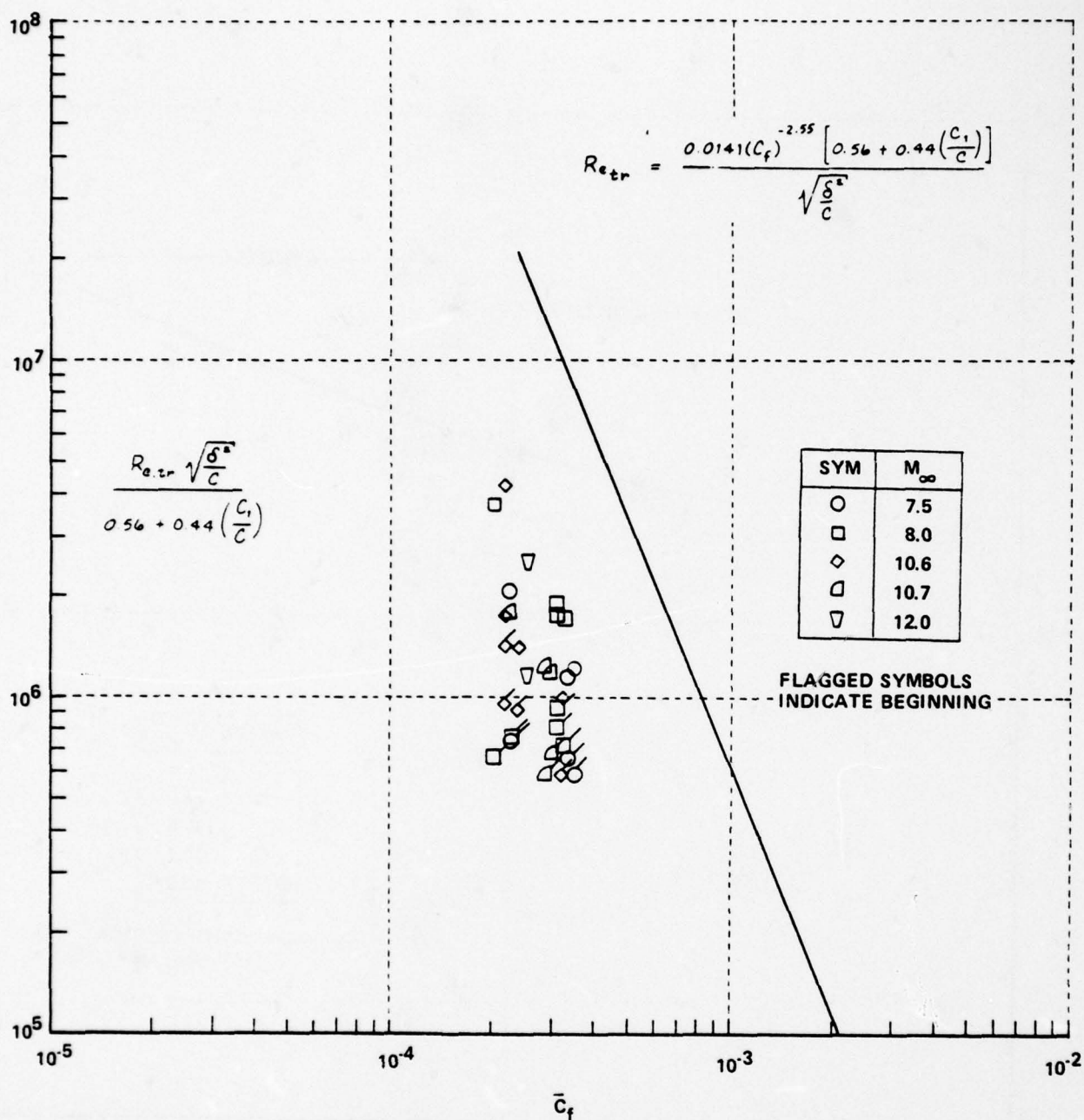


Figure 2-78 CORRELATION OF THE FLAT PLATE TRANSITION DATA IN TERMS OF THE PARAMETERS SUGGESTED BY PATE AND SCHUELER

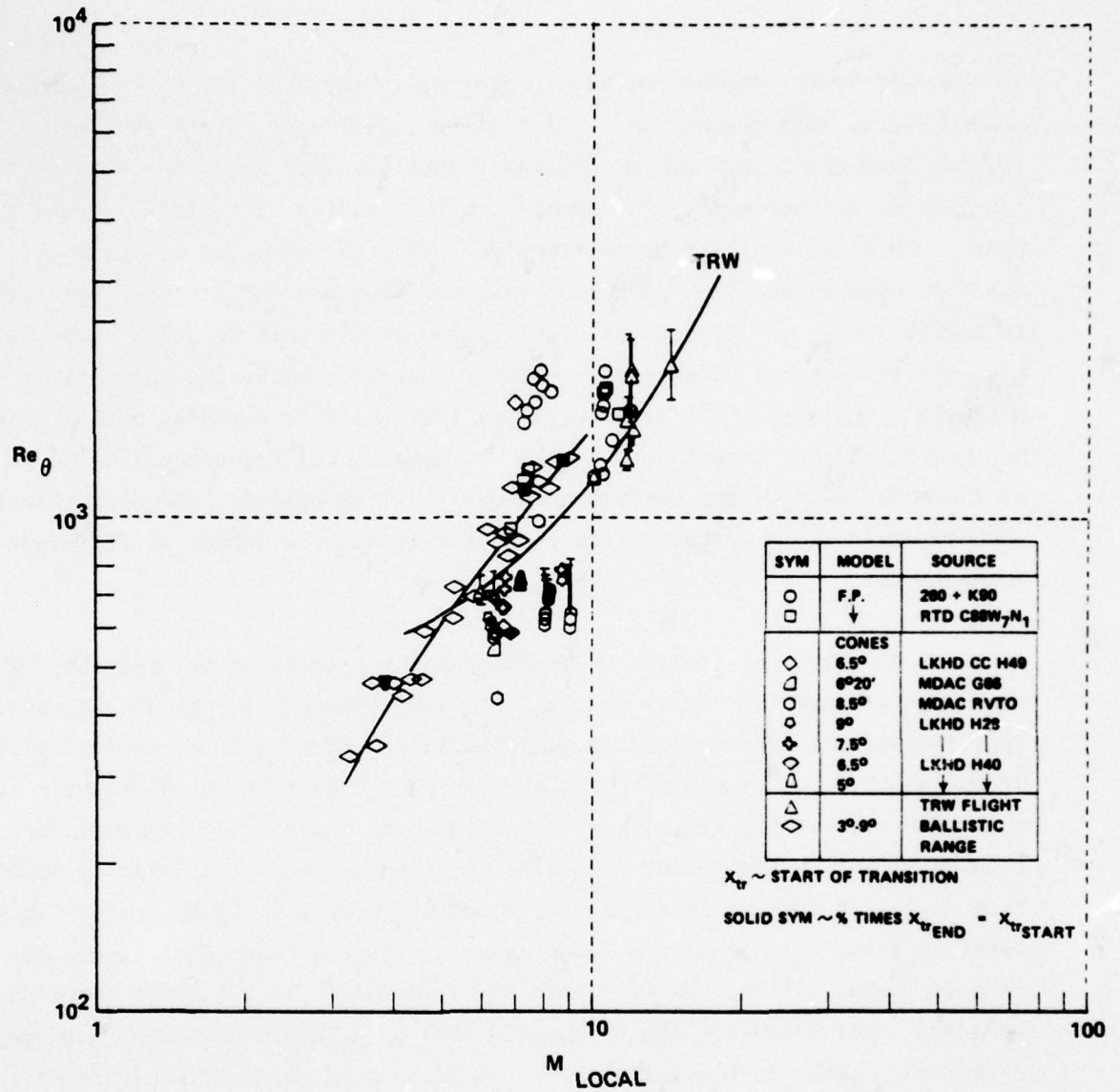


Figure 2-79 CORRELATION OF TRANSITION MEASUREMENTS IN THE CALSPAN SHOCK TUNNELS WITH BALLISTIC AND DOWNRANGE MEASUREMENTS



in the more recent studies of Reda<sup>5</sup>, plotted in terms of the unit Reynolds number, local Mach numbers and wall cooling ratio,  $T_w/T_{Aw}$ , are shown on Figures 2-80 and 2-81. Again, we find relatively good agreement between the two sets of measurements. In common with the studies of Potter<sup>6</sup>, Sheetz<sup>7</sup>, and Reda<sup>5</sup>, we observe a unit Reynolds number effect as shown in Figure 2-82. Further comparisons with the measurements of Krogmann and Stetson<sup>9</sup> are shown in Figure 2-83. The source and significance of the unit Reynolds number effect has been the subject of extensive debate. However, while the analysis of Morkovin<sup>10</sup> and Reshotko<sup>11</sup> have suggested that the unit Reynolds number effects may be traced to a sensitivity to the non-dimensional frequency ( $U_e^2 / \nu_e$ ), or the wavelength of the disturbance ( $U_e / \nu_e$ ), in reality, the disturbance inducing transition may stem from a superposition of a number of different mechanisms.

Experimental studies of boundary layer transition on hypersonic flows have demonstrated that it is difficult to induce transition in such a manner that the boundary layer downstream of the trips approaches the characteristics of an "equilibrium" turbulent boundary layer in a distance significantly less than if a natural transition had been allowed to occur. The experimental studies of Morrisette, Stone and Cary<sup>12</sup> at Langley, and studies at Calspan<sup>13</sup>, have suggested that while trips were found disturbing a highly-cooled laminar boundary layer on sharp cones, causing an increase in the local values of skin friction and heat transfer, the Reynolds number at the point where the boundary layer exhibited the characteristics of a "fully turbulent boundary layer" was almost identical to the value calculated for a natural transition. Further, Morrisette, et al., found trip-induced disturbances persisted well downstream of transition. Measurements of heat transfer for the tripped (with surface roughness) and untripped boundary layers over a sharp cone demonstrate that although roughness causes an increase in the heating rate immediately behind the trips, the heat transfer to the cone beneath the tripped and untripped boundary layer reaches the turbulent values at approximately the same distance downstream. This result suggests that in high speed-highly cooled flow, a turbulent boundary layer will develop only when the Reynolds number is large enough for the turbulence to be self-sustaining. Thus, following

SOURCE	SYM.	$\theta_c$	$M_\infty$	$M_e$	$(T_w/T_{aw})_e$	$U_e^2 / \nu_e, 1/SEC.$	FACILITY
REDA	○	5°	4.4	4.2	.22	$.28 - 1.66 \times 10^{11}$	RANGE
KROGMANN	---	5°	5.0	4.7	.79 - .67	$.08 - 0.42 \times 10^{11}$	LUDWIG TUBE
STETSON	□	8°	5.5	4.9	.17 - .23	$.11 - 0.29 \times 10^{11}$	SHOCK TUNNEL
	◇				.26 - .37	$.09 - 0.26 \times 10^{11}$	
	△				.42 - .50	$.14 - 0.17 \times 10^{11}$	
	○				.57	$0.18 \times 10^{11}$	
PRESENT STUDY	◐	6°	13.2	10.2 - 10.5	.143	$.41 \times 10^6$	SHOCK TUNNEL

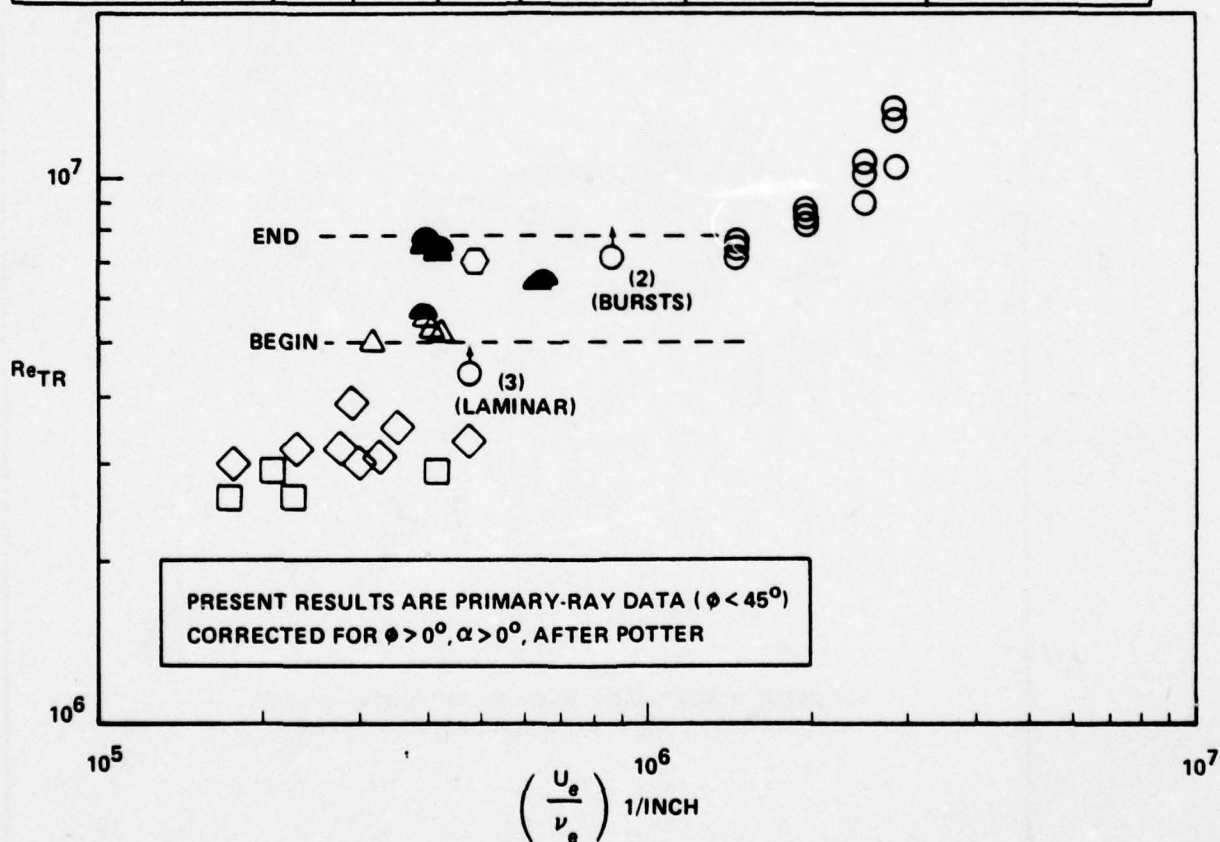


Figure 2-80 TRANSITION REYNOLDS NUMBER VS. UNIT REYNOLDS NUMBER;  
PRESENT DATA VS. KROGMANN AND STETSON

SOURCE	SYM	$\theta_c$	$M_\infty$	$M_0$	$U_0/\nu_0, 1/IN.$	$U_0^2/\nu_0, 1/SEC$	FACILITY
REDA	$\triangle$	$5^\circ$	4.4	4.2	$2.82 \times 10^6$	$1.04 - 1.66 \times 10^{11}$	RANGE
	$\bigcirc$		4.5	4.3	$0.94 \times 10^6$	$0.39 - 0.53 \times 10^{11}$	
POTTER	$\blacksquare$	$10^\circ$	5.0	4.3	$\sim 3.0 \times 10^6$	$\sim 2.0 \times 10^{11}$	RANGE
	$\boxtimes$				$\sim 0.8 \times 10^6$	$\sim 0.53 \times 10^{11}$	
	$\blacksquare$	$10^\circ$	2.3	2.1	$\sim 3.0 \times 10^6$	$\sim 0.90 \times 10^{11}$	
	$\square$				$\sim 0.9 \times 10^6$	$\sim 0.27 \times 10^{11}$	
SHEETZ	$\diamond$	$5^\circ$	4.9	4.6	$\sim 2.2 \times 10^6$	$1.3 - 2.9 \times 10^{11}$	RANGE
PRESENT STUDY	$\bullet$	$6^\circ$	13.2	10.2 - 10.5	$.41 \times 10^6$	$.34 \times 10^{11}$	SHOCK TUNNEL

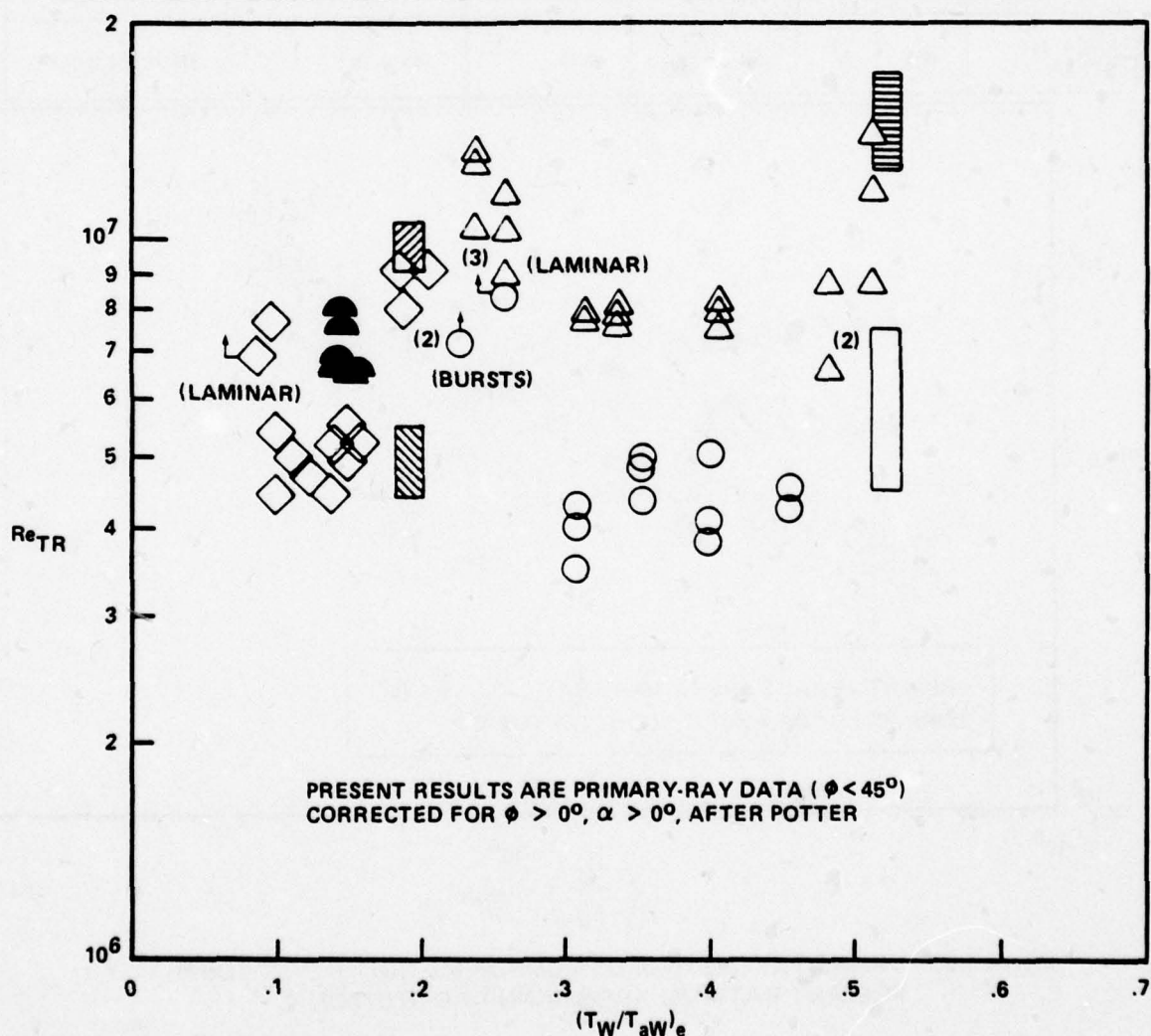


Figure 2-81 TRANSITION REYNOLDS NUMBER VS. WALL-TO-ADIABATIC WALL TEMPERATURE RATIO; PRESENT DATA VS. POTTER AND SHEETZ



SOURCE	SYM.	$\theta_C$	$M_\infty$	$M_e$	$(T_W/T_{aW})_e$	$U_e^2 / \nu_e$ , 1/SEC.	FACILITY
REDA	○	5°	4.4	4.2	.22	$.28 - 1.66 \times 10^{11}$	RANGE
POTTER	— —	10°	5.0	4.3	.19	$.42 - 5.27 \times 10^{11}$	RANGE
		10°	2.3	2.1	.52	$.17 - 1.00 \times 10^{11}$	RANGE
SHEETZ	□	5°	5.0	4.8	.19	$1.40 - 1.71 \times 10^{11}$	RANGE
PRESENT STUDY	◐	6°	13.2	10.2 - 10.5	.14	$.34 \times 10^{11}$	SHOCK TUNNEL

PRESENT RESULTS ARE PRIMARY-RAY DATA ( $\phi < 45^\circ$ )

CORRECTED FOR  $\phi > 0^\circ$ ,  $\alpha > 0^\circ$ , AFTER POTTER

— LEAST-SQUARES FIT OF PRIMARY-RAY DATA,  $\left(\frac{U_e}{\nu_e}\right) > 10^6/\text{IN.}$

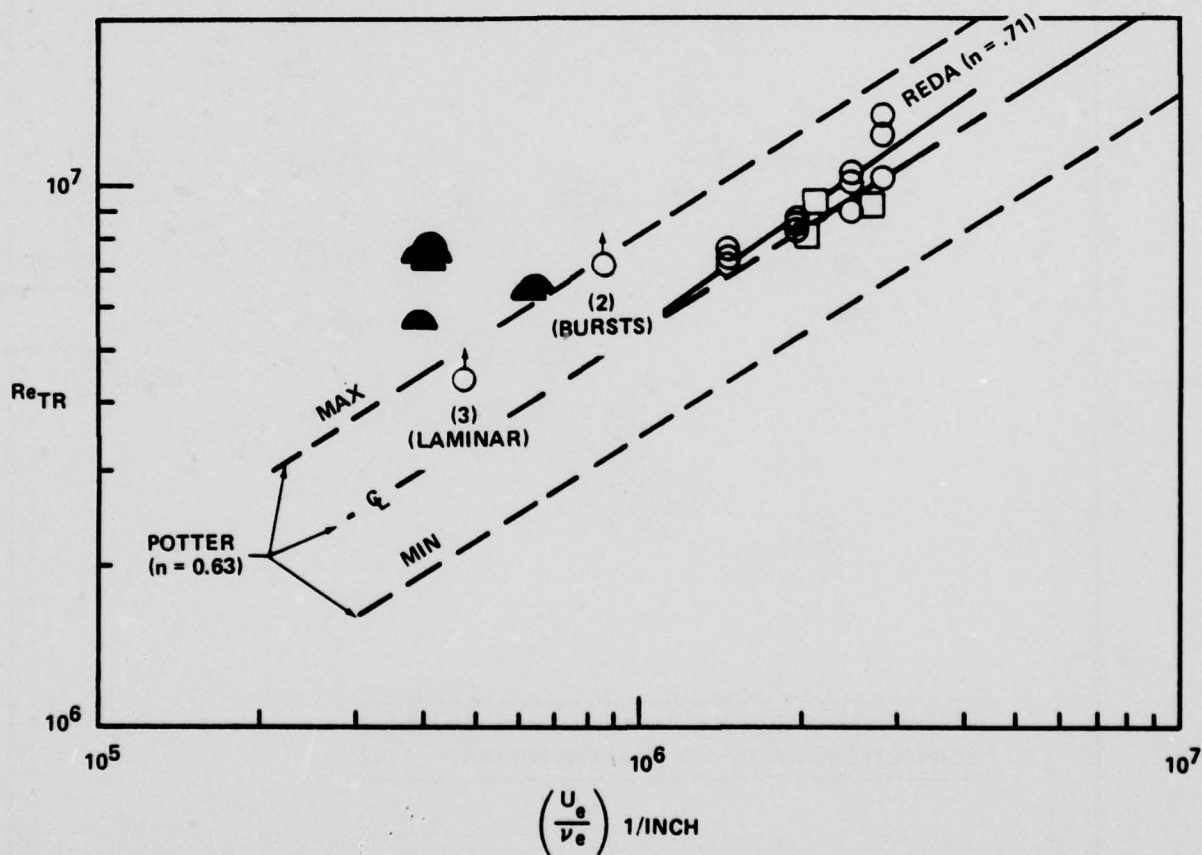


Figure 2-82 TRANSITION REYNOLDS NUMBER VS. UNIT REYNOLDS NUMBER; PRESENT DATA VS. POTTER AND SHEETZ

SOURCE	SYM.	$\theta_c$	$M_\infty$	$M_e$	$U_e / \nu_e, 1 \text{ IN.}$	$U_e^2 / \nu_e, 1 \text{ SEC.}$	FACILITY
REDA	$\triangle$	$5^\circ$	4.4	4.2	$2.82 \times 10^6$	$1.04 - 1.66 \times 10^{11}$	RANGE
	$\circ$		4.5	4.3	$0.94 \times 10^6$	$0.39 - 0.53 \times 10^{11}$	
STETSON	$\diamond$	$8^\circ$	5.5	4.9	$0.17 - 0.48 \times 10^6$	$0.09 - 0.29 \times 10^{11}$	SHOCK TUNNEL
KROGMANN	---	$5^\circ$	5.0	4.7	$0.46 \times 10^6$	$0.13 - 0.18 \times 10^{11}$	LUDWIG TUBE
	---				$0.33 - 0.79 \times 10^6$	$0.13 - 0.25 \times 10^{11}$	
PRESENT STUDY	$\bullet$	$6^\circ$	13.2	10.2 - 10.5	$.41 \times 10^6$	$.34 \times 10^{11}$	SHOCK TUNNEL

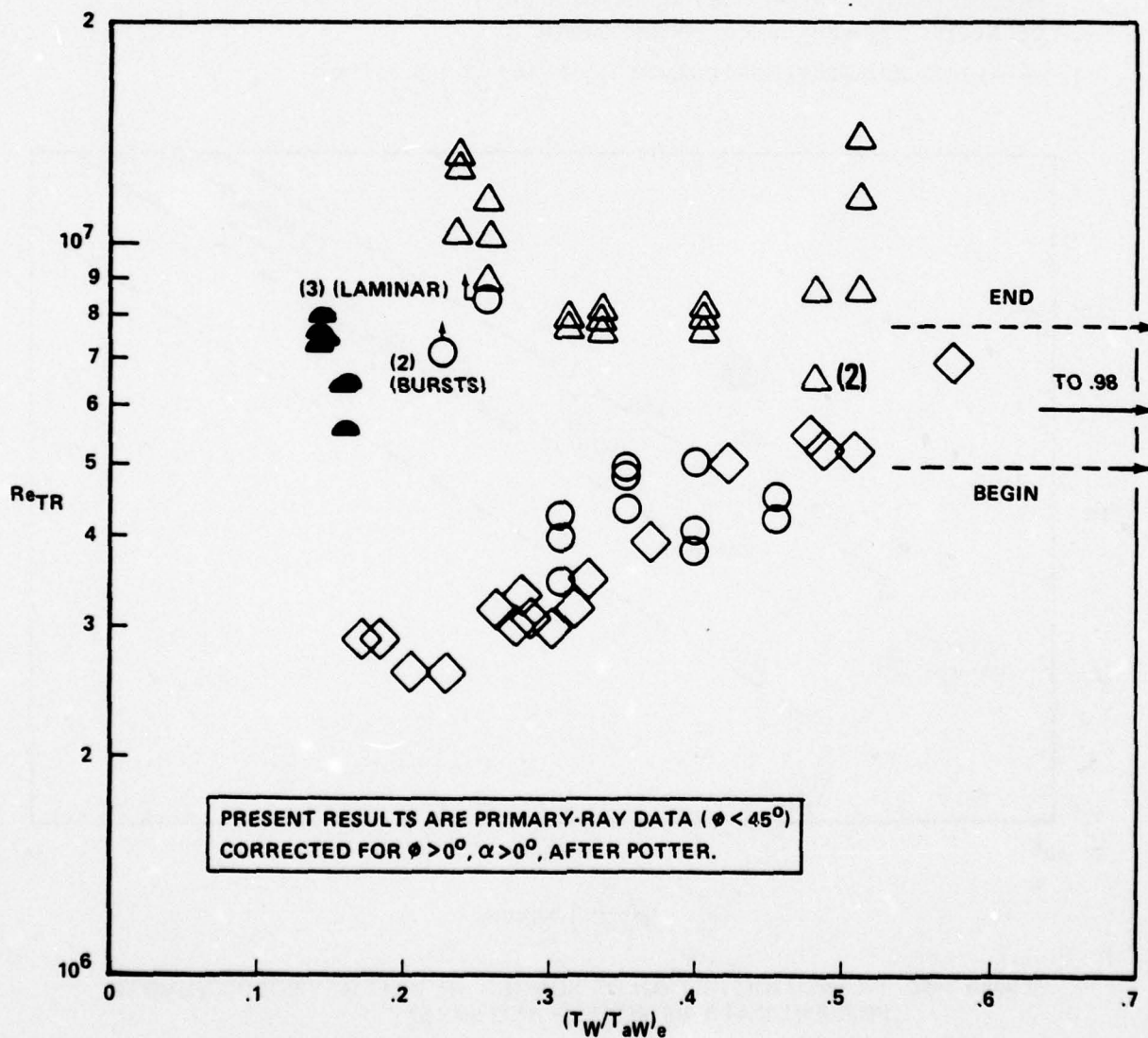


Figure 2-83 TRANSITION REYNOLDS NUMBER VS. WALL-TO-ADIABATIC WALL TEMPERATURE RATIO; PRESENT DATA VS. STETSON AND KROGMANN

Bradshaw<sup>14</sup>, we can examine the lowest Reynolds number where turbulence can be self-sustaining by comparing the energy or shear stress-producing eddy size with the dissipation-scale size. When these scale sizes are equal or overlap, production and dissipation can exist in equilibrium; however, if the Reynolds number is too low, then dissipation will dominate. This criteria can be expressed in terms of an eddy Reynolds number  $Re_\lambda$  which is derived by taking the ratio of the scale size of the energy containing eddies,  $\lambda [ = (\tau/\rho)^{3/2}/E ]$ , and the Kolmogoroff scale size,  $[\nu^3/E]^{1/4}$ , which becomes  $Re_\lambda = (\epsilon'\lambda/\nu)$  and must exceed 30 for turbulent equilibrium flow. In hypersonic boundary layers, Demetriades<sup>15</sup> has found that  $\epsilon' \approx 0.02 u_\infty$  and  $\lambda = 0.18$ ; thus by evaluating  $\epsilon'$  at the edge of the sublayer of a turbulent boundary layer, for a momentum thickness equal to that determined at the beginning and end of transition, we obtain the two correlations of flat plate data shown in Figure 2-84. Here we have used the correlations of  $\delta$ ,  $\delta^*$  and  $\theta$  generated by Wallace<sup>16</sup> and presented in Figure 2-85. Our measurements suggest that transition is complete by  $Re_\lambda \doteq 50$ , and transition begins at approximately  $Re_\lambda \doteq 25$ . We observe that the magnitude of  $Re_\lambda$  is in good agreement with Bradshaw's figure, and this parameter appears independent of Mach number. However, as shown in Figure 2-84, a small unit Reynolds number effect remains.

## 2.5 INFLUENCE OF ANGLE OF ATTACK AND BLUNTNESS ON TRANSITION PATTERN

To understand when and how wind-fixed transition can influence the stability of slender sharp and blunted cones, we must first examine how the shape of the transition front varies with angle of attack and bluntness ratio. The effect of angle of attack is to increase the Reynolds number and decrease Mach number on the windward ray and decrease Reynolds number and increase Mach number on the leeside ray. Cross flow effects act to decrease the momentum thickness on the windward ray and increase it on the leeside ray; thus, depending on the angle of attack and bluntness ratio, the product of the unit Reynolds number and the momentum thickness on the windward and leeward rays  $Re_w$  and  $Re_L$  will undergo significant variation. In earlier experimental studies, it was observed that for small bluntness ratios, increasing nose tip bluntness caused an increase in the transition Reynolds number while at large bluntness ratios the opposite trend occurred. Nose tip bluntness influences the position



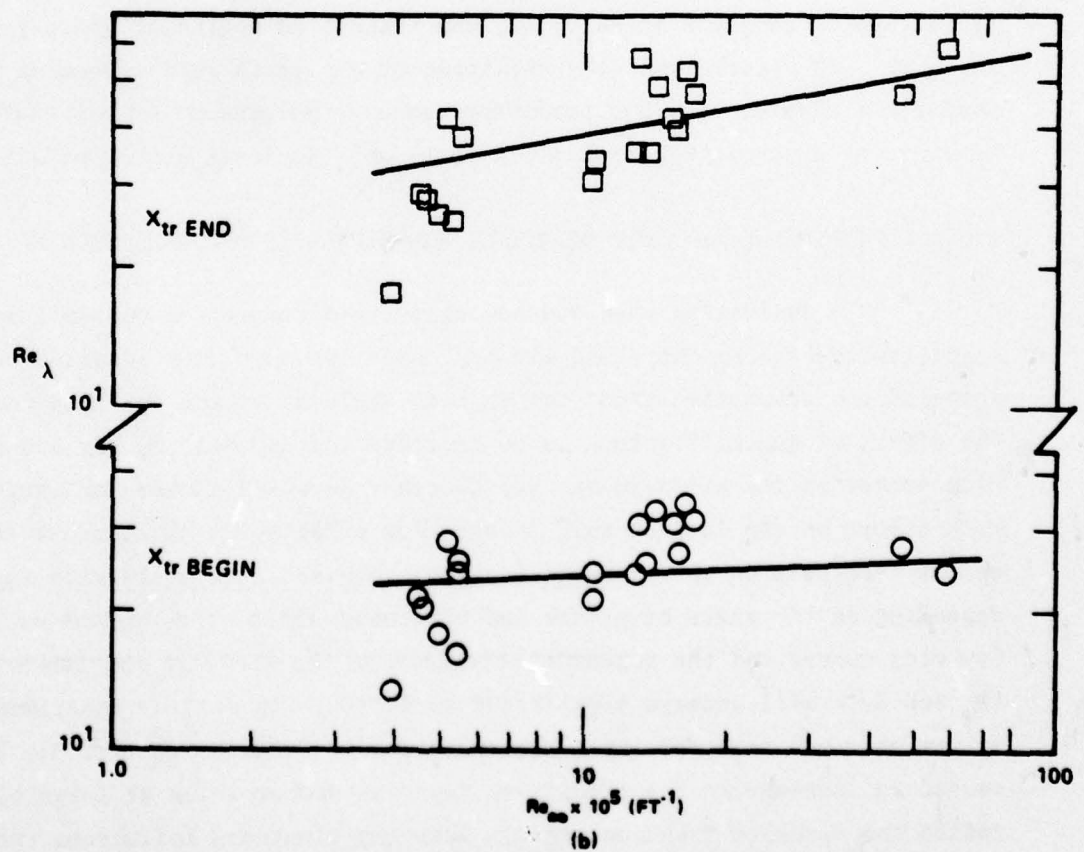
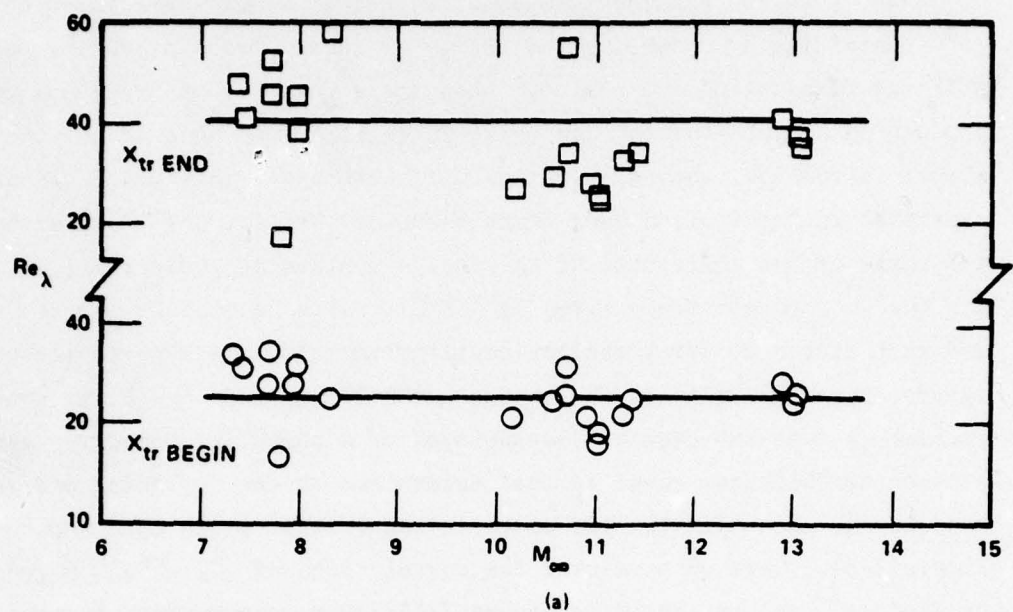


Figure 2-84 CORRELATION OF THE EDDY REYNOLDS NUMBER WITH TRANSITION MEASUREMENTS ON THE FLAT PLATES

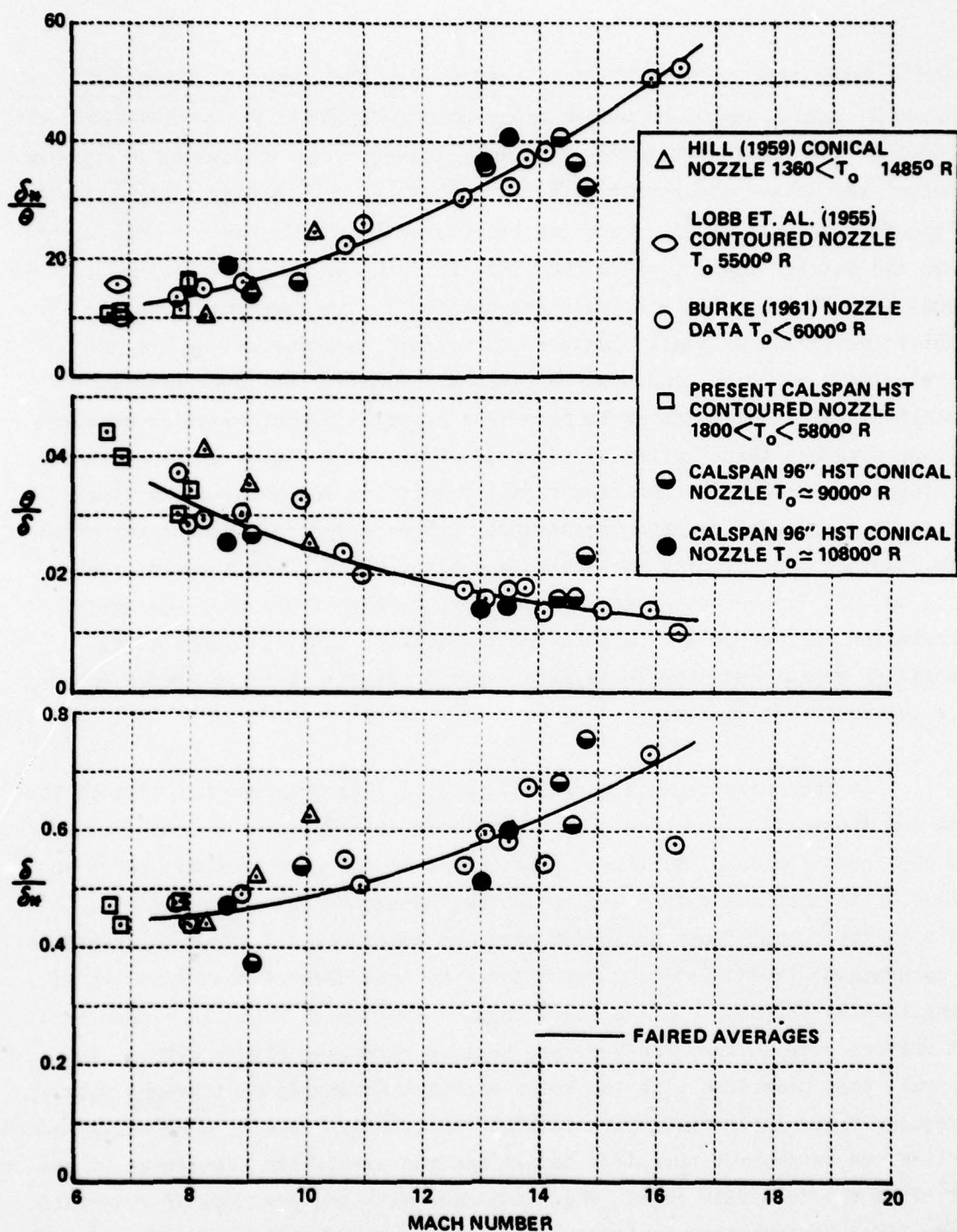


Figure 2-85 TURBULENT BOUNDARY LAYER DISPLACEMENT AND MOMENTUM THICKNESS FROM SHOCK TUNNEL NOZZLE DATA

at which transition takes place on the surface of the cone by influencing the local Mach number, Reynolds number and momentum thickness of the boundary layer, as well as the local streamwise pressure gradient. The studies of Stetson and Rushton<sup>9</sup> and others demonstrated that the position of boundary layer transition on the frustum of a blunted cone can be related to the distance to the point where the entropy layer is swallowed into the boundary layer. Plotted in this format (see Figure 2-86) Stetson's and Rushton's measurements show the strong stabilizing effect of small bluntness on transition Reynolds numbers and a lesser effect for high bluntness conditions. Finson<sup>17</sup> has demonstrated that plotting such measurements in terms of the Reynolds number based on momentum thickness rather than the length Reynolds number (see Figure 2-87) gives a monotonic variation with non-dimensional transition distance, which demonstrates a continuous decrease in Reynolds number based on momentum thickness with bluntness ratio. For both sharp and blunt bodies, the Reynolds number based on local momentum thickness appears to be one of the most successful correlation parameters for correlating transition; thus, in correlating transition measurements on cones with angle of attack, this parameter would be a logical first choice.

In the present experimental studies we made measurements of both the mean and fluctuating components of the heating rates along the cone frustum and obtained high speed Schlieren photographs of the cone boundary layer to enable us to most accurately define the beginning and end of transition. While in the correlations presented here, we have used all three observations in determining transition, for consistency we have defined the beginning of transition as the point on the model surface from which there is a monotonic and uniform rise in the time-averaged heating rate (see Figure 2-88). In general, this coincides with the point at which Schlieren photographs show an irregular increase in the growth rate of the boundary layer. However, as noted earlier, we do observe turbulent bursts and the associated transients in the outputs from the thin film gages, which coincide with the presence of systematic "wave like" disturbances upstream of points at which Schlieren photographs show an irregular increase in the boundary layer thickness. However, the time averaged increase in heating rates beneath such bursts is small, and, thus, we have



TRANSITION VS. BLUNTNESS ( $\alpha = 0$ )  
FREE-STREAM PROPERTIES – STETSON & RUSHTON DATA

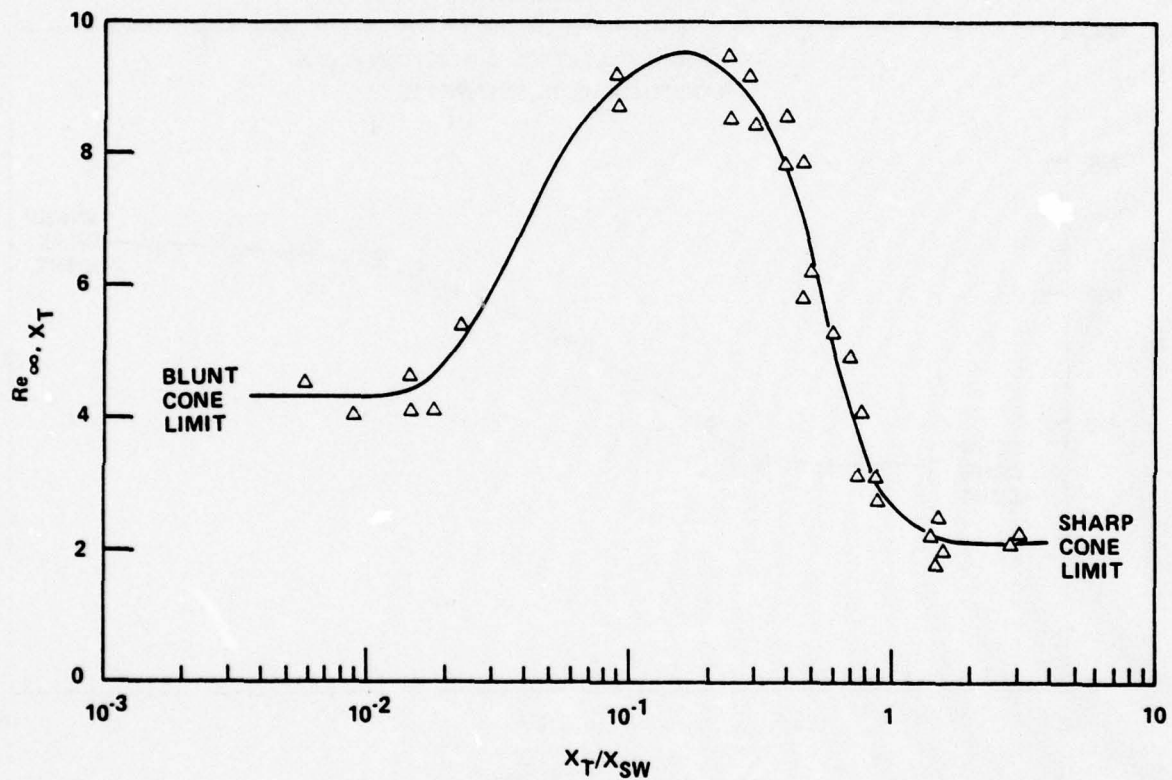
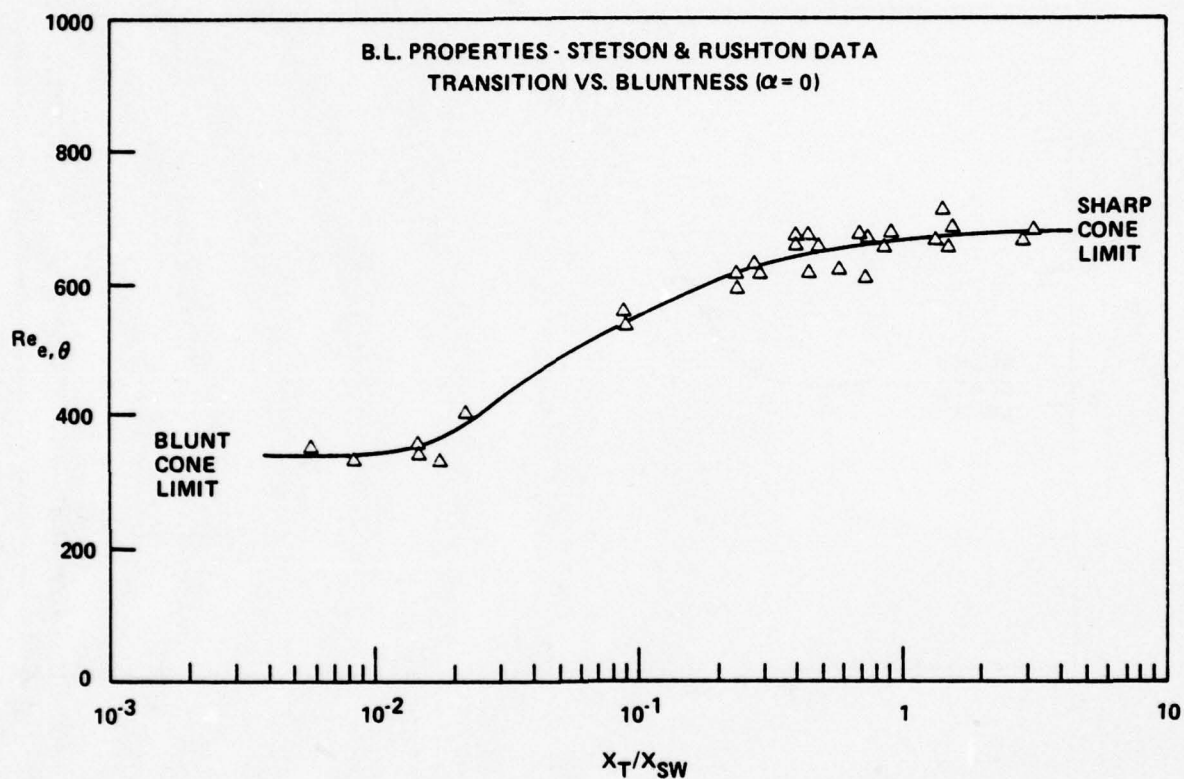


Figure 2-86 VARIATION OF TRANSITION LOCATION NON-DIMENSIONALIZED BY ENTROPY SWALLOWING DISTANCE FOR BLUNTED CONES AT  $\alpha = 0$  AS DETERMINED BY STETSON AND RUSHTON



**Figure 2-87 FINSON'S CORRELATION OF STETSON AND RUSHTON'S TRANSITION MEASUREMENTS IN TERMS OF REYNOLD NUMBER BASED ON LOCAL MOMENTUM THICKNESS AT TRANSITION**

RUN 2  
SHARP NOSE  
 $\alpha = -7^\circ$   
 $M_\infty = 13.0$   
 $Re/FT = 4.8 \times 10^6$

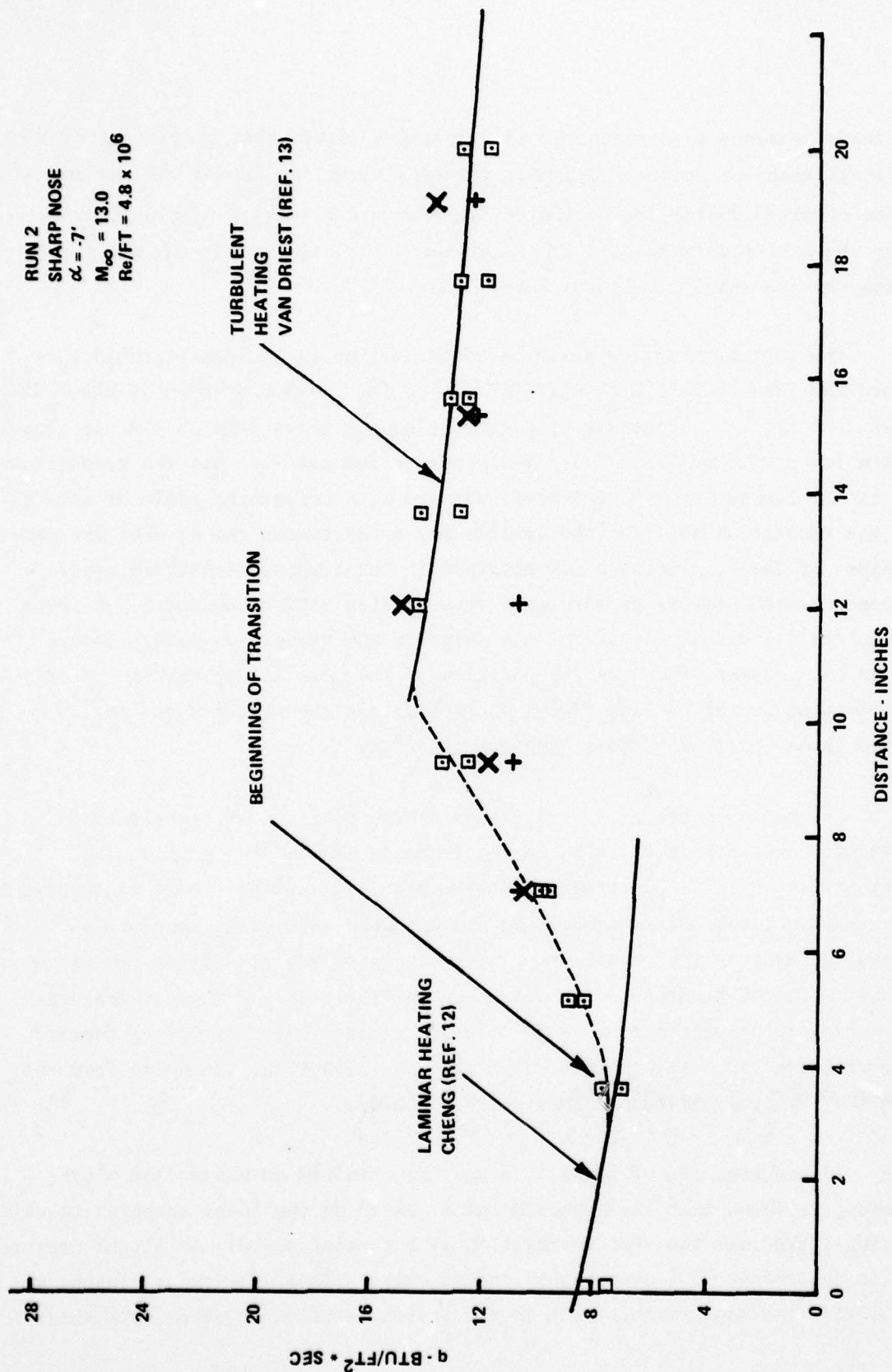


Figure 2-88 THE DISTRIBUTION OF HEAT TRANSFER THROUGH A TRANSITION REGION ON THE SURFACE OF A 6° CONE IN HYPersonic FLOW



noted their presence as a precursor to transition rather than a definition of it. The distributions of pressure and heat transfer along and around the surface of the cone obtained during these studies are shown in Figures 2-3 through 2-57, and the shape of the transition fronts selected in conjunction with those measurements are shown in Figures 2-58 through 2-72.

The variation of the position of the beginning of transition on the windward and leeward rays with angle of attack for a sharp  $6^\circ$ -cone is shown in Figures 2-89 and 2-90, together with earlier measurements made on similar cones but at a lower Mach number. These measurements demonstrate that the transition point on the leeward side of the cone moves forward with increasing angle of attack while the transition point on the leeward ray moves toward the base of the cone. The shapes of the transition point obtained in our studies with sharp cones are compared with similar measurements from earlier studies conducted at lower Mach numbers. A unique feature of the shape of the transition points determined in the present study was the position of the most aft transition point(s) which occurred on the  $90^\circ$  and  $270^\circ$ -rays rather than the windward ray as observed in the earlier studies (see Figure 2-91).

The measurements of the variation of the position of transition on the windward and leeward ray with angle of attack made in the present and earlier studies with  $6^\circ$ -blunt cones are shown in Figure 2-92. Here we observe the transition moves toward the tip on the windward ray, while there is a rearward movement on the leeward ray. The shapes of the transition fronts on the cones with the blunt nose tip are shown in Figure 2-93. These configurations show a relatively narrow wedge-like transition region extending forward on the windward ray with a relatively flat transition front extending from the  $90^\circ$  to the  $270^\circ$ -ray around the leeward side of the body.

In the analysis of transition measure obtained on sharp flat plates and cones, we found that the Reynolds number based on the local momentum thickness ( $Re_\theta$ ) provided the best correlation of both wind tunnel and flight measurements in hypersonic flow over highly cooled walls. Thus, following Finson, we have plotted the measurements made in the present studies together with those

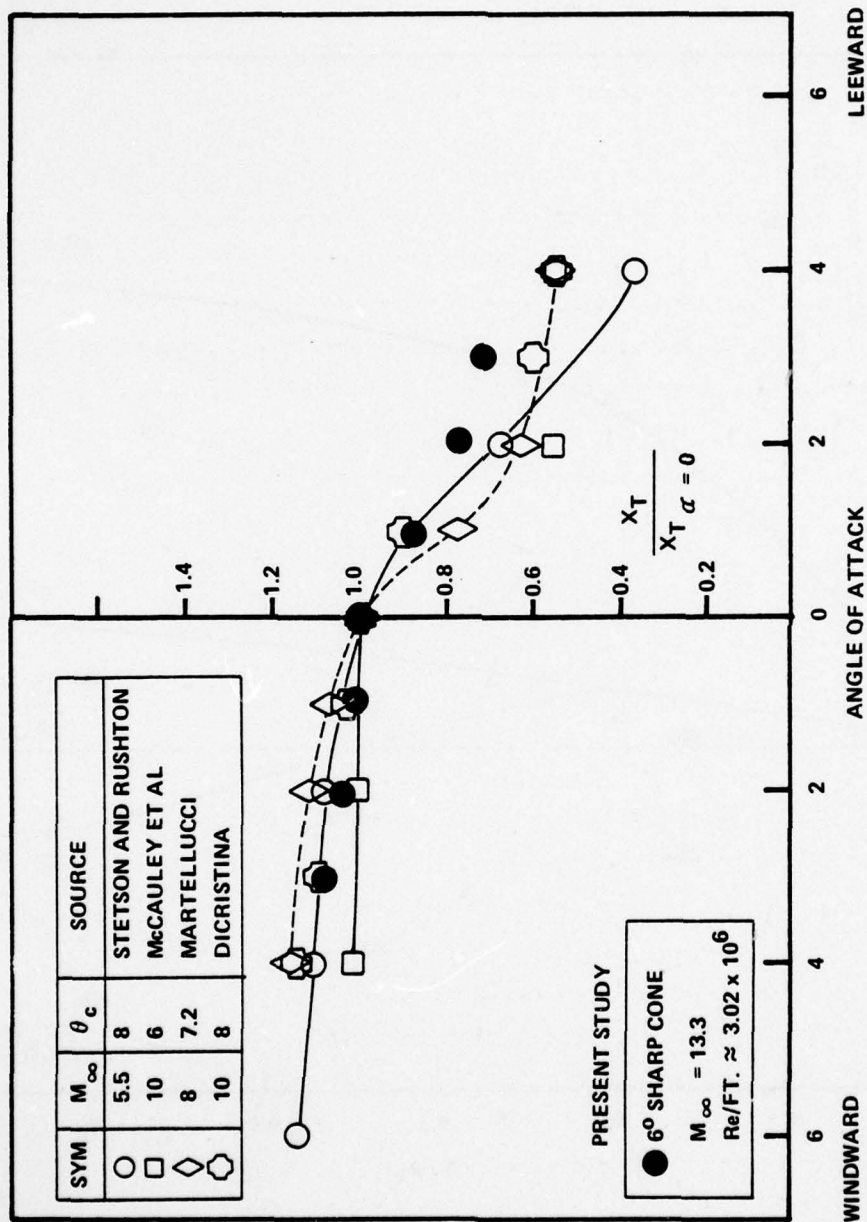
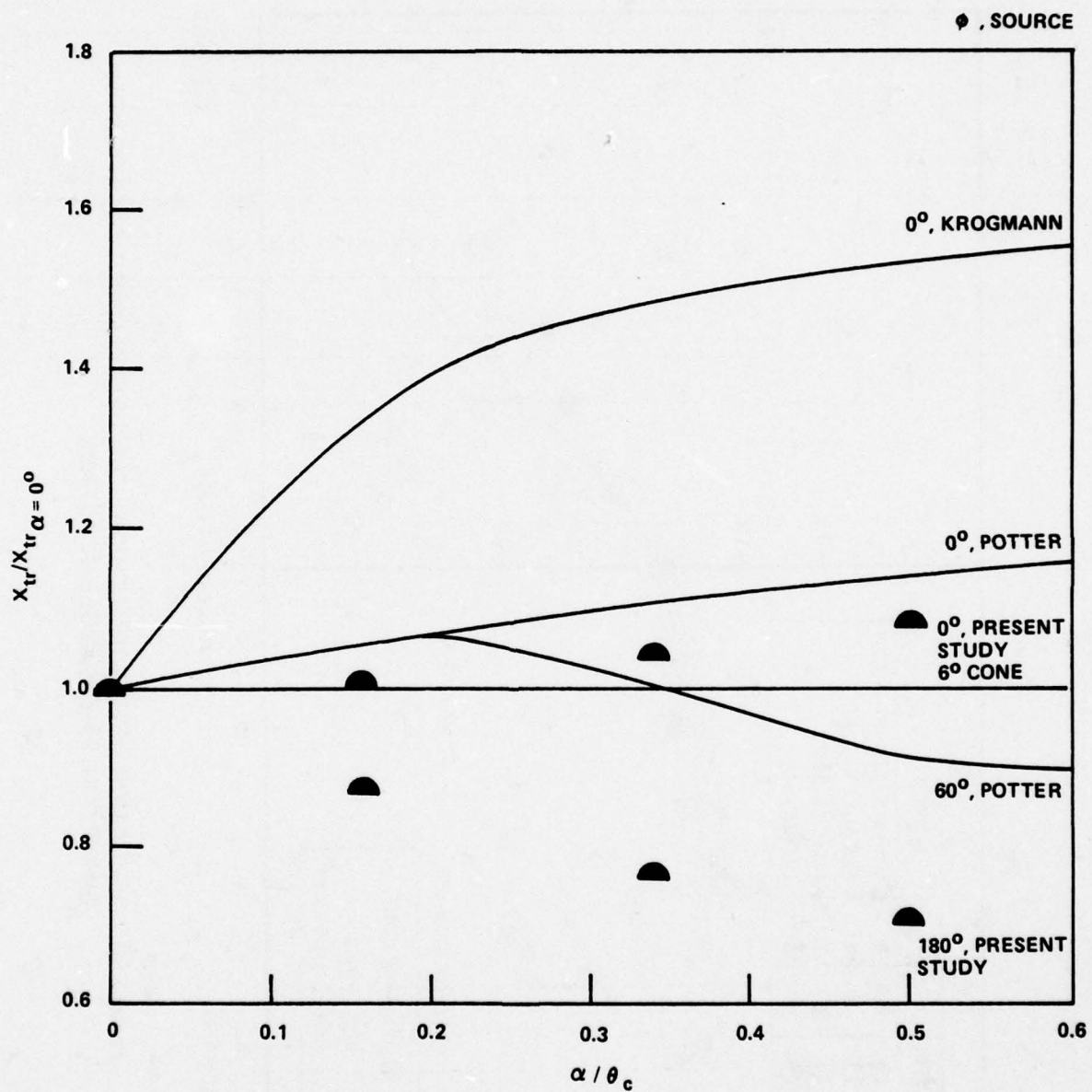


Figure 2-89 VARIATION OF NONDIMENSIONAL TRANSITION FRONT LOCATION ON SHARP CONES WITH ANGLE OF ATTACK



**Figure 2-90** COMPARISON BETWEEN RANGE, SHOCK TUNNEL AND LUDWIG TUBE MEASUREMENTS OF TRANSITION FRONT LOCATION VARIATION WITH ANGLE OF ATTACK FOR SHARP SLENDER CONES



AT  $\alpha = 0^\circ$

SOURCE	SYM.	TECHNIQUE	FACILITY	$\theta_c$	$\alpha / \theta_c$	$M_\infty$	$\left(\frac{T_W}{T_{aW_e}}\right)$	$\frac{U_e}{\nu_e} \cdot \frac{1}{IN.}$	$\frac{U_e^2}{\nu_e} \cdot \frac{1}{SEC.}$
REDA	●	DUAL-PLANE SPARK SHADOW-GRAPH (5 STATIONS)	RANGE (4 SHOTS)	$5^\circ$	.35 - .45	4.5	.22 - .48	$1.04 - 2.66 \times 10^6$	$0.48 - 1.09 \times 10^{11}$
KROGMANN	■	SURFACE HEAT TRANSFER RATES	LUDWIG TUBE	$5^\circ$	.35 - .45	5.0	—	$0.45 - 0.81 \times 10^6$	—
KORSIA & MARCILLAT	◇	SINGLE-LINE OIL FLOW ("LIMITING STREAMLINES")	TUNNEL	$7.5^\circ$	.40	5.0	~1.0	$0.632 \times 10^6$	$0.22 \times 10^{11}$
STETSON & RUSHTON	□	SURFACE HEAT TRANSFER RATES	SHOCK TUNNEL	$7^\circ$	.50	5.5	.24 - .28	$\sim 0.2 - 0.5 \times 10^6$	$\sim 0.1 - 0.25 \times 10^{11}$
PRESENT STUDY	◐ ◑	HEAT TRANSFER SCHLIEREN PHOTOGRAPHS	HST	$6^\circ$	.33 - .50	13.2	.143	$.41 \times 10^6$	$.34 \times 10^{11}$

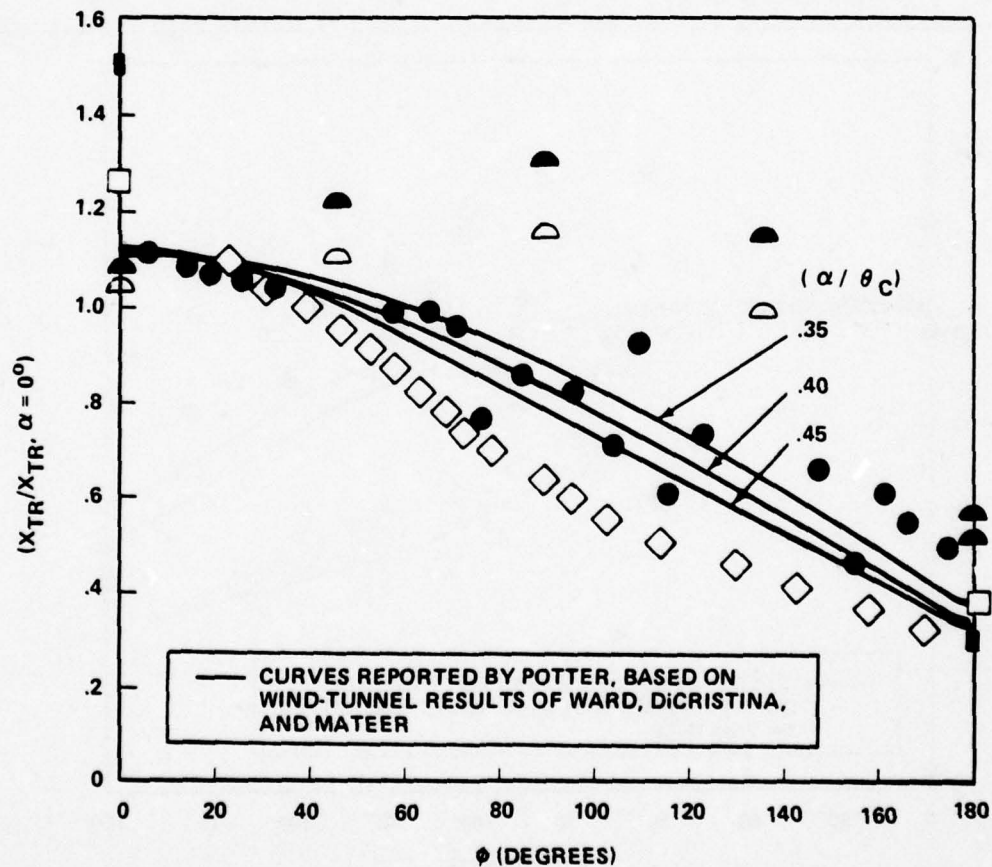


Figure 2-91a TRANSITION ZONE ASYMMETRY; COMPARISONS WITH OTHER DATA,  $.35 \leq (\alpha / \theta_c) \leq .50$

AT  $\alpha = 0^\circ$

SOURCE	SYM.	TECHNIQUE	FACILITY	$\theta_C$	$\alpha / \theta_C$	$M_\infty$	$\left(\frac{T_W}{T_{aW_e}}\right)$	$\frac{U_e}{\nu_e} \frac{1}{IN.}$	$\frac{U_e^2}{\nu_e} \frac{1}{SEC.}$
REDA	●	DUAL-PLANE SPARK SHADOW-GRAPH (5 STATIONS)	RANGE [2 SHOTS]	$5.0^\circ$	.15 - .20	4.5	.22 - .35	$0.88 - 2.50 \times 10^6$	$0.43 - 1.53 \times 10^{11}$
KROGMANN	■	SURFACE HEAT TRANSFER RATES	LUDWIG TUBE	$5.0^\circ$	.15 - .20	5.0	—	$0.45 - 0.81 \times 10^6$	—
KORSIA & MARCILLAT	◇	"LIMITING STREAMLINES"	TUNNEL	$7.5^\circ$	.20	5.0	~1.0	$0.632 \times 10^6$	$0.22 \times 10^{11}$
	○	SCHLIEREN SURFACE PITOT							
WHITFIELD & DOUGHERTY	▲	SURFACE PITOT	TUNNEL	$5.0^\circ$	.20	4.6	~1.0	—	—
STETSON & RUSHTON	□	SURFACE HEAT TRANSFER RATES	SHOCK TUNNEL	$8.0^\circ$	.25	5.5	.24 - .28	$\sim 0.2 - 0.5 \times 10^6$	$\sim 0.1 - 0.25 \times 10^{11}$
PRESENT STUDY	◐	HEAT TRANSFER SCHLIEREN PHOTOGRAPHS	HST	$6.0^\circ$	.17	13	.14	$.421 \times 10^6$	$.35 \times 10^{11}$

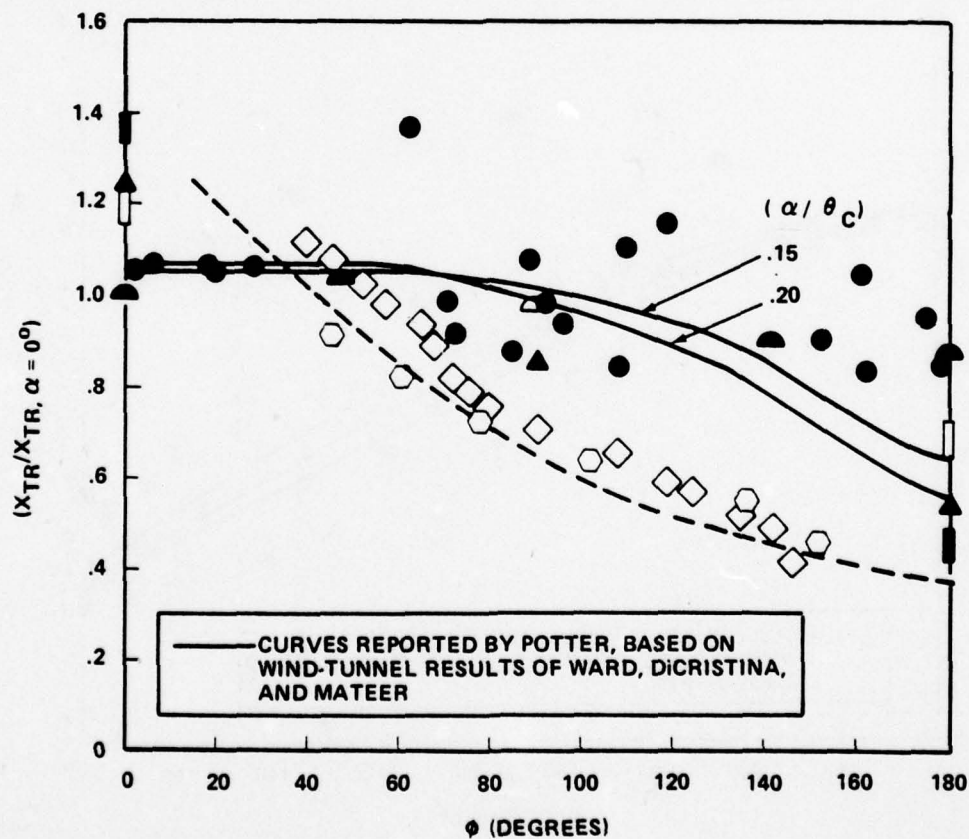


Figure 2-91b TRANSITION ZONE ASYMMETRY; COMPARISONS WITH OTHER DATA,  $.15 \leq (\alpha / \theta_C) \leq .25$

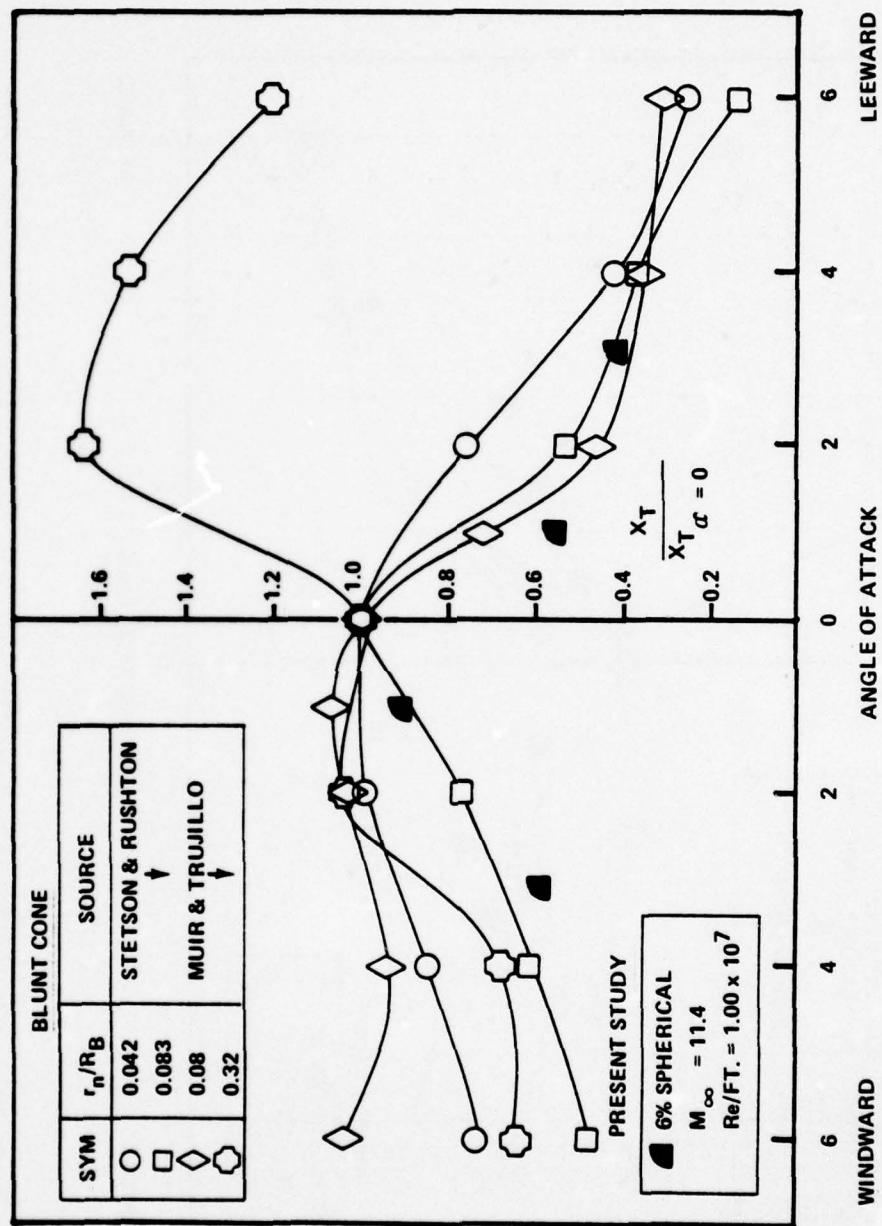


Figure 2.92 VARIATION OF TRANSITION FRONT LOCATION ON SLIGHTLY BLUNTED CONES WITH ANGLE OF ATTACK



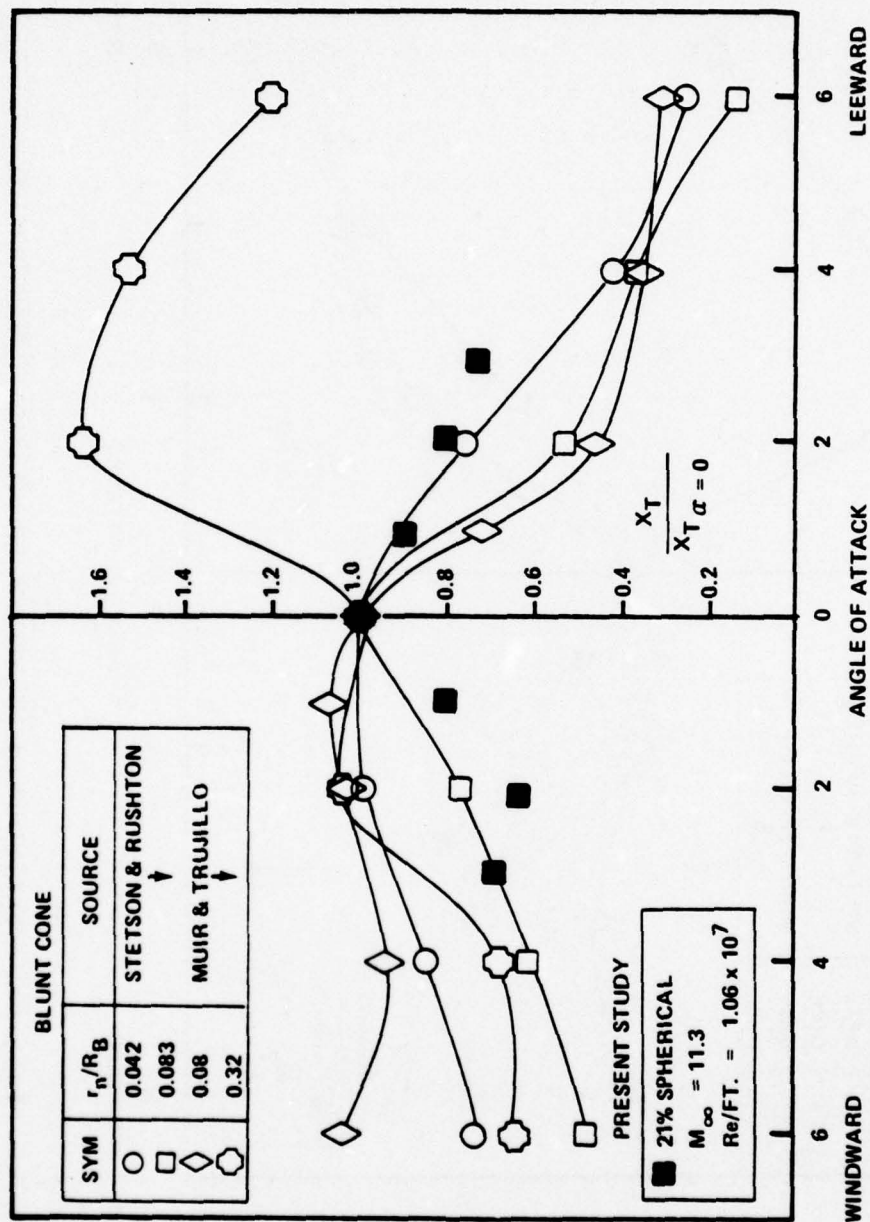


Figure 2-93 VARIATION OF NONDIMENSIONAL TRANSITION FRONT LOCATION  
ON BLUNT CONES WITH ANGLE OF ATTACK

from earlier work in terms of the Reynolds number local momentum thickness and the local Mach number for both sharp and blunt bodies (see Figure 2-94). The values of the momentum thickness used in these plots were determined from computer solutions using the GE-3DSAP and Adams codes together with measurements from the Schlieren photographs obtained in our studies. It can be seen that for both sharp and blunt configurations, that  $(Re_x / Re_{x_0}) \frac{M_0}{M}$  is relatively independent of angle of attack. Thus, for sharp cones it may be observed that transition moves forward on the leeside ray principally because of the large increase in the momentum thickness, while on the windward ray the effects of cross flow and higher unit Reynolds number combine to cause a decrease in the momentum thickness. For the blunted cones, the entropy layer is swallowed more rapidly on the windward rays, and consequently, the Reynolds number based on momentum thickness is increased and transition moves forward relative to its position at  $0^\circ$  angle of attack.

## 2.6 EFFECTS OF TRANSITION ON AERODYNAMIC STABILITY

In this study, we found that the changes which occurred in the forces and moments, which were developed as boundary layer transition moved onto the cone frustum, while small, had a measureable effect on the aerodynamic stability of sharp and blunted cones. In this program, we attempted to place transition onset (by varying the unit Reynolds number of the freestream) on the sharp and slightly blunted cones such that it fell on the leeside ray just behind the center of pressure of the unperturbed cone. From our observations of the geometry of the transition front, it was anticipated that this configuration would provide the greatest destabilizing effect. On the 18% blunt configurations, we positioned the most rearward location of transition front (which occurred on the leeside ray) at the base of the cone. A tabulation of forces and moments recorded in the present study and associated with the heat pressure transfer measurement are presented in Tables 2-6, 2-4 and 2-5, respectively. The corresponding distributions of heat transfer and pressure are plotted in Figures 2-3 through 2-57.

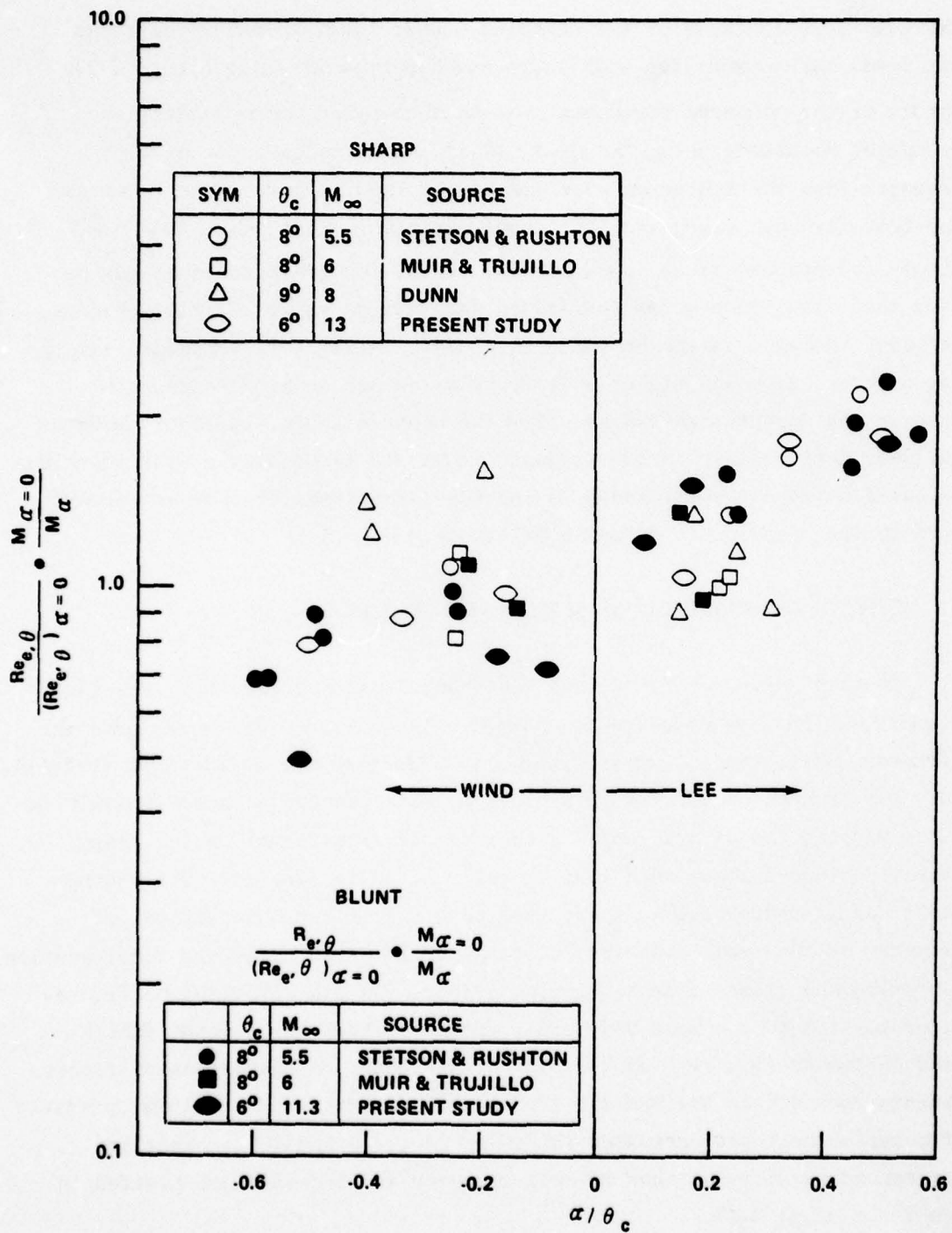


Figure 2-94 CORRELATION OF TRANSITION FRONT LOCATIONS ON SHARP AND BLUNT SLENDER CONES AT ANGLE OF ATTACK



As transition moves onto the frustum of the sharp and slightly blunted cones ( $r_n/R_b = 0.6\%$ ), the small increase in surface pressure, which acts to reduce the normal force at the base of the cone, combined with the increase in skin friction to the leeside of the frustum, which created a positive pitching moment, produces a destabilizing pitching moment. Our pressure measurements suggest that the pressure rise through the transition region is less than 5% of the local cone pressure and the destabilizing moments resulting from the increments on pressure and skin friction are of comparable magnitude.

Transition moves first onto the windward surface of the 18%-blunt cone models and the local increase on pressure and skin friction combine to yield a negative or stabilizing pitching moment about the CG. Again, calculations in which the pitching moment associated with the increased skin friction was determined from the measured heat transfer rates (assuming a Reynolds analogy factor of 1) and transition patterns demonstrated that transition-induced increments in pressure and skin friction gave restoring moments of roughly equal proportions. Taking the force and moment measurements and determining the increments in the moment in the center-of-pressure resulting from transition, we obtain the results shown in Figure 2-95. Here we have selected cases where the transition region was positioned on the core in an attempt to obtain the maximum destabilizing or stabilizing effects.

We observe, as discussed earlier, that boundary layer transition exerts a destabilizing effect on the sharp and slightly blunted configurations, and this is manifest in the forward movement of the center of pressure ( $\Delta X_{CP}/L$ ) of between 3% and 5%. Transition on the blunt configuration is stabilizing, and incremental movements of the center of the center of pressure as large as 5% were recorded. It should be reiterated that we have studied only the incremental changes in forces resulting from transition on non-ablating configurations, and it might be anticipated that the forces induced by the growth of a transition region enhanced and shortened by ablation could be significantly larger for the equivalent non-ablating body.

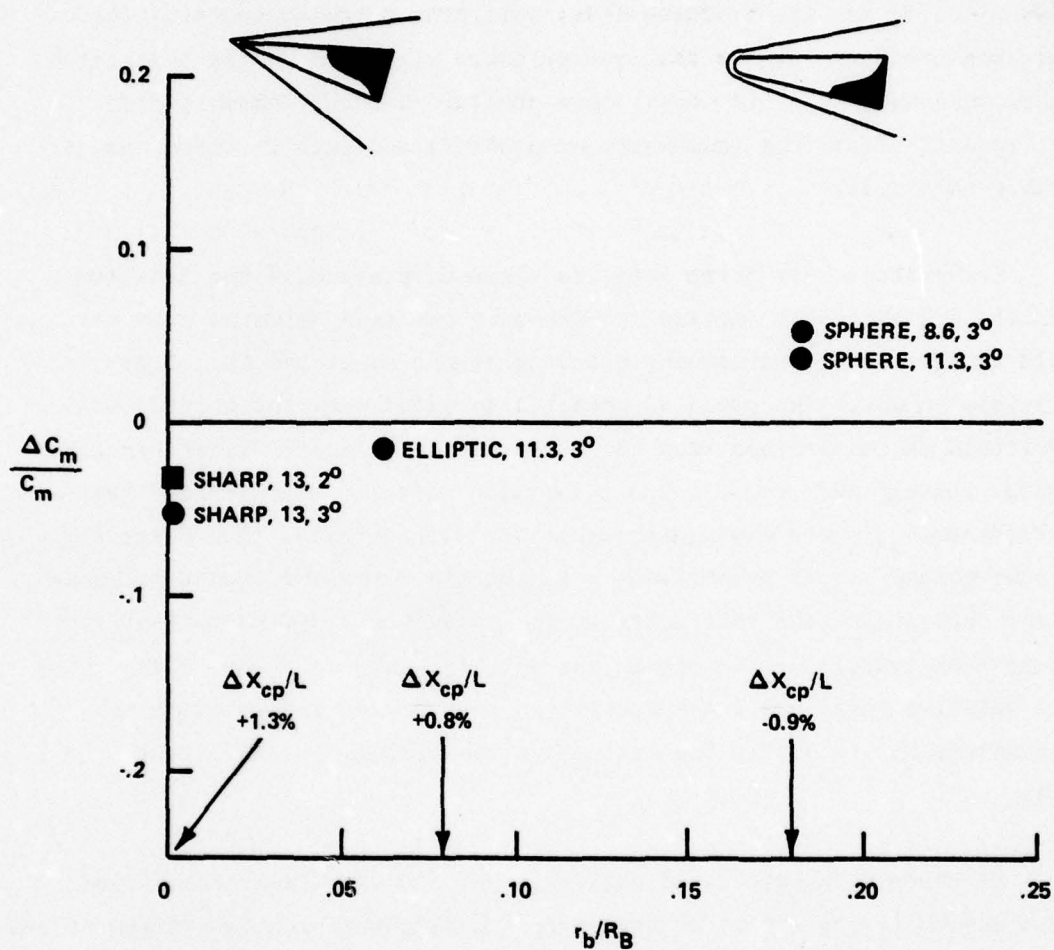
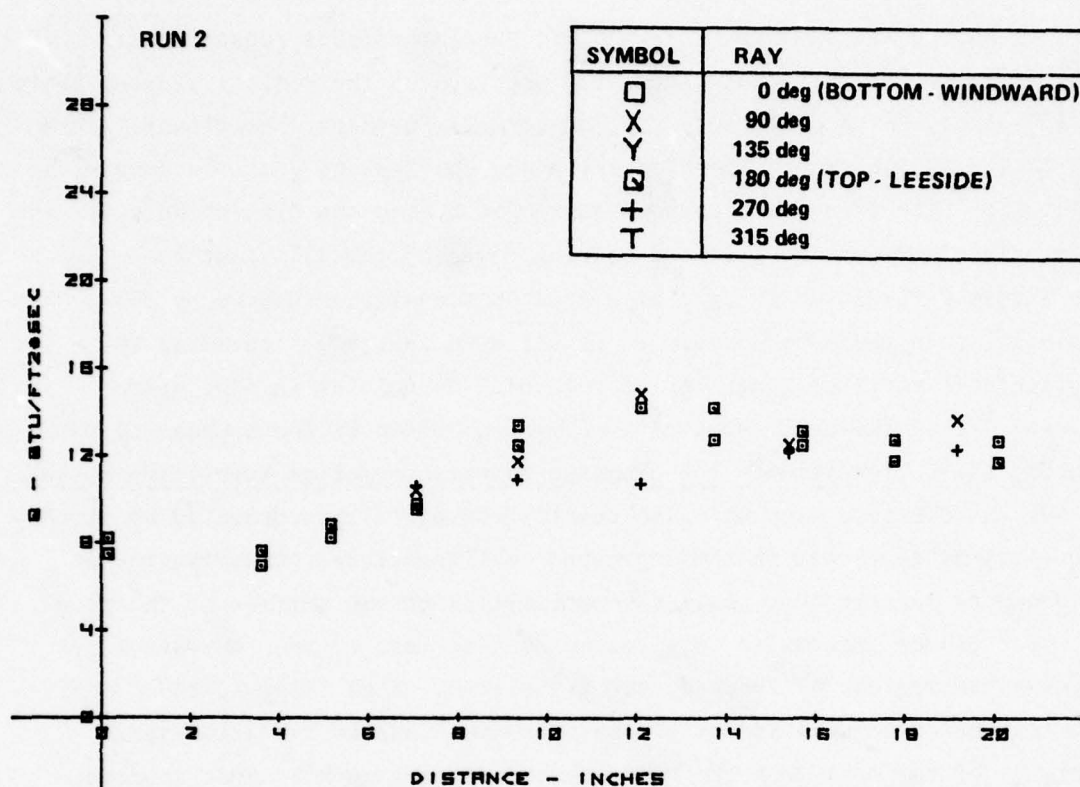


Figure 2-95 VARIATION OF THE MAXIMUM TRANSITION-INDUCED INCREMENT IN PITCHING MOMENT (ABOUT THE BASE) WITH BLUNTNESS RATIO FOR A 6° CONE

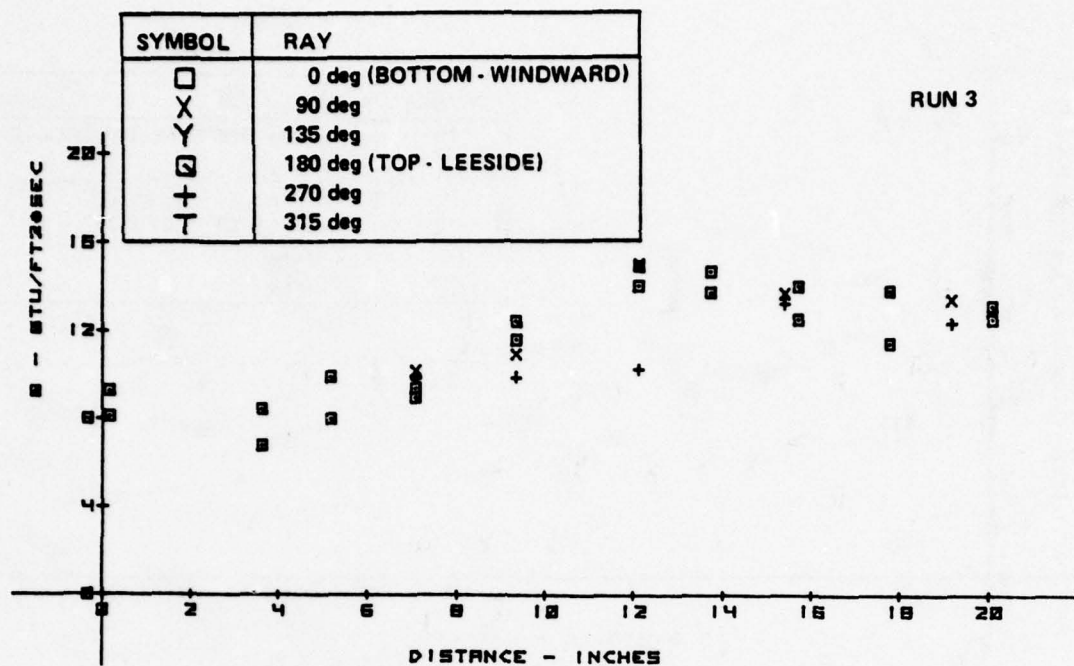
During the studies of asymmetric shaping effects (described in Section 3), we observed that transition occurred on the conical frustum behind the 45° blunt, NRV and RTE nose tips at Reynolds numbers significantly less than those for the smooth spherically-capped configuration of the same bluntness ratio. The transition regions developed behind the discontinuities at the interactions between the flat and beveled faces of the 45°-blunt nose tip (see Figure 2-71) is an example of a frustum transition induced by discontinuities in the nose shape. It is believed that the streamwise (or longitudinal) vortices generated at such discontinuities in nose shape directly excite the basic vortical instability modes of the boundary layer, inducing early transition. The dramatic forward moment of transition behind the NRV and RTE nose tips may also result from excitation promoted by streamwise vortices developed in these grooved configurations. Clearly, these measurements suggest that small discontinuities in the surface of the nose tip which induce streamwise vortices could also lead to the generation of wedge-shaped regions of "body-fixed" transition. Such "body-fixed" transition regions could well induce greater perturbations in the aerodynamic stability of the cone than the "wind-fixed" regions we have just studied.



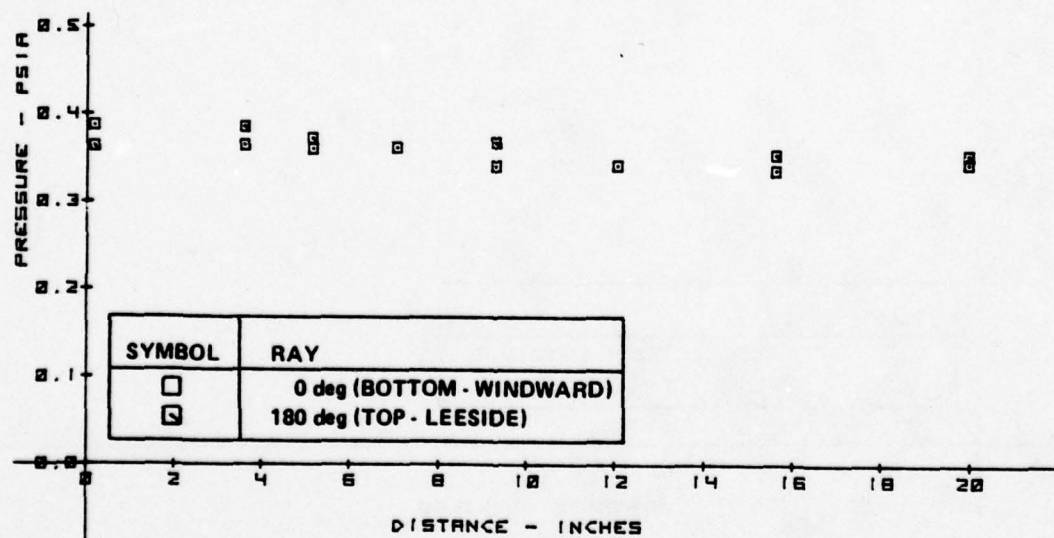


a. HEAT TRANSFER DISTRIBUTION

Figure 2-3 MEASUREMENTS ON 6° CONE MODEL FOR SHARP NOSE CONFIGURATION -  
 $M_{\infty} = 13.0$ ,  $Re/FT = 4.8 \times 10^6$ ,  $\alpha = 0^\circ .7'$

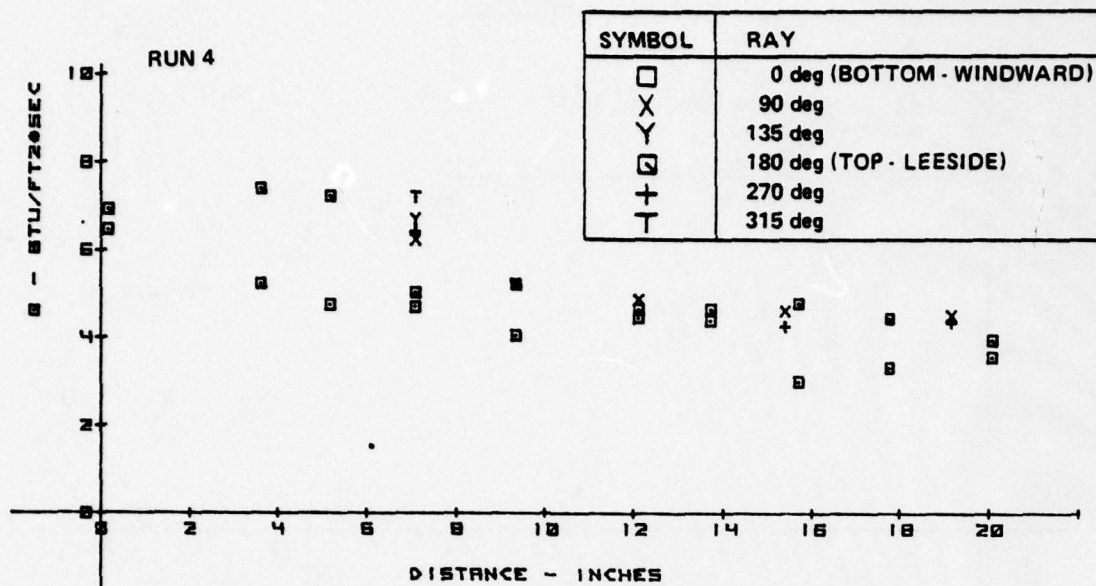


a. HEAT TRANSFER DISTRIBUTION

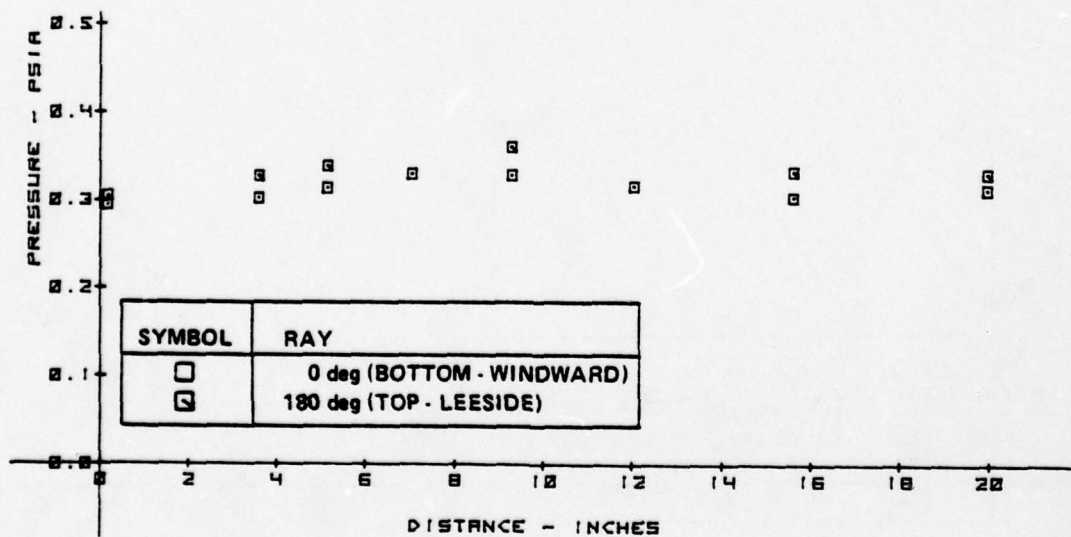


b. PRESSURE DISTRIBUTION

Figure 2-4 MEASUREMENTS ON 6° CONE MODEL FOR SHARP NOSE CONFIGURATION -  $M_\infty = 13.0$ ,  $Re/FT = 4.7 \times 10^6$ ,  $\alpha = 0^\circ .7'$



a. HEAT TRANSFER DISTRIBUTION



b. PRESSURE DISTRIBUTION

Figure 2-5 MEASUREMENT ON 6° CONE MODEL FOR 6% SPHERICAL NOSE -  
 $M_{\infty} = 13.0$ ,  $Re/FT = 4.58 \times 10^6$ ,  $\alpha = 0^\circ - 7^\circ$



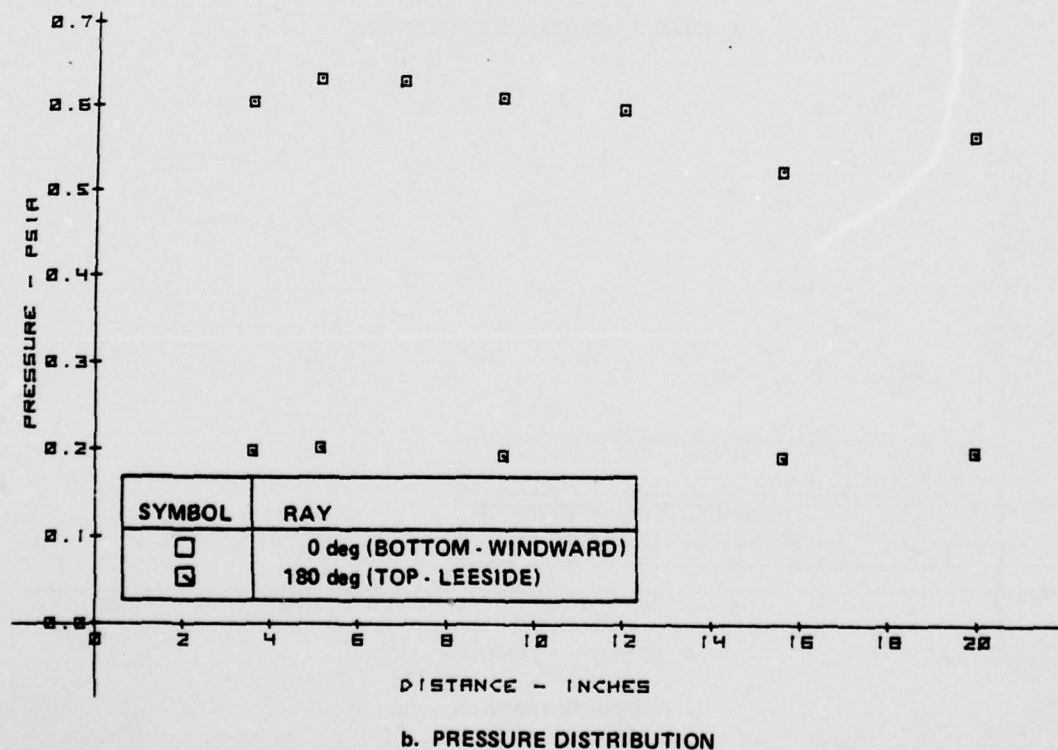
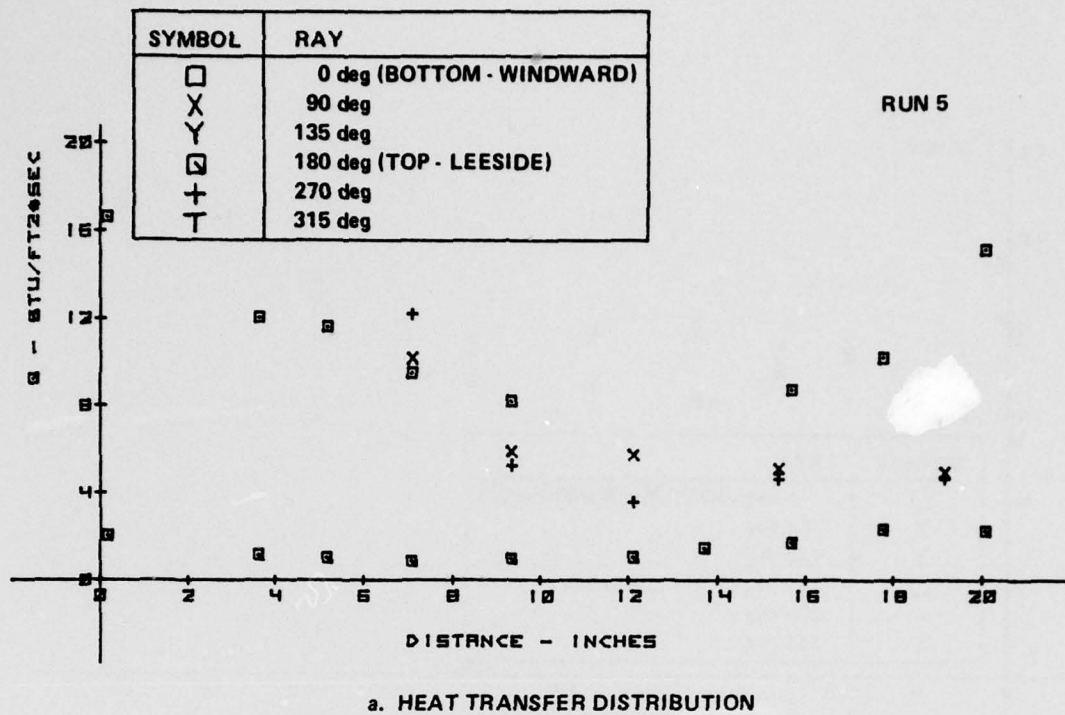
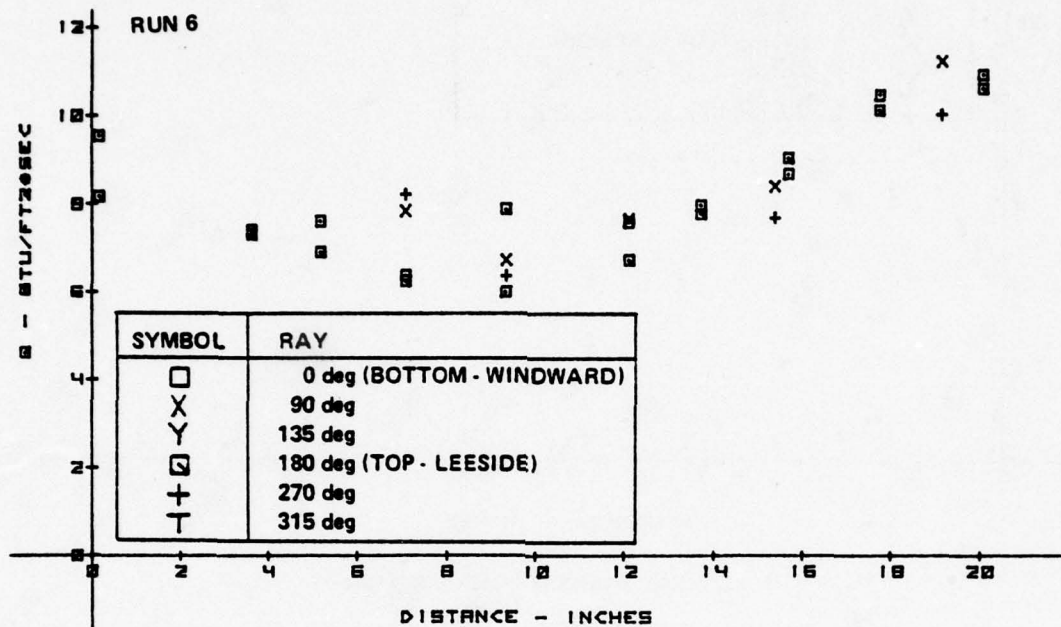
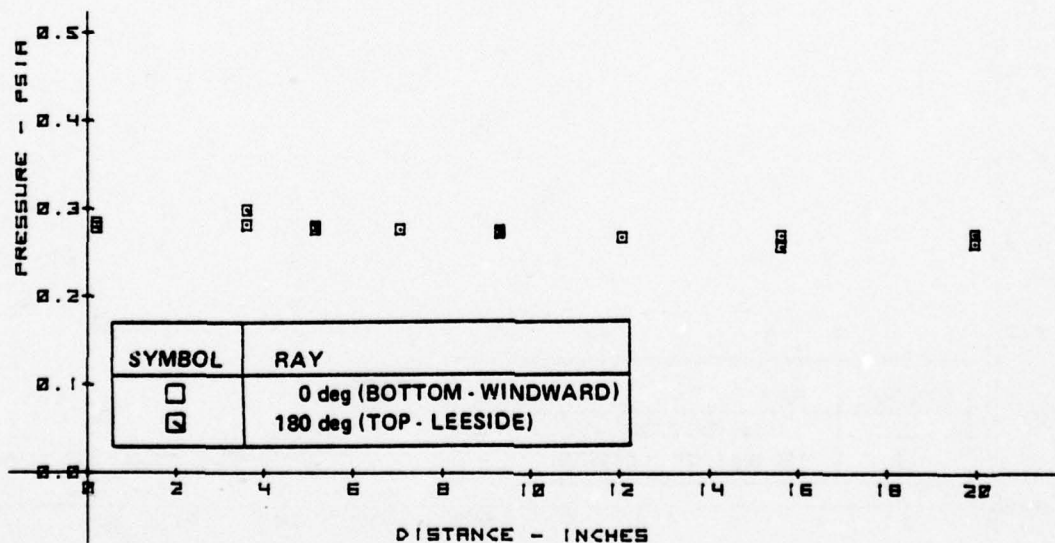


Figure 2-6 MEASUREMENT ON 6° CONE MODEL FOR 6% SPHERICAL NOSE —  
 $M_{\infty} = 13.0$ ,  $Re/FT = 5.0 \times 10^6$ ,  $\alpha = 3^{\circ} 3'$

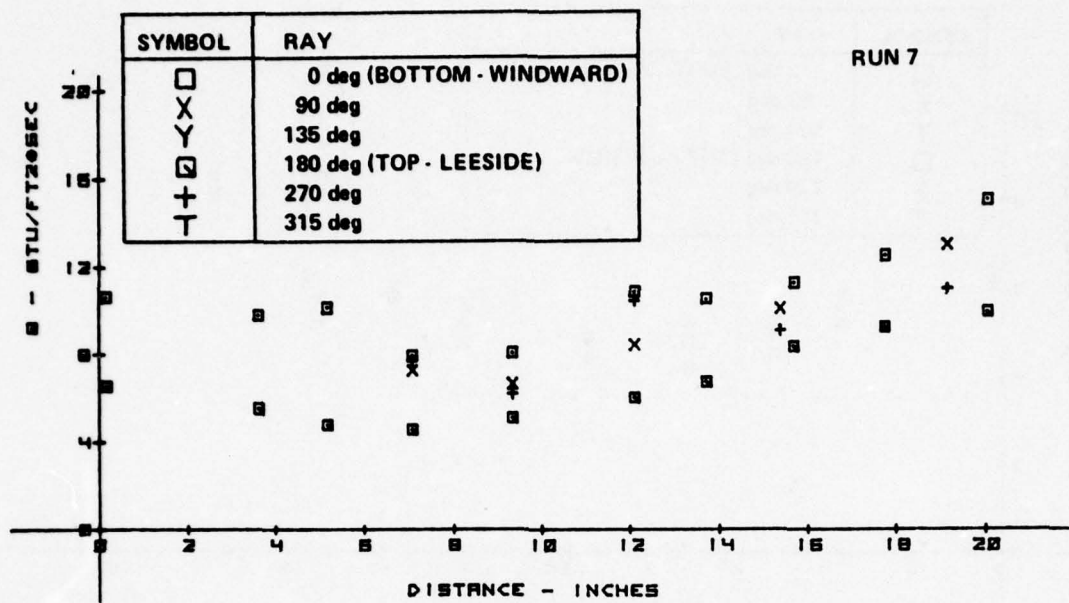


a. HEAT TRANSFER DISTRIBUTION

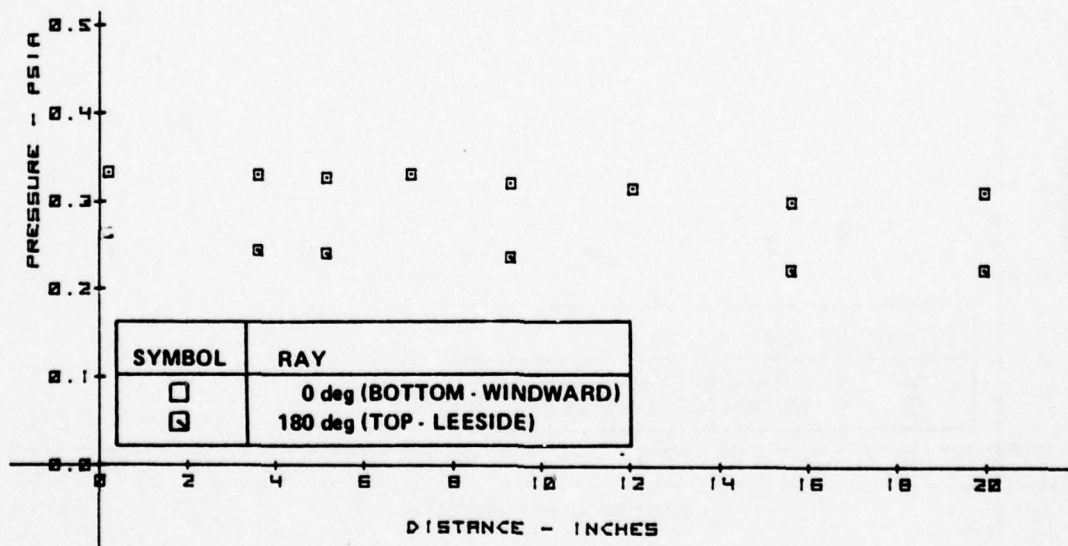


b. PRESSURE DISTRIBUTION

Figure 2-7 MEASUREMENTS ON 6° CONE MODEL FOR SHARP NOSE CONFIGURATION -  $M_\infty = 13.3$ ,  $Re/FT = 3.1 \times 10^6$ ,  $\alpha = 0^\circ$



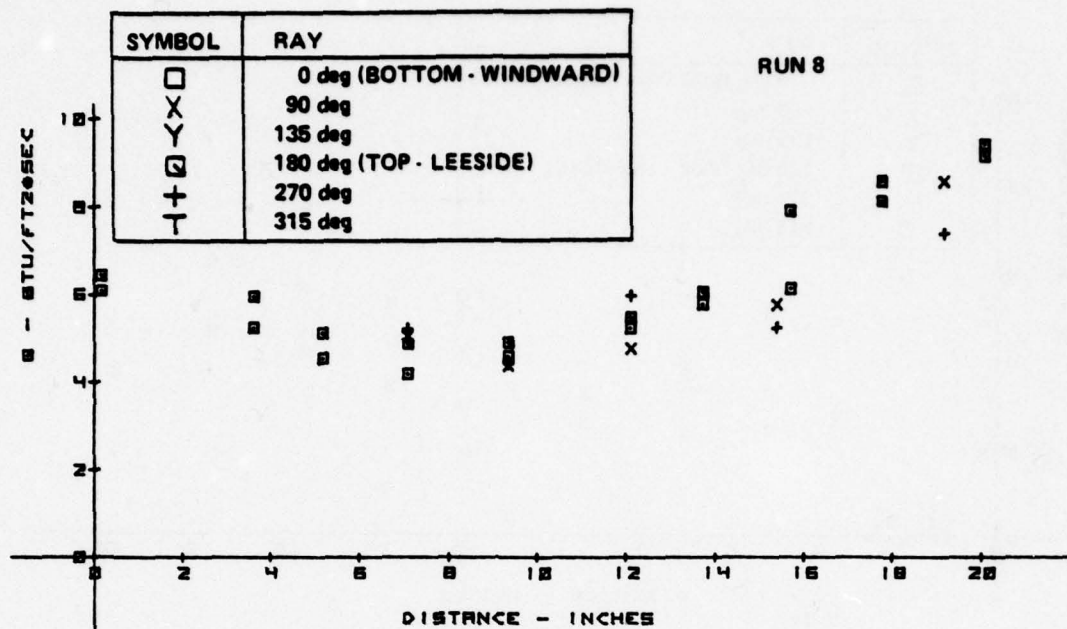
a. HEAT TRANSFER DISTRIBUTION



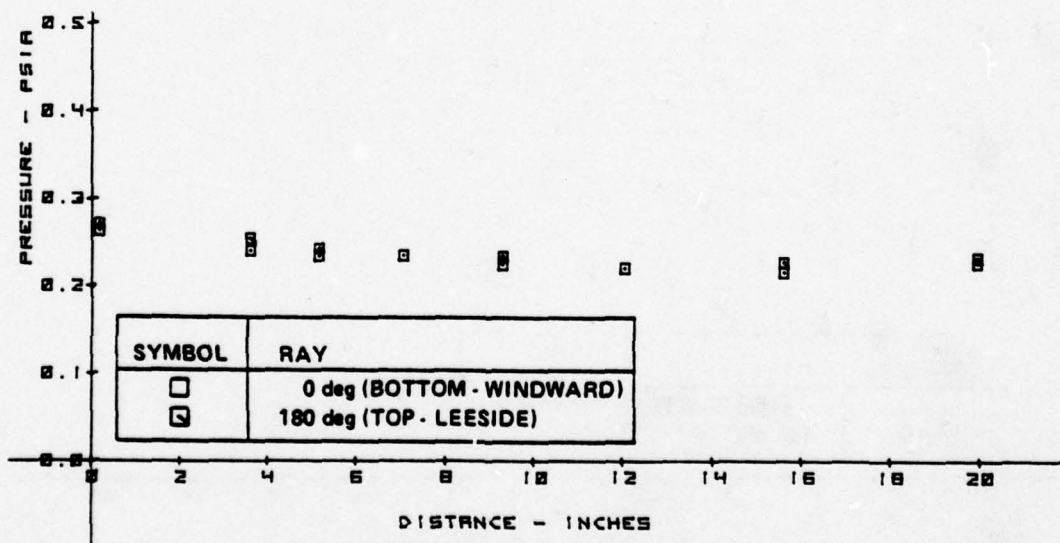
b. PRESSURE DISTRIBUTION

Figure 2-8 MEASUREMENTS ON 6° CONE MODEL FOR SHARP NOSE CONFIGURATION -  $M_\infty = 13.4$ ,  $Re/FT = 3 \times 10^6$ ,  $\alpha = 0^\circ 57'$



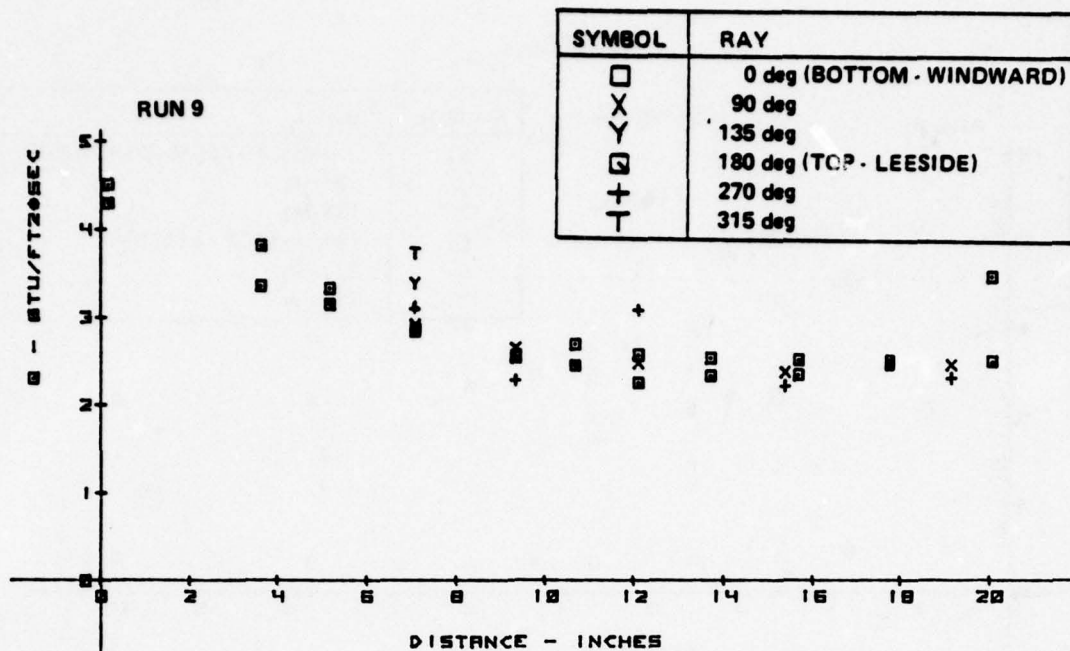


a. HEAT TRANSFER DISTRIBUTION

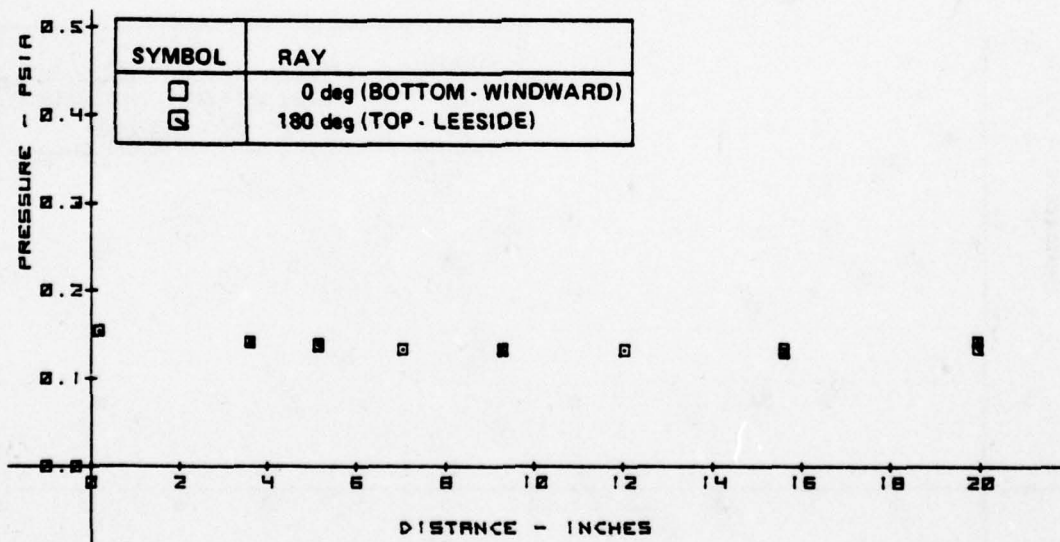


b. PRESSURE DISTRIBUTION

Figure 2-9 MEASUREMENTS ON 6° CONE MODEL FOR SHARP NOSE CONFIGURATION -  
 $M_\infty = 12.7$ ,  $Re/FT = 3 \times 10^6$ ,  $\alpha = 0^\circ - 2'$

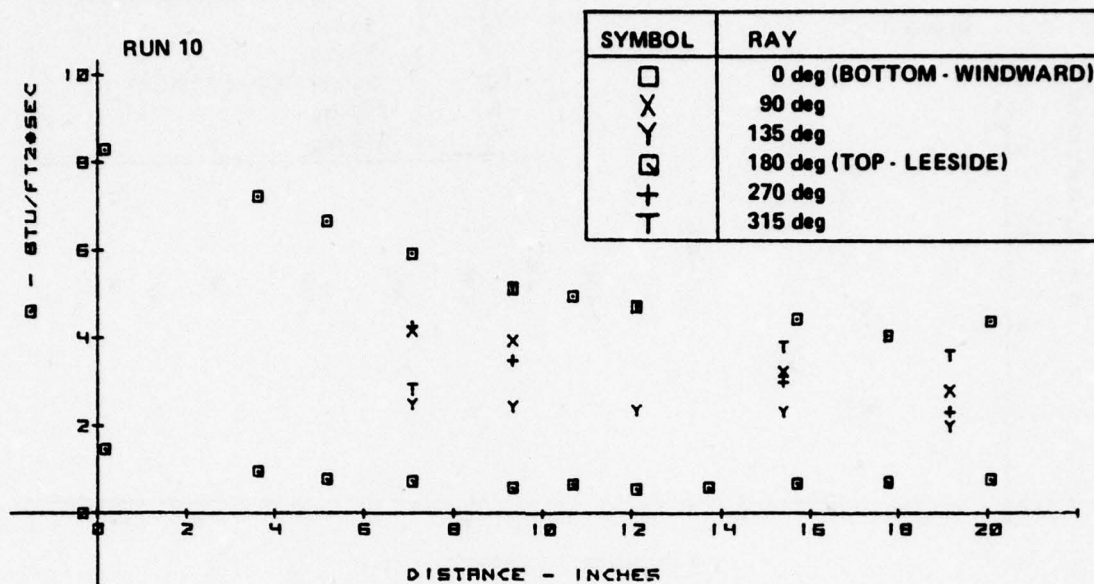


a. HEAT TRANSFER DISTRIBUTION

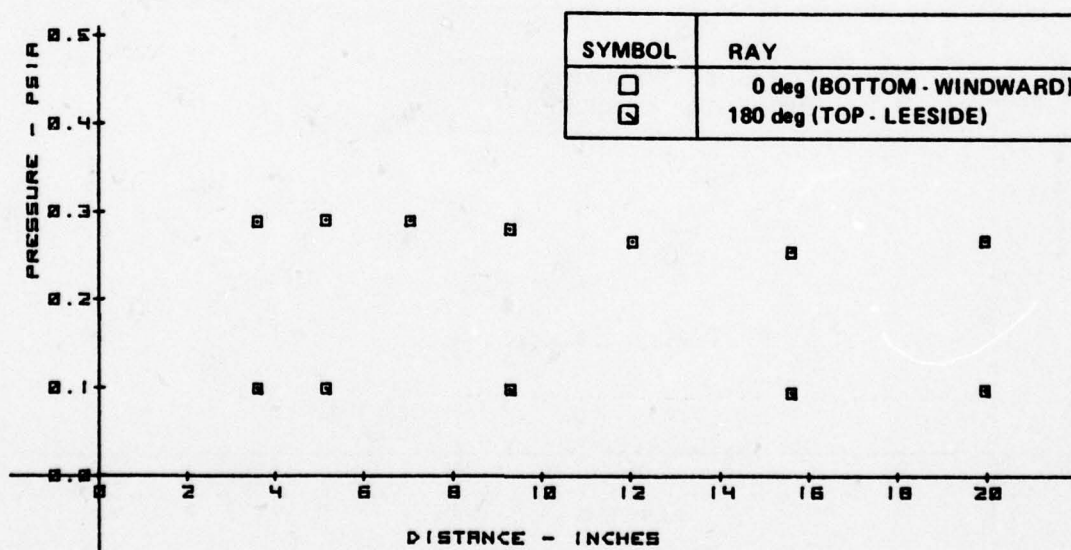


b. PRESSURE DISTRIBUTION

Figure 2-10 MEASUREMENTS ON 6° CONE MODEL FOR SHARP NOSE CONFIGURATION -  
 $M_\infty = 12.4$ ,  $Re/FT = 1.8 \times 10^6$ ,  $\alpha = 0^\circ$



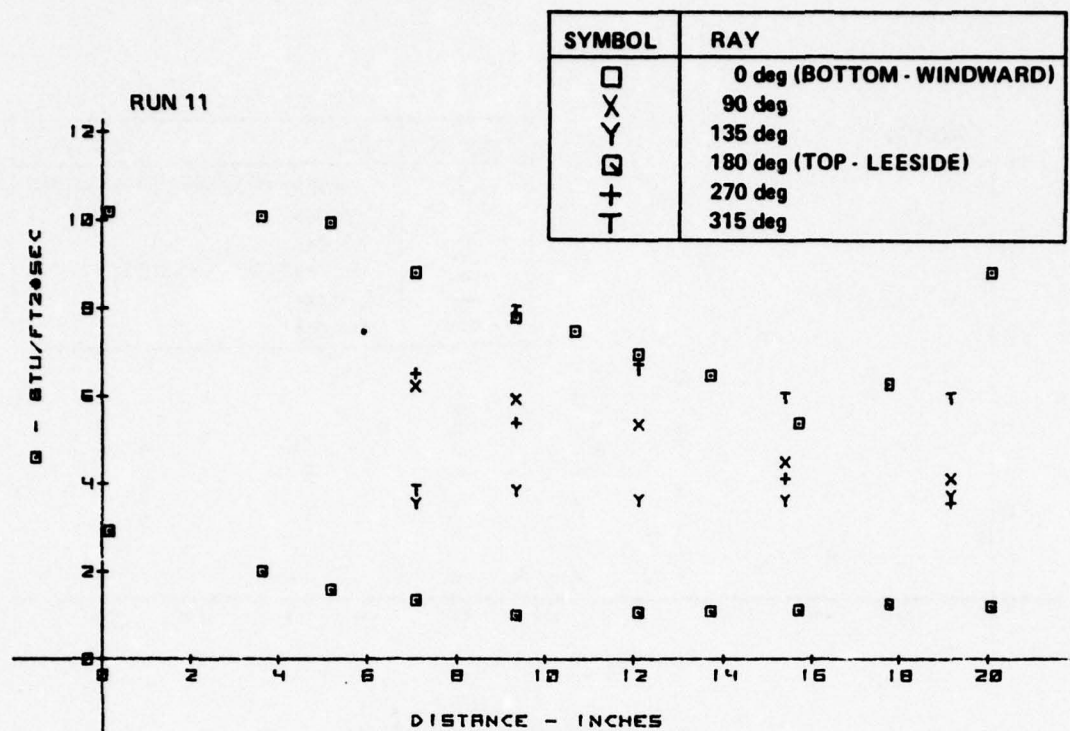
a. HEAT TRANSFER DISTRIBUTION



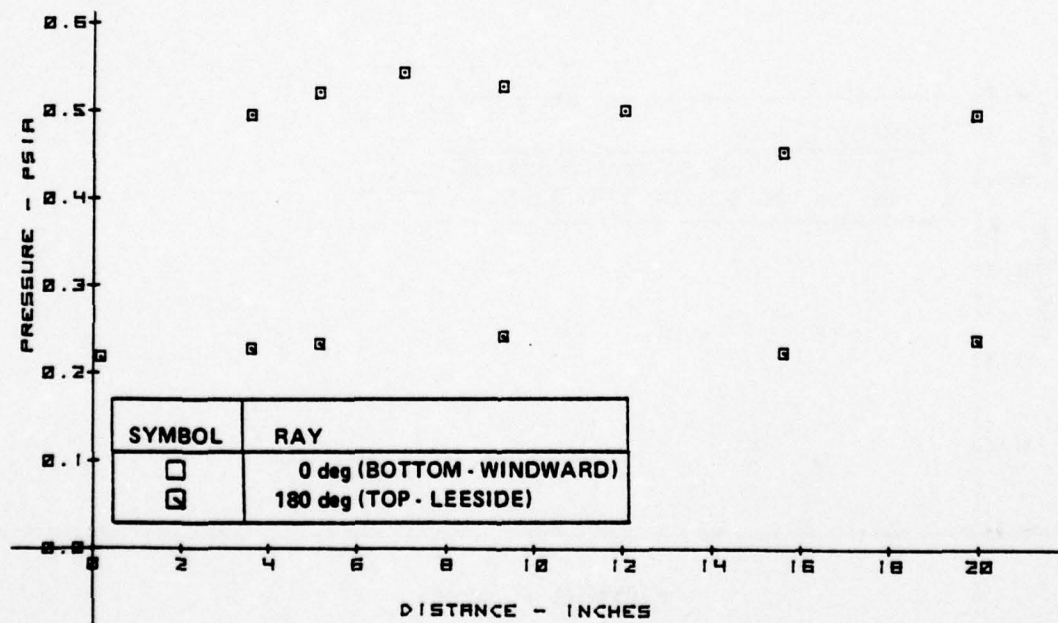
b. PRESSURE DISTRIBUTION

Figure 2-11 MEASUREMENT ON 6° CONE MODEL FOR 6% SPHERICAL NOSE -  
 $M_\infty = 12.5$ ,  $Re/FT = 2.3 \times 10^6$ ,  $\alpha = 2^\circ 59'$



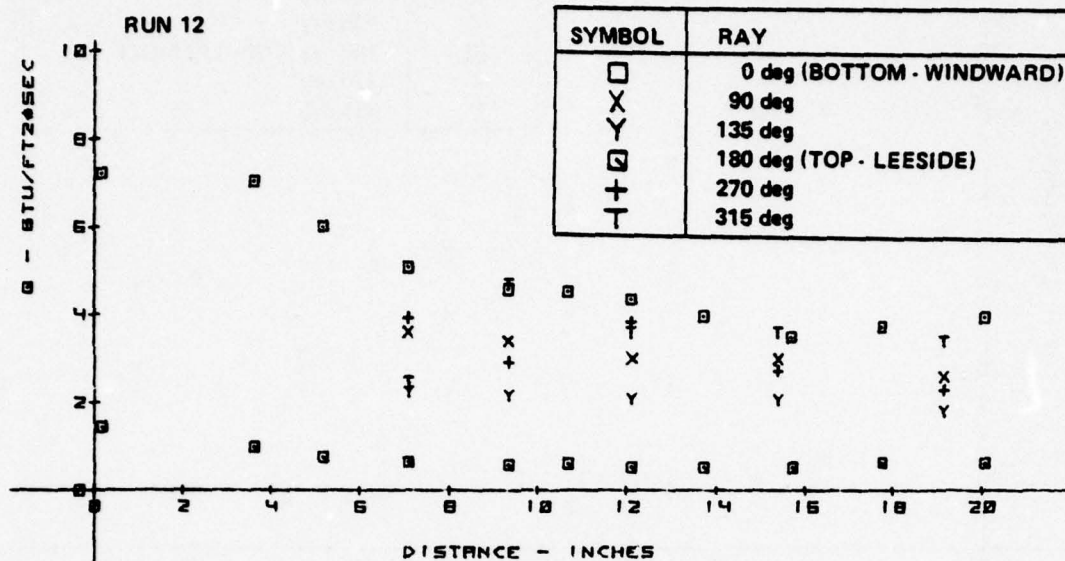


a. HEAT TRANSFER DISTRIBUTION

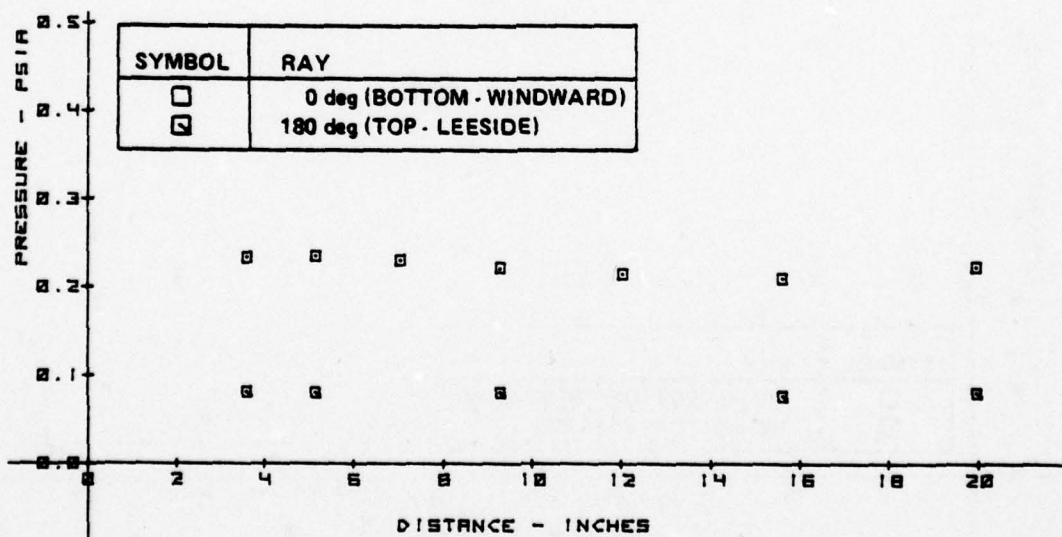


b. PRESSURE DISTRIBUTION

Figure 2-12 MEASUREMENT ON 6° CONE MODEL FOR 6% SPHERICAL NOSE -  
 $M_{\infty} = 13.0$ ,  $Re/FT = 4.9 \times 10^6$ ,  $\alpha = 2^\circ 3'$

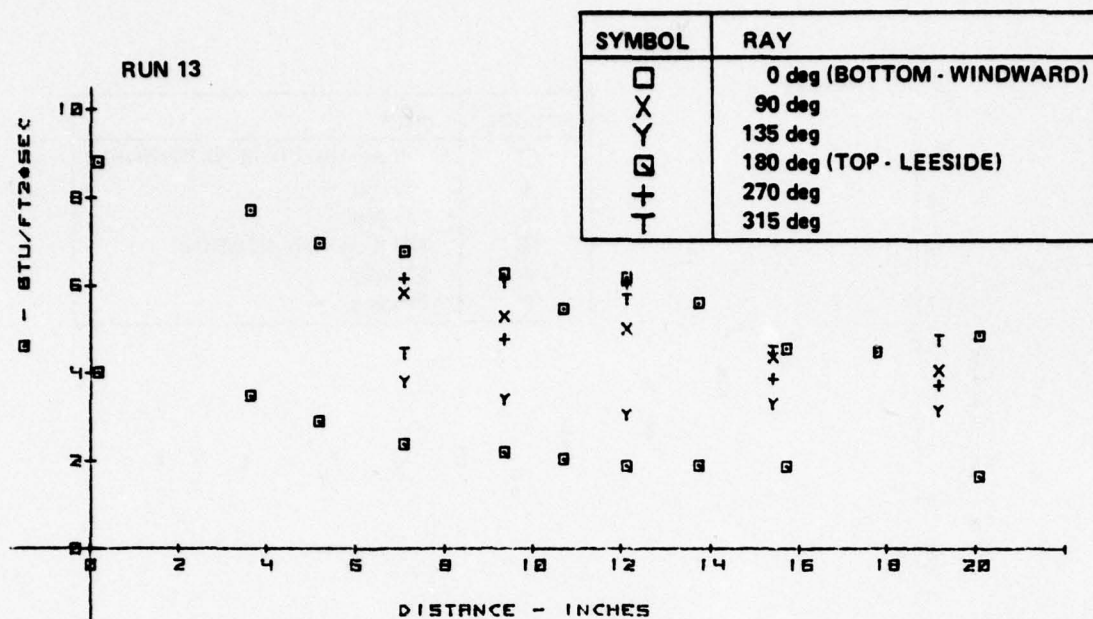


a. HEAT TRANSFER DISTRIBUTION

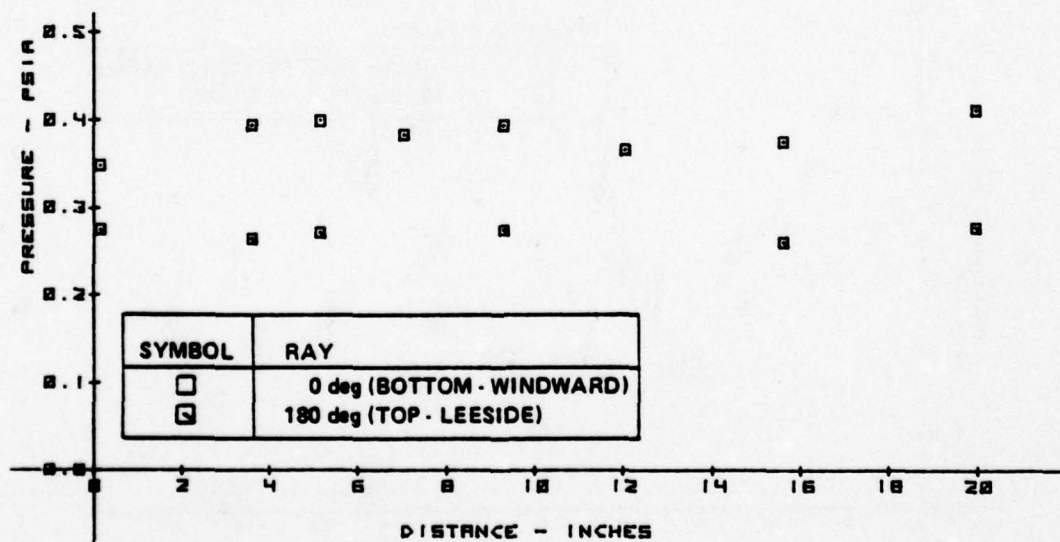


b. PRESSURE DISTRIBUTION

Figure 2-13 MEASUREMENT ON 6° CONE MODEL FOR 6% SPHERICAL NOSE -  
 $M_\infty = 12.4$ ,  $Re/FT = 1.7 \times 10^6$ ,  $\alpha = 3^\circ$



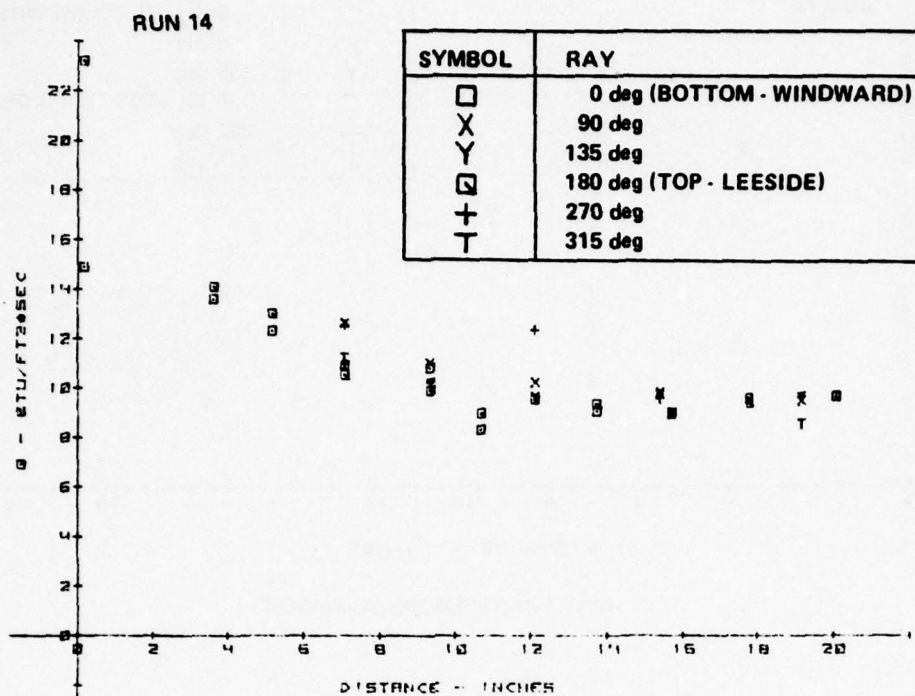
a. HEAT TRANSFER DISTRIBUTION



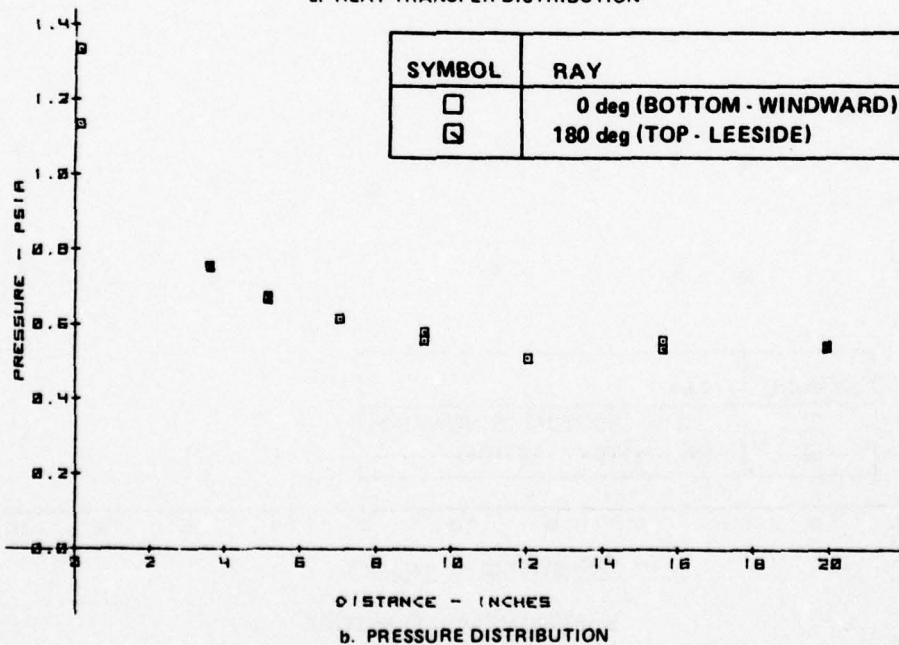
b. PRESSURE DISTRIBUTION

Figure 2-14 MEASUREMENT ON 6° CONE MODEL FOR 6% SPHERICAL NOSE -  
CONFIGURATION -  $M_\infty = 13.0$ ,  $Re/FT = 4.8 \times 10^6$ ,  $\alpha = 0^\circ 59'$



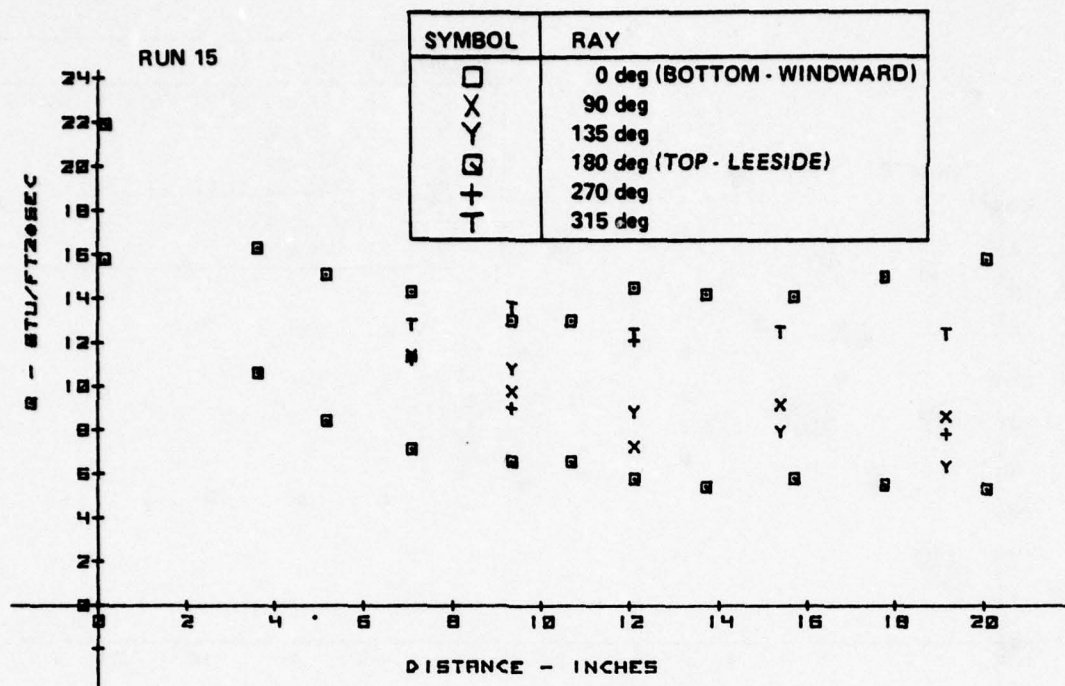


a. HEAT TRANSFER DISTRIBUTION

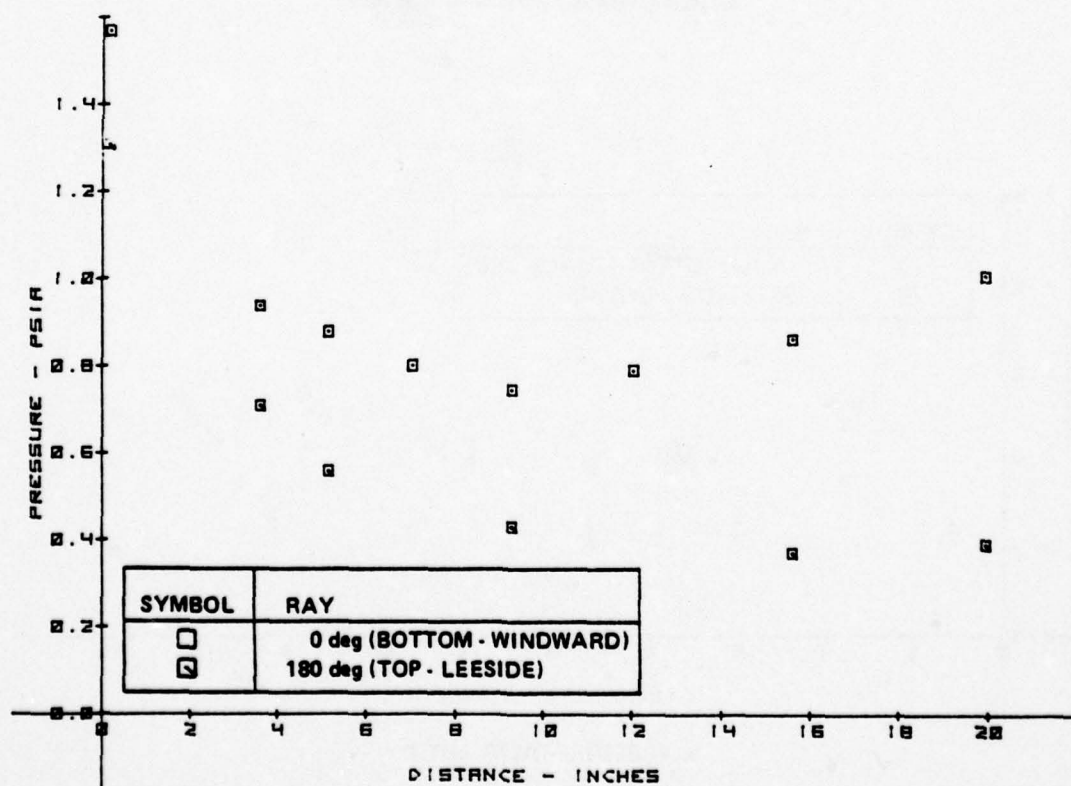


b. PRESSURE DISTRIBUTION

Figure 2-15 MEASUREMENT ON 6° CONE MODEL FOR NRV NOSE CONFIGURATION -  
 $M_{\infty} = 11.4$ ,  $Re/FT = 1.1 \times 10^7$ ,  $\alpha = 0^\circ - 2^\circ$

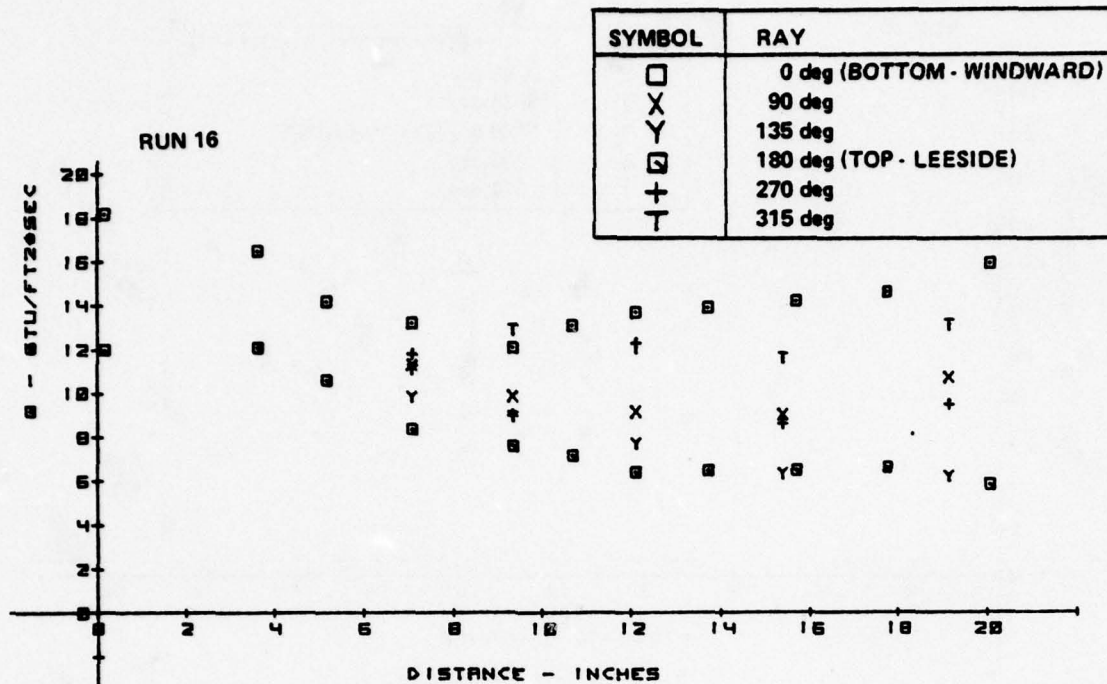


a. HEAT TRANSFER DISTRIBUTION

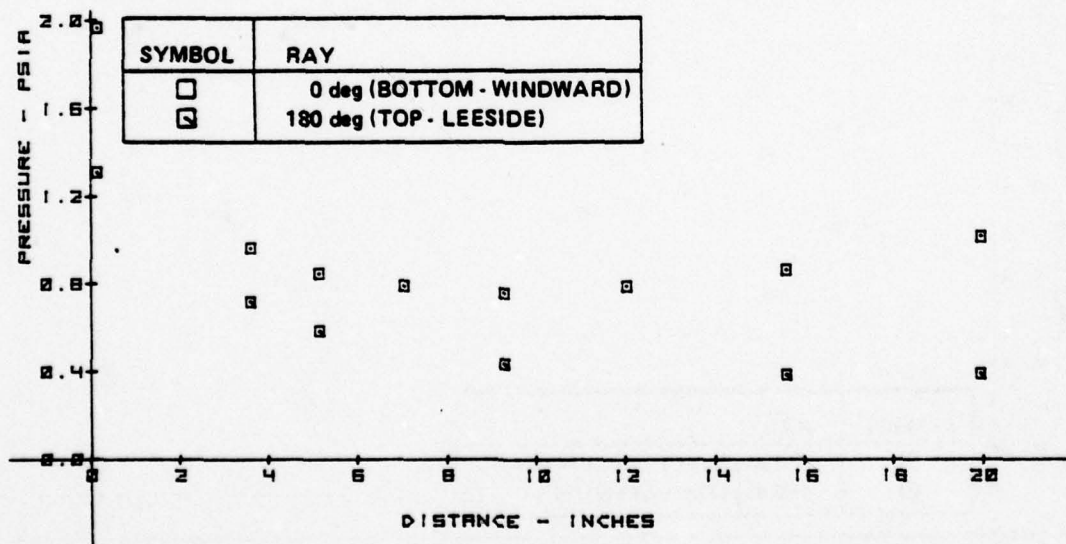


b. PRESSURE DISTRIBUTION

Figure 2-16 MEASUREMENT ON 6° CONE MODEL FOR NRV NOSE CONFIGURATION -  
 $M_\infty = 11.3$ ,  $Re/FT = 1.0 \times 10^7$ ,  $\alpha = 2^\circ 57'$



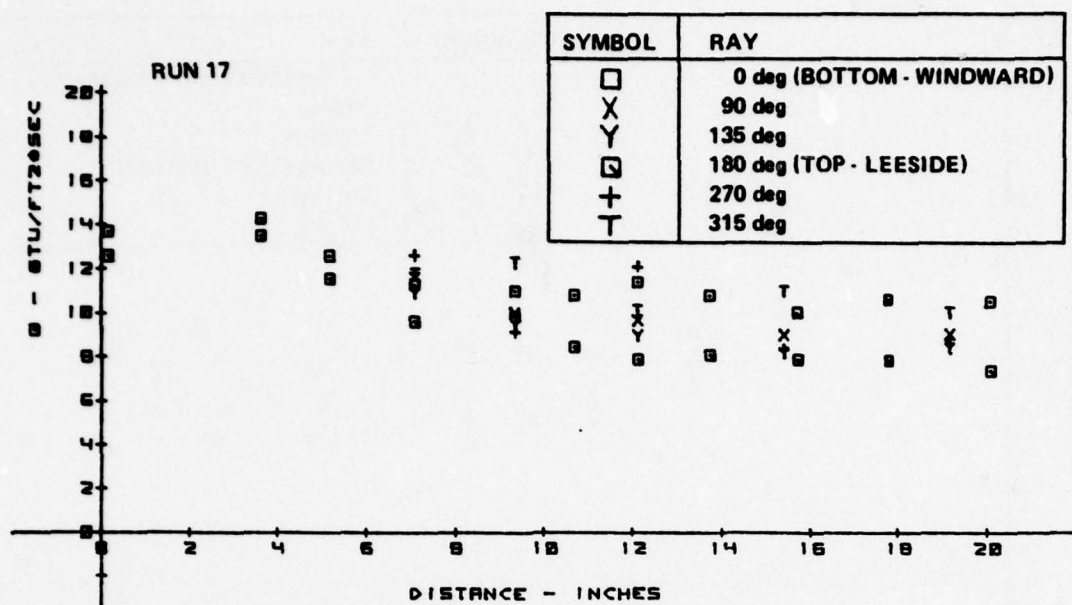
a. HEAT TRANSFER DISTRIBUTION



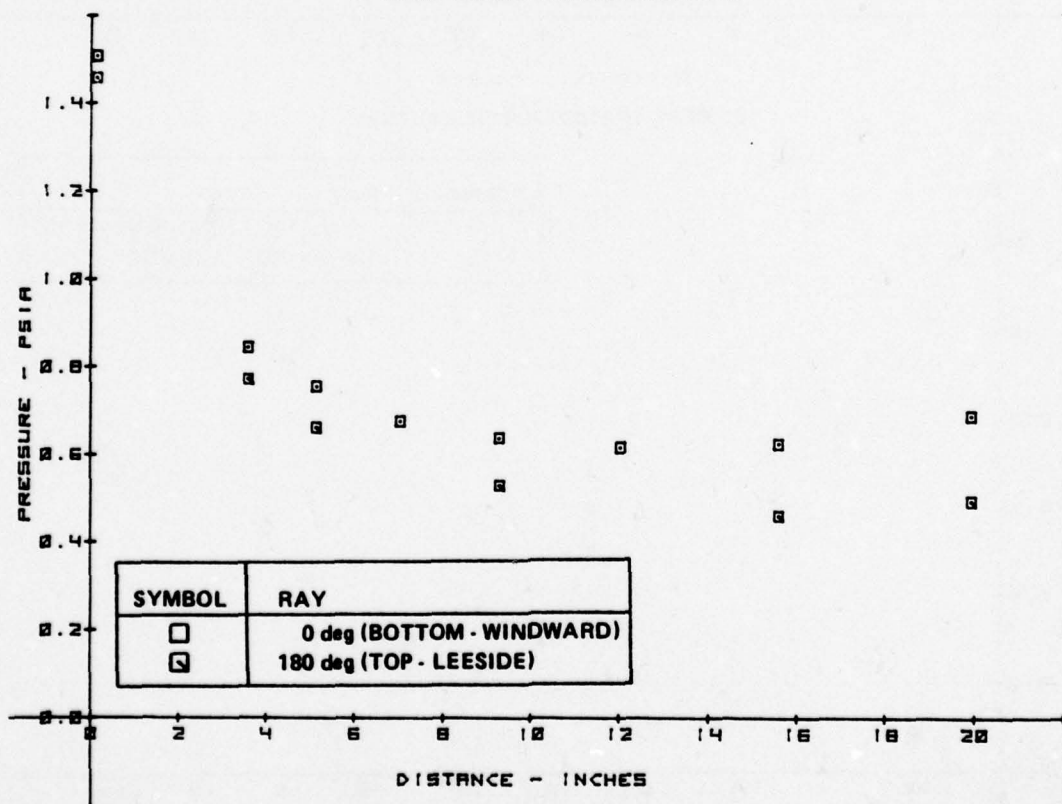
b. PRESSURE DISTRIBUTION

Figure 2-17 MEASUREMENT ON 6° CONE MODEL FOR RTE NOSE CONFIGURATION -  $M_\infty = 11.4$ ,  $Re/FT = 1.1 \times 10^7$ ,  $\alpha = 2^\circ 57'$



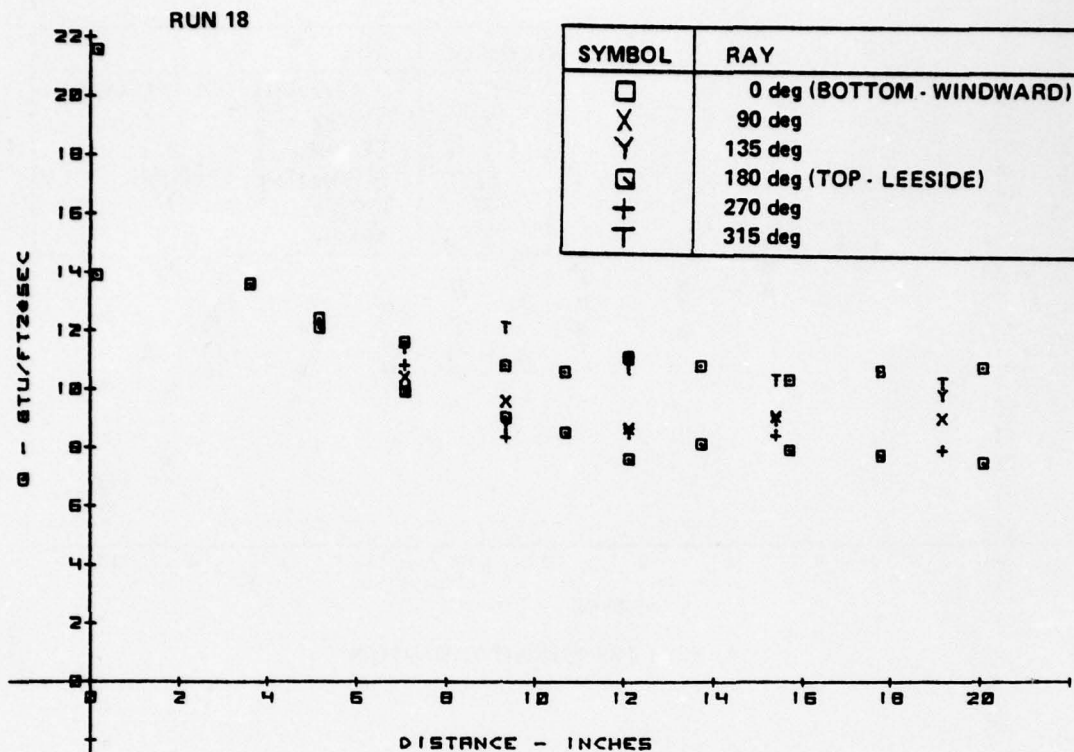


a. HEAT TRANSFER DISTRIBUTION

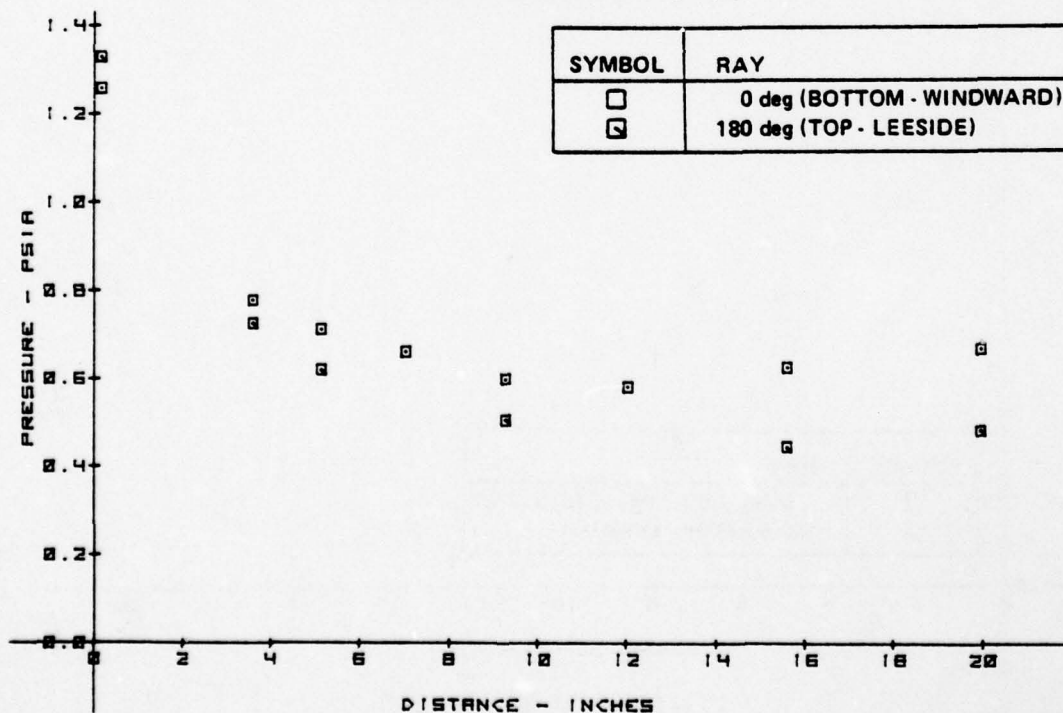


b. PRESSURE DISTRIBUTION

Figure 2-18 MEASUREMENT ON 6° CONE MODEL FOR RTE NOSE CONFIGURATION -  
 $M_{\infty} = 11.4$ ,  $Re/FT = 1.1 \times 10^7$ ,  $\alpha = 1^\circ$

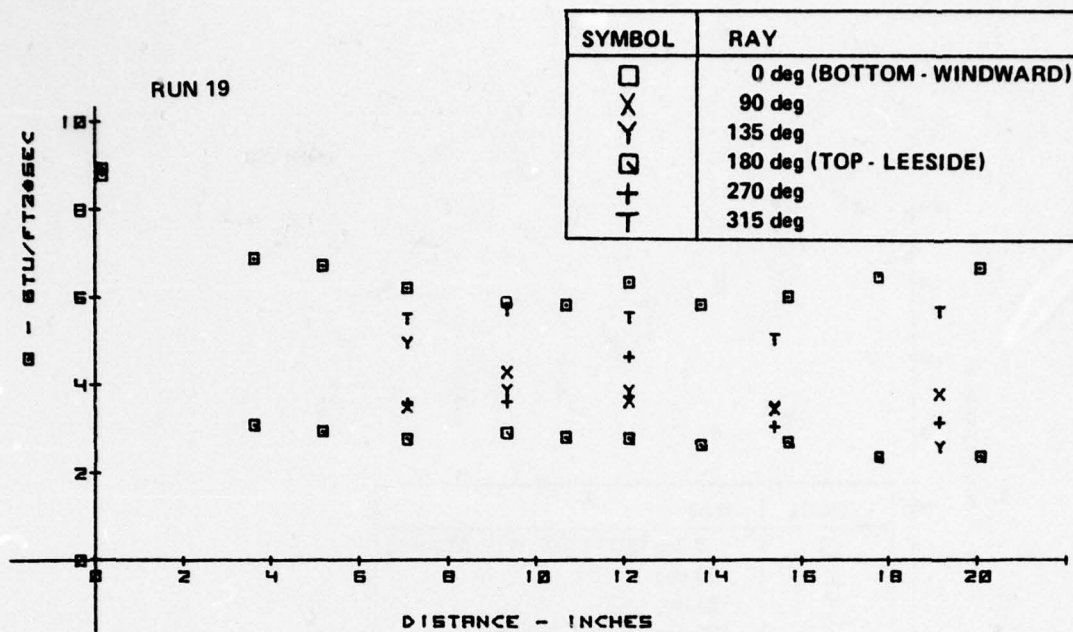


a. HEAT TRANSFER DISTRIBUTION

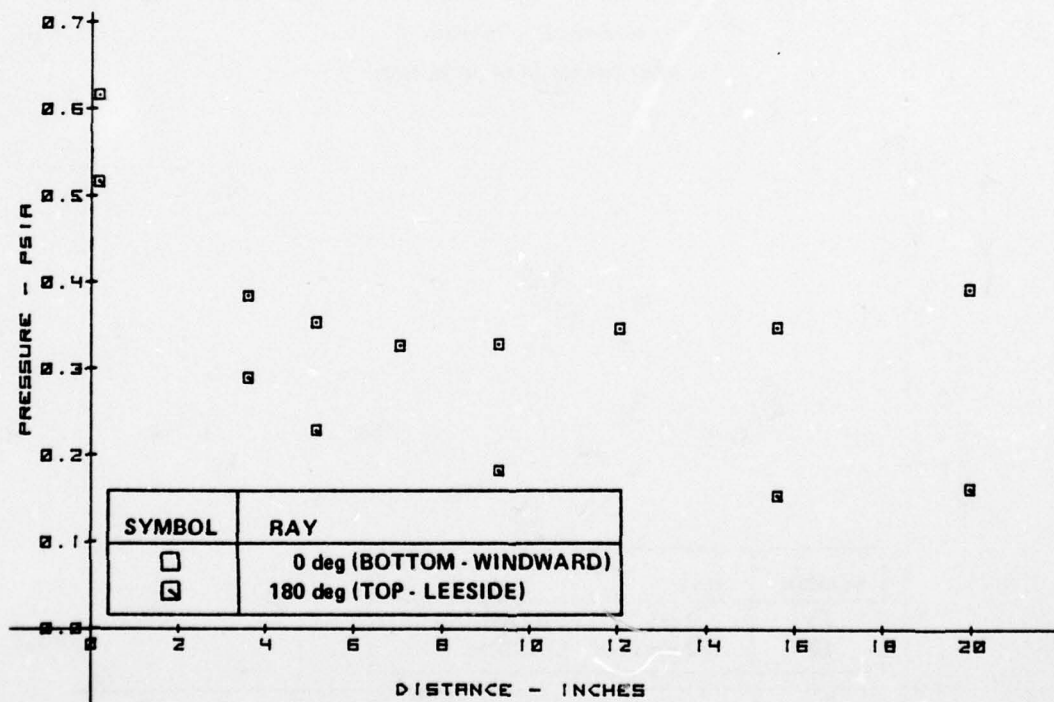


b. PRESSURE DISTRIBUTION

Figure 2-19 MEASUREMENT ON 6° CONE MODEL FOR NRV NOSE CONFIGURATION -  
 $M_\infty = 11.3$ ,  $Re/FT = 1.0 \times 10^7$ ,  $\alpha = 1^\circ$



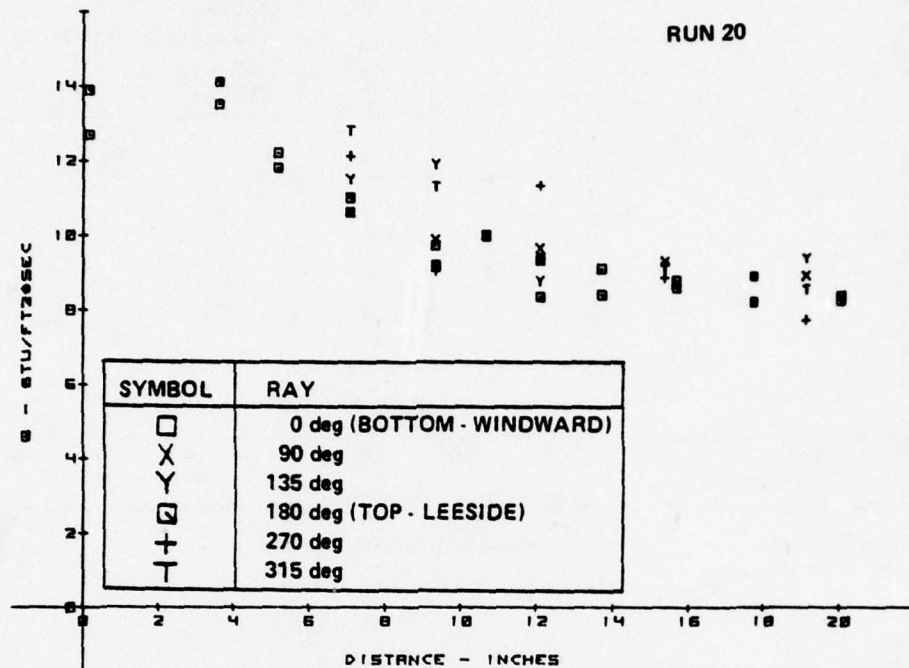
a. HEAT TRANSFER DISTRIBUTION



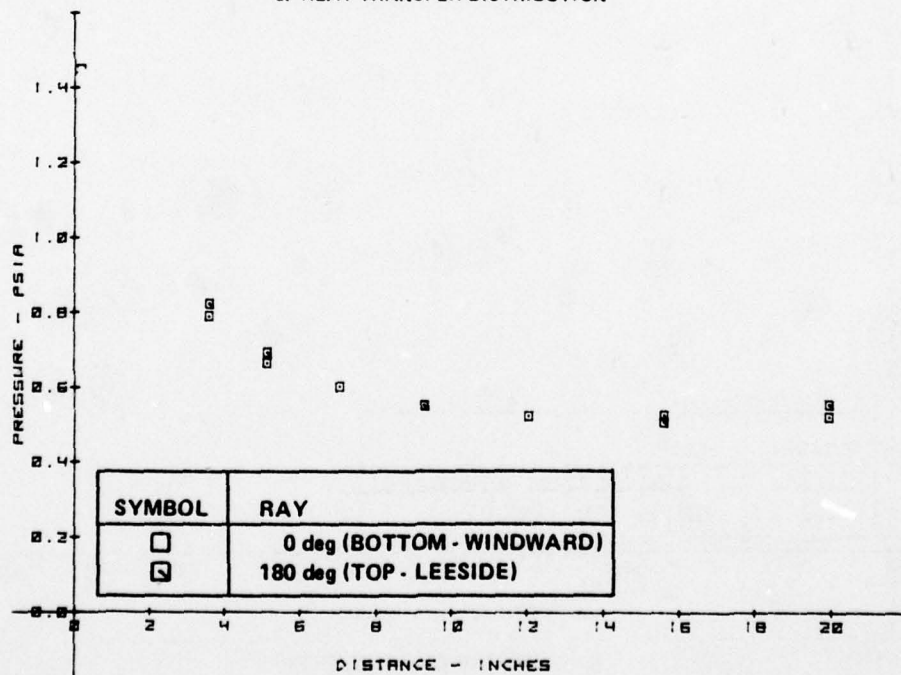
b. PRESSURE DISTRIBUTION

Figure 2-20 MEASUREMENT ON 6° CONE MODEL FOR NRV NOSE CONFIGURATION -  
 $M_\infty = 11.0$ ,  $Re/FT = 4.2 \times 10^6$ ,  $\alpha = 2^\circ 58'$



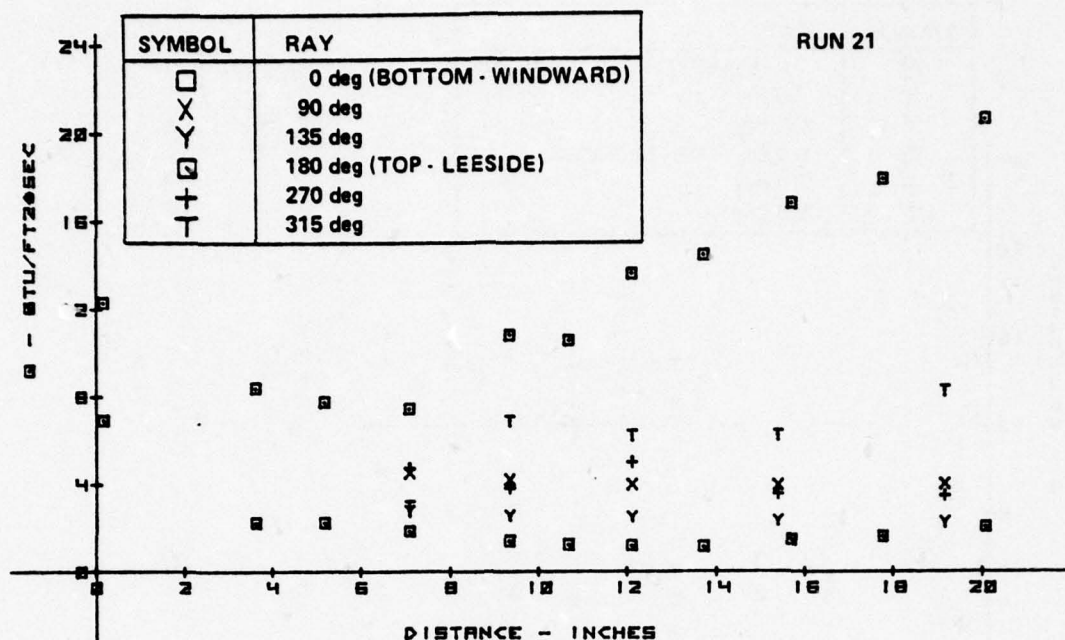


a. HEAT TRANSFER DISTRIBUTION

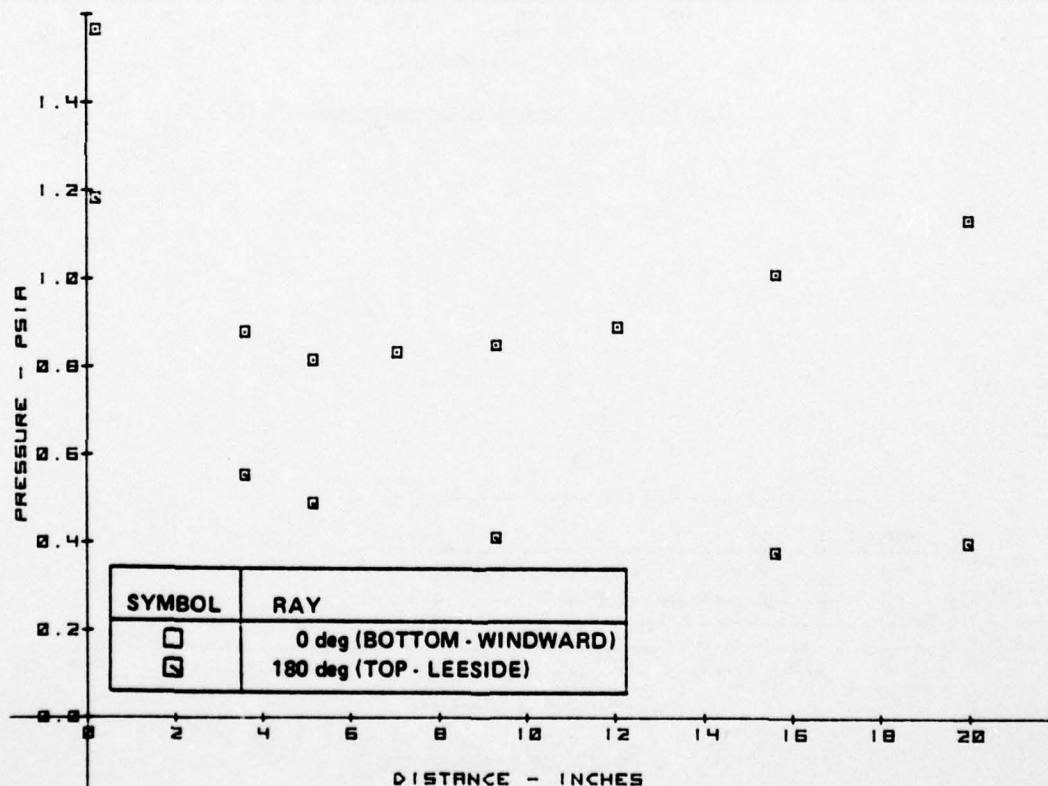


b. PRESSURE DISTRIBUTION

Figure 2-21 MEASUREMENT ON 6° CONE MODEL FOR RTE NOSE CONFIGURATION -  
 $M_\infty = 11.3$ ,  $Re/FT = 1.1 \times 10^7$ ,  $\alpha = 0^\circ 2'$

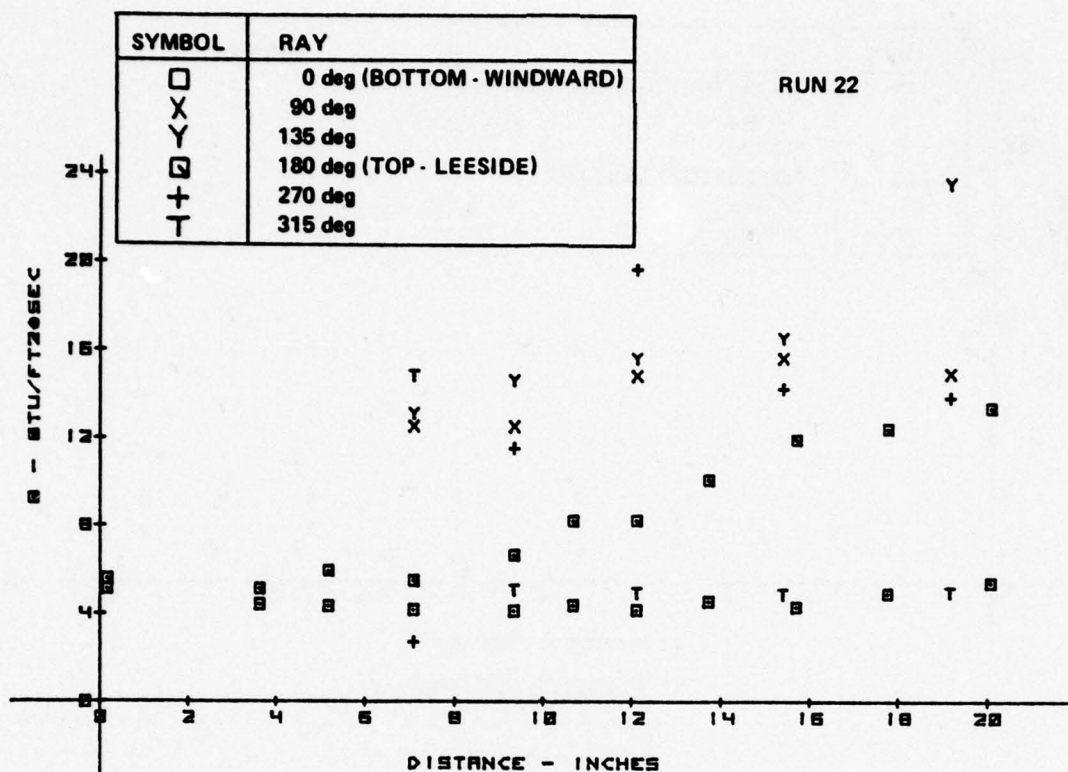


a. HEAT TRANSFER DISTRIBUTION

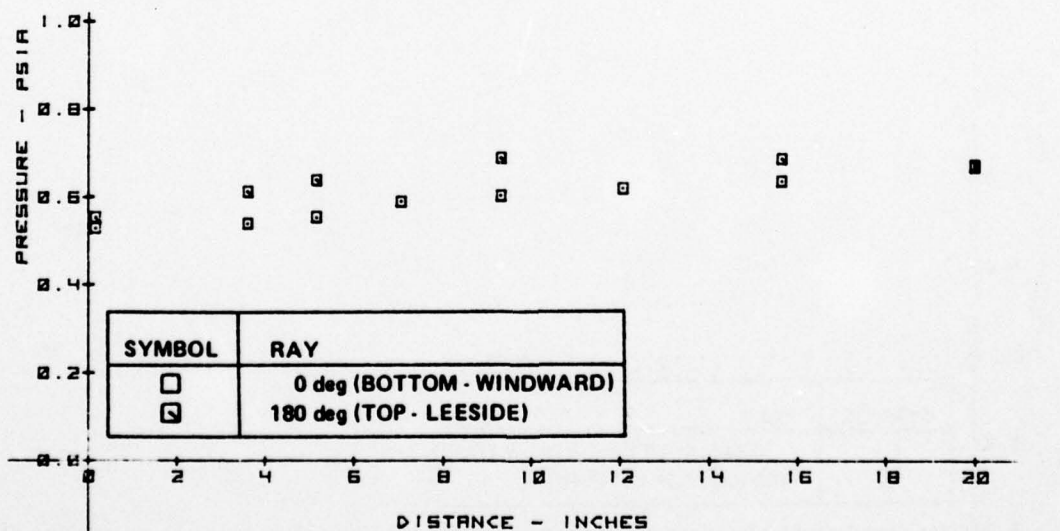


b. PRESSURE DISTRIBUTION

Figure 2-22 MEASUREMENTS ON 6° CONE MODEL FOR 21% SPHERICAL NOSE CONFIGURATION -  $M_\infty = 11.4$ ,  $Re/FT = 1.0 \times 10^7$ ,  $\alpha = 2^\circ 56'$



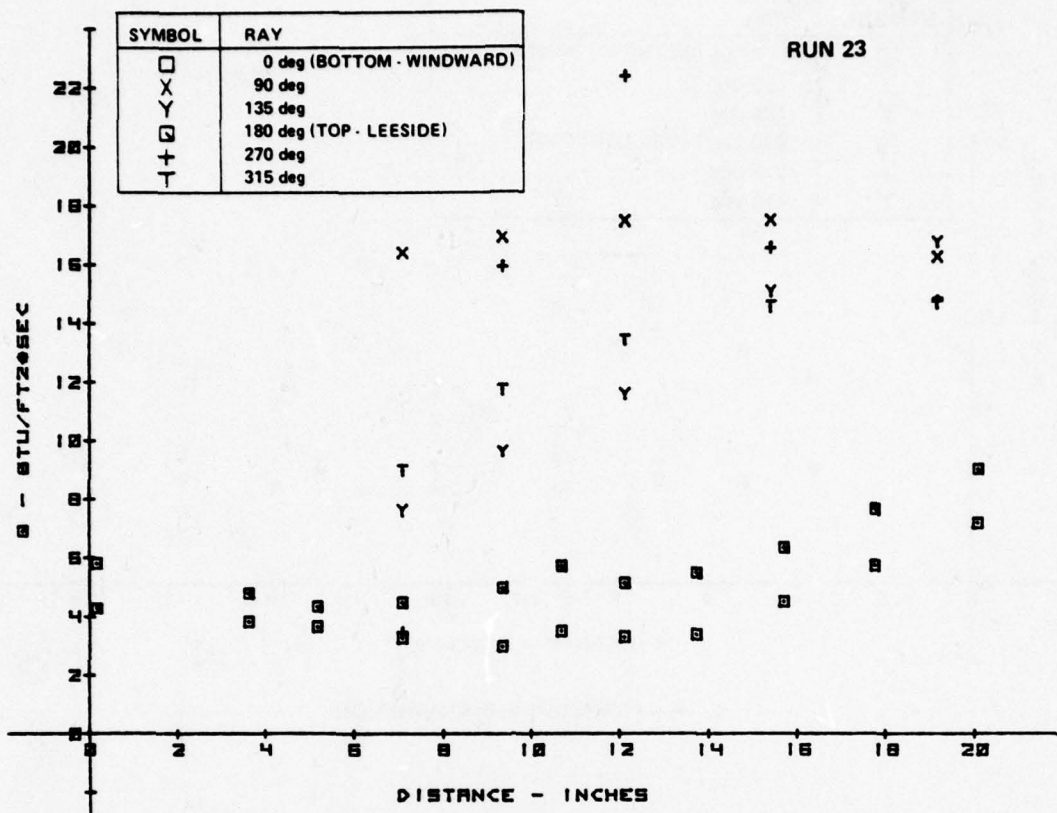
a. HEAT TRANSFER DISTRIBUTION



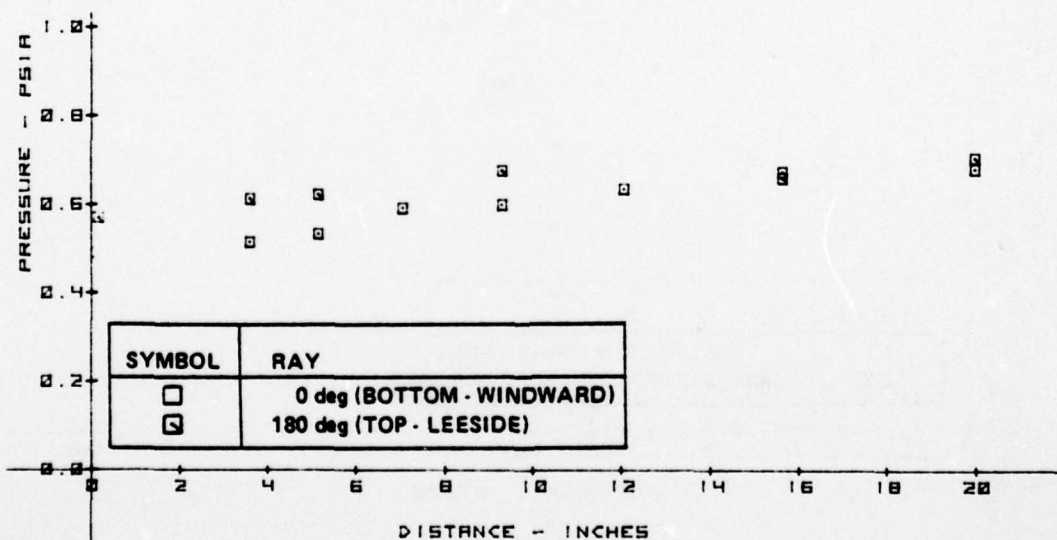
b. PRESSURE DISTRIBUTION

Figure 2-23 MEASUREMENTS ON 6° CONE MODEL FOR 6%, 0° BLUNT NOSE CONFIGURATION -  $M_\infty = 11.3$ ,  $Re/FT = 1.1 \times 10^7$ ,  $\alpha = 0^\circ$



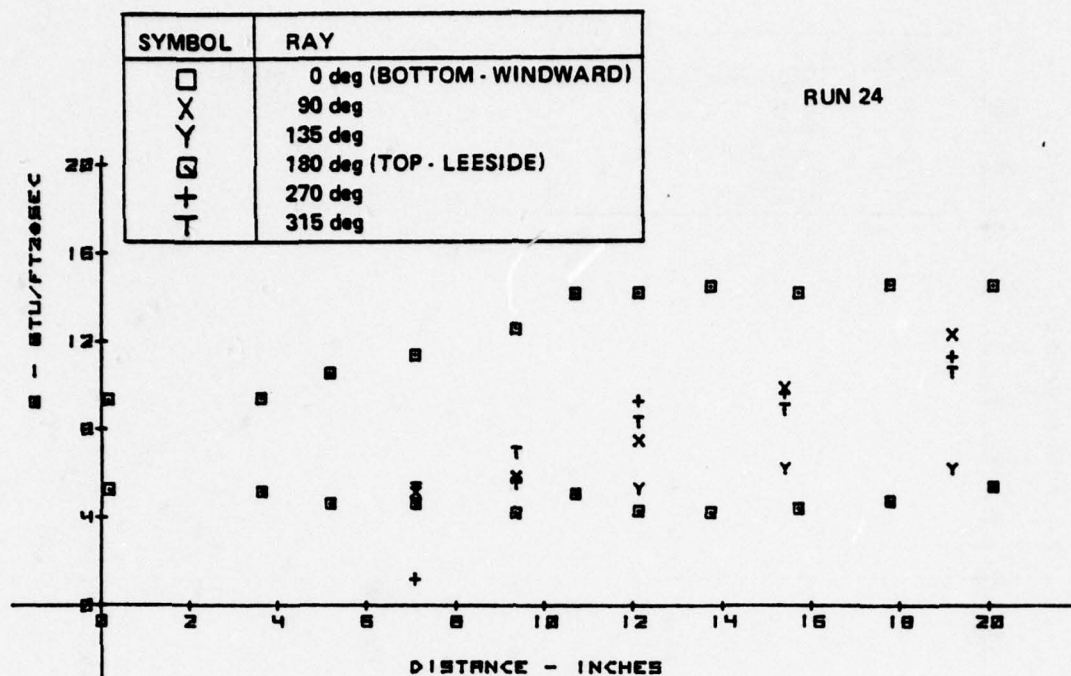


a. HEAT TRANSFER DISTRIBUTION

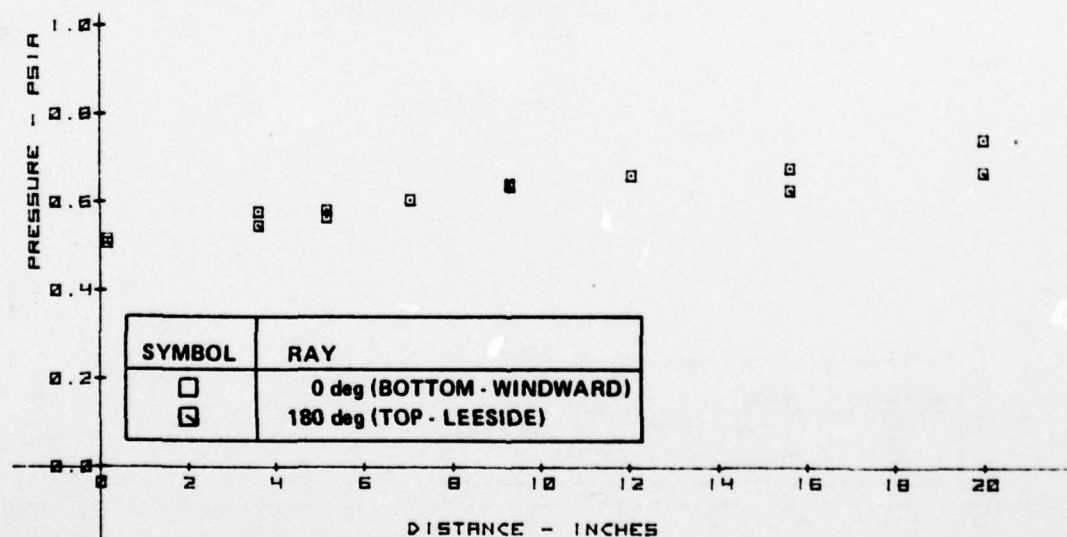


b. PRESSURE DISTRIBUTION

Figure 2-24 MEASUREMENTS ON 6° CONE MODEL FOR 6%, 45° BLUNT NOSE CONFIGURATION -  $M_\infty = 11.4$ ,  $Re/FT = 1 \times 10^7$ ,  $\alpha = 0^\circ 5'$

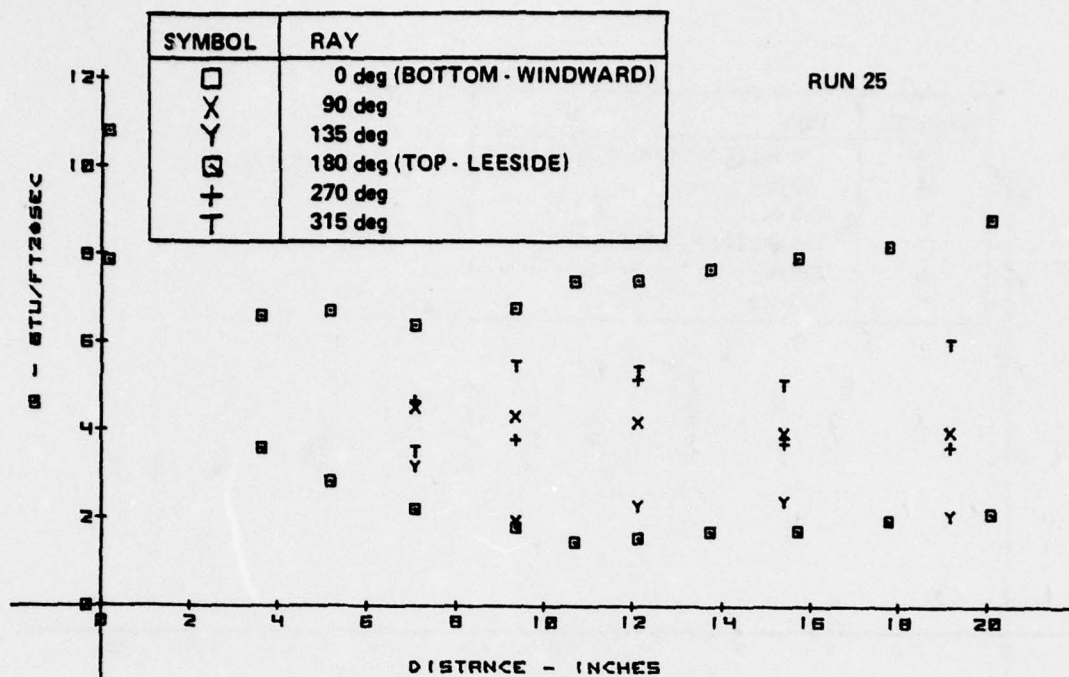


a. HEAT TRANSFER DISTRIBUTION

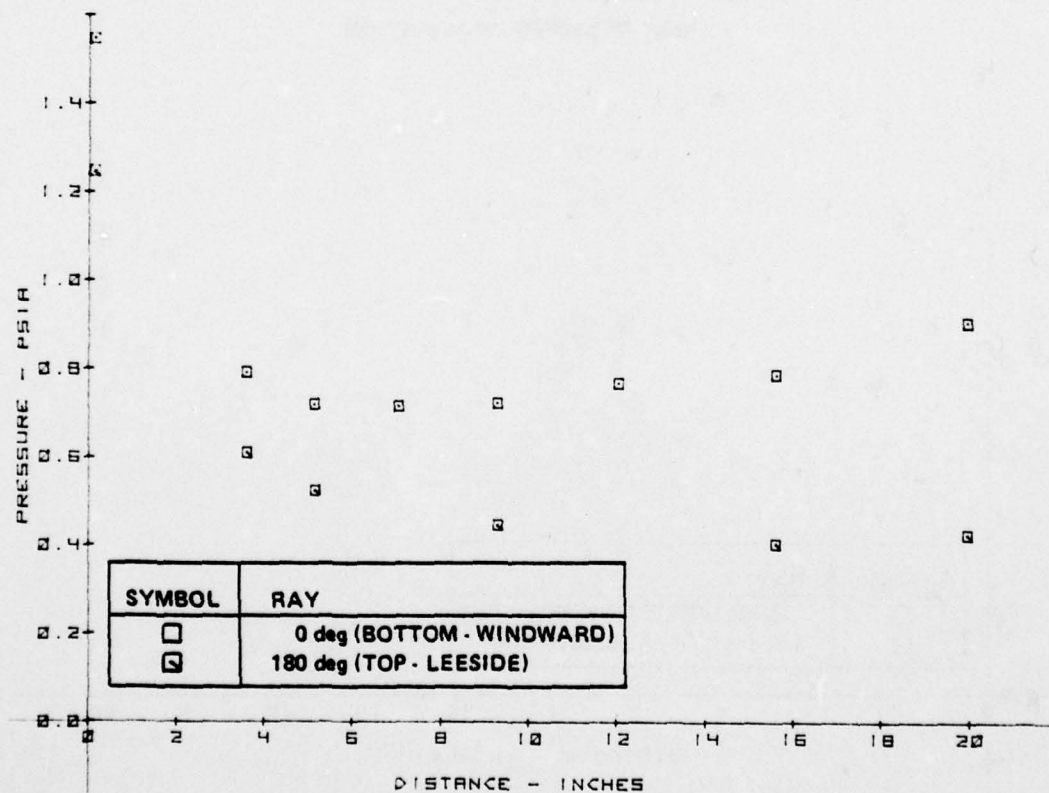


b. PRESSURE DISTRIBUTION

Figure 2-25 MEASUREMENTS ON 6° CONE MODEL FOR 6%, 0° BLUNT NOSE CONFIGURATION -  $M_\infty = 11.3$ ,  $Re/FT = 1.0 \times 10^7$ ,  $\alpha = 0^\circ 5'$



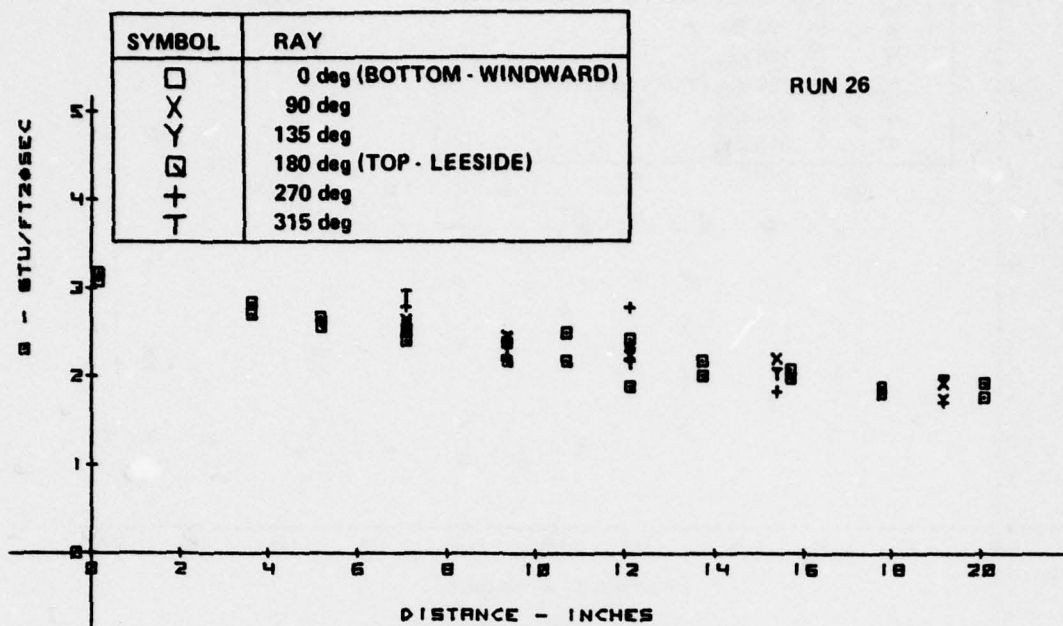
a. HEAT TRANSFER DISTRIBUTION



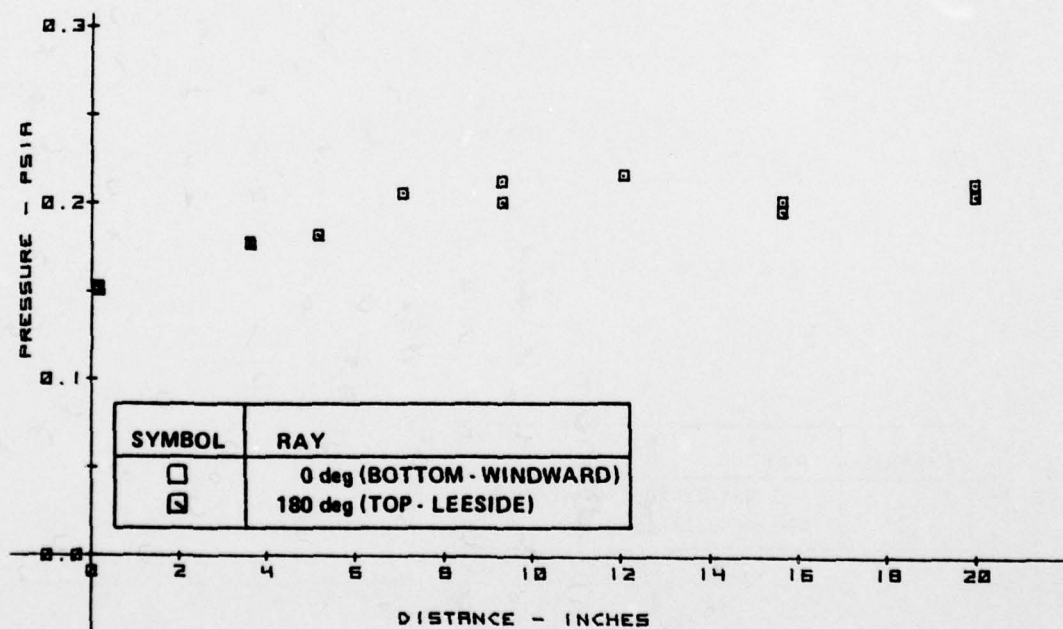
b. PRESSURE DISTRIBUTION

Figure 2-26 MEASUREMENTS ON 6° CONE MODEL FOR 21% SPHERICAL NOSE CONFIGURATION -  $M_\infty = 11.4$ ,  $Re/FT = 1.0 \times 10^7$ ,  $\alpha = 2^\circ 5'$





a. HEAT TRANSFER DISTRIBUTION



b. PRESSURE DISTRIBUTION

Figure 2-27 MEASUREMENTS ON 6° CONE MODEL FOR 6%, 0° BLUNT NOSE CONFIGURATION -  $M_\infty = 10.9$ ,  $Re/FT = 2.4 \times 10^6$ ,  $\alpha = 0^\circ 3'$

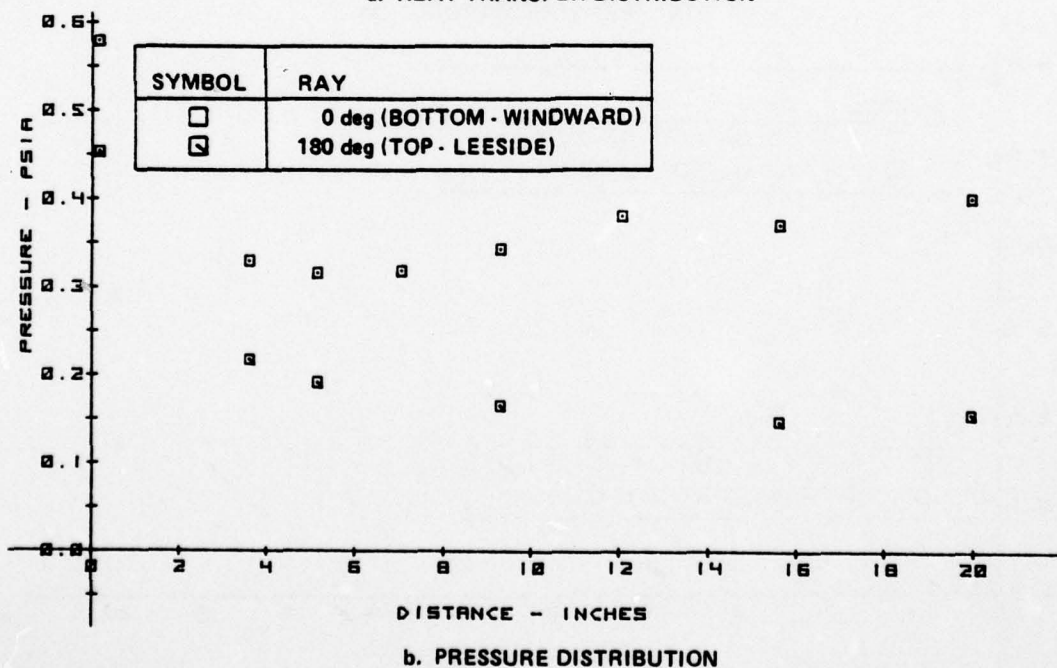
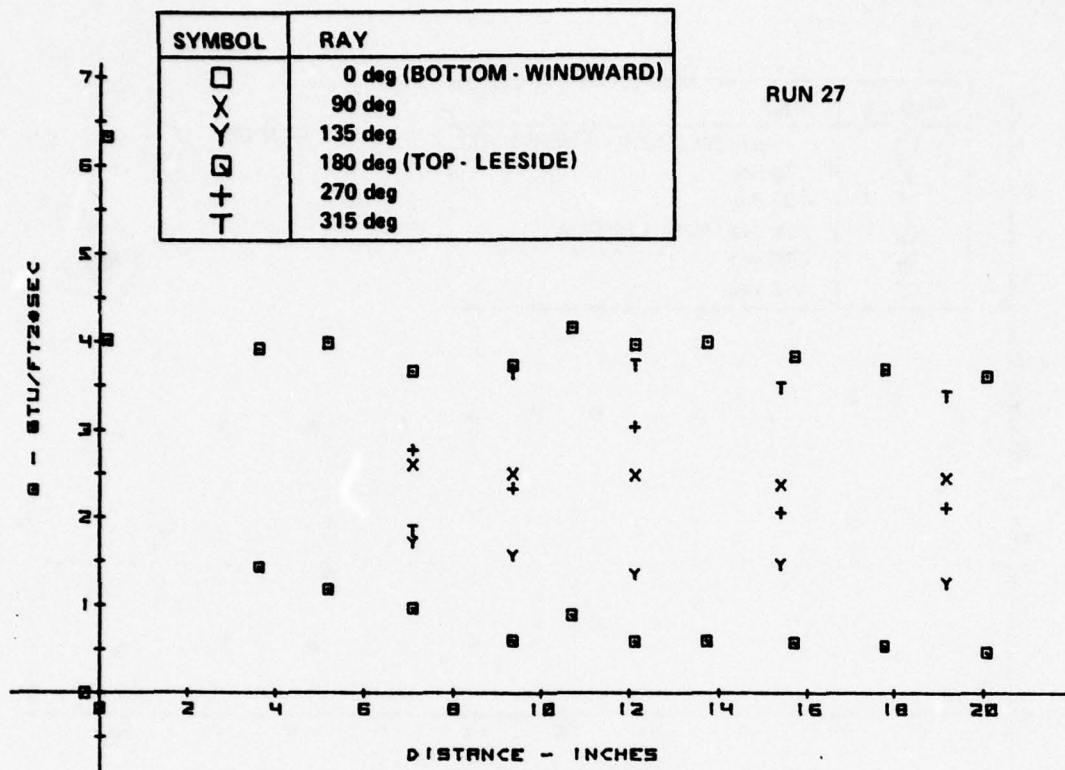
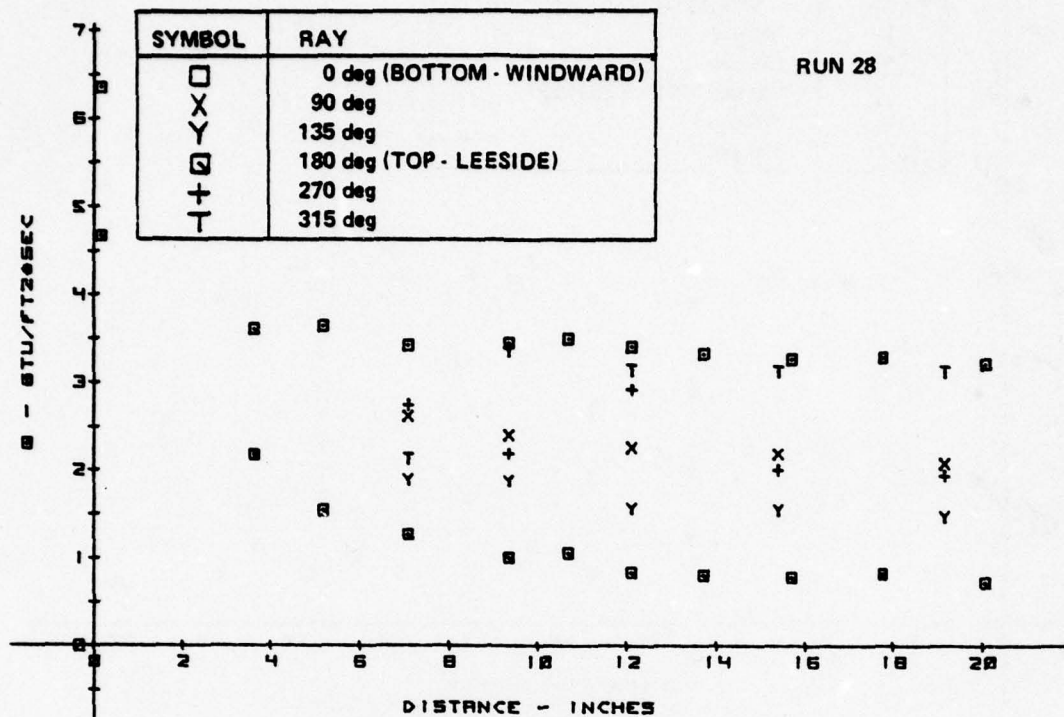
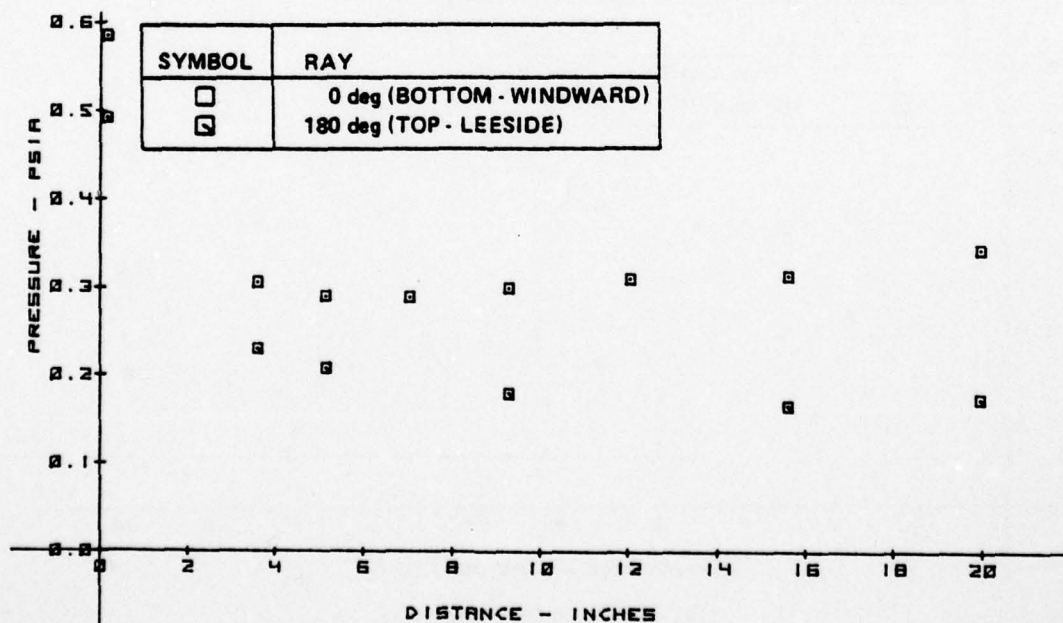


Figure 2-28 MEASUREMENTS ON 6° CONE MODEL FOR 21% SPHERICAL NOSE CONFIGURATION -  $M_\infty = 11.0$ ,  $Re/FT = 4.0 \times 10^6$ ,  $\alpha = 3^\circ 3'$



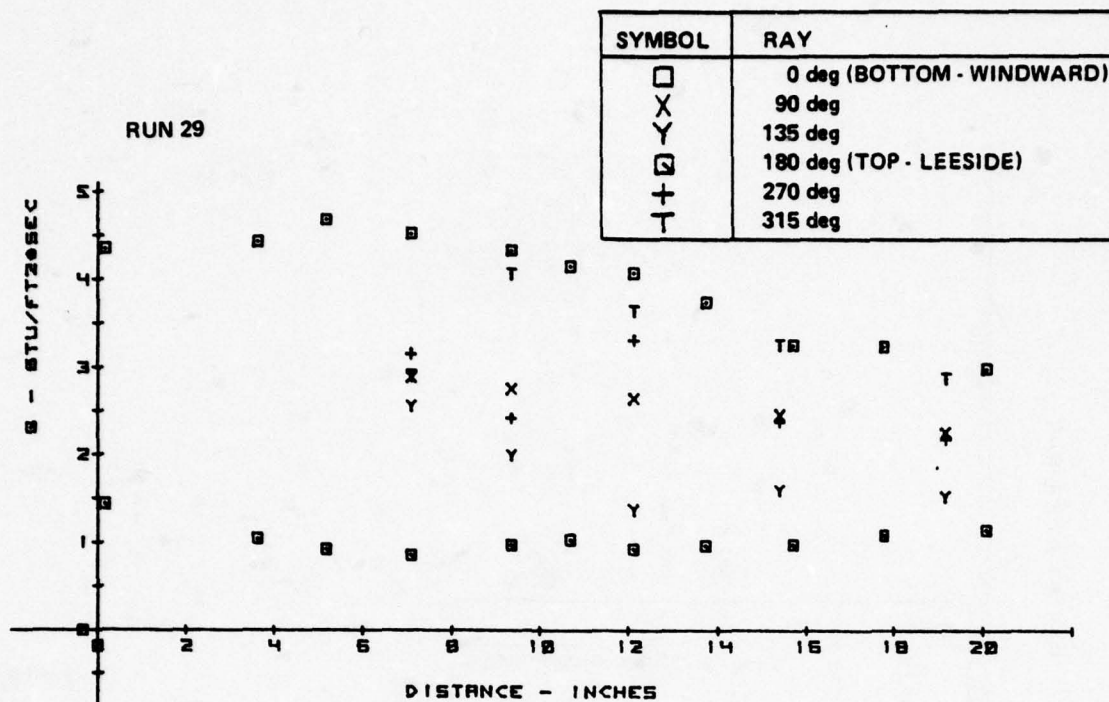
a. HEAT TRANSFER DISTRIBUTION



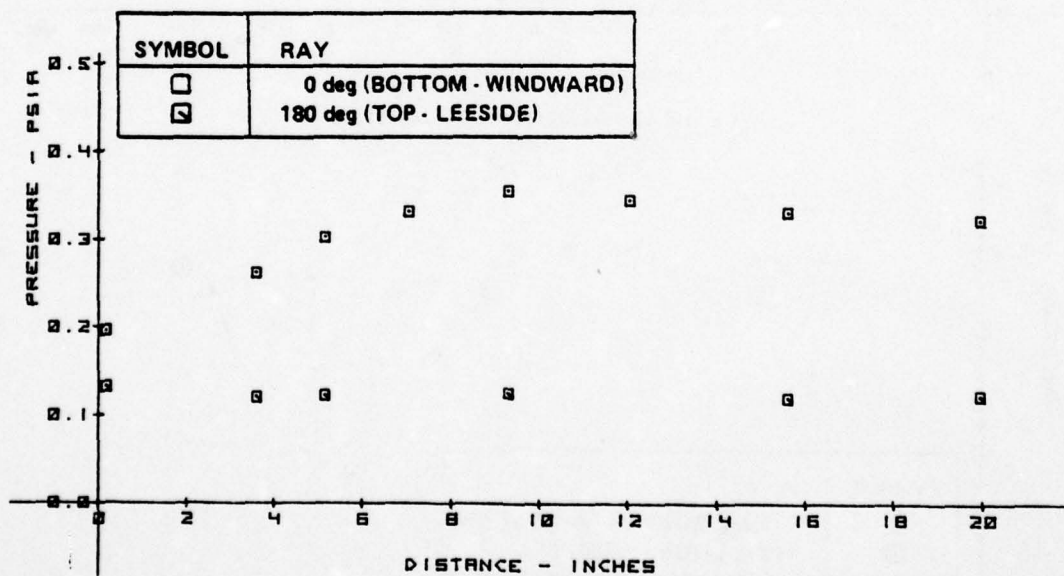
b. PRESSURE DISTRIBUTION

Figure 2-29 MEASUREMENTS ON 6° CONE MODEL FOR 21% SPHERICAL NOSE CONFIGURATION -  $M_{\infty} = 11.0$ ,  $Re/FT = 3.8 \times 10^6$ ,  $\alpha = 2^{\circ} 3'$



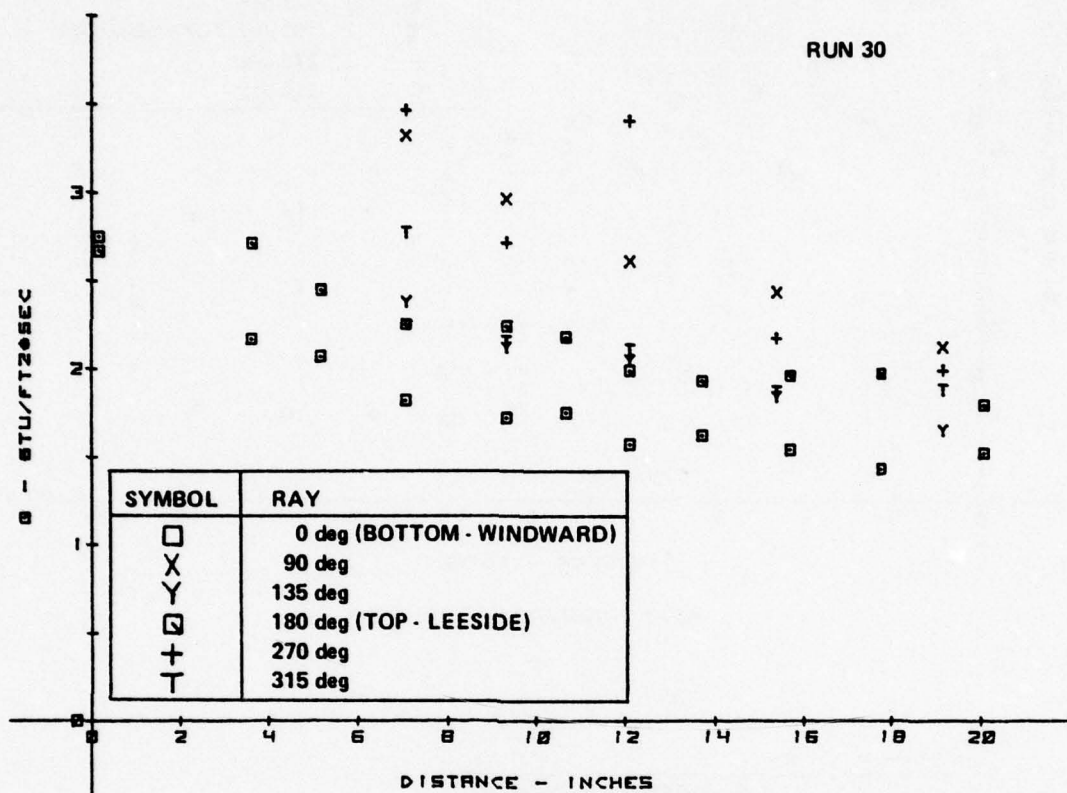


a. HEAT TRANSFER DISTRIBUTION

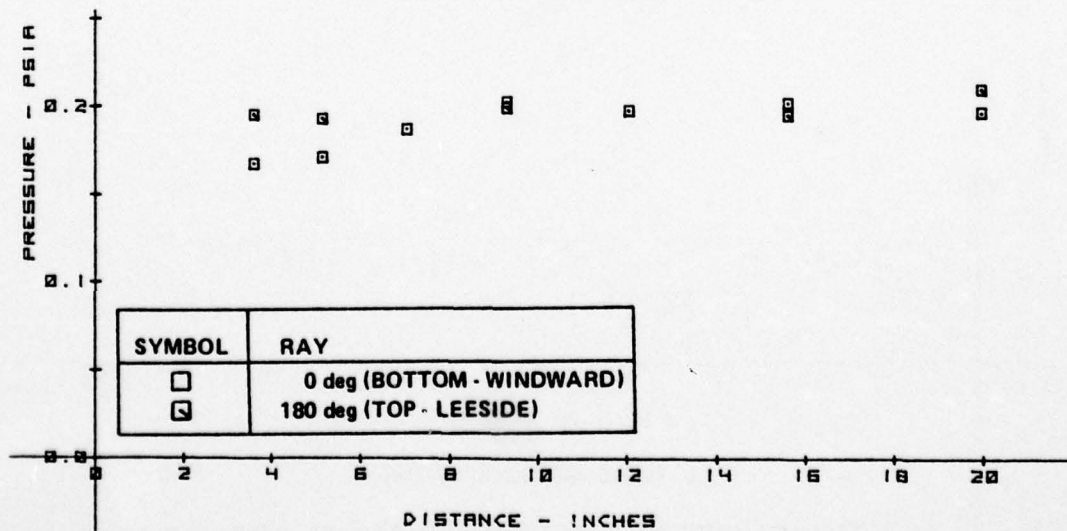


b. PRESSURE DISTRIBUTION

Figure 2-30 MEASUREMENTS ON 6° CONE MODEL FOR 6%, 45° BLUNT NOSE CONFIGURATION -  $M_\infty = 10.9$ ,  $Re/FT = 2.5 \times 10^6$ ,  $\alpha = 3^\circ 3'$

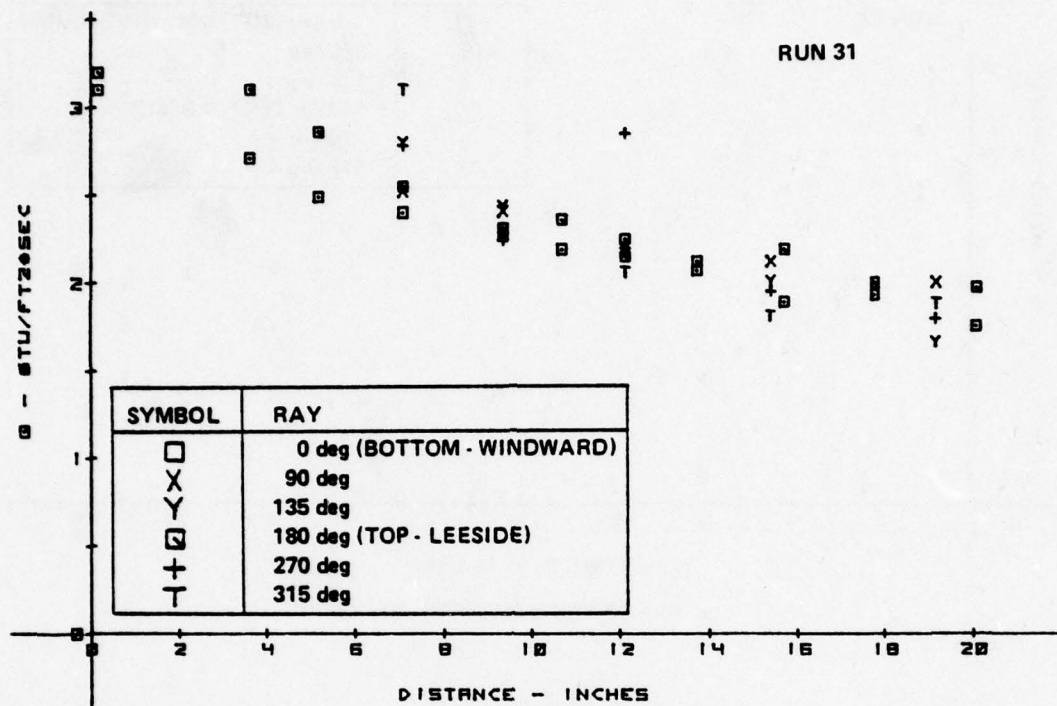


a. HEAT TRANSFER DISTRIBUTION

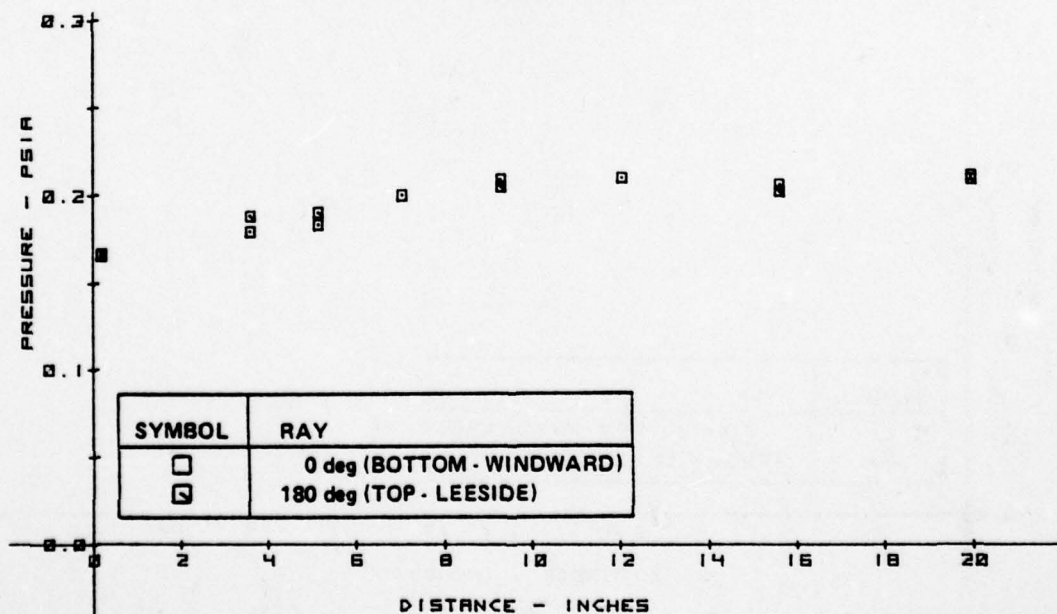


b. PRESSURE DISTRIBUTION

Figure 2-31 MEASUREMENTS ON 6° CONE MODEL FOR 6%, 45° BLUNT NOSE CONFIGURATION -  $M_\infty = 10.9$ ,  $Re/FT = 2.6 \times 10^6$ ,  $\alpha = 0^\circ 3'$



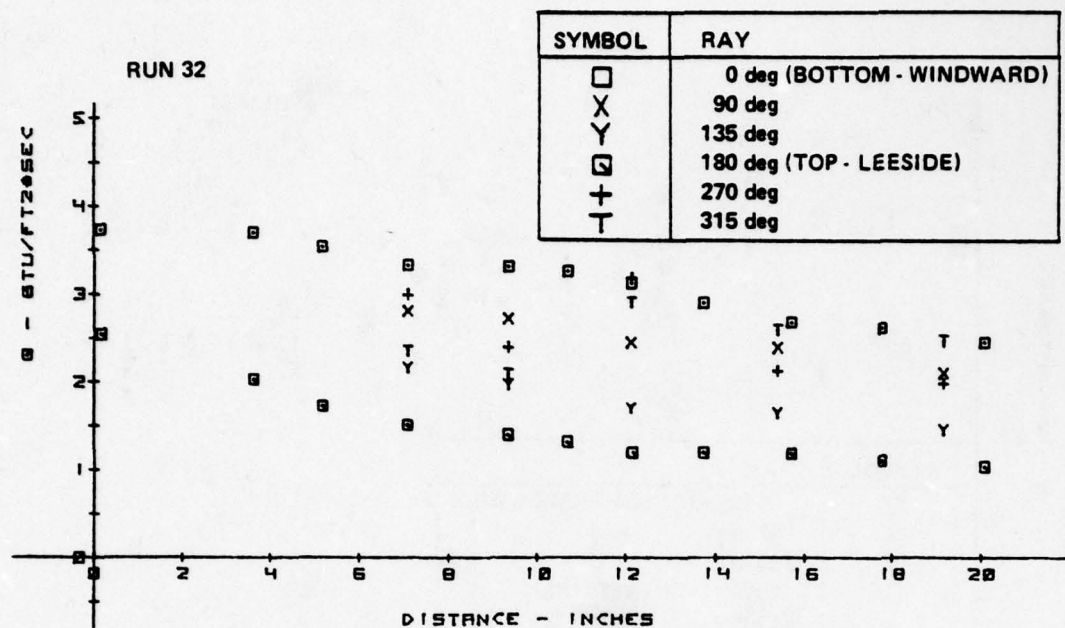
a. HEAT TRANSFER DISTRIBUTION



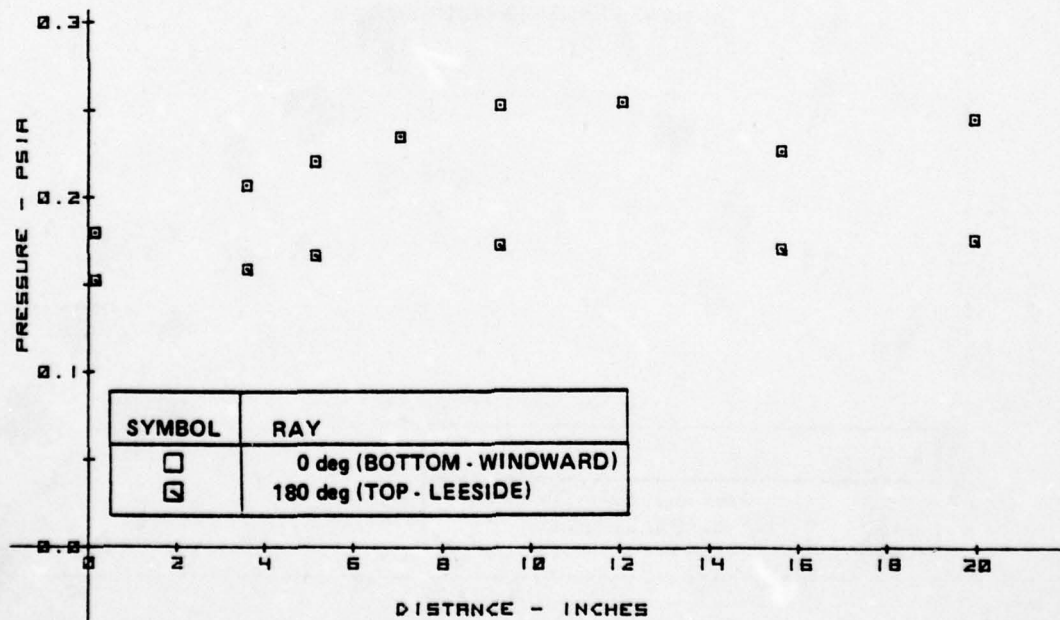
b. PRESSURE DISTRIBUTION

Figure 2-32 MEASUREMENTS ON 6° CONE MODEL FOR 6%, 0° BLUNT NOSE CONFIGURATION -  $M_\infty = 10.9$ ,  $Re/FT = 2.6 \times 10^6$ ,  $\alpha = 0^\circ 3'$





a. HEAT TRANSFER DISTRIBUTION



b. PRESSURE DISTRIBUTION

Figure 2-33 MEASUREMENTS ON 6° CONE MODEL FOR 6%, 0° BLUNT NOSE CONFIGURATION -  $M_\infty = 10.9$ ,  $Re/FT = 2.6 \times 10^6$ ,  $\alpha = 1^\circ 2'$

AD-A065 173

CALSPAN ADVANCED TECHNOLOGY CENTER BUFFALO NY  
STUDIES OF THE EFFECTS OF TRANSITIONAL AND TURBULENT BOUNDARY L--ETC(U)  
DEC 78 M S HOLDEN

F/G 20/4

F44620-76-C-0037

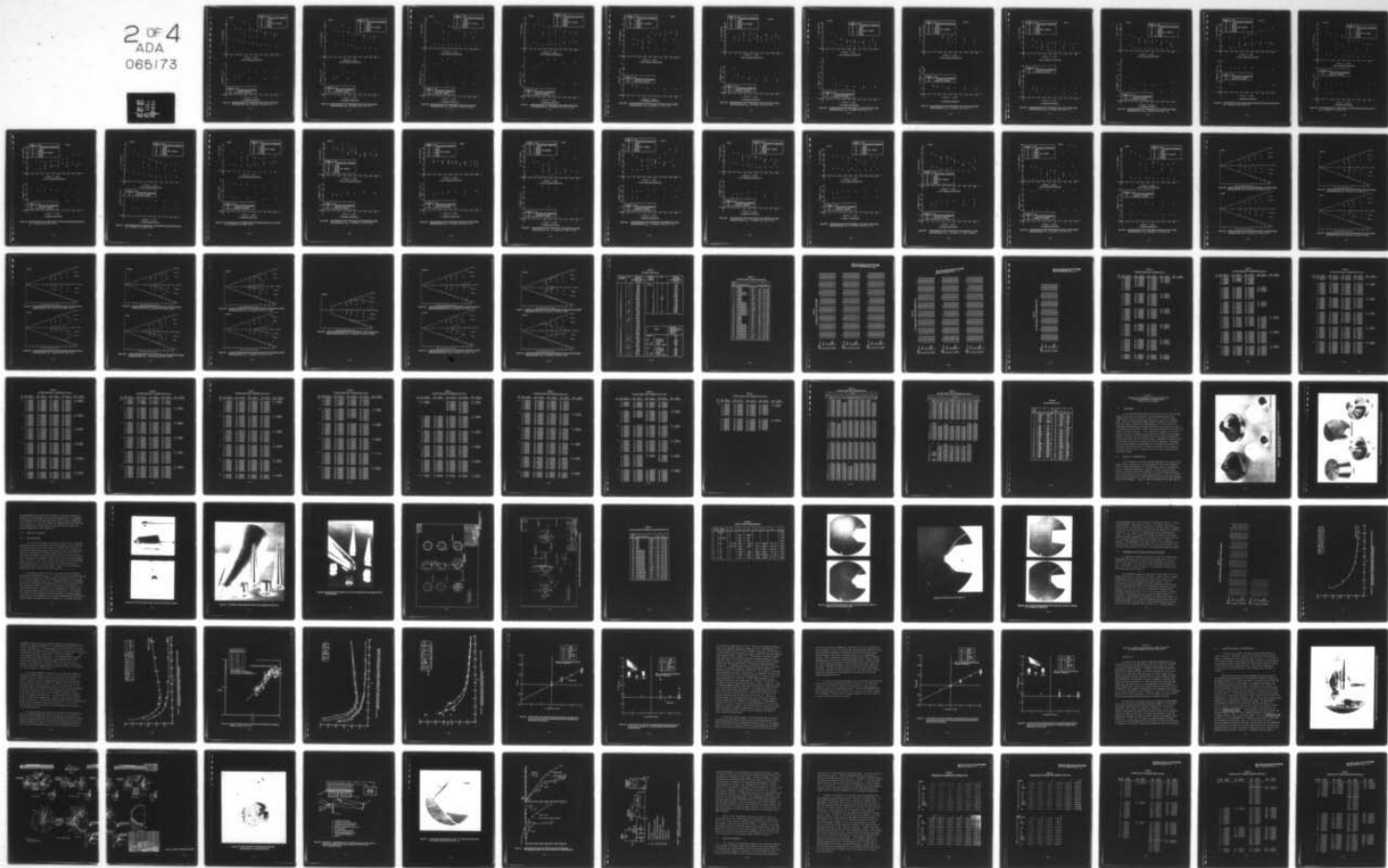
UNCLASSIFIED

CALSPAN-AB-5834-A-2

AFOSR-TR-79-0125

NL

2 OF 4  
ADA  
065173



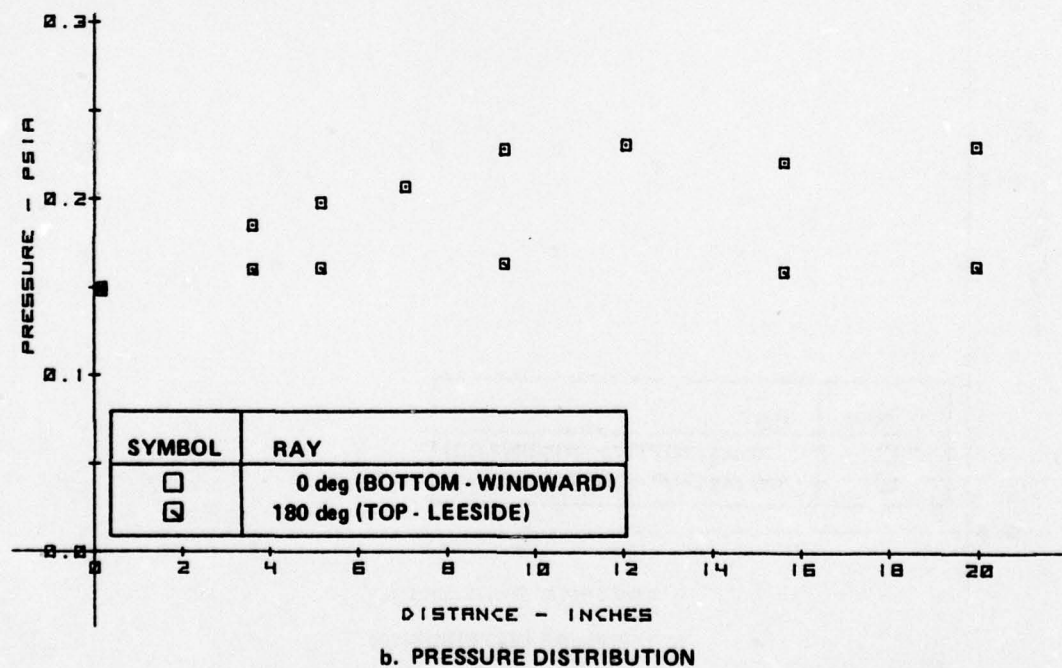
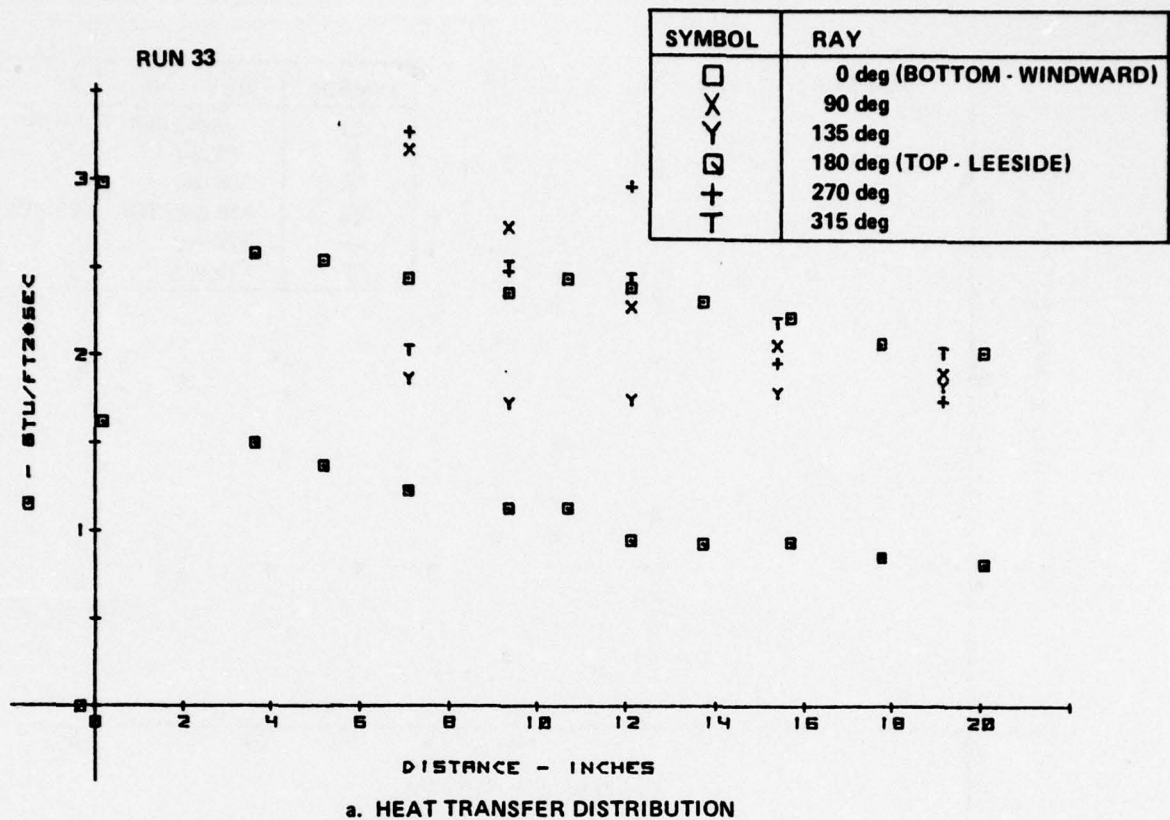
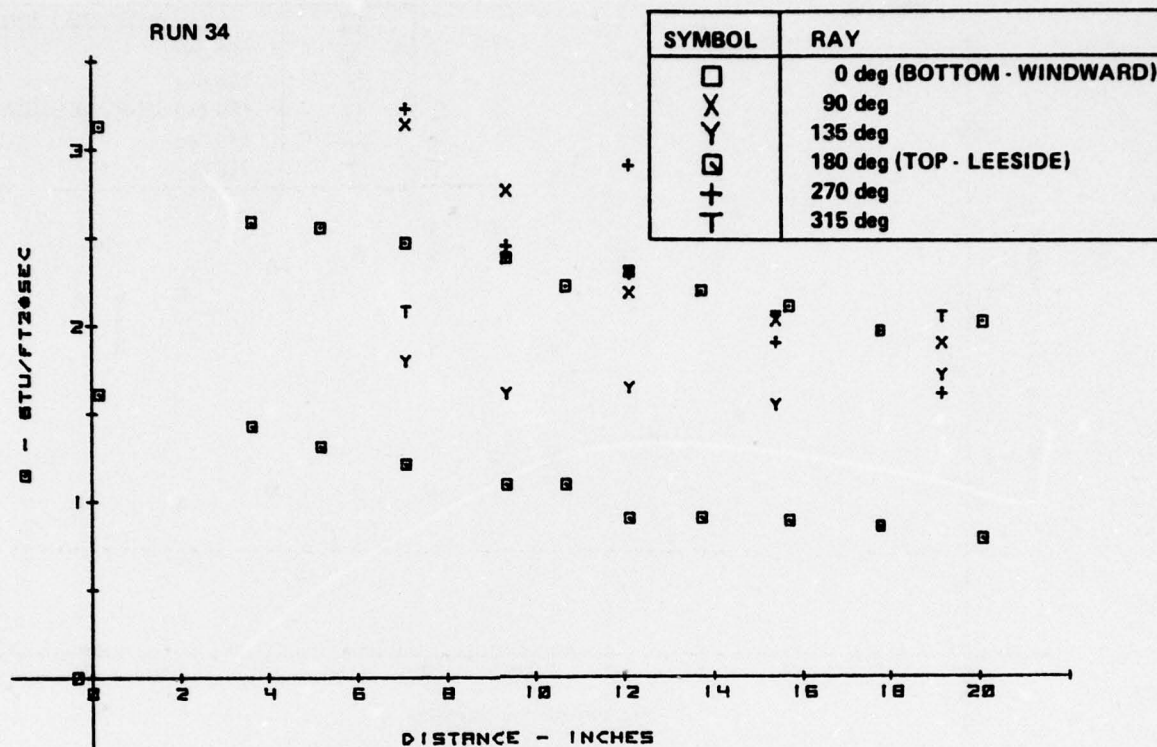
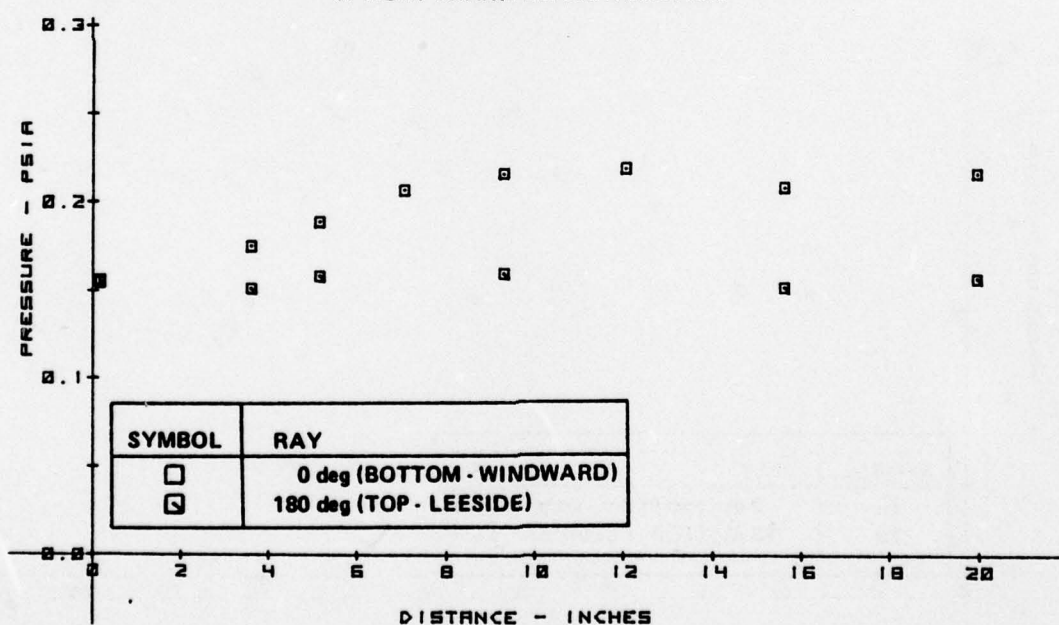


Figure 2-34 MEASUREMENTS ON 6° CONE MODEL FOR 6%, 45° BLUNT NOSE CONFIGURATION -  $M_\infty = 10.9$ ,  $Re/FT = 2.6 \times 10^6$ ,  $\alpha = 1^\circ 2'$



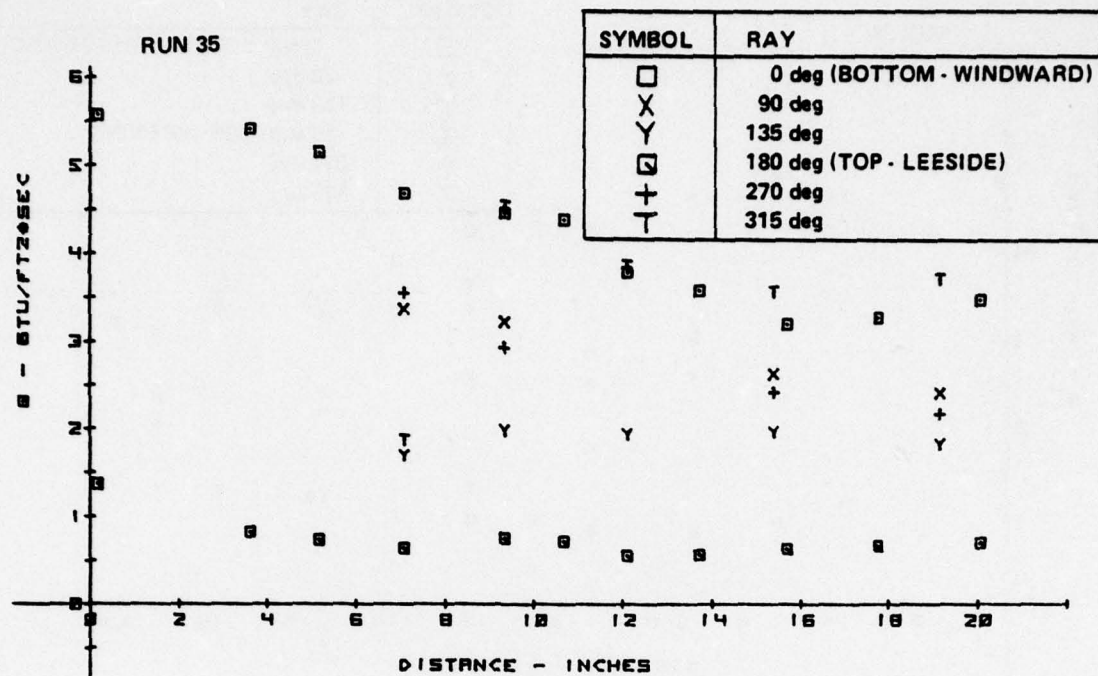


a. HEAT TRANSFER DISTRIBUTION

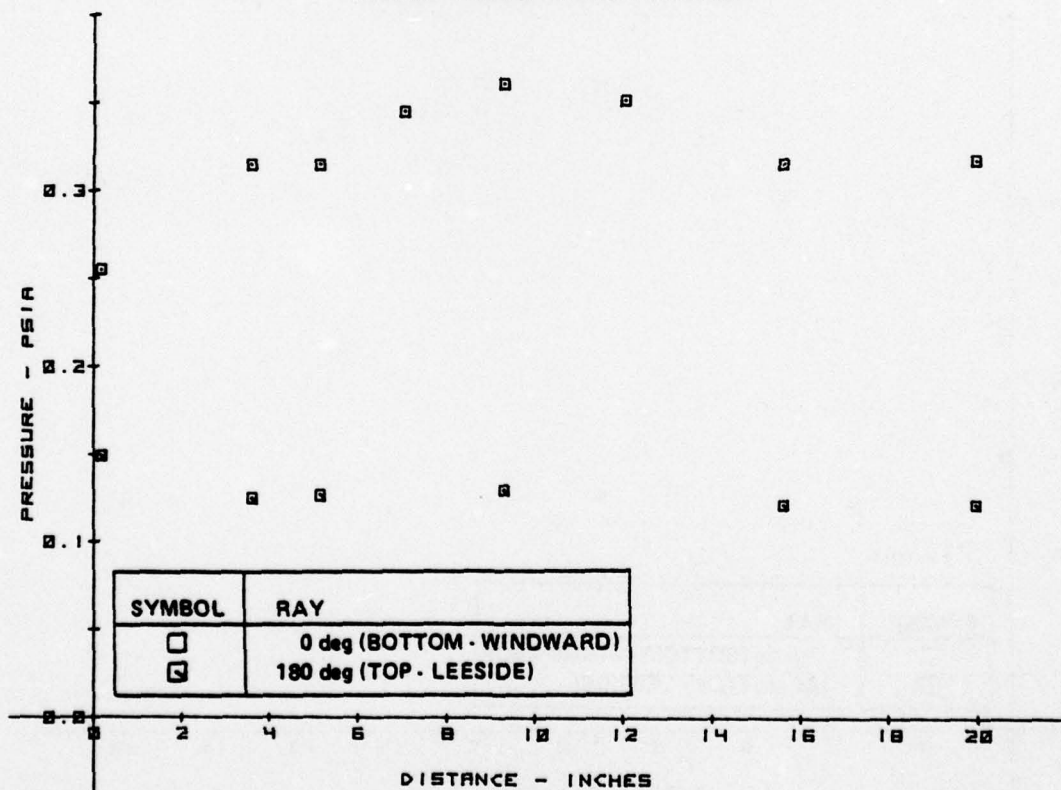


b. PRESSURE DISTRIBUTION

Figure 2-35 MEASUREMENTS ON 6° CONE MODEL FOR 6%, 45° BLUNT NOSE CONFIGURATION -  $M_\infty = 10.9$ ,  $Re/FT = 2.5 \times 10^6$ ,  $\alpha = 1^\circ 2'$



a. HEAT TRANSFER DISTRIBUTION



b. PRESSURE DISTRIBUTION

Figure 2-36 MEASUREMENTS ON 6° CONE MODEL FOR 6%, 0° BLUNT NOSE CONFIGURATION -  $M_\infty = 10.9$ ,  $Re/FT = 2.5 \times 10^6$ ,  $\alpha = 2^\circ 59'$

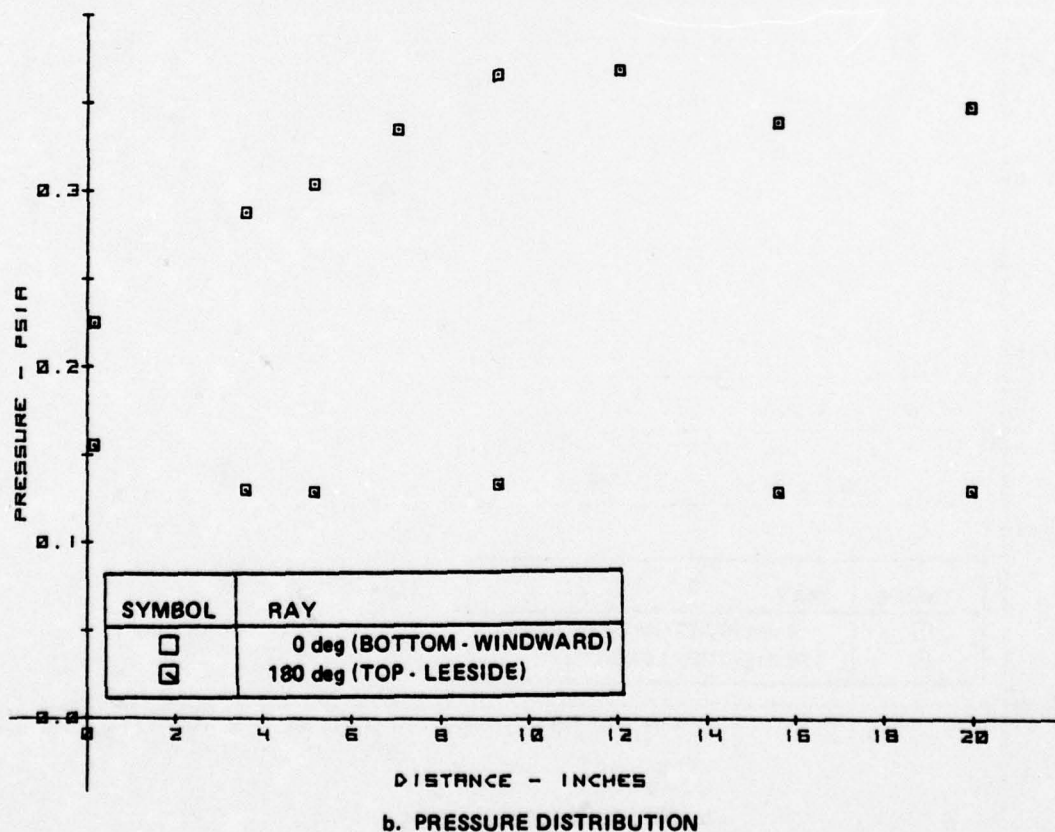
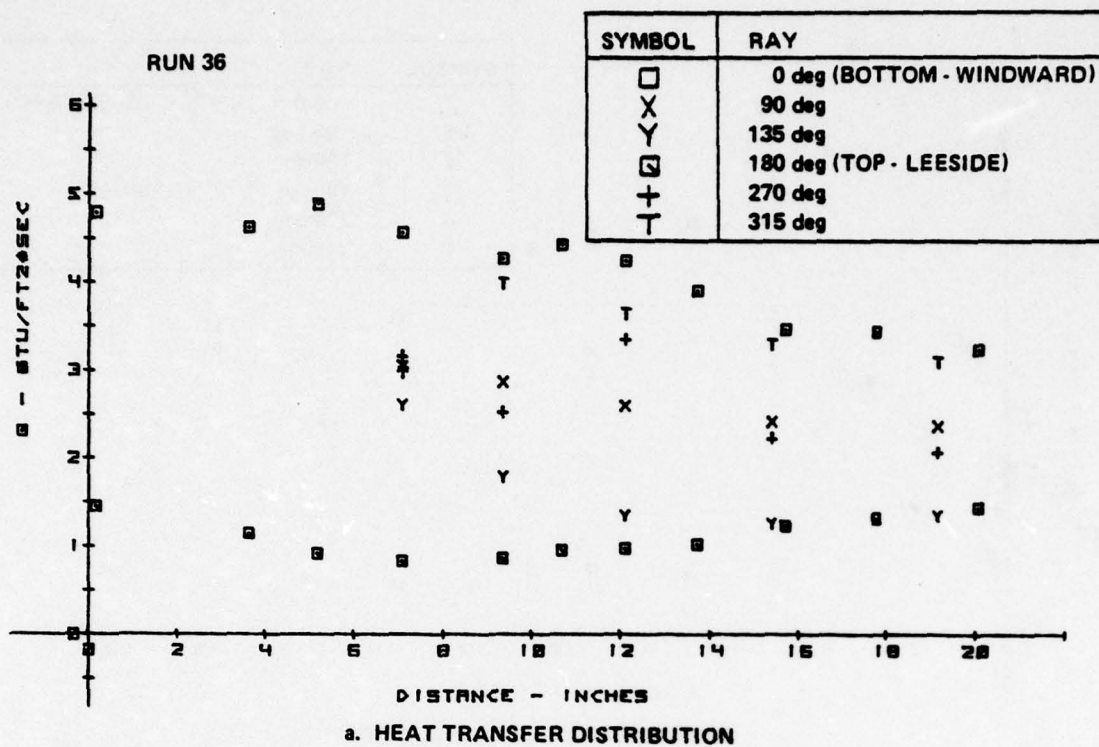
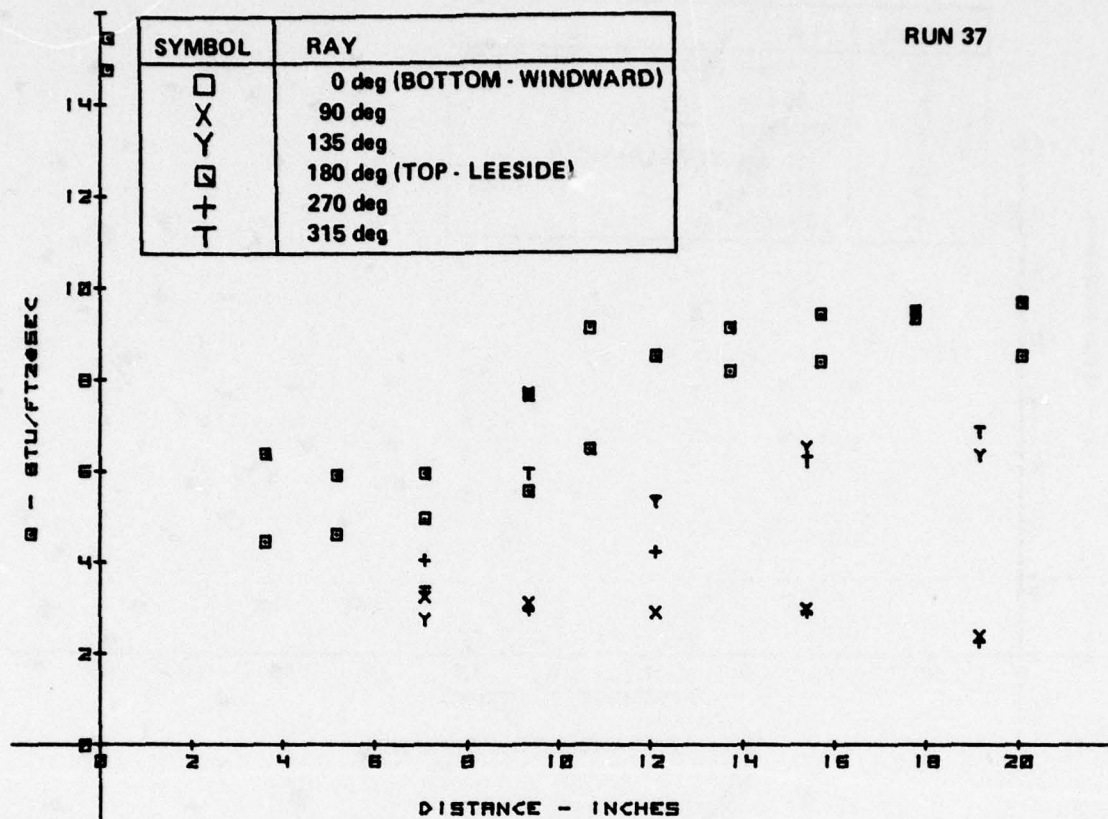
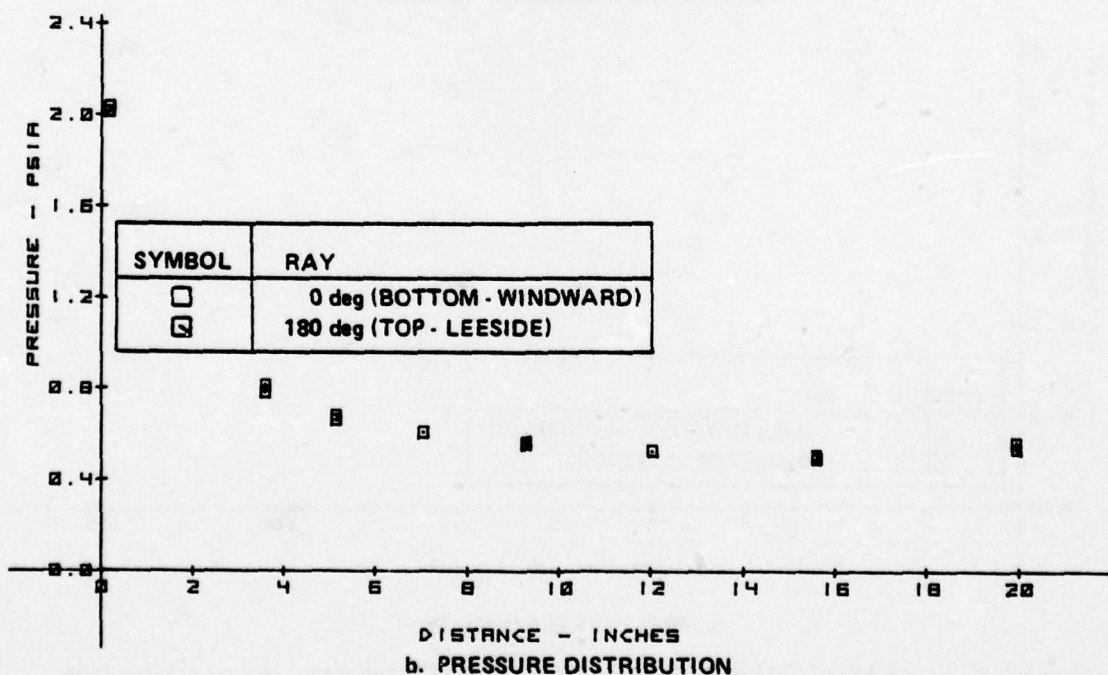


Figure 2-37 MEASUREMENTS ON 6° CONE MODEL FOR 6%, 45° BLUNT NOSE CONFIGURATION -  $M_\infty = 10.9$ ,  $Re/FT = 2.6 \times 10^6$ ,  $\alpha = 2^\circ 59'$



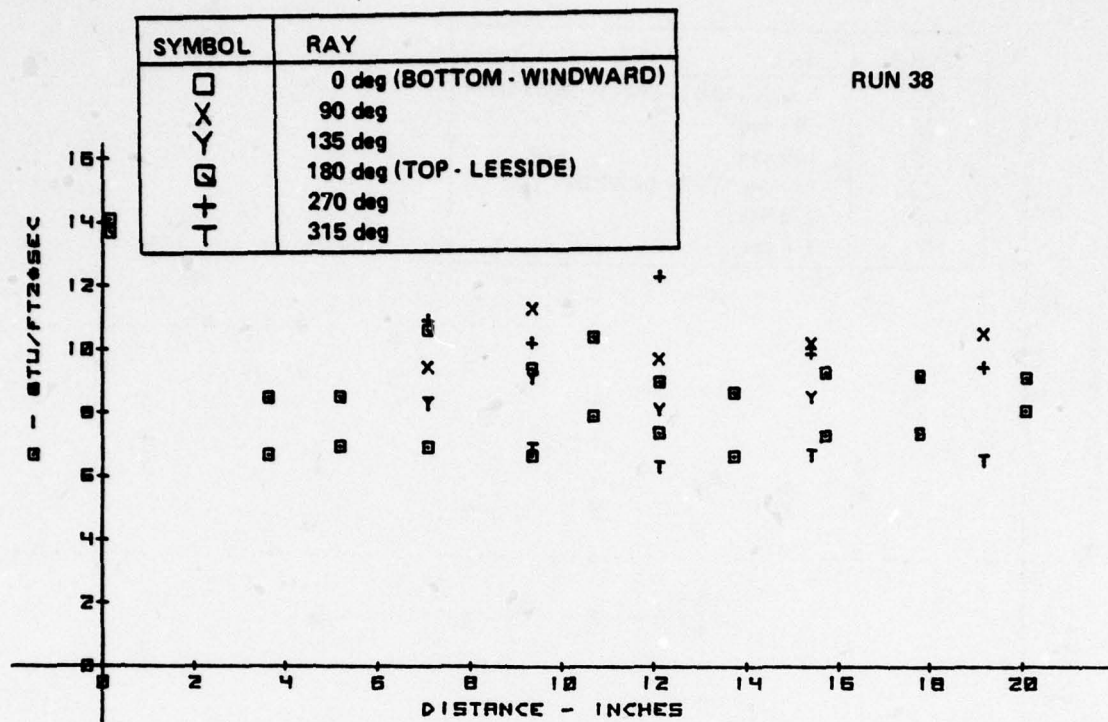


a. HEAT TRANSFER DISTRIBUTION

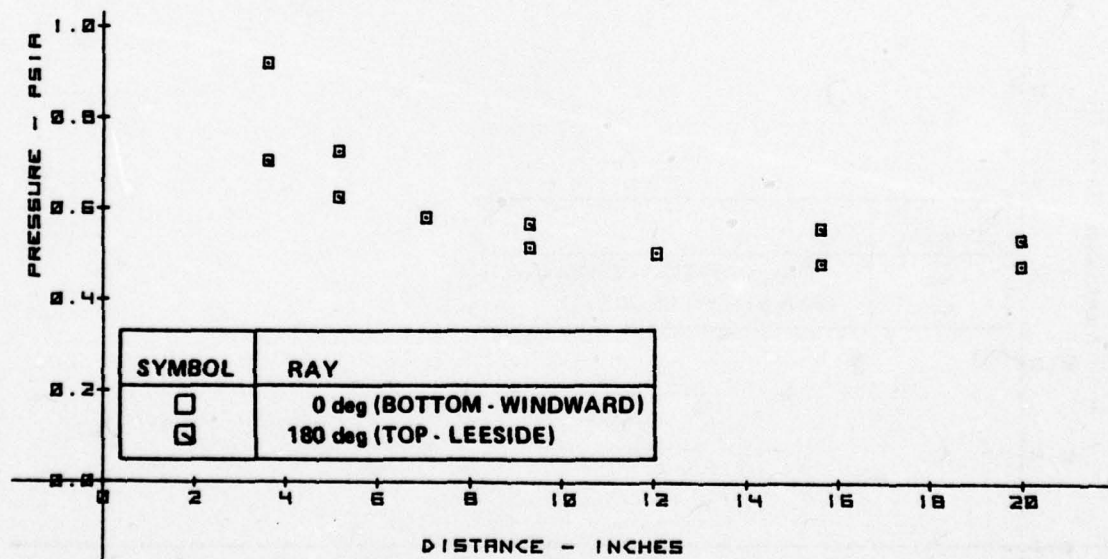


b. PRESSURE DISTRIBUTION

Figure 2-38 MEASUREMENTS ON 6° CONE MODEL FOR 21%, 0° BLUNT NOSE CONFIGURATION -  $M_\infty = 11.3$ ,  $Re/FT = 1 \times 10^7$ ,  $\alpha = 0^\circ$



a. HEAT TRANSFER DISTRIBUTION



b. PRESSURE DISTRIBUTION

Figure 2-39 MEASUREMENTS ON 6° CONE MODEL FOR 21% 45° BLUNT NOSE CONFIGURATION -  $M_\infty = 11.3$ ,  $Re/FT = 1.0 \times 10^7$ ,  $\alpha = 0^\circ$

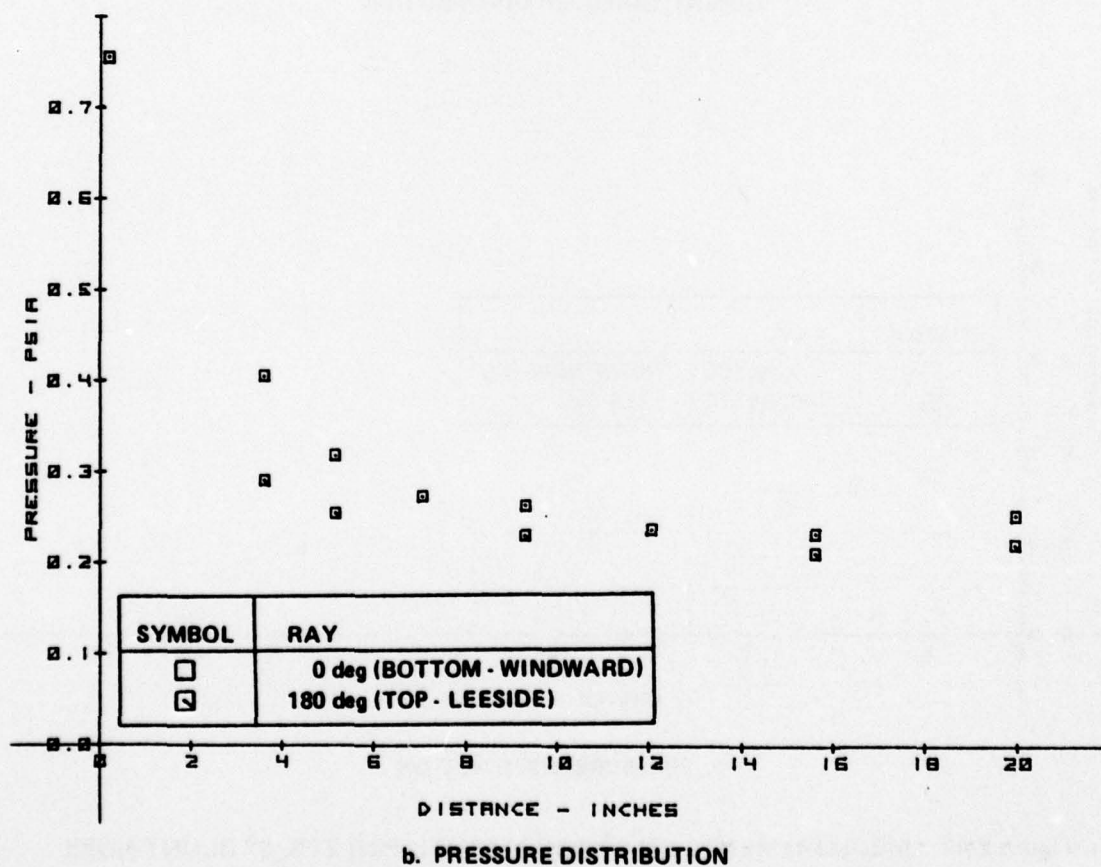
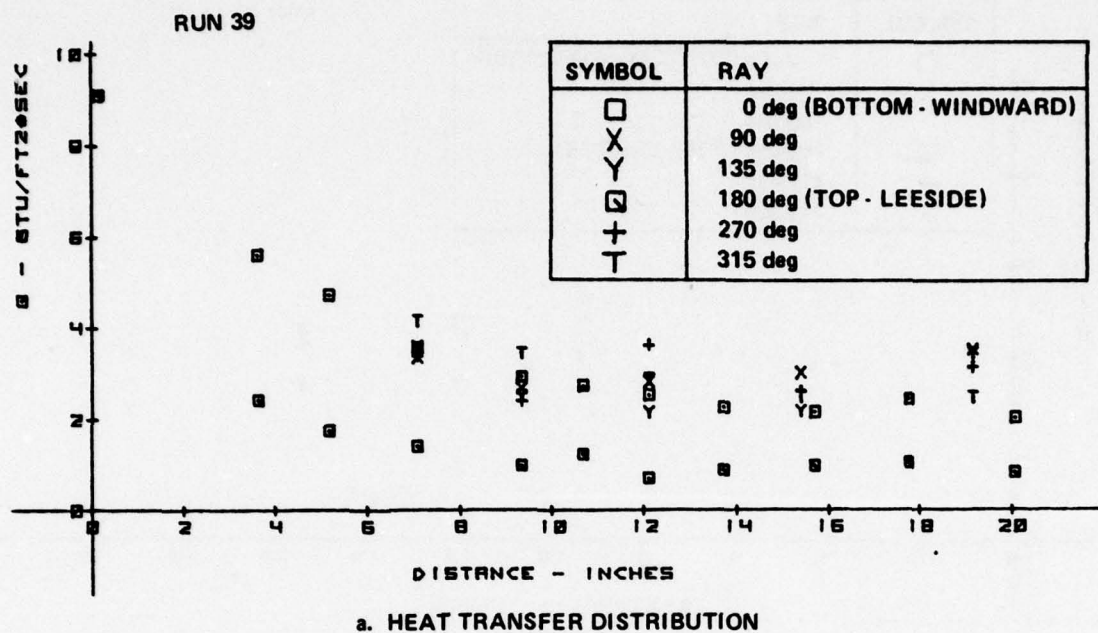
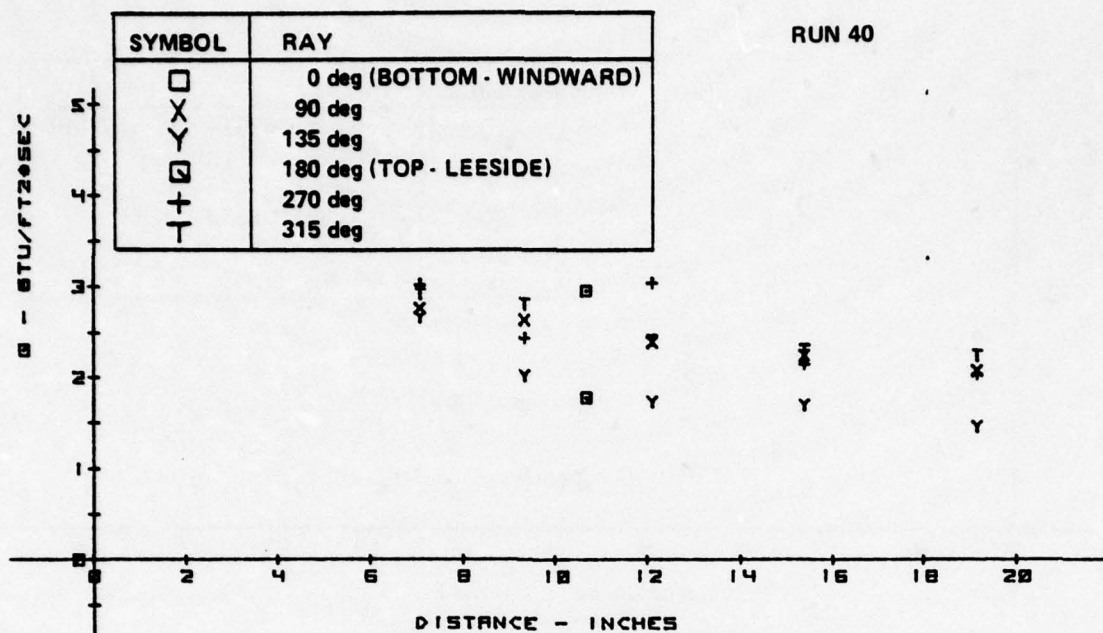
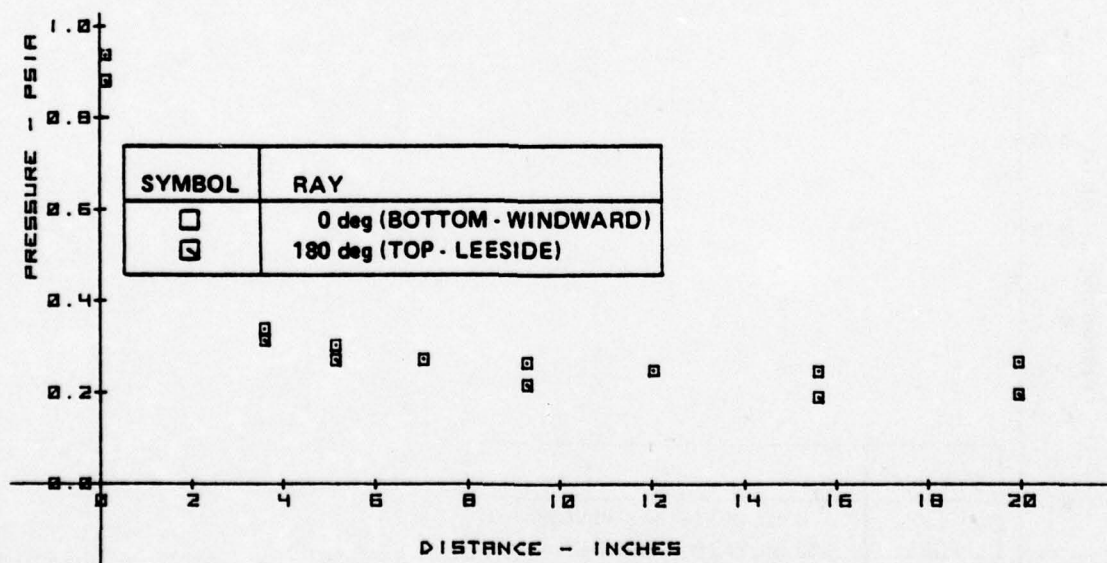


Figure 2-40 MEASUREMENTS ON 6° CONE MODEL FOR 21%, 45° BLUNT NOSE CONFIGURATION -  $M_\infty = 11.0$ ,  $Re/FT = 4.0 \times 10^6$ ,  $\alpha = 1^\circ$



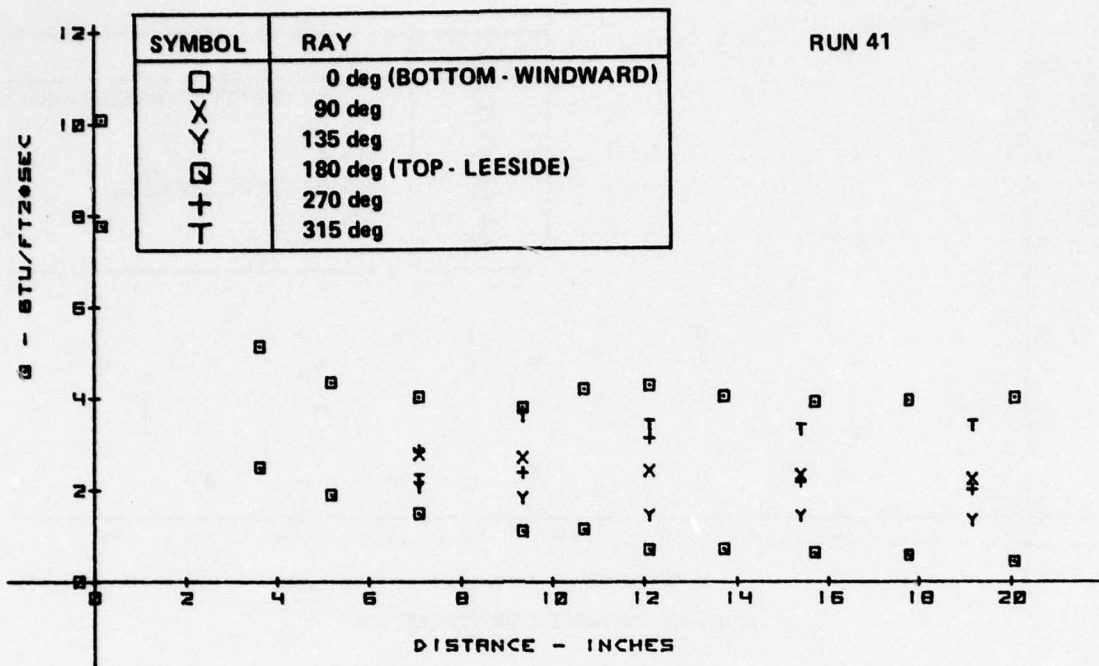


a. HEAT TRANSFER DISTRIBUTION

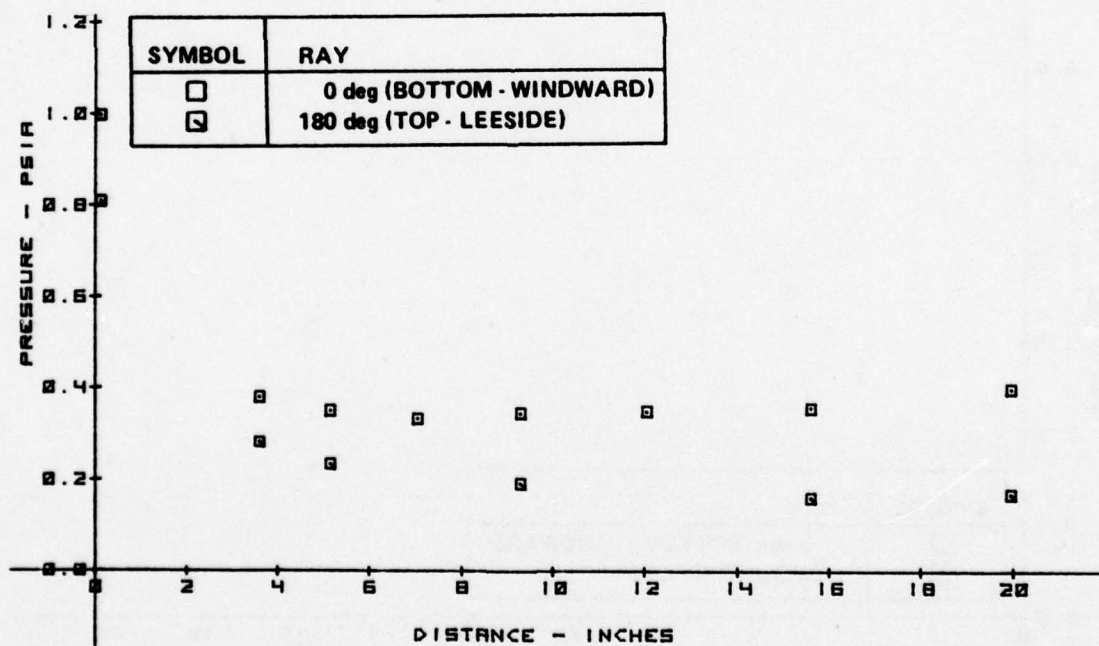


b. PRESSURE DISTRIBUTION

Figure 2-41 MEASUREMENTS ON 6° CONE MODEL FOR 21%, 0° BLUNT NOSE CONFIGURATION -  $M_\infty = 11.0$ ,  $Re/FT = 3.9 \times 10^6$ ,  $\alpha = 1^\circ$



a. HEAT TRANSFER DISTRIBUTION



b. PRESSURE DISTRIBUTION

Figure 2-42 MEASUREMENTS ON 6° CONE MODEL FOR 21%, 0° BLUNT NOSE CONFIGURATION -  $M_\infty = 11.0$ ,  $Re/FT = 3.8 \times 10^6$ ,  $\alpha = 3^\circ$

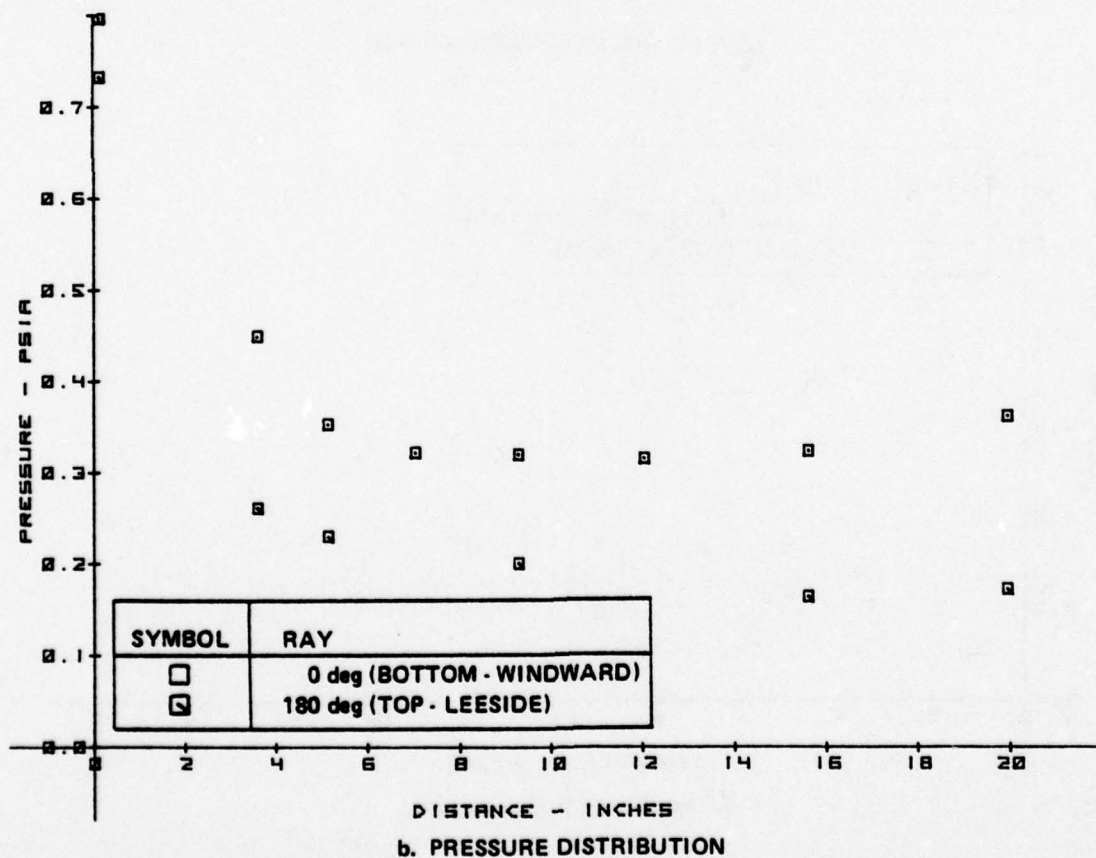
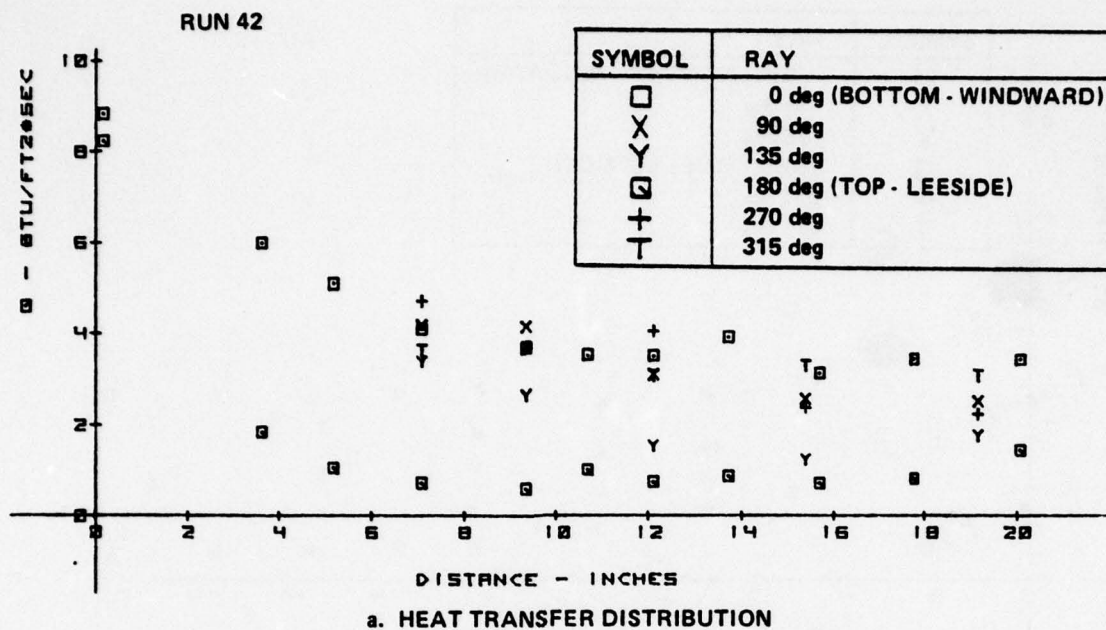
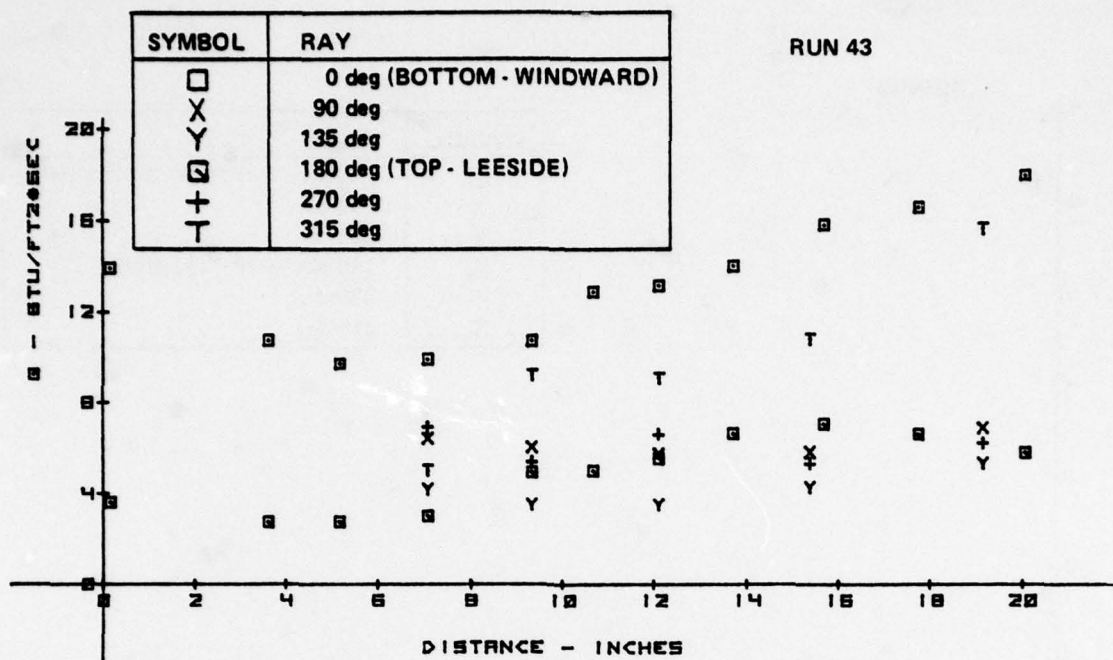
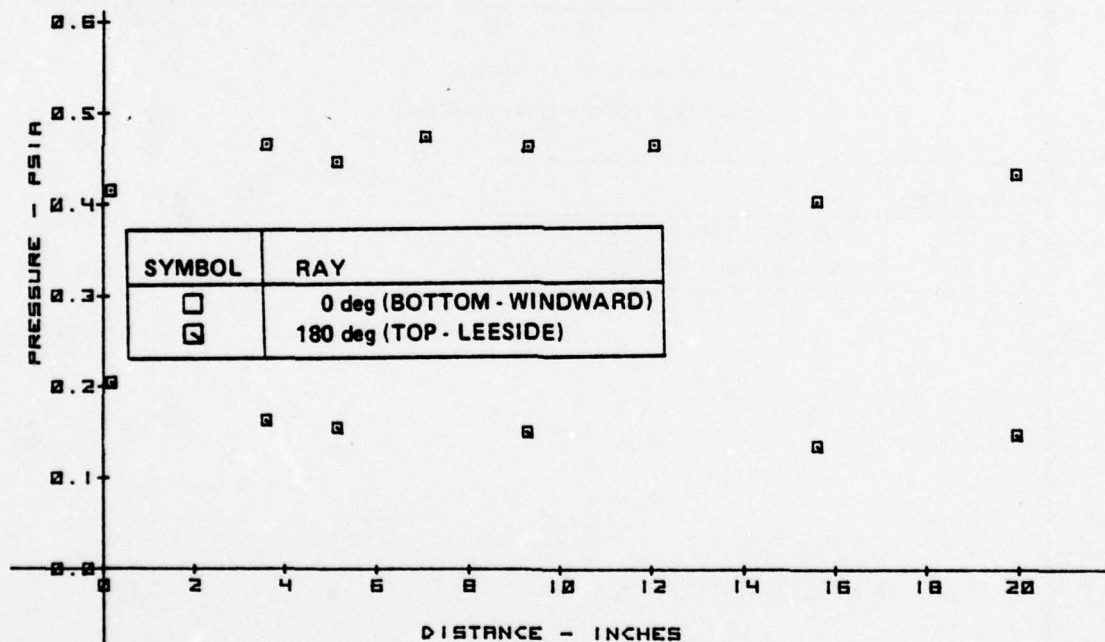


Figure 2-43 MEASUREMENTS ON 6° CONE MODEL FOR 21%, 45° BLUNT NOSE CONFIGURATION -  $M_\infty = 11.0$ ,  $Re/FT = 3.8 \times 10^6$ ,  $\alpha = 3^\circ$



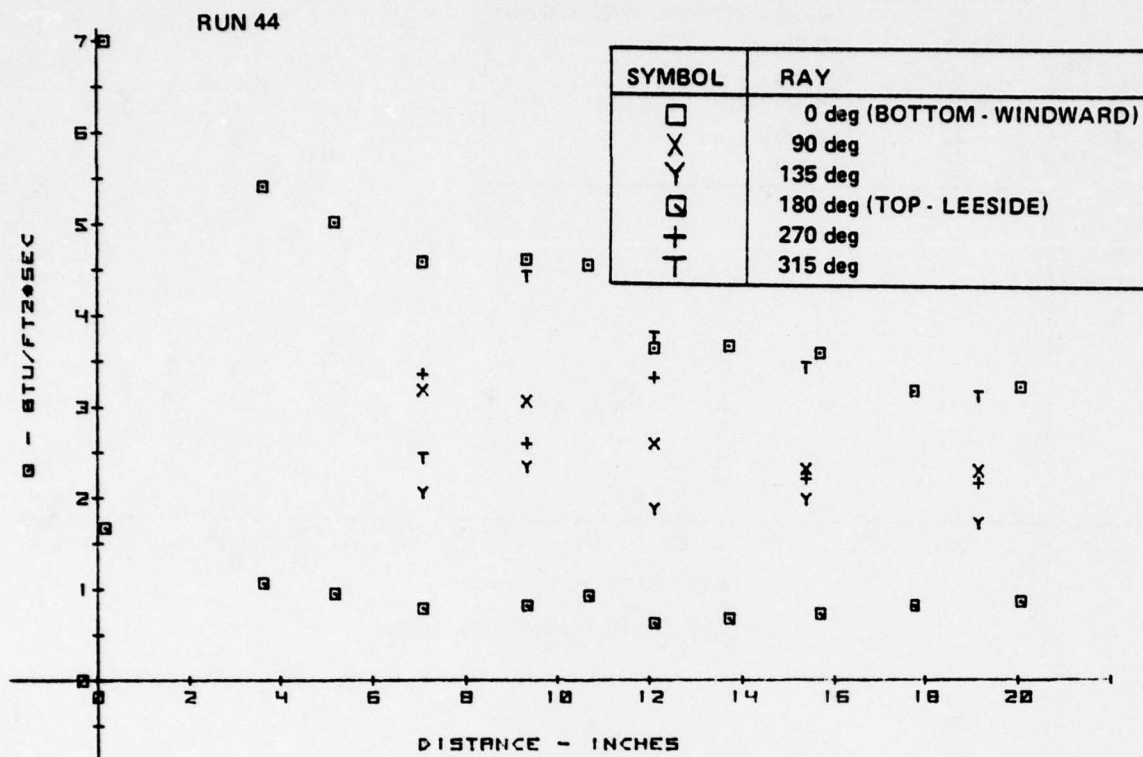


a. HEAT TRANSFER DISTRIBUTION

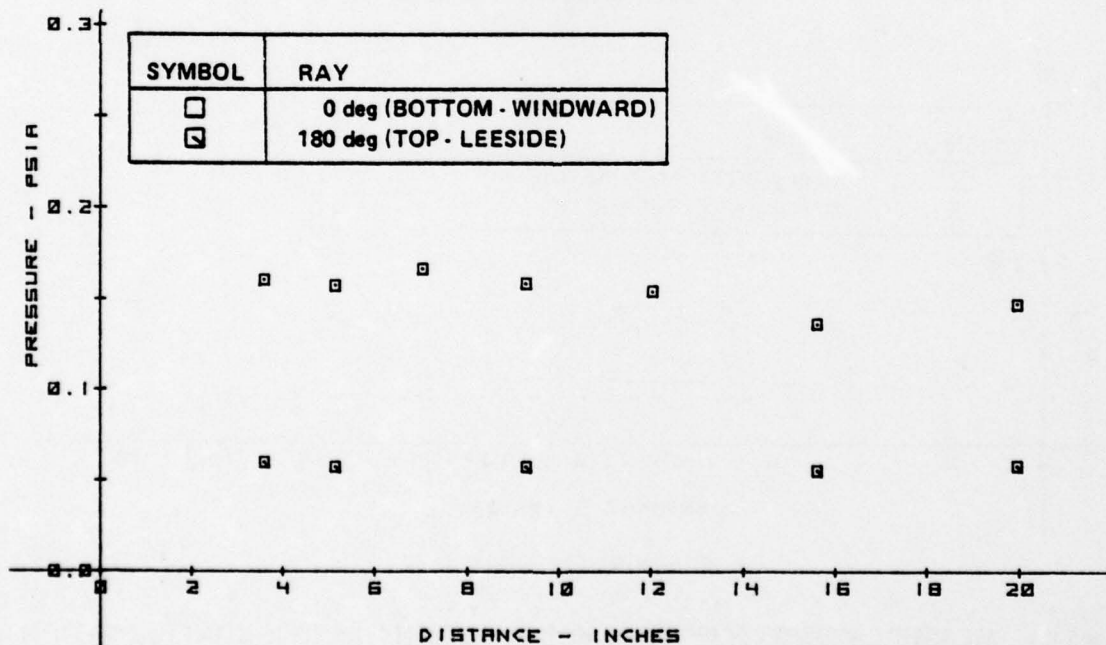


b. PRESSURE DISTRIBUTION

Figure 2-44 MEASUREMENTS ON 6° CONE MODEL FOR SHARP NOSE CONFIGURATION —  
 $M_\infty = 13.2$ ,  $Re/FT = 3.0 \times 10^6$ ,  $\alpha = 3^\circ$

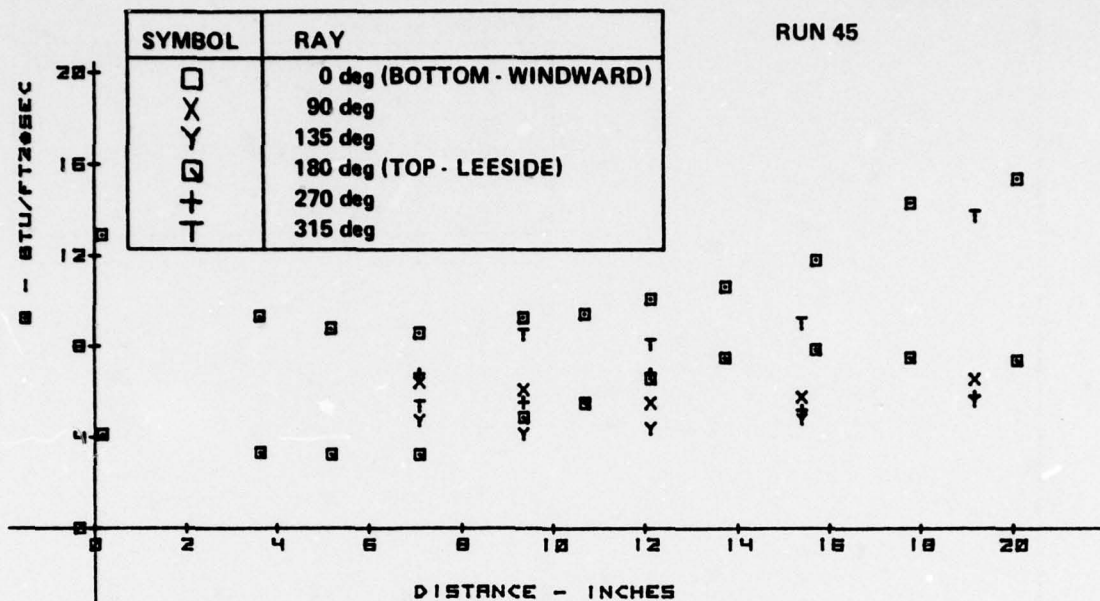


a. HEAT TRANSFER DISTRIBUTION

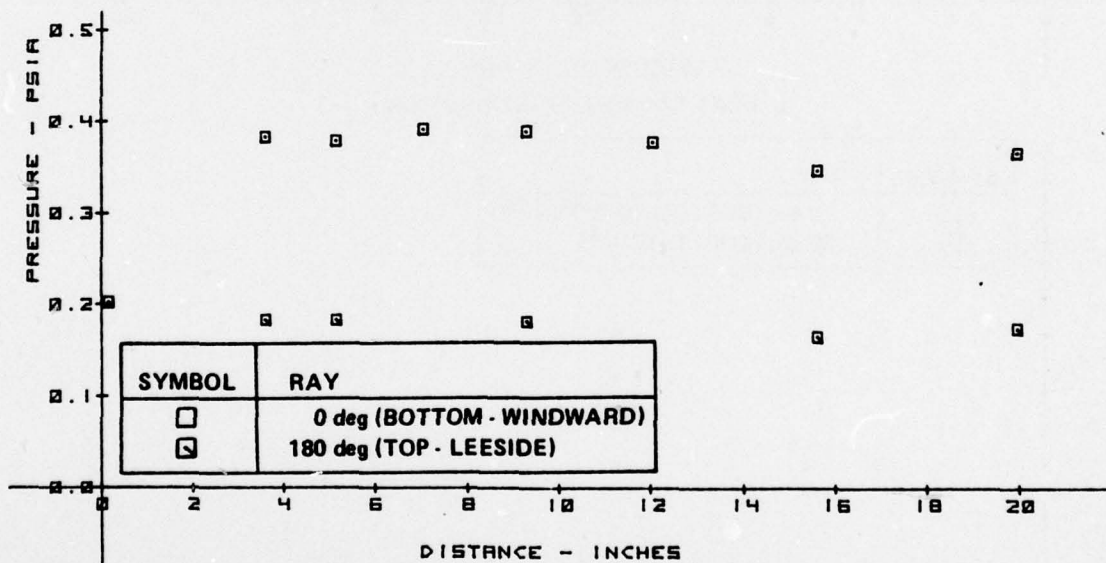


b. PRESSURE DISTRIBUTION

Figure 2-45 MEASUREMENTS ON 6° CONE MODEL FOR SHARP NOSE CONFIGURATION -  $M_\infty = 12.9$ ,  $Re/FT = 1.1 \times 10^6$ ,  $\alpha = 3^\circ$



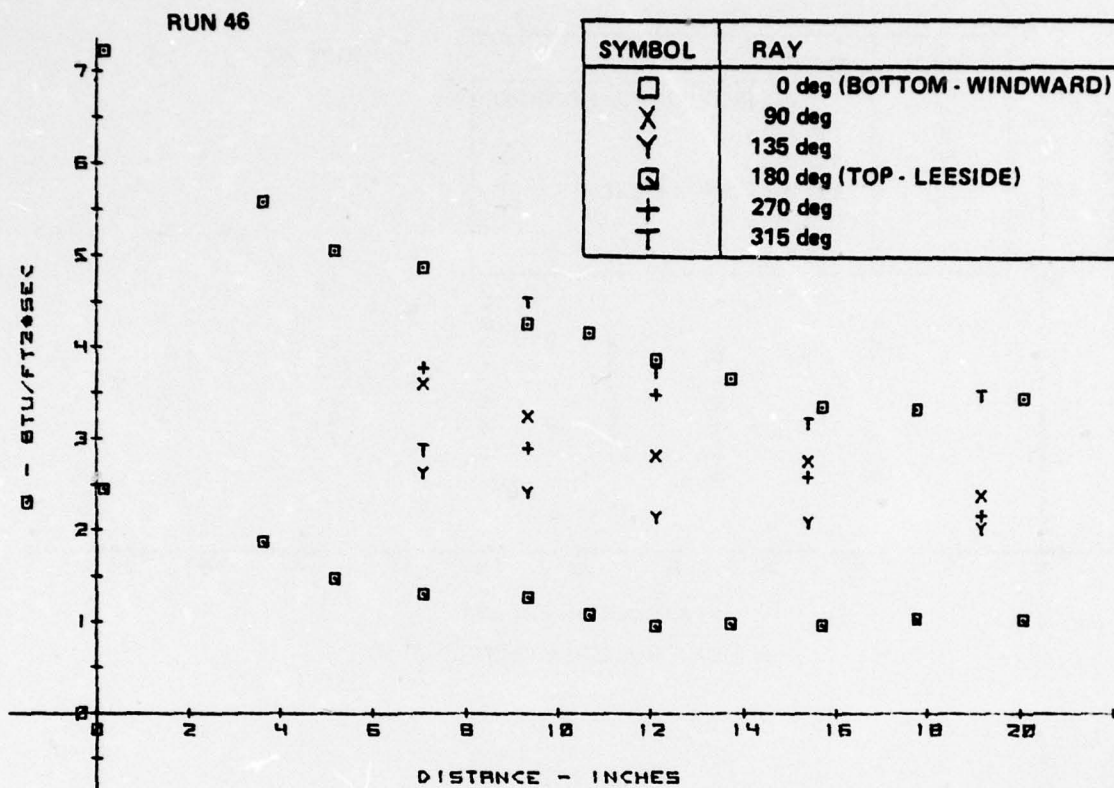
a. HEAT TRANSFER DISTRIBUTION



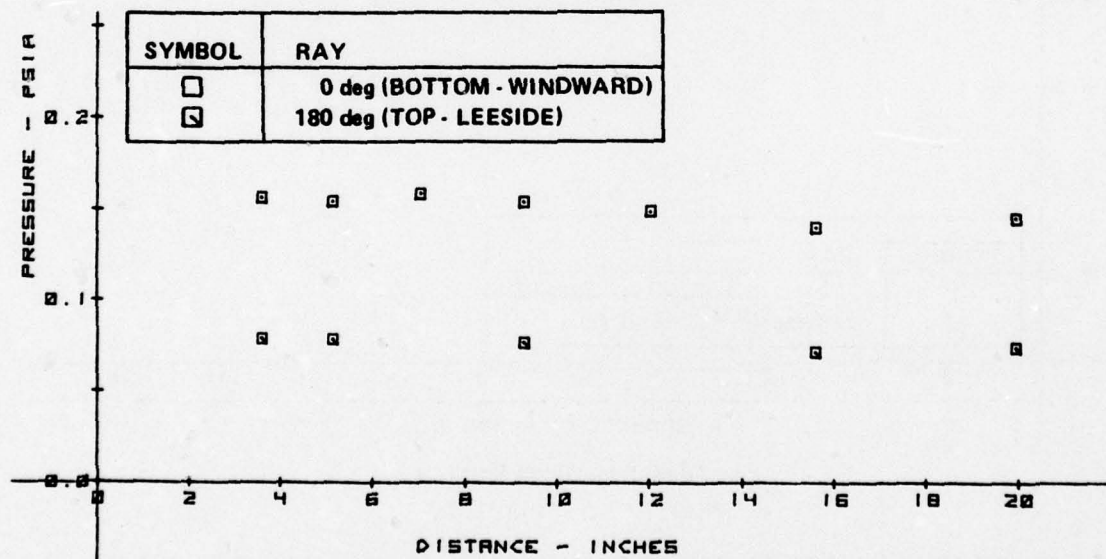
b. PRESSURE DISTRIBUTION

Figure 2-46 MEASUREMENTS ON 6° CONE MODEL FOR SHARP NOSE CONFIGURATION -  
 $M_\infty = 13.2$ ,  $Re/FT = 2.9 \times 10^6$ ,  $\alpha = 2^\circ 2'$



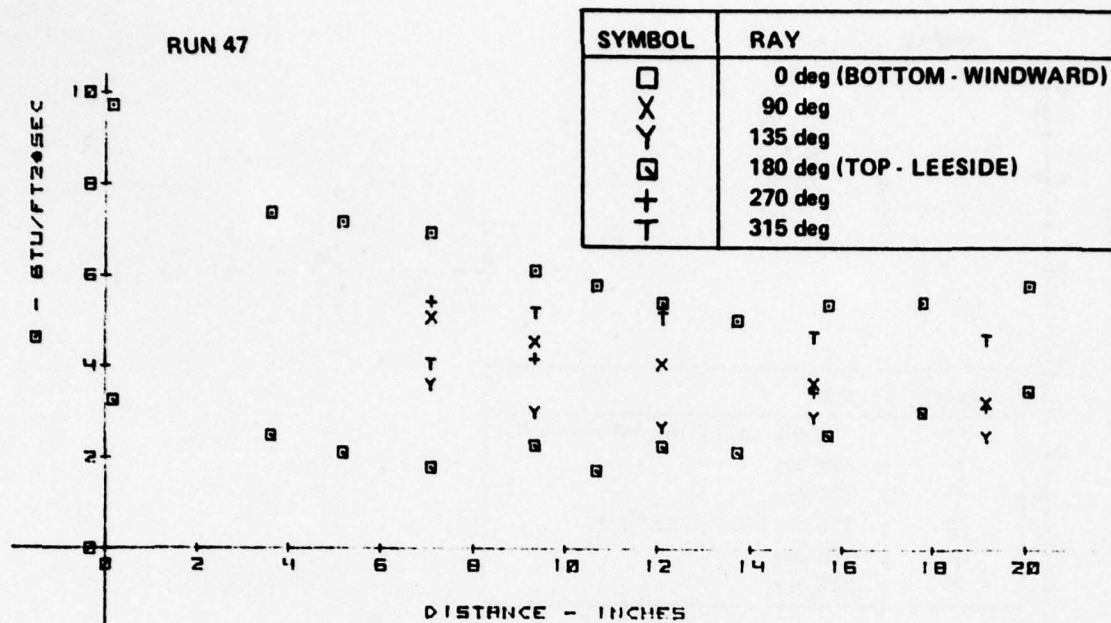


a. HEAT TRANSFER DISTRIBUTION

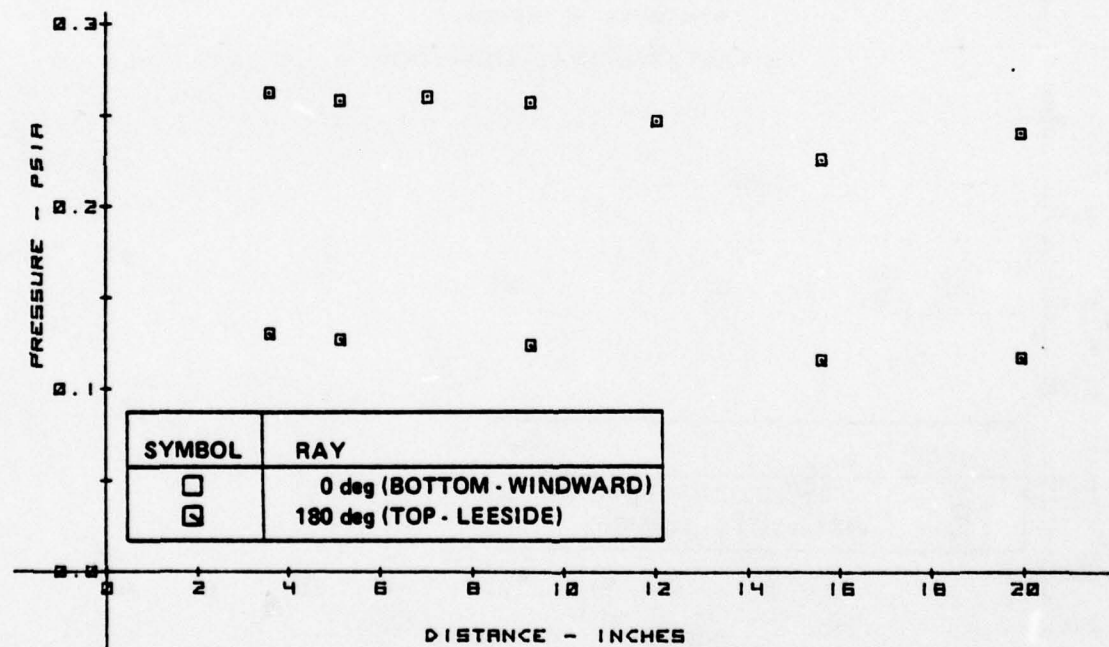


b. PRESSURE DISTRIBUTION

Figure 2-47 MEASUREMENTS ON 6° CONE MODEL FOR SHARP NOSE CONFIGURATION -  $M_\infty = 12.8$ ,  $Re/FT = 1.2 \times 10^6$ ,  $\alpha = 2^\circ 2'$

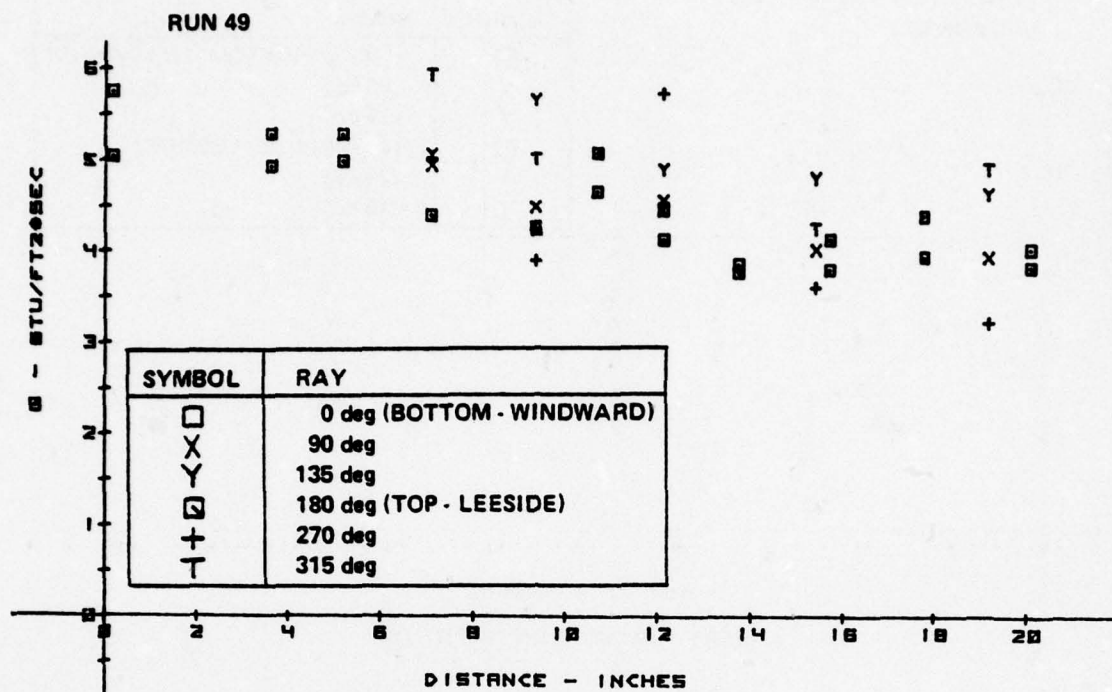


a. HEAT TRANSFER DISTRIBUTION

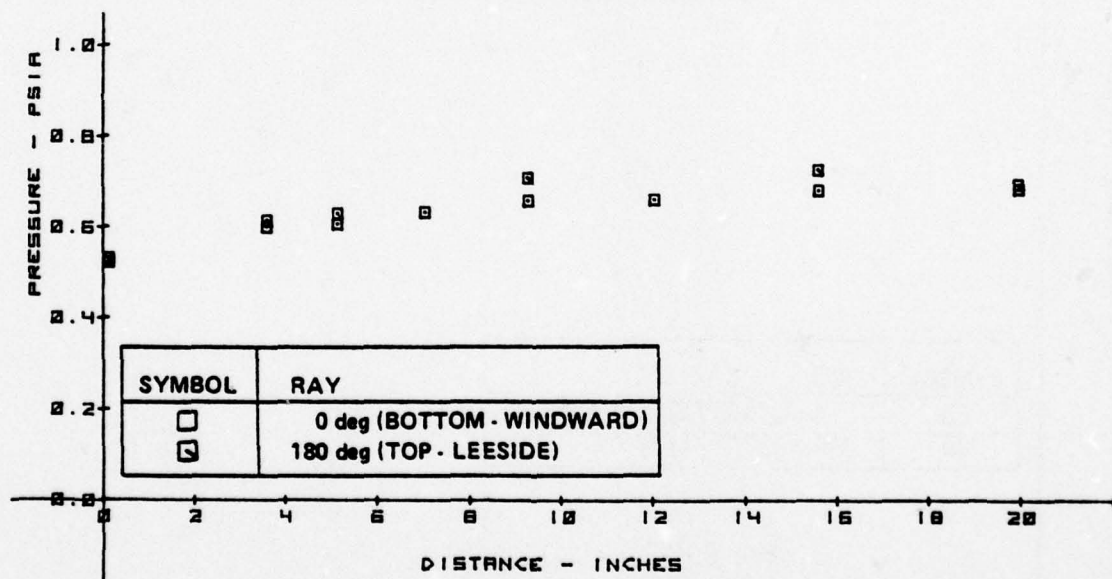


b. PRESSURE DISTRIBUTION

Figure 2-48 MEASUREMENTS ON 6° CONE MODEL FOR SHARP NOSE CONFIGURATION -  $M_\infty = 12.9$ ,  $Re/FT = 1.9 \times 10^6$ ,  $\alpha = 2^\circ 2'$



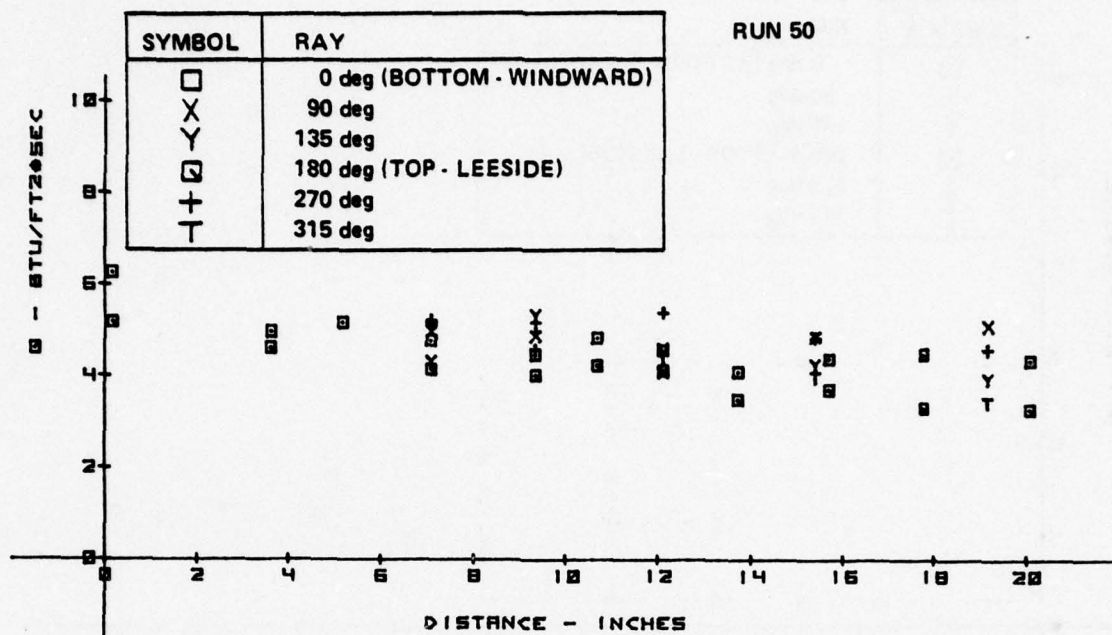
a. HEAT TRANSFER DISTRIBUTION



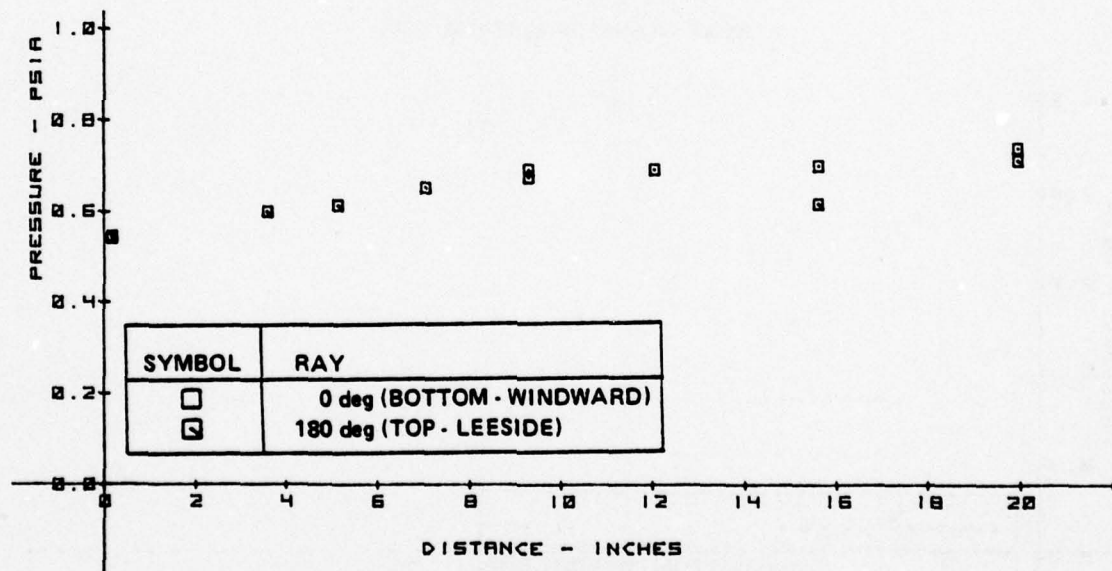
b. PRESSURE DISTRIBUTION

Figure 2-49 MEASUREMENT ON 6° CONE MODEL FOR 6% SPHERICAL NOSE CONFIGURATION -  $M_\infty = 11.3$ ,  $Re/FT = 1.1 \times 10^7$ ,  $\alpha = 0^\circ$



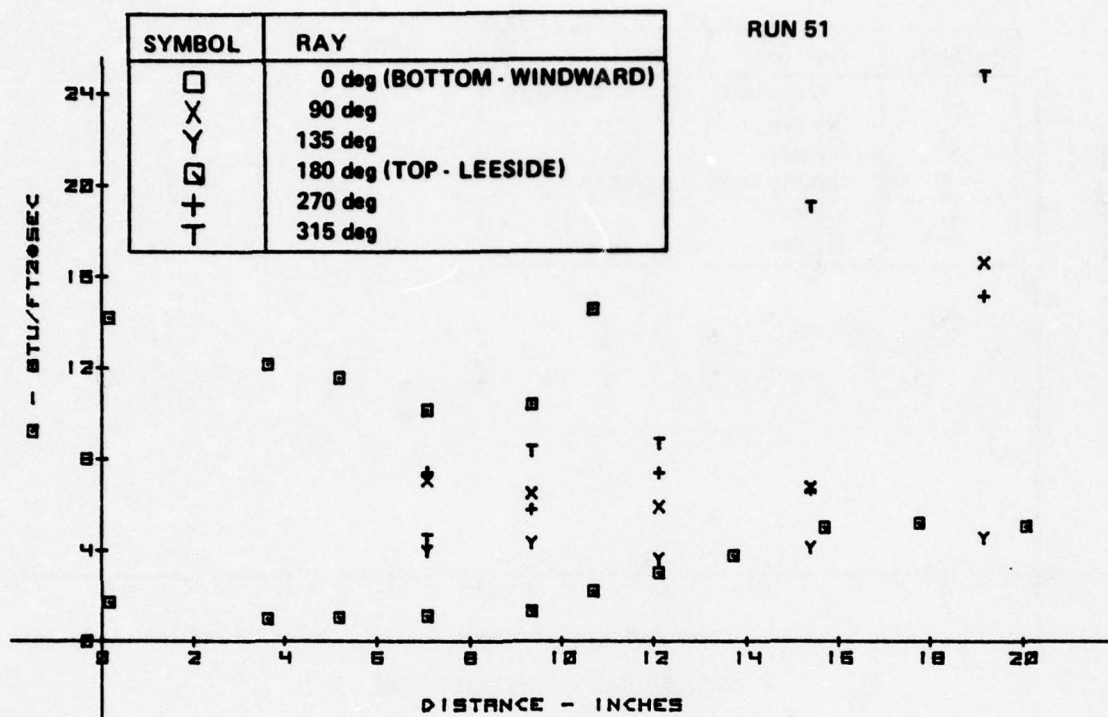


a. HEAT TRANSFER DISTRIBUTION

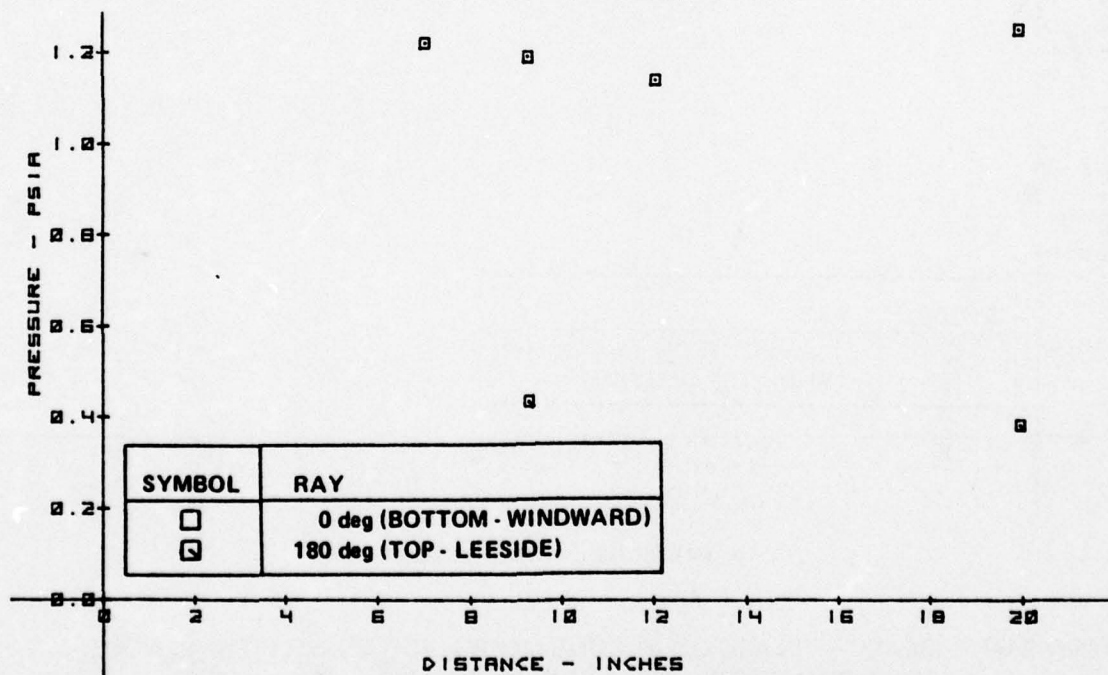


b. PRESSURE DISTRIBUTION

Figure 2-50 MEASUREMENTS ON 6° CONE MODEL FOR 6% ELLIPTICAL NOSE CONFIGURATION -  $M_\infty = 11.3$ ,  $Re/FT = 9.8 \times 10^6$ ,  $\alpha = 0^\circ 2'$

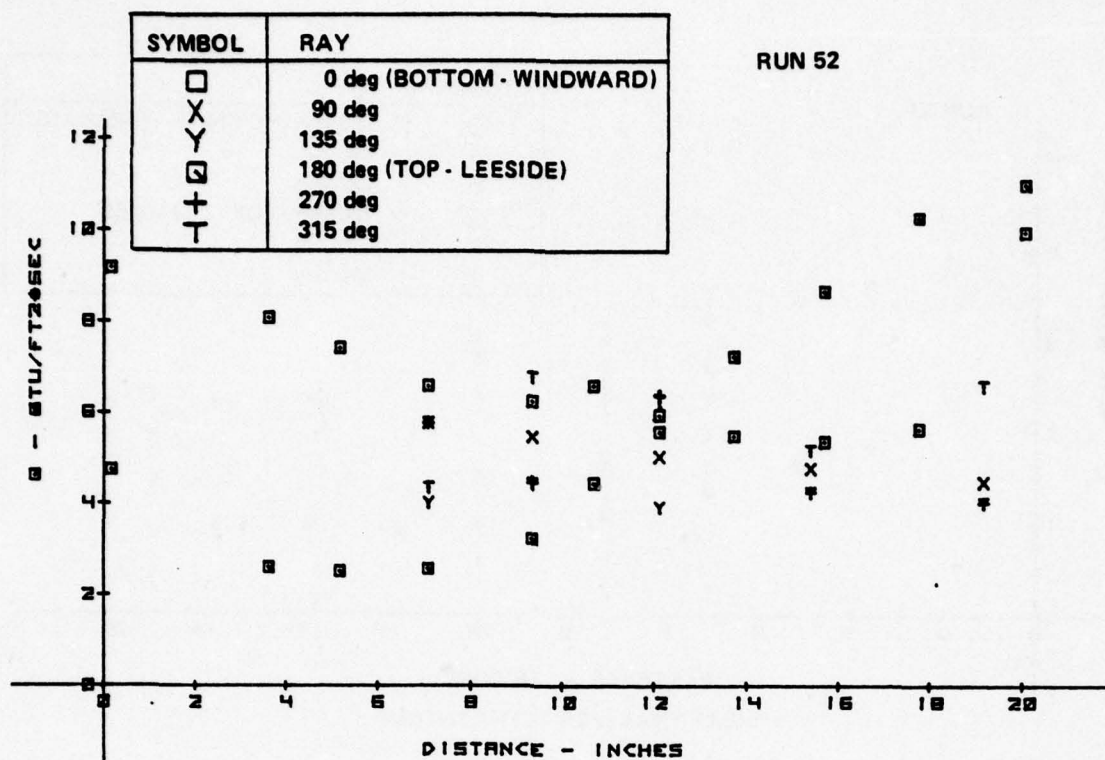


a. HEAT TRANSFER DISTRIBUTION

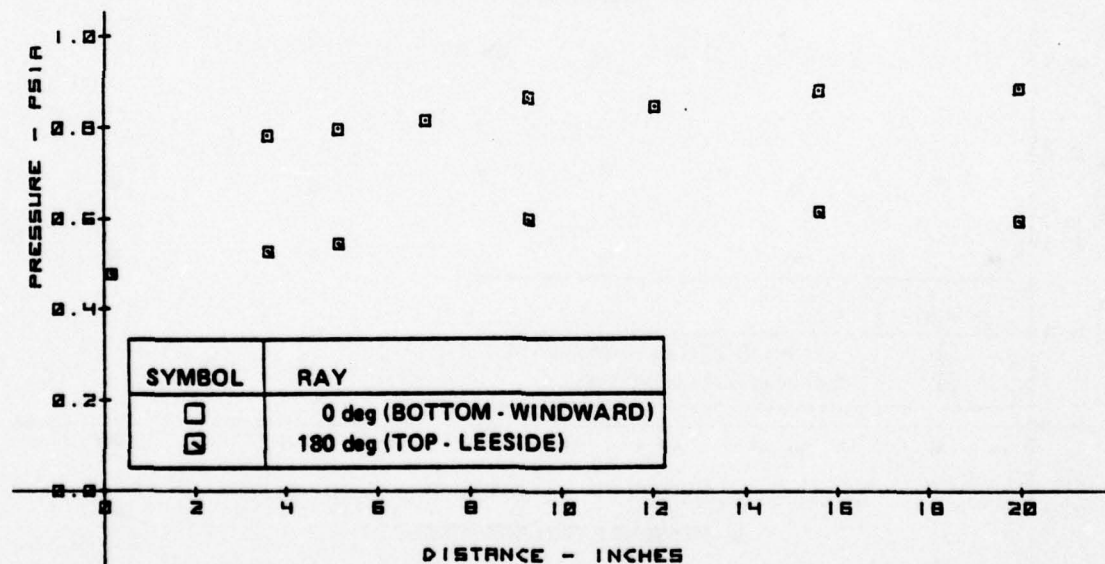


b. PRESSURE DISTRIBUTION

Figure 2-51 MEASUREMENTS ON 6° CONE MODEL FOR 6% SPHERICAL NOSE CONFIGURATION -  $M_\infty = 11.3$ ,  $Re/FT = 9.7 \times 10^6$ ,  $\alpha = 3^\circ 5'$



a. HEAT TRANSFER DISTRIBUTION



b. PRESSURE DISTRIBUTION

Figure 2-52 MEASUREMENTS ON 6° CONE MODEL FOR 6% SPHERICAL NOSE CONFIGURATION -  $M_\infty = 11.5$ ,  $Re/FT = 1.0 \times 10^7$ ,  $\alpha = 1^\circ 1'$



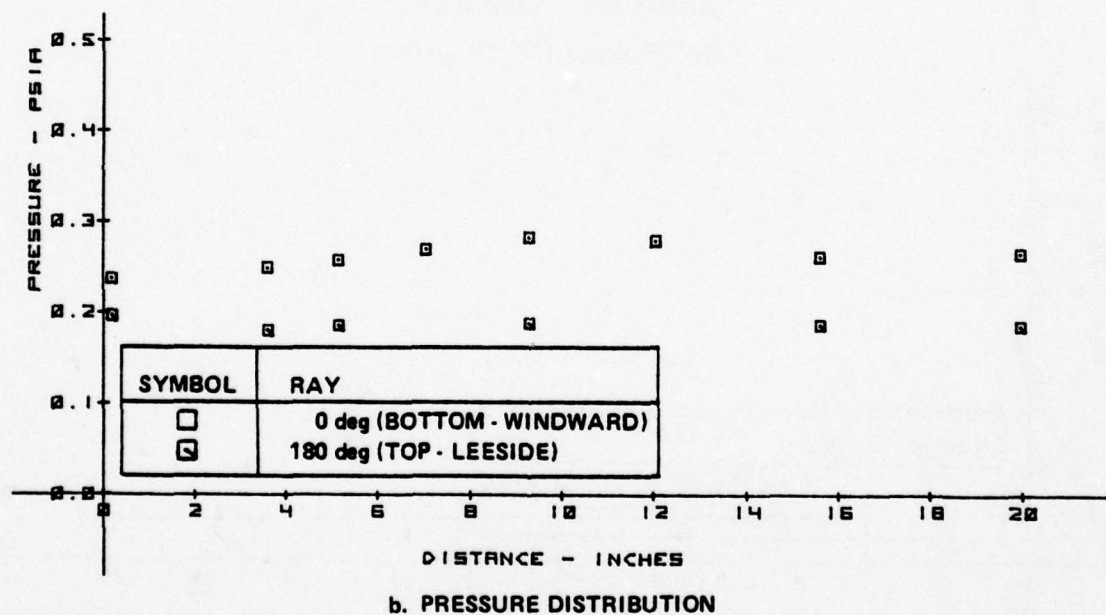
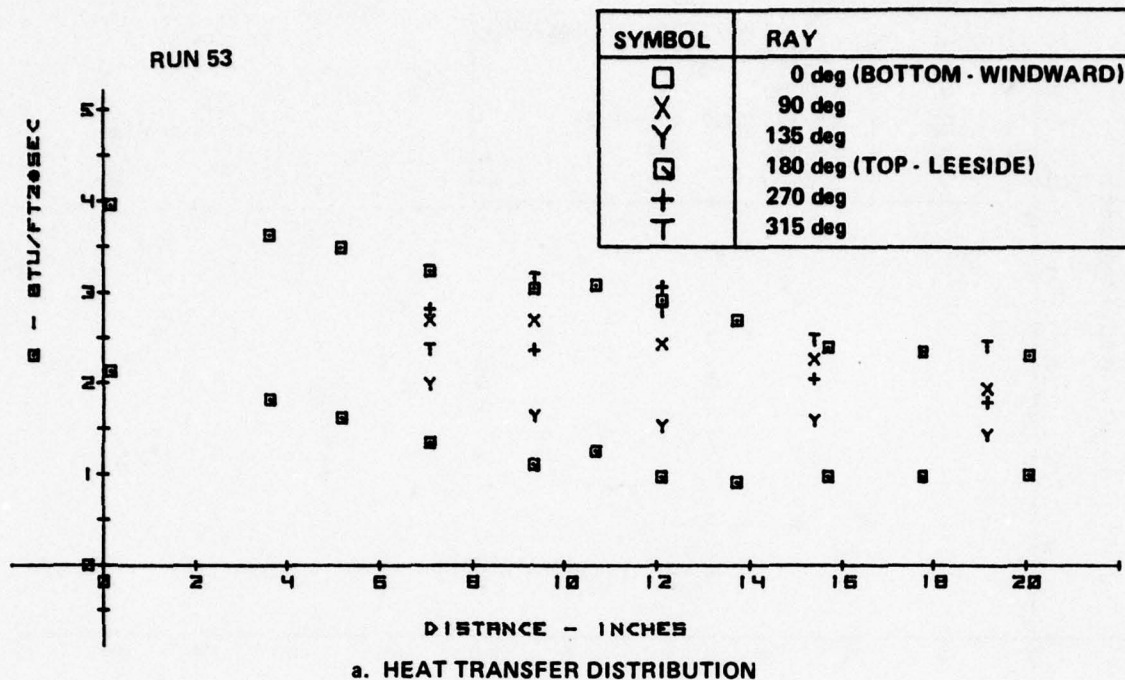
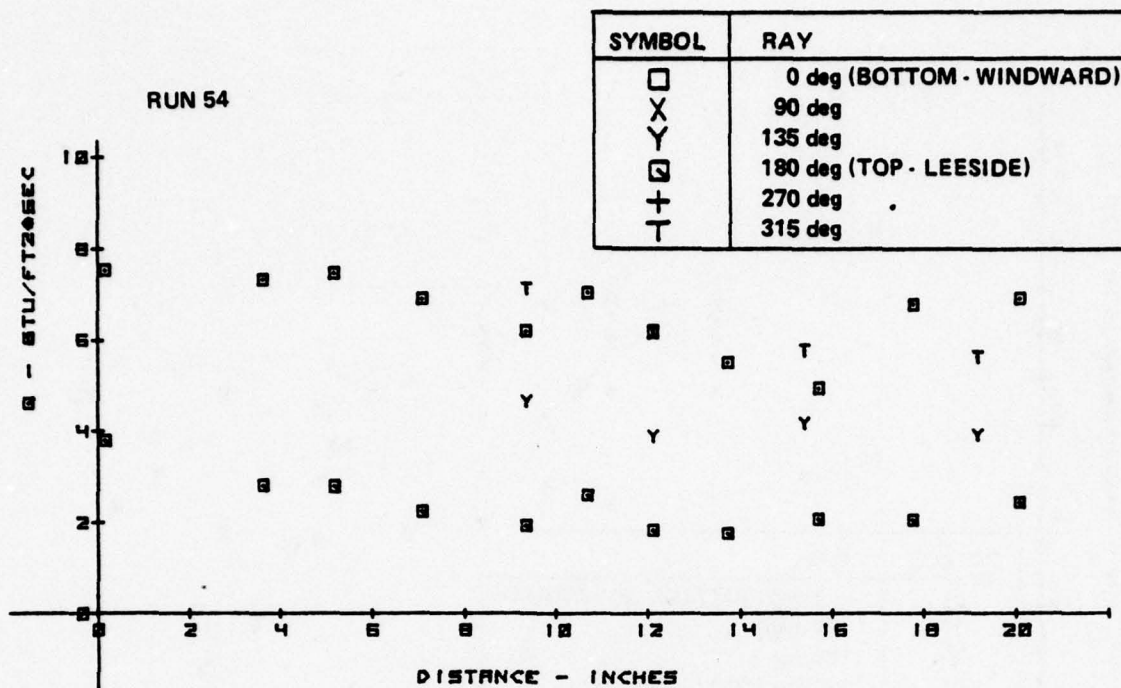
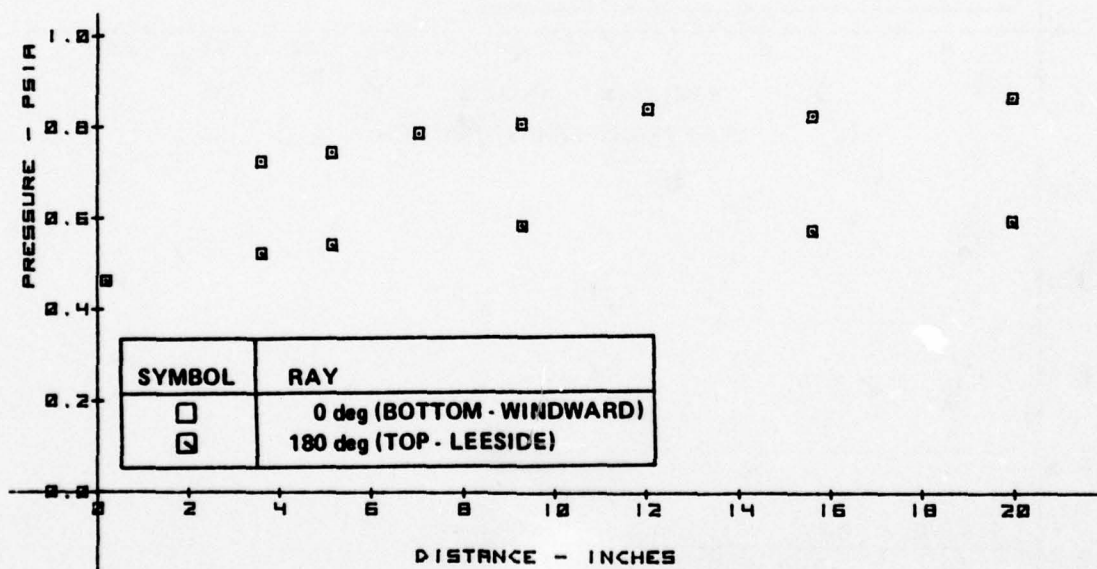


Figure 2-53 MEASUREMENTS ON 6° CONE MODEL FOR 6% SPHERICAL NOSE CONFIGURATION -  $M_\infty = 11.0$ ,  $Re/FT = 3.2 \times 10^6$ ,  $\alpha = 1^\circ 1'$



a. HEAT TRANSFER DISTRIBUTION



b. PRESSURE DISTRIBUTION

Figure 2-54 MEASUREMENTS ON 6° CONE MODEL FOR 6% ELLIPTICAL NOSE CONFIGURATION -  $M_\infty = 11.4$ ,  $Re/FT = 1.0 \times 10^7$ ,  $\alpha = 1^\circ 1'$

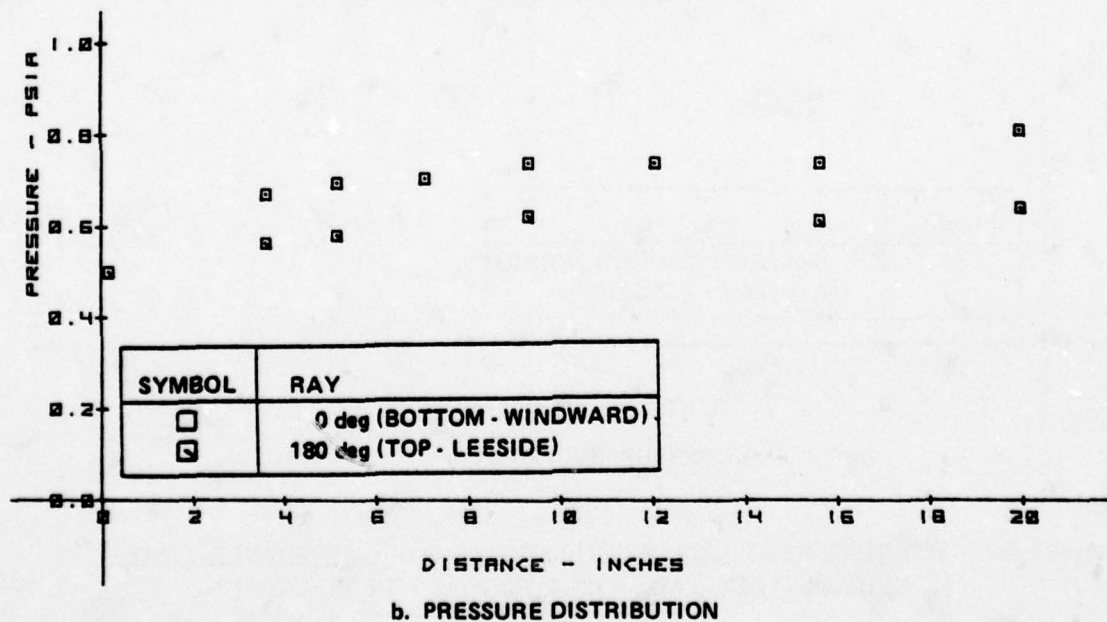
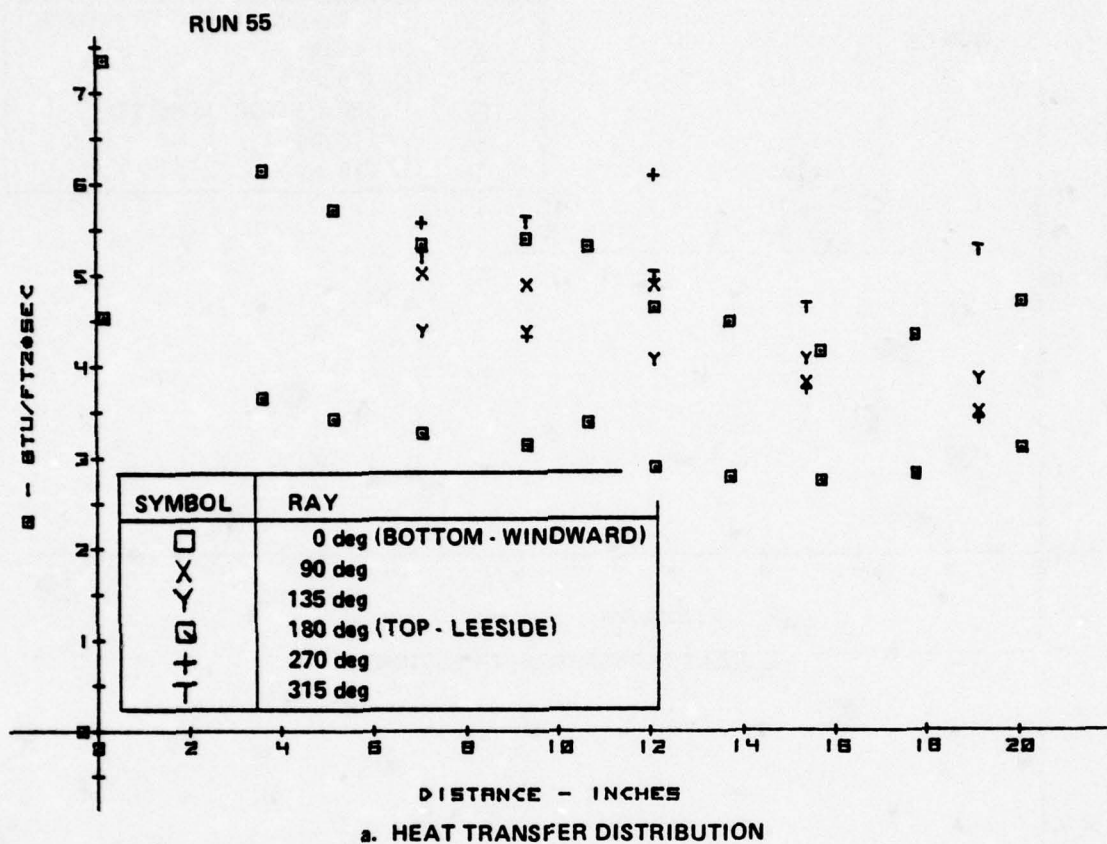
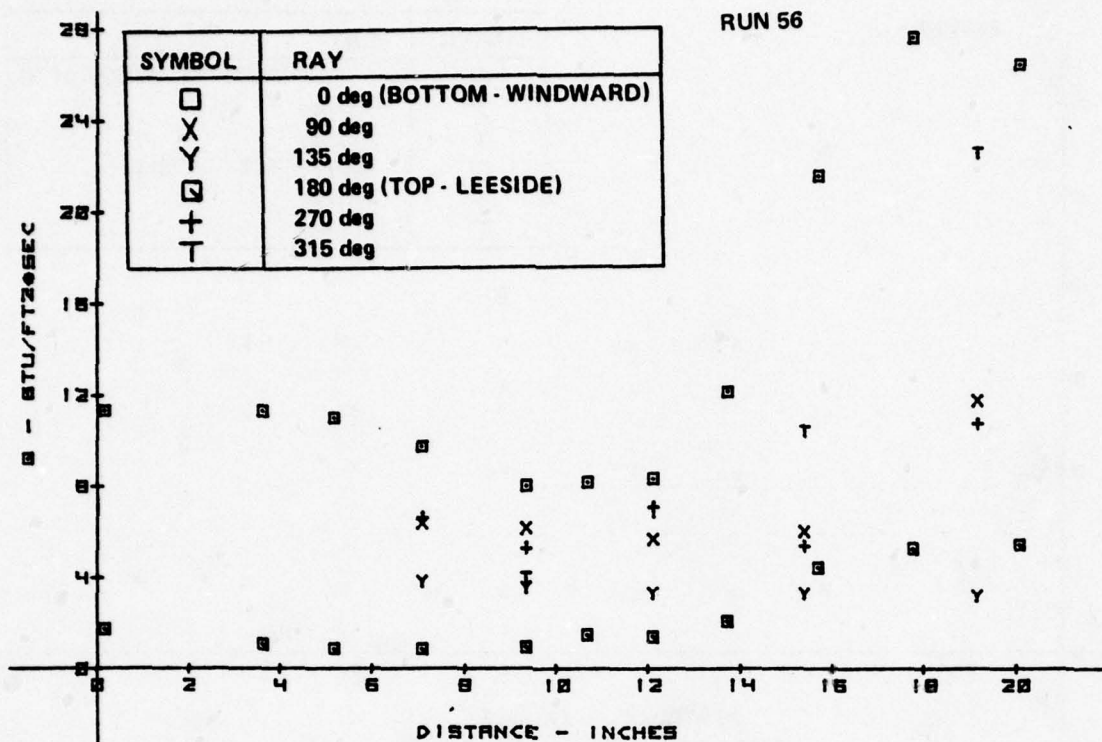
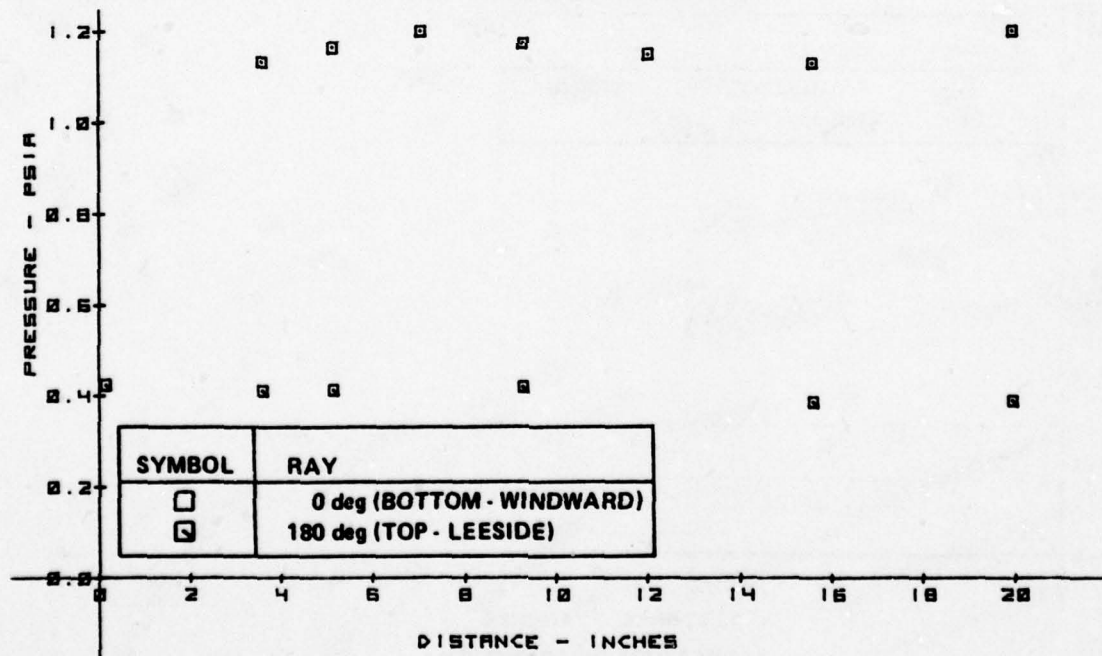


Figure 2-55 MEASUREMENTS ON 6° CONE MODEL FOR 6% SPHERICAL NOSE CONFIGURATION —  $M_\infty = 11.3$ ,  $Re/FT = 1.1 \times 10^7$ ,  $\alpha = 0^\circ 30'$



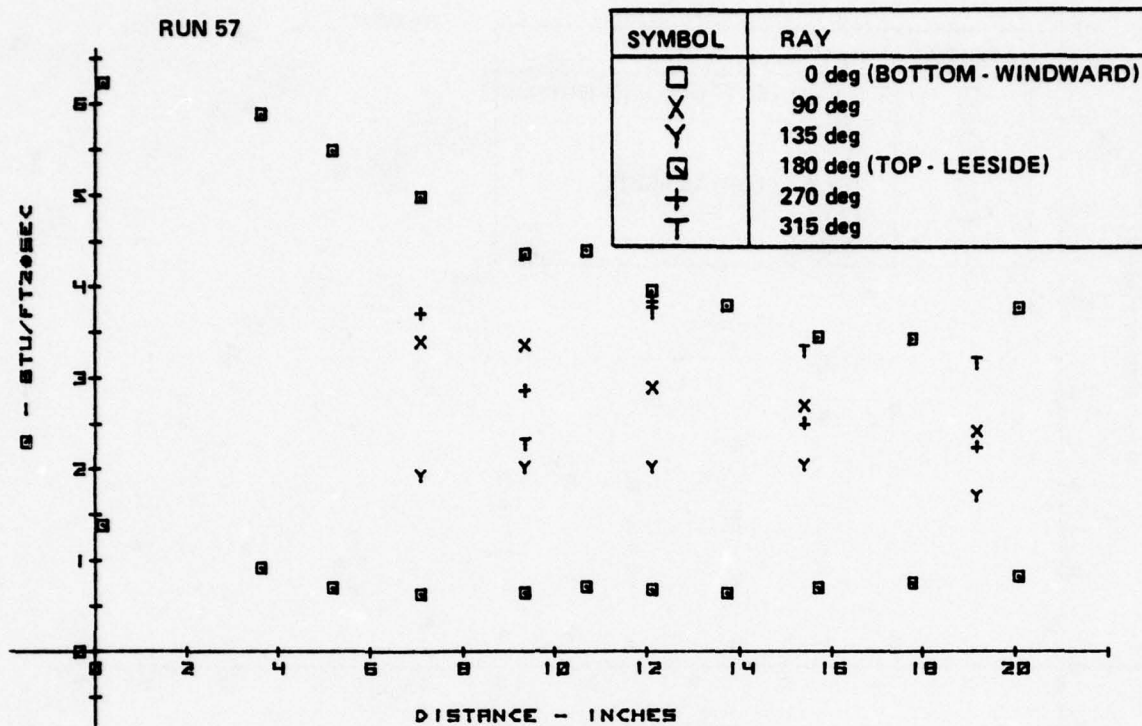


a. HEAT TRANSFER DISTRIBUTION

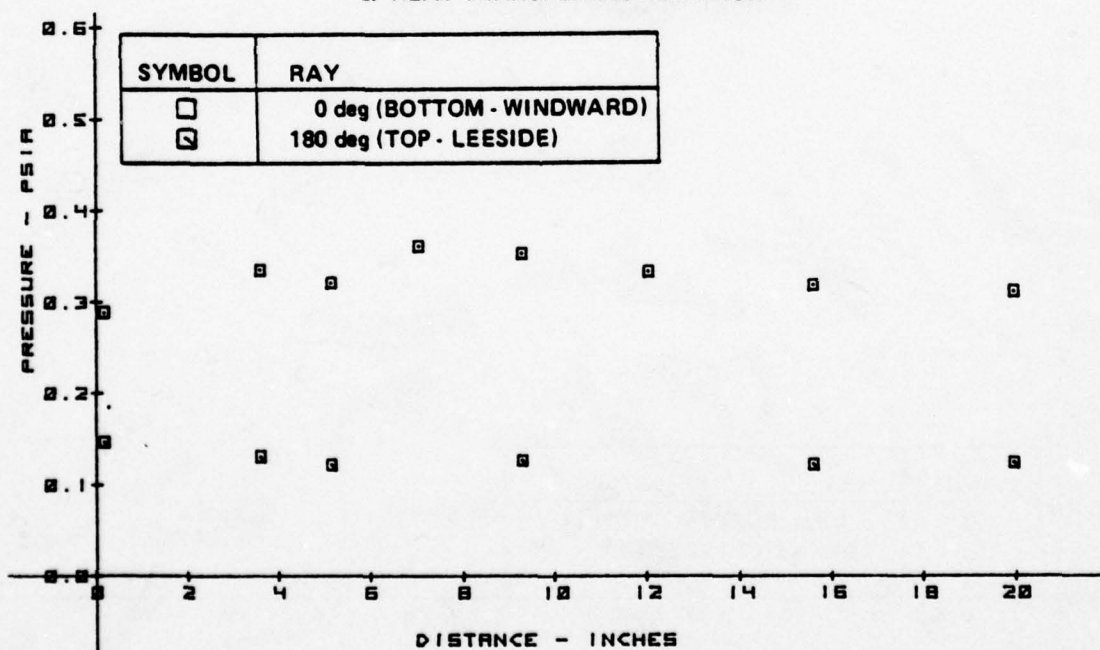


b. PRESSURE DISTRIBUTION

Figure 2-56 MEASUREMENTS ON 6° CONE MODEL FOR 6% ELLIPTICAL NOSE CONFIGURATION -  $M_\infty = 11.3$ ,  $Re/FT = 1.0 \times 10^7$ ,  $\alpha = 3^\circ$



a. HEAT TRANSFER DISTRIBUTION



b. PRESSURE DISTRIBUTION

Figure 2-57 MEASUREMENTS ON 6° CONE MODEL FOR 6% ELLIPTICAL NOSE CONFIGURATION -  $M_\infty = 10.9$ ,  $Re/FT = 2.4 \times 10^6$ ,  $\alpha = 3^\circ$

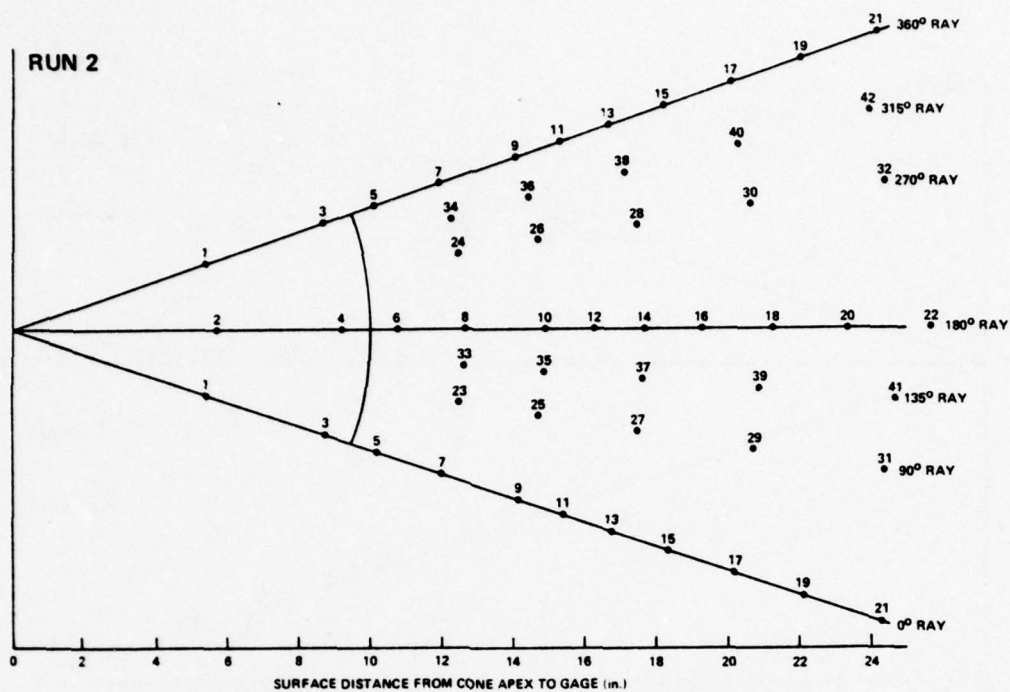


**Figure 2-58** TRANSITION BOUNDARIES ON 6° CONE MODEL FOR SHARP NOSE CONFIGURATION –  $M_\infty = 13.0$ ,  $Re/FT = 4.8 \times 10^6$ ,  $\alpha = 0^\circ - 7'$

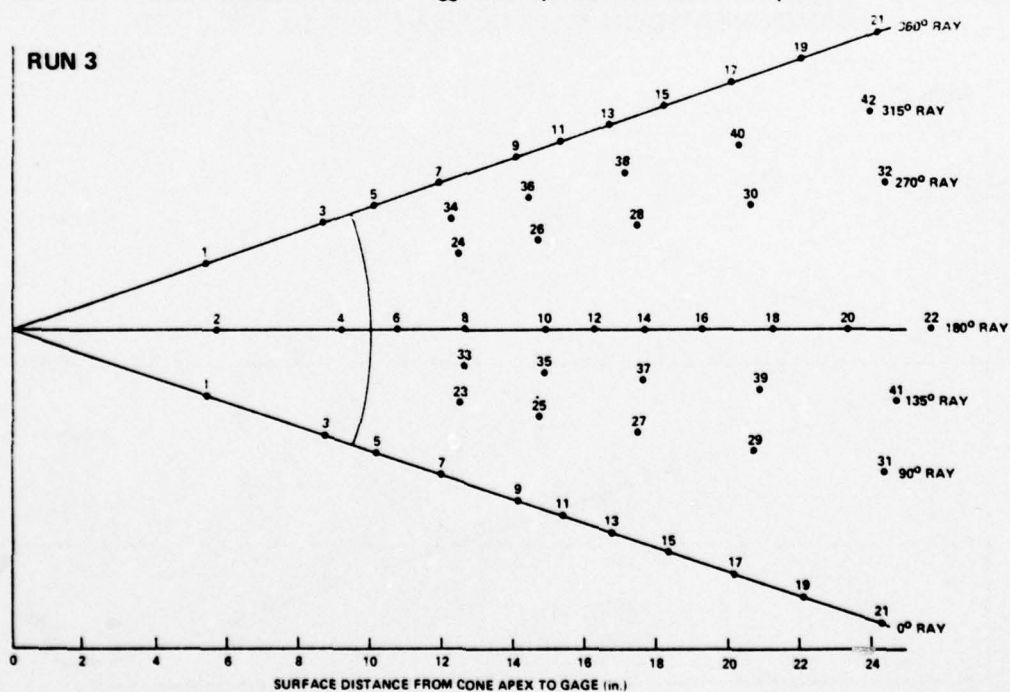


**Figure 2-59** TRANSITION BOUNDARIES ON 6° CONE MODEL FOR SHARP NOSE CONFIGURATION –  $M_\infty = 13.0$ ,  $Re/FT = 4.7 \times 10^6$ ,  $\alpha = 0^\circ - 7'$



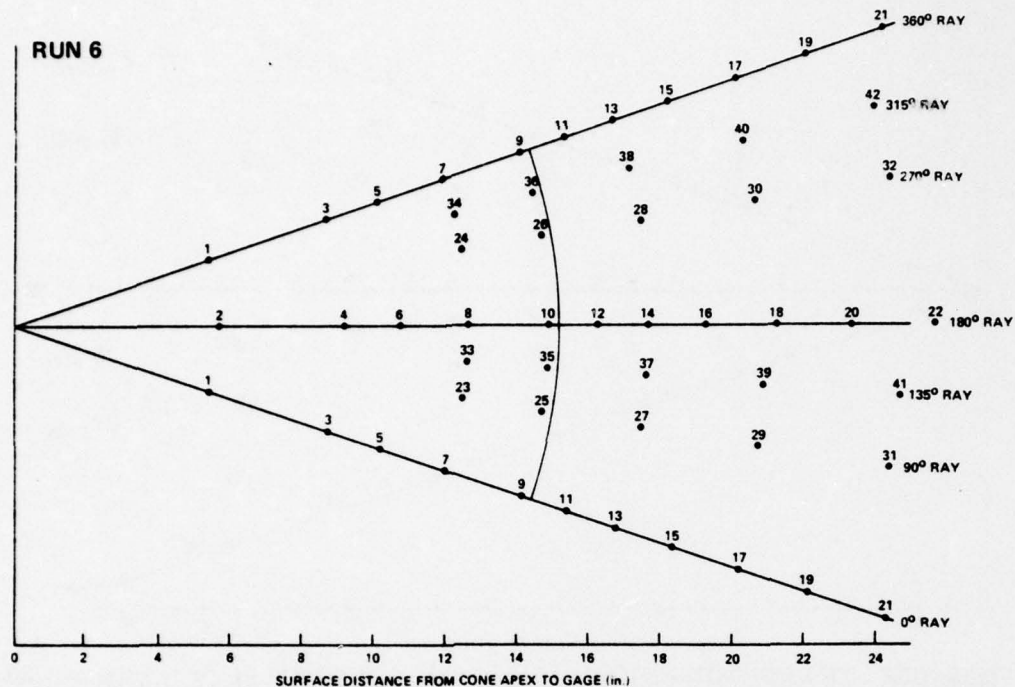


**Figure 2-60** TRANSITION BOUNDARIES ON 6° CONE MODEL FOR SHARP NOSE CONFIGURATION –  $M_\infty = 13.3$ ,  $Re/FT = 3.1 \times 10^6$ ,  $\alpha = 0^\circ$

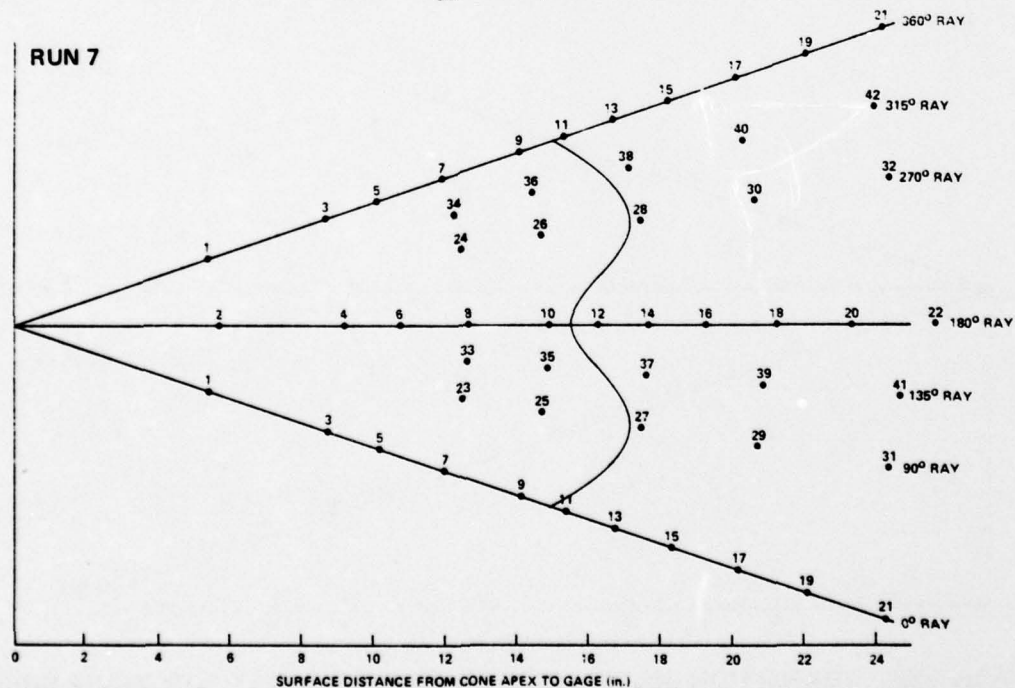


**Figure 2-61** TRANSITION BOUNDARIES ON 6° CONE MODEL FOR SHARP NOSE CONFIGURATION –  $M_\infty = 13.4$ ,  $Re/FT = 3.0 \times 10^6$ ,  $\alpha = 0^\circ 57'$

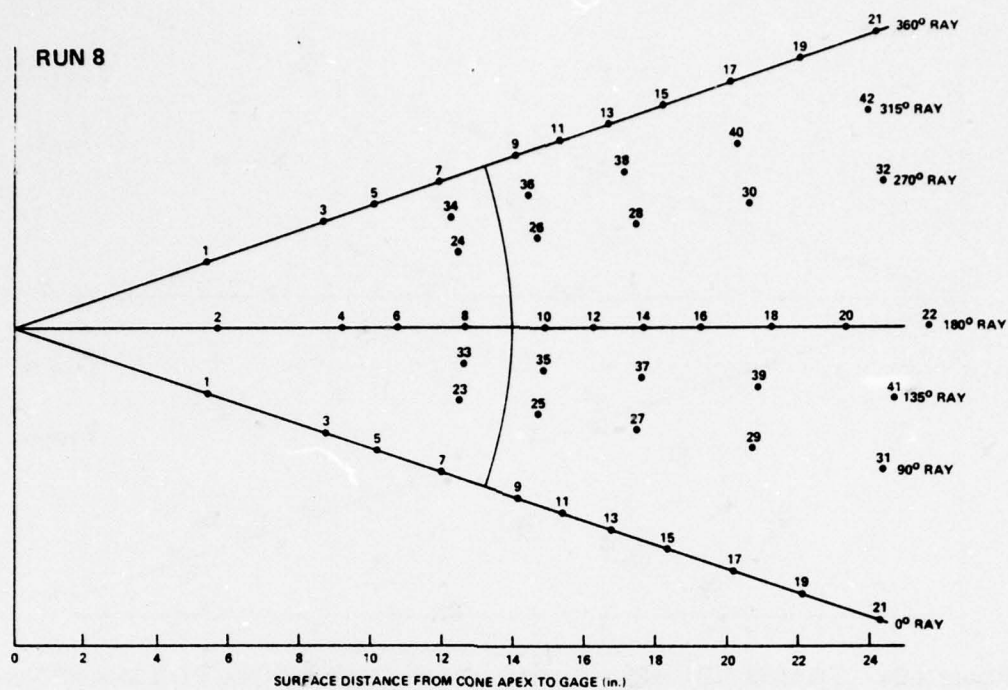


**Figure 2-62 TRANSITION BOUNDARIES ON 6° CONE MODEL FOR SHARP NOSE CONFIGURATION –  $M_\infty \approx 12.7$ ,  $Re/FT = 3 \times 10^6$ ,  $\alpha = 0^\circ - 2^\circ$**

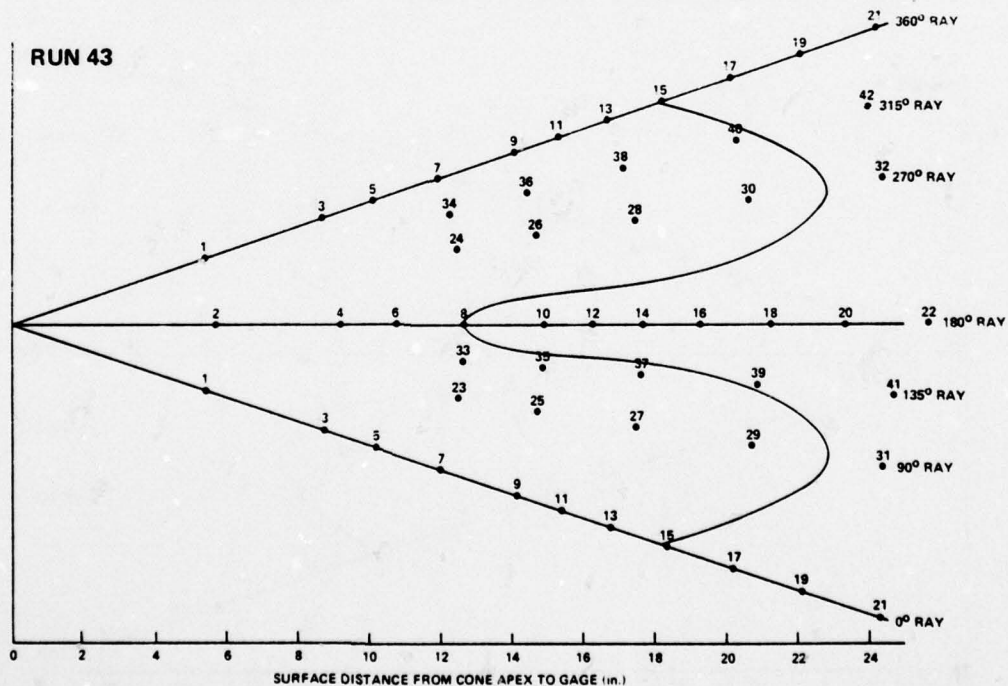


**Figure 2-63 TRANSITION BOUNDARIES ON 6° CONE MODEL FOR SHARP NOSE CONFIGURATION –  $M_\infty = 13.2$ ,  $Re/FT = 3.0 \times 10^6$ ,  $\alpha = 3^\circ$**

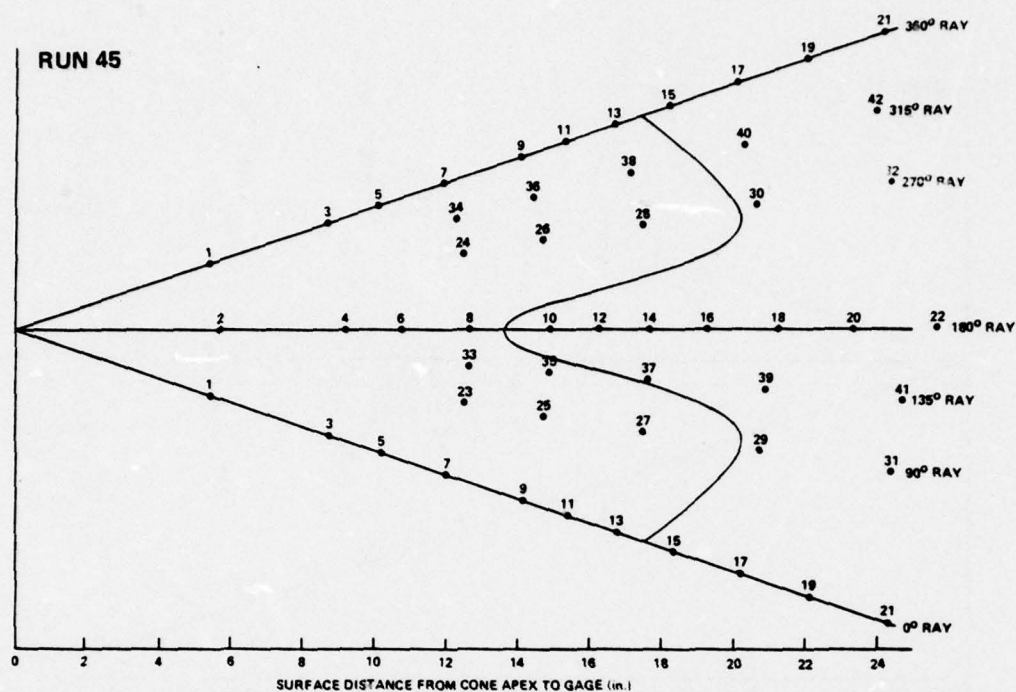


**Figure 2-64** TRANSITION BOUNDARIES ON 6° CONE MODEL FOR SHARP NOSE CONFIGURATION -  $M_\infty = 13.2$ ,  $Re/FT = 2.9 \times 10^6$ ,  $\alpha = 2^\circ 2'$

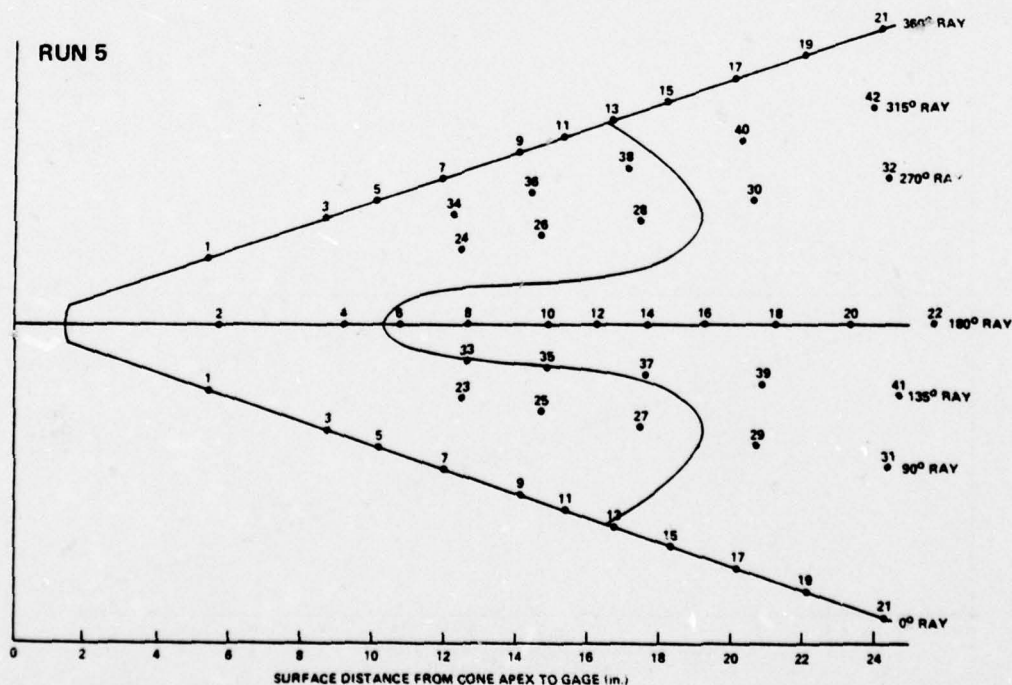


**Figure 2-65** TRANSITION BOUNDARIES ON 6° CONE MODEL FOR 6% SPHERICAL NOSE CONFIGURATION -  $M_\infty = 13.0$ ,  $Re/FT = 5.0 \times 10^6$ ,  $\alpha = 3^\circ 3'$



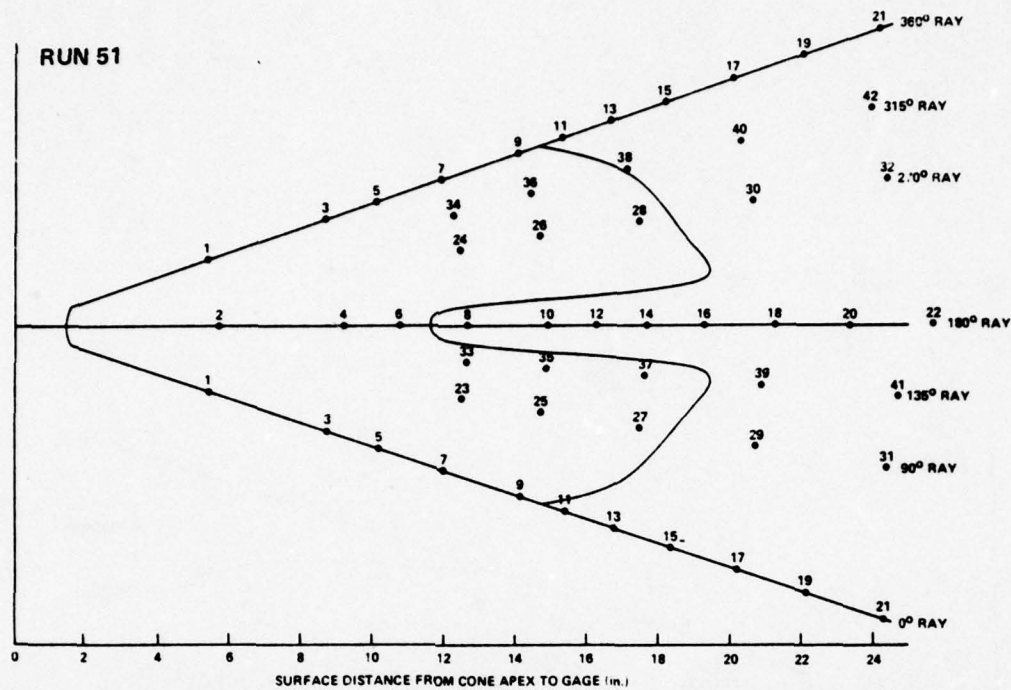


**Figure 2-66** TRANSITION BOUNDARIES ON 6° CONE MODEL FOR 6% SPHERICAL NOSE CONFIGURATION –  $M_{\infty} = 11.3$ ,  $Re/FT = 9.7 \times 10^6$ ,  $\alpha = 3^{\circ} 5'$

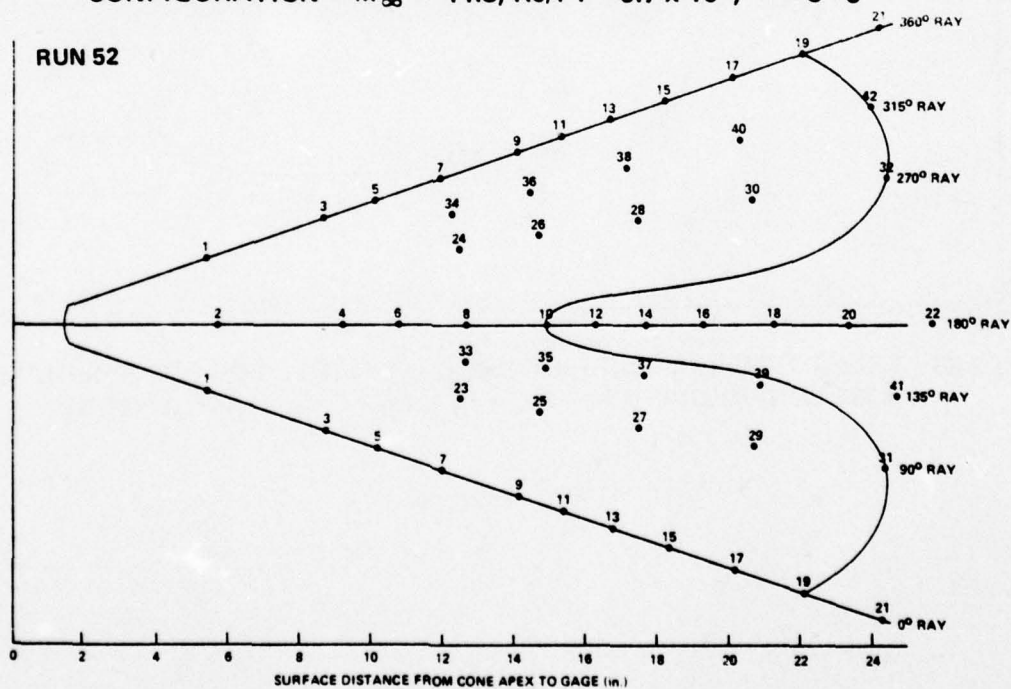


**Figure 2-67** TRANSITION BOUNDARIES ON 6° CONE MODEL FOR 6% SPHERICAL NOSE CONFIGURATION –  $M_{\infty} = 11.5$ ,  $Re/FT = 1.0 \times 10^7$ ,  $\alpha = 1^{\circ} 1'$

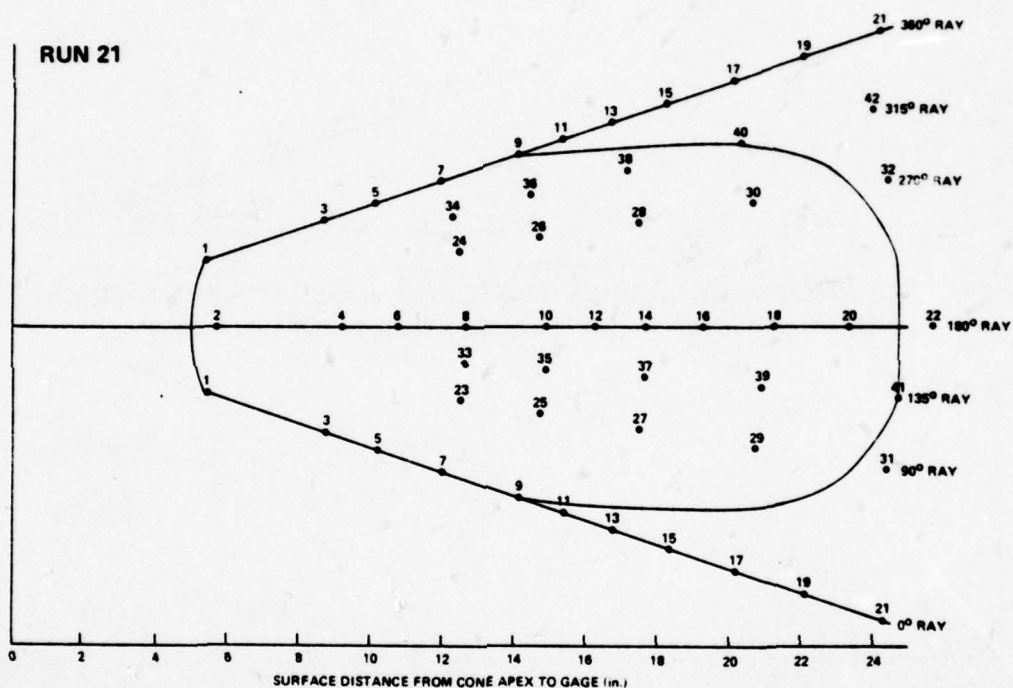


**Figure 2-68** TRANSITION BOUNDARIES ON 6° CONE MODEL FOR 21% SPHERICAL NOSE CONFIGURATION —  $M_\infty = 11.4$ ,  $Re/FT = 1.0 \times 10^7$ ,  $\alpha = 2^\circ 56'$

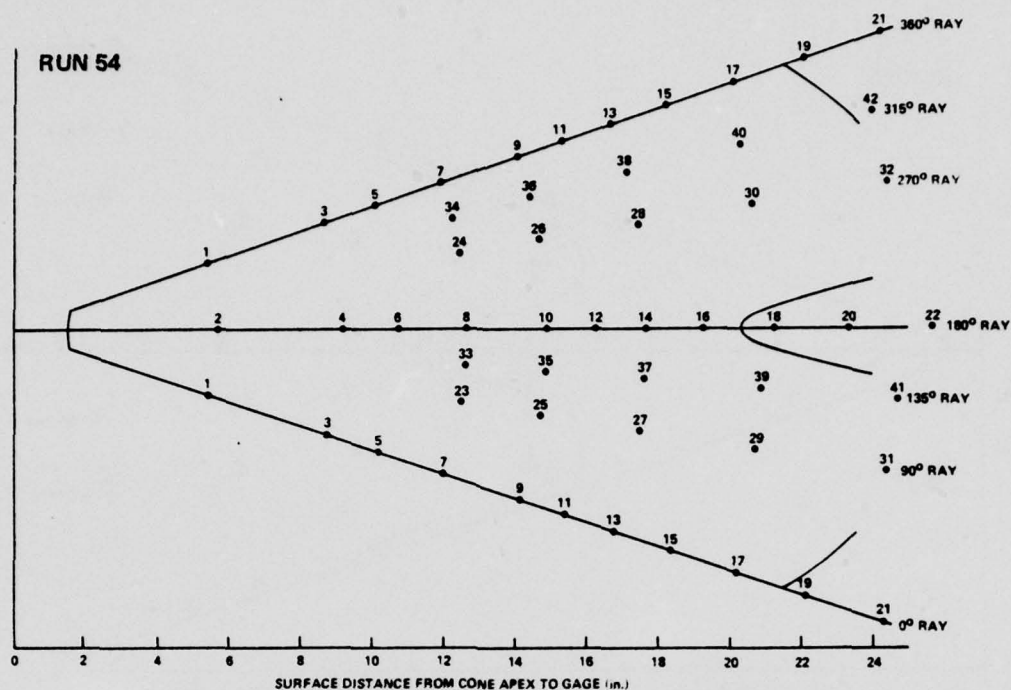


**Figure 2-69** TRANSITION BOUNDARIES ON 6° CONE MODEL FOR 6% ELLIPTICAL NOSE CONFIGURATION –  $M_{\infty} = 11.4$ ,  $Re/FT = 1.0 \times 10^7$ ,  $\alpha = 1^\circ 1'$

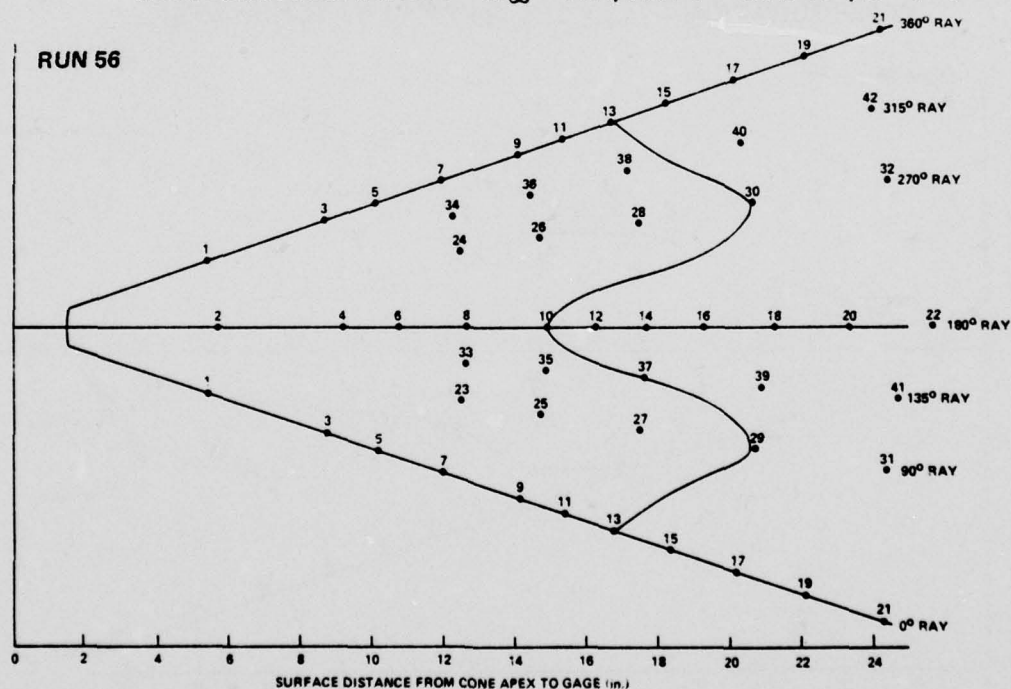


**Figure 2-70** TRANSITION BOUNDARIES ON 6° CONE MODEL FOR 6% ELLIPTICAL NOSE CONFIGURATION –  $M_{\infty} = 11.3$ ,  $Re/FT = 1.0 \times 10^7$ ,  $\alpha = 3^\circ$



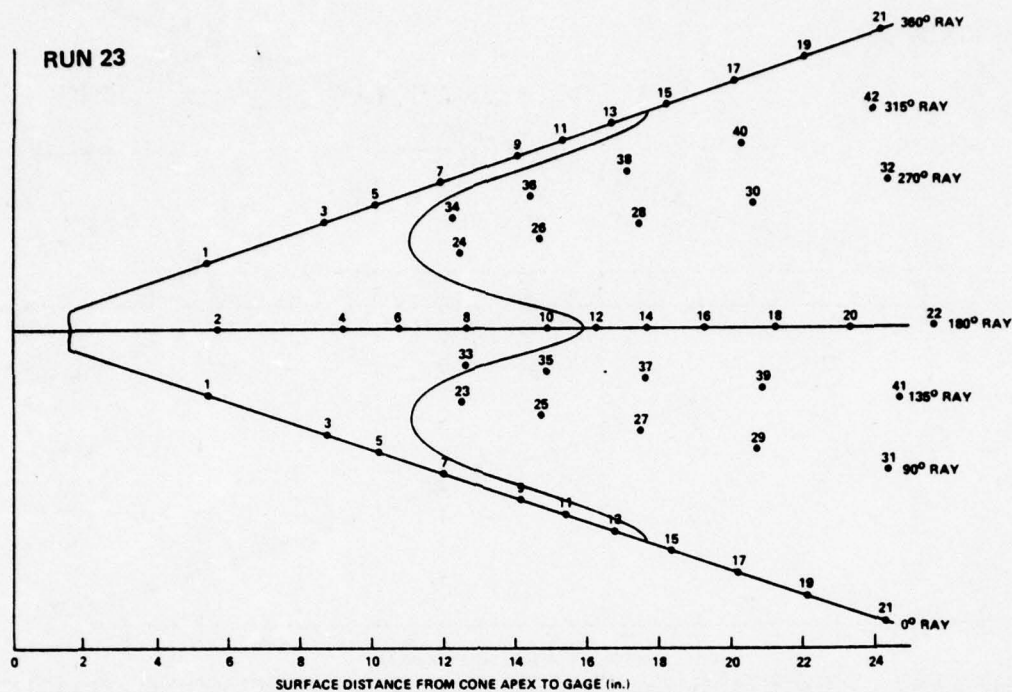


**Figure 2-71 TRANSITION BOUNDARIES ON 6° CONE MODEL FOR 6%, 45° BLUNT NOSE CONFIGURATION –  $M_\infty = 11.4$ ,  $Re/FT = 1.0 \times 10^7$ ,  $\alpha = 0^\circ 5'$**

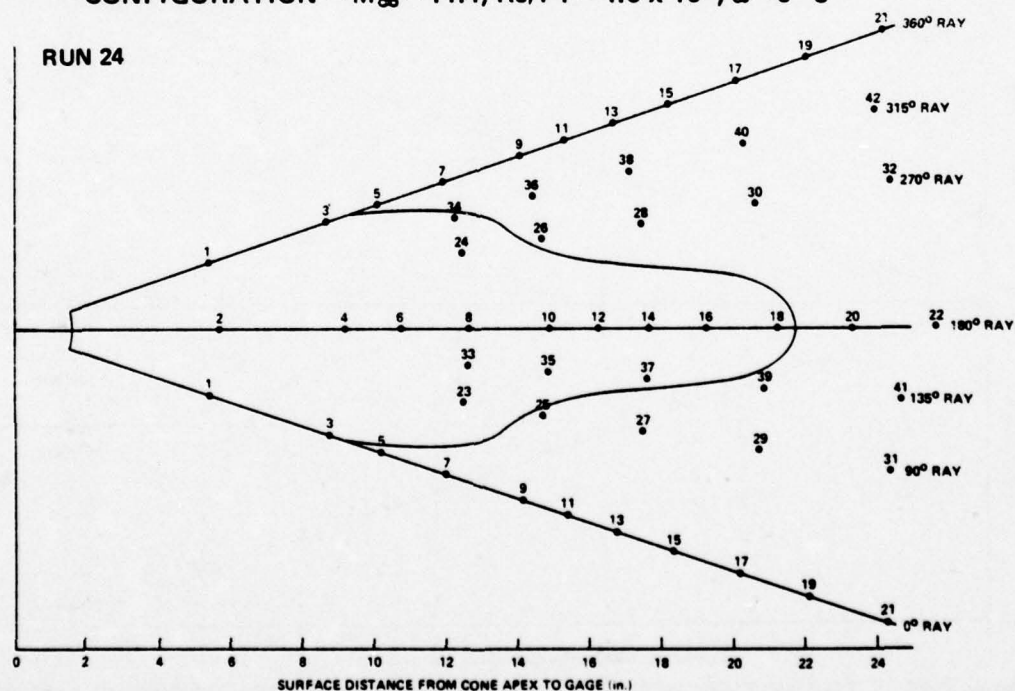


**Figure 2-72 TRANSITION BOUNDARIES ON 6° CONE MODEL FOR 6%, 0° BLUNT NOSE CONFIGURATION –  $M_\infty = 11.3$ ,  $Re/FT = 1.0 \times 10^7$ ,  $\alpha = 0^\circ 5'$**

Table 2-1  
6° CONE FORCE DATA

HT GAGE POSITION	RAY	SURFACE DISTANCE FROM REF. JOINT INCHES
1	0°	0.163
3	↓	3.620
5	↓	5.175
7	↓	7.076
9	↓	9.338
11	↓	10.679
13	↓	12.103
15	↓	13.713
17	↓	15.680
19	↓	17.747
21	↓	20.051
23	90°	7.076
25	↓	9.338
27	↓	12.103
29	↓	15.371
31	↓	19.142
33	135°	7.076
35	↓	9.338
37	↓	12.103
39	↓	15.371
41	↓	19.142
2	180°	0.163
4	↓	3.620
6	↓	5.175
8	↓	7.076
10	↓	9.338
12	↓	10.679
14	↓	12.103
16	↓	13.713
18	↓	15.680
20	↓	17.747
22	↓	20.051
24	270°	7.076
26	↓	9.338
28	↓	12.103
30	↓	15.371
32	↓	19.142
34	315°	7.076
36	↓	9.338
38	↓	12.103
40	↓	15.371
42	↓	19.142

PRESSURE GAGE POSITION	RAY	SURFACE DISTANCE FROM REF. JOINT INCHES
PRESS. 1	0°	0.163
3	↓	3.620
5	↓	5.175
7	↓	7.076
9	↓	9.338
13	↓	12.103
17	↓	15.680
21	↓	20.051
2	180°	0.163
4	↓	3.620
6	↓	5.175
8	↓	7.076
10	↓	9.338
14	↓	12.103
18	↓	15.680
43	↓	16.742
22	↓	20.051

NOSES		SURFACE DISTANCE FROM NOSE TIP TO REF. JOINT INCHES
SHARP		5.625
6%		
↓	0°	SPHERICAL 4.367
↓	45°	ELLIPTICAL 4.308
		BLUNT 4.294
		BLUNT (LOWER) 4.060
21%		
↓	0°	SPHERICAL 1.549
↓	45°	ELLIPTICAL 1.364
		NRV & RTE 1.004
		BLUNT 1.255
		BLUNT (LOWER) 0.975

Table 2-2  
6° CONE FORCE TRANSITION STUDIES

RUN NO.	CONFIGURATION	$\alpha$	$M_\infty$	Re/FT
1	SHARP	-0° 7'	-	-
2	SHARP	-0° 7'	13.0	$4.8 \times 10^6$
3	SHARP	-0° 7'	13.0	$4.8 \times 10^6$
4	6% SPHERICAL	-0° 7'	13.0	$4.8 \times 10^6$
5	6% SPHERICAL	3° 3'	13.0	$4.8 \times 10^6$
6	SHARP	0° 0'	13.3	$3.0 \times 10^6$
7	SHARP	0° 57'	13.3	$3.0 \times 10^6$
8	SHARP	-0° 2'	12.7	$3.0 \times 10^6$
9	SHARP	0° 1'	12.4	$1.7 \times 10^6$
10	6% SPHERICAL	2° 59'	12.5	$2.3 \times 10^6$
11	6% SPHERICAL	2° 3'	13.0	$4.8 \times 10^6$
12	6% SPHERICAL	3° 0'	12.4	$1.7 \times 10^6$
13	6% SPHERICAL	0° 59'	13.0	$4.8 \times 10^6$
21	21% SPHERICAL	2° 56'	11.3	$1.0 \times 10^7$
25	21% SPHERICAL	2° 5'	11.3	$1.0 \times 10^7$
27	21% SPHERICAL	3° 3'	11.0	$3.9 \times 10^6$
28	21% SPHERICAL	2° 3'	11.0	$3.9 \times 10^6$
43	SHARP	3° 0'	13.3	$3.0 \times 10^6$
44	SHARP	3° 0'	12.9	$1.1 \times 10^6$
45	SHARP	2° 2'	13.3	$3.0 \times 10^6$
46	SHARP	2° 2'	12.9	$1.1 \times 10^6$
47	SHARP	2° 2'	12.9	$1.9 \times 10^6$
49	6% SPHERICAL	0° 0'	11.3	$1.0 \times 10^7$
50	6% ELLIPTICAL	0° 2'	11.3	$1.0 \times 10^7$
51	6% SPHERICAL	3° 5'	11.3	$1.0 \times 10^7$
52	6% SPHERICAL	1° 1'	11.3	$1.0 \times 10^7$
53	6% SPHERICAL	1° 1'	11.0	$3.2 \times 10^6$
54	6% ELLIPTICAL	1° 1'	11.3	$1.0 \times 10^7$
55	6% SPHERICAL	0° 30'	11.3	$1.0 \times 10^7$
56	6% ELLIPTICAL	3° 0'	11.3	$1.0 \times 10^7$
57	6% ELLIPTICAL	3° 0'	10.9	$2.5 \times 10^6$



Table 2-3  
6° CONE FORCE TEST CONDITIONS

RUN NO.	2	3	4	5	6	7	8	9
ATTACK ANGLE	-1.167E-01	-1.167E-01	-1.167E-01	3.050F+00	0.0	9.500E-01	-3.333E-02	1.667E-02
M	3.655E+00	3.754E+00	3.772E+00	3.674E+00	4.053E+00	4.065E+00	3.703E+00	3.658E+00
P <sub>0</sub>	1.402E+04	1.911E+04	1.940E+04	1.831E+04	1.849E+04	1.793E+04	1.195E+04	6.650E+03
H <sub>0</sub>	2.179E+07	2.211E+07	2.263E+07	2.098E+07	2.549E+07	2.516E+07	2.181E+07	2.095E+07
M <sub>00</sub>	1.304E+01	1.297E+01	1.296E+01	1.300E+01	1.330E+01	1.335E+01	1.272E+01	1.244E+01
U <sub>00</sub>	6.510E+03	6.556E+03	6.633E+03	6.386E+03	7.045E+03	7.000E+03	6.508E+03	6.375E+03
T <sub>00</sub>	1.036E+02	1.063E+02	1.090E+02	1.004E+02	1.167E+02	1.143E+02	1.088E+02	1.093E+02
P <sub>00</sub>	7.865E-02	8.150E-02	8.220E-02	7.873E-02	6.001E-02	5.692E-02	5.414E-02	3.362E-02
Q <sub>00</sub>	9.371E+00	9.599E+00	9.668E+00	9.317E+00	7.439E+00	7.109E+00	6.138E+00	3.643E+00
P <sub>00</sub>	6.369E-05	6.431E-05	6.329E-05	6.579E-05	4.317E-05	4.179E-05	4.174E-05	2.581E-05
μ <sub>00</sub>	8.719E-08	8.945E-08	9.168E-08	8.449E-08	9.810E-08	9.614E-08	9.150E-08	9.192E-08
Re/ft.	4.756E+06	4.714E+06	4.579E+06	4.973E+06	3.100E+06	3.042E+06	2.967E+06	1.790E+06
P <sub>0</sub>	1.742E+01	1.785E+01	1.798E+01	1.730E+01	1.386E+01	1.325E+01	1.141E+01	6.766E+00

RUN NO.	10	11	12	13	14	15	16	17
ATTACK ANGLE	2.983E+00	2.050E+00	3.000E+00	9.833E-01	-3.333E-02	2.950E+00	2.950E+00	1.000E+00
M	3.615E+00	3.719E+00	3.649E+00	3.669E+00	3.299E+00	3.262E+00	3.293E+00	3.271E+00
P <sub>0</sub>	9.254E+03	1.913E+04	6.555E+03	1.863E+04	1.838E+04	1.762E+04	1.842E+04	1.809E+04
H <sub>0</sub>	2.089E+07	2.166E+07	2.139E+07	2.170E+07	1.733E+07	1.739E+07	1.706E+07	1.734E+07
M <sub>00</sub>	1.251E+01	1.300E+01	1.244E+01	1.297E+01	1.135E+01	1.133E+01	1.136E+01	1.136E+01
U <sub>00</sub>	6.367E+03	6.489E+03	6.441E+03	6.495E+03	5.779E+03	5.789E+03	5.734E+03	5.781E+03
T <sub>00</sub>	1.077E+02	1.036E+02	1.115E+02	1.043E+02	1.079E+02	1.086E+02	1.060E+02	1.078E+02
P <sub>00</sub>	4.111E-02	8.118E-02	3.267E-02	8.005E-02	2.202E-01	2.113E-01	2.217E-01	2.152E-01
Q <sub>00</sub>	4.509E+00	9.613E+00	3.543E+00	9.436E+00	1.988E-01	1.899E-01	2.004E-01	1.944E-01
P <sub>00</sub>	3.203E-05	6.574E-05	2.459E-05	6.441E-05	1.714E-04	1.633E-04	1.755E-04	1.675E-04
μ <sub>00</sub>	9.060E-08	8.717E-08	9.376E-08	8.774E-08	9.068E-08	9.138E-08	8.916E-08	9.066E-08
Re/ft.	2.251E+06	4.894E+06	1.689E+06	4.769E+06	1.093E+07	1.034E+07	1.129E+07	1.068E+07
P <sub>0</sub>	8.374E+00	1.787E+01	6.592E+00	1.754E+01	3.681E+01	3.517E+01	3.710E+01	3.600E+01

RUN NO.	19	20	21	22	23	24	25
ATTACK ANGLE	1.000E+00	3.333E-02	2.900E+00	0.0	8.333E-02	9.333E-02	2.083E+00
M	3.242E+00	3.269E+00	3.278E+00	3.292E+00	3.268E+00	3.237E+00	3.265E+00
P <sub>0</sub>	1.736E+04	1.793E+04	1.819E+04	1.811E+04	1.792E+04	1.727E+04	1.805E+04
H <sub>0</sub>	1.733E+07	1.695E+07	1.772E+07	1.746E+07	1.763E+07	1.709E+07	1.767E+07
M <sub>00</sub>	1.133E+01	1.134E+01	1.135E+01	1.134E+01	1.135E+01	1.133E+01	1.136E+01
U <sub>00</sub>	5.779E+03	5.692E+03	5.844E+03	5.801E+03	5.829E+03	5.739E+03	5.835E+03
T <sub>00</sub>	1.082E+02	1.079E+02	1.103E+02	1.088E+02	1.097E+02	1.067E+02	1.098E+02
P <sub>00</sub>	2.071E-01	2.146E-01	2.153E-01	2.165E-01	2.113E-01	2.072E-01	2.124E-01
Q <sub>00</sub>	1.863E+01	1.934E+01	1.942E+01	1.951E+01	1.908E+01	1.864E+01	1.919E+01
P <sub>00</sub>	1.607E-04	1.669E-04	1.639E-04	1.670E-04	1.617E-04	1.630E-04	1.623E-04
μ <sub>00</sub>	9.098E-08	9.078E-08	9.281E-08	9.152E-08	9.225E-08	8.975E-08	9.236E-08
Re/ft.	1.021E+07	1.062E+07	1.031E+07	1.059E+07	1.022E+07	1.042E+07	1.025E+07
P <sub>0</sub>	3.450E+01	3.582E+01	3.597E+01	3.614E+01	3.533E+01	3.451E+01	3.554E+01

THIS PAGE IS BEST QUALITY PRACTICABLE  
FROM COPY FURNISHED TO DDC

Table 2-3  
6° CONE FORCE TEST CONDITIONS (Cont.)

RUN NO.	26	27	28	29	30	31	32	33
ATTACK ANGLE								
M <sub>6</sub>	5.000E-02	3.050E+00	2.050E+00	3.050E+00	5.000E-02	5.000E-02	1.033E+00	1.033E+00
P <sub>0</sub>	3.260E+00	3.176E+00	3.219E+00	3.242E+00	3.242E+00	3.295E+00	3.305E+00	3.206E+00
M <sub>0</sub>	4.777E+03	6.650E+03	6.772E+03	4.634E+03	4.591E+03	4.888E+03	4.865E+03	4.522E+03
M <sub>0</sub>	1.745E+07	1.662E+07	1.712E+07	1.746E+07	1.702E+07	1.768E+07	1.758E+07	1.688E+07
M <sub>0</sub>	1.089E+01	1.101E+01	1.100E+01	1.089E+01	1.088E+01	1.089E+01	1.088E+01	1.089E+01
U <sub>0</sub>	5.377E+03	5.633E+03	5.737E+03	5.788E+03	5.718E+03	5.828E+03	5.911E+03	5.695E+03
T <sub>0</sub>	1.211E+02	1.097E+02	1.131E+02	1.176E+02	1.148E+02	1.192E+02	1.186E+02	1.137E+02
P <sub>0</sub>	6.042E-02	8.452E-02	8.555E-02	5.923E-02	5.936E-02	6.252E-02	6.248E-02	5.808E-02
Q <sub>0</sub>	5.021E+00	7.173E+00	7.254E+00	4.918E+00	4.924E+00	5.193E+00	5.185E+00	4.831E+00
M <sub>0</sub>	4.198E-05	6.465E-05	6.349E-05	4.227E-05	4.338E-05	4.403E-05	4.422E-05	4.289E-05
M <sub>0</sub>	1.019E-07	9.228E-08	9.512E-08	9.887E-08	9.657E-08	1.002E-07	9.969E-08	9.558E-08
Ra/ft.	2.417E+06	3.960E+06	3.829E+06	2.475E+06	2.568E+06	2.561E+06	2.578E+06	2.556E+06
P <sub>0</sub>	9.303E+00	1.327E+01	1.343E+01	9.107E+00	9.115E+00	9.619E+00	9.604E+00	8.941E+00

RUN NO.	34	35	36	37	38	39	40	41
ATTACK ANGLE								
M <sub>6</sub>	1.031E+00	2.983E+00	2.983E+00	0.0	0.0	1.000E+00	1.000E+00	3.000E+00
P <sub>0</sub>	3.180E+00	3.245E+00	3.270E+00	3.273E+00	3.233E+00	3.319E+00	3.291E+00	3.289E+00
M <sub>0</sub>	4.361E+03	4.634E+03	4.828E+03	1.755E+04	1.738E+04	7.521E+03	7.362E+03	7.344E+03
M <sub>0</sub>	1.676E+07	1.717E+07	1.752E+07	1.762E+07	1.757E+07	1.791E+07	1.777E+07	1.795E+07
M <sub>0</sub>	1.091E+01	1.089E+01	1.089E+01	1.132E+01	1.132E+01	1.099E+01	1.099E+01	1.099E+01
U <sub>0</sub>	5.675E+03	5.743E+03	5.801E+03	5.926E+03	5.819E+03	5.969E+03	5.846E+03	5.874E+03
T <sub>0</sub>	1.126E+02	1.157E+02	1.180E+02	1.102E+02	1.099E+02	1.187E+02	1.177E+02	1.188E+02
P <sub>0</sub>	5.568E-02	5.957E-02	6.187E-02	2.094E-01	2.071E-01	9.543E-02	9.328E-02	9.271E-02
Q <sub>0</sub>	4.640E+00	4.946E+00	5.139E+00	1.881E+01	1.860E+01	8.069E+00	7.832E+00	7.842E+00
P <sub>0</sub>	4.149E-05	4.319E-05	4.398E-05	1.595E-04	1.592E-04	6.749E-05	6.652E-05	6.547E-05
M <sub>0</sub>	9.472E-08	9.732E-08	9.925E-08	9.265E-08	9.241E-08	9.976E-08	9.895E-08	9.942E-08
Ra/ft.	2.486E+06	2.549E+06	2.571E+06	1.003E+07	9.962E+06	3.970E+06	3.929E+06	3.849E+06
P <sub>0</sub>	8.588E+00	9.157E+00	9.517E+00	3.483E+01	3.445E+01	1.495E+01	1.462E+01	1.453E+01

RUN NO.	42	43	44	45	46	47	49	50
ATTACK ANGLE								
M <sub>6</sub>	3.000E+00	3.000E+00	3.000E+00	2.033E+00	2.033E+00	2.033E+00	0.0	3.333E-02
P <sub>0</sub>	3.300E+00	3.990E+00	3.779E+00	3.975E+00	3.922E+00	4.018E+00	3.236E+00	3.269E+00
M <sub>0</sub>	7.343E+03	1.703E+04	5.556E+03	1.694E+04	6.306E+03	1.085E+04	1.771E+04	1.748E+04
M <sub>0</sub>	1.818E+07	2.479E+07	2.291E+07	2.525E+07	2.412E+07	2.546E+07	1.715E+07	1.777E+07
M <sub>0</sub>	1.098E+01	1.323E+01	1.291E+01	1.323E+01	1.279E+01	1.290E+01	1.134E+01	1.132E+01
U <sub>0</sub>	5.911E+03	6.948E+03	6.673E+03	7.011E+03	6.845E+03	7.035E+03	5.749E+03	5.852E+03
T <sub>0</sub>	1.204E+02	1.146E+02	1.111E+02	1.168E+02	1.191E+02	1.237E+02	1.069E+02	1.111E+02
P <sub>0</sub>	9.236E-02	5.750E-02	2.045E-02	5.647E-02	2.440E-02	4.045E-02	2.125E-01	2.076E-01
Q <sub>0</sub>	7.909E+00	7.052E+00	2.389E+00	6.926E+00	2.797E+00	4.717E+00	1.915E+01	1.863E+01
P <sub>0</sub>	6.436E-05	4.209E-05	1.545E-05	4.059E-05	1.719E-05	2.745E-05	1.689E-04	1.567E-04
M <sub>0</sub>	1.012E-07	9.640E-08	9.344E-08	9.818E-08	1.001E-07	1.039E-07	8.989E-08	9.347E-08
Ra/ft.	3.758E+06	3.033E+06	1.103E+06	2.998E+06	1.175E+06	1.858E+06	1.067E+07	9.812E+06
P <sub>0</sub>	1.447E+01	1.314E+01	4.444E+00	1.291E+01	5.209E+00	8.792E+00	3.546E+01	3.452E+01

Table 2-3  
6° CONE FORCE TEST CONDITIONS (Cont.)

RUN NO.	51	52	53	54	55	56	57
ATTACK ANGLE							
M	3.0R3E+00	1.017E+00	1.017E+00	1.017E+00	5.000E-01	3.000E+00	3.000E+00
P <sub>0</sub>	3.265E+00	3.282E+00	3.166E+00	3.271E+00	3.237E+00	3.255E+00	3.286E+00
H <sub>0</sub>	1.778E+04	1.846E+04	5.559E+03	1.791E+04	1.739E+04	1.774E+04	4.874E+03
M <sub>0</sub>	1.907E+07	1.757E+07	1.693E+07	1.785E+07	1.709E+07	1.758E+07	1.829E+07
U <sub>0</sub>	1.133E+01	1.149E+01	1.096E+01	1.135E+01	1.133E+01	1.134E+01	1.089E+01
T <sub>0</sub>	5.900E+03	5.821E+03	5.705E+03	5.866E+03	5.739E+03	5.820E+03	5.927E+03
Q <sub>0</sub>	1.129E+02	1.068E+02	1.128E+02	1.111E+02	1.068E+02	1.095E+02	1.232E+02
P <sub>00</sub>	2.088E-01	2.027E-01	7.056E-02	2.097E-01	2.098E-01	2.102E-01	6.145E-02
Q <sub>00</sub>	1.878E+01	1.875E+01	5.934E+00	1.893E+01	1.885E+01	1.894E+01	5.106E+00
P <sub>000</sub>	1.554E-04	1.593E-04	5.250E-05	1.585E-04	1.649E-04	1.611E-04	4.185E-05
M <sub>00</sub>	9.485E-08	8.982E-08	9.484E-08	9.341E-08	8.982E-08	9.213E-08	1.036E-07
Re/ft.	9.666E+06	1.033E+07	3.158E+06	9.950E+06	1.053E+07	1.017E+07	2.395E+06
P <sub>00</sub>	3.480E+01	3.472E+01	1.098E+01	3.507E+01	3.490E+01	3.508E+01	9.462E+00



Table 2-4  
6° CONE FORCE HEAT TRANSFER DATA

RUN NO.	GAGE POS	HT RATE (BTU/ft <sup>2</sup> sec)	GAGE POS	HT RATE (BTU/ft <sup>2</sup> sec)	GAGE POS	HT RATE (BTU/ft <sup>2</sup> sec)	GAGE POS	HT RATE (BTU/ft <sup>2</sup> sec)	GAGE POS	HT RATE (BTU/ft <sup>2</sup> sec)
2	1	8.22E+00	13	1.42E+01	21	1.26E+01	31	1.36E+01		
	2	7.48E+00	15	1.27E+01	22	1.17E+01	32	1.23E+01		
	3	6.98E+00	16	1.41E+01	23	1.04E+01	33	1.03E+01		
	4	7.64E+00	17	1.25E+01	24	1.06E+01	34	9.98E+00		
	5	8.25E+00	18	1.31E+01	25	1.17E+01				
	6	8.84E+00	19	1.18E+01	26	1.09E+01				
	7	9.75E+00	20	1.27E+01	27	1.48E+01				
	8	9.52E+00			28	1.07E+01				
	9	1.34E+01			29	1.25E+01				
	10	1.24E+01			30	1.21E+01				
3	1	8.13E+00	13	1.41E+01	21	1.26E+01	31	1.34E+01		
	2	9.27E+00	14	1.50E+01	22	1.32E+01	32	1.24E+01		
	3	6.81E+00	15	1.47E+01	23	1.02E+01	33	1.29E+01		
	4	8.45E+00	16	1.38E+01	24	9.84E+00	34	1.38E+01		
	5	9.91E+00	17	1.26E+01	25	1.10E+01				
	6	8.00E+00	18	1.41E+01	26	9.92E+00				
	7	9.40E+00	19	1.15E+01	27	1.51E+01				
	8	8.96E+00	20	1.39E+01	28	1.03E+01				
	9	1.16E+01			29	1.37E+01				
	10	1.25E+01			30	1.33E+01				
4	1	6.46E+00	13	4.46E+00	21	3.56E+00	31	4.51E+00		
	2	6.92E+00	14	4.64E+00	22	3.95E+00	32	4.34E+00		
	3	5.23E+00	15	4.39E+00	23	6.23E+00	33	6.70E+00		
	4	7.39E+00	16	4.65E+00	24	6.41E+00	34	7.25E+00		
	5	4.75E+00	17	3.00E+00	25	5.22E+00				
	6	7.22E+00	18	4.78E+00	27	4.88E+00				
	7	4.70E+00	19	3.32E+00	29	4.61E+00				
	8	5.02E+00	20	4.44E+00	30	4.25E+00				
	9	4.05E+00								
	10	5.21E+00								
5	1	1.66E+01	14	1.08E+00	21	1.51E+01	31	4.96E+00		
	2	2.05E+00	16	1.50E+00	22	2.25E+00	32	4.66E+00		
	3	1.21E+01	17	8.73E+00	23	1.02E+01	33	4.02E+00		
	4	1.18E+00	18	1.74E+00	24	1.22E+01	34	4.55E+00		
	5	1.16E+01	19	1.02E+01	25	5.89E+00				
	6	1.03E+00	20	2.34E+00	26	5.28E+00				
	7	9.49E+00			27	5.73E+00				
	8	8.80E-01			28	3.60E+00				
	9	8.22E+00			29	5.12E+00				
	10	1.00E+00			30	4.62E+00				
6	1	9.55E+00	13	7.58E+00	21	1.09E+01	31	1.12E+01		
	2	8.17E+00	14	6.72E+00	22	1.06E+01	32	1.00E+01		
	3	7.41E+00	15	7.96E+00	23	7.83E+00	33	7.31E+00		
	4	7.31E+00	16	7.77E+00	24	8.21E+00	34	7.35E+00		
	5	7.61E+00	17	8.67E+00	25	6.72E+00				
	6	6.91E+00	18	9.03E+00	26	6.36E+00				
	7	6.37E+00	19	1.05E+01	27	7.65E+00				
	8	6.24E+00	20	1.01E+01	29	8.39E+00				
	9	6.00E+00			30	7.67E+00				
	10	7.88E+00								
7	1	1.06E+01	13	1.09E+01	21	1.51E+01	31	1.30E+01		
	2	6.55E+00	14	6.02E+00	22	9.91E+00	32	1.10E+01		
	3	9.80E+00	15	1.05E+01	23	7.26E+00	33	5.88E+00		
	4	5.54E+00	16	6.74E+00	24	7.71E+00	34	6.76E+00		

Table 2-4  
6° CONE FORCE HEAT TRANSFER DATA (Cont.)

JUN NO.	GAGE POS	HT RATE (BTU/ft <sup>2</sup> sec)	GAGE POS	HT RATE (BTU/ft <sup>2</sup> sec)	GAGE POS	HT RATE (BTU/ft <sup>2</sup> sec)	GAGE POS	HT RATE (BTU/ft <sup>2</sup> sec)	GAGE POS	HT RATE (BTU/ft <sup>2</sup> sec)
	5	1.01E+01	17	1.13E+01	25	6.66E+00				
	6	4.79E+00	18	8.35E+00	26	6.19E+00				
	7	7.93E+00	19	1.25E+01	27	8.45E+00				
	8	4.56E+00	20	9.21E+00	28	1.04E+01				
	9	8.08E+00			29	1.01E+01				
	10	5.11E+00			30	9.07E+00				
8	1	6.09E+00	11	4.76E+00	21	9.41E+00	31	8.55E+00		
	2	6.43E+00	12	4.99E+00	22	9.13E+00	32	7.37E+00		
	3	5.24E+00	13	5.22E+00	23	5.03E+00	33	4.62E+00		
	4	5.95E+00	14	5.47E+00	24	5.20E+00	34	5.14E+00		
	5	4.54E+00	15	5.77E+00	25	4.38E+00				
	6	5.11E+00	16	6.05E+00	26	4.41E+00				
	7	4.19E+00	17	6.12E+00	27	4.75E+00				
	8	4.87E+00	18	7.89E+00	28	5.96E+00				
	9	4.58E+00	19	8.56E+00	29	5.75E+00				
	10	4.90E+00	20	8.10E+00	30	5.22E+00				
9	1	4.51E+00	11	2.69E+00	21	3.45E+00	31	2.45E+00		
	2	4.30E+00	12	2.45E+00	22	2.49E+00	32	2.30E+00		
	3	3.36E+00	13	2.57E+00	23	2.92E+00	33	3.39E+00		
	4	3.82E+00	14	2.25E+00	24	3.10E+00	34	3.73E+00		
	5	3.33E+00	15	2.53E+00	25	2.65E+00				
	6	3.15E+00	16	2.33E+00	26	2.28E+00				
	7	2.84E+00	17	2.34E+00	27	2.48E+00				
	8	2.87E+00	18	2.51E+00	28	3.08E+00				
	9	2.57E+00	19	2.46E+00	29	2.37E+00				
	10	2.55E+00	20	2.50E+00	30	2.21E+00				
10	1	8.30E+00	11	4.96E+00	21	4.38E+00	31	2.80E+00	41	2.00E+00
	2	1.47E+00	12	6.78E-01	22	7.80E-01	32	2.31E+00	42	3.60E+00
	3	7.23E+00	13	4.70E+00	23	4.15E+00	33	2.49E+00		
	4	9.52E-01	14	5.60E-01	24	4.24E+00	34	2.83E+00		
	5	6.66E+00	16	5.97E-01	25	3.93E+00	35	2.44E+00		
	6	7.84E-01	17	4.43E+00	26	3.47E+00	36	5.14E+00		
	7	5.92E+00	18	6.93E-01	29	3.23E+00	37	2.36E+00		
	8	7.25E-01	19	4.05E+00	30	3.00E+00	38	4.73E+00		
	9	5.12E+00	20	7.15E-01			39	2.32E+00		
	10	5.92E-01					40	3.80E+00		
11	1	1.02E+01	11	7.48E+00	21	8.80E+00	31	4.11E+00	41	3.72E+00
	2	2.92E+00	13	6.95E+00	22	1.21E+00	32	3.56E+00	42	5.95E+00
	3	1.01E+01	14	1.08E+00	23	6.22E+00	33	3.55E+00		
	4	2.02E+00	15	6.46E+00	24	6.50E+00	34	3.85E+00		
	5	9.96E+00	16	1.10E+00	25	5.93E+00	35	3.85E+00		
	6	1.60E+00	17	5.38E+00	26	5.38E+00	36	7.94E+00		
	7	8.82E+00	18	1.13E+00	27	5.35E+00	37	3.64E+00		
	8	1.35E+00	19	6.27E+00	28	6.72E+00	38	6.61E+00		
	9	7.79E+00	20	1.26E+00	29	4.49E+00	39	3.62E+00		
	10	1.01E+00			30	4.10E+00	40	5.96E+00		
12	1	7.21E+00	11	4.52E+00	21	3.93E+00	31	2.59E+00	41	1.82E+00
	2	1.44E+00	12	6.23E-01	22	6.33E-01	32	2.29E+00	42	3.40E+00
	3	7.03E+00	13	4.36E+00	23	3.61E+00	33	2.26E+00		
	4	9.90E-01	14	5.39E-01	24	3.92E+00	34	2.48E+00		
	5	6.02E+00	15	3.97E+00	25	3.41E+00	35	2.18E+00		
	6	7.71E-01	16	5.34E-01	26	2.92E+00	36	4.71E+00		
	7	5.08E+00	17	3.49E+00	27	3.03E+00	37	2.10E+00		
	8	6.55E-01	18	5.40E-01	28	3.83E+00	38	3.95E+00		

Table 2-4  
6° CONE FORCE HEAT TRANSFER DATA (Cont.)

RUN NO.	GAGE POS	HT RATE (BTU/ft <sup>2</sup> sec)	GAGE POS	HT RATE (BTU/ft <sup>2</sup> sec)	GAGE POS	HT RATE (BTU/ft <sup>2</sup> sec)	GAGE POS	HT RATE (BTU/ft <sup>2</sup> sec)	GAGE POS	HT RATE (BTU/ft <sup>2</sup> sec)
12	9	4.59E+00	19	3.72E+00	29	2.99E+00	39	2.07E+00		
	10	5.94E-01	20	6.41E-01	30	2.73E+00	40	3.50E+00		
13	1	8.82E+00	11	5.47E+00	21	4.86E+00	31	4.07E+00	41	3.16E+00
	2	4.02E+00	12	2.05E+00	22	1.66E+00	32	3.73E+00	42	4.76E+00
	3	7.72E+00	13	6.18E+00	23	5.83E+00	33	3.82E+00		
	4	3.49E+00	14	1.89E+00	24	6.16E+00	34	4.46E+00		
	5	6.96E+00	15	5.61E+00	25	5.30E+00	35	3.42E+00		
	6	2.90E+00	16	1.91E+00	26	4.77E+00	36	6.08E+00		
	7	6.78E+00	17	4.57E+00	27	5.01E+00	37	3.06E+00		
	8	2.40E+00	18	1.89E+00	28	6.02E+00	38	5.69E+00		
	9	6.27E+00	19	4.49E+00	29	4.37E+00	39	3.31E+00		
	10	2.21E+00			30	3.87E+00	40	4.51E+00		
14	1	1.49E+01	11	8.31E+00	21	9.63E+00	31	9.46E+00	41	9.62E+00
	2	2.32E+01	12	8.95E+00	22	9.60E+00	32	9.61E+00	42	8.53E+00
	3	1.36E+01	14	9.50E+00	23	1.26E+01	33	1.09E+01		
	4	1.41E+01	15	9.04E+00	24	1.25E+01	34	1.12E+01		
	5	1.23E+01	16	9.33E+00	25	1.10E+01	35	1.02E+01		
	6	1.30E+01	17	8.91E+00	26	1.02E+01	36	1.01E+01		
	7	1.09E+01	18	9.00E+00	27	1.02E+01	37	9.62E+00		
	8	1.05E+01	19	9.56E+00	28	1.23E+01	39	9.81E+00		
	9	1.08E+01	20	9.47E+00	29	9.69E+00	40	9.54E+00		
	10	9.88E+00			30	9.60E+00				
15	1	1.58E+01	11	1.30E+01	21	1.58E+01	31	8.63E+00	41	6.34E+00
	2	2.19E+01	12	6.57E+00	22	5.33E+00	32	7.81E+00	42	1.24E+01
	3	1.63E+01	13	1.45E+01	23	1.14E+01	33	1.12E+01		
	4	1.06E+01	14	5.78E+00	24	1.13E+01	34	1.28E+01		
	5	1.51E+01	15	1.42E+01	25	9.77E+00	35	1.08E+01		
	6	8.42E+00	16	5.43E+00	26	8.99E+00	36	1.36E+01		
	7	1.43E+01	17	1.41E+01	27	7.25E+00	37	8.85E+00		
	8	7.13E+00	18	5.81E+00	28	1.21E+01	38	1.24E+01		
	9	1.30E+01	19	1.50E+01	29	9.17E+00	39	7.95E+00		
	10	6.58E+00	20	5.52E+00			40	1.25E+01		
16	1	1.82E+01	11	1.31E+01	21	1.59E+01	31	1.07E+01	41	6.20E+00
	2	1.20E+01	12	7.17E+00	22	5.83E+00	32	9.45E+00	42	1.31E+01
	3	1.65E+01	13	1.37E+01	23	1.13E+01	33	9.85E+00		
	4	1.21E+01	14	6.41E+00	24	1.18E+01	34	1.11E+01		
	5	1.42E+01	15	1.39E+01	25	9.87E+00	35	8.95E+00		
	6	1.06E+01	16	6.47E+00	26	8.99E+00	36	1.29E+01		
	7	1.32E+01	17	1.42E+01	27	9.17E+00	37	7.73E+00		
	8	8.35E+00	18	6.50E+00	28	1.23E+01	38	1.21E+01		
	9	1.21E+01	19	1.46E+01	29	9.01E+00	39	6.35E+00		
	10	7.60E+00	20	6.60E+00	30	8.59E+00	40	1.16E+01		
17	1	1.37E+01	11	1.08E+01	21	1.05E+01	31	9.02E+00	41	8.39E+00
	2	1.26E+01	12	8.43E+00	22	7.35E+00	32	8.59E+00	42	1.00E+01
	3	1.43E+01	13	1.14E+01	23	1.16E+01	33	1.09E+01		
	4	1.35E+01	14	7.85E+00	24	1.26E+01	34	1.18E+01		
	5	1.26E+01	15	1.08E+01	25	9.98E+00	35	9.44E+00		
	6	1.15E+01	16	8.07E+00	26	9.11E+00	36	1.23E+01		
	7	1.13E+01	17	1.00E+01	27	9.64E+00	37	8.96E+00		
	8	9.60E+00	18	7.86E+00	28	1.21E+01	38	1.01E+01		
	9	1.10E+01	19	1.06E+01	29	8.99E+00	39	8.18E+00		
	10	9.84E+00	20	7.81E+00	30	8.30E+00	40	1.10E+01		



Table 2-4  
6° CONE FORCE HEAT TRANSFER DATA (Cont.)

RUN NO.	GAGE POS	HT RATE (BTU/ft <sup>2</sup> sec)	GAGE POS	HT RATE (BTU/ft <sup>2</sup> sec)	GAGE POS	HT RATE (BTU/ft <sup>2</sup> sec)	GAGE POS	HT RATE (BTU/ft <sup>2</sup> sec)	GAGE POS	HT RATE (BTU/ft <sup>2</sup> sec)
18	1	1.39E+01	11	1.06E+01	21	1.07E+01	31	8.99E+00	41	9.79E+00
	2	2.15E+01	12	8.54E+00	22	7.46E+00	32	7.89E+00	42	1.02E+01
	3	1.36E+01	13	1.11E+01	23	1.04E+01	33	9.98E+00		
	4	1.36E+01	14	7.60E+00	24	1.08E+01	34	1.14E+01		
	5	1.24E+01	15	1.08E+01	25	9.58E+00	35	8.77E+00		
	6	1.21E+01	16	8.13E+00	26	8.35E+00	36	1.21E+01		
	7	1.16E+01	17	1.03E+01	27	8.66E+00	37	8.52E+00		
	8	9.90E+00	18	7.90E+00	28	1.11E+01	38	1.07E+01		
	9	1.08E+01	19	1.06E+01	29	9.05E+00	39	8.94E+00		
	10	9.03E+00	20	7.73E+00	30	8.41E+00	40	1.03E+01		
19	1	8.79E+00	11	5.84E+00	21	6.66E+00	31	3.80E+00	41	2.61E+00
	2	8.95E+00	12	2.82E+00	22	2.37E+00	32	3.15E+00	42	5.69E+00
	3	6.90E+00	13	6.35E+00	23	3.50E+00	33	4.97E+00		
	4	3.10E+00	14	2.79E+00	24	3.57E+00	34	5.53E+00		
	5	6.74E+00	15	5.84E+00	25	4.30E+00	35	3.89E+00		
	6	2.96E+00	16	2.64E+00	26	3.62E+00	36	5.74E+00		
	7	6.22E+00	17	6.02E+00	27	3.64E+00	37	3.88E+00		
	8	2.78E+00	18	2.71E+00	28	4.64E+00	38	5.56E+00		
	9	5.84E+00	19	6.45E+00	29	3.45E+00	39	3.50E+00		
	10	2.93E+00	20	2.36E+00	30	3.04E+00	40	5.04E+00		
20	1	1.27E+01	11	1.00E+01	21	8.36E+00	31	8.91E+00	41	9.38E+00
	2	1.39E+01	12	9.97E+00	22	8.24E+00	32	7.71E+00	42	8.54E+00
	3	1.35E+01	13	9.31E+00	23	1.06E+01	33	1.15E+01		
	4	1.41E+01	14	8.33E+00	24	1.21E+01	34	1.28E+01		
	5	1.22E+01	15	9.10E+00	25	9.88E+00	35	1.19E+01		
	6	1.18E+01	16	8.39E+00	26	9.03E+00	36	1.13E+01		
	7	1.06E+01	17	8.78E+00	27	9.64E+00	37	8.77E+00		
	8	1.10E+01	18	8.58E+00	28	1.13E+01	38	9.38E+00		
	9	9.73E+00	19	8.20E+00	29	9.29E+00	39	9.15E+00		
	10	9.20E+00	20	8.89E+00	30	8.85E+00	40	9.09E+00		
21	1	1.23E+01	11	1.06E+01	21	2.07E+01	31	4.04E+00	41	2.28E+00
	2	6.93E+00	12	1.27E+00	22	2.07E+00	32	3.50E+00	42	8.27E+00
	3	8.41E+00	13	1.36E+01	23	4.54E+00	33	2.81E+00		
	4	2.25E+00	14	1.21E+00	24	4.73E+00	34	3.02E+00		
	5	7.78E+00	15	1.45E+01	25	4.22E+00	35	2.59E+00		
	6	2.27E+00	16	1.18E+00	26	3.83E+00	36	6.90E+00		
	7	7.46E+00	17	1.68E+01	27	4.01E+00	37	2.54E+00		
	8	1.87E+00	18	1.48E+00	28	5.02E+00	38	6.24E+00		
	9	1.08E+01	19	1.79E+01	29	3.98E+00	39	2.35E+00		
	10	1.42E+00	20	1.62E+00	30	3.57E+00	40	6.23E+00		
22	1	5.14E+00	11	4.39E+00	21	5.43E+00	31	1.49E+01	41	2.35E+01
	2	5.60E+00	12	8.22E+00	22	1.33E+01	32	1.38E+01	42	4.99E+00
	3	4.44E+00	13	4.18E+00	23	1.25E+01	33	1.31E+01		
	4	5.14E+00	14	8.24E+00	24	2.71E+00	34	1.48E+01		
	5	4.36E+00	15	4.57E+00	25	1.25E+01	35	1.46E+01		
	6	5.94E+00	16	1.01E+01	26	1.15E+01	36	5.10E+00		
	7	4.19E+00	17	4.33E+00	27	1.48E+01	37	1.56E+01		
	8	5.51E+00	18	1.19E+01	28	1.96E+01	38	4.97E+00		
	9	4.14E+00	19	4.92E+00	29	1.56E+01	39	1.65E+01		
	10	6.66E+00	20	1.24E+01	30	1.42E+01	40	4.90E+00		
23	1	5.81E+00	11	3.51E+00	21	7.18E+00	31	1.63E+01	41	1.68E+01
	2	4.28E+00	12	5.72E+00	22	9.03E+00	32	1.48E+01	42	1.47E+01
	3	3.84E+00	13	3.31E+00	23	1.64E+01	33	7.63E+00		
	4	4.78E+00	14	5.14E+00	24	3.46E+00	34	8.98E+00		
	5	3.66E+00	15	3.39E+00	25	1.69E+01	35	9.63E+00		
	6	4.33E+00	16	5.48E+00	26	1.59E+01	36	1.17E+01		

Table 2-4  
6° CONE FORCE HEAT TRANSFER DATA (Cont.)

RUN NO.	GAGE POS	HT RATE (BTU/ft <sup>2</sup> sec)	GAGE POS	HT RATE (BTU/ft <sup>2</sup> sec)	GAGE POS	HT RATE (BTU/ft <sup>2</sup> sec)	GAGE POS	HT RATE (BTU/ft <sup>2</sup> sec)	GAGE POS	HT RATE (BTU/ft <sup>2</sup> sec)
23	7	3.28E+00	17	4.50E+00	27	1.75E+01	37	1.16E+01		
	8	4.47E+00	18	6.35E+00	28	2.24E+01	38	1.34E+01		
	9	3.00E+00	19	5.73E+00	29	1.75E+01	39	1.51E+01		
	10	4.98E+00	20	7.66E+00	30	1.66E+01	40	1.46E+01		
24	1	9.33E+00	11	1.42E+01	21	1.45E+01	31	1.23E+01	41	6.21E+00
	2	5.25E+00	12	5.10E+00	22	5.41E+00	32	1.13E+01	42	1.06E+01
	3	9.41E+00	13	1.42E+01	23	5.16E+00	33	4.62E+00		
	4	5.19E+00	14	4.32E+00	24	1.20E+00	34	5.33E+00		
	5	1.05E+01	15	1.45E+01	25	5.84E+00	35	5.57E+00		
	6	4.62E+00	16	4.24E+00	26	5.70E+00	36	6.95E+00		
	7	1.14E+01	17	1.42E+01	27	7.50E+00	37	5.33E+00		
	8	4.64E+00	18	4.40E+00	28	9.29E+00	38	8.36E+00		
	9	1.26E+01	19	1.46E+01	29	9.87E+00	39	6.22E+00		
	10	4.22E+00	20	4.74E+00	30	9.62E+00	40	8.90E+00		
25	1	1.08E+01	11	7.40E+00	21	8.81E+00	31	3.97E+00	41	2.08E+00
	2	7.87E+00	12	1.46E+00	22	2.11E+00	32	3.62E+00	42	5.98E+00
	3	6.60E+00	13	7.42E+00	23	4.51E+00	33	3.17E+00		
	4	3.58E+00	14	1.55E+00	24	4.65E+00	34	3.51E+00		
	5	6.71E+00	15	7.69E+00	25	4.32E+00	35	1.95E+00		
	6	2.83E+00	16	1.71E+00	26	3.78E+00	36	5.47E+00		
	7	6.39E+00	17	7.94E+00	27	4.19E+00	37	2.29E+00		
	8	2.20E+00	18	1.72E+00	28	5.16E+00	38	5.36E+00		
	9	6.78E+00	19	8.21E+00	29	3.95E+00	39	2.40E+00		
	10	1.80E+00	20	1.97E+00	30	3.71E+00	40	5.05E+00		
26	1	3.08E+00	11	2.50E+00	21	1.77E+00	31	1.93E+00	41	1.75E+00
	2	3.17E+00	12	2.18E+00	22	1.93E+00	32	1.71E+00	42	1.96E+00
	3	2.71E+00	13	2.43E+00	23	2.64E+00	33	2.59E+00		
	4	2.84E+00	14	1.89E+00	24	2.79E+00	34	2.92E+00		
	5	2.67E+00	15	2.18E+00	25	2.46E+00	35	2.33E+00		
	6	2.57E+00	16	2.01E+00	26	2.19E+00	36	2.44E+00		
	7	2.52E+00	17	2.08E+00	27	2.24E+00	37	2.16E+00		
	8	2.40E+00	18	1.98E+00	28	2.79E+00	38	2.28E+00		
	9	2.39E+00	19	1.81E+00	29	2.21E+00	39	2.04E+00		
	10	2.18E+00	20	1.88E+00	30	1.83E+00	40	2.04E+00		
27	1	6.33E+00	11	4.16E+00	21	3.61E+00	31	2.45E+00	41	1.26E+00
	2	4.02E+00	12	8.88E-01	22	4.67E-01	32	2.11E+00	42	3.39E+00
	3	3.92E+00	13	3.97E+00	23	2.60E+00	33	1.72E+00		
	4	1.43E+00	14	5.91E-01	24	2.77E+00	34	1.85E+00		
	5	3.99E+00	15	4.00E+00	25	2.50E+00	35	1.57E+00		
	6	1.18E+00	16	5.98E-01	26	2.33E+00	36	3.64E+00		
	7	3.67E+00	17	3.84E+00	27	2.48E+00	37	1.36E+00		
	8	9.69E-01	18	5.76E-01	28	3.03E+00	38	3.74E+00		
	9	3.73E+00	19	3.69E+00	29	2.37E+00	39	1.47E+00		
	10	6.03E-01	20	5.39E-01	30	2.05E+00	40	3.48E+00		
29	1	6.35E+00	11	3.50E+00	21	3.21E+00	31	2.08E+00	41	1.48E+00
	2	4.67E+00	12	1.06E+00	22	7.26E-01	32	1.94E+00	42	3.13E+00
	3	3.61E+00	13	3.41E+00	23	2.61E+00	33	1.89E+00		
	4	2.18E+00	14	8.42E-01	24	2.74E+00	34	2.13E+00		
	5	3.64E+00	15	3.33E+00	25	2.40E+00	35	1.88E+00		
	6	1.54E+00	16	8.11E-01	26	2.19E+00	36	3.36E+00		
	7	3.42E+00	17	3.27E+00	27	2.26E+00	37	1.57E+00		
	8	1.27E+00	18	7.87E-01	28	2.92E+00	38	3.15E+00		
	9	3.45E+00	19	3.29E+00	29	2.19E+00	39	1.55E+00		
	10	1.01E+00	20	8.26E-01	30	2.00E+00	40	3.13E+00		

Table 2-4  
6° CONE FORCE HEAT TRANSFER DATA (Cont.)

RUN NO.	GAGE POS	HT RATE (BTU/ft <sup>2</sup> sec)	GAGE POS	HT RATE (BTU/ft <sup>2</sup> sec)	GAGE POS	HT RATE (BTU/ft <sup>2</sup> sec)	GAGE POS	HT RATE (BTU/ft <sup>2</sup> sec)	GAGE POS	HT RATE (BTU/ft <sup>2</sup> sec)
29	1	4.36E+00	11	4.16E+00	21	2.99E+00	31	2.26E+00	41	1.53E+00
	2	1.44E+00	12	1.04E+00	22	1.15E+00	32	2.18E+00	42	2.88E+00
	3	4.44E+00	13	4.08E+00	23	2.89E+00	33	2.56E+00		
	4	1.05E+00	14	9.31E-01	24	3.15E+00	34	2.91E+00		
	5	4.69E+00	15	3.75E+00	25	2.76E+00	35	2.00E+00		
	6	9.25E-01	16	9.71E-01	26	2.42E+00	36	4.07E+00		
	7	4.53E+00	17	3.26E+00	27	2.65E+00	37	1.38E+00		
	8	8.61E-01	18	9.84E-01	28	3.31E+00	38	3.65E+00		
	9	4.34E+00	19	3.24E+00	29	2.46E+00	39	1.60E+00		
	10	9.78E-01	20	1.09E+00	30	2.38E+00	40	3.26E+00		
30	1	2.75E+00	11	1.75E+00	21	1.52E+00	31	2.12E+00	41	1.65E+00
	2	2.67E+00	12	2.18E+00	22	1.79E+00	32	1.99E+00	42	1.88E+00
	3	2.17E+00	13	1.57E+00	23	3.32E+00	33	2.38E+00		
	4	2.71E+00	14	1.99E+00	24	3.46E+00	34	2.77E+00		
	5	2.07E+00	15	1.62E+00	25	2.96E+00	35	2.12E+00		
	6	2.45E+00	16	1.93E+00	26	2.71E+00	36	2.16E+00		
	7	1.82E+00	17	1.54E+00	27	2.61E+00	37	2.05E+00		
	8	2.25E+00	18	1.96E+00	28	3.40E+00	38	2.11E+00		
	9	1.72E+00	19	1.43E+00	29	2.43E+00	39	1.84E+00		
	10	2.24E+00	20	1.97E+00	30	2.17E+00	40	1.87E+00		
31	1	3.10E+00	11	2.19E+00	21	1.75E+00	31	2.00E+00	41	1.66E+00
	2	3.20E+00	12	2.36E+00	22	1.97E+00	32	1.79E+00	42	1.88E+00
	3	2.71E+00	13	2.25E+00	23	2.52E+00	33	2.80E+00		
	4	3.10E+00	14	2.15E+00	24	2.78E+00	34	3.10E+00		
	5	2.49E+00	15	2.07E+00	25	2.41E+00	35	2.44E+00		
	6	2.86E+00	16	2.12E+00	26	2.24E+00	36	2.27E+00		
	7	2.40E+00	17	1.89E+00	27	2.17E+00	37	2.20E+00		
	8	2.55E+00	18	2.19E+00	28	2.85E+00	38	2.06E+00		
	9	2.27E+00	19	1.93E+00	29	2.12E+00	39	2.01E+00		
	10	2.31E+00	20	2.00E+00	30	1.95E+00	40	1.81E+00		
32	1	3.73E+00	11	3.26E+00	21	2.45E+00	31	2.10E+00	41	1.46E+00
	2	2.54E+00	12	1.32E+00	22	1.04E+00	32	1.98E+00	42	2.47E+00
	3	3.70E+00	13	3.13E+00	23	2.81E+00	33	2.17E+00		
	4	2.03E+00	14	1.19E+00	24	2.99E+00	34	2.36E+00		
	5	3.54E+00	15	2.90E+00	25	2.72E+00	35	1.97E+00		
	6	1.73E+00	16	1.20E+00	26	2.39E+00	36	2.09E+00		
	7	3.33E+00	17	2.68E+00	27	2.45E+00	37	1.71E+00		
	8	1.51E+00	18	1.19E+00	28	3.18E+00	38	2.91E+00		
	9	3.31E+00	19	2.61E+00	29	2.39E+00	39	1.65E+00		
	10	1.40E+00	20	1.11E+00	30	2.12E+00	40	2.59E+00		
33	1	2.98E+00	11	2.44E+00	21	2.02E+00	31	1.90E+00	41	1.83E+00
	2	1.62E+00	12	1.13E+00	22	8.11E-01	32	1.74E+00	42	2.02E+00
	3	2.58E+00	13	2.39E+00	23	3.17E+00	33	1.87E+00		
	4	1.50E+00	14	9.47E-01	24	3.27E+00	34	2.03E+00		
	5	2.54E+00	15	2.31E+00	25	2.73E+00	35	1.73E+00		
	6	1.37E+00	16	9.28E-01	26	2.48E+00	36	2.51E+00		
	7	2.44E+00	17	2.22E+00	27	2.28E+00	37	1.75E+00		
	8	1.23E+00	18	9.35E-01	28	2.96E+00	38	2.44E+00		
	9	2.36E+00	19	2.07E+00	29	2.06E+00	39	1.79E+00		
	10	1.13E+00	20	8.53E-01	30	1.96E+00	40	2.19E+00		
34	1	3.13E+00	11	2.22E+00	21	2.01E+00	31	1.89E+00	41	1.71E+00
	2	1.61E+00	12	1.09E+00	22	7.82E-01	32	1.60E+00	42	2.04E+00
	3	2.59E+00	13	2.30E+00	23	3.14E+00	33	1.80E+00		
	4	1.43E+00	14	8.97E-01	24	3.23E+00	34	2.08E+00		



Table 2-4  
6° CONE FORCE HEAT TRANSFER DATA (Cont.)

RUN NO.	GAGE POS	HT RATE (BTU/ft <sup>2</sup> sec)	GAGE POS	HT RATE (BTU/ft <sup>2</sup> sec)	GAGE POS	HT RATE (BTU/ft <sup>2</sup> sec)	GAGE POS	HT RATE (BTU/ft <sup>2</sup> sec)	GAGE POS	HT RATE (BTU/ft <sup>2</sup> sec)
34	5	2.56E+00	15	2.19E+00	25	2.76E+00	35	1.61E+00		
	6	1.31E+00	16	8.99E-01	26	2.45E+00	36	2.42E+00		
	7	2.47E+00	17	2.10E+00	27	2.18E+00	37	1.64E+00		
	8	1.21E+00	18	8.82E-01	28	2.90E+00	38	2.29E+00		
	9	2.38E+00	19	1.96E+00	29	2.02E+00	39	1.54E+00		
	10	1.09E+00	20	8.50E-01	30	1.89E+00	40	2.04E+00		
35	1	5.57E+00	11	4.38E+00	21	3.46E+00	31	2.40E+00	41	1.82E+00
	2	1.37E+00	12	7.19E-01	22	7.01E-01	32	2.16E+00	42	3.70E+00
	3	5.41E+00	13	3.78E+00	23	3.36E+00	33	1.70E+00		
	4	8.26E-01	14	5.55E-01	24	3.54E+00	34	1.87E+00		
	5	5.15E+00	15	3.57E+00	25	3.21E+00	35	1.98E+00		
	6	7.37E-01	16	5.63E-01	26	2.92E+00	36	4.53E+00		
	7	4.68E+00	17	3.19E+00	29	2.62E+00	37	1.94E+00		
	8	6.37E-01	18	6.30E-01	30	2.41E+00	38	3.86E+00		
	9	4.45E+00	19	3.26E+00			39	1.96E+00		
	10	7.52E-01	20	6.64E-01			40	3.56E+00		
36	1	4.79E+00	11	4.43E+00	21	3.24E+00	31	2.37E+00	41	1.36E+00
	2	1.45E+00	12	9.62E-01	22	1.44E+00	32	2.07E+00	42	3.10E+00
	3	4.63E+00	13	4.25E+00	23	3.05E+00	33	2.61E+00		
	4	1.15E+00	14	9.84E-01	24	3.16E+00	34	2.98E+00		
	5	4.89E+00	15	3.91E+00	25	2.87E+00	35	1.79E+00		
	6	9.25E-01	16	1.03E+00	26	2.52E+00	36	3.99E+00		
	7	4.57E+00	17	3.47E+00	27	2.60E+00	37	1.36E+00		
	8	8.39E-01	18	1.24E+00	28	3.35E+00	38	3.65E+00		
	9	4.27E+00	19	3.44E+00	29	2.42E+00	39	1.27E+00		
	10	8.69E-01	20	1.32E+00	30	2.23E+00	40	3.30E+00		
37	1	1.48E+01	11	9.16E+00	21	8.54E+00	31	2.40E+00	41	6.36E+00
	2	1.54E+01	12	6.49E+00	22	9.70E+00	32	2.27E+00	42	6.87E+00
	3	4.45E+00	13	8.55E+00	23	3.25E+00	33	2.75E+00		
	4	6.38E+00	14	8.53E+00	24	4.04E+00	34	3.35E+00		
	5	4.61E+00	15	8.21E+00	25	3.11E+00	35	7.71E+00		
	6	5.92E+00	16	9.16E+00	26	2.95E+00	36	5.94E+00		
	7	4.96E+00	17	8.41E+00	27	2.90E+00	37	5.34E+00		
	8	5.95E+00	18	9.44E+00	28	4.23E+00	38	5.34E+00		
	9	7.67E+00	19	9.35E+00	29	2.97E+00	39	6.53E+00		
	10	5.56E+00	20	9.53E+00	30	2.91E+00	40	6.21E+00		
38	1	1.41E+01	11	7.91E+00	21	8.06E+00	31	1.05E+01	42	6.51E+00
	2	1.37E+01	12	1.04E+01	22	9.11E+00	32	9.44E+00		
	3	6.67E+00	13	7.38E+00	23	9.44E+00	33	8.31E+00		
	4	8.47E+00	14	8.99E+00	24	1.09E+01	34	8.30E+00		
	5	6.94E+00	15	6.63E+00	25	1.13E+01	35	9.13E+00		
	6	8.50E+00	16	8.64E+00	26	1.02E+01	36	6.88E+00		
	7	6.91E+00	17	7.28E+00	27	9.72E+00	37	8.12E+00		
	8	1.06E+01	18	9.27E+00	28	1.23E+01	38	6.30E+00		
	9	6.64E+00	19	7.36E+00	29	1.02E+01	39	8.52E+00		
	10	9.40E+00	20	9.18E+00	30	9.88E+00	40	6.68E+00		
39	1	9.10E+00	11	2.74E+00	21	2.03E+00	31	3.52E+00	41	3.45E+00
	2	9.11E+00	12	1.23E+00	22	8.30E-01	32	3.13E+00	42	2.48E+00
	3	5.62E+00	13	2.53E+00	23	3.35E+00	33	3.60E+00		
	4	2.43E+00	14	7.02E-01	24	3.39E+00	34	4.16E+00		
	5	4.72E+00	15	2.26E+00	25	2.69E+00	35	2.52E+00		
	6	1.76E+00	16	8.78E-01	26	2.40E+00	36	3.46E+00		
	7	3.57E+00	17	2.15E+00	27	2.82E+00	37	2.16E+00		
	8	1.41E+00	18	9.74E-01	28	3.62E+00	38	2.89E+00		
	9	2.93E+00	19	2.43E+00	29	3.01E+00	39	2.18E+00		
	10	9.86E-01	20	1.04E+00	30	2.61E+00	40	2.49E+00		

Table 2-4  
6° CONE FORCE HEAT TRANSFER DATA (Cont.)

RUN NO.	GAGE POS	HT RATE (BTU/ft <sup>2</sup> sec)	GAGE POS	HT RATE (BTU/ft <sup>2</sup> sec)	GAGE POS	HT RATE (BTU/ft <sup>2</sup> sec)	GAGE POS	HT RATE (BTU/ft <sup>2</sup> sec)	GAGE POS	HT RATE (BTU/ft <sup>2</sup> sec)
40	11	2.96E+00			23	2.76E+00	31	2.07E+00	41	1.46E+00
	12	1.78E+00			24	3.02E+00	32	2.03E+00	42	2.24E+00
					25	2.63E+00	33	2.66E+00		
					26	2.43E+00	34	2.92E+00		
					27	2.39E+00	35	2.02E+00		
					28	3.04E+00	36	2.81E+00		
					29	2.24E+00	37	1.74E+00		
					30	2.14E+00	38	2.41E+00		
							39	1.70E+00		
							40	2.30E+00		
41	1	1.01E+01	11	4.22E+00	21	4.02E+00	31	2.25E+00	41	1.35E+00
	2	7.79E+00	12	1.16E+00	22	4.49E-01	32	2.02E+00	42	3.42E+00
	3	5.15E+00	13	4.30E+00	23	2.79E+00	33	2.08E+00		
	4	2.50E+00	14	7.12E-01	24	2.86E+00	34	2.24E+00		
	5	4.36E+00	15	4.06E+00	25	2.71E+00	35	1.84E+00		
	6	1.91E+00	16	7.24E-01	26	2.38E+00	36	3.62E+00		
	7	4.04E+00	17	3.93E+00	27	2.44E+00	37	1.47E+00		
	8	1.50E+00	18	6.33E-01	28	3.14E+00	38	3.45E+00		
	9	3.80E+00	19	3.96E+00	29	2.34E+00	39	1.45E+00		
	10	1.11E+00	20	5.80E-01	30	2.18E+00	40	3.33E+00		
42	1	8.85E+00	11	3.54E+00	21	3.44E+00	31	2.53E+00	41	1.78E+00
	2	8.24E+00	12	1.02E+00	22	1.45E+00	32	2.24E+00	42	3.09E+00
	3	6.00E+00	13	3.52E+00	23	4.19E+00	33	3.40E+00		
	4	1.85E+00	14	7.59E-01	24	4.71E+00	34	3.65E+00		
	5	5.11E+00	15	3.93E+00	25	4.16E+00	35	2.66E+00		
	6	1.06E+00	16	8.77E-01	26	3.69E+00	36	3.71E+00		
	7	4.11E+00	17	3.14E+00	27	3.11E+00	37	1.55E+00		
	8	7.35E-01	18	7.25E-01	28	4.05E+00	38	3.08E+00		
	9	3.69E+00	19	3.45E+00	29	2.58E+00	39	1.25E+00		
	10	6.08E-01	20	8.22E-01	30	2.38E+00	40	3.30E+00		
43	1	1.39E+01	11	1.29E+01	21	1.80E+01	31	6.88E+00	41	5.34E+00
	2	3.62E+00	12	5.00E+00	22	5.78E+00	32	6.20E+00	42	1.56E+01
	3	1.07E+01	13	1.31E+01	23	6.40E+00	33	4.18E+00		
	4	2.74E+00	14	5.54E+00	24	6.89E+00	34	5.02E+00		
	5	9.71E+00	15	1.40E+01	25	6.01E+00	35	3.52E+00		
	6	2.75E+00	16	6.62E+00	26	5.39E+00	36	9.19E+00		
	7	9.88E+00	17	1.58E+01	27	5.74E+00	37	3.52E+00		
	8	3.00E+00	18	7.04E+00	28	6.59E+00	38	9.08E+00		
	9	1.07E+01	19	1.66E+01	29	5.81E+00	39	4.28E+00		
	10	4.92E+00	20	6.59E+00	30	5.31E+00	40	1.08E+01		
44	1	7.00E+00	11	4.55E+00	21	3.20E+00	31	2.29E+00	41	1.72E+00
	2	1.67E+00	12	9.31E-01	22	8.61E-01	32	2.15E+00	42	3.10E+00
	3	5.41E+00	13	3.64E+00	23	3.18E+00	33	2.06E+00		
	4	1.07E+00	14	6.28E-01	24	3.35E+00	34	2.44E+00		
	5	5.02E+00	15	3.66E+00	25	3.06E+00	35	2.34E+00		
	6	9.55E-01	16	6.77E-01	26	2.59E+00	36	4.43E+00		
	7	4.59E+00	17	3.58E+00	27	2.59E+00	37	1.88E+00		
	8	7.91E-01	18	7.30E-01	28	3.31E+00	38	3.76E+00		
	9	4.61E+00	19	3.16E+00	29	2.31E+00	39	1.98E+00		
	10	8.23E-01	20	8.19E-01	30	2.20E+00	40	3.42E+00		
45	1	1.29E+01	11	9.42E+00	21	1.54E+01	31	6.54E+00	41	5.60E+00
	2	4.12E+00	12	5.51E+00	22	7.37E+00	32	5.78E+00	42	1.37E+01

Table 2-4  
6° CONE FORCE HEAT TRANSFER DATA (Cont.)

RUN NO.	GAGE POS	HT RATE (BTU/ft <sup>2</sup> sec)	GAGE POS	HT RATE (BTU/ft <sup>2</sup> sec)	GAGE POS	HT RATE (BTU/ft <sup>2</sup> sec)	GAGE POS	HT RATE (BTU/ft <sup>2</sup> sec)	GAGE POS	HT RATE (BTU/ft <sup>2</sup> sec)
45	3	9.31E+00	13	1.01E+01	23	6.39E+00	33	4.73E+00		
	4	3.33E+00	14	6.55E+00	24	6.75E+00	34	5.36E+00		
	5	8.77E+00	15	1.06E+01	25	6.08E+00	35	4.16E+00		
	6	3.24E+00	16	7.48E+00	26	5.53E+00	36	8.52E+00		
	7	8.56E+00	17	1.18E+01	27	5.50E+00	37	4.39E+00		
	8	3.23E+00	18	7.84E+00	28	6.80E+00	38	8.08E+00		
	9	9.25E+00	19	1.43E+01	29	5.75E+00	39	4.79E+00		
	10	4.87E+00	20	7.49E+00	30	5.19E+00	40	9.00E+00		
46	1	7.22E+00	11	4.15E+00	21	3.43E+00	31	2.37E+00	41	2.02E+00
	2	2.45E+00	12	1.08E+00	22	1.02E+00	32	2.15E+00	42	3.46E+00
	3	5.58E+00	13	3.86E+00	23	3.59E+00	33	2.62E+00		
	4	1.87E+00	14	9.56E-01	24	3.76E+00	34	2.87E+00		
	5	5.05E+00	15	3.65E+00	25	3.24E+00	35	2.41E+00		
	6	1.47E+00	16	9.81E-01	26	2.89E+00	36	4.49E+00		
	7	4.86E+00	17	3.34E+00	27	2.81E+00	37	2.14E+00		
	8	1.30E+00	18	9.63E-01	28	3.47E+00	38	3.72E+00		
	9	4.25E+00	19	3.31E+00	29	2.75E+00	39	2.08E+00		
	10	1.27E+00	20	1.03E+00	30	2.57E+00	40	3.16E+00		
47	1	9.73E+00	11	5.80E+00	21	5.81E+00	31	3.24E+00	41	2.50E+00
	2	3.26E+00	12	1.73E+00	22	3.49E+00	32	3.14E+00	42	4.62E+00
	3	7.37E+00	13	5.42E+00	23	5.08E+00	33	3.61E+00		
	4	2.49E+00	14	2.26E+00	24	5.42E+00	34	4.05E+00		
	5	7.17E+00	15	5.03E+00	25	4.56E+00	35	3.01E+00		
	6	2.11E+00	16	2.14E+00	26	4.17E+00	36	5.19E+00		
	7	6.94E+00	17	5.38E+00	27	4.07E+00	37	2.69E+00		
	8	1.79E+00	18	2.52E+00	28	5.31E+00	38	5.09E+00		
	9	6.12E+00	19	5.44E+00	29	3.65E+00	39	2.91E+00		
	10	2.28E+00	20	3.02E+00	30	3.46E+00	40	4.67E+00		
48	1	1.31E+01	11	7.16E+00	21	5.77E+00	31	3.32E+00	41	2.36E+00
	2	2.51E+00	12	1.37E+00	22	1.28E+00	32	2.87E+00	42	5.89E+00
	3	9.02E+00	13	7.19E+00	23	4.82E+00	33	3.27E+00		
	4	1.87E+00	14	1.11E+00	24	5.13E+00	34	3.81E+00		
	5	9.05E+00	15	6.65E+00	25	4.22E+00	35	3.00E+00		
	6	1.41E+00	16	1.06E+00	26	3.87E+00	36	6.94E+00		
	7	7.84E+00	17	5.77E+00	27	3.81E+00	37	2.74E+00		
	8	1.20E+00	18	1.00E+00	28	4.93E+00	38	5.71E+00		
	9	7.34E+00	19	5.72E+00	29	3.66E+00	39	2.34E+00		
	10	1.68E+00	20	1.10E+00	30	3.41E+00	40	5.40E+00		
49	1	5.75E+00	11	4.67E+00	21	4.04E+00	31	3.95E+00	41	4.65E+00
	2	5.04E+00	12	5.09E+00	22	3.84E+00	32	3.23E+00	42	4.92E+00
	3	4.93E+00	13	4.46E+00	23	4.95E+00	33	5.07E+00		
	4	5.28E+00	14	4.14E+00	24	5.02E+00	34	5.94E+00		
	5	5.28E+00	15	3.87E+00	25	4.50E+00	35	5.67E+00		
	6	4.99E+00	16	3.78E+00	26	3.91E+00	36	5.02E+00		
	8	4.40E+00	17	3.81E+00	27	4.57E+00	37	4.91E+00		
	9	4.28E+00	18	4.14E+00	28	5.74E+00	38	4.49E+00		
	10	4.25E+00	19	4.40E+00	29	4.03E+00	39	4.82E+00		
			20	3.95E+00	30	3.61E+00	40	4.26E+00		
50	1	6.27E+00	11	4.83E+00	21	4.35E+00	31	5.11E+00	41	3.95E+00
	2	5.18E+00	12	4.23E+00	22	3.28E+00	32	4.59E+00	42	3.44E+00
	3	4.97E+00	13	4.57E+00	23	4.97E+00	33	4.32E+00		
	4	4.62E+00	14	4.12E+00	24	5.21E+00	34	5.04E+00		
	5	5.17E+00	15	4.10E+00	25	4.88E+00	35	5.34E+00		



Table 2-4  
6° CONE FORCE HEAT TRANSFER DATA (Cont.)

RUN NO.	GAGE POS	HT RATE (BTU/ft <sup>2</sup> sec)	GAGE POS	HT RATE (BTU/ft <sup>2</sup> sec)	GAGE POS	HT RATE (BTU/ft <sup>2</sup> sec)	GAGE POS	HT RATE (BTU/ft <sup>2</sup> sec)	GAGE POS	HT RATE (BTU/ft <sup>2</sup> sec)
	7	4.77E+00	16	3.50E+00	26	4.58E+00	36	5.06E+00		
	8	4.14E+00	17	4.39E+00	27	4.08E+00	37	4.60E+00		
	9	4.47E+00	18	3.71E+00	28	5.39E+00	38	4.41E+00		
	10	4.02E+00	19	4.49E+00	29	4.87E+00	39	4.26E+00		
			20	3.31E+00	30	4.83E+00	40	3.97E+00		
51	1	1.42E+01	11	1.46E+01	22	5.07E+00	31	1.66E+01	41	4.57E+00
	2	1.71E+00	12	2.21E+00	23	7.05E+00	32	1.51E+01	42	2.48E+01
	3	1.22E+01	14	3.02E+00	24	7.40E+00	33	3.98E+00		
	4	1.00E+00	16	3.78E+00	25	6.49E+00	34	4.48E+00		
	5	1.16E+01	18	5.00E+00	26	5.77E+00	35	4.34E+00		
	6	1.06E+00	20	5.20E+00	27	5.91E+00	36	8.36E+00		
	7	1.01E+01			28	7.38E+00	37	3.65E+00		
	8	1.12E+00			29	6.74E+00	38	8.68E+00		
	9	1.04E+01			30	6.63E+00	39	4.13E+00		
	10	1.33E+00					40	1.91E+01		
52	1	9.18E+00	11	6.58E+00	21	9.93E+00	31	4.47E+00	41	4.02E+00
	2	4.74E+00	12	4.44E+00	22	1.10E+01	32	4.02E+00	42	6.57E+00
	3	8.07E+00	13	5.94E+00	23	5.76E+00	33	4.02E+00		
	4	2.61E+00	14	5.57E+00	24	5.76E+00	34	4.34E+00		
	5	7.42E+00	15	5.48E+00	25	5.46E+00	35	4.43E+00		
	6	2.52E+00	16	7.22E+00	26	4.46E+00	36	6.76E+00		
	7	6.58E+00	17	5.35E+00	27	5.02E+00	37	3.92E+00		
	8	2.57E+00	18	8.64E+00	28	6.37E+00	38	6.24E+00		
	9	6.23E+00	19	5.63E+00	29	4.76E+00	39	4.24E+00		
	10	3.22E+00	20	1.03E+01	30	4.24E+00	40	5.16E+00		
53	1	3.96E+00	11	3.08E+00	21	2.30E+00	31	1.94E+00	41	1.43E+00
	2	2.13E+00	12	1.26E+00	22	9.95E-01	32	1.79E+00	42	2.41E+00
	3	3.63E+00	13	2.91E+00	23	2.69E+00	33	1.99E+00		
	4	1.82E+00	14	9.74E-01	24	2.81E+00	34	2.37E+00		
	5	3.49E+00	15	2.69E+00	25	2.69E+00	35	1.64E+00		
	6	1.62E+00	16	9.16E-01	26	2.36E+00	36	3.15E+00		
	7	3.23E+00	17	2.39E+00	27	2.43E+00	37	1.53E+00		
	8	1.35E+00	18	9.77E-01	28	3.06E+00	38	2.79E+00		
	9	3.04E+00	19	2.34E+00	29	2.26E+00	39	1.59E+00		
	10	1.11E+00	20	9.72E-01	30	2.04E+00	40	2.47E+00		
54	1	7.55E+00	11	7.04E+00	21	6.90E+00	35	4.66E+00	41	3.92E+00
	2	3.80E+00	12	2.61E+00	22	2.43E+00	36	7.13E+00	42	5.63E+00
	3	7.34E+00	13	6.16E+00			37	3.90E+00		
	4	2.82E+00	14	1.84E+00			38	6.20E+00		
	5	7.47E+00	15	5.52E+00			39	4.17E+00		
	6	2.79E+00	16	1.77E+00			40	5.78E+00		
	7	6.91E+00	17	4.93E+00						
	8	2.24E+00	18	2.07E+00						
	9	6.20E+00	19	6.77E+00						
	10	1.94E+00	20	2.05E+00						
55	1	7.35E+00	11	5.31E+00	21	4.70E+00	31	3.49E+00	41	3.85E+00
	2	4.54E+00	12	3.38E+00	22	3.09E+00	32	3.41E+00	42	5.25E+00
	3	6.14E+00	13	4.64E+00	23	5.01E+00	33	4.39E+00		
	4	3.65E+00	14	2.89E+00	24	5.56E+00	34	5.20E+00		
	5	5.71E+00	15	4.48E+00	25	4.89E+00	35	4.38E+00		
	6	3.42E+00	16	2.78E+00	26	4.33E+00	36	5.58E+00		
	7	5.33E+00	17	4.15E+00	27	4.88E+00	37	4.07E+00		
	8	3.26E+00	18	2.74E+00	28	6.08E+00	38	4.98E+00		
	9	5.39E+00	19	4.33E+00	29	3.81E+00	39	4.07E+00		
	10	3.14E+00	20	2.81E+00	30	3.74E+00	40	4.63E+00		

Table 2-4  
6° CONE FORCE HEAT TRANSFER DATA (Cont.)

RUN NO.	GAGE POS	HT RATE (BTU/ft <sup>2</sup> sec)	GAGE POS	HT RATE (BTU/ft <sup>2</sup> sec)	GAGE POS	HT RATE (BTU/ft <sup>2</sup> sec)	GAGE POS	HT RATE (BTU/ft <sup>2</sup> sec)	GAGE POS	HT RATE (BTU/ft <sup>2</sup> sec)
56	1	1.13E+01	11	8.20E+00	21	2.65E+01	31	1.18E+01	41	3.23E+00
	2	1.75E+00	12	1.50E+00	22	5.46E+00	32	1.08E+01	42	2.26E+01
	3	1.13E+01	13	8.36E+00	23	6.38E+00	33	3.86E+00		
	4	1.09E+00	14	1.43E+00	24	6.61E+00	35	3.58E+00		
	5	1.10E+01	15	1.22E+01	25	6.17E+00	36	4.00E+00		
	6	8.93E-01	16	2.09E+00	26	5.30E+00	37	3.34E+00		
	7	9.76E+00	17	2.16E+01	27	5.70E+00	38	6.90E+00		
	8	8.77E-01	18	4.45E+00	28	7.11E+00	39	3.32E+00		
	9	8.05E+00	19	2.76E+01	29	6.02E+00	40	1.04E+01		
	10	9.49E-01	20	5.27E+00	30	5.40E+00				
57	1	6.23E+00	11	4.39E+00	21	3.76E+00	31	2.41E+00	41	1.71E+00
	2	1.39E+00	12	7.16E-01	22	8.27E-01	32	2.24E+00	42	3.16E+00
	3	5.89E+00	13	3.95E+00	23	3.39E+00	33	1.93E+00		
	4	9.26E-01	14	6.81E-01	24	3.70E+00	35	2.02E+00		
	5	5.49E+00	15	3.79E+00	25	3.35E+00	36	2.27E+00		
	6	7.03E-01	16	6.46E-01	26	2.86E+00	37	2.02E+00		
	7	4.98E+00	17	3.44E+00	27	2.89E+00	38	3.71E+00		
	8	6.32E-01	18	7.03E-01	28	3.83E+00	39	2.04E+00		
	9	4.35E+00	19	3.42E+00	29	2.69E+00	40	3.29E+00		
	10	6.51E-01	20	7.58E-01	30	2.49E+00				

**Table 2-5**  
**6° CONE FORCE FINAL PRESSURE DATA**

GAGE POS	RUN NO.							
	3	4	5	6	7	8	9	10
	PRESSURE RATE (psia)							
1	0.3880	0.2960		0.2850	0.3330	0.2640	0.1550	
2	0.3640	0.3060		0.2800	0.2640	0.2730	0.1550	
3	0.3650	0.3020	0.6020	0.2820	0.3300	0.2400	0.1420	0.2880
4	0.3860	0.3270	0.1980	0.2990	0.2440	0.2540	0.1410	0.0995
5	0.3610	0.3140	0.6290	0.2770	0.3270	0.2340	0.1370	0.2900
6	0.3730	0.3390	0.2020	0.2810	0.2410	0.2430	0.1390	0.0994
7	0.3620	0.3300	0.6250	0.2770	0.3310	0.2340	0.1330	0.2890
9	0.3410	0.3290	0.6040	0.2730	0.3210	0.2240	0.1340	0.2800
10	0.3680	0.3610	0.1930	0.2760	0.2370	0.2330	0.1320	0.0987
13	0.3420	0.3170	0.5890	0.2690	0.3160	0.2200	0.1320	0.2660
17	0.3360	0.3040	0.5180	0.2700	0.3010	0.2150	0.1330	0.2540
18	0.3540	0.3330	0.1910	0.2570	0.2240	0.2260	0.1290	0.0946
21	0.3440	0.3130	0.5570	0.2610	0.3120	0.2250	0.1420	0.2670
22	0.3540	0.3310	0.2970	0.2720	0.2240	0.2310	0.1340	0.0981
	11	12	13	14	15	16	17	18
1			0.3490	1.1400	1.5700	1.9700	1.5100	1.2600
2	0.2210		0.2760	1.3400	1.3100	1.3100	1.4600	1.3300
3	0.4950	0.2330	0.3940	0.7550	0.9380	0.9620	0.8450	0.7790
4	0.2280	0.0815	0.2640	0.7520	0.7080	0.7180	0.7730	0.7260
5	0.5210	0.2350	0.3990	0.6730	0.8790	0.8480	0.7560	0.7120
6	0.2340	0.0807	0.2710	0.6660	0.5580	0.5860	0.6620	0.6200
7	0.5430	0.2300	0.3830	0.6140	0.8010	0.7910	0.6760	0.6610
9	0.5280	0.2220	0.3930	0.5580	0.7450	0.7580	0.6380	0.6010
10	0.2430	0.0809	0.2740	0.5800	0.4300	0.4370	0.5300	0.5070
13	0.5010	0.2150	0.3660	0.5100	0.7900	0.7890	0.6160	0.5830
17	0.4530	0.2100	0.3750	0.5560	0.8610	0.8620	0.6230	0.6270
18	0.2240	0.0772	0.2600	0.5350	0.3700	0.3870	0.4590	0.4470
21	0.4950	0.2230	0.4110	0.5390	1.0000	1.0200	0.6860	0.6710
22	0.2380	0.0807	0.2770	0.5440	0.3900	0.3910	0.4920	0.4850
	19	20	21	22	23	24	25	26
1	0.6170	1.4500	1.5600	0.5300	0.4920	0.5170	1.5500	0.1530
2	0.5170	1.6900	1.1800	0.5550	0.5730	0.5080	1.2500	0.1510
3	0.3850	0.7900	0.8800	0.5400	0.5150	0.5780	0.7930	0.1780
4	0.2900	0.8230	0.5540	0.6130	0.6130	0.5470	0.6100	0.1770
5	0.3540	0.6640	0.8160	0.5560	0.5340	0.5660	0.7210	0.1820
6	0.2290	0.6920	0.4890	0.6400	0.6230	0.5830	0.5250	0.1820
7	0.3270	0.6010	0.8330	0.5910	0.5930	0.6050	0.7170	0.2060
9	0.3290	0.5520	0.8500	0.6060	0.6010	0.6410	0.7250	0.2130
10	0.1830	0.5510	0.4110	0.6920	0.6780	0.6360	0.4480	0.2010
13	0.3470	0.5240	0.8900	0.6230	0.6360	0.6610	0.7710	0.2170
17	0.3480	0.5260	1.0100	0.6390	0.6750	0.6760	0.7910	0.2020
18	0.1540	0.5080	0.3770	0.6900	0.6610	0.6260	0.4060	0.1960
21	0.3920	0.5200	1.1300	0.6720	0.6820	0.7410	0.9100	0.2120
22	0.1620	0.5540	0.3990	0.6770	0.7070	0.6660	0.4280	0.2050
	27	28	29	30	31	32	33	34
1	0.5820	0.5860	0.1980		0.1660	0.1800	0.1500	0.1560
2	0.4560	0.4930	0.1340		0.1650	0.1530	0.1480	0.1550
3	0.3300	0.3060	0.2620	0.1670	0.1790	0.2070	0.1850	0.1750
4	0.2180	0.2300	0.1210	0.1950	0.1880	0.1590	0.1600	0.1510
5	0.3160	0.2900	0.3030	0.1710	0.1830	0.2210	0.1980	0.1890
6	0.1920	0.2080	0.1230	0.1930	0.1900	0.1670	0.1610	0.1580
7	0.3190	0.2890	0.3320	0.1870	0.2000	0.2350	0.2070	0.2070
9	0.3440	0.3000	0.3560	0.2030	0.2090	0.2530	0.2290	0.2170
10	0.1660	0.1800	0.1260	0.2000	0.2050	0.1730	0.1640	0.1600
13	0.3820	0.3110	0.3460	0.1980	0.2100	0.2550	0.2310	0.2200
17	0.3720	0.3140	0.3320	0.2020	0.2060	0.2270	0.2210	0.2090
18	0.1480	0.1660	0.1210	0.1950	0.2020	0.1710	0.1590	0.1520
21	0.4020	0.3440	0.3230	0.1970	0.2110	0.2450	0.2300	0.2170
22	0.1560	0.1740	0.1230	0.2100	0.2090	0.1760	0.1620	0.1570



**Table 2-5**  
**6° CONE FORCE FINAL PRESSURE DATA (Cont.)**

GAGE POS	RUN NO.							
	35	36	37	38	39	40	41	42
	PRESSURE RATE (psia)							
1	0.2560	0.2260	2.0200	1.6200	0.7560	0.9410	1.0000	0.7980
2	0.1500	0.1560	2.0400	1.7400	0.8110	0.8840	0.8110	0.7340
3	0.3150	0.2880	0.7820	0.9200	0.4060	0.3380	0.3810	0.4490
4	0.1250	0.1300	0.8140	0.7060	0.2910	0.3130	0.2820	0.2610
5	0.3150	0.3040	0.6640	0.7280	0.3190	0.3020	0.3510	0.3530
6	0.1270	0.1290	0.6840	0.6270	0.2550	0.2700	0.2340	0.2300
7	0.3450	0.3350	0.6090	0.5820	0.2740	0.2720	0.3330	0.3220
9	0.3610	0.3660	0.5570	0.5170	0.2640	0.2650	0.3460	0.3200
10	0.1300	0.1340	0.5690	0.5700	0.2310	0.2170	0.1920	0.2010
13	0.3520	0.3690	0.5290	0.5050	0.2380	0.2490	0.3500	0.3150
17	0.3160	0.3390	0.5110	0.4830	0.2320	0.2460	0.3570	0.3230
18	0.1220	0.1290	0.4960	0.5600	0.2110	0.1900	0.1610	0.1640
21	0.3180	0.3480	0.5660	0.4780	0.2530	0.2660	0.3990	0.3610
22	0.1220	0.1300	0.5380	0.5360	0.2210	0.1960	0.1690	0.1720
	43	44	45	46	47	48	49	50
1	0.4150						0.5310	0.5490
2	0.2040		0.2010				0.5230	0.5450
3	0.4660	0.1600	0.3830	0.1560	0.2620	0.2120	0.6000	0.6000
4	0.1630	0.0601	0.1830	0.0787	0.1300	0.0729	0.6140	0.5980
5	0.4470	0.1570	0.3790	0.1540	0.2580	0.2050	0.6060	0.6130
6	0.1550	0.0575	0.1830	0.0784	0.1270	0.0726	0.6290	0.6130
7	0.4750	0.1660	0.3920	0.1580	0.2600	0.2080	0.6320	0.6510
9	0.4610	0.1580	0.3900	0.1540	0.2570	0.2020	0.6580	0.6750
10	0.1500	0.0576	0.1820	0.0767	0.1240	0.0721	0.7080	0.6920
13	0.4660	0.1540	0.3780	0.1490	0.2470	0.2020	0.6610	0.6920
17	0.4040	0.1360	0.3470	0.1400	0.2260	0.1850	0.6810	0.7000
18	0.1360	0.0556	0.1650	0.0715	0.1160	0.0921	0.7260	0.6170
21	0.4340	0.1470	0.3660	0.1450	0.2400	0.1950	0.6850	0.7390
22	0.1480	0.0582	0.1740	0.0739	0.1170	0.0718	0.6950	0.7110
	51	52	53	54	55	56	57	
1			0.2390				0.2900	
2		0.4760	0.1980	0.4640	0.5010	0.4250	0.1480	
3		0.7820	0.2500	0.7250	0.6700	1.1300	0.3350	
4		0.5270	0.1810	0.5230	0.5640	0.4110	0.1310	
5		0.7970	0.2580	0.7450	0.6960	1.1700	0.3210	
6		0.5440	0.1860	0.5420	0.5810	0.4130	0.1220	
7	1.2200	0.8150	0.2700	0.7870	0.7040	1.2000	0.3610	
9	1.1900	0.8660	0.2840	0.8090	0.7390	1.1700	0.3530	
10	0.4360	0.5990	0.1890	0.5870	0.6220	0.4190	0.1270	
13	1.1400	0.9480	0.2800	0.8420	0.7390	1.1500	0.3530	
17		0.8920	0.2620	0.8260	0.7380	1.1300	0.3180	
18		0.6150	0.1870	0.5750	0.6120	0.3860	0.1220	
21	1.2500	0.8850	0.2660	0.8670	0.8090	1.2000	0.3110	
22	0.3840	0.5940	0.1860	0.5950	0.6390	0.3880	0.1240	

Figure 2-6  
6° CONE FORCE DATA

RUN NO.	C <sub>N</sub>	C <sub>m</sub>	RUN NO.	C <sub>N</sub>	C <sub>m</sub>
2	-.000778	-.00146	29	+.0932	+.137
3	-.00514	-.00742	30	-.00175	-.00139
4	-.00743	-.0112	31	-.00179	-.00342
5	+.0984	+.152	32	+.0300	+.0407
6	-.00176	-.000958	33	+.0318	+.0468
7	+.0279	+.0458	34	+.0265	+.0385
8	-	-	35	+.0958	+.140
9	+.00143	+.00171	36	+.0937	+.137
10	+.0887	+.136	37	0	-.000750
11	+.0630	+.0954	38	+.0124	+.0577
12	+.0890	+.134	39	+.0289	+.0815
13	+.0298	+.0442	40	+.0146	+.0175
14	+.000097	+.00649	41	+.0545	+.0681
15	+.0563	+.0837	42	+.0667	+.136
16	+.0494	+.0640	43	+.0959	+.152
17	+.0161	+.0206	44	+.0917	+.145
18	+.0201	+.0338	45	+.0645	+.102
19	+.0580	+.0866	46	+.0625	+.0991
20	+.000948	+.000646	47	+.0620	+.0998
21	+.0630	+.0803	49	-.00339	-.00384
22	-.00466	-.00755	50	+.00300	+.00404
23	-.00464	-.00533	51	+.107	+.159
24	+.00352	+.00155	52	+.0313	+.0466
25	+.0391	+.0485	53	+.0280	+.0395
26	+.00579	+.00980	54	+.0277	+.0388
27	+.0650	+.0826	55	+.0158	+.0226
28	+.0398	+.0497	56	+.0915	+.132
			57	+.0875	+.129

Section 3  
STUDIES OF THE AERODYNAMIC EFFECTS RESULTING FROM  
THE NOSE-TIP SHAPING OF SLENDER BLUNTED  
VEHICLES AT LOW ALTITUDES

3.1 INTRODUCTION

As the transition moves from the frustum onto the nose tip, the heat transfer to the nose tip can exhibit a local maximum downstream of the stagnation point, which can drive the ablating nose tip into an indented shape. While the current shape change programs can predict the occurrence of an axi-symmetric indented nose configuration, the intrinsically three-dimensional characteristics of regions of boundary layer transition can lead to the generation of the NRV<sup>18</sup> or RTE<sup>19</sup> nose-tip configurations (see Figure 3-1), which are far from asymmetric. In this experimental program, we set out to examine the effects of asymmetric and indented nose shapes on the aerodynamic stability of slender cones and determine how the nose shape influences the pressure distribution over the conical frustum. Measurements were made of the nose-tip forces and forces on the nose tip/frustum combination. From these two sets of measurements and measurements of the pressure distribution over the conical frustum we were able to examine the influence of nose shape on the position of the center of pressure on both the total configuration and the conical frustum.

3.2 MODELS AND INSTRUMENTATION

In this program, we used acceleration-compensated force balance techniques similar to those used in the investigation of body-fixed transition effects to make measurements of the nose-tip forces and the total forces on the nose tip/frustum combinations. Special electronics were devised to enable us to measure directly the differences in pressure between the windward or leeward rays, as well as their absolute values. In this way, we were able to measure accurately the small differences in frustum pressure resulting from nose tip asymmetry. Figure 3-2 shows a photograph of the model used in



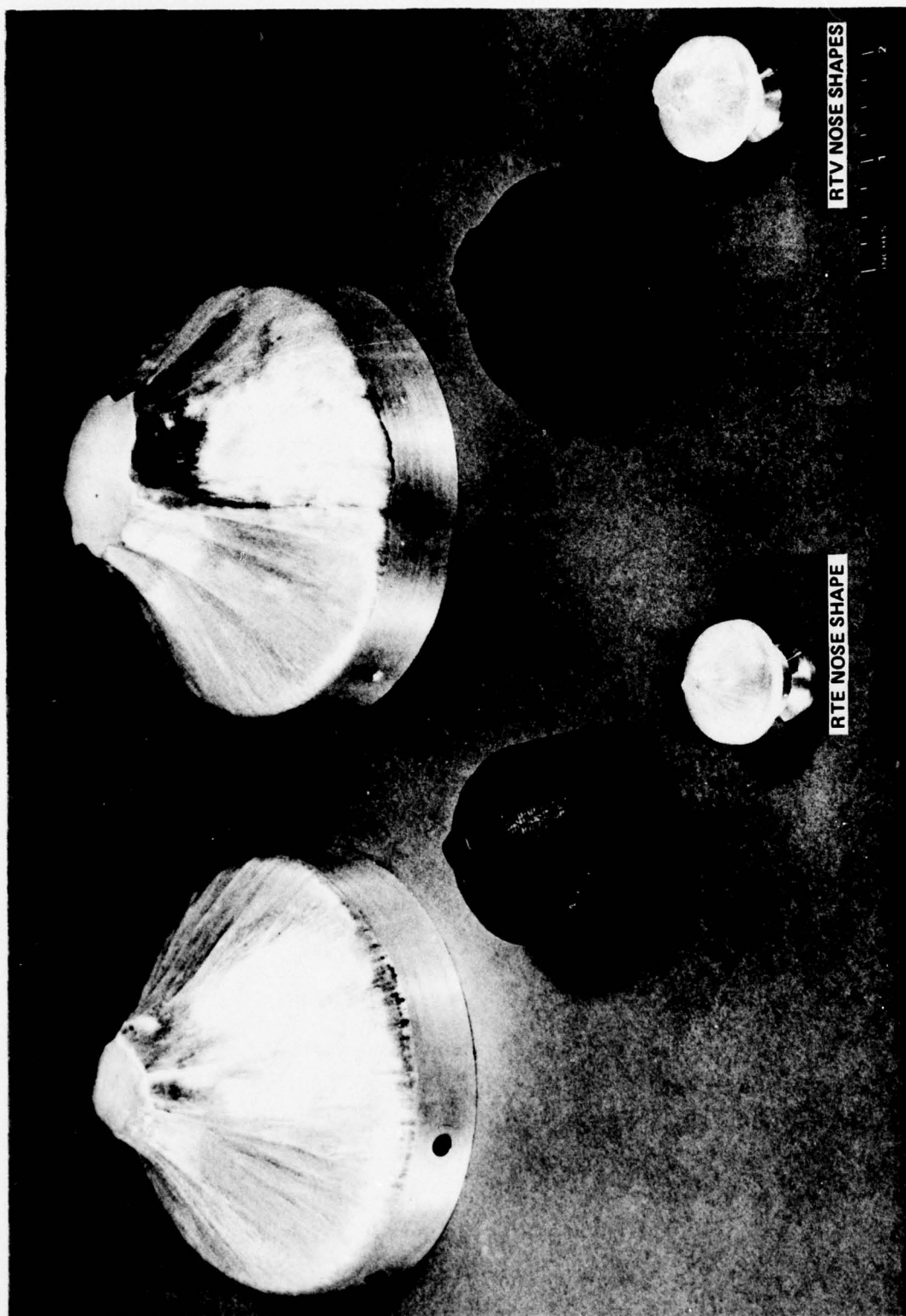


Figure 3-1 NRV (RIGHT) AND RTE FORCE, EPOXY REPLICA AND NOSE TIP MODELS (TOP TO BOTTOM)

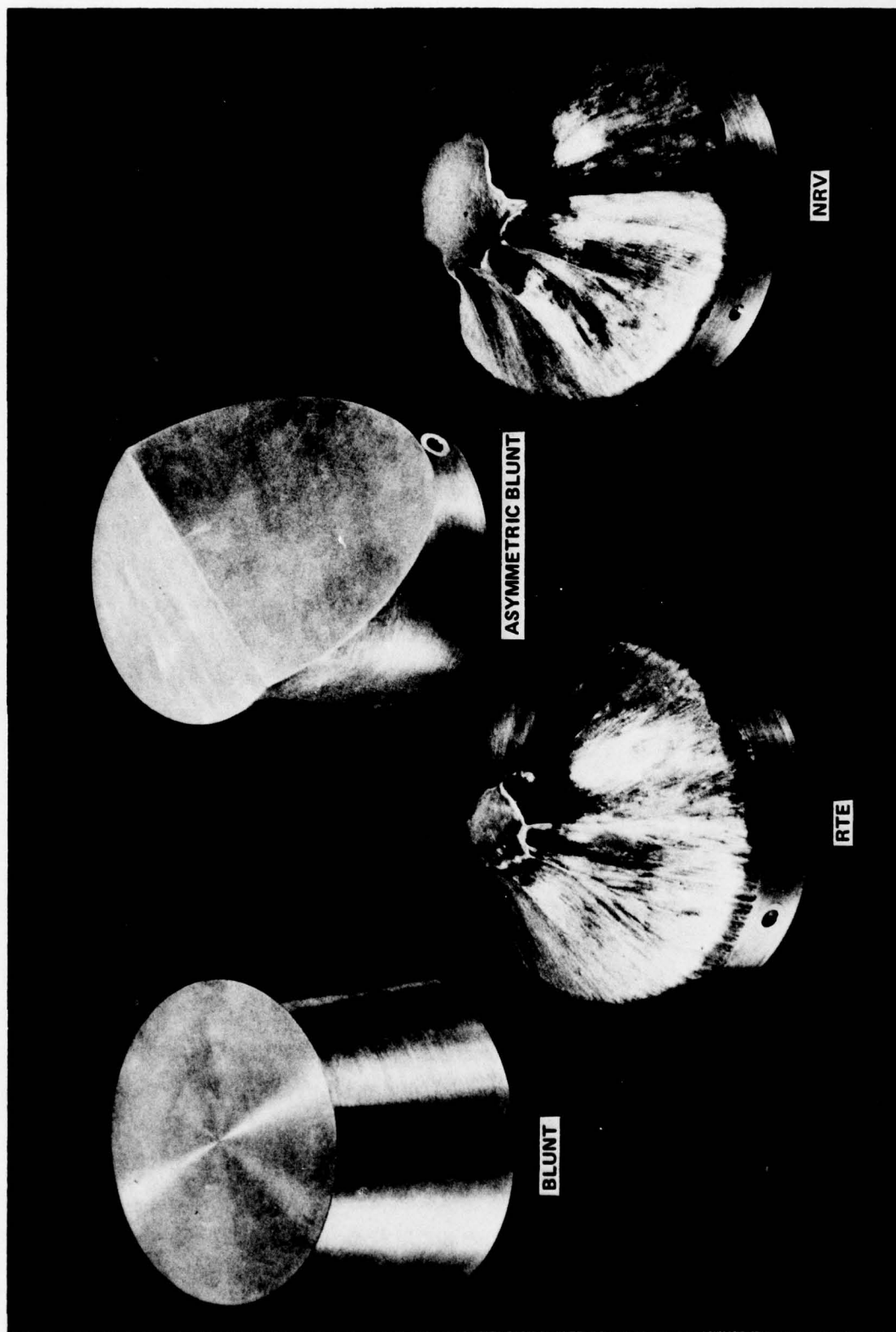


Figure 3-2 NRV RTE BLUNT AND ASYMMETRIC BLUNT FORCE MODELS

the measurement of nose-tip forces, and Figure 3-3 shows the NRV nose tip mounted on the force balance in the Calspan 96"-shock tunnel. A photograph of the equivalent nose tips that were used with the 6°-conical frustum are shown in Figure 3-4. While most studies were conducted with models that had a 21%-bluntness ratio, measurements were also made with the sharp or 6% blunted configurations shown in Figure 3-5.

### 3.3 RESULTS AND DISCUSSION

#### 3.3.1 Nose Tip Studies

The first set of studies were designed to obtain force and pressure measurements on the recovered NRV and RTE nose shapes as well as for the two "extreme" nose shapes, the "blunt" and the "45°-blunt" shown in Figure 3-1. Apart from the nose tip force data, which would be used in conjunction with total force measurements to determine frustum forces, we were also very interested in determining the roll torques generated by the NRV and RTE nose tips. The studies were conducted at Mach 8 and 14 for unit Reynolds numbers from  $8 \times 10^6$  to  $25 \times 10^6$ . Figure 3-6a shows the details of three of the four model configurations used on this program; while Figure 3-6b shows the accelerometer balance used on this program. Tables 3-1 and 3-2 lists the model characteristics and the free stream conditions.

The complex nature of the flow over the NRV nose-tip is shown in the Schlieren photographs of Figure 3-7. The model has been rotated 90° between the runs shown to display the highly asymmetric character of the flow field. In all these photographs, observe that a predominant feature is the embedded shock structure generated by the recompression of the flow downstream of the three-dimensional regions of separated flow developed in the grooves. A similar flow structure is exhibited in the photograph of the flow over the Roll Torque Experiment (RTE) nose tip shown in Figure 3-8. In this latter case, however, the flow remains attached and exhibits far greater symmetry about the axis. For completeness, the Schlieren photographs show the flow over "blunt" and the "45°-blunt" nose tips in Figure 3-9. The normal and axial



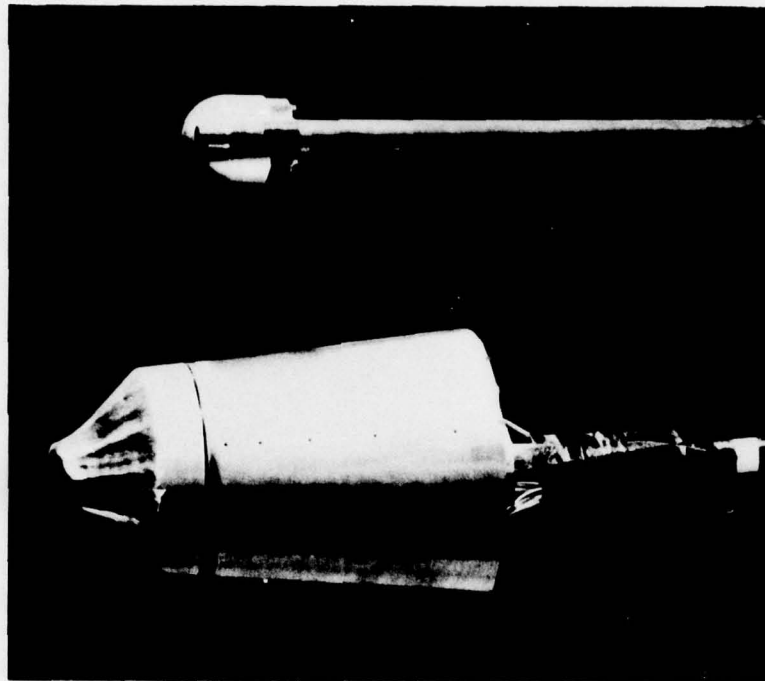


**Figure 3-3 NRV FORCE MODEL INSTALLED IN THE 96" SHOCK TUNNEL**

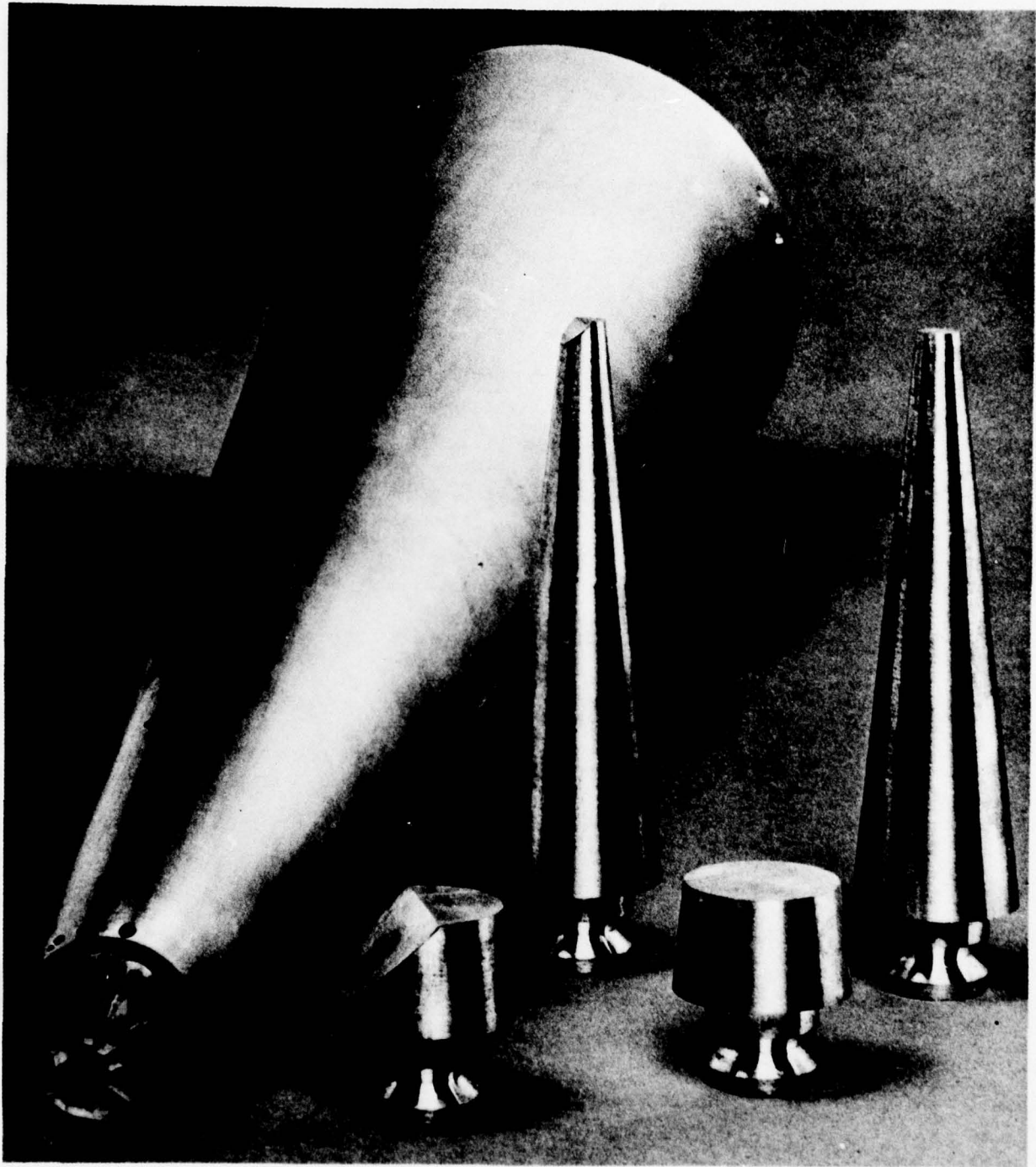


**Figure 3-4 6" CONICAL FORCE MODEL WITH NRV AND ASYMMETRIC NOSE TIPS**

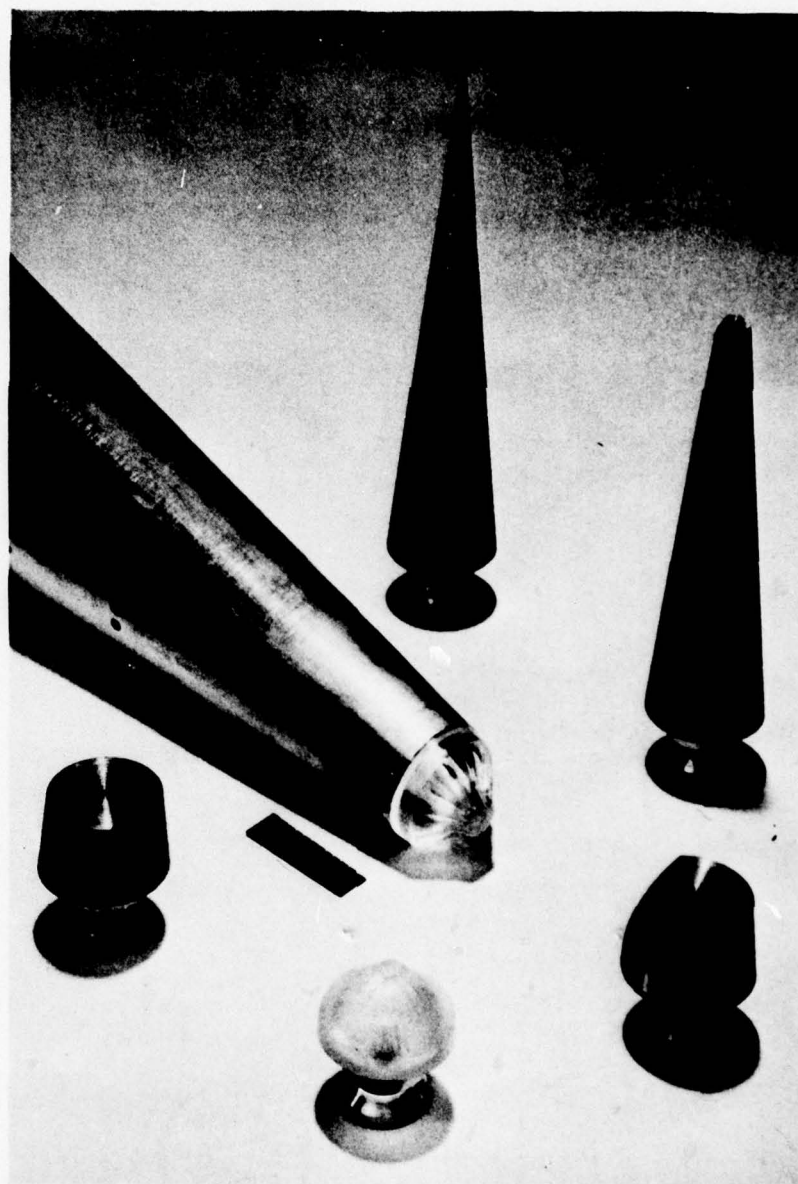


**Figure 3-5** PHOTOGRAPHS OF SOME OF THE NOSE TIPS WHICH WILL BE USED WITH THE 6° CONE MODEL



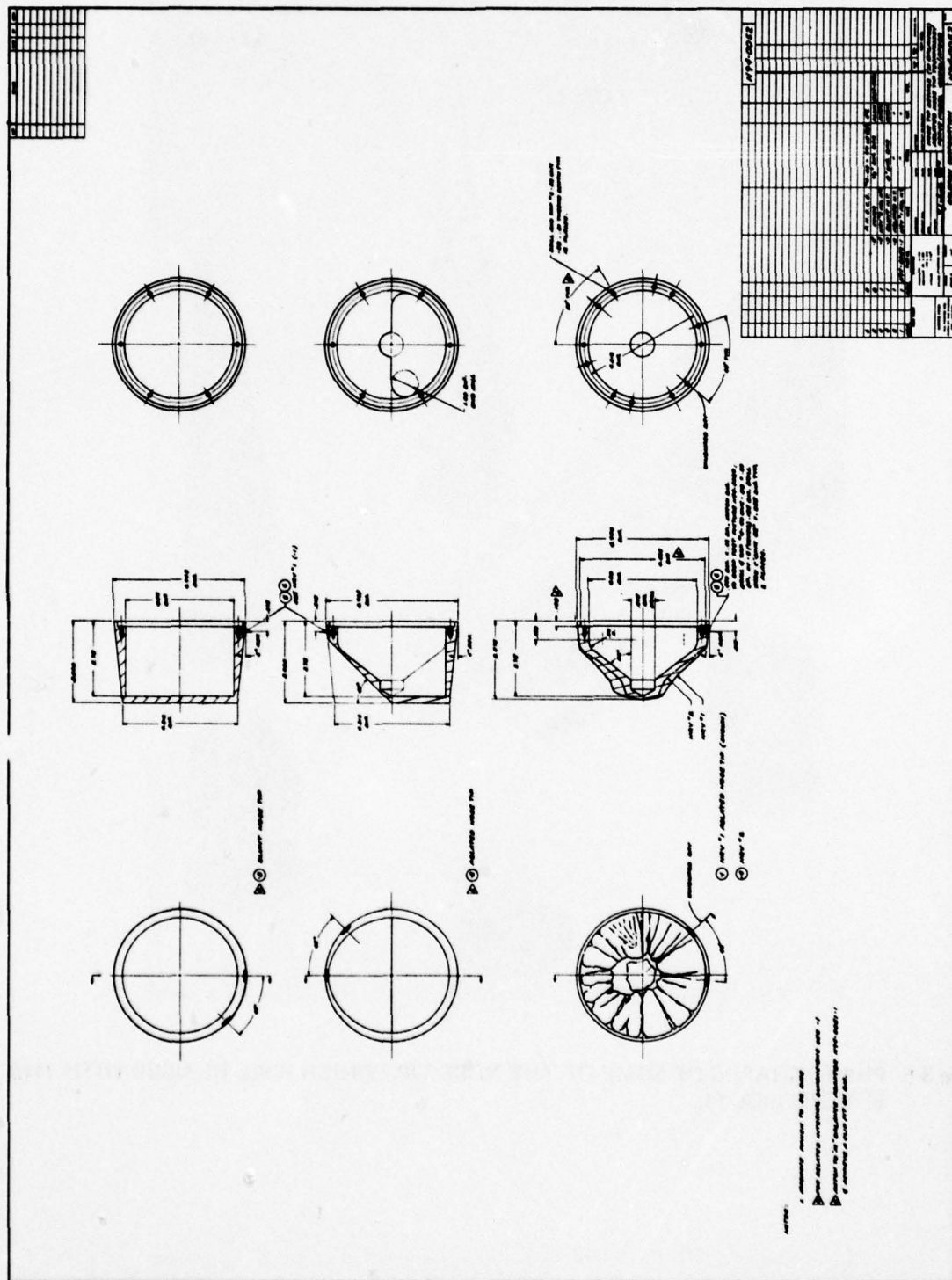


Figure 3-6a

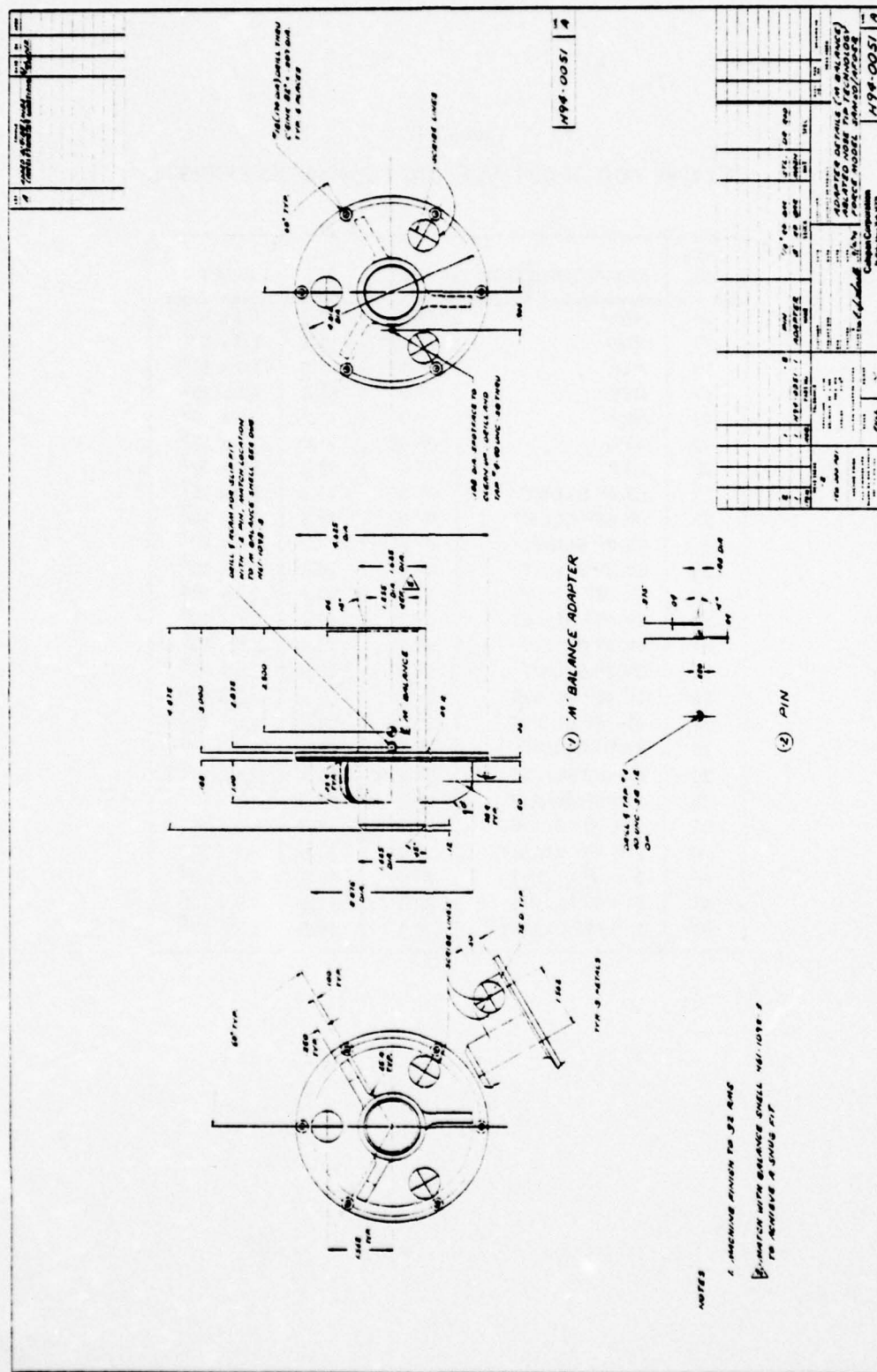


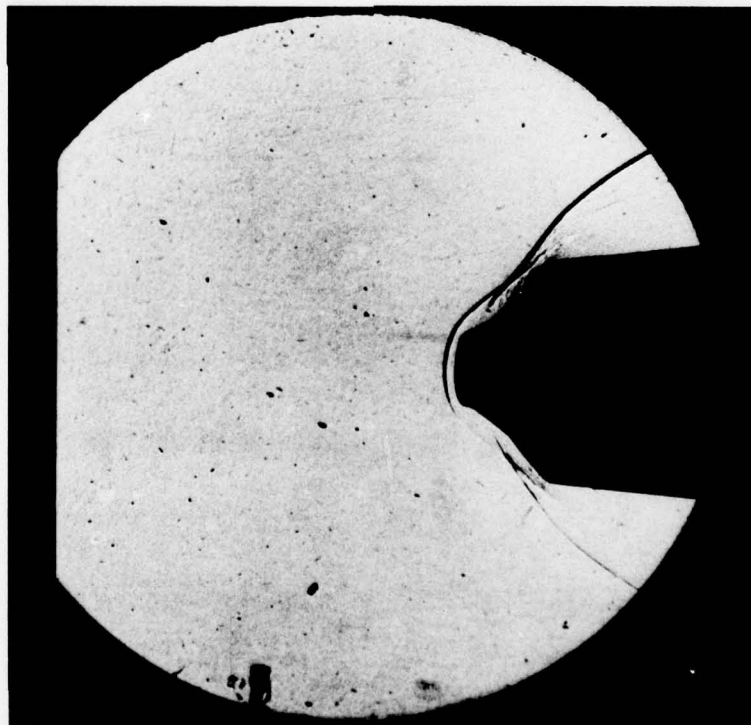
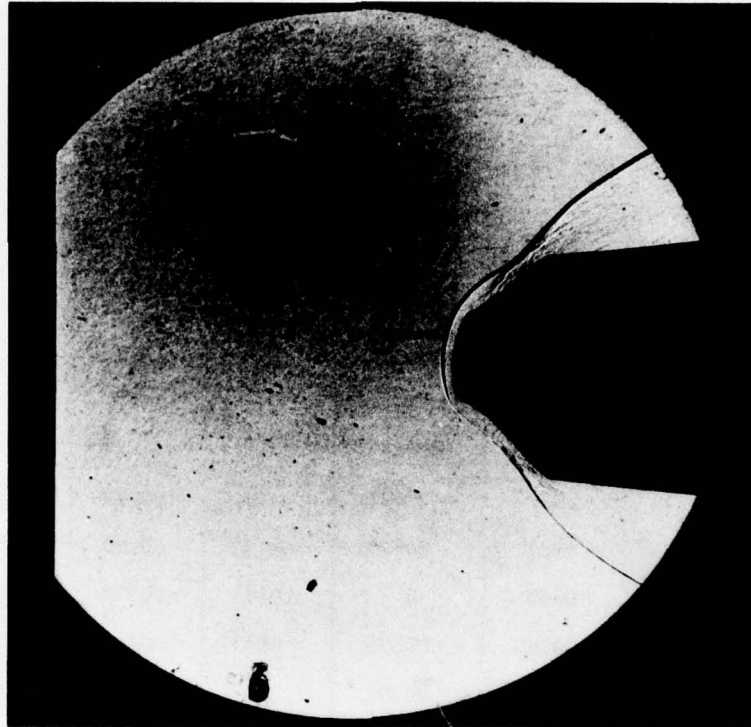
Table 3-1  
6° CONE FORCE ASYMMETRIC BLUNTNESSE EFFECTS

RUN NO.	CONFIGURATION	$\alpha$	$M_{\infty}$	$Re/FT$
14	NRV	0° 2'	11.3	$1.0 \times 10^7$
15	NRV	2° 57'	11.3	$1.0 \times 10^7$
16	RTE	2° 57'	11.3	$1.0 \times 10^7$
17	RTE	1° 0'	11.3	$1.0 \times 10^7$
18	NRV	1° 0'	11.3	$1.0 \times 10^7$
19	NRV	2° 58'	11.0	$3.9 \times 10^6$
20	RTE	0° 2'	11.3	$1.0 \times 10^7$
22	6% 0° BLUNT	0° 0'	11.3	$1.0 \times 10^7$
23	6% 45° BLUNT	0° 5'	11.3	$1.0 \times 10^7$
24	6% 0° BLUNT	0° 5'	11.3	$1.0 \times 10^7$
26	6% 0° BLUNT	0° 3'	10.9	$2.4 \times 10^6$
29	6% 45° BLUNT	3° 3'	10.9	$2.5 \times 10^6$
30	6% 45° BLUNT	0° 3'	10.9	$2.5 \times 10^6$
31	6% 0° BLUNT	0° 3'	10.9	$2.5 \times 10^6$
32	6% 0° BLUNT	1° 2'	10.9	$2.5 \times 10^6$
33	6% 45° BLUNT	1° 2'	10.9	$2.5 \times 10^6$
34	6% 45° BLUNT	1° 2'	10.9	$2.5 \times 10^6$
35	6% 0° BLUNT	2° 59'	10.9	$2.5 \times 10^6$
36	6% 45° BLUNT	2° 59'	10.9	$2.5 \times 10^6$
37	21% 0° BLUNT	0° 0'	11.3	$1.0 \times 10^7$
38	21% 45° BLUNT	0° 0'	11.3	$1.0 \times 10^7$
39	21% 45° BLUNT	1° 0'	11.0	$3.9 \times 10^6$
40	21% 0° BLUNT	1° 0'	11.0	$3.9 \times 10^6$
41	21% 0° BLUNT	3° 0'	11.0	$3.9 \times 10^6$
42	21% 45° BLUNT	3° 0'	11.0	$3.9 \times 10^6$

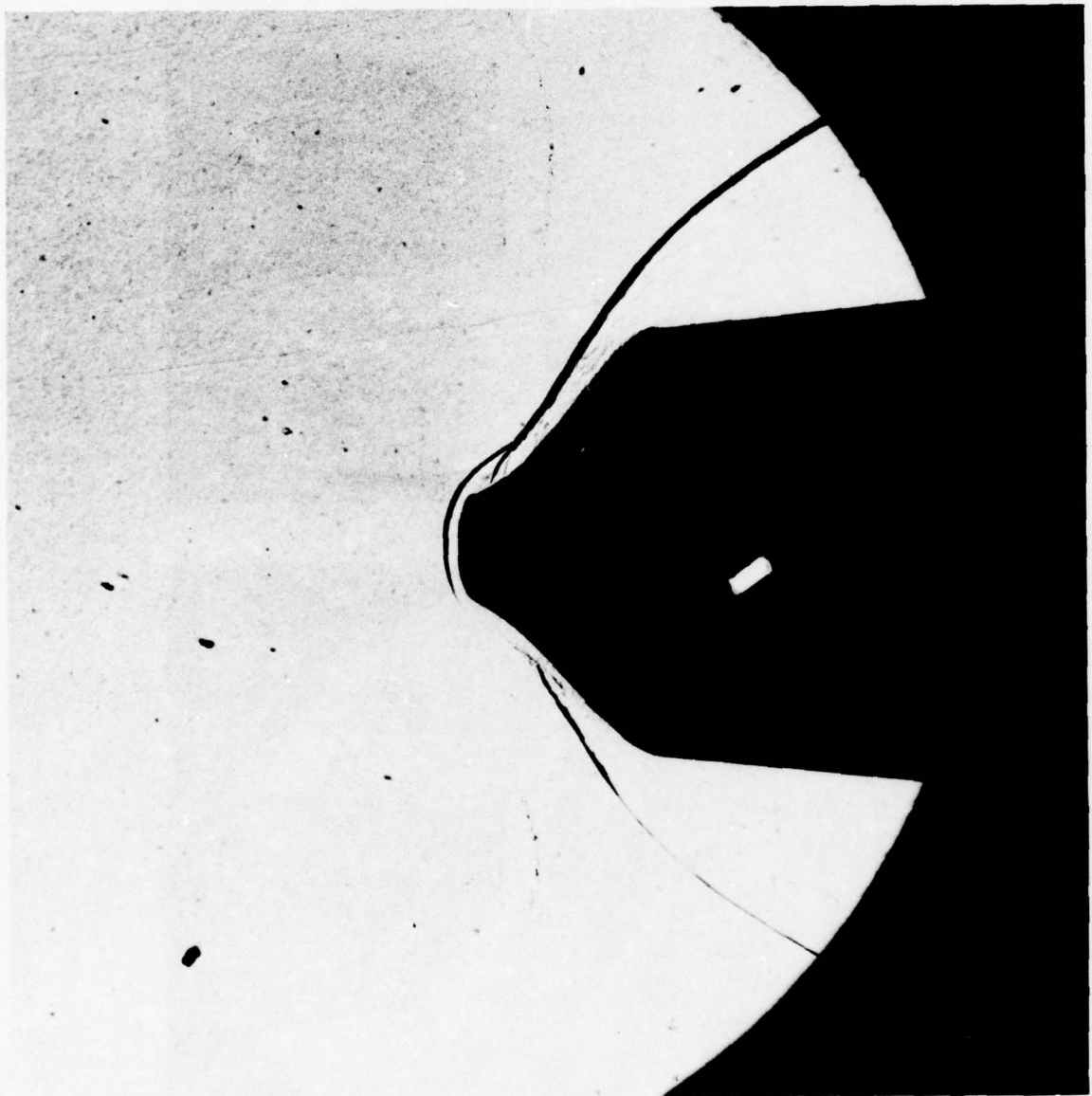


Table 3-2  
NOSE TIP FORCE MEASUREMENTS

RUN	MODEL	$\alpha$	$C_N$	$C_m$	$C_Y$	$C_n$	$C_L$	$C_A$
2	BLUNT	0						+1.26
3	↓	2	+0.116	+0.00401				+1.27
4	45° BLUNT	0	+0.382	+0.186				+1.09
5	↓	2	+0.420	+0.193				+1.09
7	NRV	0, $\phi = 74^\circ$	+0.0397	-0.000812	-0.0164	+0.000788	$+9.0 \times 10^{-5}$	+0.971
8	↓	0, $\phi = 74^\circ$	+0.0487	-0.00529	-0.0134	+0.00259	$+8.5 \times 10^{-5}$	+0.999
9	↓	2	+0.0698	0	-0.0114	+0.00214	$+2.0 \times 10^{-5}$	+0.957
10	RTE	0	-0.00985	-0.00309	+0.00437	-0.00208	$-2.5 \times 10^{-5}$	+1.03
11	↓	2	+0.0358	-0.00284	-0.00404	+0.000918	$+1.67 \times 10^{-4}$	+1.03
12	NRV	0	+0.0372	-0.00109	-0.00586	-0.000497	$+2.1 \times 10^{-5}$	+0.903



**Figure 3-7 SCHLIEREN PHOTOGRAPHS OF THE FLOW OVER THE NRV NOSE TIP  
(MODEL ROTATED BETWEEN RUNS)**



**Figure 3-8 FLOW OVER THE NTE NOSE TIP**



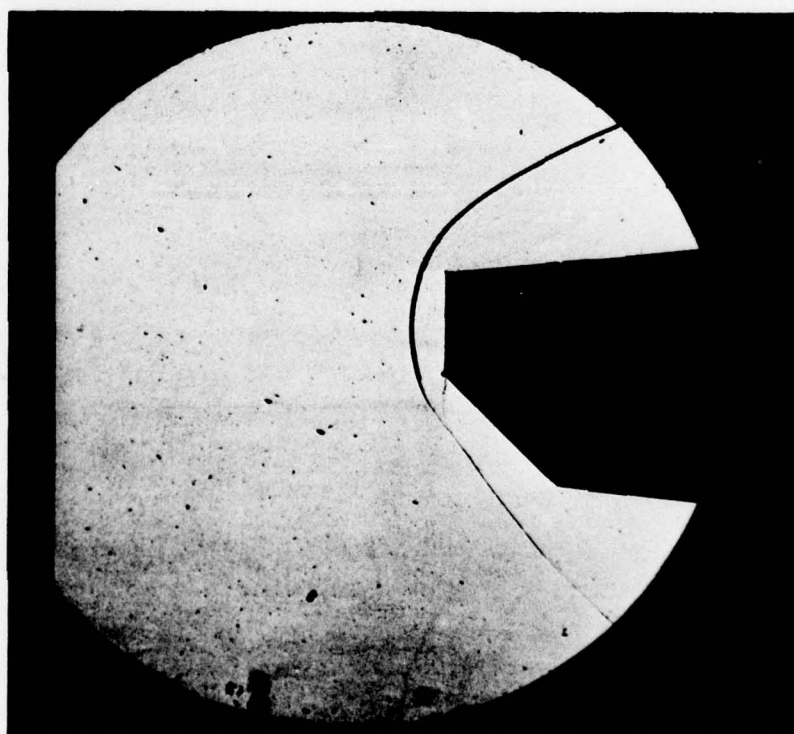
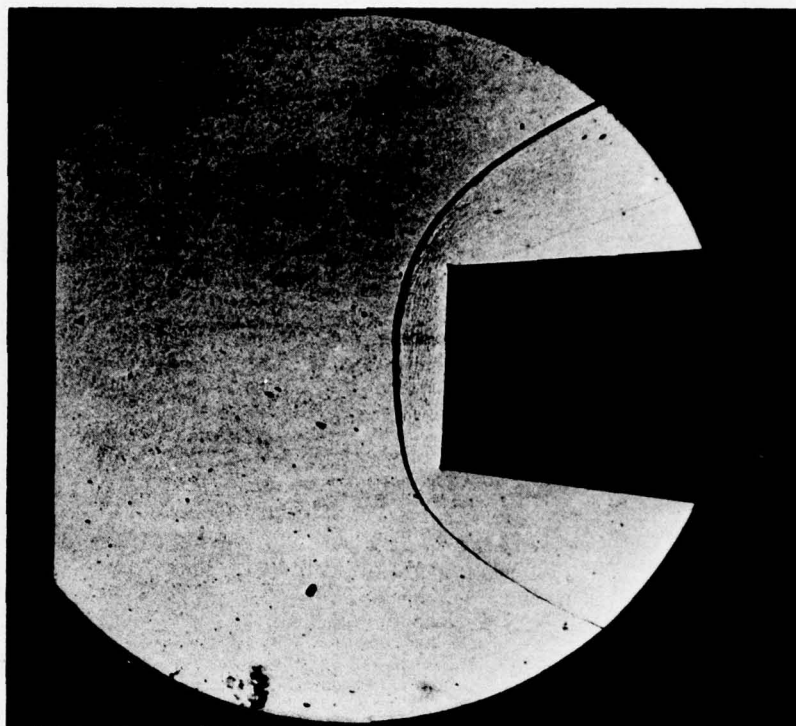


**Figure 3-9 SCHLIEREN PHOTOGRAPHS OF THE FLOW OVER THE BLUNT AND 45° BLUNT MODELS AT MACH 8.6**

force measurements made in these studies are tabulated in Table 3-3. Clearly the NRV generates a significant side force at  $0^\circ$  incidence, which as we shall see later, is reflected in a small trim of the total vehicle. Referred to the base of a 21% blunt vehicle, the NRV nose tip exhibits roll coefficients of between  $2 \times 10^{-5}$  and  $9 \times 10^{-5}$  depending upon the free stream Reynolds number. The sensitivity of nose torque to Reynolds number was anticipated because the complex characteristics of the flow field in the grooved cavities will be strongly dependent on whether the boundary layer is laminar or turbulent. The measurements of the normal and axial force coefficients also show sensitivity to Reynolds number, which as we will see later results from a variation in the structure of the flow in the reattachment compression region.

### 3.3.2 Measurements with the Nose Tip-Frustum Combinations

To complete the information necessary to obtain the frustum forces, measurements were made with a  $6^\circ$ -conical frustum capped with the nose tip configurations for which we had obtained force measurements as described above. A photograph of the cone model together with some of the nose tips used in this study is shown in Figure 3-4. The dimensions of the cone and the nose tips are shown in Figure 2-1.

The experimental program was conducted at a Mach number of 11.2 and Reynolds number of  $20 \times 10^6$  based on cone length. Table 3-1 lists the model configurations and free stream conditions for which the studies were performed, while the force measurements are listed in Tables 2-3 and 2-6. We obtained detailed heat transfer and pressure measurements along the windward and leeward meridian of the cone, and additional measurements of heat transfer on the,  $45^\circ$ ,  $90^\circ$ ,  $135^\circ$ , and  $270^\circ$  meridians. Listings of these measurements are given in Tables 2-4 and 2-5 and plots of the heat transfer and pressure distributions are shown in Figure 2-3 through Figure 2-57, respectively. The measurements of pressure on the sharp conical models at  $0^\circ$  incidence were found to be in excellent agreement with the theory, while the similar measurements on the spherically-blunted configurations were found to agree with the "NSWC solutions" shown in Figure 3-10. A second example of

Table 3-3  
TEST CONDITIONS FOR NRV NOSE TIP FORCE STUDIES

RUN NO.	ATTACK ANGLE	2	3	4	5	7	8	9	10
mi		1.633L-01	2.163L+00	0.0	2.000E+00	0.0	0.0	2.167E+00	0.0
P <sub>0</sub>	psi	2.555E+00	2.001E+00	2.579L+00	2.580E+00	2.537E+00	2.442E+00	2.537E+00	2.541E+00
H <sub>0</sub>	ft <sup>2</sup> /sec <sup>2</sup>	7.371E+00	7.534E+00	7.653E+00	7.320E+00	9.788E+00	4.046E+00	1.014E+00	1.017E+00
M <sub>0</sub>		1.105E+00	1.140E+00	1.134E+00	1.131E+00	1.100E+00	1.060E+00	1.124E+00	1.123E+00
U <sub>0</sub>	ft/sec	6.723E+00	4.705E+00	8.725L+00	3.725E+00	8.730L+00	8.040E+00	8.733E+00	8.733E+00
T <sub>0</sub>	°K	4.259E+00	4.038E+00	4.010E+00	4.009E+00	4.040E+00	4.042E+00	4.059E+00	4.059E+00
P <sub>00</sub>	psi	1.135E+00	1.131E+00	1.104E+00	1.100E+00	1.110E+00	1.095E+00	1.109E+00	1.130E+00
Q <sub>00</sub>	psi	5.077E-01	5.225E-01	5.420E-01	5.398E-01	6.737E-01	2.657E-01	6.998E-01	7.033E-01
Q <sub>00</sub>	slug/ft <sup>3</sup>	2.707E+01	2.776E+01	2.891E+01	2.880E+01	3.054E+01	1.403E+01	3.763E+01	3.802E+01
μ <sub>00</sub>	slug/ft <sup>3</sup>	3.726E-04	3.710E-04	3.903E-04	3.904E-04	3.101E-04	2.027E-04	3.133E-04	3.133E-04
Re/ft.		9.549E-00	9.926E-00	9.737E-00	9.759E-00	9.364E-00	9.241E-00	9.580E-00	9.571E-00
P <sub>0</sub>	psi	1.721E+00	1.730E+00	1.643E+00	1.644E+00	2.072E+00	9.703E+00	2.474E+00	2.490E+00
P <sub>0</sub>	psi	4.233E+01	5.117E+01	5.324E+01	5.303E+01	6.744E+01	2.541E+01	6.967E+01	7.000E+01

RUN NO.	ATTACK ANGLE	11	12
mi		2.600E+00	0.0
P <sub>0</sub>	psi	2.555E+00	3.016E+00
H <sub>0</sub>	ft <sup>2</sup> /sec <sup>2</sup>	1.001E+00	1.539E+00
M <sub>0</sub>		1.153E+00	1.240E+00
U <sub>0</sub>	ft/sec	6.723E+00	1.121E+01
T <sub>0</sub>	°K	4.057E+00	3.965E+00
P <sub>00</sub>	psi	1.109E+00	1.170E+00
Q <sub>00</sub>	psi	7.336E-01	1.049E-01
Q <sub>00</sub>	slug/ft <sup>3</sup>	3.763E+01	1.627E+01
μ <sub>00</sub>	slug/ft <sup>3</sup>	3.726E-04	1.317E-04
Re/ft.		9.549E-00	9.926E-00
P <sub>0</sub>	psi	2.443E+00	7.059E+00
P <sub>0</sub>	psi	7.209E+01	3.016E+01



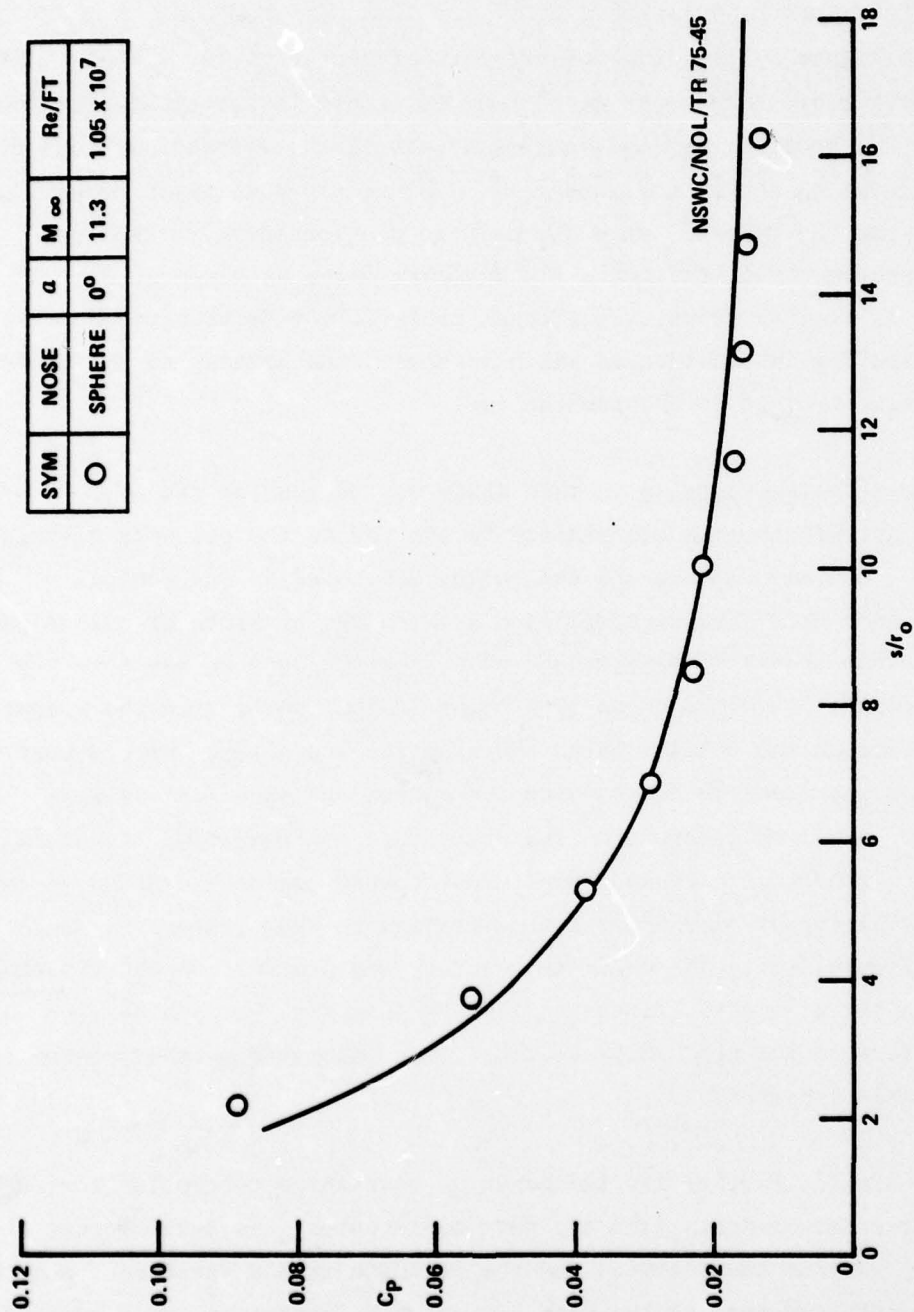


Figure 3-10 COMPARISON BETWEEN MEASURED PRESSURE DISTRIBUTION AND THEORY  
FOR SPHERICALLY CAPPED  $6^\circ$  CONE AT  $0^\circ$  INCIDENCE

agreement is demonstrated in the comparison between the measurements made on a spherically capped configuration at  $3^\circ$  incidence and the theoretical  $\gamma$  prediction (see Figure 3-11). The measurements of heat transfer on this laminar boundary layer over sharp cones at  $0^\circ$  incidence were in agreement with the simple Cheng theory<sup>20</sup>; however, at small angles of attack the effects of cross flow became important as shown on Figure 3-12. The simple prediction techniques of Eckert<sup>21</sup> and Van Driest<sup>22</sup> were found in good agreement with the heat transfer measurements in the turbulent boundary layer on cones at  $0^\circ$ ; however, as in laminar flows, significant cross flow effects were found at relatively small model incidences which increased the heating to the windward ray while decreasing it on the leeward ray.

Our principal purpose in this study was to examine the effects of an indented asymmetric nose tip similar to the NRV on the pressure distribution over the conical frustum and the forces developed by the conical frustum. Figure 3-13 shows a comparison between the pressure distribution over the frustum of the  $6^\circ$ -cone capped by a spherical and an NRV nose tip. The pressure on the frustum ahead of a point 16 body radii from the stagnation point exceeds the values behind the spherical nose tip, while downstream of this point the pressure drops below the equivalent spherical values. Clearly, the center of pressure on the NRV capped configuration lies ahead of that for a spherically capped cone. Just downstream of the NRV nose tip there is a significant circumferential variation on the pressure as demonstrated in Figure 3-14. The asymmetric forces and pressure on the frustum act in concert with the asymmetric forces on the NRV nose tip. It can be seen that the effect of the nose shape on the forces generated by the frustum is of considerable importance.

To examine further the influence of nose shape on frustum forces, we took the force measurements from the nose tip studies, the total forces on the nose tip frustum combinations and the measured frustum pressures, and calculated the separate forces on the nose tip and the frustum, as well as on the combined configuration. Figures 3-15 and 3-16 show the measured and calculated normal force coefficients and the center of pressure (CP) location on

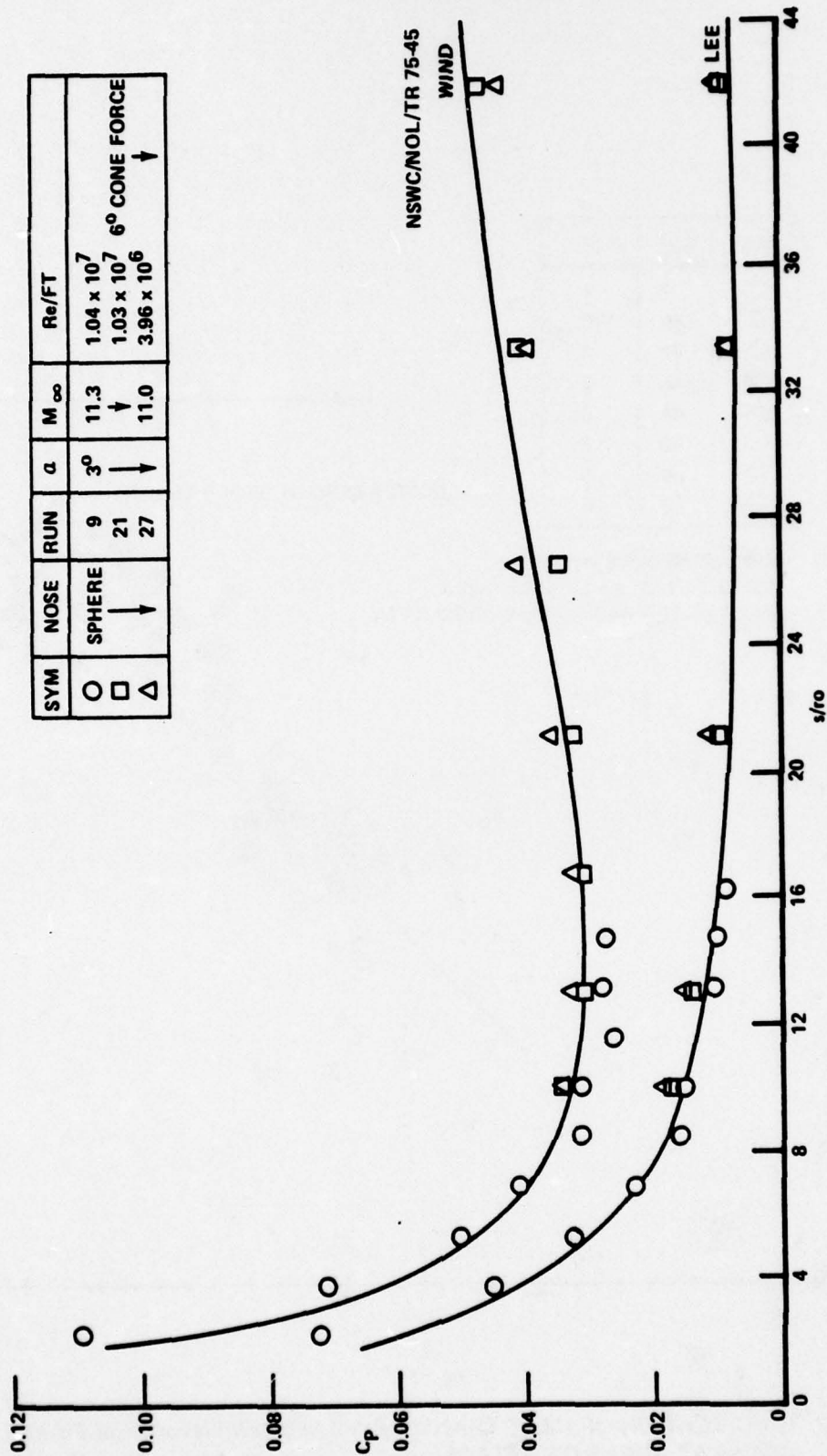


Figure 3-11 COMPARISON BETWEEN MEASURED PRESSURE DISTRIBUTION AND THEORY FOR SPHERICALLY CAPPED  $6^\circ$  CONE AT  $3^\circ$  INCIDENCE



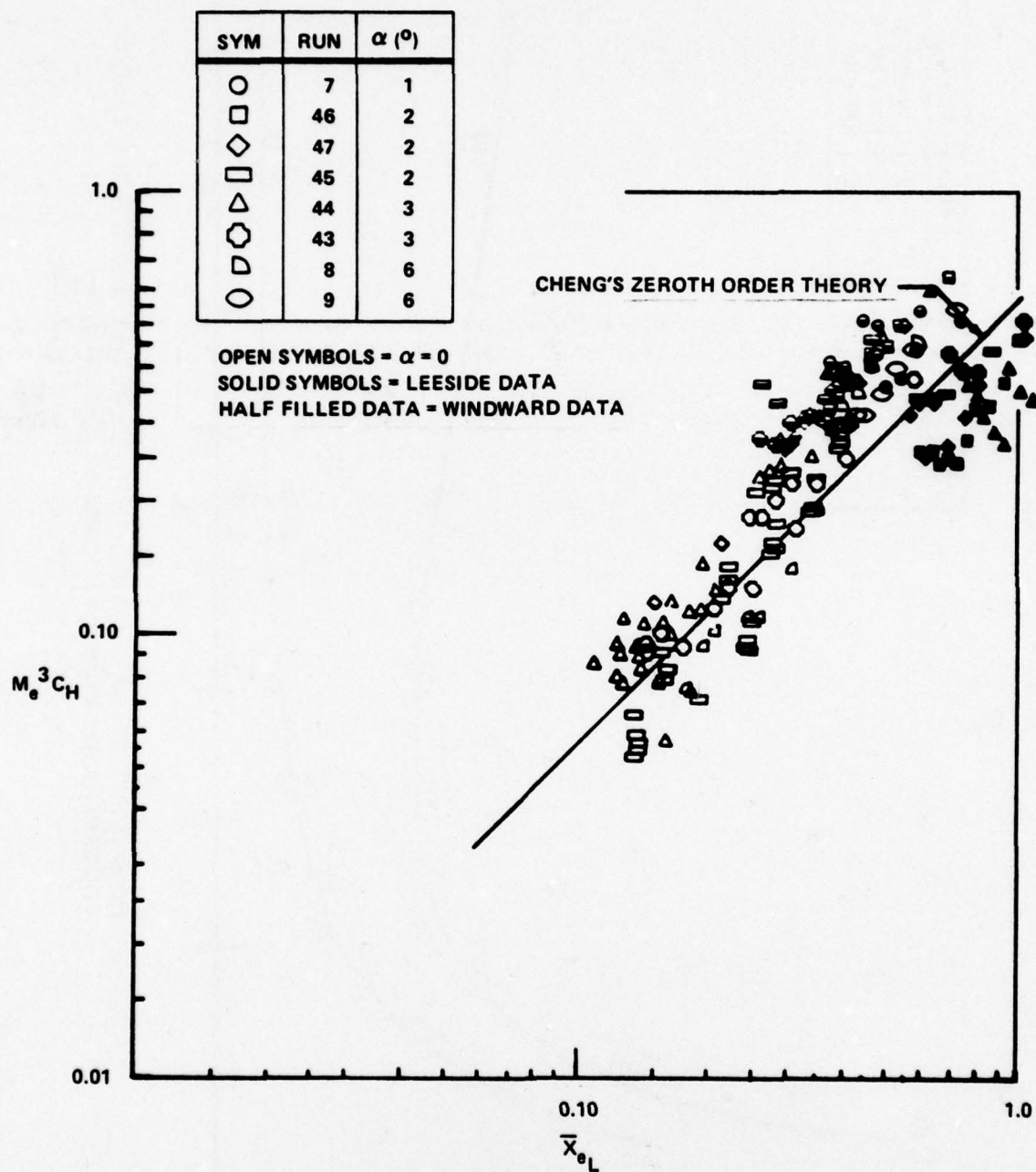


Figure 3-12 CORRELATION OF HEAT TRANSFER MEASUREMENTS ON SLENDER CONES AT ANGLE OF ATTACK

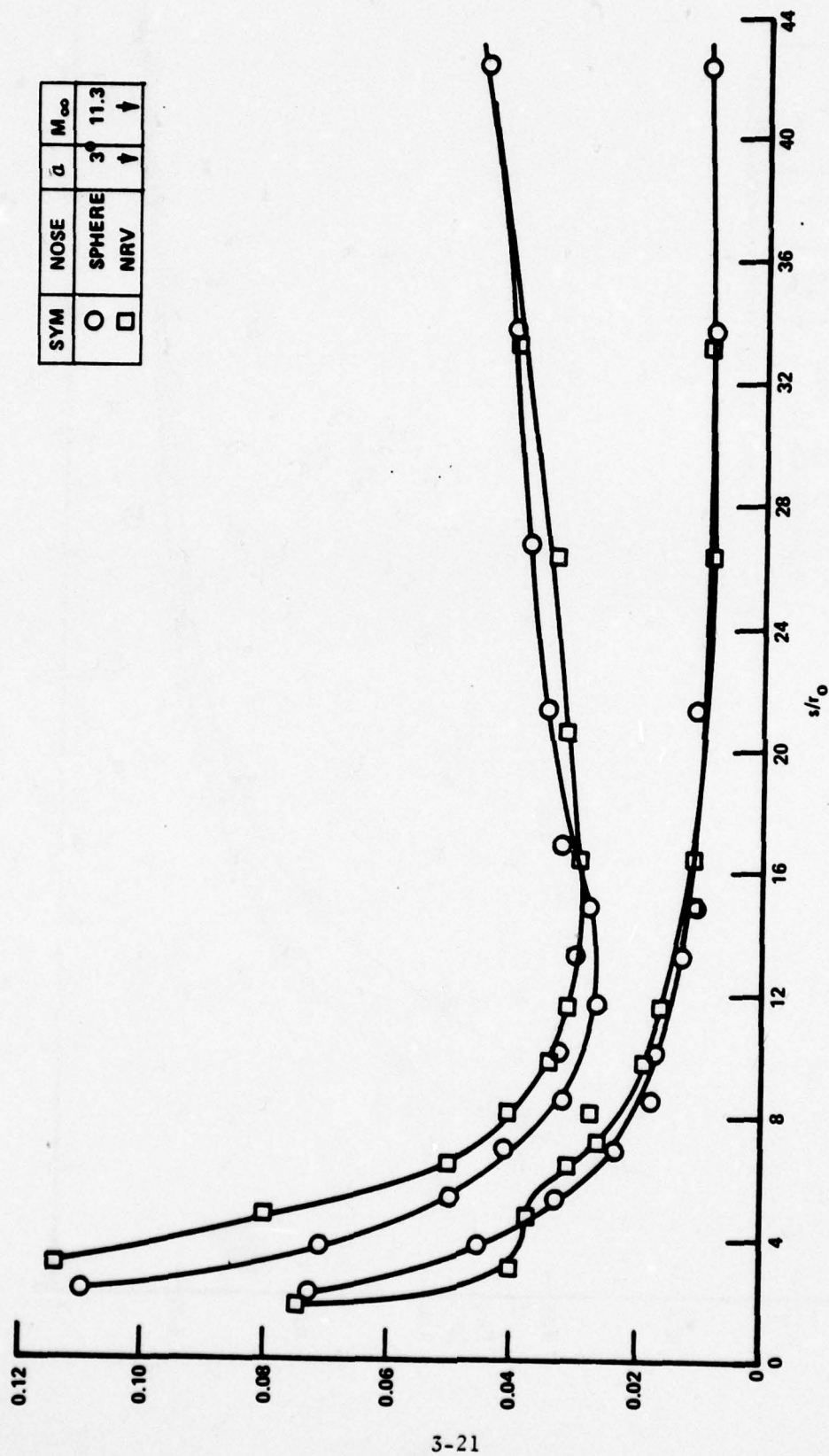


Figure 3-13 COMPARISON BETWEEN THE MEASURED PRESSURE DISTRIBUTION ON A 6° CONE CAPPED WITH THE NRV AND A SPHERICAL NOSE CAP AT 3° OF MODEL INCIDENCE

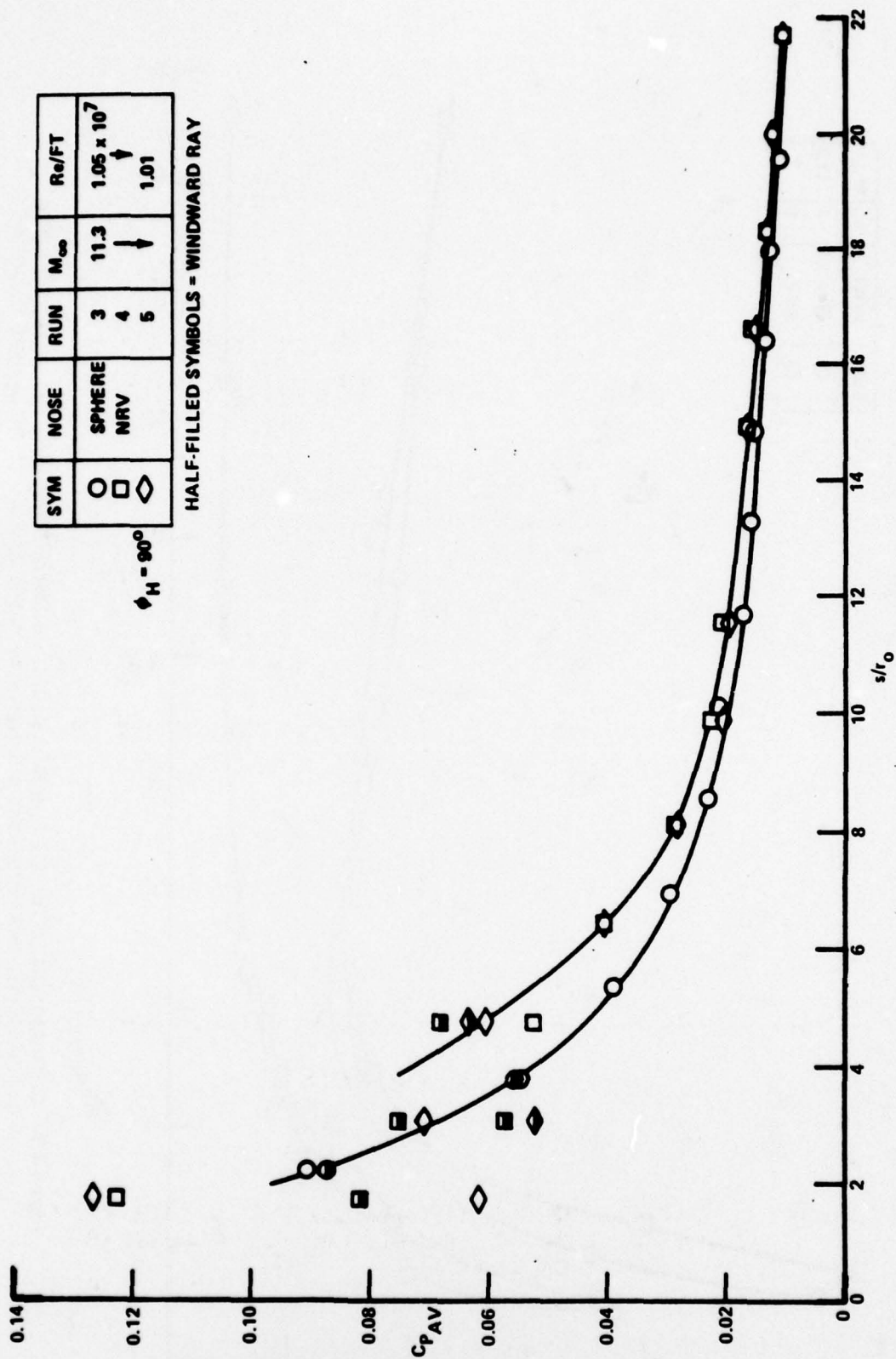


Figure 3-14 COMPARISON BETWEEN FRUSTUM PRESSURE MEASUREMENT ON A 6° CONE CAPPED WITH SPHERICAL AND NRV NOSE TIPS



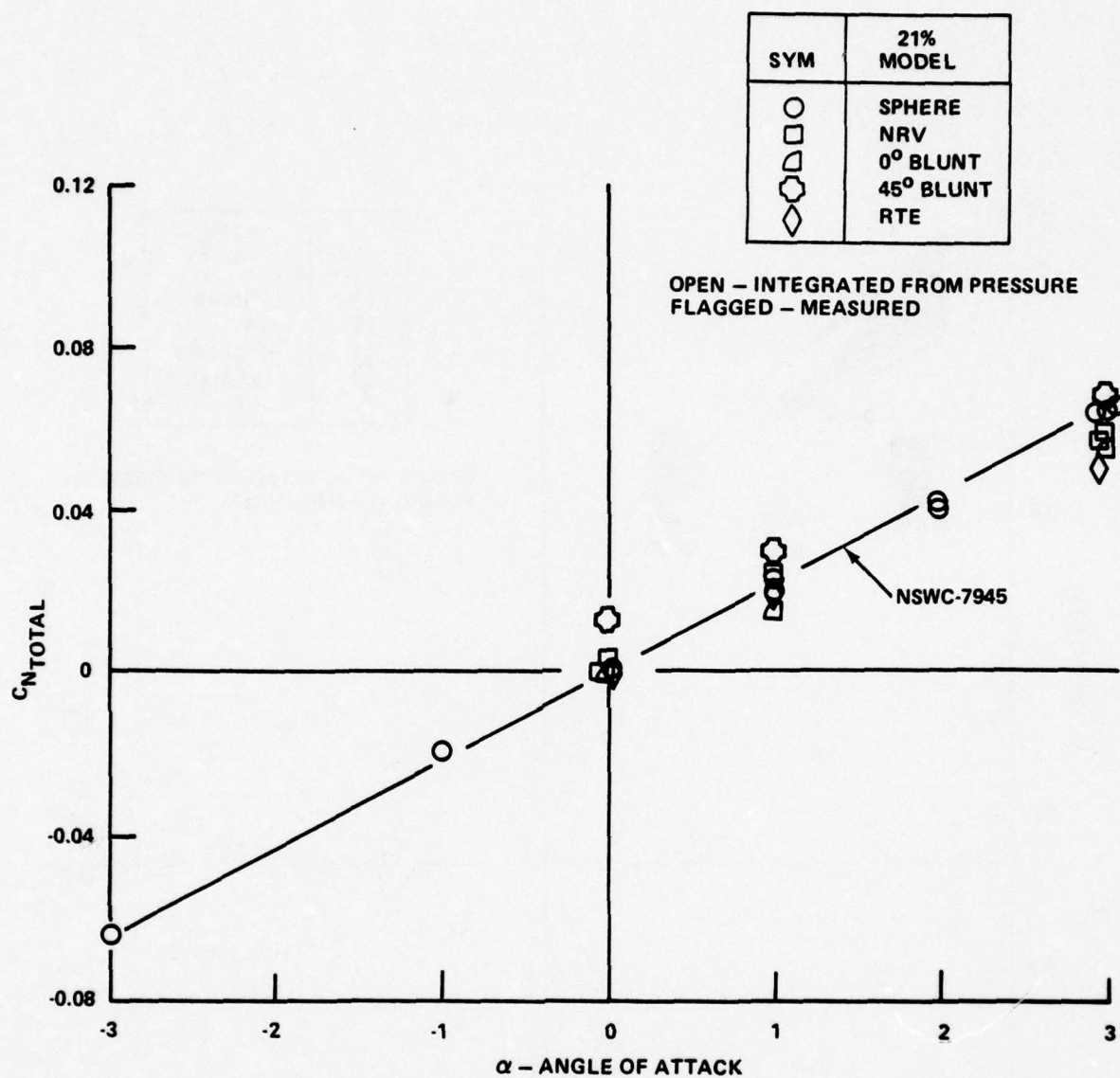


Figure 3-15 VARIATION OF THE FRUSTUM FORCE COEFFICIENT WITH ANGLE OF ATTACK FOR 21% BLUNT 6° CONES EQUIPPED WITH THE NOSE TIPS DENOTED IN THE CAPTION

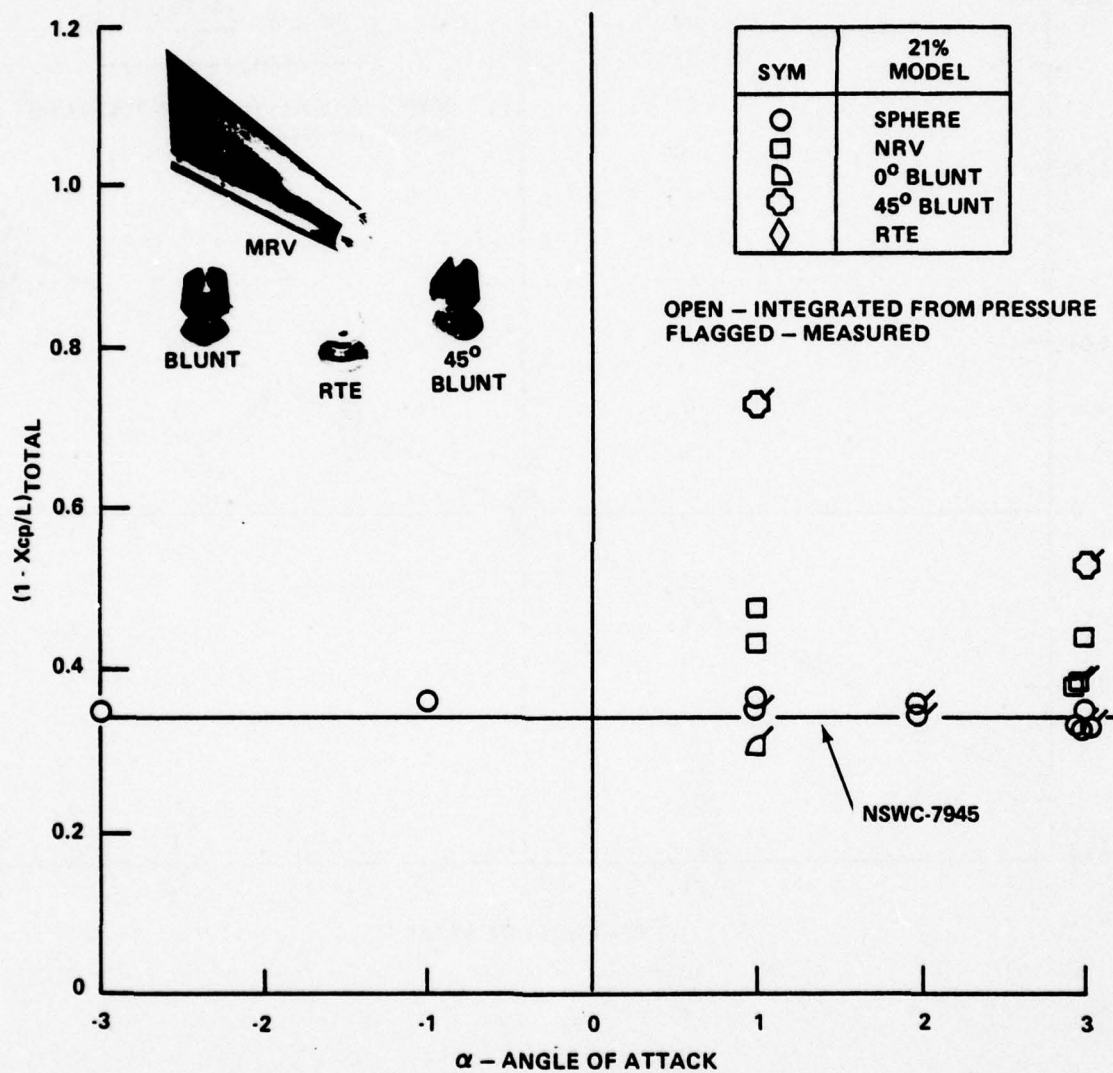


Figure 3-16 VARIATION OF THE CENTER OF PRESSURE POSITION WITH ANGLE OF ATTACK FOR THE NOSE TIP - FRUSTUM COMBINATIONS DENOTED IN THE CAPTION

the 6°-cone for a bluntness ratio of 21%. Here we have compared the measurements on the symmetric spherically capped and "blunt" configurations with those on the NRV, RTE and "45°-blunt" asymmetric nose tips. The variation of the total normal force coefficient with angle of attack for the five configurations studied is shown in Figure 3-15. The theoretical variation of normal force with angle of attack for the spherically capped configuration from NSWC-7945 is seen to be in good agreement with the measured forces (flagged symbols) and the values determined by integrating the measured pressure distribution. To integrate the pressure measurements for cones at the angle of attack, we assumed a Newtonian distribution of pressure between the measured values on the windward and leeward rays. The increase in the normal force coefficient (relative to the spherical tip) generated by the model with the 45°-blunt nose tip, which is most pronounced at a 0° angle of attack has almost disappeared by 3° incidence. The NRV-capped configuration also exhibited a measurable force coefficient at 0° incidence. The position of the center of the nose tip-frustum combination is shown in Figure 3-16. Again we find good agreement between theory and the measured and integrated results for the spherically capped configurations. The configuration with the 45° blunt nose tip does and should exhibit a large forward (destabilizing) movement of the CP while the addition of the "blunt" nose tip results in the typical stabilizing effect of blunting as the CP moves aft. However, of greatest interest is the destabilizing effect which occurs when a spherical nose tip ablates onto the asymmetric NRV configuration. Our measurements indicate that the CP of the NRV moves forward approximately 10% of the cone length at 1° incidence. However, the symmetric RTE nose tip shows the typical stabilizing effect of symmetric blunting from an initially spherical nose shape. Our primary interest, however, lies in evaluating the effects of nose tip shape on frustum forces.

For practical design purposes it has been assumed that the pressure distribution over the conical frustum of an RV can be approximated by the sphere-cone distribution for an appropriate bluntness ratio. In this present study, we were able to examine the validity of this assumption by calculating forces on the frustum by subtracting the contribution of the nose tip from



the forces on the total configuration. The results of these calculations are shown in Figures 3-17 and 3-18. We see that the pressure distribution over the conical frustum is modified by the NRV and the 45°-blunt nose tip causing a forward movement of the center of pressure relative to its "sphere-cone" position. Thus, in addition to the destabilizing nose-tip force, we obtain a complimentary nose-tip induced destabilizing frustum force. However, because the normal force on the frustum is reduced slightly behind the 45°-blunt nose tip, the net destabilizing moment is less than that for the NRV capped configuration. Therefore, we see that while the 45°-blunt nose-tip represents the "worst" case when we consider the stability of the total vehicle, when we examine the contribution of the frustum only, the NRV nose tip causes the greatest destabilizing effect.

The result of these studies suggest that calculating the destabilizing effects of nose shaping, accounting solely for changes in the normal force coefficient of the nose may adequately handle those cases where the nose shapes are simple and without embedded shocks. However, when embedded shocks and/or separated regions are developed over the nose tip our studies suggest that the changes in frustum forces and moments induced by the flow field over the nose tip should be taken into account.

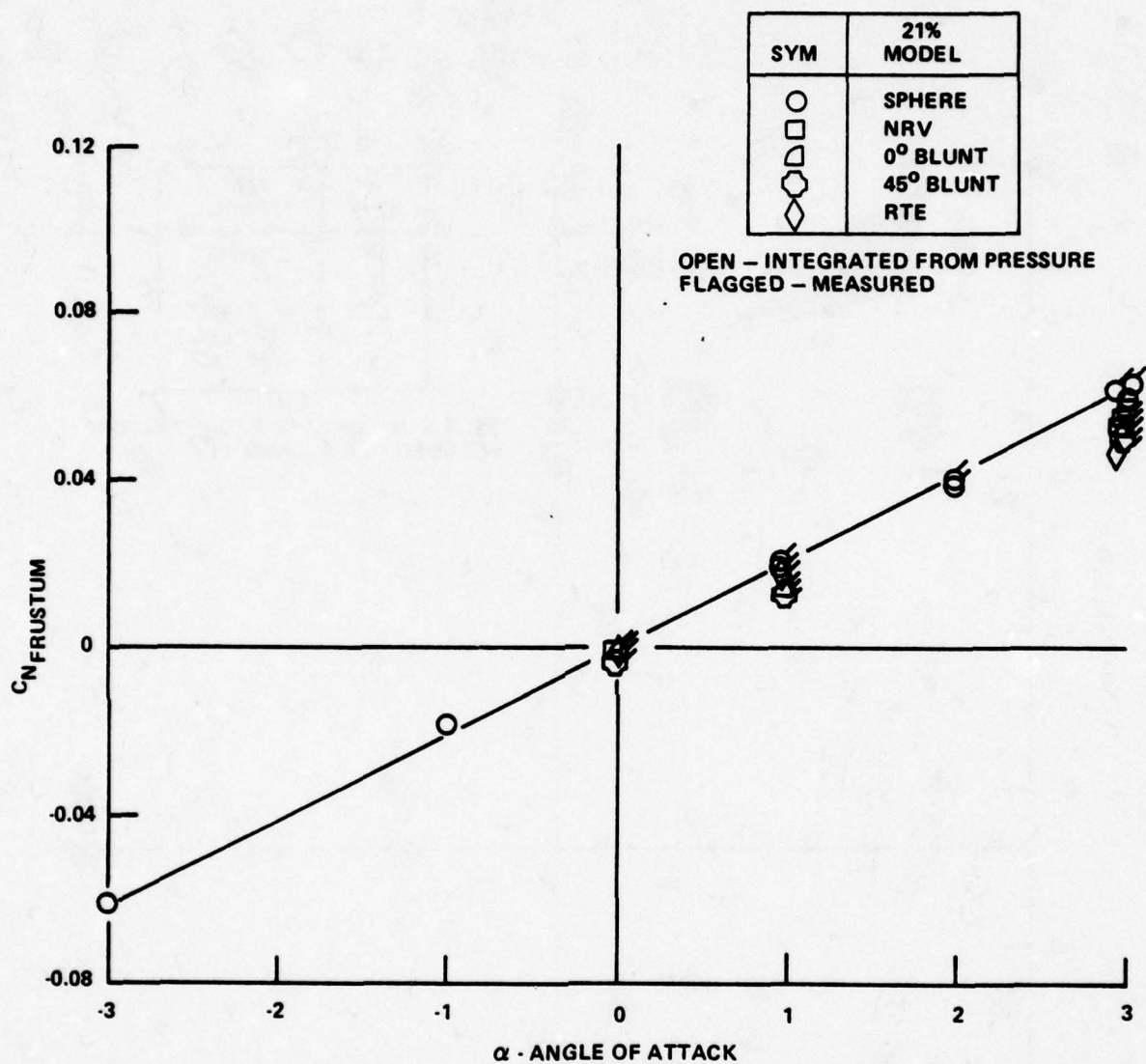
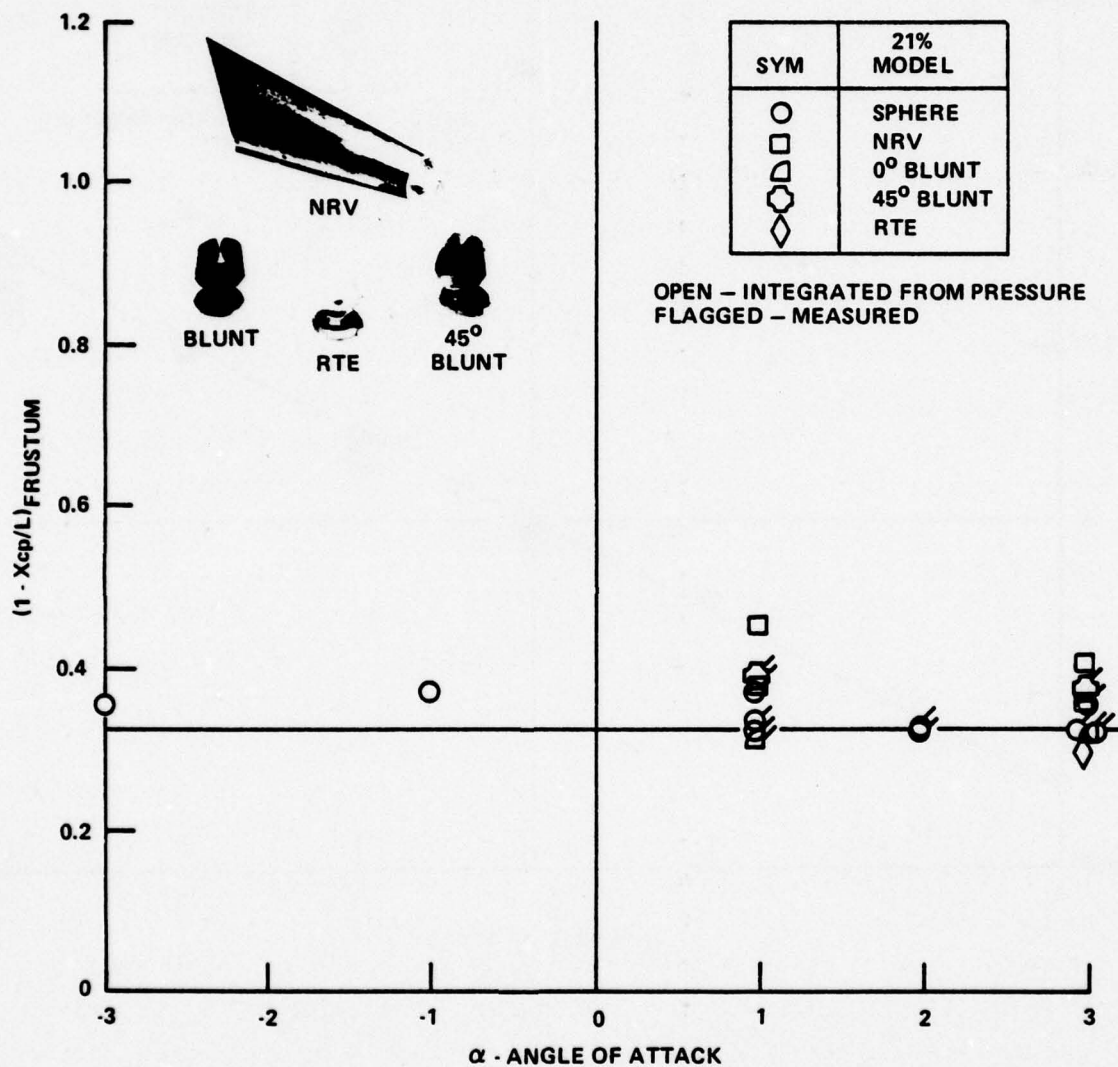


Figure 3-17 VARIATION OF THE TOTAL NORMAL FORCE COEFFICIENT WITH ANGLE OF ATTACK FOR 21% BLUNT 6° CONES EQUIPPED WITH THE NOSE TIPS DENOTED IN THE CAPTION



**Figure 3-18** VARIATION OF THE FRUSTUM CENTER OF PRESSURE POSITION WITH ANGLE OF ATTACK FOR THE NOSE TIP - FRUSTUM COMBINATIONS DENOTED IN THE CAPTION



## Section 4

### STUDIES OF BOUNDARY LAYER TRANSITION, ENTROPY SWALLOWING AND SURFACE ROUGHNESS ON ABLATED NOSE SHAPES

#### 4.1 INTRODUCTION

The prediction of the change in shape of an ablating nose tip as transition moves onto the nose requires an ability to model the development of the viscous and inviscid flow in regions of layer transition, entropy swallowing and surface roughness. In general, the theoretical analyses of the flows over blunt and slender nose tips have treated the viscous and inviscid flows as decoupled in the sense that it has been assumed that the vorticity generated by shock curvature does not directly influence boundary layer transition or the turbulence intensity in regions of boundary layer transition of fully turbulent flow. While the predictions from some shape change codes have been shown to be in good agreement with measurements on smooth "slender" nose tips where both entropy swallowing and transition were of importance, there remains a considerable lack of knowledge on the influence of surface roughness on nose tip heating. In part, this lack of knowledge reflects the dearth of measurements in high Mach numbers flow over "slender" nose tips where entropy swallowing effects are correctly simulated.

The objective of the present study was to improve our understanding of the effects of entropy swallowing and surface roughness on the distribution of heat transfer and skin friction to slender biconic nose tip configurations in the presence of boundary layer transition. In the zone of interest, measurements were made on three rough and smooth biconic configurations whose shapes were such that the entropy layer generated by nose tip bluntness was completely swallowed, partially swallowed, and remained intact, respectively. In this way, the separate and combined effects of entropy swallowing and surface roughness could be evaluated. We were also interested in examining how the Reynolds analogy factor behaved for rough wall conditions.

## 4.2 EXPERIMENTAL MODELS AND INSTRUMENTATION

A biconic nose tip model, with three nose-tip configurations was used in this study. The model, fitted with the bluntest of these nose-tip shapes, is shown mounted in the 96"-Shock Tunnel in Figure 4-1. As discussed in the previous section, sharp, medium and blunt nose tips were fabricated for these studies to impose various degrees of entropy gradient along the surface of the cone when tested in hypersonic flow. Details of the dimensions of the nose tips and the gage positions on these configurations are shown in Figure 4-2.

Heat transfer and skin friction measurements were made on each of the configurations described above for both smooth and rough wall conditions. Sand grain roughness (no. 39 grit) was bonded to the surface of the models and the diaphragm of the skin friction gages. The roughness was bonded to the skin friction gages and the main surface of the model so that as nearly as possible each grain was placed end to end. We developed a heat-transfer gage (see Figure 4-3) that measured the heat transfer to a rough surface and to the substrate beneath it. By pressing a mold containing a replica of sand-grained roughness into a molten pyrex substrate we formed a surface which had most of the characteristics of sand-grained roughness. Then we deposited the platinum sensing element over the rough substrate to complete the gage. This gage measured the average heat transfer to the surface over which the platinum is deposited; however, we can also obtain the heat transfer rate through substrate below the roughness by multiplying the heat transfer to the surface by the ratio  $R_s = \frac{\text{surface area of gage}}{\text{projected area of gage}}$ . We determined  $R_s$  by using the radiant flux calibrator shown in Figure 4-4. This apparatus generates a heat flux of calibrated intensity, which is pulsed on the gage. The ratio,  $\frac{\text{incident heat flux}}{\text{measured heat flux}}$ , is equal to  $R_s$ , if the absorptivity of the gage is close to unity. Each rough gage calibrated was coated with a thin ( $1 < 1/10 \mu\text{m}$ ) matte black film to bring the absorptivity between 95 and 100%. The exact value for the absorptivity was determined by depositing the same matte black material over flat gages and measuring directly the ratio of incident to absorbed heat flux. Details of the calibration rig are shown in Figure 4-5. A blackbody source was made by



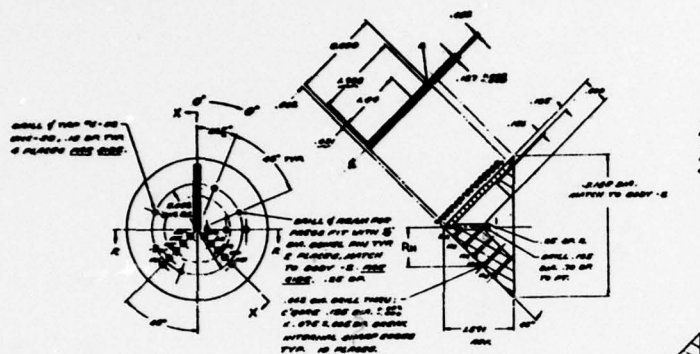
Figure 4-1 BLUNT BI-CONIC CONFIGURATION MOUNTED IN CALSPAN 96" SHOCK TUNNEL



100									
---	--	--	--	--	--	--	--	--	--

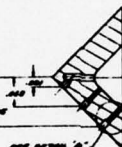


**DETAIL 'A'**

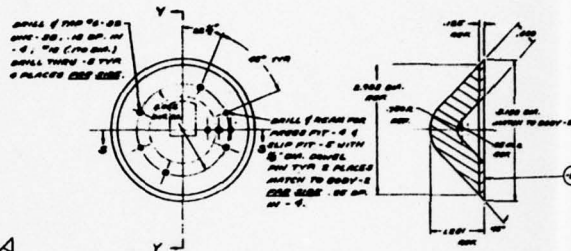


**SECTION X-X**

③ CONE SHARP

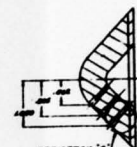


**SECTION R-R**

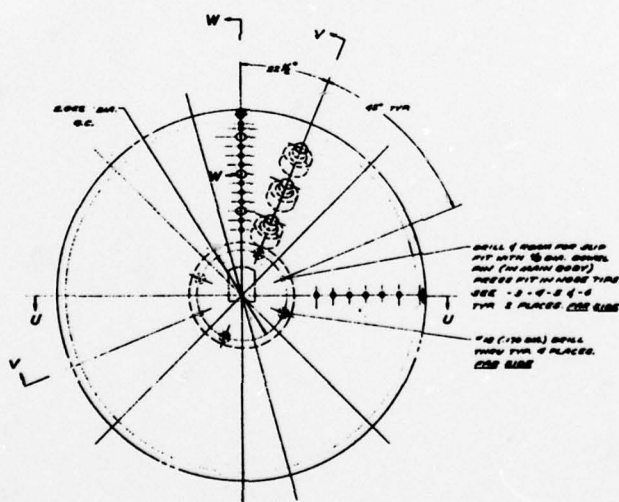


**SECTION Y-Y**

④ CONE BLUNT .75 R.



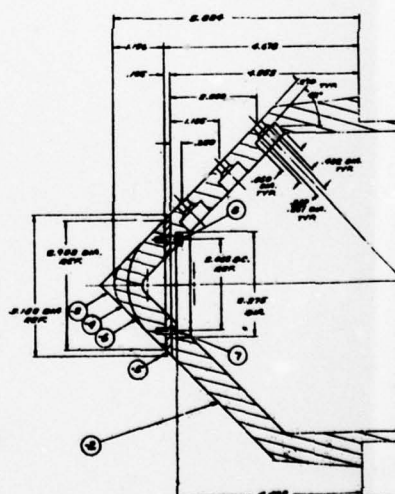
### SECTION 5-5



## NOTES

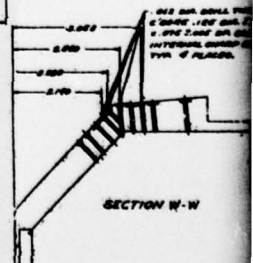
1. JOHN D. BROWN

**5. GRIND ALL INTERNAL SHARP EDGES.**

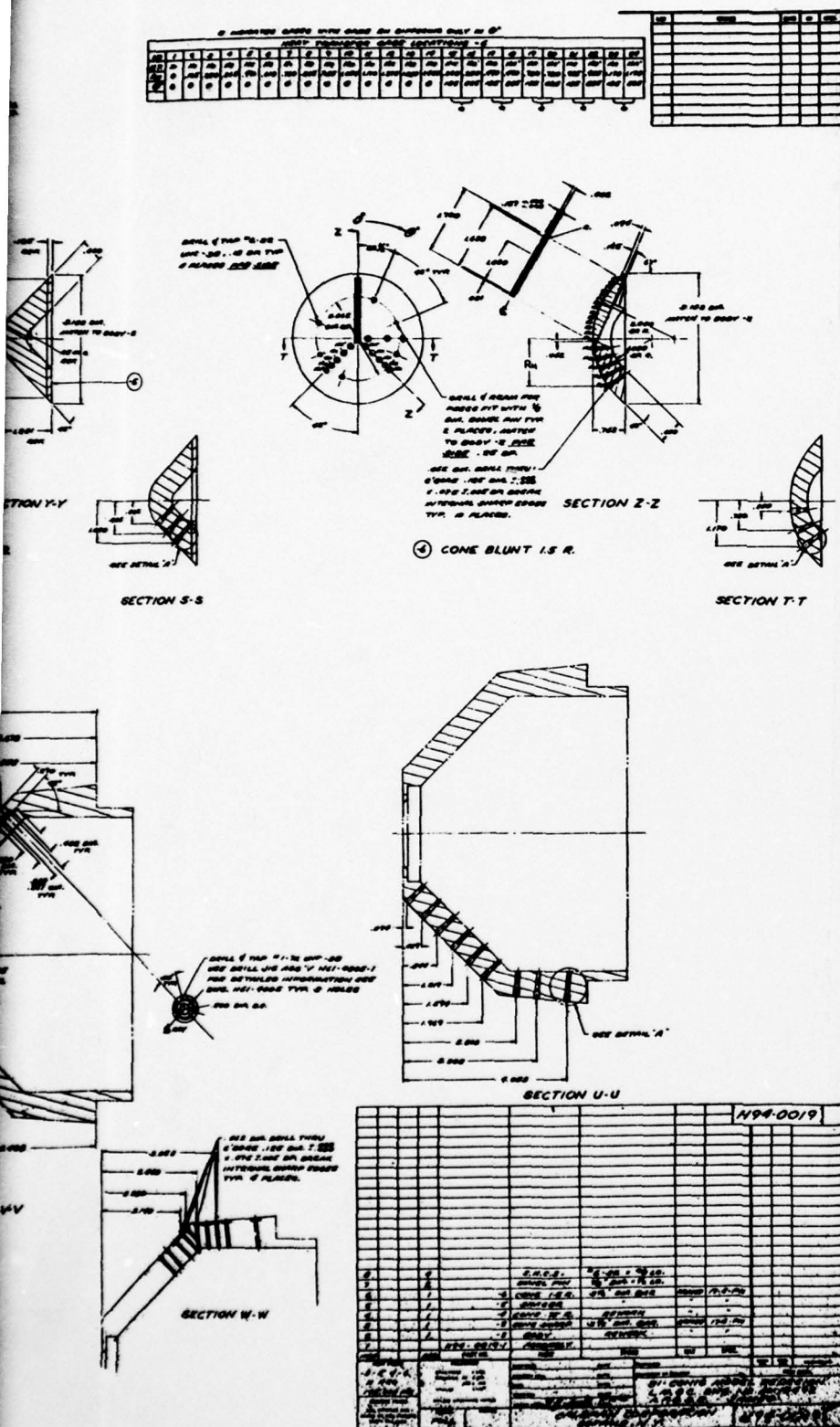


**SECTION V-V**

① BI-CONIC MODEL ASSEMBLY



**SECTION W-W**



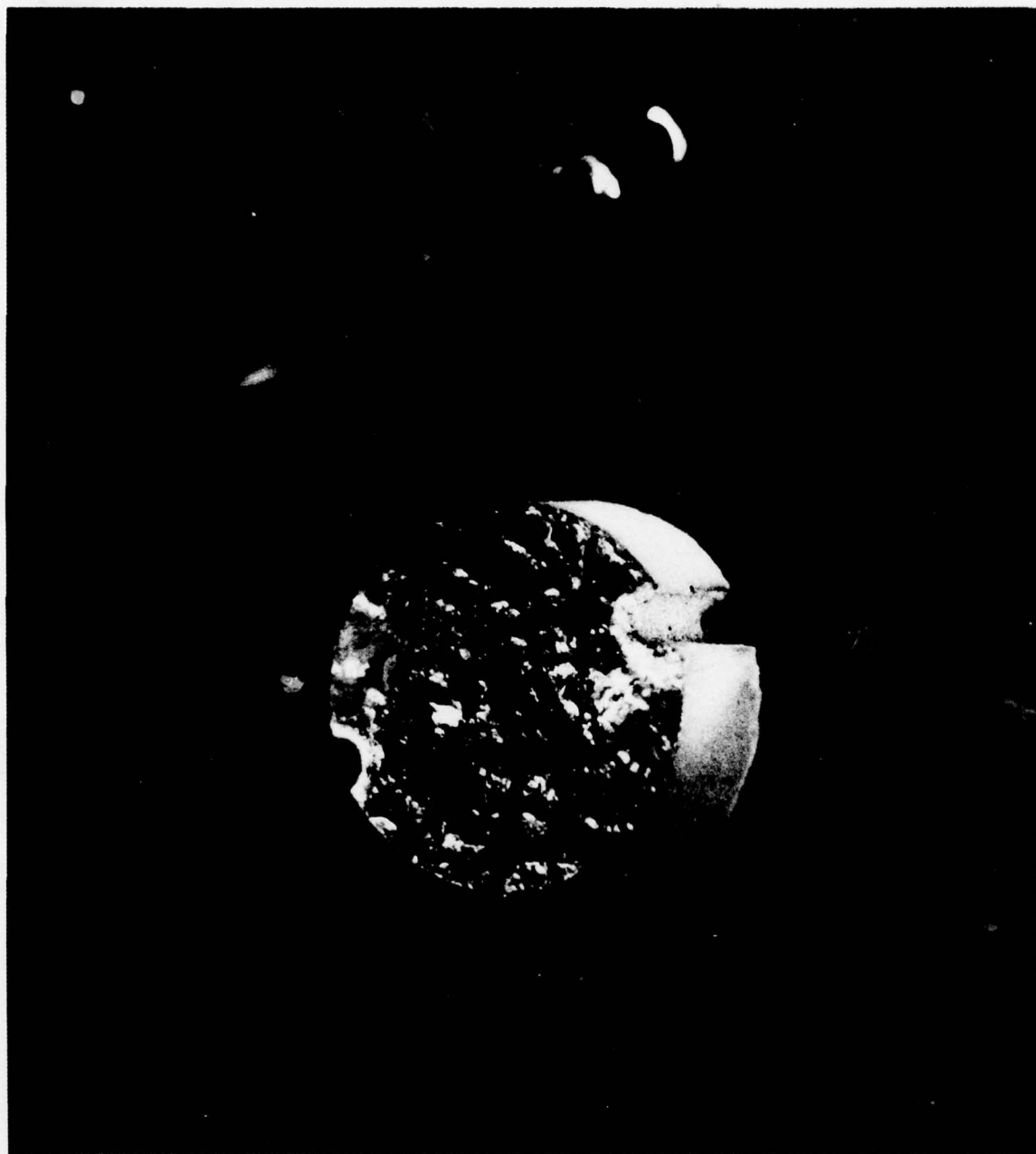
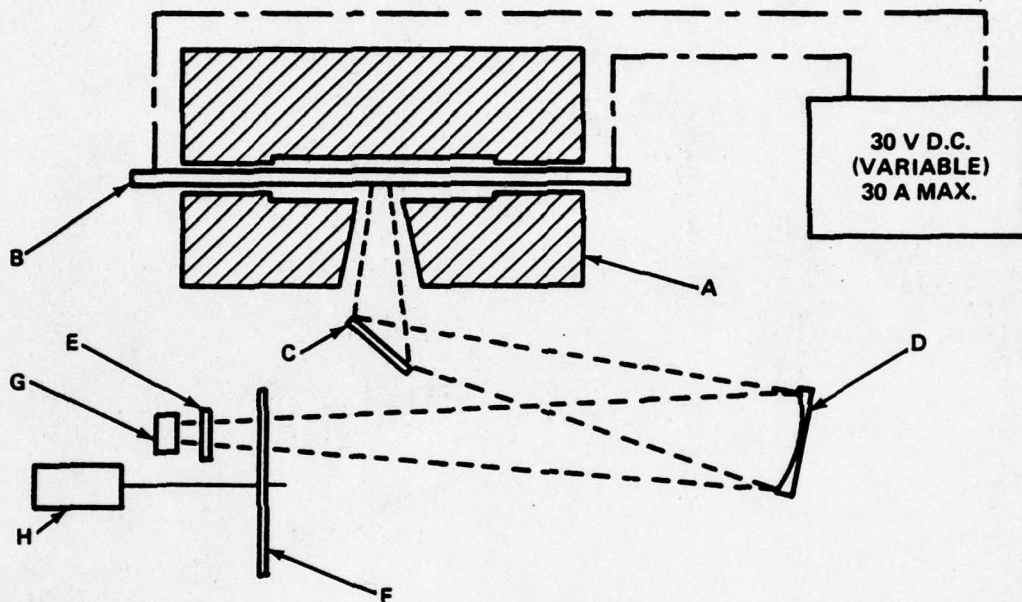


**Figure 4-3 THIN FILM GAGE TO ESTABLISH THE SURFACE  
HEATING RATE TO A ROUGH SURFACE**





- A FIREBRICK ENCLOSURE
- B GLOBAR (SILICON CARBIDE) ROD
- C FIRST-SURFACE, PLANE MIRROR
- D SPHERICAL MIRROR (4 1/4" DIA., 9" F.L.)
- E FILTER HOLDER
- F SECTOR-DISC BEAM CHOPPER
- G FOCAL PLANE (POSITION OF H.T. GAGES AND THERMOPILE)
- H MOTOR

**Figure 4-4** SCHEMATIC — ARRANGEMENT OF APPARATUS FOR CALIBRATION OF RADIATIVE ABSORPTION CHARACTERISTICS OF THIN-FILM, HEAT-TRANSFER GAGES



**Figure 4-6** A SCHLIEREN PHOTOGRAPH TYPICAL OF THOSE OBTAINED OVER THE BICONIC CONFIGURATIONS ( $M = 11$ )

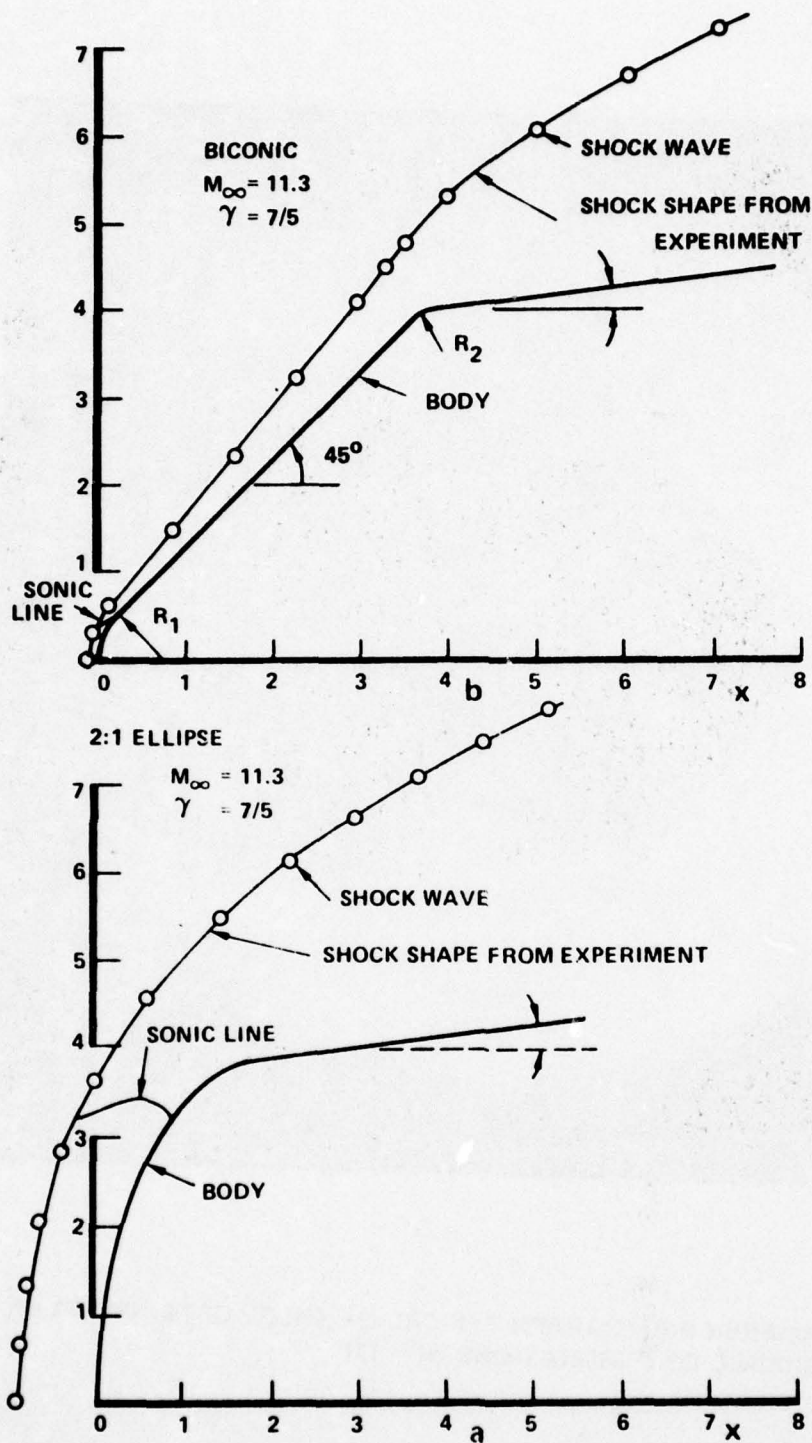


**Figure 4-7** COMPARISON BETWEEN THE SHOCK SHAPE DETERMINED BY THE GODUNOV CODE AND THE EXPERIMENTAL MEASUREMENTS



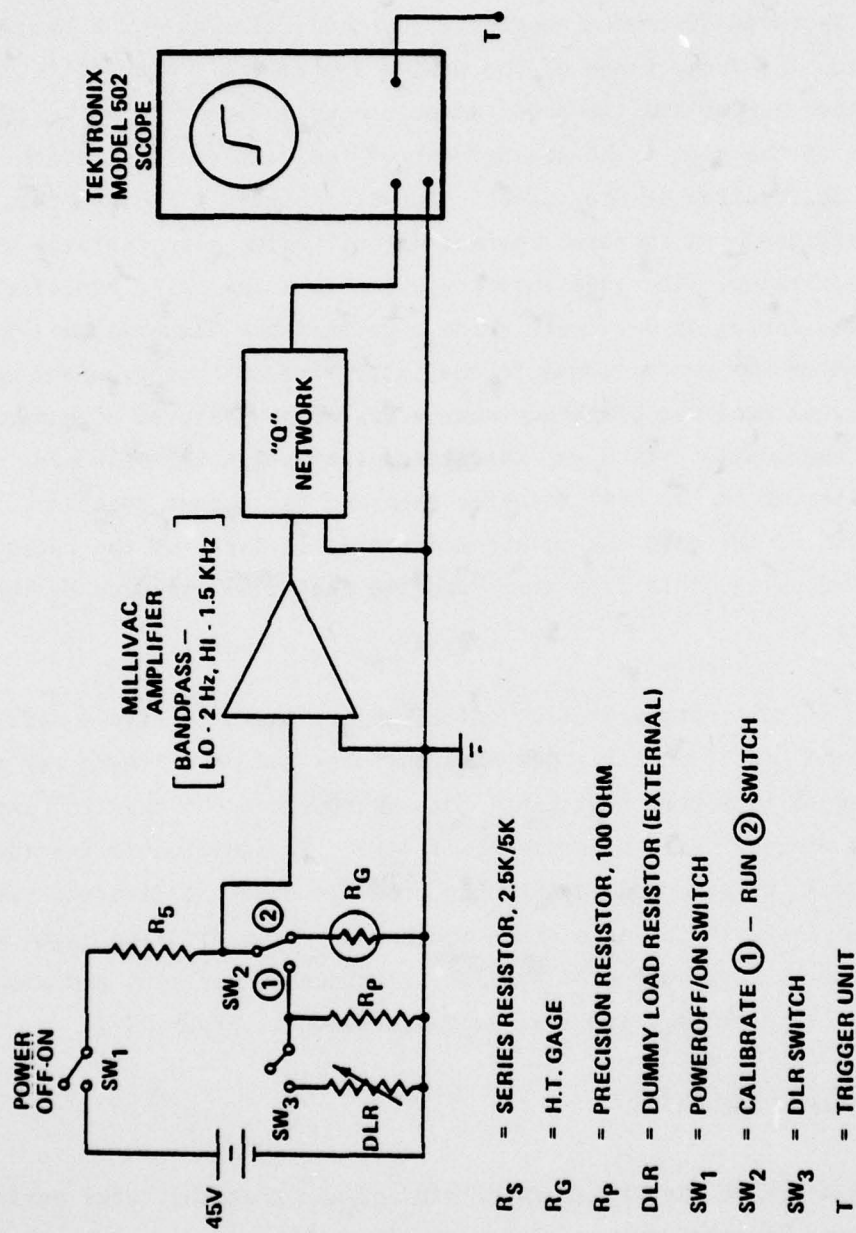


Figure 4-5 SCHEMATIC - CIRCUIT FOR CALIBRATION OF RADIANT HEAT TRANSFER CHARACTERISTICS OF THIN FILM GAGES

enclosing a GLOBAR (silicon carbide rod) in a firebrick enclosure. The heat flux from this source was turned and focused through two mirrors before it was interposed by a sectored-disc beam chopper. The thin film gage or a thermopile was placed on the focal plane of the mirror system. A  $1.8\text{ }\mu\text{m}$  filter was placed between the chopper and the gage/thermopile arrangement to maximize the absorptivity of the gage. The arrangement of the electronic circuits involved in the calibration of the gages is shown in Figure 4-5. The thin film gage ( $R_G$ ) is energized by a constant current circuit which also contains a heat transfer calibrator. The gage output was fed to a low noise amplifier and conditioned by the analog or Q-network which converted the temperature - time trace into one which was proportional to the instantaneous heat transfer rate. The output heat flux from the blackbody source was first measured directly with the Eppley thermopile, which was calibrated against an NBS standard. The beam was then directed to the heat transfer gage and the output recorded. The calibration factor of the gage was obtained directly in terms of the ratio of heat flux measured by the thin film gages and the heat flux measured by the Eppley thermopile.

Details of the instrumentation positions are shown in Figure 4-2. The majority of the heat transfer gages were concentrated on a single ray as shown in this figure; however, additional gages were placed on the  $120^\circ$  and  $240^\circ$  meridians to monitor three-dimensional effects. In addition to the rough heat-transfer gages, we recorded the outputs from conventional flat thin film gages which were placed in the sand grain roughness. Skin friction gages were placed on the conical frustra behind the interchangeable nose tips and along side the principal ray of heat-transfer gages as shown in Figure 4-2.

#### 4.3 RESULTS AND DISCUSSION

A key feature of the experimental studies was that they were performed at Mach numbers and Reynolds numbers large enough so that a good simulation of the separate and combined effects of entropy swallowing boundary layer transition and surface roughness was obtained. At each Mach number studied, we adjusted the Reynolds number so that a transition occurred just downstream of

the nose tip —  $45^\circ$  cone junction on the smooth models. The studies were conducted at Mach 11 and 13. The model configurations and test condition at which they were made are given in Table 4-1. A tabulation of the heat transfer and pressure measurements is given in Tables 4-2 and 4-3. A Schlieren photograph of the flow over one of the biconic configurations is shown on Figure 4-6. It was found that, in the absence of an embedded shock system, computer solutions based on the Godunov formulation for the shock shapes shown in Figure 4-7 were in excellent agreement with the experimental measurements.

Figures 4-8a through 4-8c show the heat transfer measurements for the configuration with sharp nose tip for both rough and smooth surface. The heat transfer measurements indicate that a transition is complete within approximately three inches from the nose tip and the heat transfer rates beneath the laminar and turbulent segments of the boundary layer were found to agree with the simple theories of Van Driest<sup>23</sup>, and Eckert<sup>21</sup> and Van Driest<sup>22</sup>, respectively. Adding roughness drove the transition almost completely to the nose tip as indicated both by the magnitude and character of the heat transfer records. In general, the heat transfer rates measured by the rough gages were generally larger than the smooth gages, which were embedded in the roughness. This suggests that the detailed microstructure of the flow around the roughness elements, as well as the modifications to the mean velocity and enthalpy profiles induced by roughness, is an important factor under high Mach number, highly cooled wall conditions. However, both rough and smooth gages indicate that there was a measurable increase in heat transfer rate above the smooth model value. Reducing the Reynolds number (see Figure 4-8c) moved the transition downstream on the smooth body but produced little change in its position on the rough model. While roughness enhanced the heating levels, we observed little effect of unit Reynolds number on the roughness augmentation factor. The measurements at Mach 13 were again in good agreement with the laminar and turbulent theories. However, while a fully developed turbulent boundary layer was developed within one inch of the tip on the rough model, the boundary layer on the smooth conical frustum remained transitional.



Table 4-1

BICONIC I HEAT TRANSFER AND PRESSURE TEST

RUN NO.	1	2	3	4	5	6
Mt	3.193E 00	3.296E 00	3.695E 00	3.395E 00	3.256E 00	3.693E 00
P <sub>o</sub> psia	1.724E 04	1.787E 04	1.803E 04	1.816E 04	1.776E 04	1.850E 04
H <sub>o</sub> ft <sup>2</sup> /sec <sup>2</sup>	1.828E 07	1.718E 07	2.143E 07	1.724E 07	1.695E 07	2.116E 07
M <sub>∞</sub>	1.134E 01	1.133E 01	1.297E 01	1.119E 01	1.133E 01	1.298E 01
U <sub>∞</sub> ft/sec	5.601E 03	5.754E 03	6.453E 03	5.761E 03	5.715E 03	6.414E 03
T <sub>∞</sub> °R	1.015E 02	1.072E 02	1.000E 02	1.100E 02	1.058E 02	1.015E 02
P <sub>∞</sub> psia	2.107E-01	2.160E-01	7.749E-02	1.614E-01	2.158E-01	7.993E-02
Q <sub>∞</sub> psia	1.899E 01	1.940E 01	9.128E 00	1.415E 01	1.941E 01	9.437E 00
ρ <sub>∞</sub> slugs/ft <sup>3</sup>	1.743E-04	1.690E-04	6.314E-05	1.228E-04	1.712E-04	6.605E-05
μ <sub>∞</sub> slugs/ft-sec	8.536E-08	9.021E-08	8.665E-08	9.277E-08	8.900E-08	8.543E-08
Re/ft.	1.144E 07	1.078E 07	4.702E 06	7.624E 06	1.099E 07	4.959E 06
P <sub>o</sub> psia	3.512E 01	3.597E 01	1.696E 01	2.619E 01	3.594E 01	1.753E 01

RUN NO.	7	8	9	10	11	12
Mt	3.287E 00	3.289E 00	3.278E 00	3.689E 00	3.284E 00	3.296E 00
P <sub>o</sub> psia	1.316E 04	1.302E 04	1.754E 04	1.794E 04	1.345E 04	1.750E 04
H <sub>o</sub> ft <sup>2</sup> /sec <sup>2</sup>	1.793E 07	1.750E 07	1.734E 07	2.183E 07	1.765E 07	1.771E 07
M <sub>∞</sub>	1.119E 01	1.118E 01	1.132E 01	1.295E 01	1.120E 01	1.131E 01
U <sub>∞</sub> ft/sec	5.875E 03	5.804E 03	5.780E 03	6.515E 03	5.829E 03	5.841E 03
T <sub>∞</sub> °R	1.146E 02	1.121E 02	1.085E 02	1.052E 02	1.128E 02	1.109E 02
P <sub>∞</sub> psia	1.580E-01	1.588E-01	2.117E-01	7.671E-02	1.625E-01	2.094E-01
Q <sub>∞</sub> psia	1.387E 01	1.391E 01	1.900E 01	9.014E 00	1.428E 01	1.877E 01
ρ <sub>∞</sub> slugs/ft <sup>3</sup>	1.157E-04	1.189E-04	1.638E-04	6.117E-05	1.210E-04	1.585E-04
μ <sub>∞</sub> slugs/ft-sec	9.639E-08	9.426E-08	9.127E-08	8.853E-08	9.483E-08	9.328E-08
Re/ft.	7.052E 06	7.321E 06	1.037E 07	4.501E 06	7.437E 06	9.922E 06
P <sub>o</sub> psia	2.569E 01	2.576E 01	3.518E 01	1.675E 01	2.644E 01	3.477E 01

Table 4-1  
BICONIC I HEAT TRANSFER AND PRESSURE TEST (Cont.)

RUN NO.	13	14	15	16	17	18
Mi	3.705E 00	3.305E 00	3.291E 00	3.282E 00	3.691E 00	3.709E 00
P <sub>o</sub> psia	1.818E 04	1.341E 04	1.789E 04	1.758E 04	1.812E 04	1.853E 04
H <sub>o</sub> ft <sup>2</sup> /sec <sup>2</sup>	2.184E 07	1.829E 07	1.785E 07	1.764E 07	2.202E 07	2.188E 07
M <sub>∞</sub>	1.296E 01	1.119E 01	1.133E 01	1.132E 01	1.297E 01	1.297E 01
U <sub>∞</sub> ft/sec	6.517E 03	5.934E 03	5.865E 03	5.830E 03	6.543E 03	6.522E 03
T <sub>∞</sub> °R	1.051E 02	1.170E 02	1.114E 02	1.104E 02	1.058E 02	1.051E 02
P <sub>∞</sub> psia	7.753E-02	1.598E-01	2.119E-01	2.104E-01	7.649E-02	7.884E-02
Q <sub>∞</sub> psia	9.125E 00	1.402E 01	1.906E 01	1.887E 01	9.015E 00	9.293E 00
ρ <sub>∞</sub> slugs/ft <sup>3</sup>	6.188E-05	1.146E-04	1.596E-04	1.599E-04	6.065E-05	6.293E-05
μ <sub>∞</sub> slugs/ft-sec	8.845E-08	9.834E-08	9.370E-08	9.284E-08	8.903E-08	8.845E-08
Re/ft.	4.559E 06	6.918E 06	9.990E 06	1.004E 07	4.457E 06	4.640E 06
P <sub>o</sub> ' psia	1.696E 01	2.598E 01	3.531E 01	3.496E 01	1.676E 01	1.727E 01

RUN NO. ATTACK ANGLE	19	20	21	22
Mi	3.288E 00	3.266E 00	3.692E 00	3.302E 00
P <sub>o</sub> psia	1.363E 04	1.700E 04	1.877E 04	1.336E 04
H <sub>o</sub> ft <sup>2</sup> /sec <sup>2</sup>	1.807E 07	1.742E 07	2.194E 07	1.775E 07
M <sub>∞</sub>	1.121E 01	1.131E 01	1.300E 01	1.119E 01
U <sub>∞</sub> ft/sec	5.898E 03	5.794E 03	6.532E 03	5.846E 03
T <sub>∞</sub> °R	1.152E 02	1.091E 02	1.051E 02	1.135E 02
P <sub>∞</sub> psia	1.622E-01	2.034E-01	7.889E-02	1.615E-01
Q <sub>∞</sub> psia	1.427E 01	1.824E 01	9.336E 00	1.417E 01
ρ <sub>∞</sub> slugs/ft <sup>3</sup>	1.182E-04	1.565E-04	6.302E-05	1.194E-04
μ <sub>∞</sub> slugs/ft-sec	9.690E-08	9.179E-08	8.838E-08	9.545E-08
Re/ft.	7.193E 06	9.876E 06	4.658E 06	7.313E 06
P <sub>o</sub> ' psia	2.645E 01	3.377E 01	1.735E 01	2.625E 01

THIS PAGE IS BEST QUALITY PRACTICABLE  
FROM COPY FURNISHED TO DDC

Table 4-2  
BICONIC I HEAT TRANSFER COMPUTATIONS

RUN NO.	GAGE POS	HT RATE (BTU/ft <sup>2</sup> sec)	GAGE POS	HT RATE (BTU/ft <sup>2</sup> sec)	GAGE POS	HT RATE (BTU/ft <sup>2</sup> sec)	GAGE POS	HT RATE (BTU/ft <sup>2</sup> sec)
1	1	1.42E+02	1A	6.32E+01	H 4A	1.02E+02	H20	8.45E+00
	2	1.39E+02	2A	6.43E+01	H 5A	1.21E+02	H15A	8.87E+00
	3A	1.25E+02			H15	1.19E+02	H25	7.04E+00
	4	9.27E+01			H 6A	1.56E+02	H26	6.27E+00
	5	7.73E+01			H 7A	1.28E+02	H17	1.26E+02
	8	8.18E+01			H 8A	1.37E+02	H18	1.30E+02
	9	6.09E+01			H16	1.36E+02	H21	9.27E+00
	10	6.22E+01			H 9A	1.29E+02	H22	7.95E+00
	11	1.13E+02			H10A	1.33E+02	H23	8.13E+00
	12	1.09E+02			H11A	1.37E+02	H24	8.31E+00
	13	5.78E+01			H19	1.32E+02		
	14	7.84E+01			H12A	1.28E+02		
					H14A	1.53E+01		
2	1	1.48E+02	1A	8.42E+01	H 4A	1.18E+02	H20	9.77E+00
	2	1.50E+02	2A	9.23E+01	H 5A	1.31E+02	H15A	9.32E+00
	3A	1.39E+02			H15	1.27E+02	H25	7.18E+00
	4	1.09E+02			H 6A	1.54E+02	H26	6.62E+00
	5	8.61E+01			H 7A	1.35E+02	H17	1.37E+02
	7	1.06E+02			H 8A	1.46E+02	H18	1.45E+02
	8	9.13E+01			H16	1.42E+02	H21	9.09E+00
	9	7.63E+01			H10A	1.37E+02	H22	9.03E+00
	10	8.11E+01			H11A	1.49E+02	H23	9.61E+00
	11	1.19E+02			H19	1.39E+02	H24	8.88E+00
	12	1.18E+02			H12A	1.36E+02		
	13	7.95E+01			H14A	1.63E+01		
	14	9.60E+01						
3	1	1.48E+02	1A	6.22E+01	H 4A	5.55E+01	H20	6.82E+00
	2	1.42E+02	2A	5.65E+01	H 5A	5.57E+01	H15A	6.54E+00
	3A	1.26E+02			H15	7.22E+01	H25	5.18E+00
	4	9.72E+01			H 6A	6.56E+01	H26	5.28E+00
	5	7.69E+01			H 7A	6.86E+01	H17	7.16E+01
	7	8.92E+01			H 8A	6.54E+01	H18	7.71E+01
	8	8.24E+01			H16	6.89E+01	H21	7.51E+00
	9	6.59E+01			H 9A	7.57E+01	H22	7.61E+00
	10	4.63E+01			H10A	6.63E+01	H23	7.58E+00
	11	4.88E+01			H11A	7.43E+01	H24	7.47E+00
	12	5.31E+01			H19	7.29E+01		
	13	5.21E+01			H12A	7.67E+01		
	14	4.68E+01			H13A	7.53E+01		
					H14A	1.17E+01		
					H 4A	4.88E+01	H17	5.16E+01
					H 5A	4.63E+01	H18	6.29E+01
					H15	6.16E+01		
					H 6A	5.27E+01		
					H 7A	5.65E+01		
					H 8A	4.70E+01		
					H16	5.22E+01		
					H 9A	5.76E+01		
					H10A	4.59E+01		



THIS PAGE IS BEST QUALITY PRACTICABLE  
FROM COPY FURNISHED TO DDC

Table 4-2  
BICONIC I HEAT TRANSFER COMPUTATIONS (Cont.)

RUN NO.	GAGE POS	HT RATE (BTU/H <sup>2</sup> sec)	GAGE POS	HT RATE (BTU/H <sup>2</sup> sec)	GAGE POS	HT RATE (BTU/H <sup>2</sup> sec)	GAGE POS	HT RATE (BTU/H <sup>2</sup> sec)
3					H11A	4.94E+01		
					H19	4.82E+01		
					H12A	5.62E+01		
					H13A	5.21E+01		
					H 4A	7.06E+01	H17	9.36E+01
					H 5A	7.66E+01	H18	9.88E+01
					H15	8.69E+01		
					H 6A	8.26E+01		
					H 7A	8.51E+01		
					H 8A	8.82E+01		
					H16	8.79E+01		
					H 9A	9.98E+01		
					H10A	9.00E+01		
					H11A	1.00E+02		
					H19	1.02E+02		
					H12A	1.05E+02		
					H13A	1.01E+02		
4	1	1.34E+02	1A	5.78E+01	H 4A	6.68E+01	H20	8.20E+00
	2	1.32E+02	2A	7.20E+01	H 5A	7.72E+01	H15A	7.75E+00
	3A	1.10E+02			H15	9.81E+01	H25	5.49E+00
	4	8.73E+01			H 6A	1.12E+02	H26	5.36E+00
	5	7.11E+01			H 7A	1.08E+02	H17	1.05E+02
	7	9.38E+01			H16	1.11E+02	H21	7.46E+00
	8	7.69E+01			H 9A	1.10E+02	H22	7.33E+00
	9	6.05E+01			H10A	1.11E+02	H23	7.34E+00
	10	5.26E+01			H11A	1.20E+02	H24	7.75E+00
	11	6.48E+01			H19	1.12E+02		
	12	6.89E+01			H12A	1.08E+02		
	13	5.27E+01			H13A	1.06E+02		
	14	4.76E+01			H14A	1.34E+01		
5	1	2.02E+02	15	1.03E+02	H 4A	1.46E+02	H20	8.55E+00
	2	1.57E+02	16	1.22E+02	H 5A	1.53E+02	H15A	8.98E+00
	3	1.06E+02	17	1.40E+02	H15	1.34E+02	H25	6.87E+00
	4	1.08E+02	18	1.07E+02	H 6A	1.53E+02	H26	6.18E+00
	5	5.97E+01	19	1.05E+02	H 7A	1.39E+02	H17	1.19E+02
	6	6.24E+01	17A	1.39E+02	H 8A	1.58E+02	H18	1.39E+02
	7	6.19E+01	18A	1.10E+02	H16	1.41E+02	H21	8.39E+00
	8	7.83E+01	19A	9.67E+01	H 9A	1.33E+02	H22	8.10E+00
	9	5.92E+01			H10A	1.27E+02	H23	8.22E+00
	10	6.33E+01			H11A	1.36E+02	H24	8.32E+00
	11	6.51E+01			H19	1.24E+02		
	12	6.20E+01			H12A	1.23E+02		
	13	7.50E+01			H13A	1.32E+02		
	14	7.60E+01			H14A	1.52E+01		
6	1	1.99E+02	15	5.44E+01	H 4A	5.42E+01	H20	9.31E+00
	2	1.44E+02	16	5.64E+01	H 5A	4.49E+01	H15A	6.51E+00
	3	1.18E+02	17	1.44E+02	H15	6.22E+01	H25	4.72E+00

THIS PAGE IS BEST QUALITY PRACTICABLE  
FROM COPY FURNISHED TO DDC

Table 4-2  
BICONIC I HEAT TRANSFER COMPUTATIONS (Cont.)

RUN NO.	GAGE POS	HT RATE (BTU/ft <sup>2</sup> sec)	GAGE POS	HT RATE (BTU/ft <sup>2</sup> sec)	GAGE POS	HT RATE (BTU/ft <sup>2</sup> sec)	GAGE POS	HT RATE (BTU/ft <sup>2</sup> sec)
6	4	1.12E+02	18	1.05E+02	H 6A	7.77E+01	H26	4.92E+00
	5	9.39E+01	19	9.79E+01	H 7A	9.54E+01	H21	5.53E+00
	6	8.51E+01	20	7.36E+01	H 8A	1.07E+02	H22	4.75E+00
	7	8.12E+01	21	6.64E+01	H16	1.16E+02	H23	5.11E+00
	8	7.65E+01	17A	1.46E+02	H 9A	1.12E+02	H24	5.05E+00
	9	6.87E+01	18A	1.14E+02	H10A	1.18E+02		
	10	6.58E+01	19A	8.25E+01	H11A	1.28E+02		
	11	6.48E+01	20A	7.40E+01	H19	1.16E+02		
	12	6.40E+01	21A	6.48E+01	H12A	1.17E+02		
	13	6.01E+01			H13A	1.15E+02		
	14	5.76E+01			H14A	1.45E+01		
					H 6A	4.58E+01		
					H 7A	5.37E+01		
					H 8A	5.34E+01		
					H16	4.89E+01		
					H 9A	4.74E+01		
					H10A	4.58E+01		
					H11A	4.74E+01		
					H19	4.93E+01		
					H12A	4.98E+01		
					H13A	4.44E+01		
7	1	1.71E+02	15	4.76E+01	H 4A	6.97E+01	H20	8.28E+00
	2	1.25E+02	16	4.71E+01	H 5A	9.07E+01	H15A	7.80E+00
	3	1.05E+02	17	1.26E+02	H15	1.05E+02	H25	6.04E+00
	4	9.28E+01	18	9.44E+01	H 6A	1.26E+02	H26	5.59E+00
	5	8.55E+01	19	8.66E+01	H 7A	1.28E+02	H21	4.67E+00
	6	7.48E+01	20	6.94E+01	H 8A	1.43E+02	H22	1.01E+01
	7	6.86E+01	21	8.35E+01	H16	1.30E+02	H23	7.10E+00
	8	6.69E+01	17A	1.28E+02	H 9A	1.13E+02	H24	7.38E+00
	9	6.20E+01	18A	9.96E+01	H10A	1.16E+02		
	10	5.67E+01	19A	7.54E+01	H11A	1.20E+02		
	11	5.61E+01	20A	6.81E+01	H19	1.29E+02		
	12	5.19E+01	21A	6.67E+01	H12A	1.09E+02		
	13	5.31E+01			H13A	1.06E+02		
	14	5.34E+01			H14A	1.31E+01		
8	1	1.67E+02	15	4.65E+01	H 4A	6.50E+01	H20	7.64E+00
	2	1.23E+02	16	4.66E+01	H 5A	7.35E+01	H15A	7.64E+00
	3	1.01E+02	17	1.21E+02	H15	9.02E+01	H25	5.94E+00
	4	8.92E+01	18	8.79E+01	H 6A	1.26E+02	H26	5.48E+00
	5	8.05E+01	19	8.46E+01	H 7A	1.28E+02	H21	5.38E+00
	6	7.14E+01	20	6.69E+01	H16	1.27E+02	H22	4.04E+00
	7	6.59E+01	21	7.95E+01	H 9A	1.13E+02	H23	7.04E+00
	8	6.40E+01	17A	1.25E+02	H10A	1.17E+02	H24	7.15E+00
	9	5.74E+01	18A	9.76E+01	H11A	1.18E+02		
	10	5.47E+01	19A	7.20E+01	H19	1.10E+02		
	11	5.29E+01	20A	6.66E+01	H12A	1.10E+02		
	12	5.44E+01	21A	6.65E+01	H13A	1.06E+02		
	13	4.94E+01			H14A	1.37E+01		
	14	4.78E+01						

AD-A065 173

CALSPAN ADVANCED TECHNOLOGY CENTER BUFFALO NY

F/G 20/4

STUDIES OF THE EFFECTS OF TRANSITIONAL AND TURBULENT BOUNDARY L--ETC(U)

DEC 78 M S HOLDEN

F44620-76-C-0037

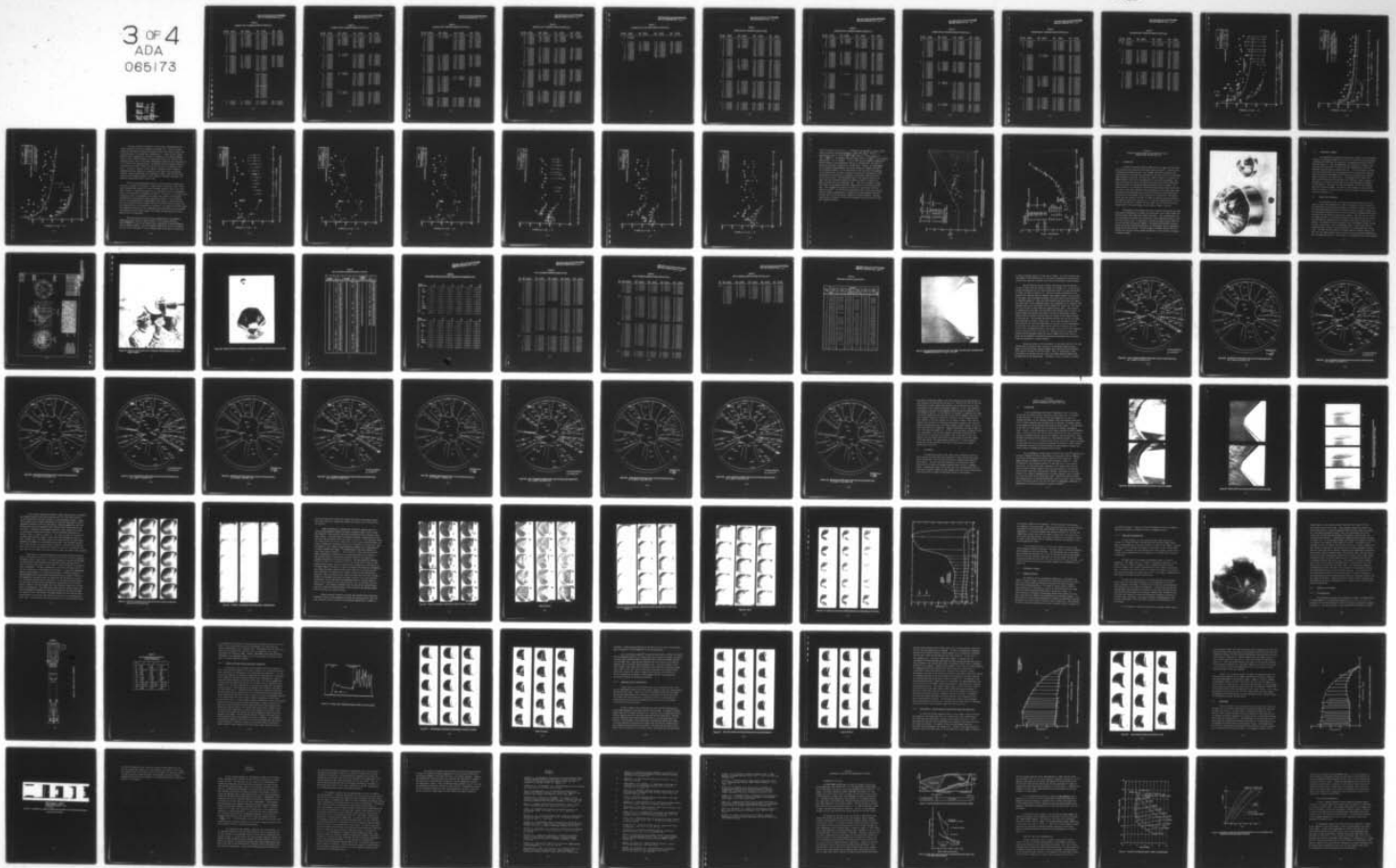
UNCLASSIFIED

CALSPAN-AB-5834-A-2

AFOSR-TR-79-0125

NL

3 OF 4  
ADA  
065173





THIS PAGE IS BEST QUALITY PRACTICABLE  
FROM COPY FURNISHED TO DDG

Table 4-2

BICONIC I HEAT TRANSFER COMPUTATIONS (Cont.)

RUN NO.	GAGE POS	HT RATE (BTU/ft <sup>2</sup> sec)	GAGE POS	HT RATE (BTU/ft <sup>2</sup> sec)	GAGE POS	HT RATE (BTU/ft <sup>2</sup> sec)	GAGE POS	HT RATE (BTU/ft <sup>2</sup> sec)
9	1	9.12E+01	15	8.34E+01	H 4A	1.06E+02	H20	1.12E+01
	2	9.27E+01	16	8.52E+01	H 5A	1.11E+02	H15A	1.20E+01
	3	8.31E+01	17	8.95E+01	H15	1.05E+02	H25	8.12E+00
	4	8.38E+01	18	8.24E+01	H 6A	1.13E+02	H26	6.68E+00
	5	8.14E+01	19	7.66E+01	H16	1.04E+02	H18	1.08E+02
	6	7.79E+01	15A	1.11E+02	H 9A	9.65E+01	H21	9.19E+00
	7	8.09E+01	16A	1.07E+02	H10A	1.03E+02	H22	8.27E+00
	8	7.83E+01	17A	8.89E+01	H11A	1.04E+02	H23	1.08E+01
	9	7.89E+01	18A	8.71E+01	H19	9.87E+01	H24	1.09E+01
	10	7.19E+01	19A	7.61E+01	H12A	9.69E+01		
	11	7.21E+01			H13A	1.00E+02		
	12	6.01E+01			H14A	2.06E+01		
	13	5.90E+01						
	14	5.81E+01						
10	1	9.26E+01	15	9.50E+01	H 4A	3.83E+01	H20	9.81E+00
	2	8.89E+01	16	9.06E+01	H 5A	3.62E+01	H15A	9.10E+00
	3	8.84E+01	17	8.68E+01	H15	4.98E+01	H25	6.98E+00
	4	8.75E+01	18	8.07E+01	H 6A	4.38E+01	H26	5.82E+00
	5	8.89E+01	19	6.96E+01	H16	4.69E+01	H17	2.67E+01
	6	8.11E+01	15A	9.77E+01	H 9A	4.67E+01	H18	3.07E+01
	7	7.59E+01	16A	8.67E+01	H10A	5.51E+01	H21	7.73E+00
	8	7.75E+01	17A	8.19E+01	H11A	5.26E+01	H23	9.77E+00
	9	7.37E+01	18A	7.43E+01	H19	5.27E+01	H24	8.45E+00
	10	6.59E+01	19A	6.48E+01	H12A	5.49E+01		
	11	6.41E+01			H13A	5.58E+01		
	12	5.86E+01			H14A	1.60E+01		
	13	5.41E+01						
	14	5.22E+01						
11	1	8.21E+01	15	8.08E+01	H 4A	6.63E+01	H20	9.71E+00
	2	7.04E+01	16	8.10E+01	H 5A	7.79E+01	H15A	8.65E+00
	3	7.73E+01	17	7.81E+01	H15	7.91E+01	H25	6.73E+00
					H16	4.52E+01		
					H 6A	3.44E+01		
					H16	4.12E+01		
					H 9A	3.45E+01		
					H10A	3.98E+01		
					H11A	4.06E+01		
					H19	3.91E+01		
					H12A	4.13E+01		
					H13A	4.44E+01		
					H15	6.57E+01		
					H 6A	6.73E+01		
					H16	8.07E+01		
					H 9A	7.79E+01		
					H10A	8.24E+01		
					H11A	8.31E+01		
					H19	7.53E+01		
					H12A	7.61E+01		
					H13A	8.11E+01		

THIS PAGE IS BEST QUALITY PRACTICABLE  
FROM COPY FURNISHED TO DDC

Table 4-2  
BICONIC I HEAT TRANSFER COMPUTATIONS (Cont.)

RUN NO.	GAGE POS	HT RATE (BTU/ft <sup>2</sup> sec)	GAGE POS	HT RATE (BTU/ft <sup>2</sup> sec)	GAGE POS	HT RATE (BTU/ft <sup>2</sup> sec)	GAGE POS	HT RATE (BTU/ft <sup>2</sup> sec)
11	4	7.14E+01	18	7.12E+01	H 6A	8.93E+01	H26	5.70E+00
	5	6.91E+01	19	6.26E+01	H16	8.15E+01	H18	6.27E+01
	6	7.07E+01	15A	8.55E+01	H 9A	7.26E+01	H21	6.94E+00
	7	6.46E+01	16A	8.88E+01	H10A	7.91E+01	H23	8.83E+00
	8	6.51E+01	17A	8.22E+01	H11A	8.09E+01	H24	9.21E+00
	9	6.09E+01	18A	6.74E+01	H19	7.67E+01		
	10	5.44E+01	19A	5.90E+01	H12A	7.62E+01		
	11	5.62E+01			H13A	7.84E+01		
	12	5.11E+01			H14A	1.66E+01		
	13	4.54E+01						
	14	4.34E+01						
12	1	1.48E+02	1A	1.58E+02	H 4A	1.78E+02	H20	1.18E+01
	2	1.67E+02	2A	1.56E+02	H 5A	1.67E+02	H15A	1.29E+01
	3A	2.15E+02			H 6A	1.76E+02	H25	1.29E+01
	4	1.77E+02			H 7A	1.81E+02	H26	1.19E+01
	5	1.64E+02			H 8A	1.89E+02	H17	1.45E+02
	8	1.49E+02			H 9A	1.86E+02	H18	1.38E+02
	9	1.46E+02			H10A	1.73E+02	H21	1.35E+01
	10	1.49E+02			H11A	1.87E+02	H23	1.36E+01
	11	1.49E+02			H19	1.45E+02	H24	1.41E+01
	12	1.42E+02			H12A	1.83E+02		
	13	1.46E+02			H13A	1.67E+02		
	14	1.34E+02						
13	1	1.14E+02	1A	1.48E+02	H 4A	1.67E+02	H20	5.57E+00
	2	1.13E+02	2A	1.50E+02	H 5A	1.53E+02	H15A	5.44E+00
	3A	1.36E+02			H 6A	1.45E+02	H25	3.79E+00
	4	1.27E+02			H 7A	1.59E+02	H26	4.42E+00
	5	1.38E+02			H 8A	1.58E+02	H17	1.26E+02
	8	1.24E+02			H 9A	1.45E+02	H18	1.20E+02
	9	1.32E+02			H10A	1.45E+02	H21	3.64E+00
	10	1.32E+02			H11A	1.53E+02	H23	3.87E+00
	11	1.26E+02			H19	1.22E+02	H24	4.48E+00
	12	1.20E+02			H12A	1.57E+02		
	13	1.30E+02						
	14	1.14E+02						
14	1	9.96E+01	1A	1.39E+02	H 4A	1.58E+02	H20	6.99E+00
	2	1.19E+02	2A	1.38E+02	H 5A	1.41E+02	H15A	7.69E+00
	3A	1.67E+02			H 6A	1.52E+02	H25	7.13E+00
	4	1.41E+02			H 7A	1.57E+02	H26	8.06E+00
	5	1.33E+02			H 8A	1.15E+02	H17	1.23E+02
	8	1.30E+02			H 9A	1.53E+02	H18	1.12E+02
	9	1.25E+02			H10A	1.51E+02	H21	6.25E+00
	10	1.23E+02			H11A	1.57E+02	H23	7.23E+00
	11	1.30E+02			H19	1.30E+02	H24	7.94E+00
	12	1.19E+02			H12A	1.56E+02		
	13	1.25E+02			H13A	1.36E+02		
	14	1.18E+02						

Table 4-2  
BICONIC I HEAT TRANSFER COMPUTATIONS (Cont.)

RUN NO.	GAGE POS	HT RATE (BTU/ft <sup>2</sup> sec)	GAGE POS	HT RATE (BTU/ft <sup>2</sup> sec)	GAGE POS	HT RATE (BTU/ft <sup>2</sup> sec)	GAGE POS	HT RATE (BTU/ft <sup>2</sup> sec)
15	1	1.54E+02	1A	1.76E+02	H 4A	1.84E+02	H20	1.17E+01
	2	1.83E+02	2A	1.63E+02	H 5A	1.68E+02	H15A	1.24E+01
	3A	2.32E+02			H 6A	1.91E+02	H25	1.24E+01
	4	1.82E+02			H 7A	2.02E+02	H26	1.31E+01
	5	1.64E+02			H 8A	1.85E+02	H17	1.57E+02
	8	1.47E+02			H 9A	1.92E+02	H18	1.47E+02
	9	1.49E+02			H10A	1.86E+02	H21	1.40E+01
	10	1.69E+02			H11A	2.03E+02	H23	1.31E+01
	11	1.48E+02			H19	1.57E+02	H24	1.54E+01
	12	1.39E+02			H12A	1.86E+02		
	13	1.49E+02			H13A	1.73E+02		
	14	1.39E+02						
16	1	3.36E+02	15	1.87E+02	H 4A	2.05E+02	H20	1.18E+01
	2	2.95E+02	16	1.81E+02	H 5A	1.82E+02	H15A	1.47E+01
	3	2.31E+02	17	2.73E+02	H 6A	1.87E+02	H25	1.27E+01
	4	2.09E+02	18	2.44E+02	H 7A	2.09E+02	H26	1.27E+01
	5	2.00E+02	19	2.71E+02	H 8A	1.85E+02	H17	1.45E+02
	6	2.05E+02	20	2.40E+02	H 9A	1.85E+02	H18	1.45E+02
	7	1.91E+02	21	2.27E+02	H10A	1.71E+02	H21	1.25E+01
	8	1.91E+02	17A	2.47E+02	H11A	1.85E+02	H23	1.14E+01
	9	1.87E+02	18A	2.42E+02	H19	1.48E+02	H24	1.43E+01
	10	1.86E+02	19A	1.71E+02	H12A	1.82E+02		
	11	1.80E+02	20A	2.38E+02	H13A	1.62E+02		
	12	1.75E+02	21A	2.04E+02				
	13	1.88E+02						
	14	1.65E+02						
17	1	1.46E+02	15	1.63E+02	H 4A	1.56E+02	H20	5.62E+00
	2	1.86E+02	16	1.48E+02	H 5A	1.46E+02	H15A	4.88E+00
	3	1.83E+02	17	1.94E+02	H19	1.23E+02	H25	3.77E+00
	4	1.71E+02	18	1.75E+02			H26	4.80E+00
	5	1.58E+02	19	2.48E+02			H18	1.19E+02
	6	1.56E+02	20	1.82E+02			H21	3.24E+00
	7	1.58E+02	21	1.91E+02			H23	3.64E+00
	8	1.75E+02	17A	1.81E+02			H24	4.32E+00
	9	1.57E+02	18A	2.32E+02				
	10	1.55E+02	19A	1.45E+02				
	11	1.47E+02	20A	1.86E+02				
	12	1.55E+02	21A	1.50E+02				
	13	1.53E+02						
	14	1.35E+02						
18	1	1.42E+02	15	1.63E+02	H 4A	1.59E+02	H20	6.51E+00
	2	1.99E+02	16	1.36E+02	H 5A	1.49E+02	H15A	4.81E+00
	3	1.96E+02	17	1.97E+02	H 6A	1.52E+02	H25	3.60E+00
	4	1.69E+02	18	1.96E+02	H 7A	1.61E+02	H26	5.01E+00
	5	1.67E+02	19	2.36E+02	H 8A	1.46E+02	H17	1.19E+02
	6	1.49E+02	20	2.10E+02	H 9A	1.42E+02	H18	1.26E+02
	7	1.57E+02	21	1.97E+02	H10A	1.45E+02	H21	3.25E+00



Table 4-2  
BICONIC I HEAT TRANSFER COMPUTATIONS (Cont.)

RUN NO.	GAGE POS	HT RATE (BTU/H <sup>2</sup> sec)	GAGE POS	HT RATE (BTU/H <sup>2</sup> sec)	GAGE POS	HT RATE (BTU/H <sup>2</sup> sec)	GAGE POS	HT RATE (BTU/H <sup>2</sup> sec)
18	8	1.82E+02	17A	1.64E+02	H11A	1.50E+02	H23	3.93E+00
	9	1.60E+02	18A	2.42E+02	H19	1.28E+02	H24	4.42E+00
	10	1.53E+02	19A	1.46E+02	H12A	1.53E+02		
	11	1.56E+02	20A	2.05E+02	H13A	1.35E+02		
	12	1.60E+02	21A	1.57E+02	H14A	1.15E+01		
	13	1.52E+02						
	14	1.36E+02						
19	1	2.18E+02	15	1.58E+02	H 4A	1.60E+02	H20	6.94E+00
	2	2.31E+02	16	1.50E+02	H 5A	1.51E+02	H15A	7.50E+00
	3	2.08E+02	17	1.97E+02	H 6A	1.67E+02	H25	7.10E+00
	4	1.80E+02	18	1.97E+02	H 7A	1.72E+02	H26	8.39E+00
	5	1.66E+02	19	2.43E+02	H 8A	1.55E+02	H17	1.15E+02
	6	1.46E+02	20	2.18E+02	H 9A	1.59E+02	H18	1.20E+02
	7	1.59E+02	21	2.17E+02	H10A	1.51E+02	H21	6.18E+00
	8	1.77E+02	17A	2.06E+02	H11A	1.51E+02	H23	7.00E+00
	9	1.62E+02	18A	2.27E+02	H19	1.27E+02	H24	8.65E+00
	10	1.55E+02	19A	1.45E+02	H12A	1.52E+02		
	11	1.51E+02	20A	1.97E+02	H13A	1.37E+02		
	12	1.59E+02	21A	1.62E+02	H14A	1.78E+01		
	13	1.61E+02						
	14	1.35E+02						
20	1	7.51E+01	15	1.07E+02	H 4A	1.27E+02	H20	1.51E+01
	2	7.12E+01	16	1.10E+02	H 5A	1.22E+02	H15A	1.61E+01
	3	7.34E+01	17	1.62E+02	H 6A	1.32E+02	H25	1.41E+01
	4	1.04E+02	18	1.59E+02	H 7A	1.44E+02	H26	1.26E+01
	5	1.20E+02	15A	8.74E+01	H 8A	1.34E+02	H17	1.21E+02
	6	1.16E+02	16A	1.18E+02	H 9A	1.36E+02	H18	1.16E+02
	7	1.35E+02	17A	1.75E+02	H10A	1.37E+02	H21	1.77E+01
	8	1.37E+02	18A	1.41E+02	H11A	1.48E+02	H23	1.58E+01
	9	1.30E+02	19A	1.26E+02	H19	1.24E+02	H24	1.78E+01
	10	1.31E+02			H12A	1.42E+02		
	11	1.30E+02			H13A	1.39E+02		
	12	1.18E+02			H14A	3.02E+01		
	13	1.11E+02						
	14	1.09E+02						
21	1	8.15E+01	15	8.50E+01	H 4A	1.14E+02	H20	6.05E+00
	2	7.80E+01	16	7.49E+01	H 5A	1.02E+02	H15A	6.27E+00
	3	6.33E+01	17	1.13E+02	H 6A	1.14E+02	H25	4.65E+00
	4	6.40E+01	18	1.36E+02	H 7A	1.16E+02	H26	5.39E+00
	5	6.92E+01	15A	7.33E+01	H 8A	1.06E+02	H17	1.05E+02
	6	8.61E+01	16A	8.33E+01	H 9A	1.05E+02	H18	9.90E+01
	7	1.16E+02	17A	1.22E+02	H10A	1.18E+02	H21	4.20E+00
	8	1.16E+02	18A	1.16E+02	H11A	1.18E+02	H23	4.49E+00
	9	1.04E+02	19A	1.01E+02	H19	1.02E+02	H24	6.23E+00
	10	1.12E+02			H12A	1.15E+02		
	11	1.09E+02			H13A	1.21E+02		
	12	1.01E+02			H14A	1.40E+01		

THIS PAGE IS BEST QUALITY PRACTICABLE  
FROM COPY FURNISHED TO DDG

Table 4-2  
BICONIC I HEAT TRANSFER COMPUTATIONS (Cont.)

RUN NO.	GAGE POS	HT RATE (BTU/h <sup>2</sup> sec)	GAGE POS	HT RATE (BTU/h <sup>2</sup> sec)	GAGE POS	HT RATE (BTU/h <sup>2</sup> sec)	GAGE POS	HT RATE (BTU/h <sup>2</sup> sec)
	13	9.73E+01						
	14	9.74E+01						
22	1	9.75E+01	16	9.55E+01	H 4A	1.18E+02	H20	9.54E+00
	2	7.20E+01	17	1.17E+02	H 5A	1.04E+02	H15A	9.91E+00
	3	6.14E+01	18	1.38E+02	H 6A	1.12E+02	H25	9.65E+00
	4	8.66E+01	16A	1.07E+02	H 7A	1.24E+02	H26	8.12E+00
	5	1.01E+02	17A	1.50E+02	H 8A	1.08E+02	H17	1.05E+02
	6	9.84E+01	18A	1.13E+02	H 9A	1.12E+02	H18	9.62E+01
	7	1.14E+02	19A	1.10E+02	H10A	1.14E+02	H21	9.40E+00
	8	1.17E+02			H11A	1.17E+02	H23	9.55E+00
	9	1.10E+02			H19	9.96E+01	H24	1.19E+01
	10	1.09E+02			H12A	1.15E+02		
	11	1.07E+02			H13A	1.14E+02		
	12	9.39E+01			H14A	2.01E+01		
	13	9.23E+01						
	14	9.54E+01						

THIS PAGE IS BEST QUALITY PRACTICABLE  
FROM COPY FURNISHED TO DDG

Table 4-3

BICONIC II HEAT TRANSFER COMPUTATIONS

RUN NO.	GAGE POS	HT RATE (BTU/ft <sup>2</sup> sec)	GAGE POS	HT RATE (BTU/ft <sup>2</sup> sec)	GAGE POS	HT RATE (BTU/ft <sup>2</sup> sec)	GAGE POS	HT RATE (BTU/ft <sup>2</sup> sec)
24	1	2.84E+01	15	3.79E+01	H 4A	4.31E+01	H20	7.20E+00
	3	2.93E+01	16	3.51E+01	H 5A	3.90E+01	H15A	8.66E+00
	4	3.44E+01	17	4.36E+01	H 6A	4.31E+01	H26	5.96E+00
	5	3.40E+01	18	4.21E+01	H 7A	4.20E+01	H17	3.46E+01
	6	3.97E+01	16A	3.66E+01	H 8A	3.79E+01	H18	3.49E+01
	7	4.26E+01	18A	3.52E+01	H16	2.81E+01	H21	7.66E+00
	8	4.21E+01	19A	3.64E+01	H 9A	4.15E+01	H22	7.57E+00
	9	3.94E+01			H10A	4.26E+01	H23	6.50E+00
	10	3.97E+01			H11A	4.24E+01	H24	7.28E+00
	11	3.81E+01			H19	3.53E+01	S25	4.42E+00
	12	3.76E+01			H12A	4.22E+01	S26	5.74E+00
	13	3.87E+01			H13A	4.14E+01	S30	4.07E+00
	14	3.70E+01			H14A	1.33E+01	S32	5.11E+00
25	1	6.80E+01	15	8.80E+01	H 4A	1.08E+02	H20	2.17E+01
	2	8.61E+01	16	1.03E+02	H 5A	9.80E+01	H15A	2.47E+01
	3	7.44E+01	17	1.05E+02	H 6A	1.03E+02	H25	1.81E+01
	4	8.76E+01	18	1.05E+02	H 7A	1.06E+02	H26	1.48E+01
	5	9.75E+01	16A	7.58E+01	H 8A	8.91E+01	H17	8.27E+01
	6	1.16E+02	17A	8.55E+01	H16	6.68E+01	H18	8.06E+01
	7	1.23E+02	18A	8.13E+01	H 9A	9.61E+01	H21	1.88E+01
	8	1.18E+02	19A	8.35E+01	H10A	9.70E+01	H22	2.03E+01
	9	1.07E+02			H11A	1.09E+02	H23	1.51E+01
	10	1.02E+02			H19	7.90E+01	H24	1.69E+01
	11	9.61E+01			H12A	9.77E+01	S25	1.10E+01
	12	8.78E+01			H13A	9.27E+01	S26	1.13E+01
	13	9.47E+01			H14A	3.62E+01	S30	1.16E+01
	14	9.08E+01					S32	1.21E+01
26	1	9.70E+01	15	5.72E+01	H 4A	6.51E+01	H20	5.88E+00
	2	7.76E+01	16	5.73E+01	H 5A	5.64E+01	H15A	7.34E+00
	3	7.16E+01	17	6.66E+01	H 6A	5.89E+01	H25	6.92E+00
	4	7.06E+01	18	8.19E+01	H 7A	5.90E+01	H26	6.52E+00
	5	5.65E+01	19	7.16E+01	H 8A	6.75E+01	H17	4.57E+01
	6	5.63E+01	20	7.04E+01	H16	3.90E+01	H18	4.49E+01
	7	5.35E+01	21	6.83E+01	H 9A	5.57E+01	H21	6.65E+00
	9	5.90E+01	17A	7.52E+01	H10A	5.39E+01	H22	5.94E+00
	10	5.66E+01	18A	8.74E+01	H11A	5.70E+01	H23	5.11E+00
	11	5.42E+01	19A	5.64E+01	H19	4.84E+01	H24	5.78E+00
	12	5.44E+01			H12A	5.59E+01	S25	4.85E+00
	13	5.79E+01			H13A	5.13E+01	S26	5.02E+00
	14	5.45E+01			H14A	1.32E+01	S30	4.52E+00
							S32	4.91E+00
27	1	1.55E+02	15	1.10E+02	H 4A	1.28E+02	H20	2.15E+01
	2	1.47E+02	16	1.15E+02	H 5A	1.24E+02	H15A	2.28E+01
	3	1.34E+02	17	1.16E+02	H 6A	1.34E+02	H25	1.85E+01
	4	1.39E+02	18	1.46E+02	H 7A	1.24E+02	H26	1.51E+01
	5	1.18E+02	19	1.40E+02	H 8A	1.12E+02	H17	9.96E+01
	6	1.20E+02	20	1.41E+02	H16	8.74E+01	H18	8.91E+01



Table 4-3

BICONIC II HEAT TRANSFER COMPUTATIONS (Cont.)

RUN NO.	GAGE POS	HT RATE (BTU/ft <sup>2</sup> sec)	GAGE POS	HT RATE (BTU/ft <sup>2</sup> sec)	GAGE POS	HT RATE (BTU/ft <sup>2</sup> sec)	GAGE POS	HT RATE (BTU/ft <sup>2</sup> sec)
7		1.14E+02	21	1.23E+02	H 9A	1.27E+02	H21	1.77E+01
9		1.20E+02	17A	1.31E+02	H10A	1.17E+02	H22	1.97E+01
10		1.19E+02	18A	1.32E+02	H11A	1.21E+02	H23	1.48E+01
11		1.16E+02	19A	1.10E+02	H19	9.87E+01	H24	1.70E+01
12		1.13E+02			H12A	1.14E+02	S25	1.13E+01
13		1.18E+02			H13A	1.02E+02	S26	1.21E+01
14		1.06E+02			H14A	3.66E+01	S30	1.51E+01
							S32	1.36E+01
28	1	4.32E+02	15	3.05E+02	H 4A	3.17E+02	H20	4.92E+01
	2	3.85E+02	16	2.75E+02	H 5A	2.83E+02	H15A	5.59E+01
	3	3.55E+02	17	3.54E+02	H 6A	2.92E+02	H25	4.64E+01
	4	3.77E+02	18	3.69E+02	H 7A	2.98E+02	H26	3.85E+01
	5	3.32E+02	19	3.62E+02	H 8A	3.29E+02	H17	2.43E+02
	7	2.67E+02	20	3.86E+02	H16	2.09E+02	H18	2.40E+02
	9	3.04E+02	21	3.80E+02	H 9A	2.96E+02	H21	4.54E+01
	10	3.17E+02	17A	4.01E+02	H10A	2.99E+02	H22	4.64E+01
	11	3.16E+02	18A	3.48E+02	H11A	2.88E+02	H23	3.52E+01
	12	2.73E+02	19A	2.76E+02	H19	2.42E+02	H24	4.16E+01
	13	3.07E+02			H12A	2.97E+02	S25	2.89E+01
	14	2.87E+02			H13A	2.62E+02	S26	2.94E+01
					H14A	8.33E+01	S30	2.89E+01
							S32	3.17E+01
29	1	3.41E+01	2A	4.54E+01	H 4A	5.25E+01	H20	5.78E+00
	2	5.50E+01			H 5A	4.96E+01	H25	7.83E+00
	3A	7.40E+01			H 6A	5.55E+01	H17	4.60E+01
	4	5.33E+01			H 7A	5.75E+01	H18	4.47E+01
	5	4.86E+01			H 8A	5.25E+01	H21	6.37E+00
	8	4.27E+01			H16	3.94E+01	H22	5.73E+00
	9	4.19E+01			H 9A	5.82E+01	H23	5.13E+00
	10	4.25E+01			H10A	5.75E+01	H24	6.09E+00
	11	3.99E+01			H11A	5.79E+01		
	12	3.84E+01			H19	4.68E+01		
	13	4.33E+01			H12A	5.83E+01		
	14	3.58E+01			H13A	4.71E+01		
					H14A	1.29E+01		
30	1	5.96E+01	2A	1.09E+02	H 4A	1.19E+02	H20	1.99E+01
	2	8.01E+01			H 5A	1.16E+02	H15A	2.55E+01
	3A	1.40E+02			H 6A	1.19E+02	H26	1.62E+01
	4	1.14E+02			H 7A	1.25E+02	H17	1.05E+02
	5	1.05E+02			H 8A	1.22E+02	H18	1.06E+02
	8	8.71E+01			H16	8.47E+01	H21	1.78E+01
	9	9.61E+01			H 9A	1.26E+02	H22	1.89E+01
	10	9.27E+01			H10A	1.26E+02	H23	1.50E+01
	11	9.01E+01			H19	1.04E+02	H24	1.64E+01
	12	8.34E+01			H12A	1.32E+02	S25	1.21E+01
	13	8.60E+01			H13A	1.09E+02	S26	1.21E+01
	14	8.00E+01			H14A	3.65E+01	S30	1.27E+01

THIS PAGE IS BEST QUALITY PRACTICABLE  
FROM COPY FURNISHED TO DDC

Table 4-3  
BICONIC II HEAT TRANSFER COMPUTATIONS (Cont.)

RUN NO.	GAGE POS	HT RATE (BTU/ft <sup>2</sup> sec)	GAGE POS	HT RATE (BTU/ft <sup>2</sup> sec)	GAGE POS	HT RATE (BTU/ft <sup>2</sup> sec)	GAGE POS	HT RATE (BTU/ft <sup>2</sup> sec)
31	1	3.11E+01	15	2.76E+01	H 4A	3.68E+01	H20	2.74E+00
	3	2.55E+01	16	2.86E+01	H 5A	3.45E+01	H15A	4.03E+00
	4	2.50E+01	17	2.66E+01	H 6A	3.20E+01	H25	3.04E+00
	5	2.44E+01	18	3.09E+01	H 7A	3.48E+01	H26	2.46E+00
	6	2.26E+01	19	2.82E+01	H16	3.07E+01	H17	2.98E+01
	7	2.27E+01	16A	3.63E+01	H 9A	3.05E+01	H18	3.14E+01
	8	2.22E+01	18A	2.82E+01	H10A	3.24E+01	H21	2.33E+00
	9	1.98E+01	19A	3.43E+01	H19	3.05E+01	H22	3.05E+00
	10	1.93E+01			H12A	2.56E+01	H23	3.10E+00
	11	1.87E+01			H13A	2.96E+01	H24	2.95E+00
	12	1.69E+01			H14A	5.70E+00	S25	5.20E+00
	13	1.72E+01					S26	5.18E+00
	14	1.64E+01					S30	5.01E+00
							S32	5.53E+00
32	1	6.13E+01	15	7.28E+01	H 4A	8.06E+01	H20	2.30E+01
	3	7.74E+01	16	1.01E+02	H 5A	8.96E+01	H15A	2.14E+01
	4	6.69E+01	17	1.08E+02	H 7A	8.61E+01	H26	1.66E+01
	5	9.89E+01	18	1.22E+02	H16	8.11E+01	H17	8.09E+01
	6	9.09E+01	19	1.03E+02	H 9A	8.65E+01	H21	2.49E+01
	7	9.97E+01	16A	9.70E+01	H10A	8.55E+01	H22	2.11E+01
	8	1.05E+02	19A	1.06E+02	H12A	7.61E+01	H23	2.31E+01
	9	9.86E+01			H14A	2.24E+01	H24	3.15E+01
	10	9.87E+01					S25	1.59E+01
	11	9.48E+01					S26	1.47E+01
	12	9.01E+01					S30	1.46E+01
	13	8.95E+01					S32	1.54E+01
	14	8.55E+01						
33	1	4.40E+01	1A	3.86E+01	H 4A	3.64E+01	H20	3.28E+00
	2	4.19E+01	2A	3.50E+01	H 5A	3.89E+01	H15A	3.48E+00
	4	2.68E+01			H 6A	4.54E+01	H25	2.36E+00
	5	2.49E+01			H 7A	4.52E+01	H26	5.55E+00
	7	3.39E+01			H 8A	3.80E+01	H17	4.03E+01
	8	3.66E+01			H16	4.17E+01	H18	3.98E+01
	9	2.74E+01			H 9A	4.47E+01	H21	3.02E+00
	10	3.79E+01			H10A	4.32E+01	H22	2.58E+00
	11	4.01E+01			H11A	4.10E+01	H23	2.27E+00
	12	4.59E+01			H19	4.22E+01	H24	2.33E+00
	14	3.70E+01			H12A	3.76E+01	S25	7.49E+00
					H13A	4.14E+01	S26	7.00E+00
					H14A	2.60E+01	S30	4.80E+00
							S32	6.01E+00
34	1	6.52E+01	1A	8.27E+01	H 4A	7.79E+01	H20	1.60E+01
	2	6.76E+01	2A	8.38E+01	H 5A	7.80E+01	H15A	1.56E+01
	4	4.64E+01			H 6A	8.63E+01	H25	1.44E+01
	5	5.96E+01			H 7A	8.60E+01	H26	1.52E+01
	7	7.48E+01			H 8A	7.96E+01	H17	9.12E+01
	8	8.19E+01			H16	8.96E+01	H18	8.80E+01

THIS PAGE IS BEST QUALITY PRACTICABLE  
FROM COPY FURNISHED TO DDG

Table 4-3  
BICONIC II HEAT TRANSFER COMPUTATIONS (Cont.)

RUN NO.	GAGE POS	HT RATE (BTU/ft <sup>2</sup> sec)	GAGE POS	HT RATE (BTU/ft <sup>2</sup> sec)	GAGE POS	HT RATE (BTU/ft <sup>2</sup> sec)	GAGE POS	HT RATE (BTU/ft <sup>2</sup> sec)
34	9	8.60E+01			H 9A	9.36E+01	H21	1.55E+01
	10	8.11E+01			H10A	9.58E+01	H22	1.50E+01
	11	8.11E+01			H11A	9.00E+01	H23	1.53E+01
	12	7.58E+01			H19	9.42E+01	H24	1.47E+01
	14	7.52E+01			H12A	8.29E+01	S25	1.52E+01
					H13A	9.08E+01	S26	1.44E+01
					H14A	1.60E+01	S30	1.51E+01
							S32	1.51E+01
35	1	3.51E+01	1A	3.40E+01	H 4A	3.55E+01	H20	2.76E+00
	2	3.69E+01	2A	3.51E+01	H 5A	3.70E+01	H15A	3.11E+00
	4	2.63E+01			H 6A	3.96E+01	H25	2.45E+00
	5	2.22E+01			H 7A	4.32E+01	H26	4.45E+00
	7	2.90E+01			H 8A	3.75E+01	H17	4.21E+01
	8	3.26E+01			H16	4.13E+01	H18	4.14E+01
	9	3.56E+01			H 9A	4.35E+01	H21	2.58E+00
	10	3.47E+01			H10A	4.37E+01	H22	2.55E+00
	11	3.70E+01			H19	4.09E+01	H23	2.56E+00
	12	3.68E+01			H12A	3.79E+01	H24	2.47E+00
	13	3.34E+01			H13A	4.17E+01	S25	6.66E+00
	14	3.42E+01			H14A	5.20E+00	S26	6.39E+00
							S30	6.50E+00
							S32	5.78E+00
36	1	5.00E+01	15	4.99E+01	H 4A	4.59E+01	H20	2.61E+00
	2	3.73E+01	19	4.84E+01	H 5A	4.25E+01	H15A	2.84E+00
	3	3.05E+01	20	4.69E+01	H 6A	4.23E+01	H25	2.11E+00
	4	2.65E+01	21	4.83E+01	H 7A	4.54E+01	H26	4.55E+00
	5	2.47E+01	17A	3.20E+01	H 8A	3.89E+01	H17	3.87E+01
	7	1.97E+01	18A	3.88E+01	H16	4.11E+01	H18	4.14E+01
	8	2.10E+01	19A	5.06E+01	H 9A	4.21E+01	H21	2.37E+00
	9	2.64E+01	20A	4.61E+01	H10A	3.96E+01	H22	2.26E+00
	10	3.05E+01			H11A	3.77E+01	H23	2.38E+00
	11	3.44E+01			H19	4.04E+01	H24	2.41E+00
	12	4.10E+01			H12A	3.59E+01	S25	1.53E+01
	13	4.69E+01			H13A	3.76E+01	S26	1.23E+01
	14	5.09E+01			H14A	4.98E+00	S30	1.31E+01
							S32	1.20E+01
37	1	4.93E+01	15	4.94E+01	H 4A	4.53E+01	H20	2.53E+00
	2	3.55E+01	18	3.25E+01	H 5A	4.13E+01	H15A	3.12E+00
	3	2.98E+01	19	5.39E+01	H 6A	4.33E+01	H25	2.09E+00
	4	2.63E+01	20	5.29E+01	H 7A	4.90E+01	H26	3.44E+00
	5	2.33E+01	21	4.82E+01	H 8A	3.95E+01	H17	4.04E+01
	7	2.06E+01	17A	3.34E+01	H16	4.24E+01	H18	4.03E+01
	8	2.18E+01	18A	4.32E+01	H 9A	4.37E+01	H21	2.31E+00
	9	2.67E+01	19A	5.66E+01	H10A	4.72E+01	H22	2.42E+00
	10	3.09E+01	20A	4.88E+01	H11A	4.26E+01	H23	2.33E+00
	11	3.34E+01			H19	4.03E+01	H24	2.27E+00



Table 4-3  
BICONIC II HEAT TRANSFER COMPUTATIONS (Cont.)

RUN NO.	GAGE POS	HT RATE (BTU/ft <sup>2</sup> sec)	GAGE POS	HT RATE (BTU/ft <sup>2</sup> sec)	GAGE POS	HT RATE (BTU/ft <sup>2</sup> sec)	GAGE POS	HT RATE (BTU/ft <sup>2</sup> sec)
37	12	4.13E+01			H12A	3.64E+01	S25	8.17E+00
	13	4.59E+01			H13A	3.85E+01	S26	7.64E+00
	14	4.95E+01			H14A	5.61E+00	S30	6.83E+00
							S32	8.13E+00
39	1	2.60E+02	15	2.52E+02	H 4A	2.72E+02	H20	2.18E+01
	2	1.93E+02	18	2.88E+02	H 5A	2.39E+02	H15A	3.35E+01
	3	1.86E+02	19	2.69E+02	H 6A	2.45E+02	H25	4.03E+01
	4	2.17E+02	20	2.51E+02	H 7A	2.74E+02	H26	3.85E+01
	7	2.64E+02	21	2.51E+02	H 8A	2.60E+02	H17	2.14E+02
	9	2.87E+02	17A	2.06E+02	H16	2.34E+02	H18	2.14E+02
	10	2.76E+02	18A	3.05E+02	H 9A	2.50E+02	H21	2.04E+01
	11	2.47E+02	19A	2.69E+02	H10A	2.65E+02	H22	1.94E+01
	12	2.52E+02	20A	2.70E+02	H11A	2.68E+02	H23	1.92E+01
	13	2.57E+02	21A	3.66E+02	H19	2.33E+02	H24	1.83E+01
	14	2.49E+02			H12A	2.13E+02	S25	3.93E+01
					H13A	2.47E+02	S26	3.72E+01
					H14A	3.71E+01	S30	3.42E+01
							S32	3.79E+01
40	1	1.08E+02	15	8.77E+01	H 4A	9.78E+01	H20	1.42E+01
	2	1.16E+02	18	1.06E+02	H 5A	8.57E+01	H15A	1.43E+01
	3	1.10E+02	19	9.48E+01	H 6A	9.40E+01	H25	1.33E+01
	4	1.05E+02	20	8.86E+01	H 7A	9.91E+01	H26	1.34E+01
	5	9.62E+01	21	9.04E+01	H 8A	8.82E+01	H17	7.70E+01
	7	9.27E+01	17A	1.17E+02	H16	8.74E+01	H18	7.60E+01
	8	9.28E+01	18A	1.01E+02	H 9A	8.71E+01	H21	1.27E+01
	9	9.24E+01	19A	9.54E+01	H10A	9.38E+01	H22	1.31E+01
	10	9.75E+01	20A	9.14E+01	H11A	7.74E+01	H23	1.16E+01
	11	8.39E+01	21A	1.18E+02	H19	8.55E+01	H24	1.28E+01
	12	8.82E+01			H12A	8.03E+01	S25	1.39E+01
	13	9.33E+01			H13A	9.49E+01	S26	1.28E+01
	14	8.98E+01			H14A	1.27E+01	S30	1.24E+01
							S32	1.37E+01

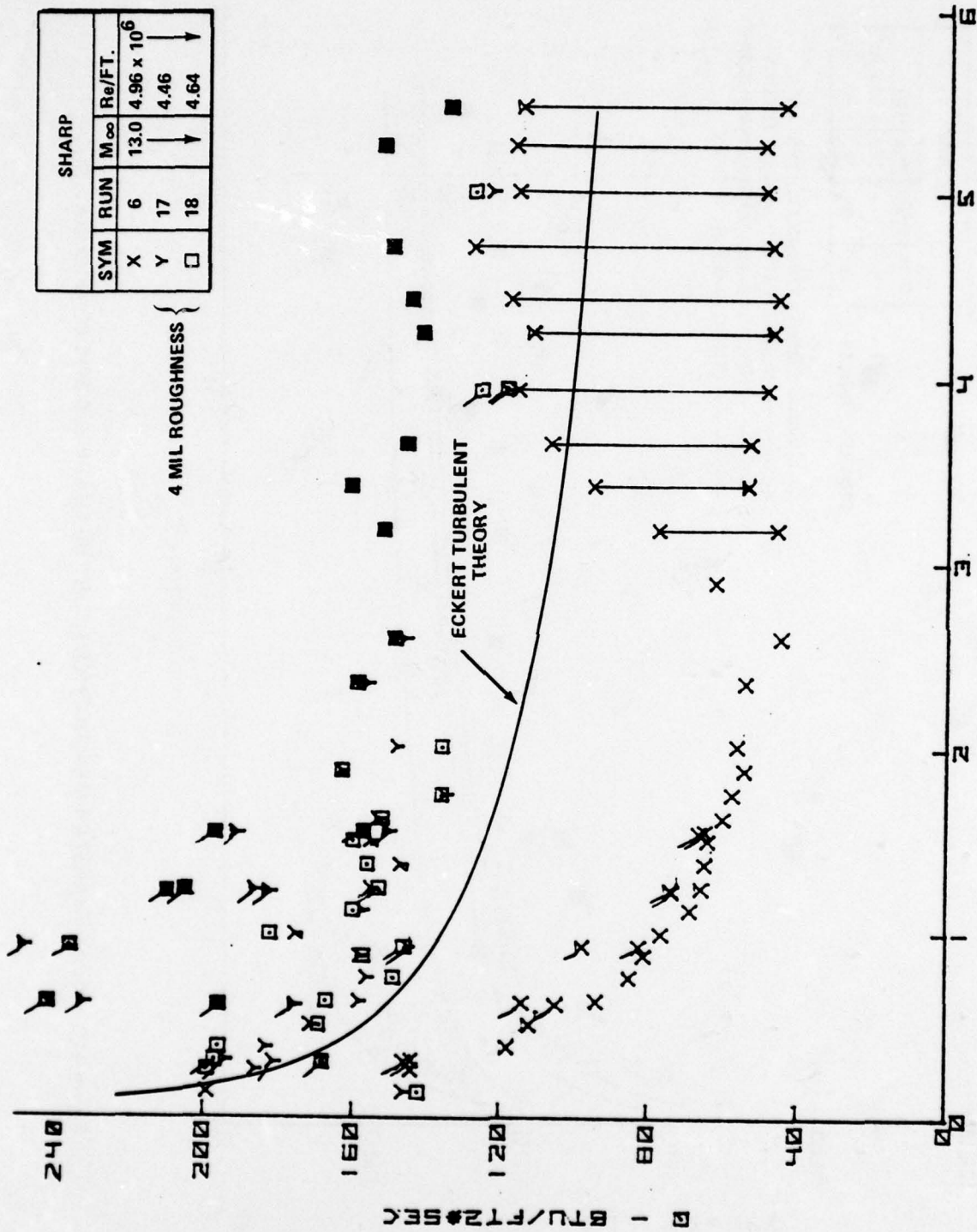


Figure 4-8a HEAT TRANSFER MEASUREMENTS ON THE SHARP BI-CONIC CONFIGURATION

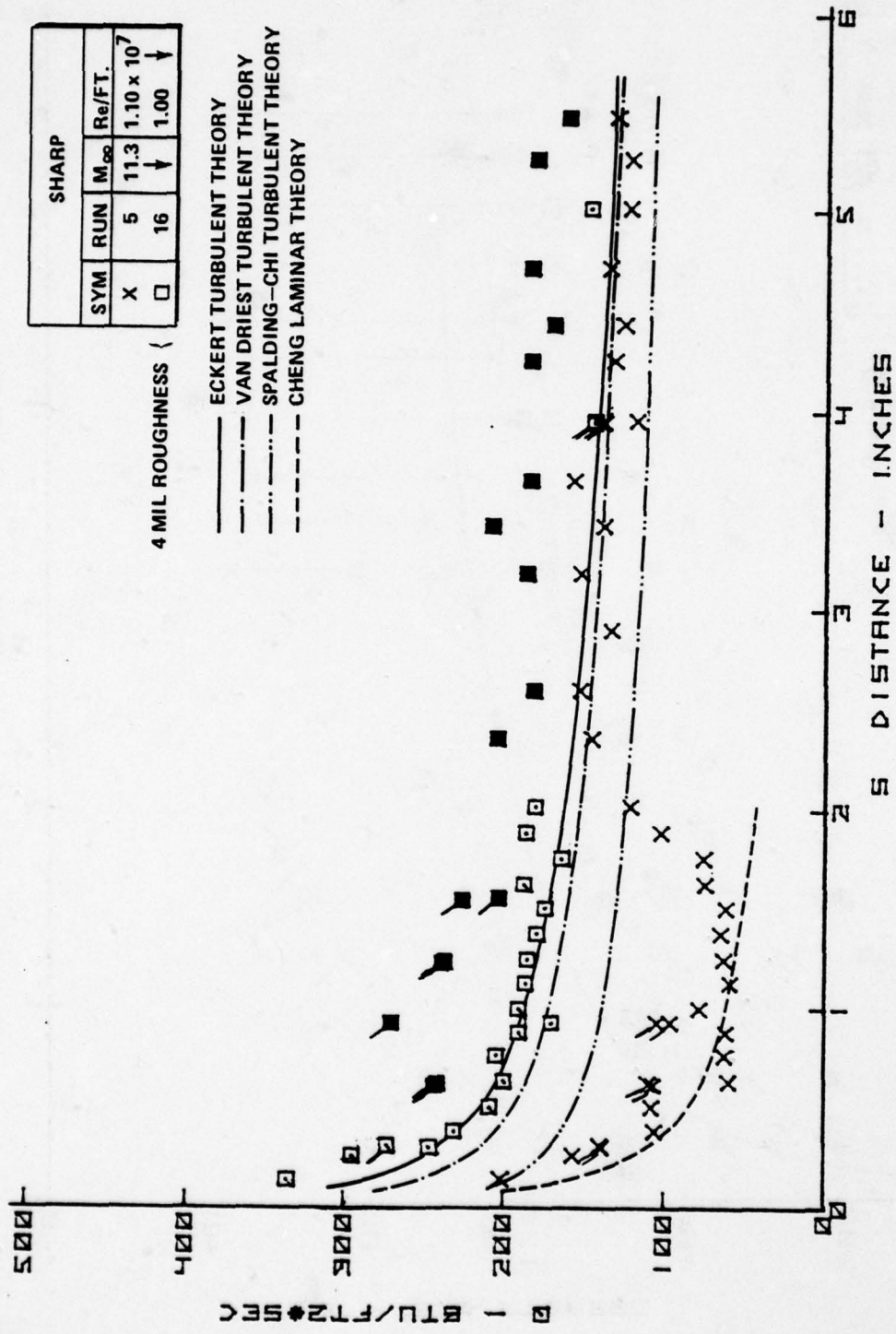


Figure 4-8b HEAT TRANSFER MEASUREMENTS ON THE SHARP BI-CONIC CONFIGURATION



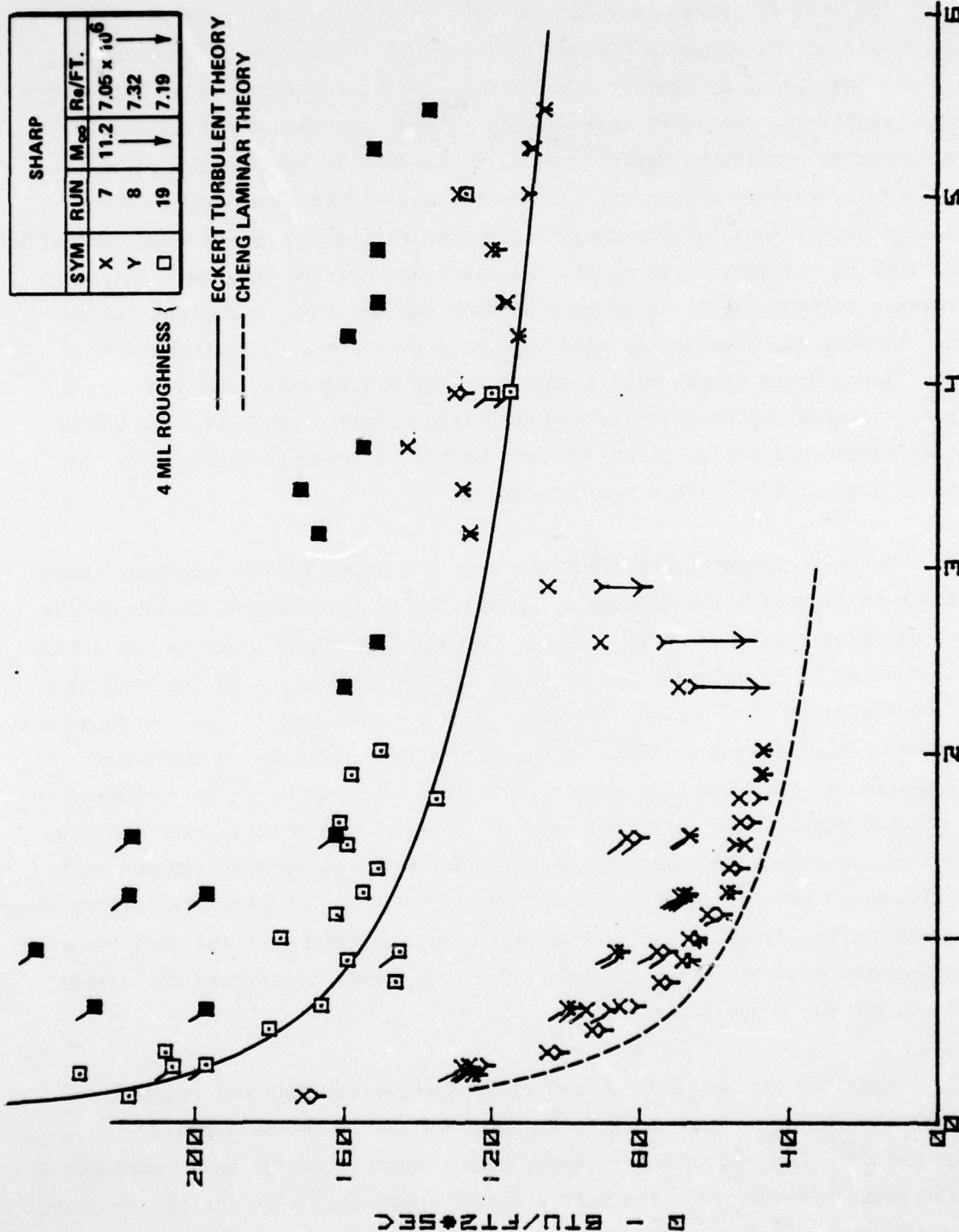


Figure 4-8c HEAT TRANSFER MEASUREMENTS ON THE SHARP BI-CONIC CONFIGURATION

The heat transfer distributions to the biconic configurations with medium bluntness are shown in Figures 4-9a through 4-9c. Here the boundary growth was influenced by entropy swallowing, and the local values of  $Re_\theta$  were reduced relative to the sharp nosed configuration. At both the free stream Reynolds number conditions for the Mach 11.3 studies on the smooth configurations, a fully turbulent boundary was established within four inches of the stagnation point, while on the rough configuration transition was completed within 0.5 inch of the stagnation point. We observed that the roughness induced an increase in the heat transfer rate of over 30% for fully turbulent conditions. At Mach 13, however, we were unable to generate a fully turbulent boundary layer under smooth wall conditions (see Figure 4-9a) and although roughness tripped the boundary layer generating a fully turbulent flow within one inch of the stagnation point, we were unable to determine accurately the roughness augmentation factor for this case.

The heat transfer distributions over the blunt biconic configurations are shown in Figures 4-10a through c. Again, while a transition occurs on the smooth configuration at Mach 13, a fully turbulent boundary layer is not developed. However, a turbulent boundary layer is developed close to the stagnation point on the rough blunt configuration at Mach 13. At Mach 11, it was found that a transition occurs just downstream of the sphere cone junction on the smooth configuration at both Reynolds number conditions; however, a fully turbulent flow was not established until approximately three lengths of laminar run from the tip as opposed to the two lengths observed on the sharp nose tip and as was also assumed in many of the theoretical approaches. We observed the largest roughness augmentation factors on this configuration and found that the heat transfer rates measured with the smooth gages in the rough model approached the levels measured with the rough gages.

Both the present and earlier studies suggested that the roughness augmentation factor is not a simple function of the roughness Reynolds number  $\left(\frac{\rho_e u \tau k}{\mu_w}\right)$  or  $\frac{K}{\delta^*}$  but may depend upon a combination of these parameters and the roughness spacing. The heat transfer augmentation factor was compared with the Powars correlation<sup>24</sup> and measurements given in the paper by Grabor and

MEDIUM			
SYM	RUN	$M_{\infty}$	$Re/FT.$
X	3	13.0	$4.70 \times 10^6$
□	13	13.0	$4.56 \times 10^6$

4 MIL ROUGHNESS {

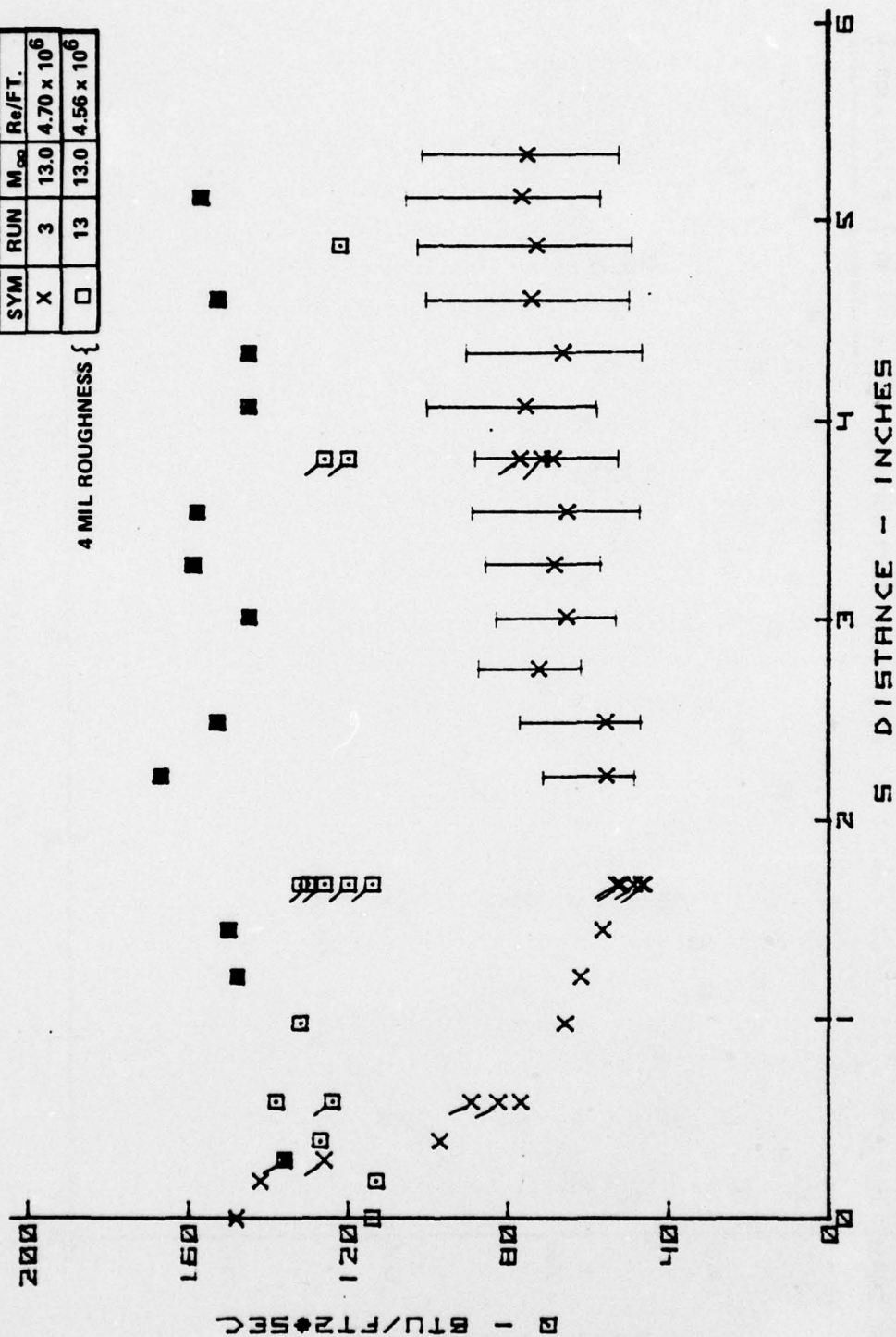


Figure 4-9a HEAT TRANSFER MEASUREMENTS ON THE MEDIUM BI-CONIC CONFIGURATION



MEDIUM			
SYM	RUN	$M_{\infty}$	$Re/FT.$
X	1	11.3	$1.14 \times 10^7$
□	12	↓	$9.92 \times 10^6$

4 MIL ROUGHNESS {

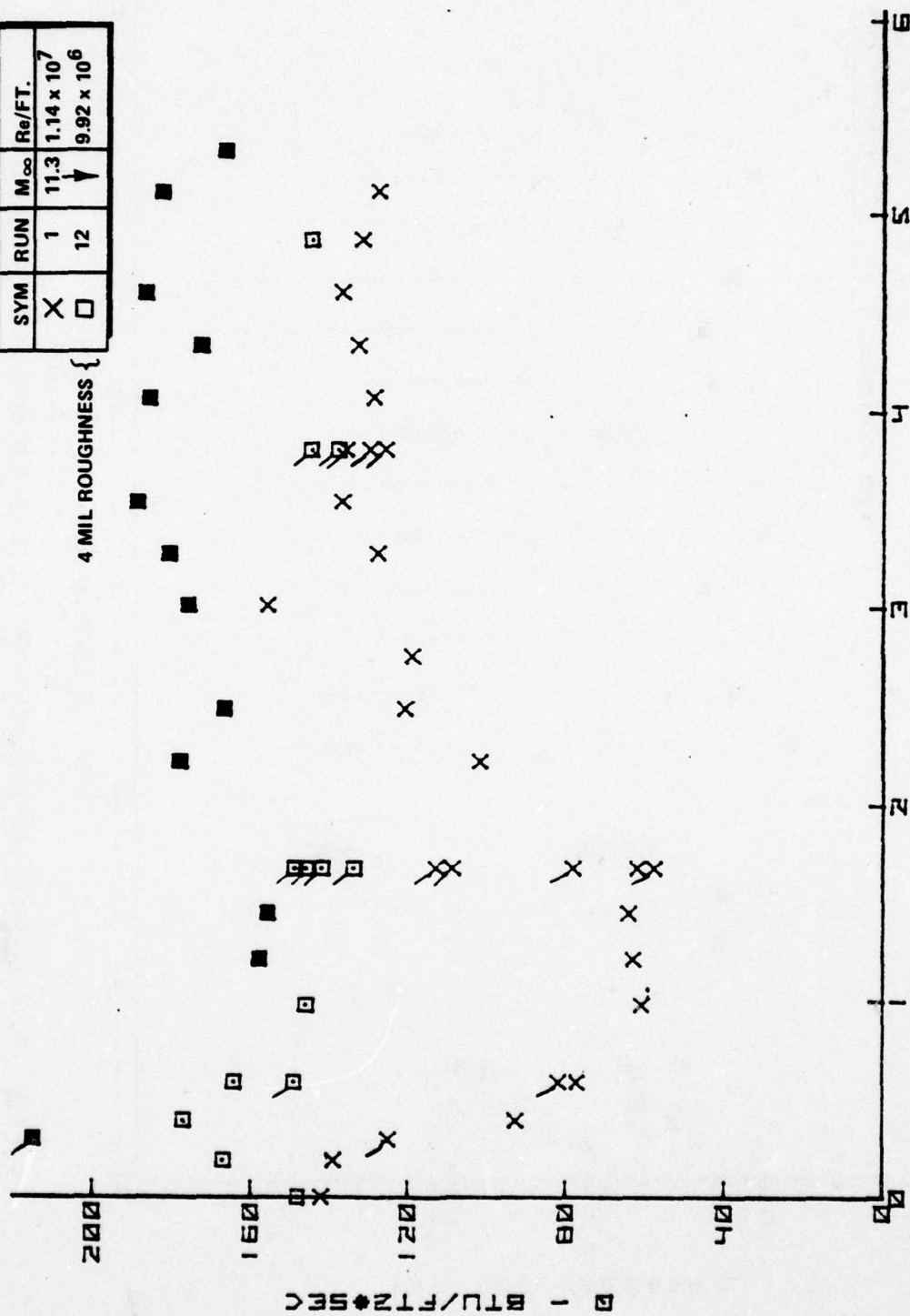


Figure 4-9b HEAT TRANSFER MEASUREMENTS ON THE MEDIUM BI-CONIC CONFIGURATION

MEDIUM			
SYM	RUN	$M_{\infty}$	$Re/ft.$
X	4	11.2	$7.62 \times 10^6$
□	14	↑	6.92 ↑

4 MIL ROUGHNESS (

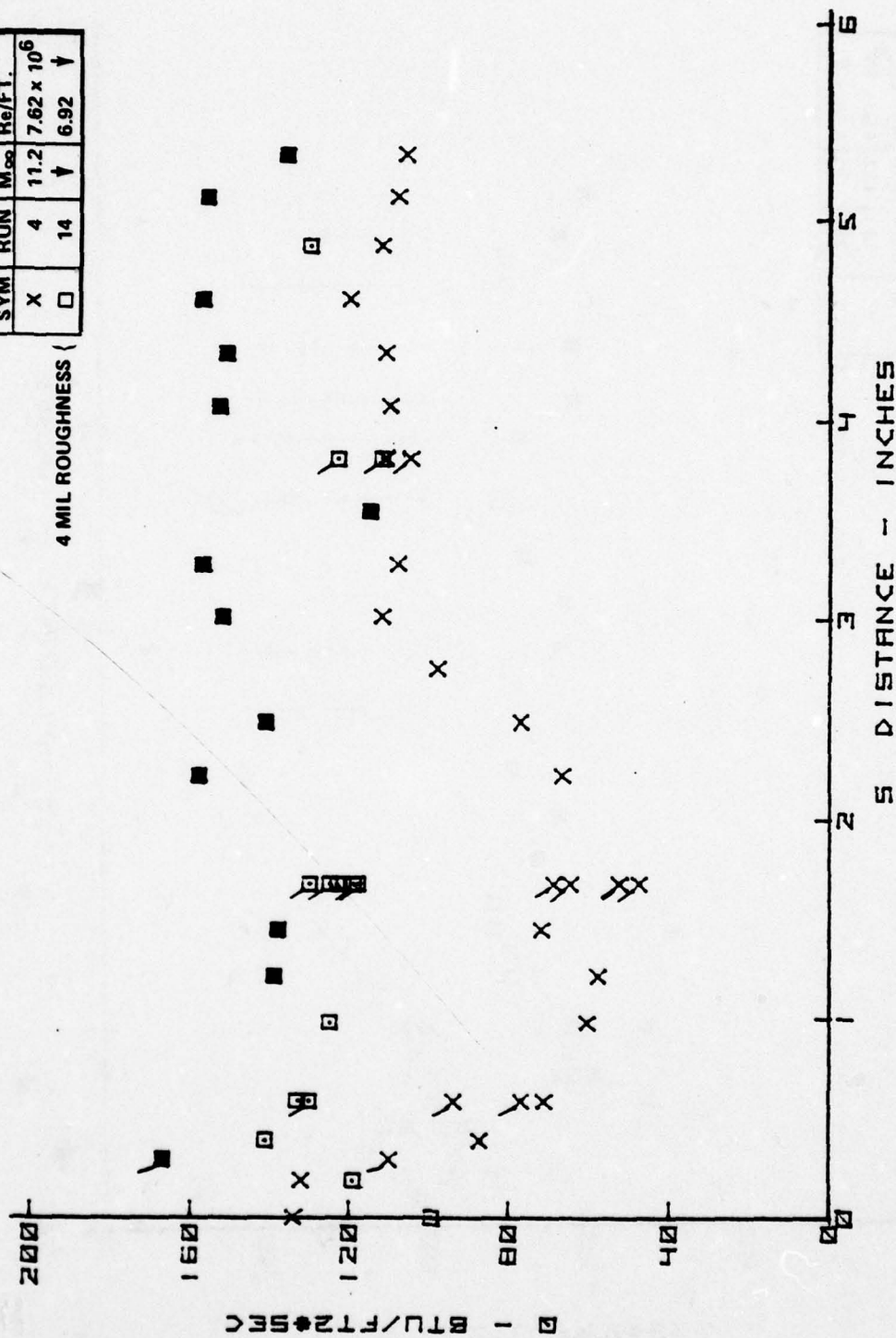


Figure 4-9c: HEAT TRANSFER MEASUREMENTS ON THE MEDIUM BI-CONIC CONFIGURATION

BLUNT			
SYM	RUN	$M_\infty$	Re/FT.
X	10	13.0	$4.50 \times 10^6$
□	21	↓	4.66

4 MIL ROUGHNESS {

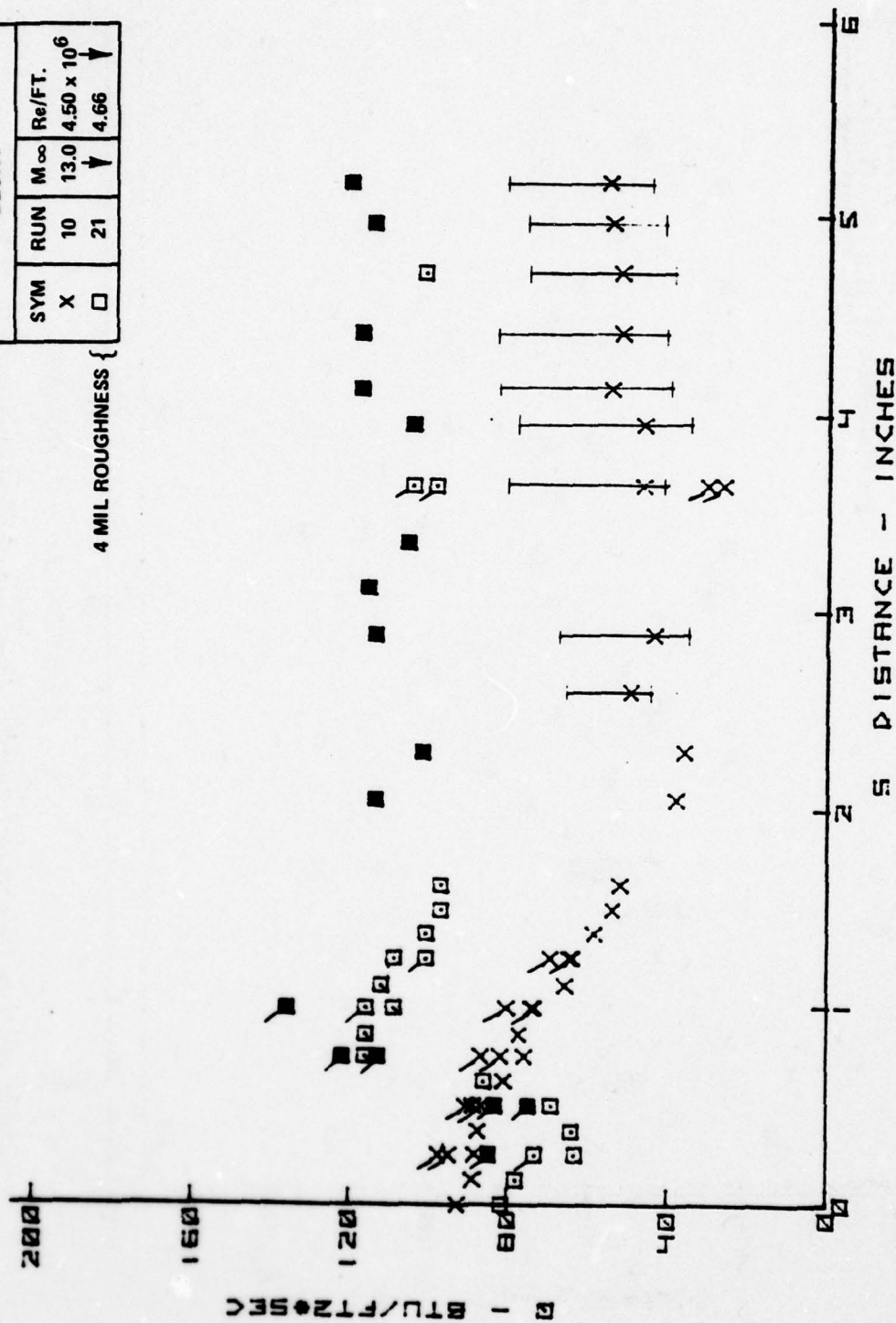


Figure 4-10a HEAT TRANSFER MEASUREMENTS ON THE BLUNT BI-CONIC CONFIGURATION



BLUNT			
SYM	RUN	$M_{\infty}$	$Re/FT.$
X	9	11.3	$1.04 \times 10^7$
□	20	✓	$9.88 \times 10^6$

4 MIL ROUGHNESS {

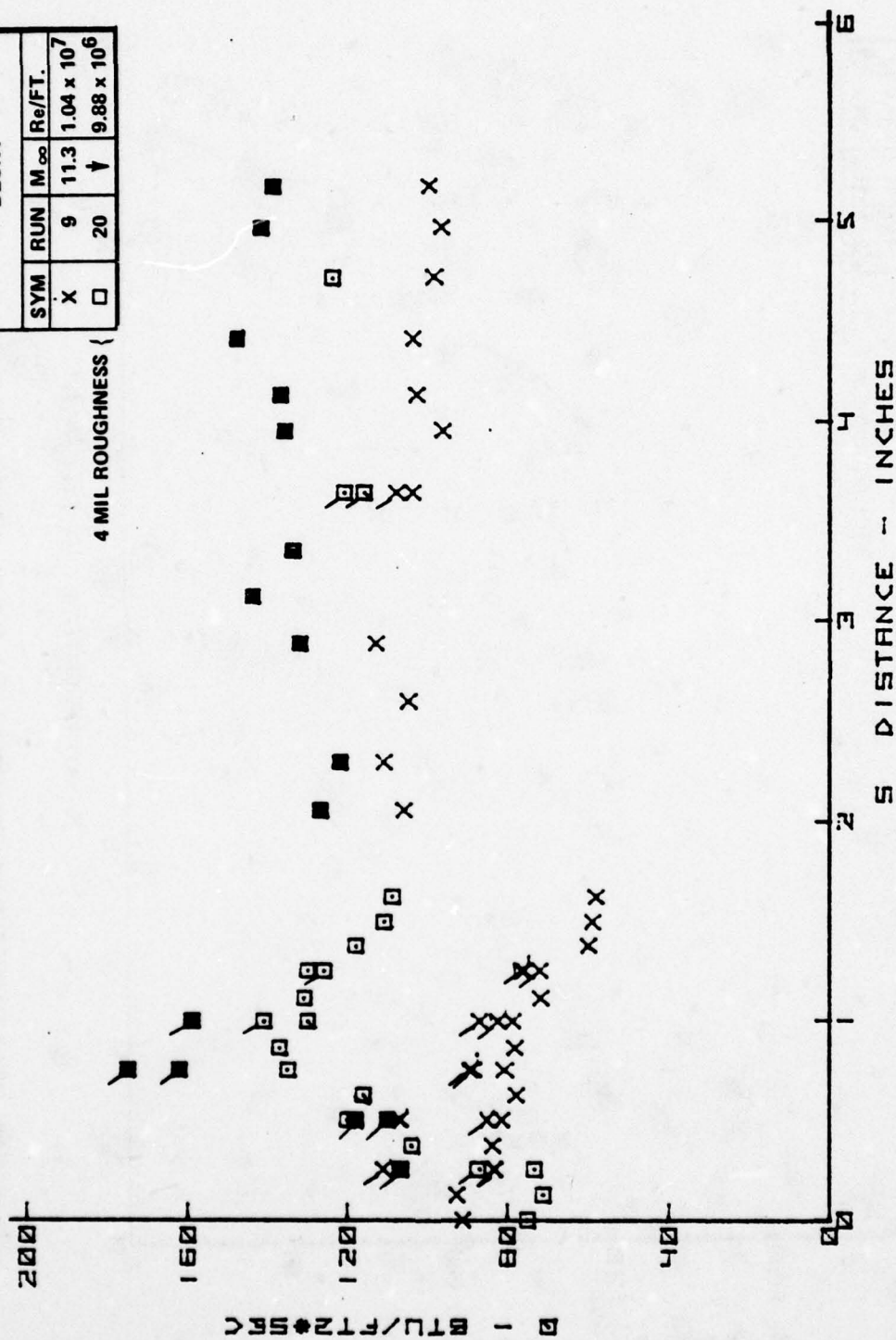


Figure 4-10b HEAT TRANSFER MEASUREMENTS ON THE BLUNT BI-CONIC CONFIGURATION

BLUNT			
SYM	RUN	$M_\infty$	$Re/FT.$
X	11	11.2	$7.44 \times 10^6$
□	22	11.3	$7.31 \times 10^6$

4 MIL ROUGHNESS (

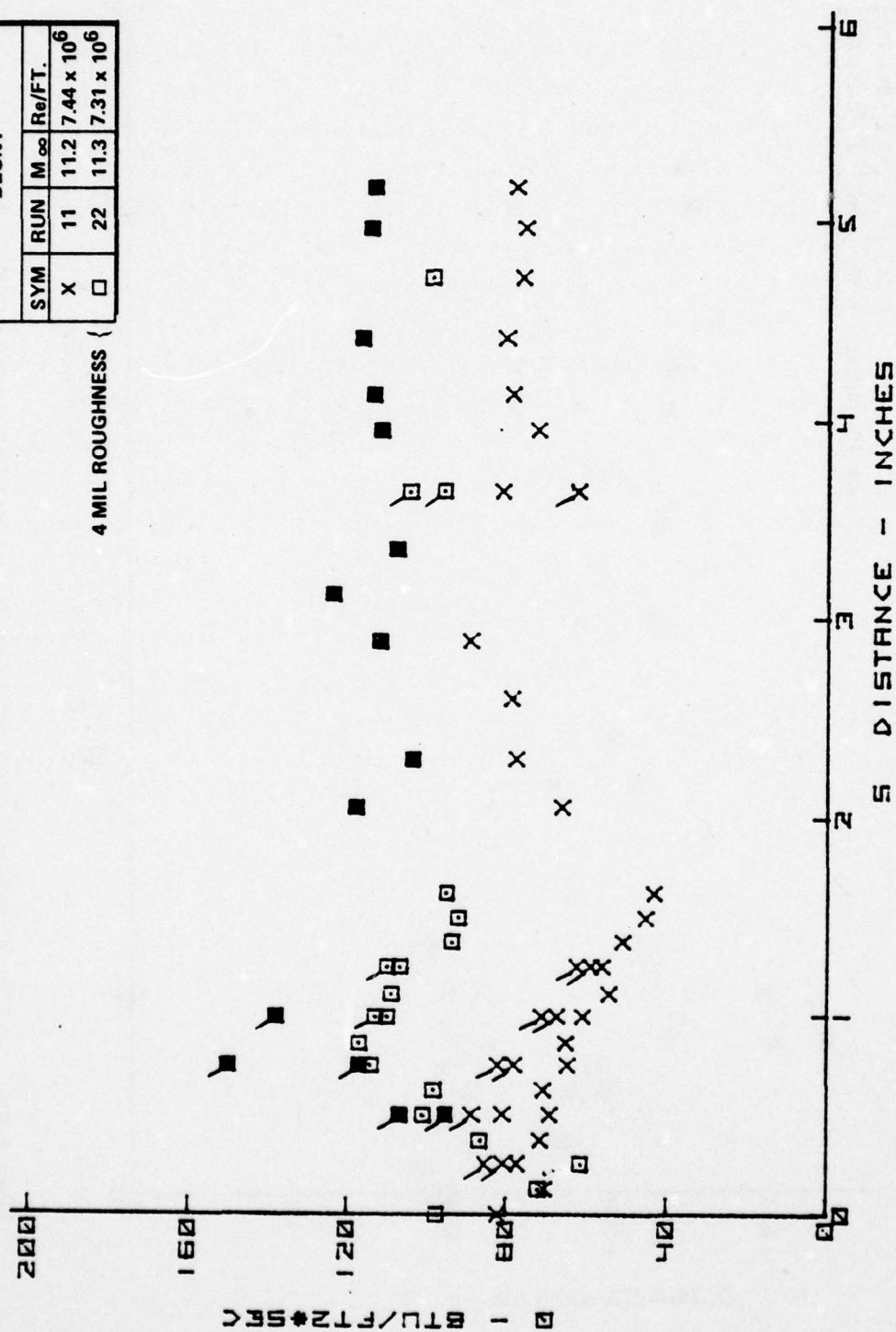


Figure 4-10c HEAT TRANSFER MEASUREMENTS ON THE BLUNT BI-CONIC CONFIGURATION

White<sup>25</sup> in Figures 4-11 and 4-12. In Figure 4-11 we plotted  $C_{H \text{ rough}}/C_{H \text{ smooth}}$  versus the Powars correlation parameter  $(\frac{u_e R}{\nu_e}) \sqrt{C_{H_0}} (\frac{T_e}{T_w})^{1.3}$  which is approximately equal to  $Re(C_H)^{1/2} (\frac{\rho_w}{\rho_e})^{0.5} (\frac{\mu_e}{\mu})$  which is in turn is equal to  $\tilde{Re}_k (= \frac{\rho_w u_\tau}{\mu}) k$ , the roughness Reynolds number where  $u_\tau = (\frac{\tau_w}{\rho_w})^{1/2}$ , and a Reynolds analog factor of 1 is assumed. It can be seen that the roughness augmentation factor obtained in our experimental studies was significantly less than predicted by the Powars correlation of the PANT data. However, our measurements are in relatively good agreement with those obtained by Brandon and Masek<sup>26</sup> for corrugated surfaces. It is interesting to note that while the augmentation heating factor is slightly larger for the bluntest configuration, these measurements do not appear to be strongly influenced by entropy gradients on the inviscid flow. The measurements made in the present study are compared with the correlation presented by Grabor and White in Figure 4-12. Grabor and White choose the parameter  $\frac{k}{\delta^*}$ , the ratio of effective roughness height to displacement thickness, against which to correlate the PANT data. This parameter was chosen on the basis of a theoretical study performed by Dvorak<sup>27</sup>. We see that the measurements made in this and a previous study of biconic configurations at Calspan are in good agreement with both the PANT data and the correlation suggested by Grabor and White. Clearly, further study is required to select the parameters which characterize roughness augmented heating.



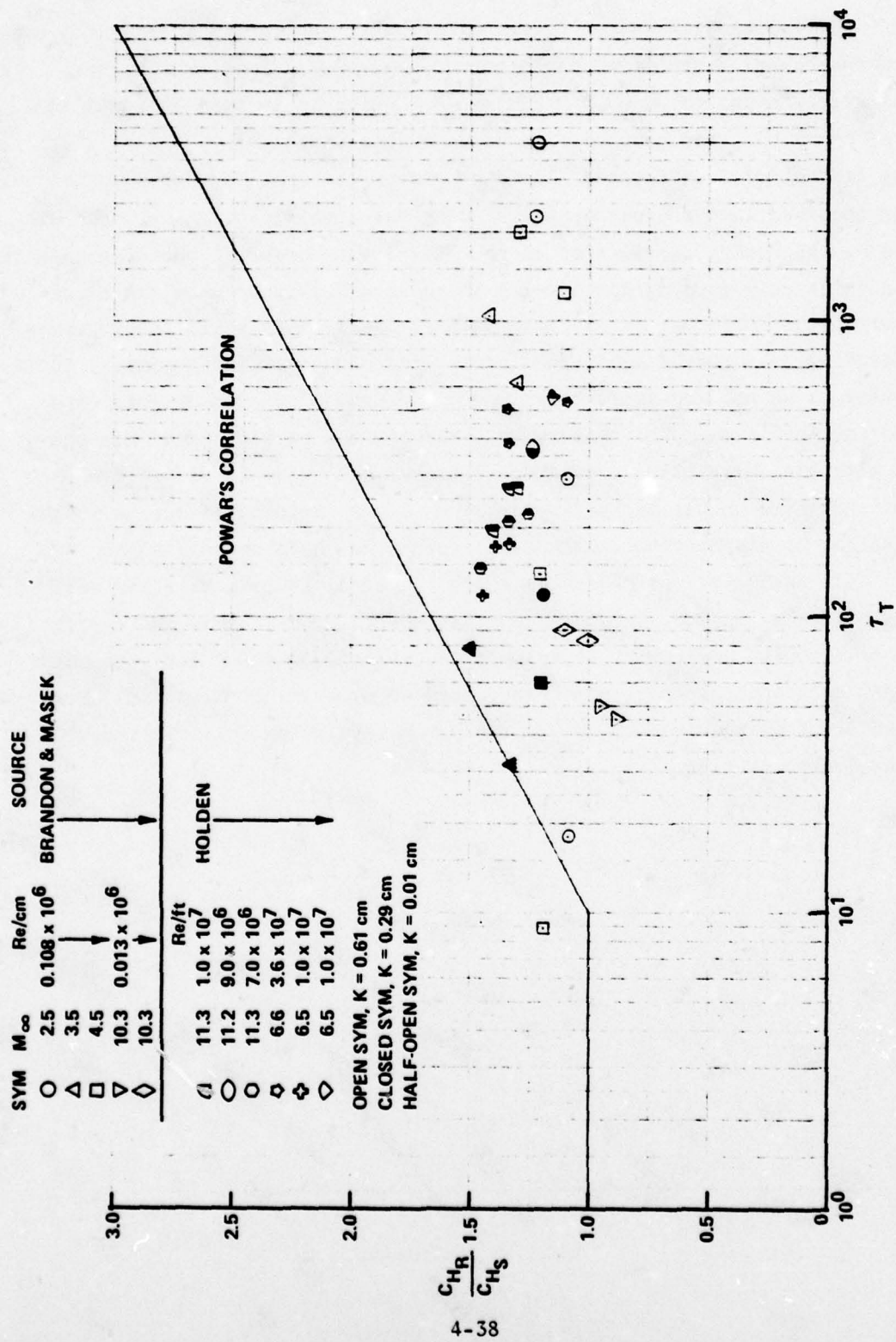


Figure 4-11 COMPARISON BETWEEN POWER'S CORRELATION AND RECENT MEASUREMENTS  
 BY HOLDEN AND BRANDON & MASEK

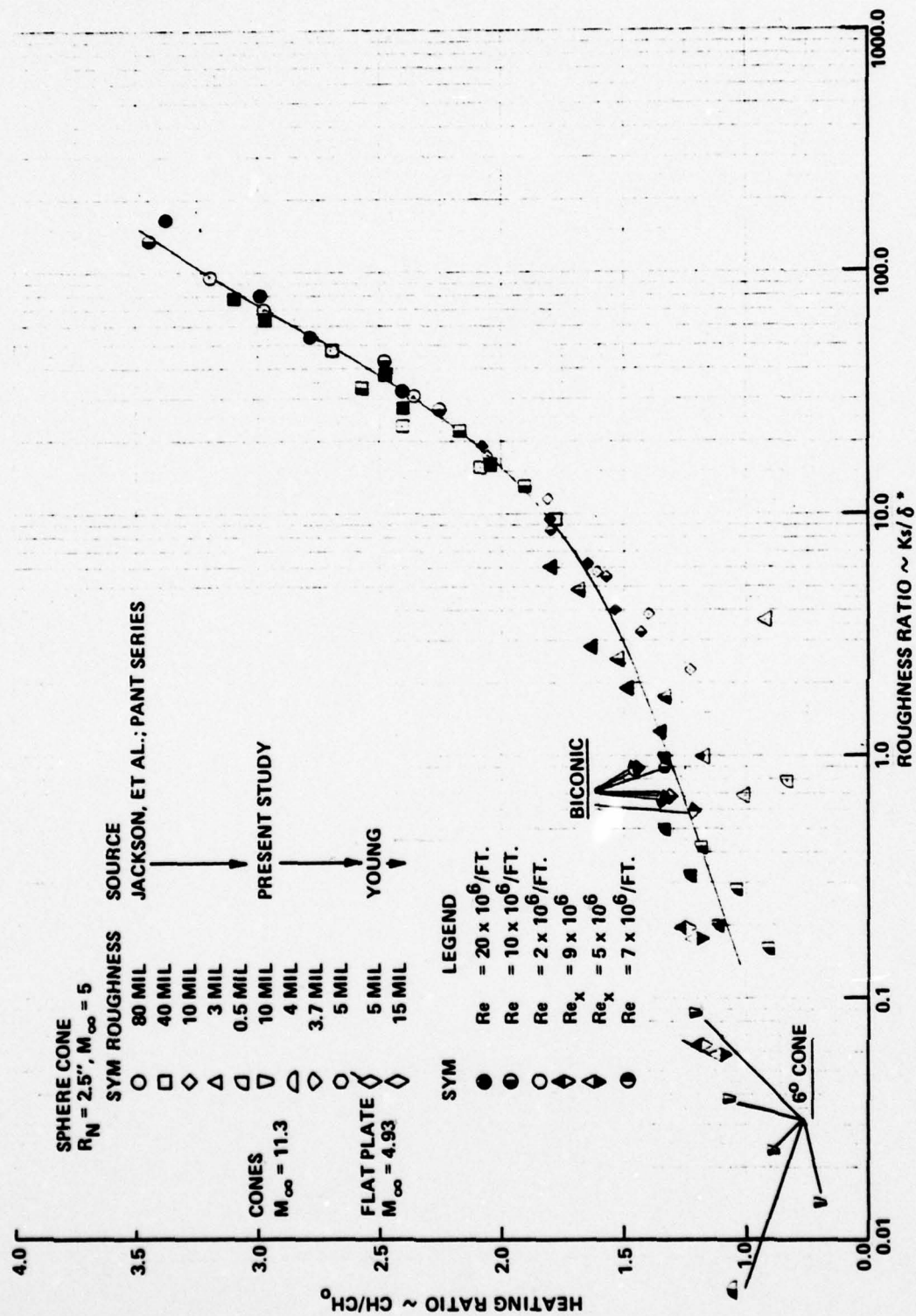


Figure 4-12 COMPARISON BETWEEN THE GRABER AND WHITE CORRELATION OF THE PANT DATA AND THE RECENT CALSPAN MEASUREMENTS OF ROUGHNESS HEATING ON BICONIC AND 6° CONE CONFIGURATIONS

Section 5  
STUDIES OF THE FLOW AND THE DISTRIBUTION OF HEAT  
TRANSFER OVER THE NRV NOSE TIP

5.1 INTRODUCTION

The Nose Tip Recovery Vehicle (NRV) nose tip is one of the few nose tips which has been recovered from flight during re-entry<sup>18</sup>. The nose tip is of particular interest because it was "caught" during the portion of the trajectory where transition was spreading over the nose tip, and a non-similar shape change was occurring. The nose tip, shown in Figure 5-1, displays two characteristics which are of key importance to the nose tip designer. The first is that the nose tip is indented to the point where three-dimensional separated regions of significant proportions must have been formed. The second feature is the distinctive three-dimensional grooved shape of the NRV nose tip, a shape which could not have been predicted from shape change codes. It could be speculated that because of the intrinsically three-dimensional characteristics of boundary layer transition, an intrinsically three-dimensional nose tip similar to the NRV is formed on ablating nose tips whenever the transition moves onto the nose tip. If such nose shaping occurs, it will not only be difficult to predict but also induce nose-tip forces which can change rapidly with small changes in nose shape or angle of attack.

The purpose of the present study was to obtain detailed heat transfer and pressure measurements on a model of the NRV nose tip at a Mach number and Reynolds number which duplicated flight conditions. The instrumentation was to be positioned to examine the intrinsically three-dimensional nature of the flow over the nose tip. In particular we wished to examine whether pairs of counter-rotating vortices were formed in the grooves and determine the magnitude of the heat transfer generated in the reattachment and re-compression regions on the NRV nose tip. We also wished to determine whether the flow pattern over the nose tip was steady and whether it was sensitive to changes in Reynolds number.



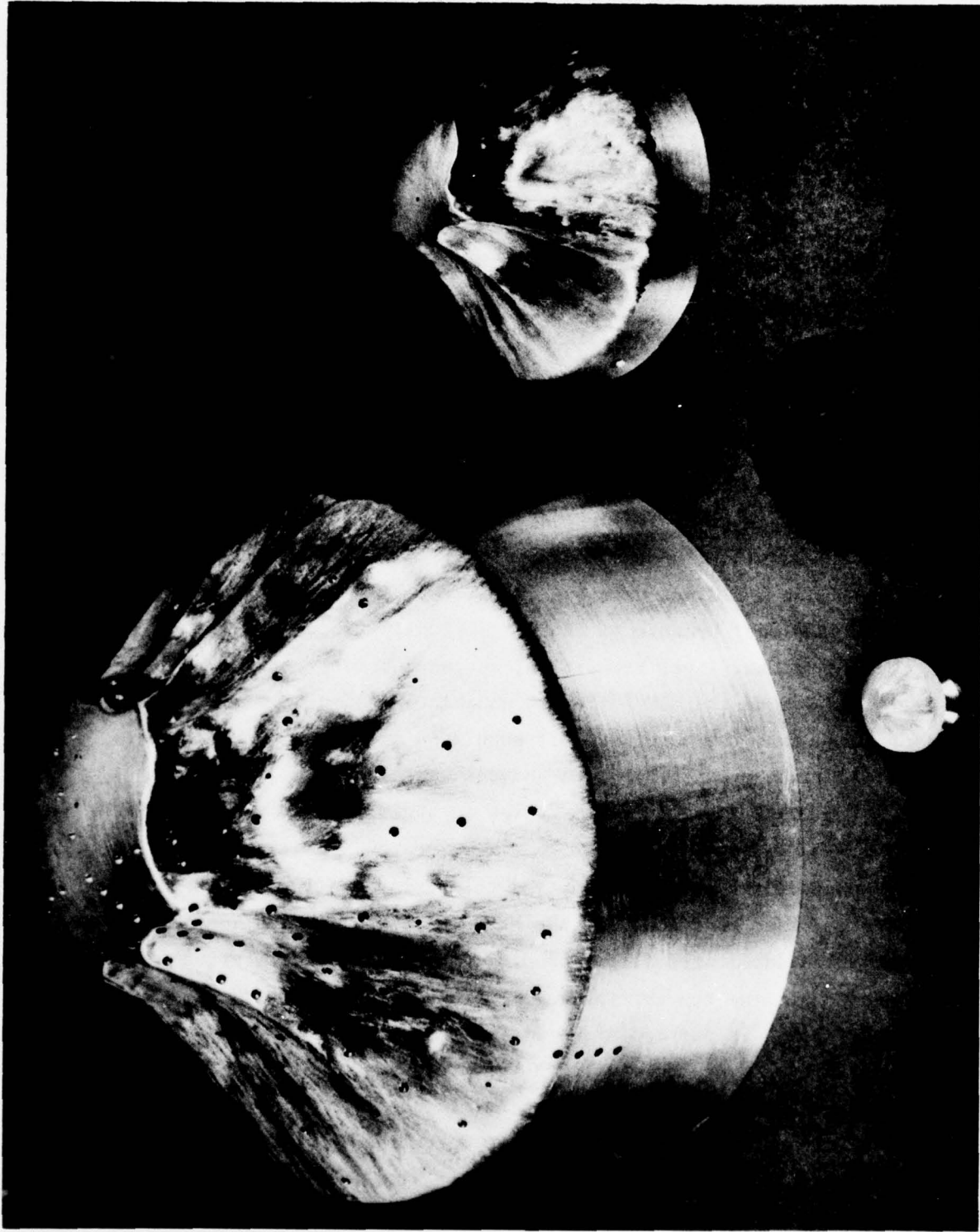


Figure 5-1 NRV HEAT TRANSFER & PRESSURE, FORCE, EPOXY REPLICA AND NOSE TIP MODELS (CLOCKWISE FROM TOP LEFT)

## 5.2 EXPERIMENTAL PROGRAM

The experimental program was conducted in Calspan's 96"-Shock Tunnel at Mach 11 for Reynolds numbers of up to  $10 \times 10^6$  based on nose tip diameter. A drawing of the NRV nose tip showing the instrumentation pattern chosen is shown in Figure 5-2. The instrumentation was connected on a number of key rays which were positioned in grooves and were representative of the key geometric features found on the NRV nose tips. A 4X scale model of the NRV nose tip was constructed for this program so that we could obtain detailed spatially resolved measurements and the ability to duplicate the Reynolds numbers obtained in the flight tests. A photograph of this model and a replica of the NRV nose tip from which it was copied is shown in Figure 5-1. The model was constructed using a precision three-dimensional pantagraph/milling machine. This model was then instrumented with 100 heat transfer gages and 43 pressure gages. The model is shown mounted in the 96" Shock Tunnel in Figure 5-3. The locations of the heat transfer and pressure gages are listed in Table 5-1.

## 5.3 RESULTS AND DISCUSSION

An experimental study of 15 runs were conducted which covered the range of free stream conditions and model configurations listed in Table 5-2. The measurements made during this program are tabulated in Tables 5-3 and 5-4. A Schlieren photograph of the flow over the NRV model is shown in Figure 5-4. This photograph illustrates the two classes of flow with embedded shocks which are typical of the flow over indented nose shapes. The flow over the top of the model separates as it expands downstream of the spherical cap and a small three-dimensional separated region is formed in the cavity formed by the grooves. The compression waves generated in the reattachment region coalesce to form a single shock - the re-compression shock. The bow shock and re-compression shock interact with the formation of a single shock and a shear layer. The flow over the bottom of the model remains attached; however, the flow over the roughly conical section of the nose tip was again characterized by a re-compression process. Here, however, re-compression takes place through







**Figure 5-3a** INSTALLATION OF NRV HEAT TRANSFER AND PRESSURE MODEL IN 96" SHOCK TUNNEL



**Figure 5-3b VIEW OF NRV HEAT TRANSFER AND PRESSURE MODEL SHOWING GAGE LOCATIONS**

Table 5-1  
HEAT TRANSFER IMPRESSION MODEL FOR NRV

H.T. GAGE POSITION	$\theta$ (deg)	$R_H$	H.T. GAGE POSITION	$\theta$ (deg)	$R_H$	PRESSURE GAGE POSITION	$\theta$ (deg)	$R_P$
1	0	0	51	220	3.73	1	8	2.78
2	8	2.47	52	↓	4.11	2	↓	3.87
3	↓	3.11	53	↓	4.49	3	20	.94
4	↓	3.48	54	240	.31	4	↓	1.56
5	↓	4.27	55	↓	.63	5	35	2.83
6	20	2.90	56	↓	.94	6	↓	3.50
7	↓	3.98	57	↓	1.48	7	↓	4.23
8	35	.63	58	↓	1.87	8	90	.94
9	↓	1.25	59	↓	2.24	9	↓	1.25
10	↓	1.88	60	↓	2.61	10	↓	2.21
11	↓	2.47	61	↓	2.98	11	↓	3.21
12	↓	3.15	62	↓	3.36	12	110	1.84
13	↓	3.85	63	↓	3.74	13	↓	2.50
14	↓	4.58	64	↓	4.11	14	↓	3.23
15	53	2.28	65	↓	4.49	15	188	.31
16	↓	2.93	66	250	1.88	16	↓	.94
17	↓	3.65	67	↓	2.98	17	↓	2.19
18	↓	4.39	68	↓	3.74	18	↓	2.90
19	83	2.13	69	↓	4.49	19	230	2.24
20	↓	2.50	70	260	1.87	20	↓	3.36
21	↓	2.86	71	↓	2.61	21	↓	4.48
22	↓	3.29	72	↓	3.36	22	280	2.24
23	100	1.27	73	↓	4.11	23	↓	3.75
24	↓	1.84	74	↓	4.49	24	280	3.37
25	↓	2.86	75	280	1.87	25	310	2.18
26	↓	3.62	76	↓	2.62	26	↓	2.79
27	↓	4.03	77	↓	3.74	27	↓	3.45
28	110	.63	78	↓	4.12	28	↓	4.12
29	↓	.94	79	↓	4.49	29	35	4.74
30	↓	1.27	80	295	.63	30	↓	4.83
31	↓	1.57	81	↓	.94	31	230	4.73
32	↓	2.16	82	↓	1.87	32	↓	4.84
33	↓	2.85	83	↓	2.62			
34	↓	3.63	84	↓	3.00			
35	↓	4.03	85	↓	3.37			
36	↓	4.50	86	↓	3.76			
37	135	1.58	87	↓	4.13			
38	↓	2.85	88	↓	4.51			
39	145	1.38	89	320	3.17			
40	↓	1.93	90	330	3.31			
41	↓	2.75	91	↓	4.17			
42	↓	4.05	92	340	2.55			
43	188	1.57	93	↓	3.36			
44	↓	3.71	94	↓	4.21			
45	↓	4.47	95	35	4.69			
46	210	3.37	96	↓	4.79			
47	↓	4.12	97	↓	4.88			
48	220	1.87	98	240	4.71			
49	↓	2.61	99	↓	4.78			
50	↓	2.98	100	↓	4.81			
			101	↓	4.87			



THIS PAGE IS BEST QUALITY PRACTICABLE  
FROM COPY FURNISHED TO DDG

Table 5-2  
TEST CONDITIONS FOR NRV HEAT TRANSFER AND PRESSURE TEST

RUN NO.	15	16	17	18	19	20
ATTACK ANGLE	0°	0°	2°	2°	0°	0°
MI	3.296E 00	3.299E 00	3.302E 00	3.254E 00	3.302E 00	3.276E 00
P <sub>o</sub> psia	1.758E 04	1.767E 04	1.753E 04	1.765E 04	8.371E 03	8.021E 03
H <sub>o</sub> ft <sup>2</sup> /sec <sup>2</sup>	1.712E 07	1.715E 07	1.750E 07	1.668E 07	1.744E 07	1.709E 07
M <sub>∞</sub>	1.131E 01	1.131E 01	1.130E 01	1.130E 01	1.102E 01	1.101E 01
U <sub>∞</sub> ft/sec	5.744E 03	5.748E 03	5.807E 03	5.669E 03	5.791E 03	5.733E 03
T <sub>∞</sub> °R	1.073E 02	1.074E 02	1.098E 02	1.047E 02	1.149E 02	1.127E 02
P <sub>∞</sub> psia	2.140E-01	2.156E-01	2.125E-01	2.198E-01	1.069E-01	1.031E-01
Q <sub>∞</sub> psia	1.919E 01	1.933E 01	1.901E 01	1.967E 01	9.091E 00	8.755E 00
ρ <sub>∞</sub> slugs/ft <sup>3</sup>	1.675E-04	1.685E-04	1.624E-04	1.762E-04	7.806E-05	7.672E-05
μ <sub>∞</sub> slugs/ft-sec	9.022E-08	9.033E-08	9.236E-08	8.805E-08	9.666E-08	9.482E-08
Re/ft.	1.066E 07	1.072E 07	1.021E 07	1.135E 07	4.677E 06	4.639E 06
P <sub>o</sub> psia	3.552E 01	3.579E 01	3.521E 01	3.639E 01	1.684E 01	1.621E 01

RUN NO.	21	22	23	24	26	27
ATTACK ANGLE	0°	0°	0°	0°	1°	1°
MI	3.741E 00	3.757E 00	3.134E 00	3.180E 00	3.261E 00	3.257E 00
P <sub>o</sub> psia	1.665E 04	1.889E 04	1.838E 03	1.977E 03	1.746E 04	1.729E 04
H <sub>o</sub> ft <sup>2</sup> /sec <sup>2</sup>	2.149E 07	2.157E 07	1.615E 07	1.661E 07	1.713E 07	1.722E 07
M <sub>∞</sub>	1.296E 01	1.296E 01	1.076E 01	1.076E 01	1.132E 01	1.131E 01
U <sub>∞</sub> ft/sec	6.463E 03	6.476E 03	5.568E 03	5.647E 03	5.745E 03	5.760E 03
T <sub>∞</sub> °R	1.035E 02	1.039E 02	1.113E 02	1.146E 02	1.071E 02	1.079E 02
P <sub>∞</sub> psia	8.101E-02	8.205E-02	2.491E-02	2.672E-02	2.112E-01	2.093E-01
Q <sub>∞</sub> psia	9.528E 00	9.649E 00	2.021E 00	2.166E 00	1.896E 01	1.876E 01
ρ <sub>∞</sub> slugs/ft <sup>3</sup>	6.569E-05	6.626E-05	1.878E-05	1.956E-05	1.655E-04	1.628E-04
μ <sub>∞</sub> slugs/ft-sec	8.707E-08	8.742E-08	9.364E-08	9.637E-08	9.008E-08	9.072E-08
Re/ft.	4.876E 06	4.909E 06	1.116E 06	1.146E 06	1.055E 07	1.034E 07
P <sub>o</sub> psia	1.770E 01	1.793E 01	3.738E 00	4.008E 00	3.511E 01	3.473E 01

Table 5-3  
HEAT TRANSFER COMPUTATIONS FOR NRV

RUN NO.	GAGE POS	HT RATE (BTU/ft <sup>2</sup> sec)	GAGE POS	HT RATE (BTU/ft <sup>2</sup> sec)	GAGE POS	HT RATE (BTU/ft <sup>2</sup> sec)	GAGE POS	HT RATE (BTU/ft <sup>2</sup> sec)	GAGE POS	HT RATE (BTU/ft <sup>2</sup> sec)
1710	1	6.76E+01	21	1.05E+02	42	9.48E+01	61	1.14E+02	81	6.82E+01
	2	4.15E+01	22	1.14E+02	43	2.58E+01	62	1.08E+02	82	3.86E+01
	3	1.27E+02	23	7.63E+00	44	1.10E+02	63	9.57E+01	83	7.62E+01
	4	1.21E+02	24	1.04E+02	46	1.20E+02	64	1.01E+02	84	7.98E+01
	5	1.04E+02	25	1.09E+02	47	1.25E+02	65	1.23E+02	86	1.10E+02
	6	5.64E+01	26	9.82E+01	48	6.60E+01	66	2.13E+01	87	1.05E+02
	7	9.42E+01	27	9.03E+01	49	4.04E+01	67	1.09E+02	88	1.28E+02
	8	6.75E+01	28	6.92E+01	51	1.64E+02	68	1.10E+02	89	1.06E+02
	9	6.74E+01	29	7.08E+01	52	1.44E+02	69	1.45E+02	90	1.16E+02
	10	5.62E+01	30	2.35E+01	54	6.87E+01	70	6.12E+01	91	1.20E+02
	11	1.26E+01	31	2.64E+01	55	6.78E+01	71	6.27E+01	92	4.03E+01
	12	7.60E+01	32	8.69E+01	56	6.72E+01	72	1.18E+02	93	1.15E+02
	13	6.47E+01	33	1.17E+02	57	1.66E+01	73	1.35E+02	94	1.13E+02
	14	7.44E+01	34	1.05E+02	58	4.01E+01	74	1.03E+02	95	1.51E+01
	15	1.53E+01	35	1.14E+02	59	7.14E+01	75	3.74E+01	96	1.06E+01
	16	1.10E+02	36	1.04E+02	60	9.23E+01	76	6.88E+01	97	7.51E+00
	17	1.04E+02	37	6.35E+01			77	1.27E+02	98	3.84E+01
	18	9.82E+01	38	1.03E+02			78	1.19E+02	99	9.78E+00
	19	5.95E+01	39	5.14E+01			79	1.65E+02	100	1.04E+01
	20	6.11E+01	40	1.02E+02			80	6.04E+01		
1718	1	6.72E+01	21	7.37E+01	41	9.55E+01	61	1.08E+02	81	6.61E+01
	2	4.44E+01	22	1.06E+02	42	9.36E+01	62	1.03E+02	82	4.99E+01
	3	1.16E+02	23	6.71E+00	43	3.57E+01	63	1.00E+02	83	7.48E+01
	4	1.16E+02	24	9.63E+01	44	1.25E+02	64	1.03E+02	84	9.32E+01
	5	9.51E+01	25	1.15E+02	45	1.34E+02	65	1.20E+02	86	1.08E+02
	6	6.36E+01	26	9.75E+01	47	1.24E+02	66	2.46E+01	87	1.10E+02
	7	8.19E+01	29	6.93E+01	48	1.05E+02	67	1.10E+02	88	1.44E+02
	8	6.74E+01	30	1.72E+01	49	6.65E+01	68	1.09E+02	89	1.20E+02
	9	6.42E+01	31	1.94E+01	50	1.21E+02	69	1.48E+02	90	1.17E+02
	10	5.33E+01	32	6.47E+01	51	1.40E+02	70	7.13E+01	91	1.21E+02
	11	1.12E+01	33	1.32E+02	52	1.56E+02	71	1.08E+02	92	4.60E+01
	12	7.34E+01	34	1.10E+02	53	1.48E+02	72	1.50E+02	93	1.09E+02
	13	6.42E+01	35	1.01E+02	54	6.77E+01	73	1.87E+02	94	1.12E+02
	14	9.08E+01	36	9.76E+01	55	6.06E+01	74	1.37E+02	95	1.95E+01
	15	1.26E+01	37	6.37E+01	57	1.50E+01	75	4.37E+01	96	1.88E+01
	16	8.43E+01	38	9.85E+01	58	4.44E+01	76	6.93E+01	97	1.45E+01
	17	9.36E+01	39	6.35E+01	59	9.14E+01	77	1.16E+02	98	4.35E+01
	18	1.04E+02	40	1.07E+02	60	9.31E+01	78	1.28E+02	99	1.08E+01
	19	5.29E+01					79	1.94E+02	100	1.25E+01
	20	5.85E+01					80	6.49E+01	101	8.94E+00
1720	1	4.11E+01	21	4.66E+01	41	6.26E+01	61	6.48E+01	81	4.63E+01
	2	1.46E+01	22	6.24E+01	42	5.44E+01	62	5.39E+01	82	2.14E+01
	3	6.31E+01	23	1.68E+01	43	1.34E+01	64	4.87E+01	83	3.50E+01
	4	6.20E+01	24	3.88E+01	44	6.54E+01	66	6.95E+00	84	4.10E+01
	5	6.14E+01	26	6.61E+01	45	7.04E+01	67	4.65E+01	86	6.47E+01
	6	2.25E+01	28	4.77E+01	46	6.80E+01	68	5.98E+01	87	5.95E+01
	7	4.46E+01	29	4.62E+01	47	6.47E+01	69	6.13E+01	88	7.11E+01
	8	3.66E+01	30	1.63E+01	48	2.40E+01	70	3.88E+01	89	5.63E+01
	9	3.46E+01	31	3.07E+01	49	2.75E+01	71	5.22E+01	90	5.78E+01
	10	3.75E+01	32	5.37E+01	50	4.20E+01	72	6.45E+01	91	6.86E+01
	11	5.38E+00	33	7.34E+01	51	7.48E+01	73	7.41E+01	92	2.23E+01
	12	4.86E+01	34	6.86E+01	52	7.32E+01	74	5.97E+01	93	5.66E+01
	13	5.79E+01	35	5.76E+01	53	7.13E+01	75	2.23E+01	94	6.91E+01

THIS PAGE IS BEST QUALITY PRACTICABLE  
FROM COPY FURNISHED TO DDG

Table 5-3  
HEAT TRANSFER COMPUTATIONS FOR NRV (Cont.)

RUN NO.	GAGE POS	HT RATE (BTU/ft <sup>2</sup> sec)	GAGE POS	HT RATE (BTU/ft <sup>2</sup> sec)	GAGE POS	HT RATE (BTU/ft <sup>2</sup> sec)	GAGE POS	HT RATE (BTU/ft <sup>2</sup> sec)	GAGE POS	HT RATE (BTU/ft <sup>2</sup> sec)
	14	4.26E+01	36	5.41E+01	54	4.14E+01	76	3.58E+01	95	7.27E+00
	15	8.40E+00	37	4.43E+01	55	3.43E+01	77	7.13E+01	96	5.65E+00
	16	8.04E+01	38	6.47E+01	57	9.40E+00	78	6.85E+01	97	3.05E+00
	17	4.99E+01	39	4.92E+01	58	3.36E+01	79	7.53E+01	98	2.12E+01
	18	2.37E+01	40	6.36E+01	59	4.77E+01	80	4.02E+01	99	5.48E+00
	19	3.55E+01			60	6.22E+01			100	5.69E+00
	20	5.49E+01							101	4.94E+00
2422	1	6.70E+01	21	6.76E+01	41	8.76E+01	61	9.15E+01	81	7.27E+01
	2	3.14E+01	22	7.52E+01	42	8.46E+01	62	7.81E+01	82	2.93E+01
	3	8.44E+01	24	5.49E+01	43	3.47E+01	63	7.30E+01	83	5.14E+01
	4	8.48E+01	26	9.76E+01	44	1.03E+02	64	7.51E+01	84	6.61E+01
	5	6.72E+01	28	7.49E+01	45	1.13E+02	65	8.64E+01	86	9.12E+01
	6	3.31E+01	29	7.53E+01	46	1.04E+02	66	1.90E+01	87	9.11E+01
	7	6.81E+01	30	1.96E+01	47	1.00E+02	67	8.25E+01	88	9.52E+01
	8	6.25E+01	31	3.34E+01	48	4.17E+01	68	8.20E+01	89	7.86E+01
	9	6.02E+01	32	7.93E+01	49	5.74E+01	69	8.26E+01	90	9.26E+01
	10	5.56E+01	33	1.16E+02	50	6.50E+01	70	5.88E+01	91	1.05E+02
	11	7.34E+00	34	9.22E+01	51	1.20E+02	71	6.78E+01	92	2.48E+01
	12	7.43E+01	35	8.42E+01	52	1.15E+02	72	1.31E+02	93	8.37E+01
	13	9.05E+01	36	6.47E+01	53	9.31E+01	73	1.08E+02	94	1.02E+02
	14	6.23E+01	37	4.25E+01	54	6.95E+01	74	8.04E+01	95	1.20E+01
	15	1.34E+01	38	6.74E+01	55	7.5E+01	75	2.94E+01	96	7.58E+00
	16	1.10E+02	39	4.51E+01	57	1.31E+01	76	5.95E+01	97	4.74E+00
	17	7.55E+01	40	8.82E+01	58	2.90E+01	77	1.11E+02	98	3.26E+01
	18	3.40E+01			60	5.89E+01	78	1.01E+02	99	9.34E+00
	19	4.79E+01					79	1.04E+02	100	9.67E+00
	20	7.28E+01					80	6.83E+01	101	7.96E+00
2424	1	2.01E+01	21	1.80E+01	41	2.15E+01	61	2.36E+01	81	2.05E+01
	2	2.80E+00	22	2.09E+01	42	1.60E+01	62	2.06E+01	82	6.04E+00
	3	1.67E+01	23	4.27E+00	43	6.90E+00	63	1.99E+01	83	1.39E+01
	4	2.28E+01	24	1.53E+01	44	1.98E+01	64	1.96E+01	84	1.60E+01
	5	1.70E+01	26	2.17E+01	45	2.19E+01	65	1.75E+01	86	1.50E+01
	6	7.84E+00	28	2.23E+01	46	1.98E+01	66	1.94E+00	87	2.02E+01
	7	1.56E+01	29	2.08E+01	47	1.79E+01	67	2.54E+01	88	1.63E+01
	8	1.94E+01	30	1.09E+00	48	4.70E+00	68	2.27E+01	89	1.94E+01
	9	1.74E+01	31	4.90E+00	49	1.63E+01	69	1.83E+01	90	2.31E+01
	10	1.52E+01	32	1.84E+01	50	1.95E+01	70	1.37E+01	91	2.22E+01
	11	1.16E+00	33	2.58E+01	51	2.44E+01	71	1.99E+01	92	5.75E+00
	12	1.81E+01	34	1.75E+01	52	2.37E+01	72	2.43E+01	93	2.23E+01
	13	1.66E+01	35	1.71E+01	53	1.97E+01	73	2.04E+01	94	2.39E+01
	14	1.50E+01	36	1.52E+01	54	2.09E+01	74	1.67E+01	95	3.62E+00
	15	2.36E+00	37	6.88E+00	55	2.14E+01	75	3.70E+00	96	2.16E+00
	16	2.01E+01	38	1.69E+01	57	2.00E+00	76	1.56E+01	97	1.71E+00
	17	1.41E+01	39	4.70E+00	58	2.80E+00	77	2.23E+01	98	8.56E+00
	18	8.68E+00	40	1.29E+01	59	5.16E+00	78	2.22E+01	99	2.57E+00
	19	8.12E+00			60	1.39E+01	79	2.06E+01	100	2.64E+00
	20	1.75E+01					80	1.96E+01	101	1.97E+00
2427	1	6.65E+01	21	9.42E+01	41	1.01E+02	61	1.06E+02	81	6.42E+01
	2	4.35E+01	22	1.10E+02	43	4.74E+01	63	9.26E+01	82	3.07E+01
	3	1.25E+02	23	7.03E+00	44	1.23E+02	64	9.57E+01	83	6.01E+01
	4	1.20E+02	24	9.30E+01	45	1.29E+02	65	1.37E+02	84	8.42E+01
	5	1.04E+02	26	9.43E+01	46	1.19E+02	66	2.03E+01	87	1.10E+02



THIS PAGE IS BEST QUALITY PRACTICABLE  
FROM COPY FURNISHED TO DDC

Table 5-3  
HEAT TRANSFER COMPUTATIONS FOR NRV (Cont.)

RUN NO.	GAGE POS	HT RATE (BTU/ft <sup>2</sup> sec)	GAGE POS	HT RATE (BTU/ft <sup>2</sup> sec)	GAGE POS	HT RATE (BTU/ft <sup>2</sup> sec)	GAGE POS	HT RATE (BTU/ft <sup>2</sup> sec)	GAGE POS	HT RATE (BTU/ft <sup>2</sup> sec)
2027	6	5.38E+01	28	6.85E+01	47	1.22E+02	67	1.06E+02	88	1.47E+02
	7	4.29E+01	29	7.21E+01	48	6.53E+01	68	1.05E+02	89	1.16E+02
	8	7.39E+01	30	2.06E+01	49	5.85E+01	69	1.54E+02	90	9.83E+01
	9	6.32E+01	31	1.97E+01	50	7.51E+01	70	6.11E+01	91	1.09E+02
	10	5.55E+01	32	8.13E+01	52	1.48E+02	71	8.76E+01	92	3.97E+01
	11	1.01E+01	35	1.32E+02	53	1.47E+02	72	1.39E+02	93	9.40E+01
	12	7.38E+01	37	6.29E+01	54	7.11E+01	73	1.48E+02	94	1.13E+02
	13	7.90E+01	38	3.05E+01	57	1.85E+01	74	1.09E+02	95	1.79E+01
	14	6.74E+01	39	6.04E+01	58	3.72E+01	75	3.56E+01	96	1.18E+01
	15	1.28E+01	40	1.02E+02	59	5.47E+01	76	6.77E+01	97	1.13E+01
	16	8.76E+01			60	8.54E+01	77	1.35E+02	98	4.17E+01
	17	4.72E+01					78	1.33E+02	99	1.07E+01
	18	1.01E+02					79	1.79E+02	100	1.14E+01
	19	5.29E+01					80	7.25E+01	101	8.81E+00
	20	5.90E+01								

THIS PAGE IS BEST QUALITY PRACTICABLE  
FROM COPY FURNISHED TO DDG

Table 5-4  
PRESSURE COMPUTATIONS FOR NRV

GAGE POS	RUN NO.					
	15/16	17/18	19/20	21/22	23/24	26/27
	PRESSURE RATE (psia)					
1	7.49	6.89	4.14	3.06	0.60	
2	13.70	13.90	6.45		1.66	13.80
3	33.80	33.40	15.30	14.50	3.80	33.60
4	30.30	28.60	13.80	16.50	3.30	29.70
5	6.78		2.89	3.40	0.64	6.50
6	13.90	13.80	7.22	10.60	1.70	
7	20.20	11.60	9.25	10.70	2.18	16.10
8	32.40	29.80	14.90	18.00	3.69	33.10
9	29.90	29.00	13.70	16.50	3.35	29.30
10	2.73		4.62		1.06	2.72
11	12.70	13.60	6.03	7.01	1.41	12.30
12	9.06		4.73	5.22	0.89	2.21
13	21.10		6.33	7.54	1.68	19.60
14	23.50	12.10	9.75	11.00	2.26	22.00
15	33.60	32.70	16.00	19.60	3.98	34.60
16	29.10	28.70	13.80	16.70	3.36	30.10
17	12.50	13.10	6.25	6.25	1.29	12.90
18	16.40	19.60	7.79	9.39	2.10	20.50
19	4.74		2.35	2.22	0.35	3.51
20	18.90	22.00	8.60	10.20	2.37	19.70
21	21.90	24.20	10.40	11.90	2.38	21.10
22	7.47		4.46	3.86	0.98	7.97
23	23.80	24.40	11.20	13.00	2.60	24.20
24	20.40	21.20	8.99	10.50	2.11	18.60
25	9.05	9.06	4.12	4.90	0.93	8.90
26	11.70	13.30	5.64	6.39	1.51	12.20
27	20.00	22.80	9.50	10.50	2.06	20.10
28	25.20	25.40	11.30	13.10	2.39	24.40
29	2.65		1.20	1.15	0.34	2.80
30	2.05	2.71	1.02	1.15	0.24	2.15
31						
32	1.24		0.54	0.46	0.16	1.30

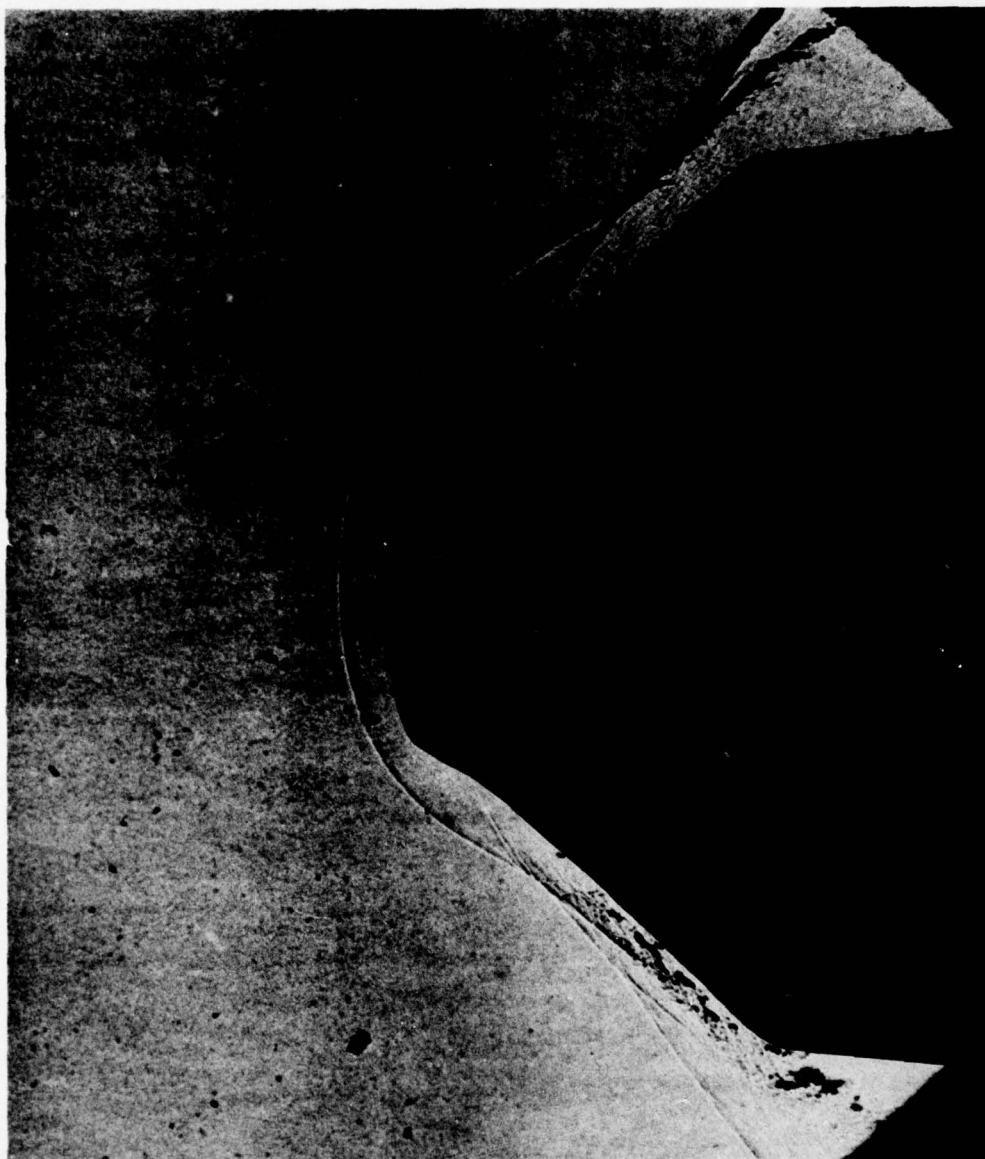


**Figure 5-4 SCHLIEREN PHOTOGRAPH OF THE FLOW OVER THE NRV HEAT TRANSFER AND PRESSURE MODEL ( $M = 11.3$  Re/FT =  $10 \times 10^6$ )**



a series of oblique shocks as a wall jet is formed. It is the structure and development of the boundary layer at the base re-compression processes which controls the large heat transfer rates which are developed in these regions.

The distributions of heat transfer and pressure over the NRV nose tip made in this study are shown in Figures 5-5 through 5-10. A typical heat transfer distribution for free stream conditions closest to those encountered in flight are shown in Figure 5-5a. The heat transfer measurements on the spherical cap indicate that the boundary layer remains laminar over this part of the model, with transition occurring in the free shear layer downstream of the shoulder expansion. While the heat transfer rates drop below the stagnation point value in the separated regions just downstream of the shoulder, heat transfer rates in the reattachment and re-compression regions over the model can rise to close to three times the stagnation point value. This increase is influenced by transition, the thinning of the boundary layer in the re-compression region and entropy swallowing. However, the measurements clearly indicate that the surface recession would be largest on the conical frustum of this nose tip. The pressure distribution over the nose tip for the conditions discussed is shown in Figure 5-5b. As we would anticipate from our observations on the Schlieren photographs and the heat transfer measurements, the pressure rises along the roughly conical portion of the nose tip as a result of the re-compression process and reaches close to 89% of the stagnation pressure toward the base of the nose tip. However, there is a significant variation in the pressure around the conical segment of the nose tip as a result of the different re-compression processes associated with the circumferential variations in surface geometry.

During the design of this experiment, we speculated that the flow over the NRV nose tip would be very sensitive to the Reynolds number and Mach number of the free stream, because boundary layer transition and separation were intrinsic features of the flow field. Thus, we constructed a large scale replica of the NRV nose tip so that the flight Reynolds number could be duplicated in the Shock Tunnel. Therefore, it was of interest to examine

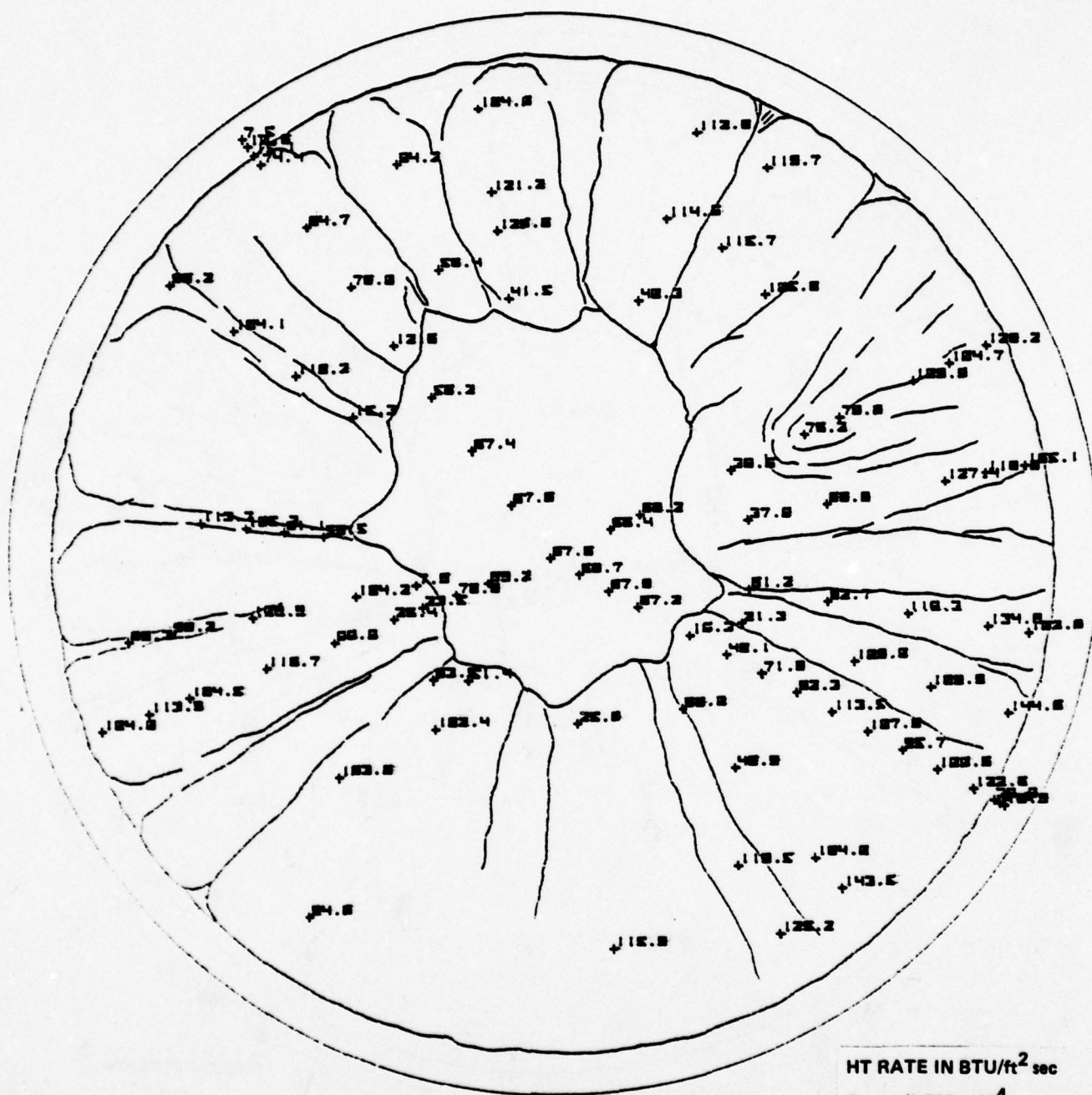
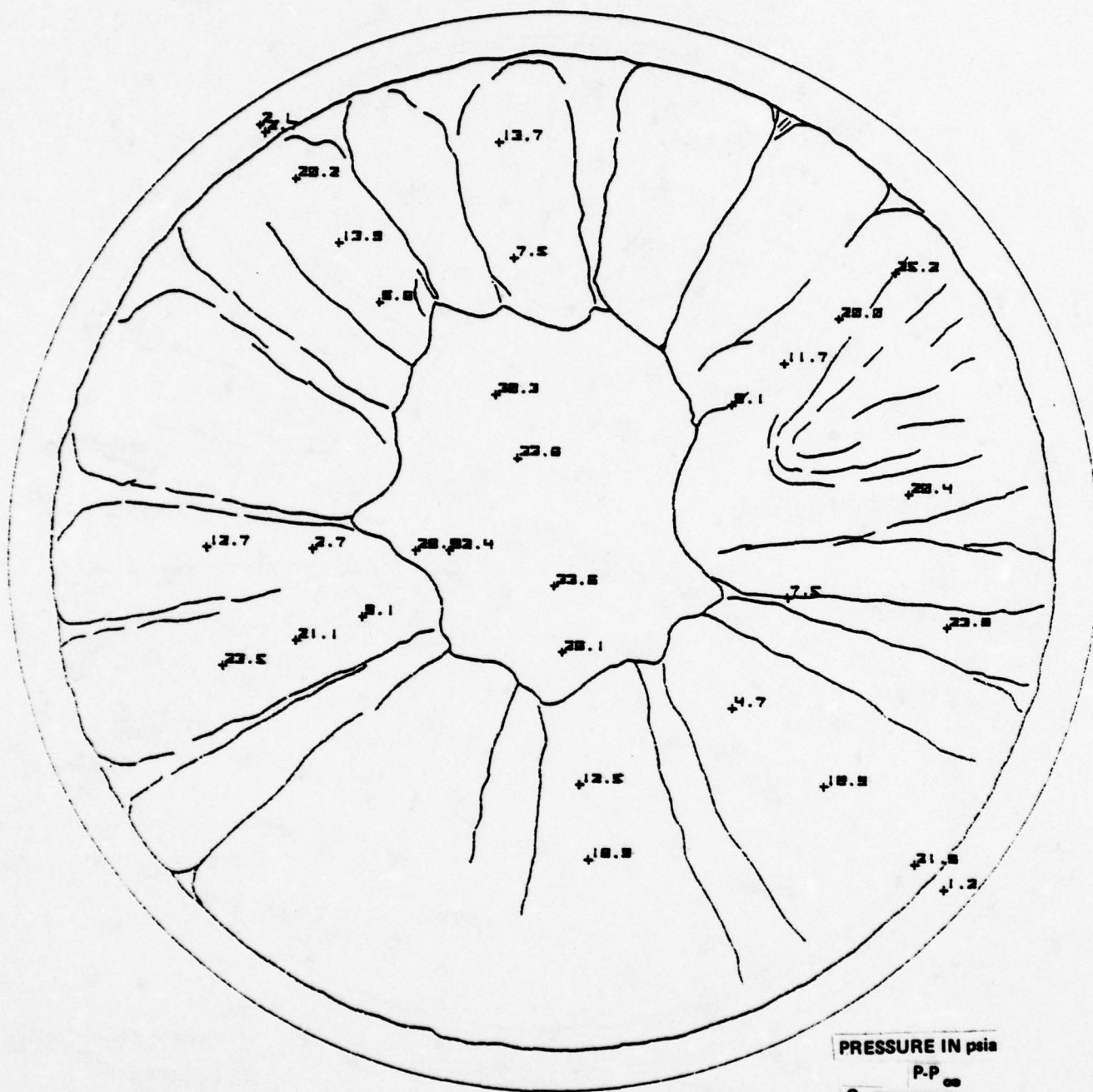


Figure 5-5a HEAT TRANSFER DISTRIBUTION OVER THE NRV CONFIGURATION -  
 $M = 11$ ,  $Re/FT = 10 \times 10^6$ ,  $\alpha = 0^\circ$



PRESSURE IN psia

$$C_p = \frac{P - P_\infty}{\frac{1}{2} \rho V_\infty^2}$$

19.28

Figure 5-5b PRESSURE DISTRIBUTION OVER THE NRV CONFIGURATION —  
 $M = 11$ ,  $Re/FT = 10 \times 10^6$ ,  $\alpha = 0^\circ$



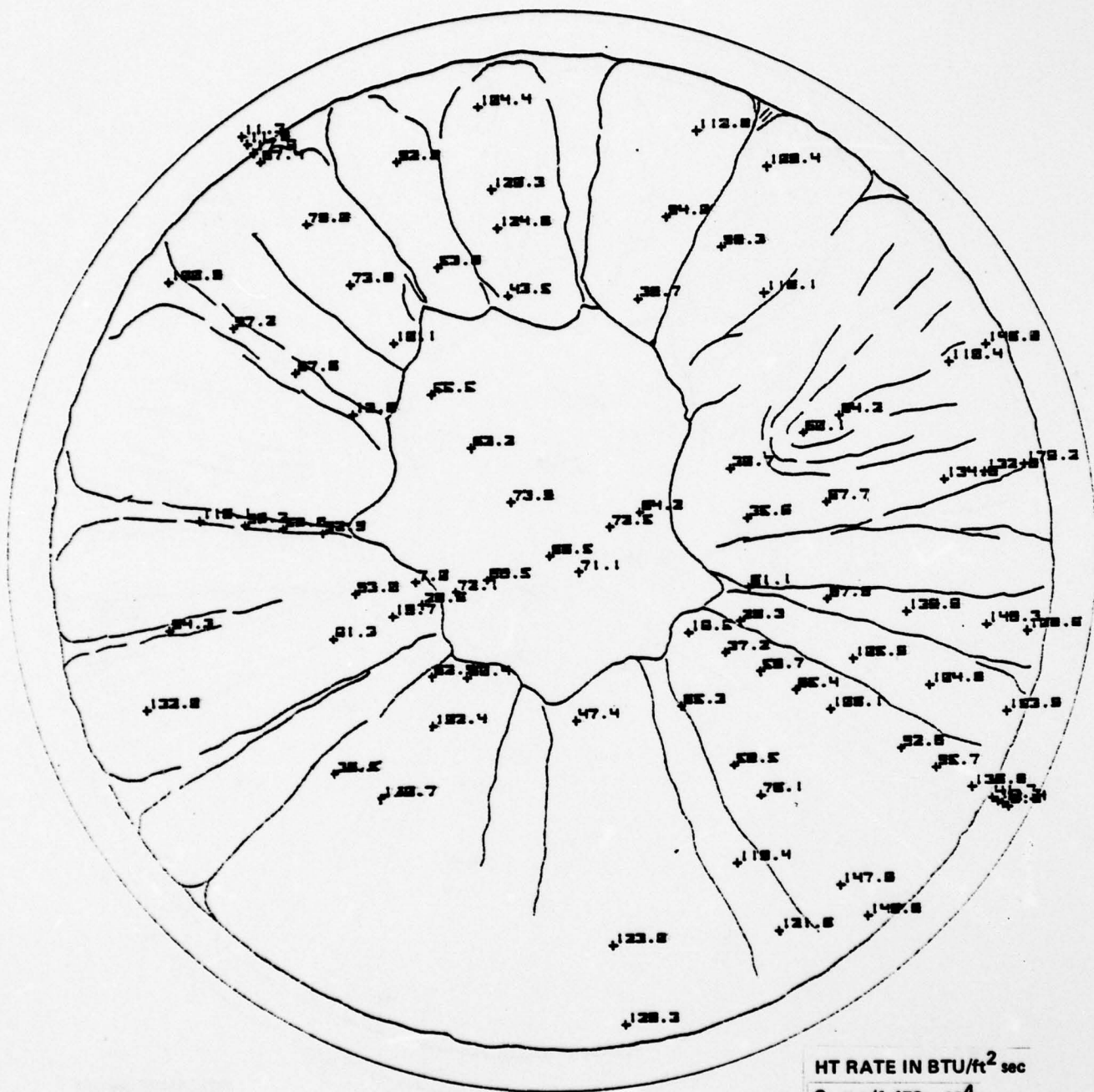
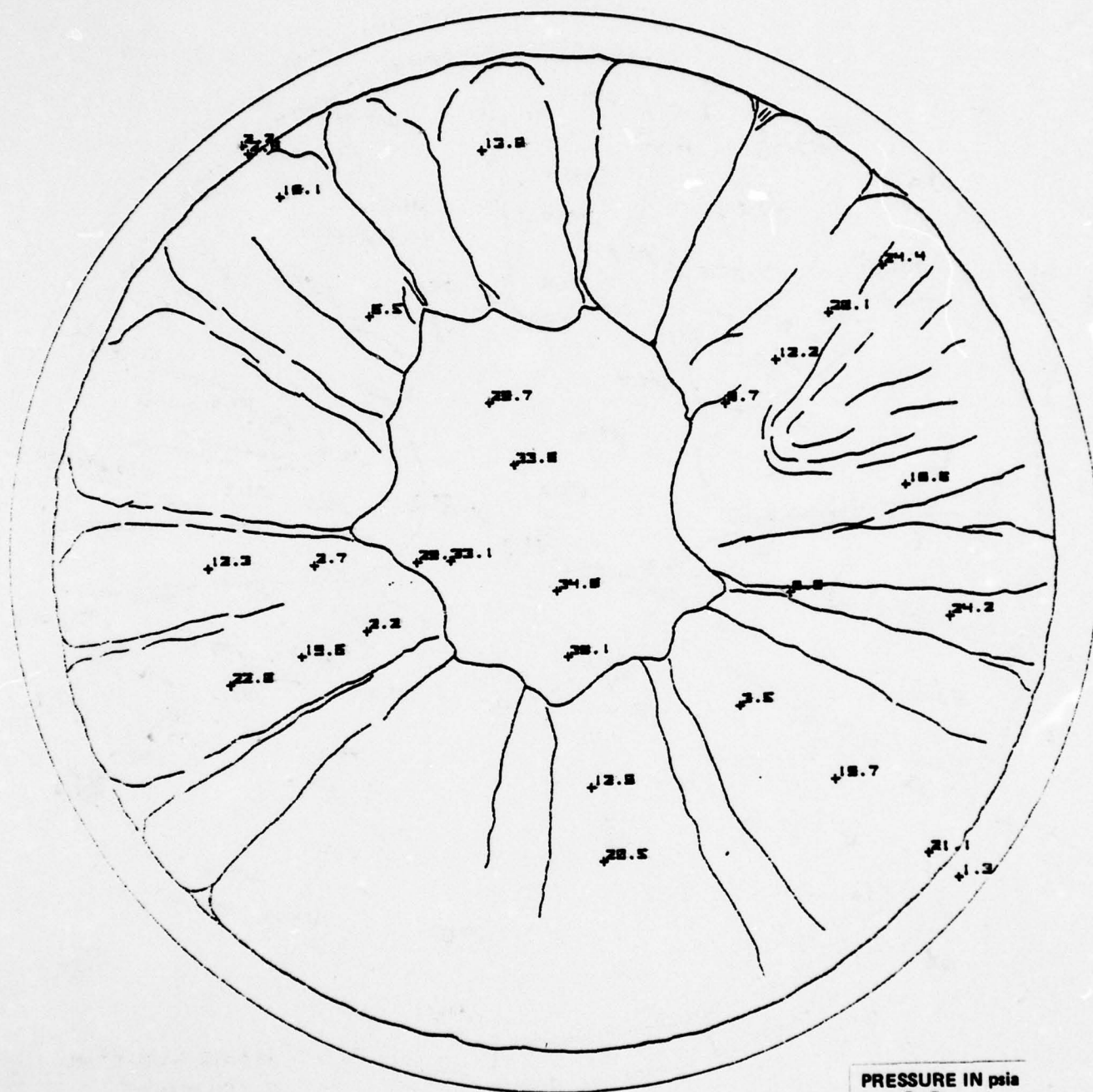


Figure 5-6a HEAT TRANSFER DISTRIBUTION OVER THE NRV CONFIGURATION -  
 $M = 11$ ,  $Re/FT = 10 \times 10^6$ ,  $\alpha = 10$



PRESSURE IN psia  
 $C_p = \frac{P - P_\infty}{18.86}$

Figure 5-6b PRESSURE DISTRIBUTION OVER THE NRV CONFIGURATION -  
 $M = 11, Re/FT = 10 \times 10^6, \alpha = 1^\circ$

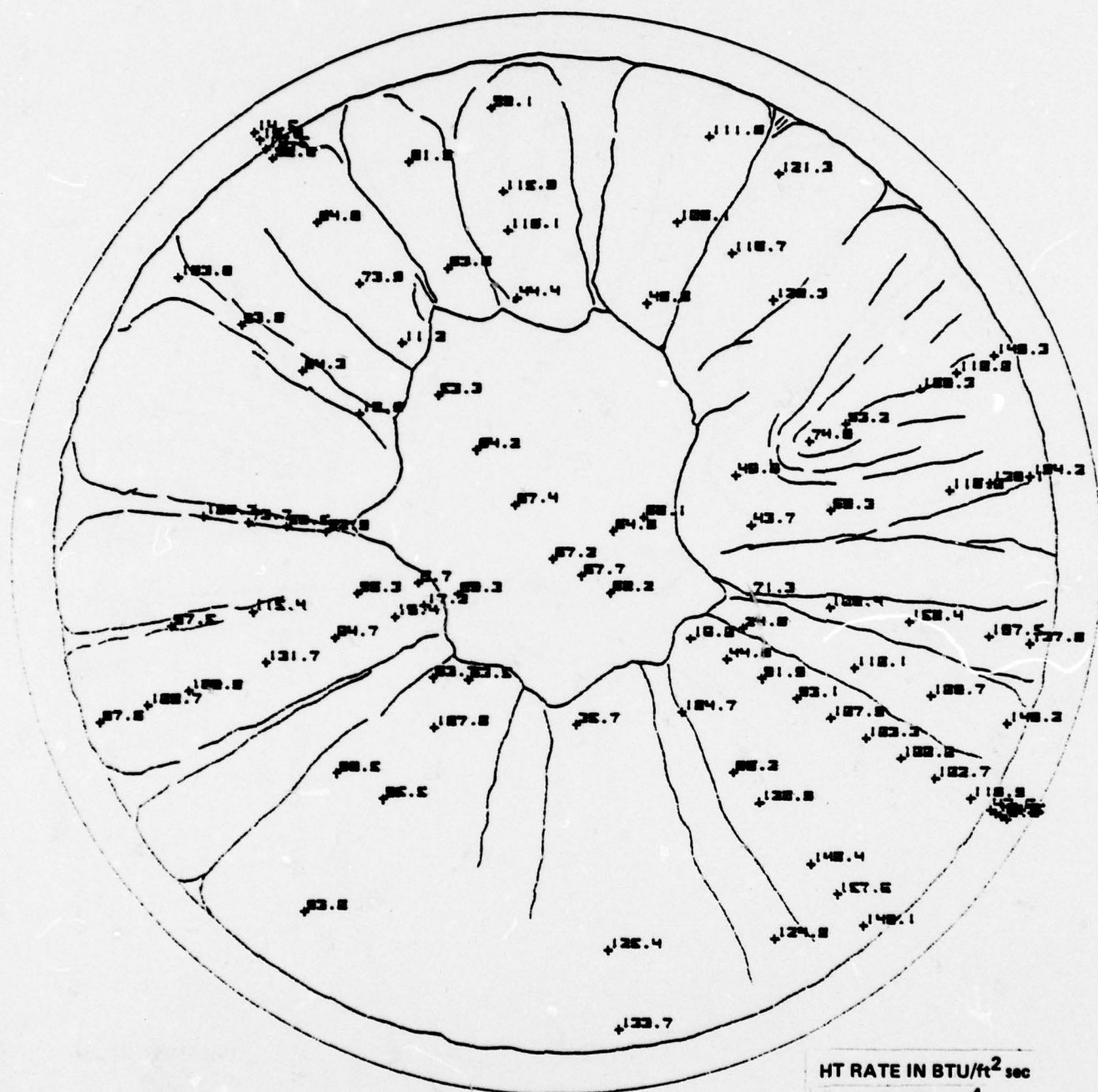
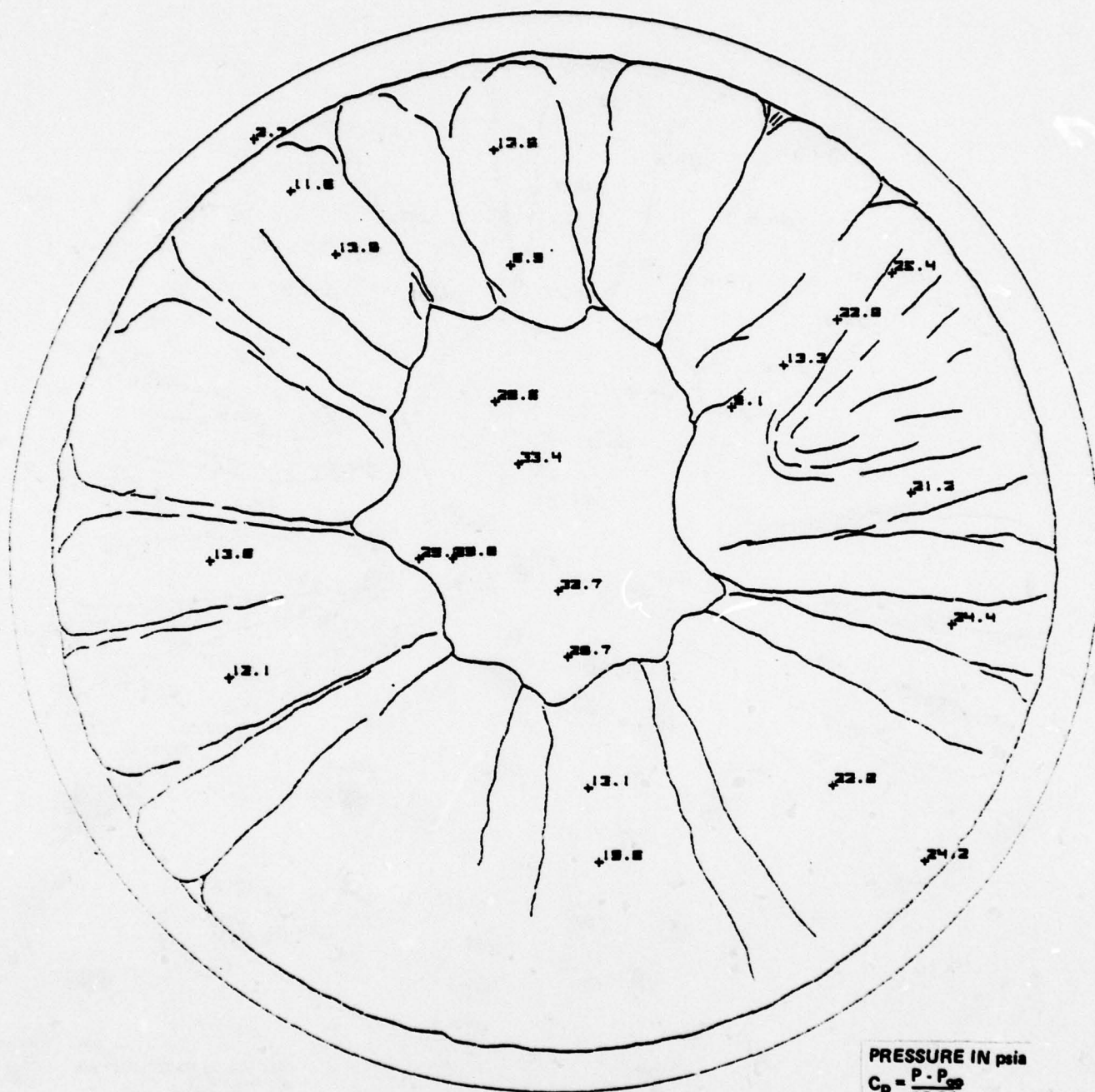


Figure 5-7a HEAT TRANSFER DISTRIBUTION OVER THE NRV CONFIGURATION -  
 $M = 11$ ,  $Re/FT = 10 \times 10^6$ ,  $\alpha = 20^\circ$





PRESSURE IN psia  
 $C_p = \frac{P - P_\infty}{P_\infty - P_\infty}$   
 19.34

Figure 5-7b PRESSURE DISTRIBUTION OVER THE NRV CONFIGURATION -  
 $M = 11, Re/FT = 10 \times 10^6, \alpha = 2^\circ$

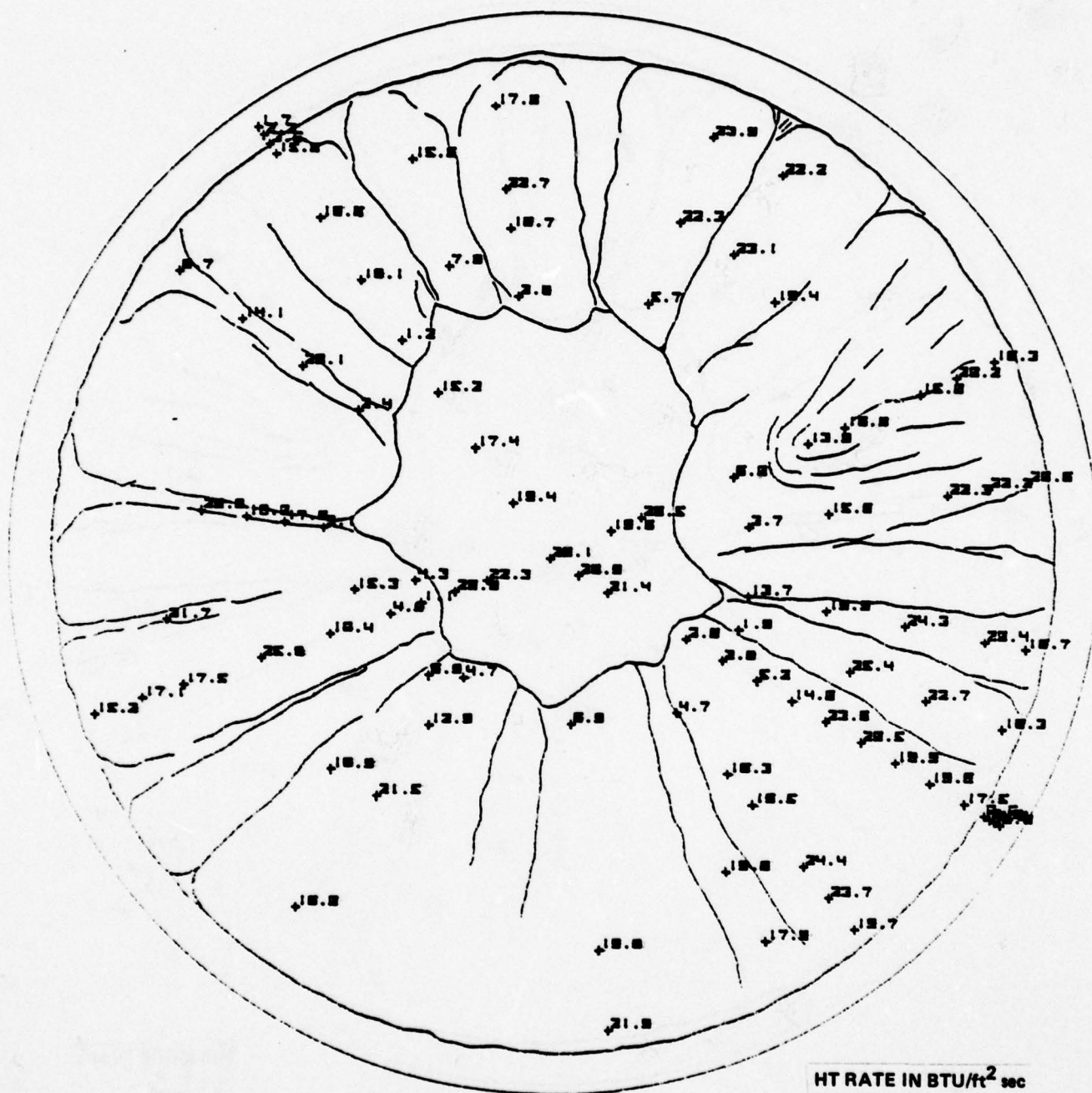
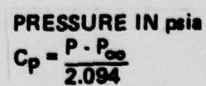
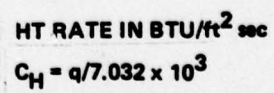


Figure 5-8a HEAT TRANSFER DISTRIBUTION OVER THE NRV CONFIGURATION -  
 $M = 11$ ,  $Re/FT = 1 \times 10^6$ ,  $\alpha = 0^\circ$



5-22





5-23

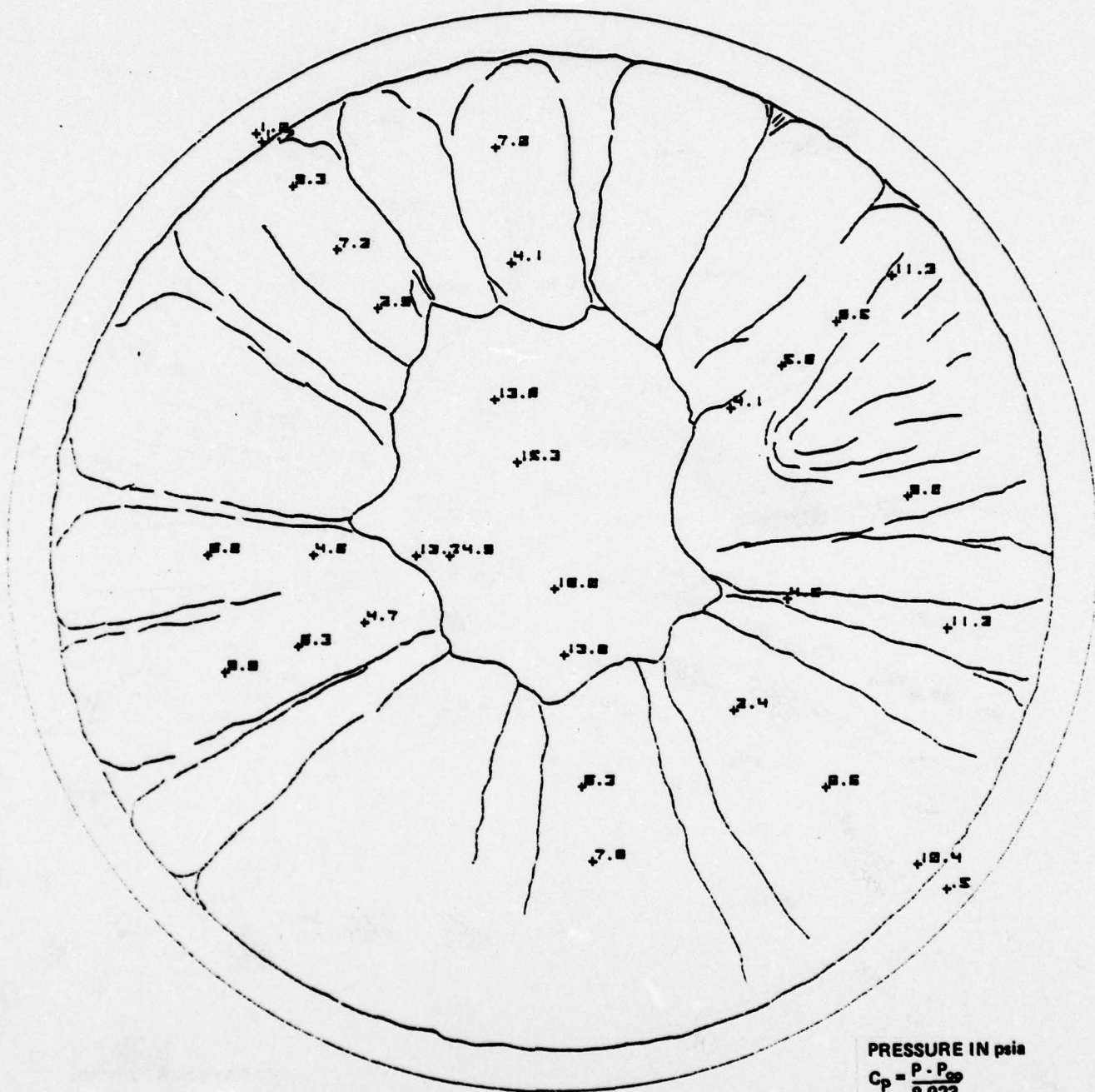


Figure 5-9b PRESSURE DISTRIBUTION OVER THE NRV CONFIGURATION -  
 $M = 11$ ,  $Re/FT = 4.6 \times 10^6$ ,  $\alpha = 0^\circ$

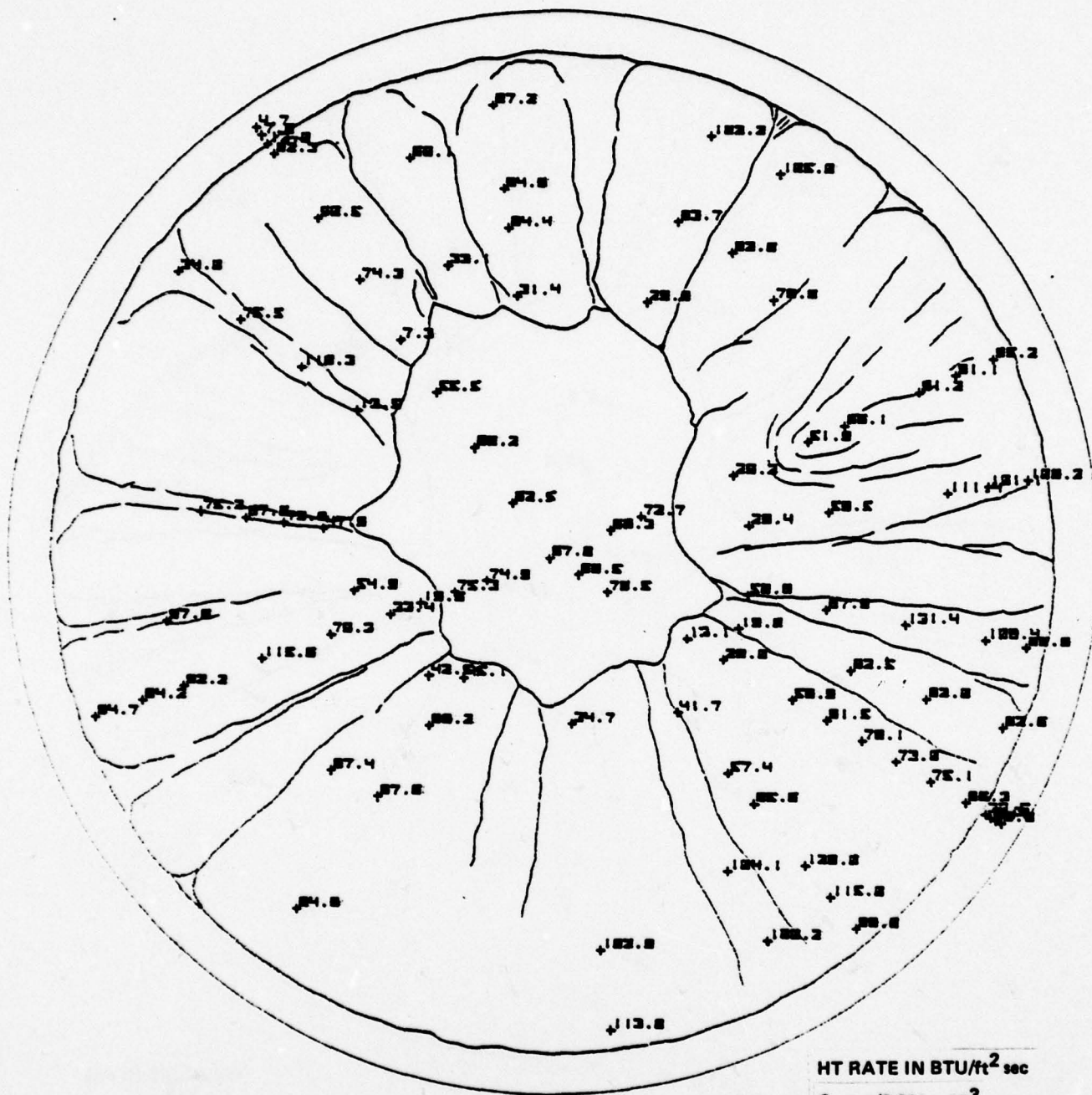


Figure 5-10a HEAT TRANSFER DISTRIBUTION OVER THE NRV CONFIGURATION -  
 $M = 13$ ,  $Re/FT = 4.8 \times 10^6$ ,  $\alpha = 0^\circ$





the effects of Reynolds number on the flow structure and the distribution of heat transfer and pressure over the nose tip. Figures 5-8a and 5-8b show the distribution of heat transfer and pressure over the NRV nose tip for conditions where we have lowered the Reynolds number to  $1 \times 10^6$ . This results in an increase in the size of the separated region and the aft movement of the re-compression regions. It also results in a decrease in pressure rise (relative to the stagnation point pressure) on the conical segment of the nose tip and a dramatic reduction (a factor of 3 relatively to the stagnation point heat transfer) in the heat transfer to the conical frustum. These results underline the importance of conducting experimental studies of the flow over complex indented nose shapes at Reynolds numbers and Mach numbers as close to the flight conditions as possible. Further measurements were made at Mach 11 and 13 with Reynolds numbers of  $5 \times 10^6/\text{ft}$ , which are shown in Figures 5-9 and 5-10, demonstrate that the heat transfer and pressure distribution are sensitive to the position of the boundary layer transition and the flow pattern, which are again controlled by the Mach number and Reynolds number of the free stream. The measurements conducted at a  $2^\circ$  angle of attack showed that the heat transfer to the lips of the grooves are strongly influenced by cross flow.

#### 5.4 CONCLUSIONS

The measurements made in this study clearly demonstrate that the flow field and the distribution of properties on "real" ablated nose shapes differ significantly from the idealized biconic configurations assumed by many analysts. The flow over NRV configuration is intrinsically three-dimensional with regions of embedded separated flows as well as embedded shocks. Experimental studies of the flows over such configurations must be conducted at Reynolds numbers and Mach numbers which come close to duplicating those encountered in flight for meaningful results to be obtained.

## Section 6

### MULTIPLE PARTICLE INDUCED CONVECTIVE HEATING AUGMENTATION TO BLUNT NOSE TIPS

#### 6.1 INTRODUCTION

A critical phenomenon which must be addressed in nose tip design occurs when the reentry vehicle encounters clouds formed from ice crystals or dust particles. In the study of nose tip shaping and integrity in a "weather encounter" we are concerned primarily with two phenomena which give rise to surface recession and increased nose tip heating. Of primary concern is the damage and direct heating which results from the impact of the particles on the nose tip; this subject has, and continues to receive considerable study. However, a second phenomenon, which causes significant heating augmentation, is associated with the increased heating which results when a particle is ejected or rebounds from the nose tip and interacts with the bow shock. This has been recognized as being important in light weather encounter. The studies of Wilkinson, et al.<sup>29</sup>, in conjunction with studies in the dust tunnels at Boeing and AEDC identified this interaction phenomenon by observing a sudden increase in aerodynamic heating for conditions where the dust particles attained sufficient energy to rebound and penetrate the bow shock.

Early photographic studies made in Boeing<sup>28</sup> and Calspan<sup>29</sup> suggested the principal mechanism of heating enhancement was associated with the formation of a vortex system induced by particle shock-bow shock interaction. Photographs showing an interaction of this kind are shown in Figure 6-1. When the momentum of the rebounding particle is such that only a small penetration occurs, the free shear layer, generated at the annulus where the bow shock and particle shock interact, rolls up as the particle is driven back into the shock layer and a ring vortex is formed. This vortex is then convected to the surface as demonstrated by the movie sequence, shown in Figure 6-2, which was taken in the Boeing dust tunnel. While the particle-induced vortex generation is an intriguing phenomenon, which can cause a small increase in nose tip heating, this is but one of a number of enhancement mechanisms as demonstrated in detailed experimental studies by Holden<sup>29</sup>.



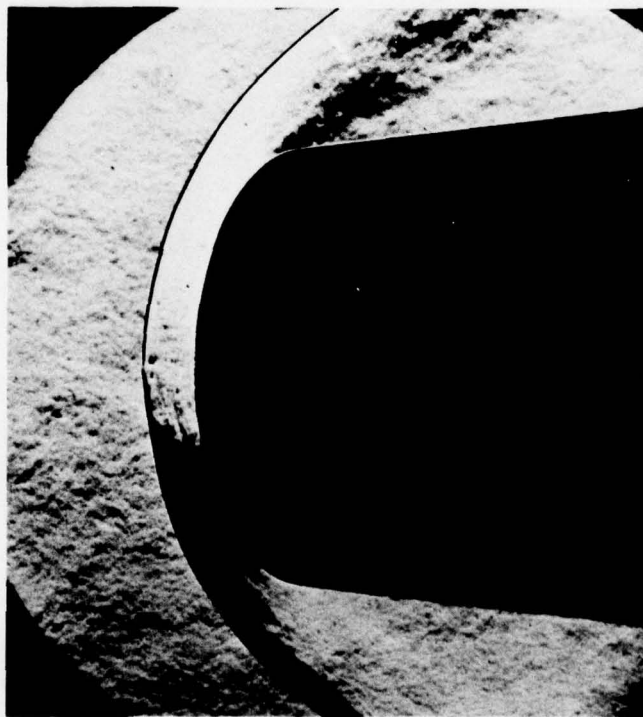


**Figure 6-1a SHOCK-PARTICLE INTERACTION OVER A BLUNT ELLIPSOID**

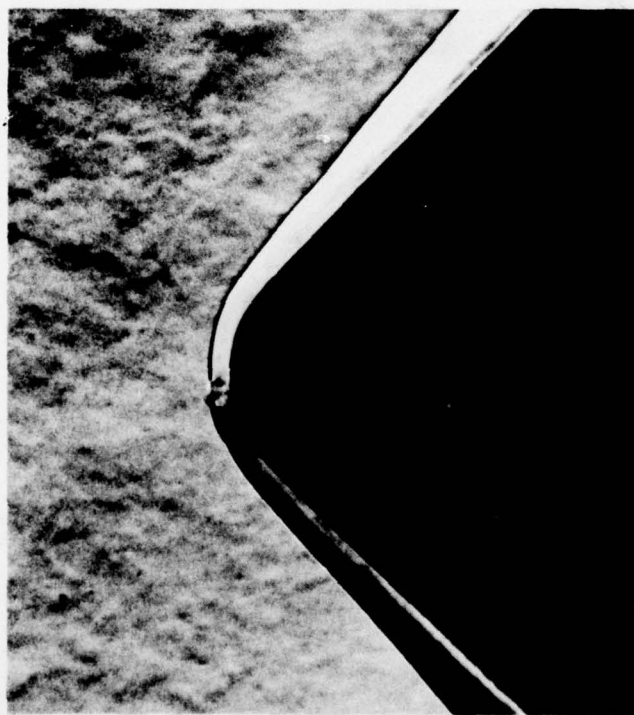
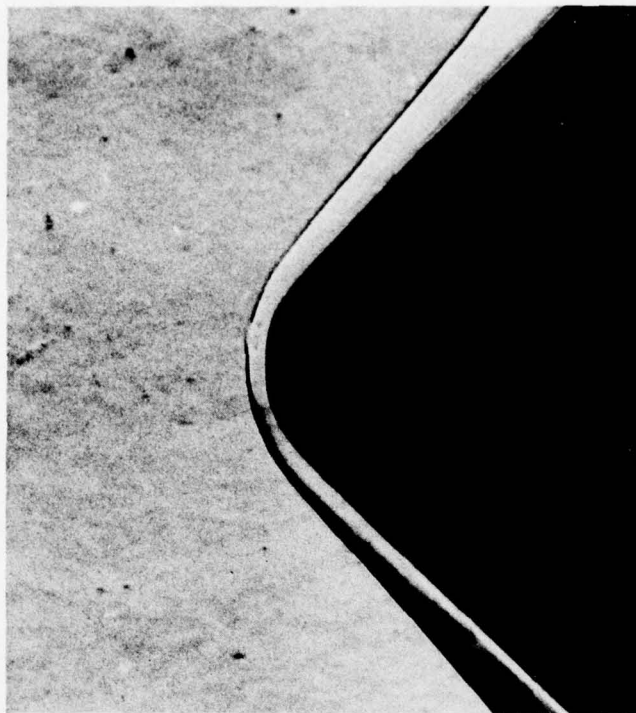
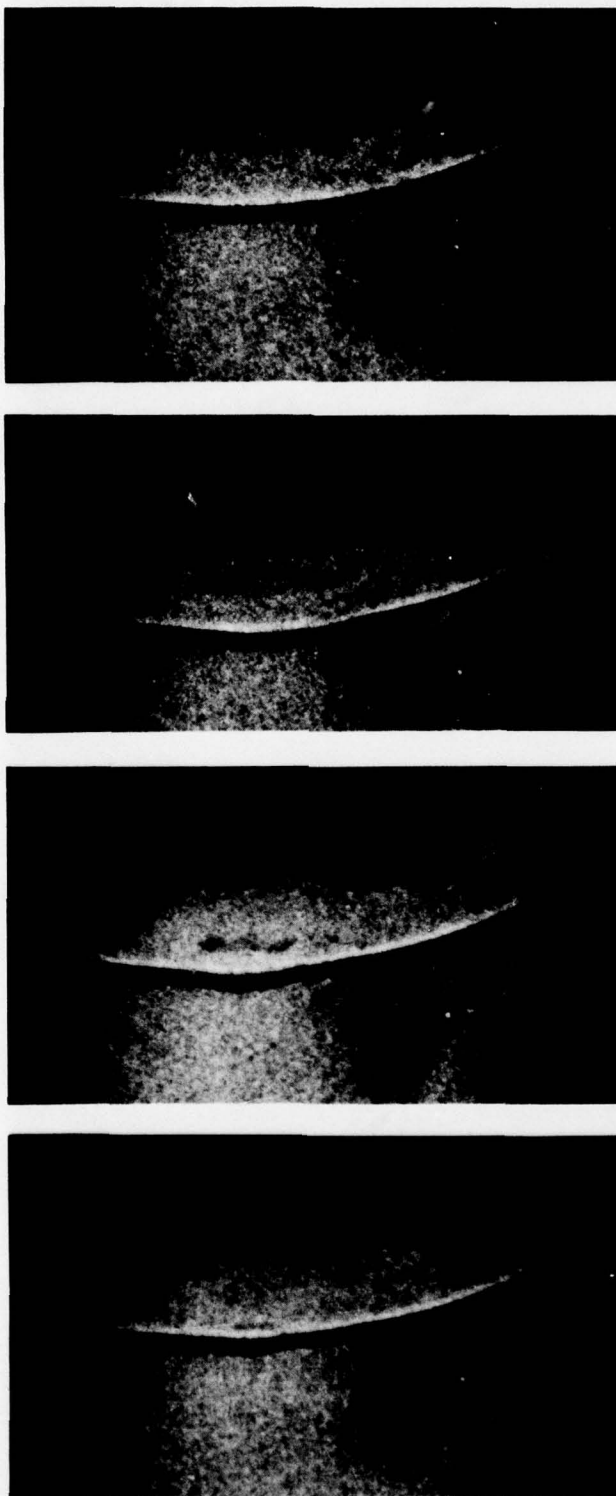


**Figure 6-1b SHOCK-PARTICLE INTERACTION OVER A BLUNTED CONE**



(d)

(c)

(b)

(a)

**Figure 6-2** VORTEX GENERATION RESULTING FROM PARTICLE REBOUND,  
A SEQUENCE TAKEN IN THE BOEING MACH 6 TUNNEL



In the studies conducted by Holden a single small particle (100-800  $\mu$ s) was launched toward the bow shock along the axis of a flat-ended cylinder. It was observed that the wake of particles with insufficient energy to reach the bow shock did not create disturbances of sufficient magnitude to cause a measurable increase in the nose tip heating. Heating augmentation was first observed for particle trajectories which caused a small penetration of the bow shock. A sequence of photographs showing the small dimple which occurs as the particle reaches the bow shock, and the subsequent formation of a toroidal vortex, is shown in Figure 6-3. The shock curvature at the particle and body shock junction creates a shear layer which subsequently rolls up into a vortex ring. This vortex ring is then convected into the shock layer expanding in diameter as it approaches the surface. Heat transfer time histories indicate that a localized heating increase of between 150 and 200 percent occurs at the model surface for a period of just over 1 millisecond, the time taken for the vortex to traverse the shear layer and expand across the model.

When there is a sustained movement of the particle ahead of the bow shock, the interaction between the particle shock and the bow shock enveloping the model creates a shear layer or jet which attaches to the face of the model. The heating rates associated with such interactions have been explored by Holden in spiked body flows<sup>30</sup>, and by Edney<sup>31</sup>, Keyes and Hains<sup>32</sup> in regions of shock interference. The major augmentation occurs when the "Edney Type IV" or "jet" interaction is established over the model. A sequence of photographs showing the development of a region of shock-shock interaction leading to heating augmentation resulting from small penetration is shown in Figure 6-4. The momentum of the particle was just sufficient for the particle to reach 0.7 of the body diameter ahead of the model. As the particle moves ahead of the bow shock, the shock wave associated with the particle and the flow behind it interacts with the original bow shock inducing a shear layer at their point of intersection. This shear layer sweeps radially outward across the face of the model increasing the local heat transfer at its base by as much as a factor of ten. The period of increased heating was just over one millisecond, which is the time it takes for the particle to exit and reenter the shock layer. Pressure levels just above the pitot level were observed at the

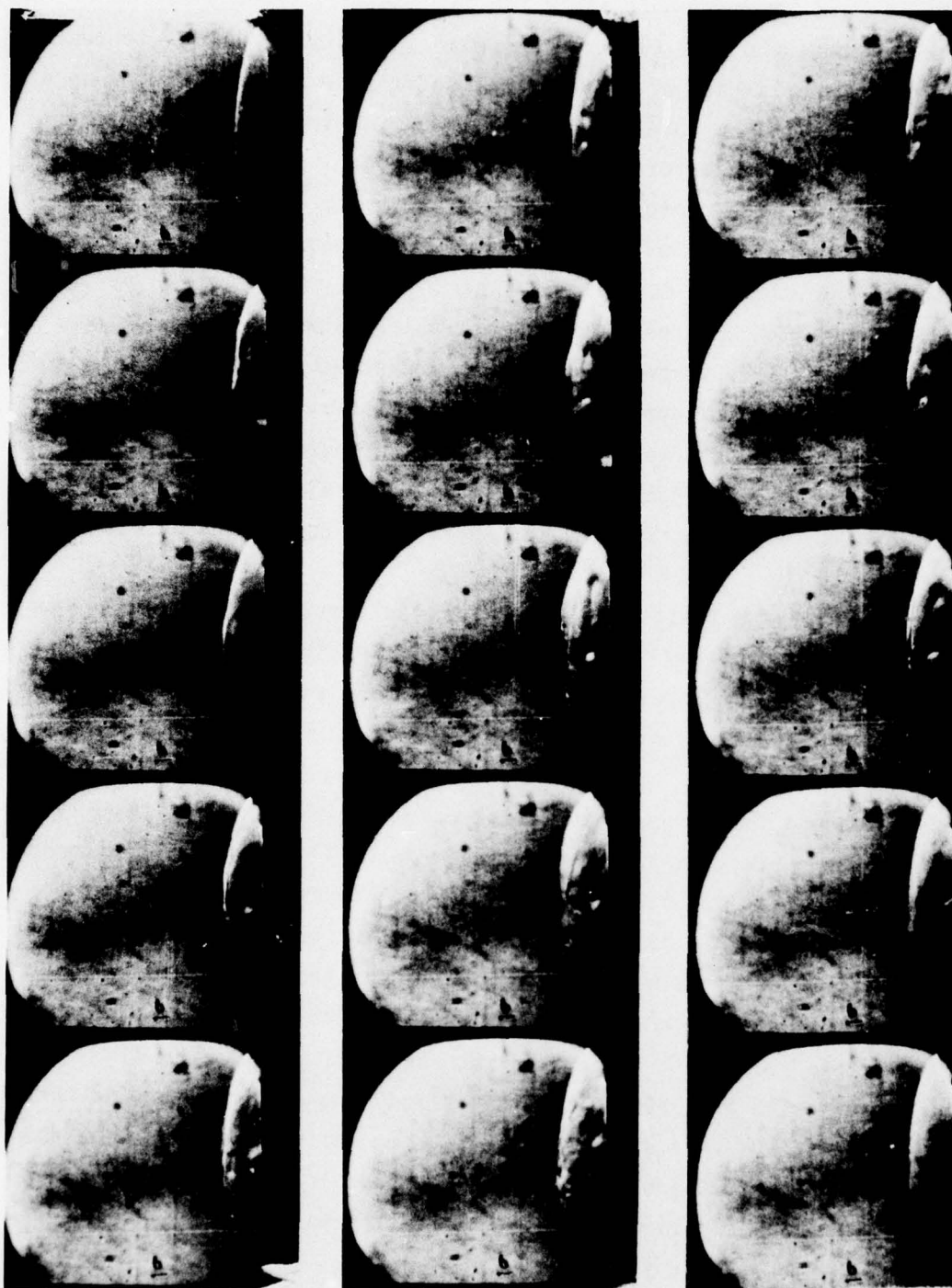


**Figure 6-3** HEATING AUGMENTATION ASSOCIATED WITH PARTICLE-INDUCED RING VORTEX INTERACTION

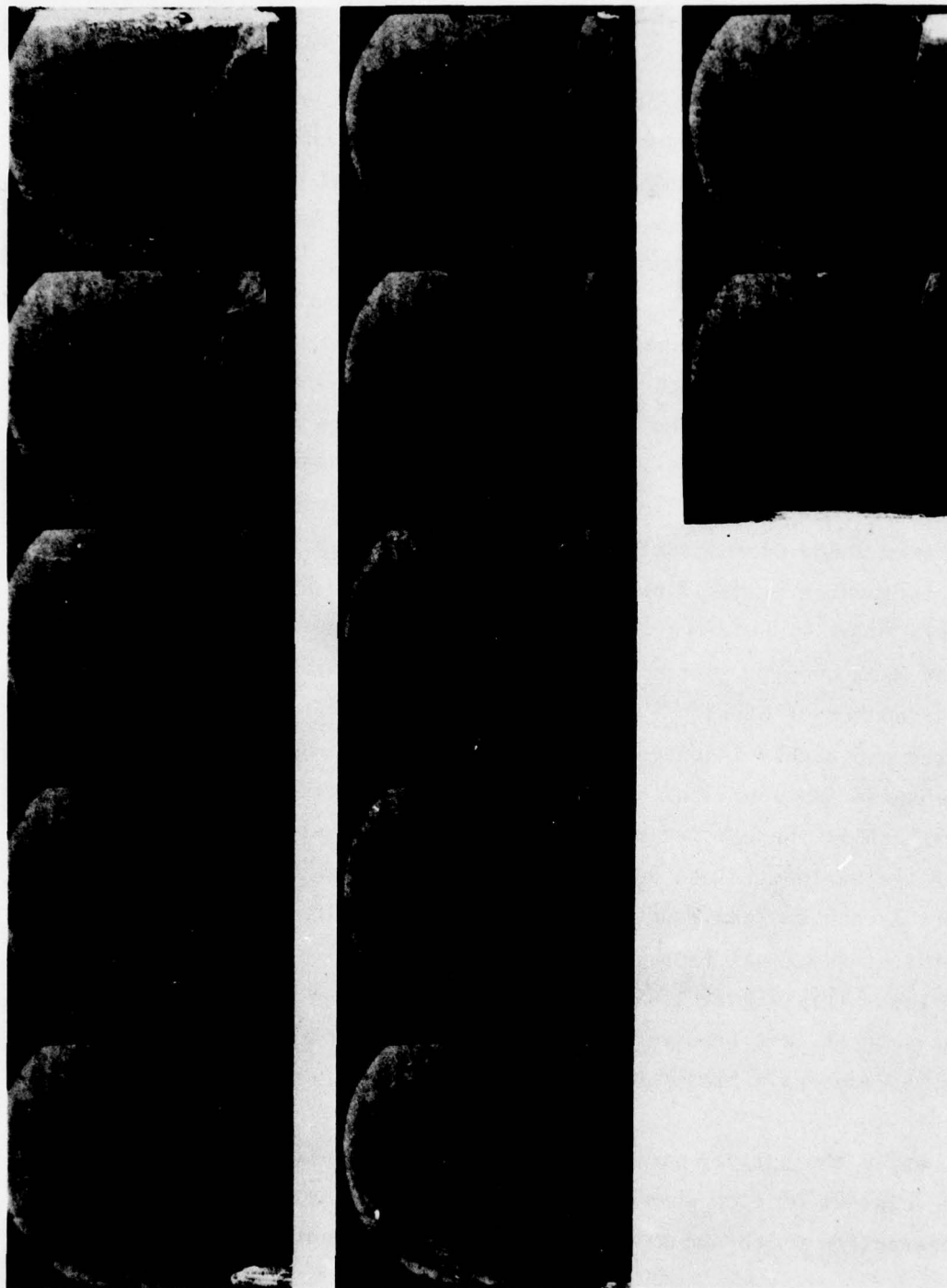


**Figure 6-4 "STABLE" FLOW RESULTING FROM SMALL PENETRATION**



base of the shear layer while those within the annulus corresponded roughly with those achieved by compression through the conical shock associated with the particle.

When the particle is launched with sufficient momentum for it to reach one body diameter ahead of the body, a dramatic change occurs in both the character of the inviscid flow and the pressure and heat transfer on the model surface. The entire flow field begins pulsating as demonstrated in the high speed movie sequences shown in Figures 6-5 and 6-6. These sequences, which were taken at Mach 6.5 and 13, respectively, and at similar Reynolds number conditions, demonstrate considerable similarity in mechanics of oscillation. This oscillation is very similar to pulsating flows observed over spiked bodies<sup>30</sup> or highly indented nose shapes<sup>33</sup> as demonstrated by the movie sequence of these flows shown in Figure 6-7. The occurrence of these massive pulsations appears independent of particle size, and once the particle has reached a body diameter ahead of the surface, the axial motion of the particle is strongly influenced by the flow oscillations. The non-dimensional frequency ( $fD/U_\infty$ ) was found to lie between 0.17 and 0.19 and appeared relatively independent of Mach number, particle velocity size or penetration, and model size. A Strouhal number of between 0.17 and 0.20 typifies the frequencies encountered over spiked and highly indented bodies and reinforces the concept that the basic mechanism is associated with a simple inviscid filling and spilling mechanism. While the heating rates across the model vary with time, the magnitude of the maximum values does not appear sensitive to the exact particle trajectory as can be seen from the measurements made in two runs (shown in Figure 6-8) at identical free stream conditions but with different particle trajectories. This figure illustrates that the edge of the cylinder experiences the largest heat transfer rates, which can exceed the ambient heating levels by as much as a factor of five.

While the earlier studies at Calspan had identified four distinctly different classes of flow phenomena resulting from single particle shock-bow shock interaction which can give rise to heating augmentation, a number of

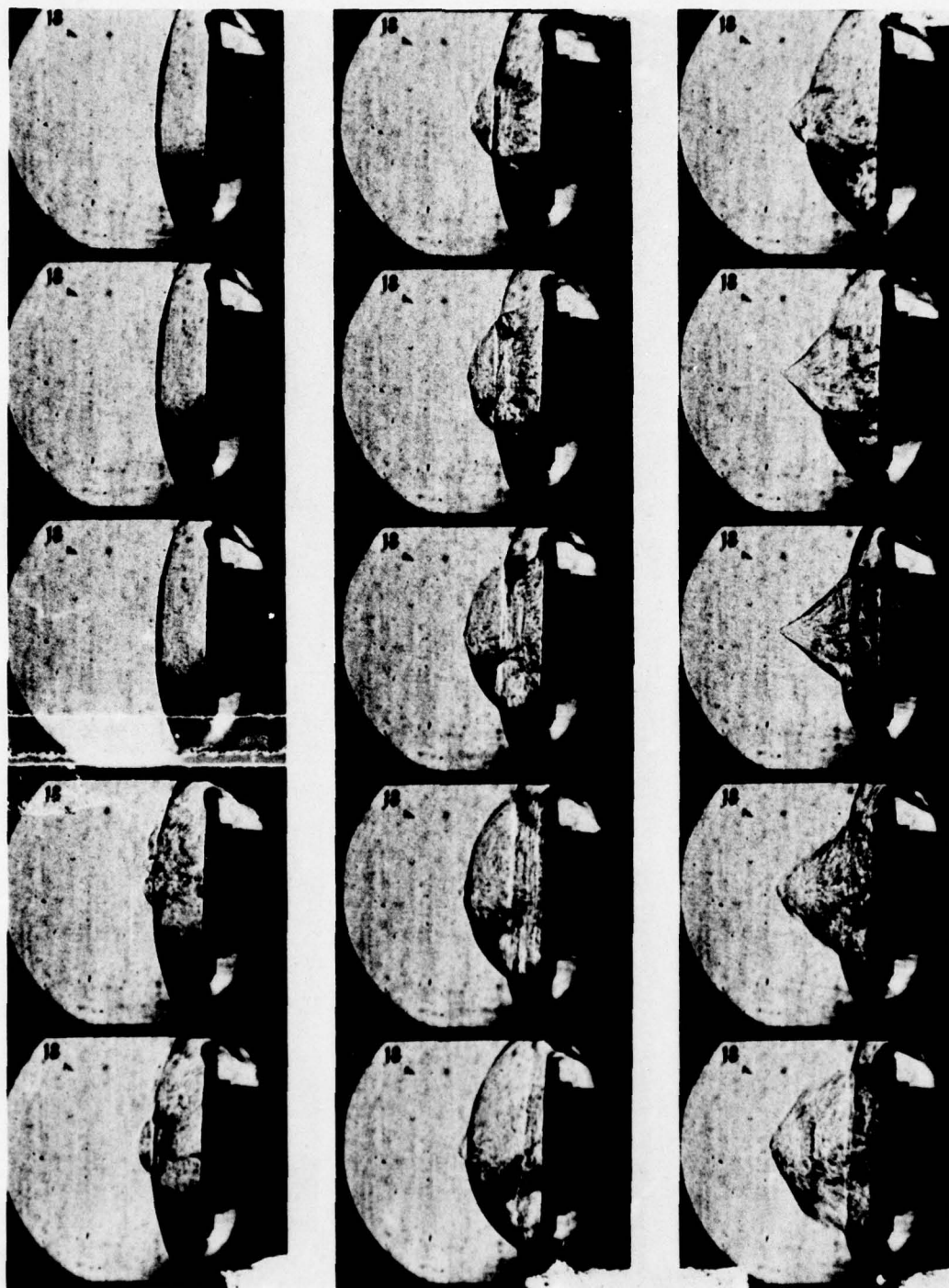


Figure 6-5 PARTICLE-INDUCED LARGE SCALE OSCILLATION (E) (MACH 6.5)

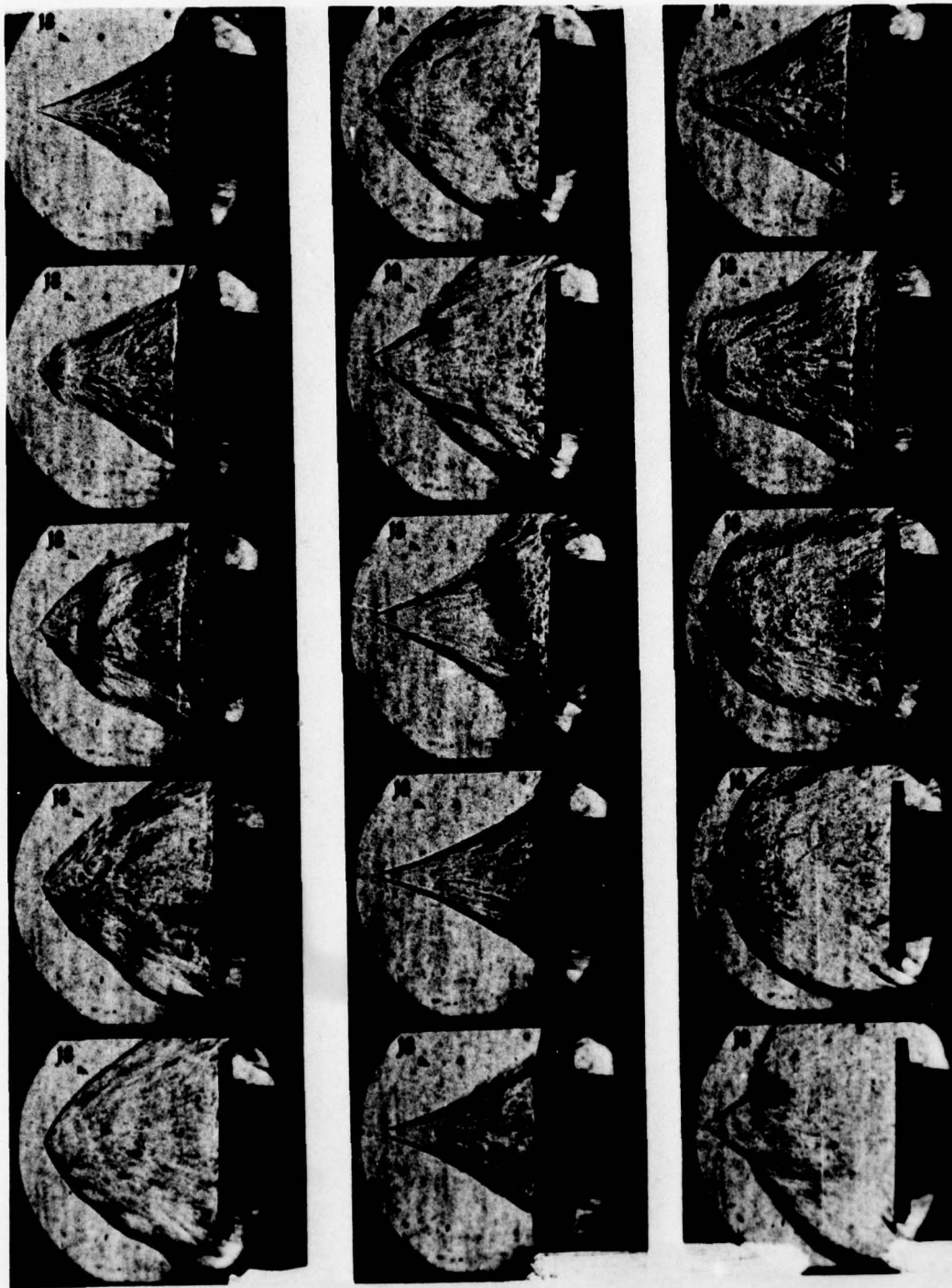
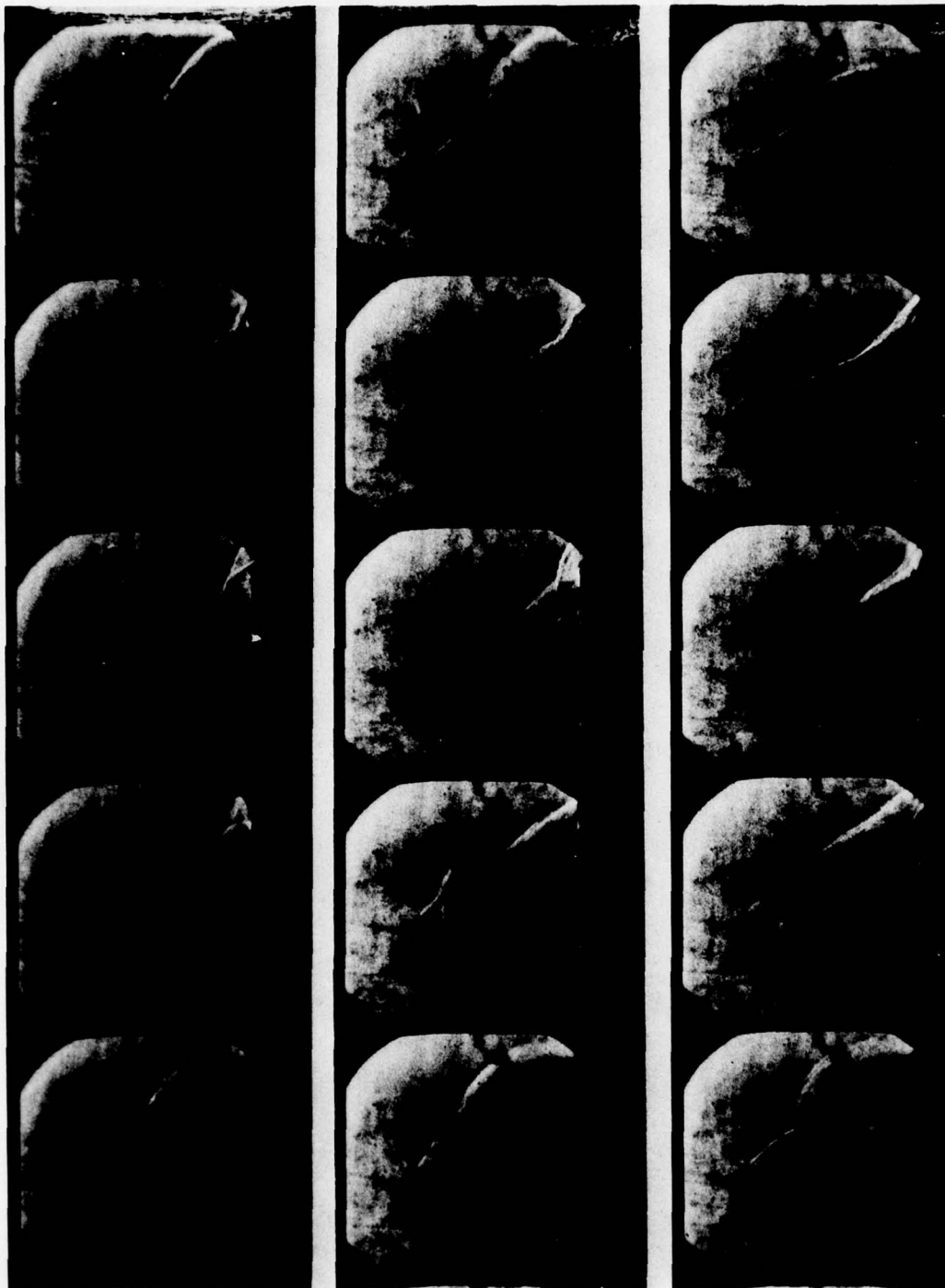


Figure 6-5 (Cont.)





**Figure 6-6** PARTICLE-INDUCED LARGE SCALE OSCILLATION (E) OF FLOW FIELD  
(MACH 13)

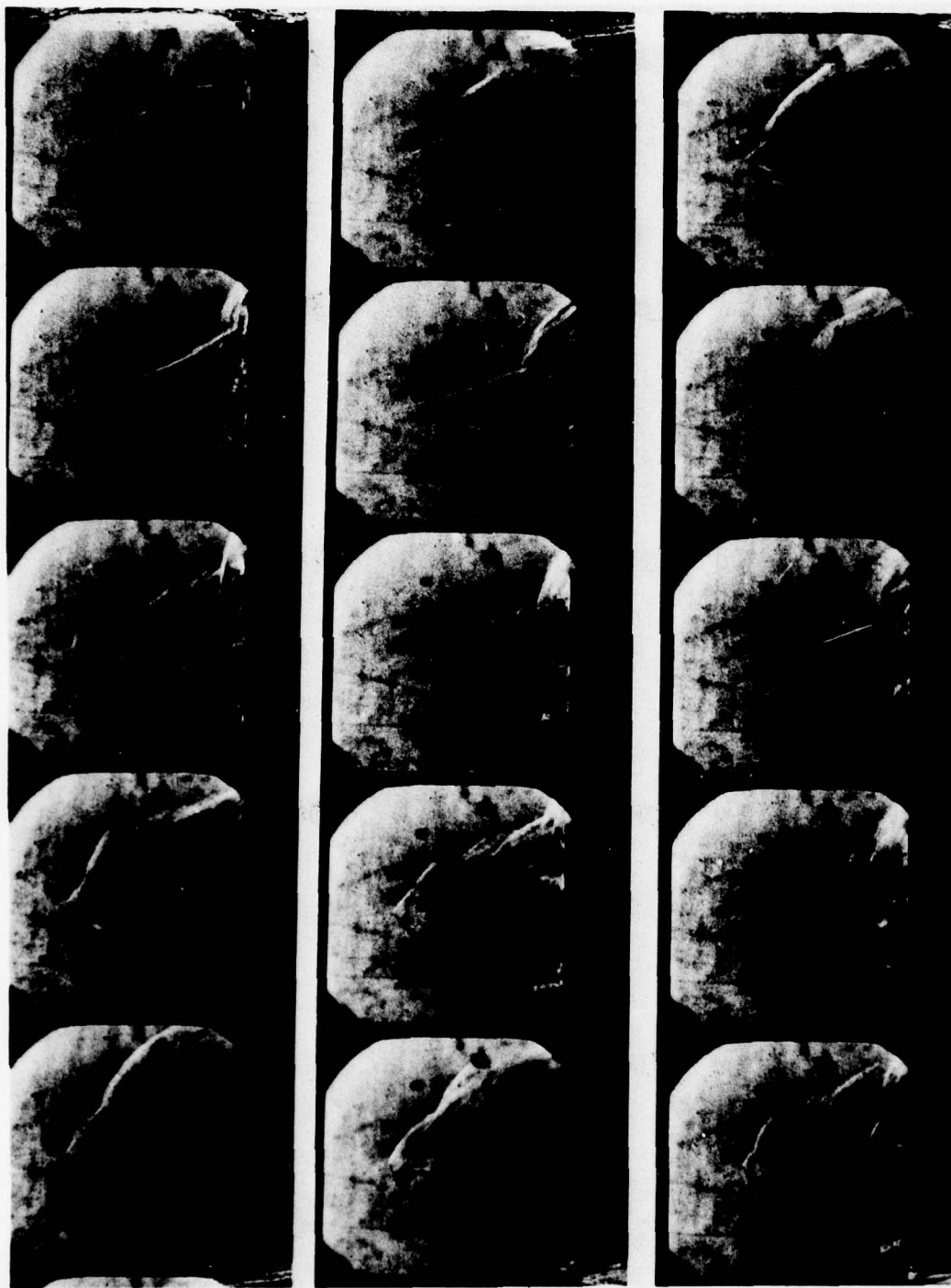


Figure 6-6 (Cont.)

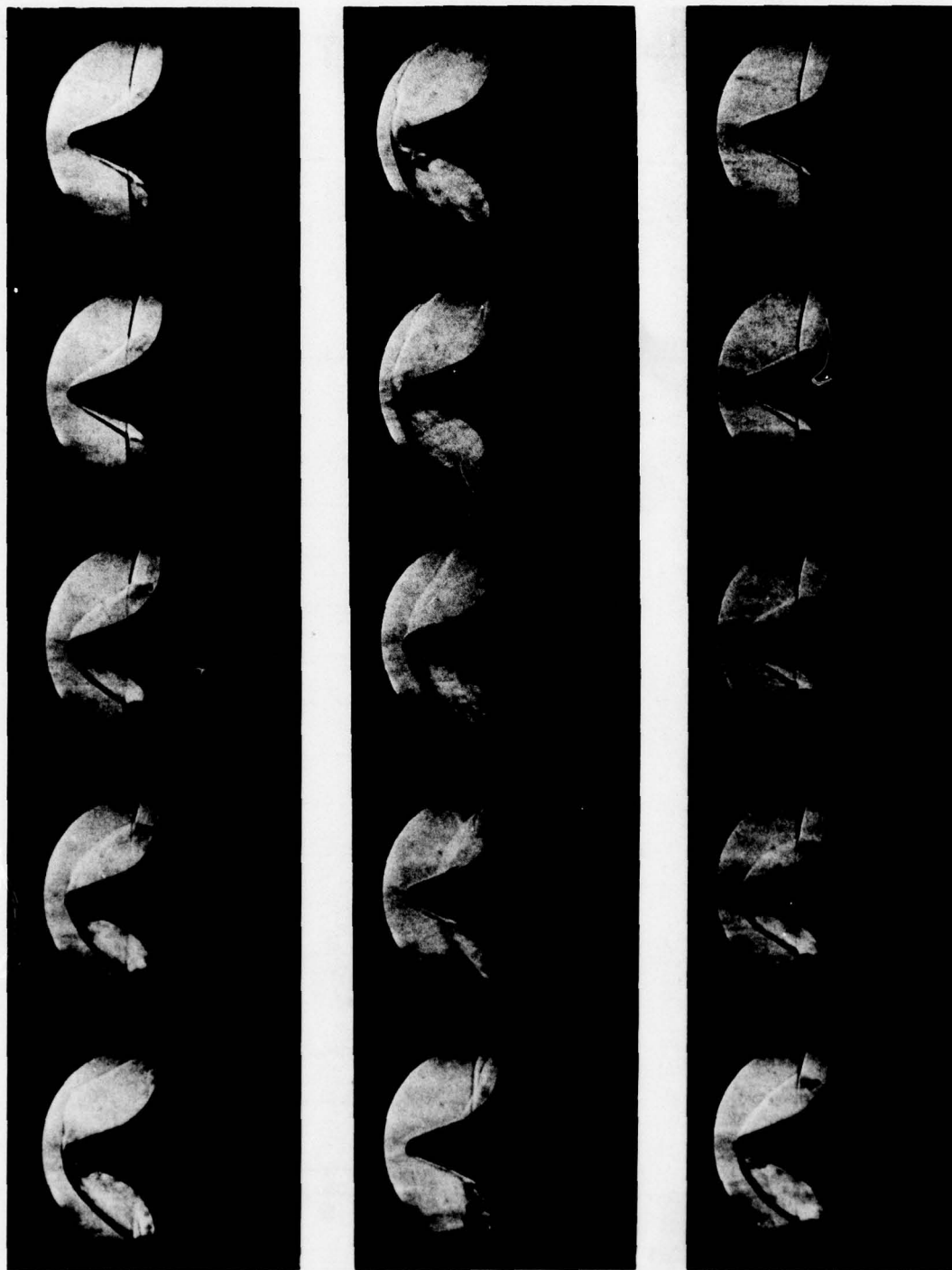


Figure 6-7 "E" OSCILLATION ON AO CONFIGURATION AT ZERO ANGLE OF ATTACK



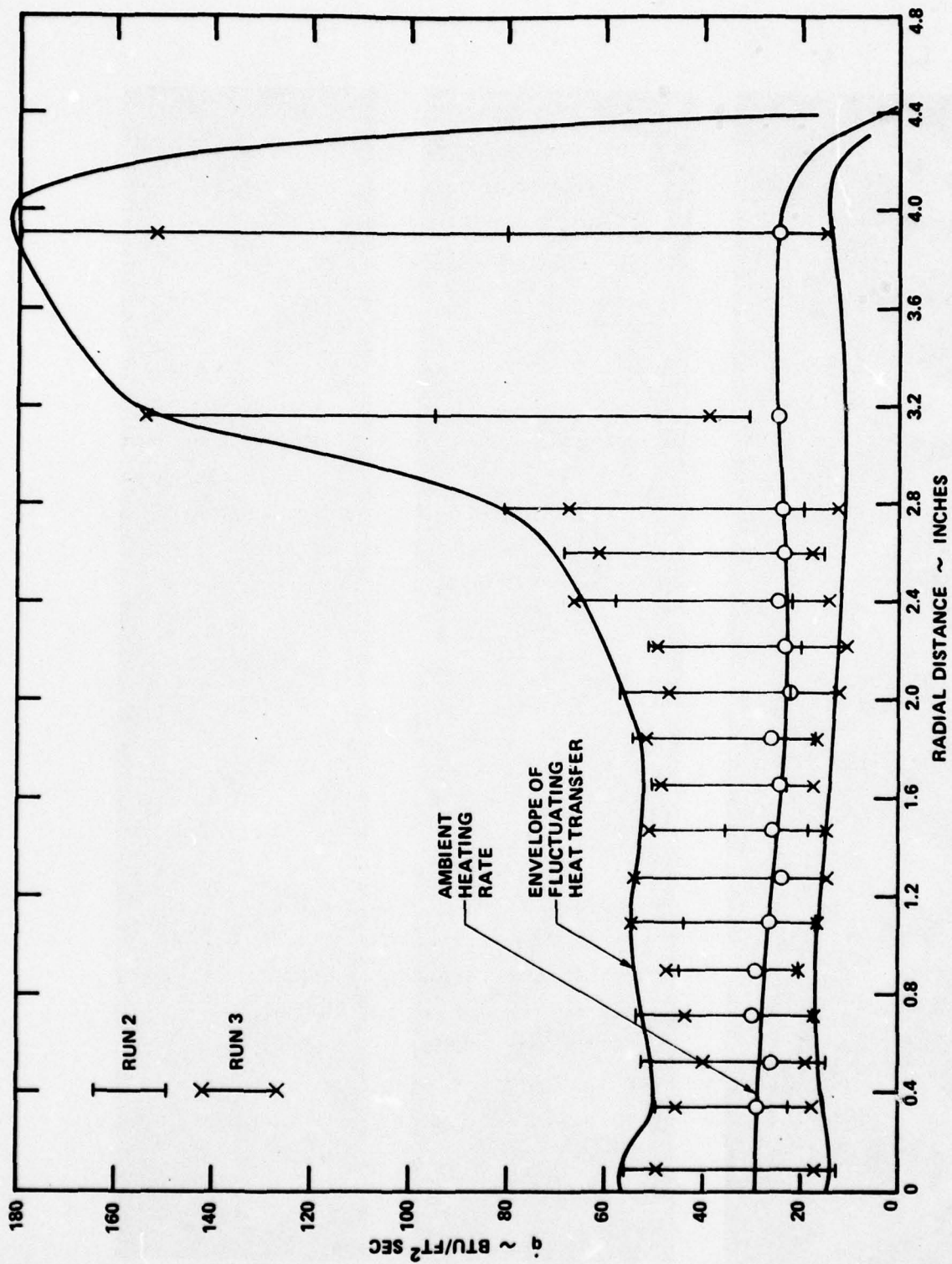


Figure 6-8 HEAT TRANSFER DISTRIBUTION TO MODEL FACE FOR A SINGLE PARTICLE LAUNCH

key questions remained to be addressed. The first question revolved about the importance of the nose shape. Would pulsating flow exist on blunt ablating nose shapes, and how would body shape influence the magnitude of heating augmentation? A second and perhaps more important question was how does the augmentation heating scale with the number of particles in the shock layer and how does multiple particle interactions interact with one another? Finally we wished to know whether nose tip roughness influences the magnitude of the heating augmentation factor.

In the following section, we discuss the objectives of the experimental program and method of approach. The model, particle launching apparatus and instrumentation are then described. The measurements made in the experimental program are described with the aid of high speed Schlieren photography; details of the heat transfer measurements of the flow regimes observed and the heating augmentation with which they are associated with are discussed. Conclusions from this study are then presented together with recommendations for future work.

## 6.2 EXPERIMENTAL PROGRAM

### 6.2.1 Program Objectives

The objective of this experimental program was to investigate the effects of nose tip shape, multiple particle interactions and nose tip roughness on the fluid mechanical phenomena associated with particle-induced convective heating augmentation. We wished to examine particle shock-bow shock interaction on configurations similar to the blunt ablated nose shape rather than the flat-ended cylinder used in our earlier studies. We were particularly interested in determining whether major pulsations of the shock layer were also obtained on configurations with rounded shoulders. The main objective of the present program was to examine the mechanisms of heating enhancement for multiple particle shock-bow shock interactions. Understanding how multiple particles interacted and induced increased convective heating was

our principal concern. Lastly, we wished to determine if nose tip roughness modified or changed the mechanism of particle augmented heating.

#### 6.2.2 Model and Instrumentation

For this program, as in the earlier Calspan study described in Section 1, we choose to launch the particles from the model surface rather than by adding particles to the free stream as is done in dust tunnels. We used the impact particle launcher developed for this purpose in the earlier AFOSR program<sup>33</sup>. A new model was also constructed for these studies, a model which is more closely representative of the geometry of a "laminar blunt" nose tip configuration.

The model used in the present experimental studies is shown in Figure 6-9. This model, which is 12-inches in diameter is made up of a flat center section, 6 inches in diameter, which contains positions for five particle launchers and is highly instrumented with heat transfer and pressure gages. An annular ring with a radius of curvature of 3-inches in the stream-wise direction surrounds the center section and is also highly instrumented with high frequency pressure and heat transfer gages.

As can be seen from Figure 6-9 the model contained over 100 transducers which were concentrated primarily on two perpendicular axis which bound a quadrant of the model. Our object was to trace the three-dimensional characteristics of the asymmetric disturbances. Flush mounted piezoelectric pressure gages were installed on the surface of the model, and both the pressure and heat transfer gages had a frequency response which exceeded 300 kHz, well above that required to follow the disturbances resulting from particle shock-bow shock interaction. High speed Schlieren cinematography was used to obtain photographs of the flow field at intervals of approximately 200 microseconds.

In this program, we employed three particle launchers mounted along a



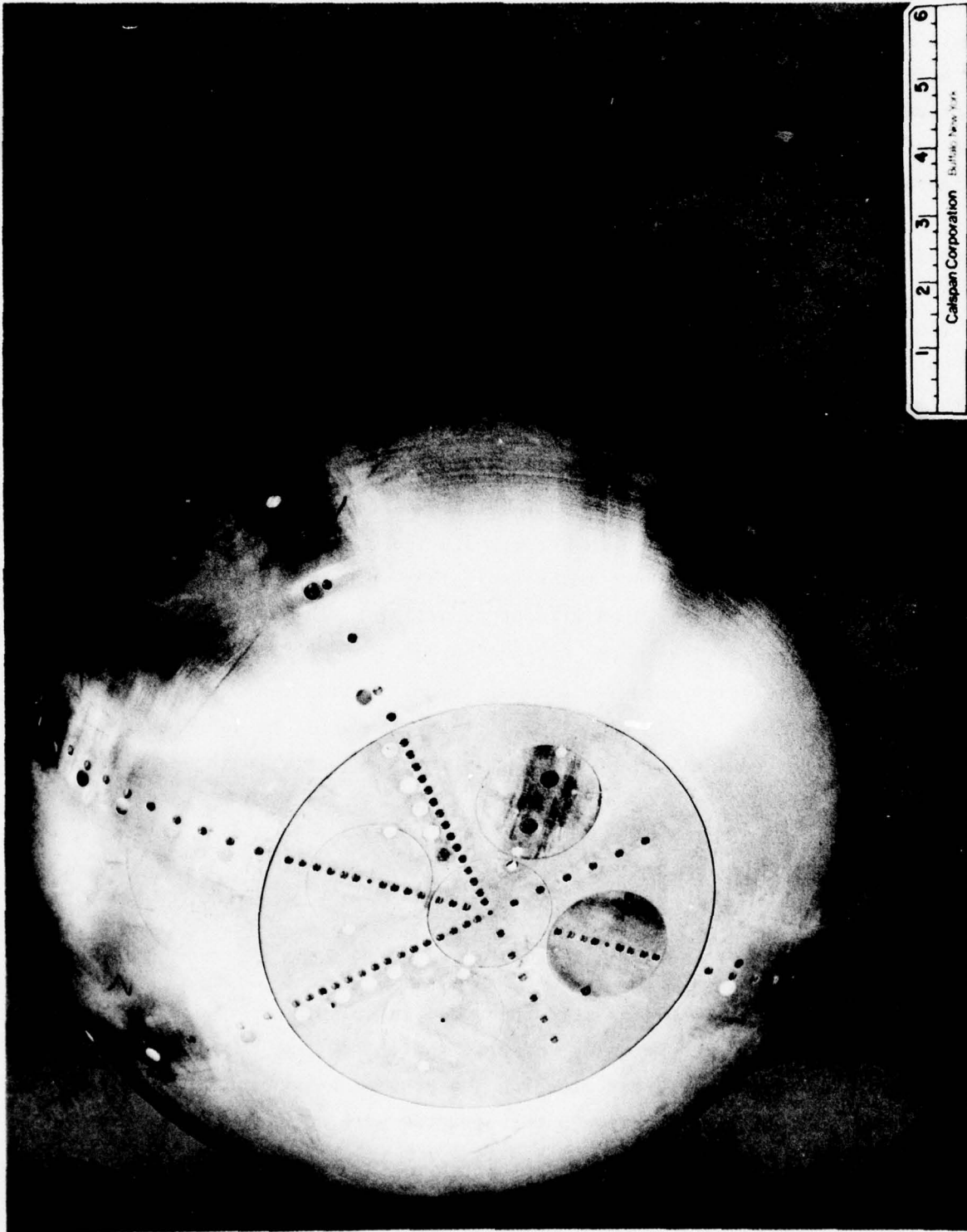


Figure 6-9 PARTICLE LAUNCH MODEL EQUIPPED WITH THREE PARTICLE LAUNCHERS,  
105 HEAT TRANSFER GAGES, 27 PRESSURE GAGES AND 4 SKIN FRICTION GAGES

model diameter in the center section of the model (see Figure 6-9) and positioned on the vertical plane. Each launcher assembly was mounted in a seismic mass, which in turn was supported within the main frame of the model on a soft rubber suspension system. Thus, the instrumented section was effectively isolated from the mechanical disturbances generated when the launchers were activated. A drawing of the impact particle launcher is shown in Figure 6-10. In this design we employ two pistons, the second of which has the launcher "cue" mounted on the center of its face. The particle to be launched is placed in contact with the face of the cue as shown in Figure 6-10. When helium is released by a quick-action valve, the driver piston is driven down the launch tube and its motion is monitored with photodiodes activated by LEDs mounted along the internal surface of the launch tube. When the driver piston strikes the second piston, which rests in contact with a rubber energy absorption system, an elastic compression wave is propagated down and then is reflected from the face of this cue. The particle is launched through a small cavity in the surface of the model, which is sealed by the cue as the second piston is driven into the rubber stops. The disturbance induced by the mechanism of launch was shown to be negligible in measurements made when the launch mechanism was activated without a particle. The velocity of the second piston was measured with the LED-photodiode system and correlated with the particle velocity measured with an inductive transducer placed in the exit plane of the model. Particles from 30 to 800  $\mu\text{m}$  could be launched from the surface of the model simultaneously or in a phased array, with velocities from 50 to 300 ft/sec.

### 6.3 RESULTS AND DISCUSSION

#### 6.3.1 Test Conditions

The experimental studies were conducted in Calspan's 48"-Shock Tunnel at a Mach number of 6.5 for Reynolds numbers from  $1 \times 10^6$  to  $30 \times 10^6$ . A tabulation of the test conditions at which the program was conducted is given in Table 6-1. The initial studies in this program were conducted to examine

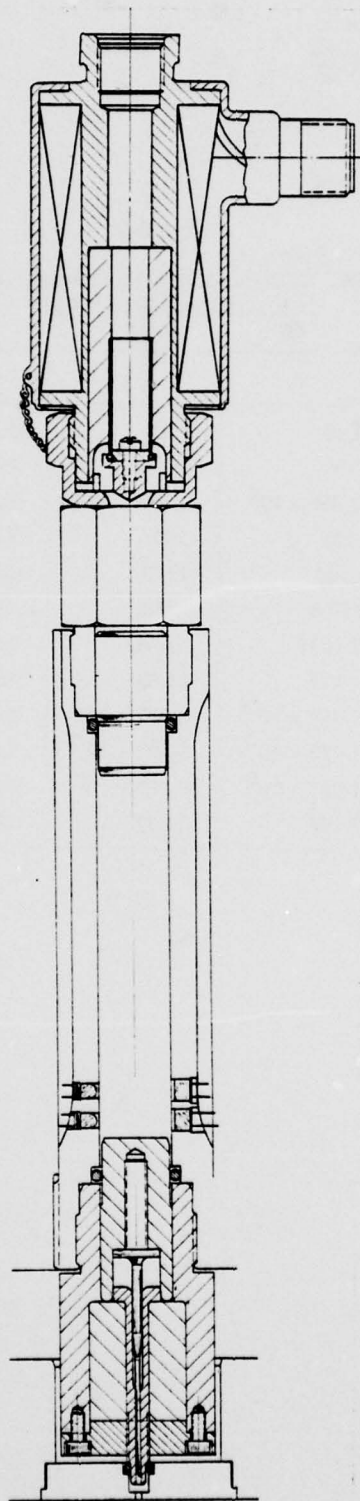


Figure 6-10 IMPACT PARTICLE LAUNCHER



Table 6-1  
TEST CONDITIONS FOR PARTICLE  
LAUNCH PROGRAM

T.C.	A	B	C
Mi	2.29	2.23	2.15
P <sub>o</sub>	354	968.3	2178
H <sub>o</sub>	$9.709 \times 10^6$	$9.190 \times 10^6$	$8.752 \times 10^6$
M <sub>∞</sub>	6.38	6.45	6.55
U <sub>∞</sub>	4160	4053	3961
T <sub>∞</sub>	177.0	164.2	152.1
P <sub>∞</sub>	0.1548	0.4062	0.8688
Q <sub>∞</sub>	4.411	11.84	26.12
ρ <sub>∞</sub>	$7.340 \times 10^{-5}$	$2.077 \times 10^{-4}$	$4.794 \times 10^{-4}$
μ <sub>∞</sub>	$1.478 \times 10^{-7}$	$1.373 \times 10^{-7}$	$1.275 \times 10^{-7}$
Re/FT	$1.067 \times 10^6$	$6.130 \times 10^6$	$1.490 \times 10^7$
P <sub>o</sub> '	8.189	21.97	48.45

the interactions occurring for a single particle launched along the axis of the model. These studies were followed by measurements with three particles launched simultaneously and in phased arrays. Measurements were then made with dust particles launched into the shock layer for comparison with studies conducted on the ballistic range. Finally, measurements were made of heating enhancement to a rough model, where 5 mil grit was bonded to the face of the model to achieve sand-grain roughness.

#### 6.3.2 Studies of Single Particle Bow Shock Interaction

These initial set of studies were performed to determine whether the gross flow pulsations observed in our earlier studies with a flat-ended cylinder model would occur on configurations with rounded shoulder geometries. As in our earlier investigation, we launched a single particle along the axis of the model, with a range of velocities to achieve different shock penetrations. Again we found that unless the particle reached the bow shock, the heating augmentation resulting from the wake of the particle on the shock layer was negligible (see Figure 6-11). For small penetrations, a ring vortex was formed and a measurable increase ( $q_p/q_o = 1.5$ ) was observed on the surface heat transfer to the model as the vortex part over it. However, our major interest was centered on observing the particle-bow shock interaction which occurred when the particle penetrated a body radius beyond the model surface. Figure 6-12 shows a photographic sequence of the interactions which result when the particle penetrates a body radius beyond the bow shock. In this sequence, particle penetration occurs 3 milliseconds after the flow over the model has been established. During the initial movement of the particle ahead of the bow shock, the particle shock pulsates independently of the bow shock as the annular shear layer, which is formed by particle shock-shock interaction, is driven to the shoulder of the model. When the shear layer reaches the shoulder and the entrapped gas escapes around the shoulder of the model, the interaction partially collapses and a gross shock layer pulsation occurs as the sequence of events is repeated. This pulsation is observed to subside as the particle falls below the model axis and the flow becomes asymmetric. However, as found in our earlier studies we observed a large increase in heat transfer as the shear layer sweeps across the face of

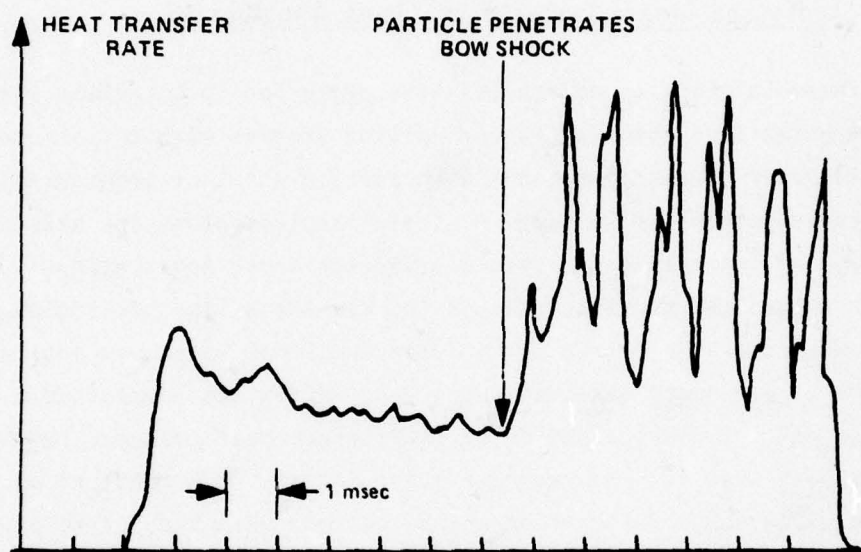
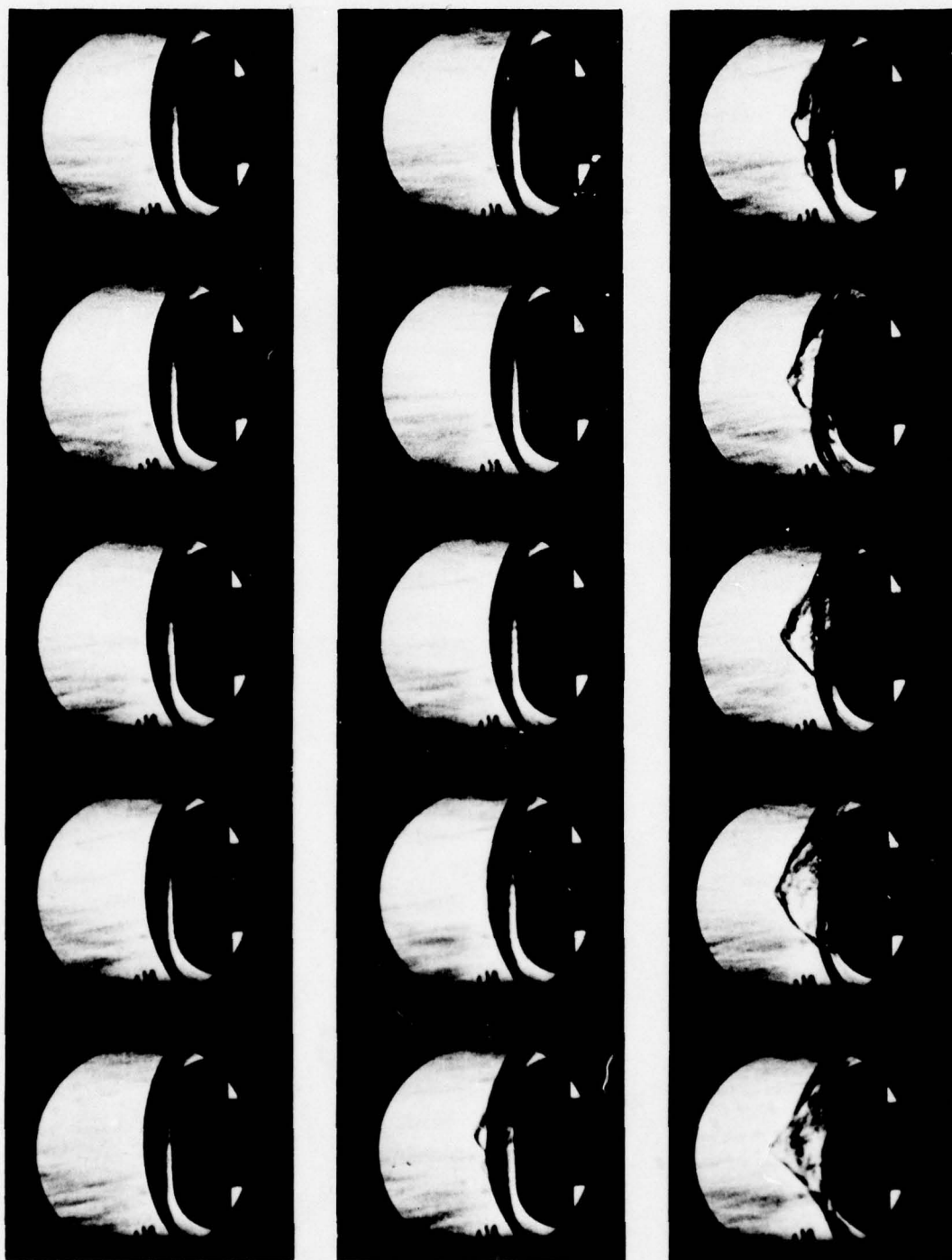


Figure 6-11 TYPICAL HEAT TRANSFER RECORD FROM THIN FILM GAGES





**Figure 6-12 PHOTOGRAPHIC SEQUENCE FROM SINGLE PARTICLE LAUNCH**

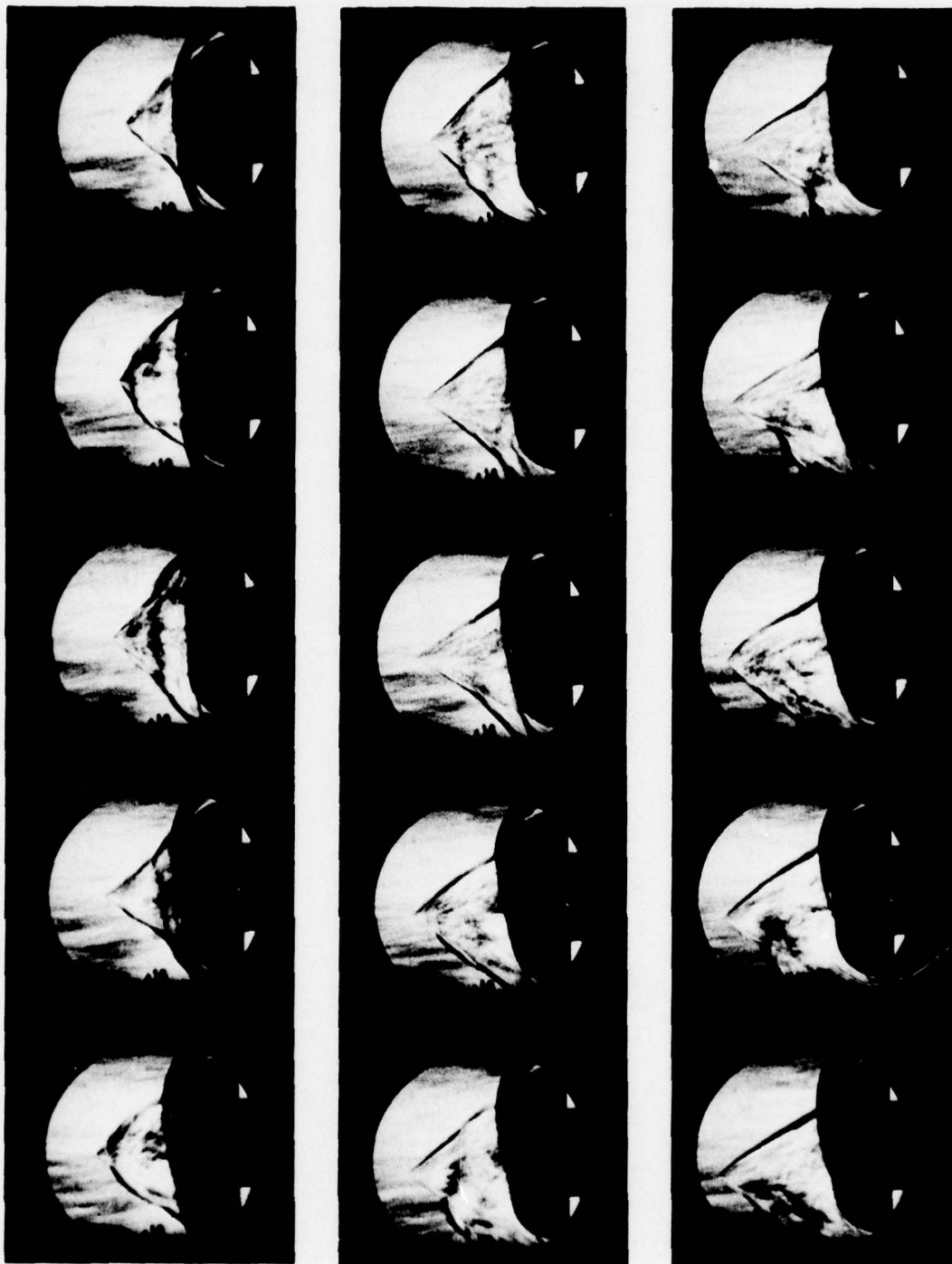


Figure 6-12 (Cont.)

the model. Clearly gross pulsations of the shock layer can exist on blunt nose shape irrespective of their geometry in the shoulder region.

As in our earlier studies<sup>33</sup>, we observed the largest increase in particle-induced augmented heating in the outer region of the model (see Figure 6-8) where the shear layer formed by particle shock-bow shock interaction sweeps directly over the model face. Here the heat transfer rate can increase by an order of magnitude for an initially laminar boundary layer. The heat transfer to the center region of the model which immersed in the turbulent recirculating region varies from a value just less than the ambient heating level to approximately double this value as the particle induces pulsating flow over the nose tip. For this interaction, we measure a time-averaged increase of approximately 300 percent relative to the ambient condition.

#### 6.3.3 Multiple Particle Interactions

A major objective of the present study was to examine the flow field and the enhancement heating which result when a number of particles simultaneously penetrate the bow shock. Here we set out to determine whether the flow about one particle would dominate the interaction or whether flow pulsations would occur about each of the particles. Basically we wished to investigate the mechanism which controlled how augmentation heating scaled with the number of particles in the shock layer.

In these studies, three 30  $\mu\text{m}$  particles were launched simultaneously from launchers mounted in the model for the vertical plane. A sequence of photographs from run 10 is shown in Figure 6-13. Here the particle propelled from the launcher mounted above the centerline penetrates the bow shock first, inducing particle shock-bow shock interaction which results in a pulsation about this particle. This pulsation can be observed in the following twenty five frames. A similar pulsation can be observed to begin when the particle launched below the centerline interacts with the bow shock. The pulsating flow occurs alternately about the particles in this shock layer, and despite the fact that these





**Figure 6-13**    **MULTIPLE PARTICLE INTERACTIONS OVER THE BLUNT NOSE TIP**



Figure 6-13 (Cont.)

particles were, launched with the same velocity as the single particle described earlier, far less penetration is observed. In fact, the mechanism of pulsation observed in the multiple particle studies appears to be intrinsically different from the gross pulsation described for the single particle. For not only is the frequency of the pulsation significantly higher, it appears that the instability resulting from particle shock bow shock interaction does not involve the attachment of the annular shear layer to the model surface and its subsequent movement to the shoulder. Rather, here it appears to be a more localized mechanism. The augmentation heating associated with multiple particle interactions is significantly larger than observed for a single particle because a larger percentage of the area of the nose tip is exposed to the direct shear layer heating. The measured distribution of heat transfer to the surface of the model immersed in a multiple particle interaction is shown in Figure 6-14. In contrast to the heating experienced for a single particle interaction, the maximum heating occurs close to the axis of the model and the peak heating is experienced for a greater percentage of the time. Our studies suggest that as long as the major structure associated with the bow shock remains intact, then increasing the number of particles in the shock layer will cause an increase in heating to the nose tip. However, if the particles become so numerous that the bow shock is destroyed, then the heat transfer may decrease because the nose tip is immersed in the wake of an effectively new body. To investigate the heating rates developed when a large number of particles were launched into the shock layer, we performed studies with the particle launchers loaded with dust particles.

#### 6.3.4 Dust Particle - Shock Layer Interaction for Rough Wall Conditions

To study the heating enhancement when a large number of small particles were present in the shock layer over 30, 12  $\mu\text{m}$  particles were launched into the shock layer from three guns. Because of their small size ( $d = 4 \times 10^{-3}$ ), these particles achieved little penetration and remained in the shock layer for less than 1 millisecond. A sequence of Schlieren photographs shows the dust-shock layer interaction (see Figure 6-15). Because of the small particle residence time in the shock layer, we do not observe the large number of particle



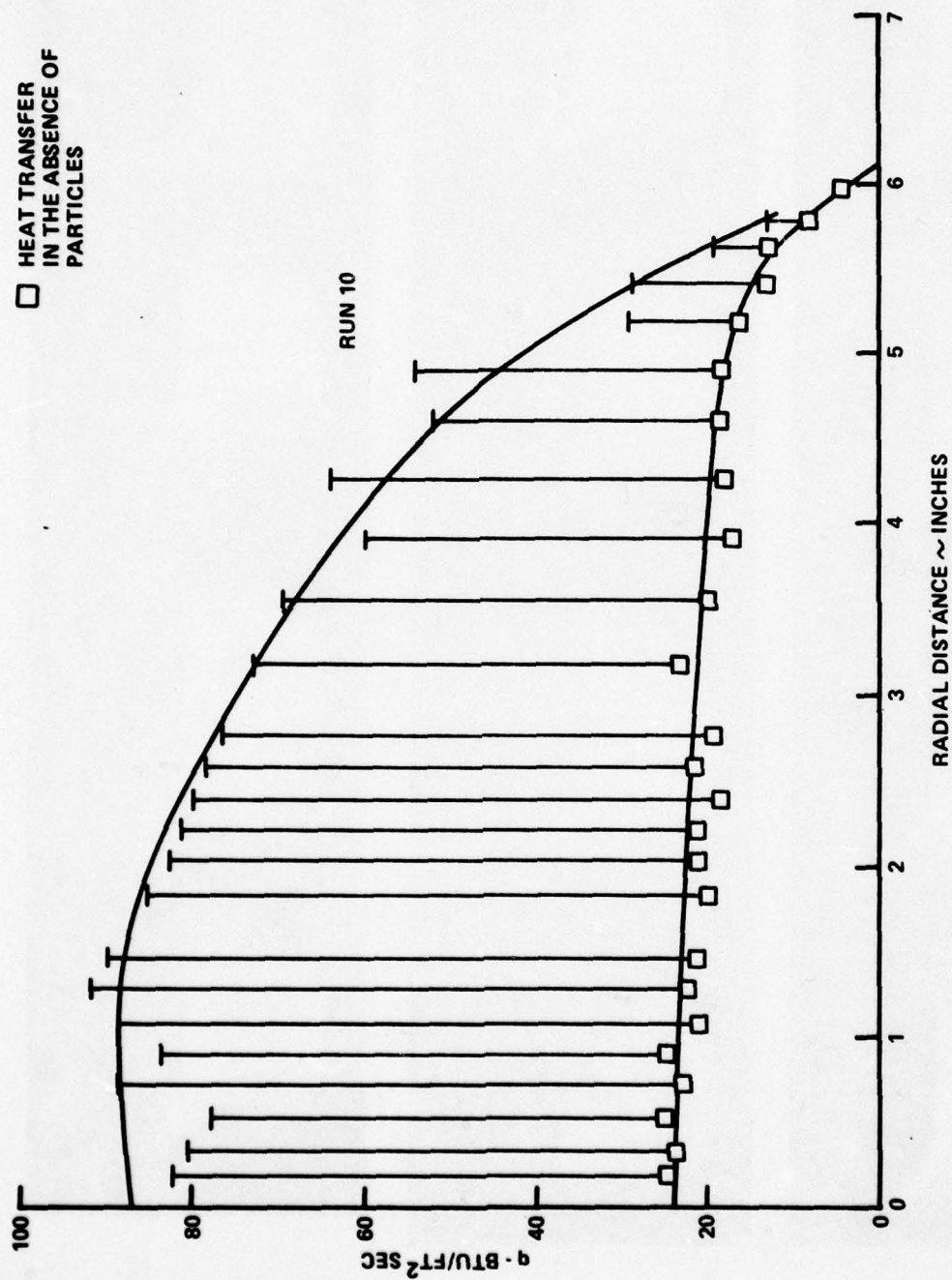
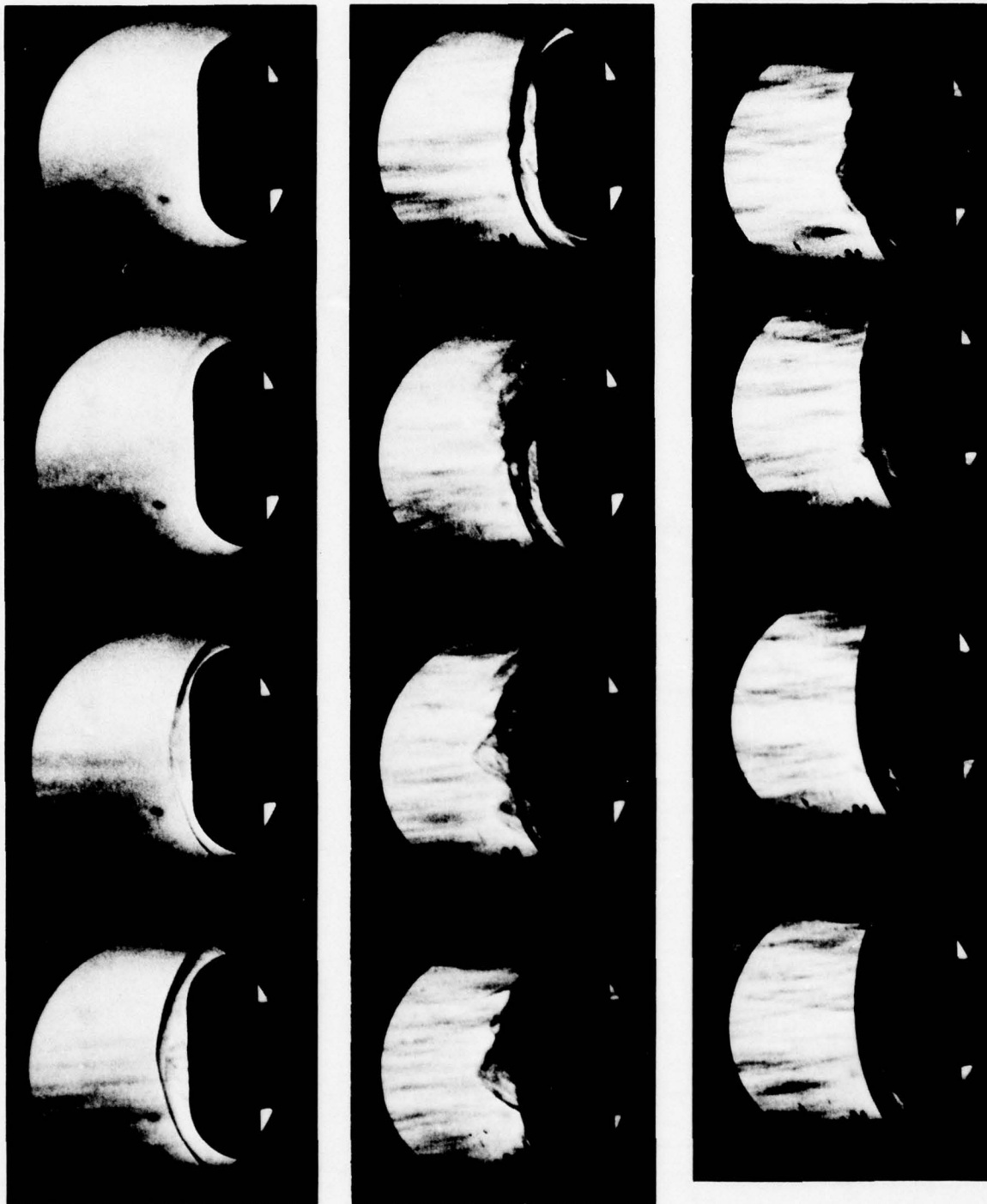


Figure 6-14 HEATING RATES RESULTING FROM MULTIPLE PARTICLE INTERACTIONS



**Figure 6-15 DUST INTERACTIONS IN THE SHOCK LAYER**

shock pulsations which occur when the heavier particles penetrate the bow shock. However, multiple shear layer nose tip interactions remain the major source of enhancement heating. The heat transfer distribution associated with the interactions shown in Figure 6-16. Again we observe that the maximum heating is fairly uniform across the nose tip at a level which exceeds the ambient by a factor of 4. Since the ambient heating level shown is for turbulent boundary layers induced by bonding 4 mil sand grain roughness to the face of the model, it is clear that large heating augmentation occurs in the presence of both turbulent boundary layers and roughness.

Finally it is of great interest to compare the geometric features of the interactions observed in the studies reported here with those taken with high speed photography in the ballistic range. Figure 6-17 shows a sequence of photographs taken of the shock interactions resulting from the impact of a water droplet on a flat nose tip. The debris from the impact is driven through the bow shock, and the particle shocks exhibit the same geometric features and pulsing characteristics that were observed on the present studies. Since heating measurements were not made in the ballistic range studies we cannot compare the augmentation heating; however, we would anticipate similar factors because of the similarity between the flow fields.

#### 6.4 CONCLUSIONS

The gross features of the single particle shock-bow shock interaction phenomena were not strongly influenced by the shoulder geometry for the blunt configurations studied. The four types of interactions identified in the previous studies using flat-ended cylindrical models were again observed, and the augmentation factors measured in the present series of experiments differed little from that obtained earlier. The aerodynamics of the multiple particle interactions are significantly different from those for a single particle, and the augmentation heating factors are measurably larger. The principal mode of oscillation observed for the multiple particle interactions was associated with the pulsations of the particle shocks. The geometric features of the



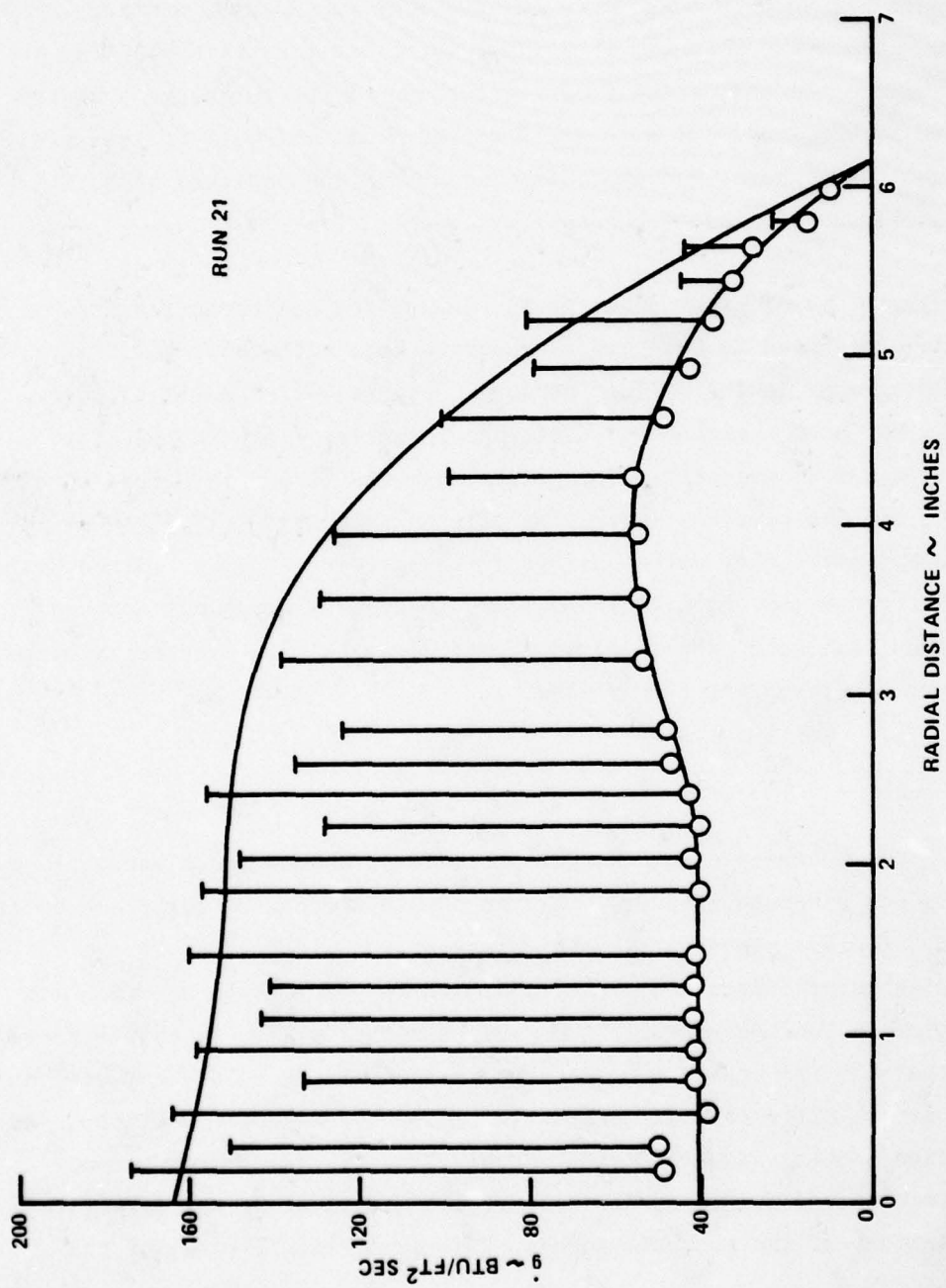


Figure 6-16 HEAT TRANSFER AUGMENTATION IN A DUST ENVIRONMENT



MODEL VELOCITY: 11,500 fps  
RANGE PRESSURE: 350 torr  
WATER DROP DIAMETER - 1.5 mm  
 $\Delta t = 5.5 \mu\text{sec}$

Figure 6-17 SEQUENTIAL LASER PHOTOGRAPHS OF DEBRIS FROM WATER DROP IMPACT  
(AEDC BALLISTIC RANGE)

interactions observed in this study were similar to those observed on the ballistic range where impacts with water droplets were studied. Our studies for conditions where the boundary layer over the model was turbulent and where the model surface was rough indicated that mechanism of particle-induced augmentation heating was not modified or the augmentation factor significantly reduced by these factors.



## Section 7

### CONCLUSIONS

In this research program, we investigated a number of aero-thermodynamic phenomena which influence the accuracy and survivability of slender reentry vehicles. The first phase of this study was an investigation of aerodynamic mechanisms which can perturb the stability of slender conical vehicles when transition moves, first onto the frustum, and then onto the nose tip. Simultaneous measurements of cone force and the distribution of heat transfer and pressure were made to determine the influence of angle of attack and bluntness ratio on the characteristics of the frustum transition region and the associated perturbations in cone forces. Measurements of the characteristics of the transition regions are presented, together with correlations with earlier range and wind tunnel measurements. These measurements demonstrate that transition moved first onto the leeside of sharp or slightly blunted cones inducing a destabilizing effect; while, on blunter bodies ( $0.1 < r/R_B < 0.2$ ) transition occurred first on the windward ray, resulting in a stabilizing effect. On both sharp and blunt configurations, the incremental forces and the corresponding movements of the center of pressure associated with such "wind-fixed" transition regions were small ( $\frac{\Delta x_{CP}}{L_{cone}} \approx 1\%$ ). The measurements with the NRV, RTE and 45°-blunt nose tips demonstrated that asymmetric regions of "body-fixed" transition can be induced and may produce forces of significant proportions.

The influence of nose shaping, induced by nose tip transition, on the pressure distribution over the conical frustum, and the contribution of the cone frustum to the aerodynamic stability of the total configuration was studied in detail. In this study of the "low altitude" stability problem, we employed the NRV and RTE nose tips, together with simple symmetric and asymmetric nose shapes in an experimental program where direct measurements were made of the nose tip and frustum forces, together with detailed pressure and heat transfer distributions. These studies demonstrated that the pressure

over the conical frustum is modified by an asymmetric nose shape such that the destabilizing effect of the nose tip forces is enhanced by the forces generated by the frustum. The asymmetric nose shaping which involves the sharpening of one side of the nose tip will generally be accomplished by the forward movement of the center-of-pressure (CP) on the frustum. Thus, to make accurate predictions of the "low altitude trim effect," the effect of nose shape (particularly if the tip is indented like the NRV configuration) on the frustum pressures must be determined accurately.

The program to explore the aero-thermodynamics of nose tip shaping has centered about (1) detailed measurements on a four-times scale model of the NRV nose tip for conditions which duplicated those encountered during re-entry, and (2) studies to determine the effects of surface roughness and entropy swallowing on transitional and turbulent flows over biconic configurations. The Measurements on the NRV nose tip indicated that flow separation and regions of shock wave-boundary layer interaction occurred in the complex three-dimensional flow over this configuration. The large heat transfer rates generated in the reattachment regions (up to three times the stagnation point heating rate) would clearly drive an ablating nose shape into a more highly indented configuration. Our measurements suggest that, in contrast with the assumption of axisymmetric flow made in all the shape-change codes, the flow, and hence, the ablation mechanism, was dominated by pairs of streamwise counter-rotating vortices nestled in the grooved surface of the NRV. It might be speculated that these grooves resulted from an intrinsically three-dimensional transition process in which the basic instability mode was helical, as discussed in Section 2. The measurements of roughness heating augmentation made in the nose-tip studies of transition, entropy swallowing and roughness were found to agree well with earlier data on spheres and flat plates when correlated in terms of the roughness parameter  $K/\theta$  but were poorly correlated when plotted versus the roughness Reynolds number  $Re_K$ , the essential parameters used in the PANT correlation. Further studies are required to better define the key roughness parameters and the role of the roughness characteristics and spacing on heating augmentation.

The studies of multiple particle-shock interaction heating demonstrated that the mechanism of heating augmentation was not strongly affected by the shoulder geometry of the blunt nose tip or its surface roughness. However, the aerodynamics of multiple particle interaction are significantly different from those for a single particle interaction, and the augmentation factors are significantly larger. Particle enhanced heating factors of up to five times the undisturbed values were recorded in these studies. The geometric features of the interactions observed in this investigation were similar to those observed in ballistic range studies of water droplet-bow shock interaction.



Section 8  
REFERENCES

1. Reynolds, O., An Experimental Investigation of the Circumstances Which Determine Whether the Motion of Water Shall be Direct or Sinuous and of the Law of Resistance in Parallel Channels, Trans. Roy. Soc. (London) A174, 1883 pp. 935-982 Sci. Papers 2:51.
2. Schubauer, G.B., and Skramstad, H.K., Laminar-Boundary-Layer Oscillations and Transition on a Flat Plate, NACA 909 1948.
3. Pate, S.R. and Schueler, C.J., An Investigation of Radiated Aerodynamic Noise Effects on Boundary-Layer Transition in Supersonic and Hypersonic Wind Tunnels, AIAA Paper No. 68-375, April 1968.
4. Stainbeck, P.C., Fischer, M.C. and Wagner, R.D., Effects of Wind-Tunnel Disturbances on Hypersonic Boundary Layer Transition, AIAA 10th Aerospace Sciences Meeting, San Diego, California, 17-19 January 1972.
5. Reda, D.C., Boundary-Layer Transition Experiments on Sharp, Slender Cones in Supersonic Freeflight, AIAA Paper 78-1129, July 1978.
6. Potter, J.L., Boundary-Layer Transition on Supersonic Cones in an Aeroballistic Range, AIAA Journal, Vol. 13, No. 3, March 1975, pp. 270-277.
7. Sheetz, N.W., Jr., Free-Flight Boundary Layer Transition Investigations at Hypersonic Speeds, AIAA Paper No. 65-127, 2nd Aerospace Sciences Meeting, New York, N.Y., Jan. 1965.
8. Krogmann, P., An Experimental Study of Boundary-Layer Transition on a Slender Cone at Mach 5, AGARD Symposium on Laminar-Turbulent Transition, Technical University of Denmark, Copenhagen, Denmark, 2-4 May 1977.
9. Stetson, K.F. and Rushton, G.H., Shock Tunnel Investigation of Boundary-Layer Transition at  $M = 5.5$ , AIAA Journal, Vol. 5, No. 5, May 1967, pp. 899-906.
10. Morkovin, M.V., Instability, Transition to Turbulence and Predictability, Keynote Address to AGARD Symposium on Laminar-Turbulent Transition, Technical University of Denmark, Copenhagen, Denmark, 2-4 May 1977.
11. Reshotko, E., Boundary-Layer Stability and Transition, Annual Review of Fluid Mechanics, Vol. 8, 1976, pp. 311-349.
12. Morrisette, E.L., Stone, D.R., and Cary, A.M., Downstream Effects of Boundary Layer Trips in Hypersonic Flow, Langley Symposium on Compressible Turbulent Boundary Layers, NASA SP 216, December 1968.

13. Holden, M.S., Shock Wave-Turbulent Boundary Layer Interaction in Hypersonic Flow, AIAA 10th Aerospace Sciences Meeting, San Diego, California, 17-19 January 1972.
14. Bradshaw, P., A Note on Reverse Transition, JFM (1969), Vol. 35, Part 2, pp. 387-390.
15. Demetriades, A. and Laderman, A.J., Measurements of the Mean and Turbulent Flow in a Cooled Wall Boundary Layer at Mach 9.37, AIAA Paper 72-73, January 1972.
16. Wallace, J.E., Hypersonic Turbulent Boundary Layer Studies at Cold Wall Conditions, Proceedings of the 1967 Heat Transfer and Fluid Mechanics Institute, 1967.
17. Finson, M., Frustum Transition Modeling, Proceedings of the ABRES Accuracy Review, 8, 9 November 1977.
18. English, E.A., Nosetip Recovery Vehicle Postflight Development Report, SAND75-8059, Sandia Laboratories, Livermore, January 1976.
19. Kryvoruka, J.K., Roll Torque Evaluation (RTE) Vehicle Postflight Test Report, SAND76-8001, Sandia Laboratories.
20. Cheng, H.K., et. al., Boundary Layer Displacement and Leading-Edge Bluntness Effects in High-Temperature Hypersonic Flow, Journal of Aerospace Science, Vol. 28, No. 5, 1961, pp. 353-381.
21. Eckert, E.R.G., Engineering Relations for Friction and Heat Transfer to Surfaces in High Velocity Flow, J. Aeronautical Sciences, 1956, 23 (8), pp. 585-587.
22. Van Driest, E.R., Turbulent Boundary Layer in Compressible Fluids, J. Aero. Sci., 1951, 18, N. 3., pp. 145-160.
23. Van Driest, E.R., Problem of Aerodynamic Heating, Aeronautical Engineering Review, Vol. 15, No. 10, October 1956.
24. Powars, C.A., Passive Nose Tip Technology Program, Interim Report Vol. III Surface Roughness Effects, Part II - Roughness Augmented Heating Data Analysis and Correlation Aerotherm Report 74-96, January 1973.
25. Grabow, R.M., White, C.O., Surface Roughness Effects on Nosetip Ablation Characteristics, AIAA Paper 74-513.
26. Brandon, M.J., and Masek, R.V., Aerodynamic Heating Corrugation Stiffened Structures in Thick Turbulent Boundary Layers, AIAA J., Vol. 13, No. 11, pp. 1460-1465.

27. Dvorak, F.A., Calculation of Turbulent Boundary Layers on Rough Surfaces in Pressure Gradient, AIAA J., Vol. 7, No. 9, pp. 1752-1759, September 1969.
28. Wilkinson, R., Minuteman Hot-Structure Heating Augmentation Study, Vol. 1 Mechanisms and Analyses, SAMSO Technical Report No. 73-273, August 1973.
29. Holden, M.S., Gustafson, G.Q., Duryea, G.R., and Hudack, L.T., An Experimental Study of Particle-Induced Convective Heating Augmentation, AIAA Paper No. 76-320, AIAA 9th Fluid and Plasma Dynamics Conference, San Diego, California, July 14-16, 1976.
30. Holden, M.S., Experimental Studies of Separated Flows at Hypersonic Speeds--Part I: Separated Flows over Axisymmetric Spiked Bodies, AIAA Journal, Vol. 4, No. 4, April 1966.
31. Edney, B.E., Anomalous Heat Transfer and Pressure Distributions on Blunt Bodies in the Presence of an Impinging Shock, The Aeronautical Research Institute of Sweden, Report FFA-115, February 1968.
32. Keyes, J.W. and Hains, F.D., Analytical and Experimental Studies of Shock Interference Heating in Hypersonic Flows, NASA TN D-7139, May 1973.
33. Holden, M.S., Studies of Transitional Flow Unsteady Separation Phenomena and Particle-Induced Augmentation Heating on Ablated Nose Tips, AFOSR TR-76-1066.



APPENDIX A  
EXPERIMENTAL FACILITIES AND MEASUREMENT TECHNIQUES

EXPERIMENTAL FACILITIES

The experimental program was conducted in Calspan's 48-inch and 96-inch Hypersonic Shock tunnels (Ref. A-1). The operation of these tunnels can be shown simply with the aid of the wave diagram shown in Figure A-1. The tunnel is started by rupturing a double diaphragm which permits the high pressure air in the driver section to expand into the driven section, and in so doing generates a normal shock which propagates through the low pressure air. A region of high temperature, high pressure air is produced between this normal shock front and the gas interface between the driver and driven gas, often referred to as the contact surface. When the primary or incident shock strikes the end of the driven section, it is reflected leaving a region of almost stationary high pressure heated air. This air is then expanded through a nozzle to the desired free stream conditions in the test section.

The duration of the flow in the test section is controlled by the interactions between the reflected shock, the interface, and the leading expansion wave generated by the non-stationary expansion process occurring in the driver section. At Calspan we normally control the initial conditions of the gases in the driver and driven sections so that the gas interface becomes transparent to the reflected shock, as shown in Figure A-1; thus, there are no waves generated by interface-reflected shock interaction. This is known as operating under "Tailored-Interface" conditions. Under this condition, the test time is controlled by the time taken for the driver-driven interface to reach the throat, or the leading expansion wave to deplete the reservoir of pressure behind the reflected shock; the flow duration is said to be either driver gas limited or expansion limited, respectively. Figure A-2 shows the flow duration in the test section as a function of the Mach number of the incident shock. Here it can be seen that for operation at low  $M_1$ , running times of over 25 milliseconds can be obtained with a long driver section. When run under these latter conditions at high pressures and Reynolds numbers,

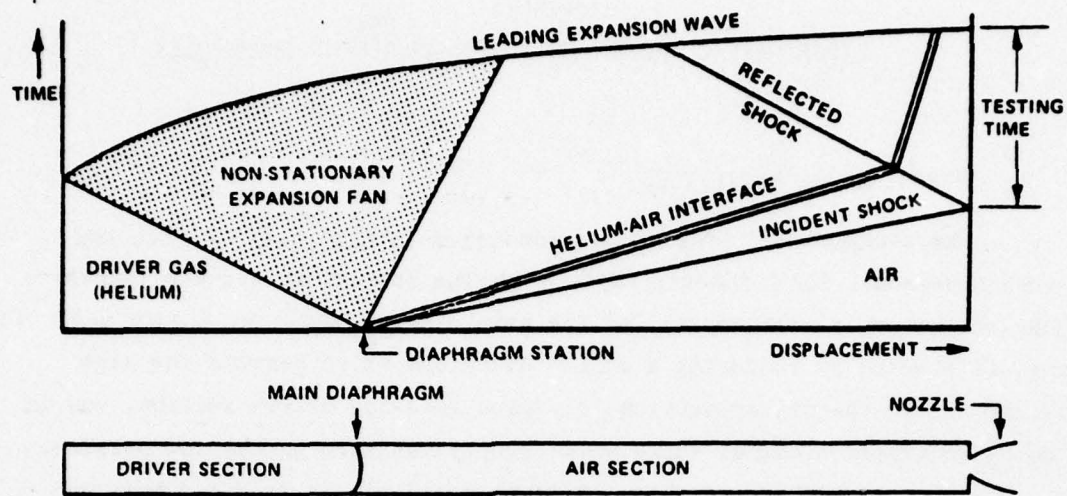


Figure A-1 WAVE DIAGRAM FOR TAILORED-INTERFACE SHOCK TUNNEL

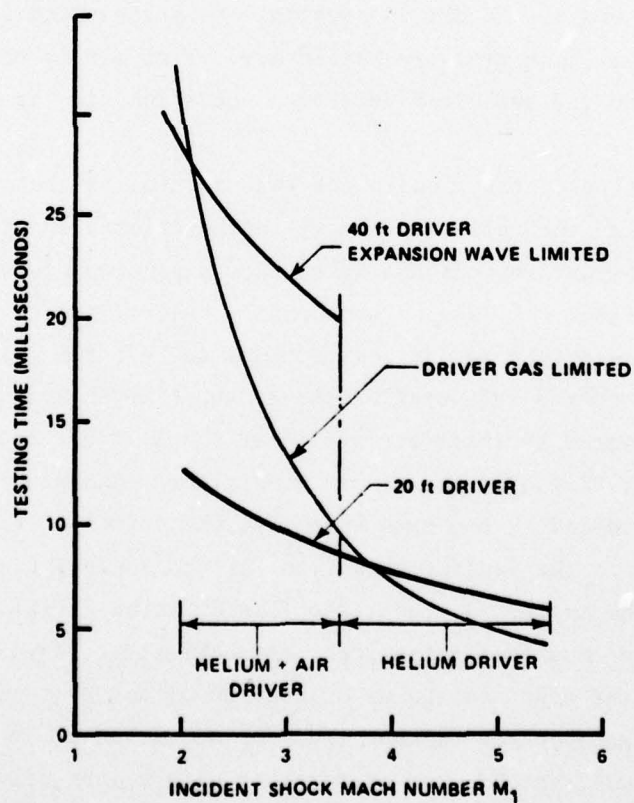


Figure A-2 TEST TIME AVAILABLE FOR TAILORED-INTERFACE OPERATION OF 48-INCH SHOCK TUNNEL

the test running times are of the same magnitude or longer than for piston driven tunnels (Ref. A-2, A-3) with comparable stagnation temperature, and the reservoir conditions and flow quality are superior to piston driven tunnels. This is due to the fact that the test gas has been processed by a simple reflected shock rather than multiple shocks as in piston tunnels. A further consequence is that the free stream conditions can be calculated with far more accuracy in a shock tunnel.

It is interesting to note that if sensitive high frequency instrumentation is to be used in the very severe heating conditions encountered in turbulent interaction regions in hypersonic flow, running times longer than 20 milliseconds present distinct problems because the sensing element can be damaged or destroyed by overheating since it must be placed close to the flow environment.

By running the shock tunnels at low incident shock Mach numbers and high driver pressures, we can generate test conditions in which we can obtain very large Reynolds numbers. The large test core allows us to use models which are at least 3 feet in length. The maximum Reynolds number capabilities of the tunnels are shown in Figure A-3. Under these maximum Reynolds number conditions, the location of the end of natural transition on flat plate models as determined from heat transfer and other measurements, is shown in Figure A-4.

#### MODEL AND FLOW FIELD INSTRUMENTATION

To make a meaningful study of regions of transitional boundary layers over nose-tip and frustum configurations, measurements of both the mean and the fluctuating flow field should be obtained. Our recent studies indicated that to obtain the complete power spectrum for the surface pressure, a frequency response from 200 Hz to 100 kHz was required. The measurements of skin friction and heat transfer in the separation and reattachment regions indicated that a frequency of at least 10 kHz was required to follow the



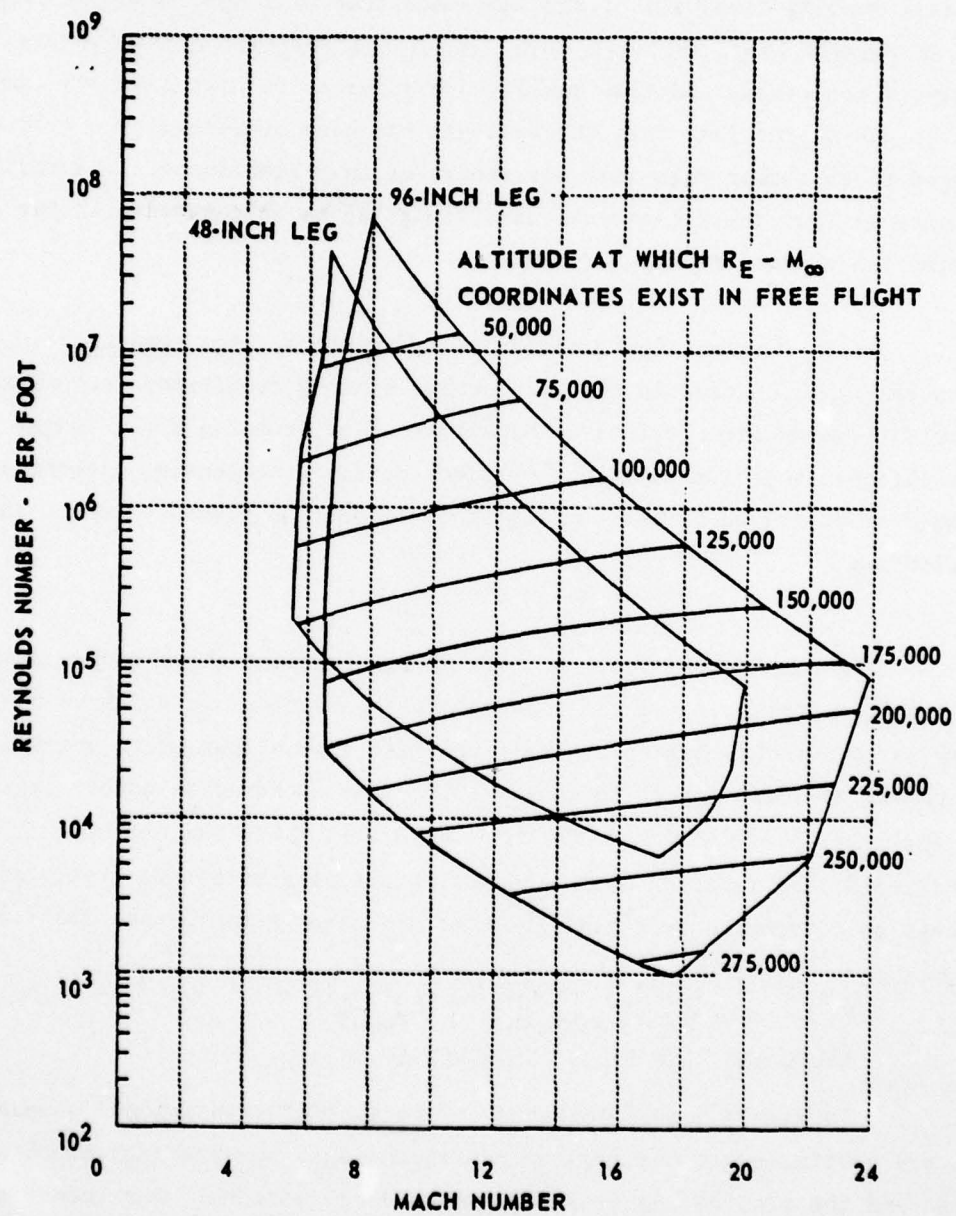


Figure A-3 CALSPAN HYPERSONIC SHOCK TUNNEL PERFORMANCE

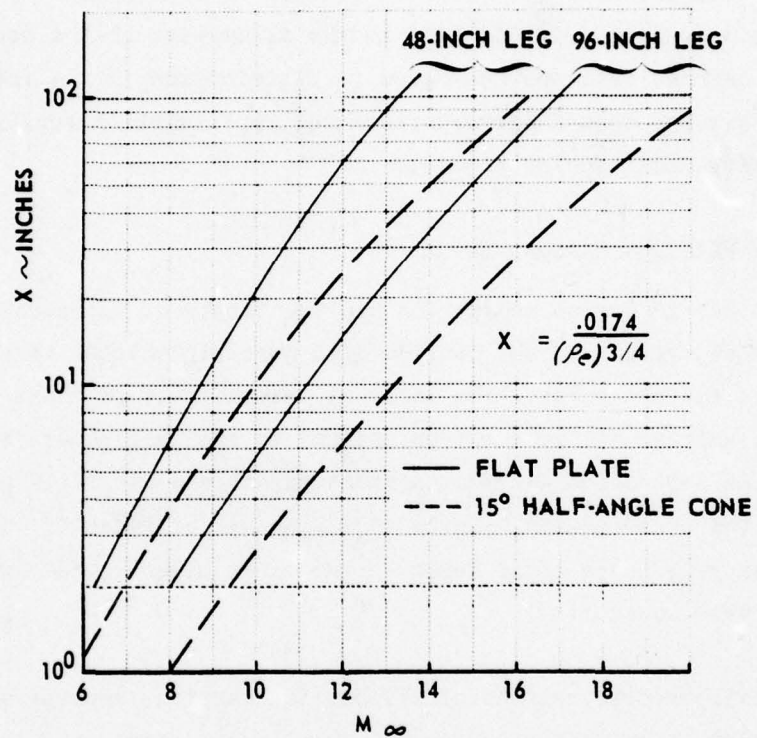


Figure A-4 MINIMUM TRANSITION DISTANCE ON SHARP FLAT PLATE MODELS FOR CALSPAN HYPERSONIC SHOCK TUNNELS

motion of the separation and reattachment points. It is also desirable to make fluctuation measurements through the flow field to help establish the source and mechanism which generated the high level of pressure fluctuation observed in earlier studies. Fluctuation measurements both on the wall and in the flow field are also available as a check on the validity of earlier theoretical models which, in addition to the assumption that a mean flow model can be used to describe the velocity distribution in the interaction region, also assumes that a large part of the recirculation region can be described by a laminar sublayer model.

#### SKIN FRICTION MEASUREMENTS

In order to define separation and the length of separated regions accurately in separated regions over ablated nose tip shapes, it is important to measure the surface shear. The inherent unsteadiness of these regions also makes it desirable to follow the fluctuations in the wall shear to trace the movement of the separation and reattachment points and hopefully gain some insight into the fluid mechanics of such motions. Our recent studies indicate that a frequency response of at least 10 kHz is required to follow these movements in hypersonic flow.

In axisymmetric regions of viscous interaction, separation is defined as the condition at which the surface is zero at one point only in the interaction region. Because direct measurements of surface shear are difficult to make, pressure distribution, surface pitot, and oil flow measurements have been used to determine separation. Pressure distribution measurements have been shown by Green (Ref. A-4) and by Spaid and Frishett (Ref. A-5) to be an extremely poor indicator of boundary layer separation in supersonic flow. Holden (Ref. A-6) found this technique was even more insensitive at hypersonic speeds. From our studies we have noted that the introduction of a small disturbance into the laminar sublayer beneath the sonic line can cause dramatic effects both in the immediate vicinity and downstream of the disturbance.



AD-A065 173

CALSPAN ADVANCED TECHNOLOGY CENTER BUFFALO NY  
STUDIES OF THE EFFECTS OF TRANSITIONAL AND TURBULENT BOUNDARY L--ETC(U)  
DEC 78 M S HOLDEN F44620-76-C-0037

UNCLASSIFIED

CALSPAN-AB-5834-A-2

AFOSR-TR-79-0125

NL

4 OF 4  
ADA  
065173



END  
DATE  
FILMED

4 - 79  
DDC

On our studies of the separation of turbulent boundary layers in hypersonic flow, we have used a gage (Ref. A-7) which directly measures surface shear to indicate the separation condition. A diagram of the skin friction transducer which we would use in the proposed studies is shown in Figure A-5. The transducer consists of a diaphragm which is supported flush with the model surface by two piezo-ceramic beams, which develop a charge when placed in bending by a surface shear on the diaphragm. A third beam is used to provide acceleration compensation; the beams are connected electrically to eliminate thermal, normal, and transverse pressure effects. An FET impedance transform circuit is mounted internally to eliminate cable noise effects at low levels of skin friction. The gage, which has been refined and developed over the past 12 years, has been used to measure very low levels of skin friction encountered in separated regions in low Reynolds number hypersonic flow and more recently very high levels in regions of shock wave-turbulent boundary layer interactions in hypersonic flow. Because of the very severe heating conditions encountered in the latter studies, special care was taken to minimize the heat conduction through the flexures. The very large dynamic loads generated on the transducers during tunnel shutdown when run at the high dynamic pressure conditions used in our studies caused the diaphragms to be torn from the supporting beam. This problem was overcome by careful design of the flexure and by mounting the transducer in the seismic mass-rubber suspension system shown in Figure A-5.

#### HEAT TRANSFER INSTRUMENTATION

A knowledge of the heat transfer distribution on nose tips is of great importance because of the very severe heating rates generated in the reattachment region. Almost as important as the severity of reattachment, heating is the extremely large heat transfer gradients which occur both in the separation and reattachment regions. Regions of high heat transfer gradient present a problem to the experimenter because they can cause transverse heat conduction problems in the model. This can distort heat transfer distributions and in some cases dramatically reduce the maximum indicated heating. An example which illustrates this feature is given in the report

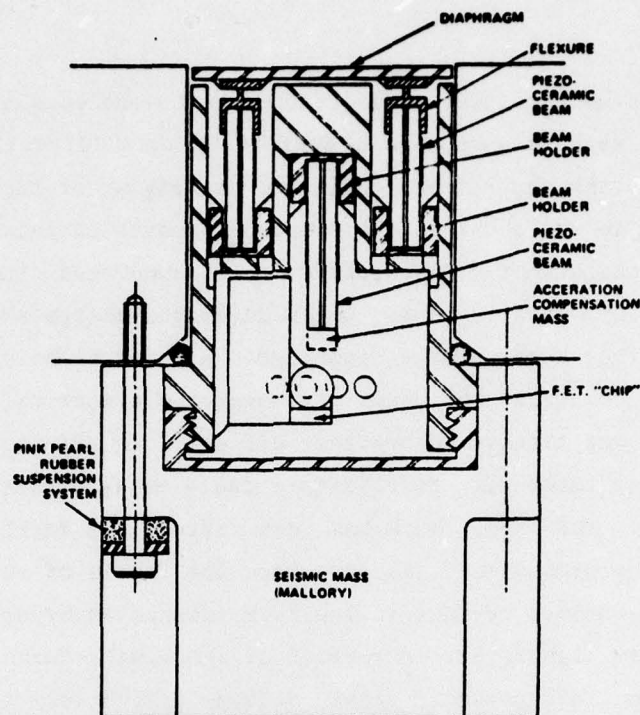
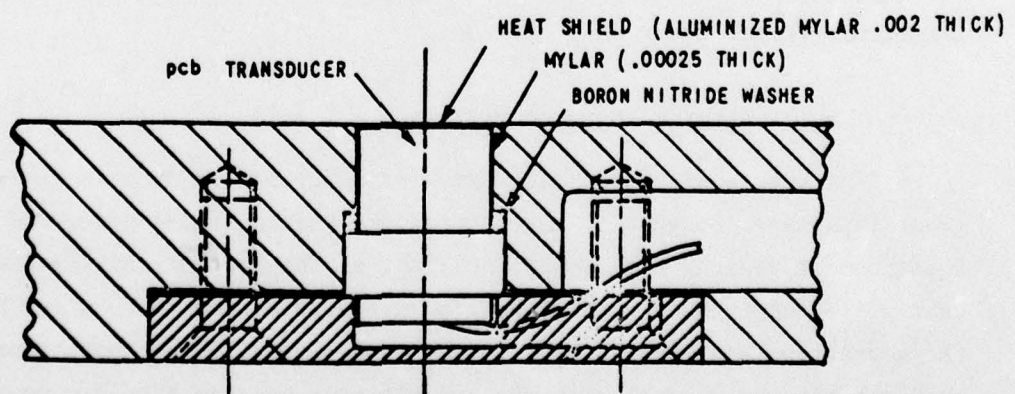


Figure A-5 DRAWING OF SECTION THROUGH SKIN FRICTION TRANSDUCER



(a) TYPICAL MOUNTING TECHNIQUE USED IN MODEL

Figure A-6 HIGH-FREQUENCY PRESSURE MOUNTING



of Hiers and Loubsky (Ref. A-8) where they used a thin skin technique to obtain heat transfer measurements in regions of turbulent viscous layer attachment. They found that the corrections to their measurements were of the same magnitude as the measurements themselves. To reduce transverse heat conduction along the model surface, the model should be made from a non-conducting material; this is incompatible with the thin skin technique unless a segmented model is used. To overcome these problems we use a measurement of heat transfer which relies on sensing the transient surface temperature of a non-conducting model by means of thin-film resistance thermometers. Because the thermal capacity of the gage is negligible, the instantaneous surface temperature of the backing material is related to the heat transfer rate by the classical semi-infinite slab theory. Analog networks are used to convert the outputs of the gages, which are proportional to surface temperature, to a voltage directly proportional to heat transfer. The thin film gage has a frequency response to 1 MHz.

The gages are fabricated on either small pyrex buttons or on contoured insert, the ability of this technique to make closely spaced measurements in regions of shock impingement is demonstrated in Figure A-7.

#### SURFACE AND FLOW FIELD PRESSURE MEASUREMENTS

We employed two types of surface pressure transducers in our shock tunnel studies. The Calspan-designed and constructed lead zirconium titanate piezoelectric pressure transducers (Ref. A-9) were used to obtain essentially the mean pressure distribution through the interaction region, though the transducer and orifice combination could follow fluctuations up to 15 kHz. A second flush-mounted transducer, especially designed for high frequency measurements by PCB in Buffalo, was used to obtain surface pressure fluctuation measurements from 200 Hz to 120 kHz. To prevent a resonance, a special mounting system was developed (as shown in Figure A-6) to lock the gage firmly into the model. A thin insulating barrier of aluminized mylar was attached to the diaphragm of the transducer to prevent thermal heating effect caused by the large heat transfer rates (over 500 Btu/ft<sup>2</sup> sec) generated in the re-attachment regions.

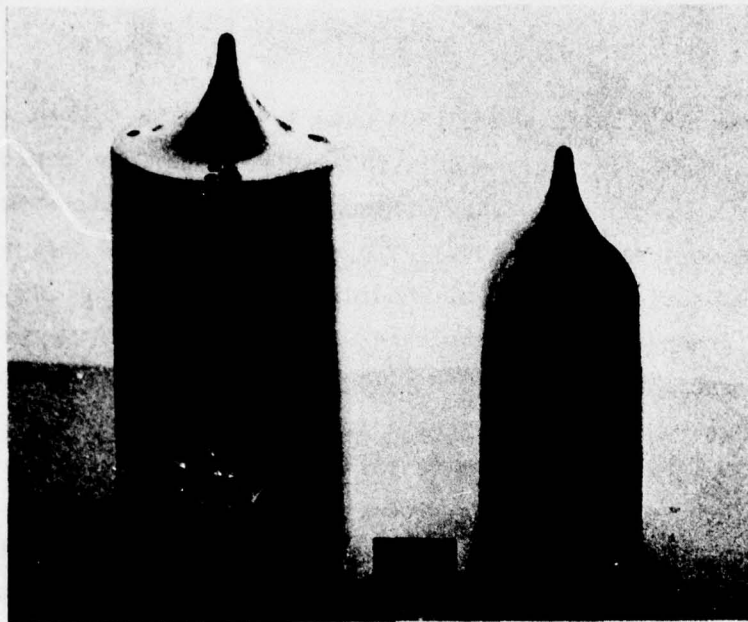


**Figure A-7 MODELS SHOWING TYPICAL HEAT TRANSFER GAGE INSTALLATION**

## TOTAL TEMPERATURE AND HOT WIRE ANEMOMETER MEASUREMENTS

Total temperature measurements have been made with a shielded fine-wire probe. This probe which is shown in Figure A-8 is basically a resistance thermometer mounted in a vented cavity so that it senses the total temperature of a low-speed flow behind the normal shock. A 0.0001 inch diameter wire with a sensing length of 0.060 is supported between two steel needles and insulated from the housing which is 0.060 in height. The response time of the probe is approximately 2 milliseconds. The recovery factor of the probe varies between 0.94 and 0.995, depending upon the local Reynolds number of the flow; however, for most of the high Reynolds number conditions encountered in our studies the recovery factor is very close to unity.

The hot wire probe is constructed on the same basic support system as the total temperature probe, however a 0.00025-inch diameter wire 0.040 inches in length is used to obtain a more rugged probe. The probe, which is shown in Figure A-9, is used in a standard bridge circuit and run in constant temperature mode. The system has a bandwidth of between 50 and 65 kHz.

## DATA RECORDING AND PROCESSING

The outputs from the transducers are recorded on a NAVCOR (Ref. A-1) magnetic drum system and on CEC and AMPEX FM tape recorders, and monitored on oscilloscopes. The NAVCOR system, which can hold 48 channels of data in digital form, is essentially a low frequency response system which will record the mean output of the gages over the running time. The fluctuation measurements will be recorded on the FM tape recorders in analog form and subsequently converted into digital form by the analog-to-digital conversion/data storage system developed at Calspan.

The fluctuation data, in punched card form, are then processed by an existing digital computer program to obtain the statistical properties -- Root Mean Square Pressure, Power- and Cross-Spectra, and Auto- and Cross-Correlation functions.





**Figure A-8 TOTAL TEMPERATURE PROBE**



**Figure A-9 HOT WIRE PROBE**

## REFERENCES

- A-1 "Calspan Hypersonic Shock Tunnel, Description and Capabilities Brochure", March 1973.
- A-2 Needham, D.A., Elfstrom, G.M. and Stollery, J.L. "Design and Operation of the Imperial College Number 2 Hypersonic Gun Tunnel" I.C. Aero Report No. 70-04, May 1970.
- A-3 Enkenhus, K.R. and Parazzoli, C. "The Longshot Free-Piston Cycle-- Part I: Theory" vonKarman Inst. for Fluid Dynamics, Technical Note 51, November 1968.
- A-4 Green, J.E. "Interactions Between Shock Waves and Turbulent Boundary Layers" vonKarman Inst. for Fluid Dynamics (Lecture), Report Lecture Series 10, Part 2, January 1969.
- A-5 Spaid, F.W. and Frishnett, J.C. "Incipient Separation of a Supersonic Turbulent Boundary Layer Including the Effects of Heat Transfer" AIAA Paper, November 1971.
- A-6 Holden, M.S. "Shock Wave-Turbulent Boundary Layer Interaction in Hypersonic Flow" AIAA Preprint No. 72-74.
- A-7 MacArthur, R.C. "Contoured Skin Friction Transducer" Calspan Report No. AN-2403-Y-1, August 1967.
- A-8 Hiers, R.S. and Loubsky, W.J. "Effects of Shock-Wave Impringement on the Heat Transfer on a Cylindrical Leading Edge" NASA TN D-3859, February 1967.
- A-9 Martin, J.F., Duiyea, G.R. and Stevenson, L.M. "Instrumentation for Force and Pressure Measurements in a Hypersonic Shock Tunnel, Advances in Hypervelocity Techniques" Calspan Report No. 113 (Plenum Press, 1962).